Reconstruction of the eruptive history of central Ecuador volcanoes : constraints on the spatio-temporal evolution of the Andean volcanism

Santiago Santamaría Freire

▶ **To cite this version:**

Santiago Santamaría Freire. Reconstruction of the eruptive history of central Ecuador volcanoes : constraints on the spatio-temporal evolution of the Andean volcanism. Volcanology. Université Paris-Saclay, 2021. English. NNT : 2021UPASJ024 . tel-03893419

HAL Id: tel-03893419

https://theses.hal.science/tel-03893419

Submitted on 11 Dec 2022

HAL is a multi-disciplinary open access archive for the deposit and dissemination of scientific research documents, whether they are published or not. The documents may come from teaching and research institutions in France or abroad, or from public or private research centers.

L'archive ouverte pluridisciplinaire **HAL**, est destinée au dépôt et à la diffusion de documents scientifiques de niveau recherche, publiés ou non, émanant des établissements d'enseignement et de recherche français ou étrangers, des laboratoires publics ou privés.

THÈSE DE DOCTORAT

NNT : 2021UPASJ024

université PARIS-SACLAY

Reconstruction of the eruptive history of central Ecuador volcanoes: constraints on the spatio-temporal evolution of the Andean volcanism

Reconstruction de l'histoire éruptive des volcans du centre de l'arc équatorien : contraintes pour l'évolution spatio-temporelle du volcanisme andin

Thèse de doctorat de l'université Paris-Saclay

École doctorale n°579 : sciences mécaniques et énergétiques, matériaux et géosciences (SMEMaG)
Spécialité de doctorat : Structure et évolution de la terre et des autres planètes
Graduate School : Géosciences, climat, environnement et planètes.
Référent : Faculté des sciences d'Orsay

Thèse préparée dans l'unité de recherche **GEOPS (Université Paris-Saclay, CNRS)**, sous la direction de **Xavier QUIDELLEUR**, Professeur.

Thèse soutenue à Paris-Saclay, le 10 décembre 2021, par

Santiago David SANTAMARÍA FREIRE

Composition du Jury

Hervé GUILLOU Directeur de Recherche, CEA-LSCE	Président
Benjamin VAN WYK DE VRIES Professor, Univ. Clermont Auvergne	Rapporteur & Examinateur
Pablo GROSSE Chargé de Recherche, CONICET	Rapporteur & Examinateur
Laurence AUDIN Directrice de Recherche, IRD-ISTerre	Examinatrice
Silvana HIDALGO Professeure, Escuela Politécnica Nacional	Examinatrice
Xavier QUIDELLEUR Professeur, Université Paris-Saclay	Directeur de thèse

A quienes dieron todo por mi presente y mi futuro,

Mariela, Carmen, Edwin, y Javier

¡Lo hicimos de nuevo!

Acknowledgments

I thank Xavier Quidelleur, my thesis director, for his constant supervision and support in the completion of this work. But more than anything else, for being a constant guide and mentor, for not letting me give up in the hardest moments of my stay in France, for teaching me that it is more important to be an excellent person than to be an empty person full of knowledge. Thank you for these three years of adventure! I never imagined that a three-month internship in France would culminate in a PhD project and the realization of a personal goal with a great scientific team.

Thanks to Pablo Samaniego, for his constant support, encouragement and dedication to improve this research. His valuable remarks created new challenges at each stage of the research development. It was greatly appreciated to receive your comments because of the academic challenge they represented. I learned from you to never be completely satisfied, because there are always new questions to be answered. I also thank you for agreeing to participate in the jury of my thesis as Invited Researcher.

I wish to thank Jean-Luc Le Pennec and Silvana Hidalgo for their significant contributions to the realization of this project. You were a fundamental support in discussing the ideas presented, proposing new approaches, and pointing out that there will always be new things to learn. I firmly believe that with you, we completed the best scientific team for the realization of this research. Thank you for your constant encouragement and supervision of this thesis.

Thanks to Laurence Audin, Hervé Guillou, Pablo Grosse, Benjamin van Wyk de Vries and Giuseppe Siani for their valuable contributions to the improvement of this study. Thank you for agreeing to be part of the different committees and juries that evaluated my thesis.

I am especially grateful to my parents and my siblings, who never let me falter and who were my spiritual guide during these three years away from home. I will never cease to be grateful to God for having given me the wisdom of my family.

Thanks to Mathilde Bablon, Pierre Lahitte, Stéphane Dibacto, Anthony Hildenbrand, Céline Liorzou, Patricia Mothes, Patricio Ramon, Pedro Espín, Marco Córdova, Stefanie Almeida, Marjorie Encalada and all those who accompanied me in the completion of this work. Your knowledge, teachings, feedback, advice and support were fundamental during the completion of this PhD thesis. I always counted on you to give me the encouragement I needed when things seemed to get complicated. It was always you to whom I shared the small successes I was achieving every day.

This work is part of an Ecuadorian-French cooperation program carried out between the *Instituto Geofísico, Escuela Politécnica Nacional* (IGEPN), Quito, Ecuador, and the French *Institut de Recherche pour le Développement* (IRD), thought the *Laboratoire Mixte International "Séismes et Volcans dans les Andes du Nord"* (LMI-SVAN) program. This work was supported by the CNRS/INSU TelluS and the LMI-SVAN programs. My PhD grant was funded by the *Secretaria Nacional de Educación Superior, Ciencia, Tecnología e Innovación* (SENESCYT), Ecuador.

Reconstruction of the eruptive history of central Ecuador volcanoes: constraints on the spatio-temporal evolution of the Andean volcanism

Santiago David SANTAMARIA FREIRE

General index

Résumé en français 1

1. Contexte géochronologique de l'arc volcanique équatorien 3
2. L'Iliniza, un volcan étonnamment jeune 4
3. Evolution chronologique de l'arc volcanique équatorien 6
   - 3.1. Stade initial (*early stage*): ~2.5 à ~1.4 Ma 6
   - 3.2. Stade intermédiaire (*intermediary stage*): ~1.4 à ~0.6 Ma 7
   - 3.3. Stade final (*late stage*) : à partir de ~0.6 Ma 8
4. Perspectives sur la relation entre le volcanisme et la tectonique 9

General introduction 13

Chapter 1

Ecuadorian volcanic arc: geologic and tectonic setting 18

- 1.1 Segmentation of the Andean margin 19
- 1.2 Ecuadorian geodynamic setting 25
  - 1.2.1 Guiana Shield Realm (Guiana Shield and Oriente Foreland Basin) 28
  - 1.2.2 Central Tectonic Realm (Para-autochthonous Terrains and Cretaceous Volcanic Arc Fragments) 29
  - 1.2.3 Western Tectonic Realm (Western Cordillera and Coastal Forearc) 33
  - 1.2.4 Nazca Plate Domain 39
  - 1.2.5 Geodynamics of The North Andean Sliver 44
- 1.3 Ecuadorian volcanic arc 46
  - 1.3.1 Previous stages: the Neogene volcanism 46
  - 1.3.2 Distribution of volcanic edifices 50
  - 1.3.3 Geochronology of the volcanic arc 54
  - 1.3.4 Geochemical characterization and petrogenetic models 56

Chapter 2

Methodology 64

2.1 Sampling strategy and fieldtrips 65

2.2 Potassium–argon radiometric dating 67

2.2.1 Dating principles 67

2.2.2 Sample preparation protocol 69

2.2.3 The K-Ar method 71

2.2.4 The $^{40}Ar/^{39}Ar$ method 76

2.2.5 Dating method limits 80

2.3 Volcanic Surface Modeling 82

2.3.1 Principles 82

2.3.2 Extraction of the representative points of the paleotopography 84

2.3.3 Modeling of paleotopography 86

2.3.4 Calculation of volumes, and construction and erosion rates 89

Chapter 3

Geochronological evolution of the potentially active Iliniza Volcano 92

ABSTRACT 96

1. INTRODUCTION 97

2. GEOLOGICAL CONTEXT 99

3. METHODS 100

3.1. Sampling strategy 100

3.2. K-Ar dating 102

3.3. Geochemical analyses 103

3.4. Geomorphological reconstructions 105

4. RESULTS 106

4.1. Morphology 106

4.2. Eruptive Chronology 108

4.3. Reconstructed morphology for volume estimations 120

4.4. Geochemical characterization 123

5. DISCUSSION 127

5.1. Iliniza and Santa Cruz geochronological evolution 127

5.2. The Jatuncama explosive phase 130

5.3. Growth and erosion patterns in Iliniza Volcano 132

5.4. Overall geochemical nature 134

5.5. Exploring the implications for the hazard assessment 136

6. CONCLUSIONS 137
Acknowledgments 138
REFERENCES 139
Appendix A. 150
Appendix B 157
Appendix C 161
Appendix D 162

Chapter 4

Timing of Pleistocene volcanism and its relationship with geodynamics in the central segment of the Ecuadorian Andes 166
ABSTRACT 170
1. INTRODUCTION 171
2. GEOLOGICAL CONTEXT 173
2.1. Ecuadorian geological setting 173
2.2. Volcanism from the central segment 174
3. METHODS 177
3.1. Sampling strategy 177
3.2. K-Ar dating 179
3.3. Whole-rock geochemical analyses 180
3.4. Numerical reconstructions of paleotopographies for volume calculations 181
4. RESULTS 182
4.1. K-Ar dating 182
4.2. Construction and erosion volumes of the central segment volcanoes 185
4.3. Geochemical characterization 187
5. DISCUSSION 190
5.1. Comparison with previous geochronological data 190
5.2. Eruptive history of the central segment 191
5.3. Temporal and spatial arrangement of the central segment volcanoes 198
6. CONCLUSIONS 202
REFERENCES 203
Appendix A. 213
Appendix B 218
Appendix C 222

Chapter 5

Evolution of the Pleistocene volcanism in the Ecuadorian Andes 224

ABSTRACT 228

1. INTRODUCTION 229

2. GEOLOGICAL CONTEXT 230

2.1. Ecuadorian geological setting 230

2.2. Overview of the Ecuadorian volcanic arc 232

2.3. Volcanism from the Quito segment 235

3. METHODS 239

3.1. Sampling strategy 239

3.2. K-Ar dating 240

3.3. Whole-rock geochemical analyses 241

4. RESULTS 242

4.1. K-Ar dating 242

4.2. Geochemical characterization 244

5. DISCUSSION 246

5.1. Comparison with previous geochronological data on the Quito segment 246

5.2. Geochronological data compilation of the Ecuadorian volcanic arc 247

5.3. Pleistocene eruptive history 252

5.4. Geochemical characterization 260

5.5. Relationship between volcanism and tectonics 263

5.6. Relationship between volcanism and the Nazca slab 267

6. CONCLUSIONS 269

REFERENCES 271

Appendix A. 284

Appendix B 287

Appendix C 290

Chapter 6

Summary 293

6.1 Geochronological background of the Ecuadorian volcanic arc 294

6.2 Iliniza volcano, a surprisingly young volcano 297

6.2.1 Eruptive history of Iliniza and Santa Cruz volcanoes 297

6.3 Geochronological evolution of the Ecuadorian volcanic arc 305

6.3.1 New K-Ar ages obtained for the central segment volcanoes 305

6.3.2 Volcanism at the Ecuadorian volcanic arc scale 326

6.4 Relationship between volcanism and tectonics 334

Chapter 7

Conclusions and perspectives 339

References 346

Annexes 374

Volcanic history reconstruction in northern Ecuador: insights for eruptive and erosion rates on the whole Ecuadorian arc

Bablon, M., Quidelleur, X., Samaniego, P., Le Pennec, J.-L., Santamaría, S., Liorzou, C., Hidalgo, S., Eschbach, B. (*Bulletin of Volcanology*, 2020) 376

Glass shard K-Ar dating of the Chalupas caldera major eruption: Main Pleistocene stratigraphic marker of the Ecuadorian volcanic arc

Bablon, M., Quidelleur, X., Siani, G., Samaniego, P., Le Pennec, J.-L., Nouet, J., Liorzou, C., Santamaría, S., Hidalgo, S. (*Quaternary Geochronology*, 2020) 378

Pululahua dome complex, Ecuador: eruptive history, total magma output and potential hazards

Andrade, S.D., Müller, A.V., Vasconez, F.J., Beate, B., Aguilar, J., Santamaría, S. (J*ournal of South American Earth Sciences*, 2021) 380

Instituto Geofísico – Escuela Politécnica Nacional, the Ecuadorian Seismology and Volcanology Service

Ramón, P., Vallejo, S., Mothes, P., Andrade, D., Vásconez, F., Yepes, H., Hidalgo, S., Santamaría, S. (Volcanica, 2021) 382

New groundmass K-Ar ages of Iliniza Volcano, Ecuador

Santamaria, S., Quidelleur, X., Hidalgo. S., Samaniego, P., Le Pennec, J.-L. (ISAG 2019) 384

Résumé en français

View of the Western Cordillera from the summit of Guagua Pichincha. The twin-peaked shape of Iliniza volcano is visible in the horizon.

Résumé en français

Contents

1. Contexte géochronologique de l'arc volcanique équatorien 3
2. L'Iliniza, un volcan étonnamment jeune 4
3. Evolution chronologique de l'arc volcanique équatorien 6
   3.1. Stade initial (*early stage*): ~2.5 à ~1.4 Ma 6
   3.2. Stade intermédiaire (*intermediary stage*): ~1.4 à ~0.6 Ma 7
   3.3. Stade final (*late stage*) : à partir de 600 ka 8
4. Perspectives sur la relation entre le volcanisme et la tectonique 9

1. Contexte géochronologique de l'arc volcanique équatorien

Située dans la zone de convergence nord-ouest de l'Amérique du Sud, la partie continentale de l'Équateur accueille la terminaison sud de la *Northern Volcanic Zone (NVZ)*, un arc volcanique formé sur la cordillère des Andes par la subduction de la plaque océanique de Nazca (e.g., McGeary et al., 1985; Ramos, 1999; Stern, 2004; Thorpe, 1984). Le nombre de volcans quaternaires en Équateur est l'un des plus élevé de la région andine, avec plus de 70 volcans identifiés (Fig. 1.1; Hall, 1977; Hall and Beate, 1991; Bernard and Andrade, 2011). Bien que la plupart de ces volcans aient été classés comme "éteints ou dormants", les données géologiques suggèrent qu'au moins 21 édifices étaient actifs pendant l'Holocène. De plus, cinq volcans sont entrés en éruption au cours des deux dernières décennies, causant des dommages aux réseaux routier et électrique, aux infrastructures et à de vastes terres agricoles, et affectant plusieurs villes, dont la capitale Quito (e.g., Hall and Mothes, 2008a). Cette concentration particulièrement élevée de volcans s'explique par des anomalies thermiques et par la géométrie de la plaque subduite, déduites à partir de la composition des magmas éruptifs, des discontinuités rhéologiques de la croûte océanique et de la sismicité de la plaque profonde (e.g., Gutscher et al., 1999; Michaud et al., 2009; Yepes et al., 2016; Bablon et al., 2019, 2020a).

L'histoire éruptive de l'arc équatorien au cours des dernières décennies a été décrite principalement sur la base d'études géochronologiques effectuées sur un nombre limité de volcans sélectionnés. Comme décrit dans le Chapitre 1, ces études se sont principalement concentrées sur les épisodes récents de formation des volcans "actifs" de la région. La priorité avait été donnée aux volcans dont l'activité éruptive est documentée par des archives historiques (depuis la colonisation espagnole de l'Équateur en AD 1534; Hall, 1977; Hall and Beate, 1991) ou dont les preuves morphologiques et stratigraphiques suggèrent une activité éruptive holocène. Cependant, l'histoire éruptive de plusieurs édifices anciens, reconnus par leur état d'érosion avancé, reste mal définie. Peu de publications ont fourni des données géochronologiques sur leurs anciennes étapes de construction (e.g., Barberi et al., 1988; Lavenu et al., 1992; Bigazzi et al., 2005; Opdyke et al., 2006; Hoffer et al., 2008). De plus, la fiabilité des âges K-Ar obtenus sur roche totale (Barberi et al., 1988; Lavenu et al., 1992) a récemment

été remise en question en raison des biais causés par la présence d'argon hérité dans les phénocristaux et/ou la présence de phases minéralogiques altérées (voir Chapitre 2).

Ces dernières années, plus d'une centaine de nouveaux âges K-Ar mesurés sur la mésostase ont été acquis (Alvarado et al., 2014; Almeida, 2016; Almeida et al., 2019; Bablon et al., 2018, 2019, 2020a, 2020b; Telenchana, 2017) dans le cadre de la coopération entre le laboratoire GEOPS de l'Université Paris-Saclay (France), l'Institut de Recherche pour le Développement (IRD, France), et l'Instituto Geofísico de la Escuela Politécnica Nacional (IG-EPN, Equateur). Ces données géochronologiques ont fourni une nouvelle perspective sur l'évolution des segments nord et sud de l'arc (Fig. 6.5). La présente thèse de doctorat fournit 49 nouveaux âges K-Ar provenant de 15 volcans situés dans le segment central de l'arc équatorien (Fig. 6.5b), complétant ainsi les études précédentes d'autres volcans de la région. Avec de nouvelles observations de terrain, des corrélations stratigraphiques, des analyses morphologiques et des données géochimiques, notre nouvel ensemble de données géochronologiques nous permet de décrire l'histoire éruptive des volcans de cette région et, pour la première fois, de l'ensemble de l'arc équatorien.

2. L'Iliniza, un volcan étonnamment jeune

La première partie de la présente thèse de doctorat consiste en une étude détaillée de l'Iliniza, un volcan à double pic, situé à 50 km au sud de Quito (voir Chapitre 3). Les travaux sur le terrain ont également inclus le volcan Santa Cruz situé à proximité, à des fins de comparaison stratigraphique. Les profondes vallées glaciaires présentes dans les zones les plus élevées du volcan Iliniza, en particulier celles observées sur son édifice nord, suggèrent que l'âge de ce volcan pourrait atteindre ~1 Ma par comparaison avec d'autres volcans érodés de la région (Hidalgo et al., 2007). Par ailleurs, un âge de formation proche de l'Holocène a été proposé pour un dôme satellite peu érodé sur le flanc sud du volcan (Hall and Beate, 1991).

Nous avons acquis les 14 premiers âges K-Ar de ces volcans (Fig. 6.2) qui, avec les nouvelles observations de terrain et les résultats précédents de Hidalgo (2001, 2002) et Hidalgo et al. (2007), nous

ont permis de contraindre le développement du volcan Iliniza au cours du temps. Contrairement aux hypothèses précédentes, l'activité volcanique plus ancienne est attribuée au volcan Santa Cruz, daté ici à 702 ± 11 ka (Fig. 6.2). Après une longue période d'apparente inactivité, son activité a repris à 79 ± 2 ka et 60 ± 3 ka, formant le cône Loma Saquigua de faible volume. L'activité initiale d'Iliniza correspond à l'extrusion du dôme rhyodacitique de Pilongo à 353 ± 6 ka (Fig. 6.2). La forme en double pic du volcan Iliniza a impliqué la construction de deux édifices superposés construits en plusieurs phases (Fig. 6.3). L'édifice Iliniza Nord a été formé principalement par des laves andésitiques et des brèches monolithologiques datées entre 116 ± 2 et 123 ± 6 ka. L'histoire éruptive de cet édifice ancien comprend la formation du pic satellite Huayrapungo à 121 ± 2 ka (Fig. 6.3a). Après une période de repos, l'activité éruptive a repris 1,7 km au sud-ouest, formant l'édifice Iliniza Sud construit sur les pentes de l'édifice Iliniza Nord. Les laves dacitiques supérieures de l'édifice basal d'Iliniza Sur ont été datées à 46 ± 1 et 45 ± 2 ka. Nos résultats suggèrent l'occurrence d'une phase hautement explosive qui a détruit le sommet de cet édifice basal et créé une succession pyroclastique dacitique de grand volume à sa base (Fig. 6.4). Le volume minimum estimé de ces dépôts, appelés ignimbrite de Jatuncama, est de 2,1 km^3, ce qui correspond à une éruption avec un indice d'explosivité volcanique (*VEI*) de 5. L'activité éruptive ultérieure a permis de reconstruire l'édifice Iliniza Sud avec la mise en place d'un complexe de dômes, daté de 34 ± 1 ka, à son sommet.

Contrairement aux autres volcans du Front Volcanique (e.g., von Hillebrandt, 1989; Robin et al., 2008; Hidalgo et al., 2008; Almeida et al., 2019; Andrade et al., 2021), la dernière activité éruptive de l'édifice Iliniza Sud a inclus l'émission de multiples coulées de lave andésitique datées entre 31 ± 4 et 25 ± 3 ka (Fig. 6.2). L'histoire éruptive plus récente du volcan Iliniza comprend l'extrusion du dôme satellite de Tishigcuchi, et l'émission de la coulée de lave Pongo probablement à partir d'un cône adventif ou d'une fissure éruptive. Ces deux structures sont situées à la base du flanc sud du volcan Iliniza. Nous avons obtenu un âge K-Ar holocène de 6 ± 4 ka pour la lave de Pongo (Fig. 6.2). Sur la base de ces données géologiques et géochronologiques, nous proposons de considérer le volcan Iliniza comme un centre volcanique potentiellement actif. Nous reconnaissons que ces âges sont à la limite de la méthode de datation K-Ar. Ainsi, nous suggérons fortement que les futures investigations détaillées

de l'histoire éruptive récente d'Iliniza emploient, dans la mesure du possible, des méthodes géochronologiques alternatives mieux adaptées à cette gamme d'âges, comme la datation au radiocarbone. Néanmoins, nos résultats fournissent déjà contraintes fortes sur le comportement du volcan Iliniza et leurs implications possibles pour l'évaluation des risques.

3. Evolution chronologique de l'arc volcanique équatorien

La deuxième partie de cette thèse presente l'étude du volcanisme équatorien à l'échelle régionale. Une trentaine de nouveaux âges K-Ar nous a permis de décrire l'histoire éruptive de la partie centrale de l'arc volcanique, entre les latitudes 0,1° N et 0,7° S. Notre étude s'est focalisée sur les volcans du bassin de Guayllabamba situé dans la vallée inter-andine (Fig. 6.5). Sur la base des résultats obtenus, la base de données géochronologiques présentée par Santamaría (2017) a été mise à jour pour obtenir une cartograohie complète du développement du volcanisme quaternaire dans les Andes équatoriennes (voir Chapitre 5). Ces travaux nous ont permis de définir les 77 volcans quaternaires qui composent l'arc équatorien, lequel a développé son histoire éruptive en trois étapes principales caractérisées par une augmentation globale du nombre de volcans actifs.

Comme détaillé dans les Chapitres 1 et 5, la distribution des volcans n'est pas homogène. En fait, sept segments transversaux à l'arc peuvent être distingués en fonction du nombre de volcans situés dans chaque zone. Les limites entre chaque segment sont définies par des lignes perpendiculaires à l'axe N70°E formé par les volcans du Front Volcanique. En accord avec la proposition d'Andrade (2009), ces segments ont été nommés en fonction de la plus grande ville située dans chaque segment, comme le montre la Figure 6.14.

3.1. Stade initial (*early stage*): ~2.5 à ~1.4 Ma

Nos données suggèrent que l'activité volcanique documentée la plus ancienne était principalement concentrée au nord du bassin de Guayllabamba (segments de Quito et Machachi ; Fig.

6.15). Plus précisément, ce stade initial du volcanisme inclue l'activité du volcan Chacana, daté ici à 2228 ± 34 ka et à ~2400 ka par Opdyke et al. (2006), et du volcan Coturco, daté ici à 1959 ± 28 ka. Par ailleurs, plusieurs éruptions fissurales ont eu lieu à plusieurs kilomètres au sud de Guayllamaba, dans l'arrière-arc de l'actuelle terminaison sud de l'arc (segment d'Ambato). Ce volcanisme a été daté entre 2670 ± 60 et 1920 ± 100 ka (Hoffer et al., 2008). En considérant que l'échantillonnage et la datation des plus anciennes séquences volcaniques de l'arc n'étaient pas exhaustifs dans les études antérieures, nous n'excluons pas l'existence d'un volcanisme dans d'autres zones de l'arc pendant ce stade initial.

3.2. Stade intermédiaire (*intermediary stage*): ~1.4 à ~0.6 Ma

Au cours du stade intermédiaire (~1.4-0.6 Ma), plusieurs édifices volcaniques ont été construits principalement autour du bassin de Guayllabamba (segments d'Ibarra, Quito et Machachi ; Fig. 6.15). Nos âges suggèrent que les volcans Pambamarca (1374 ± 21 à 1261 ± 18 ka), Ilaló (1273 ± 20 à 1112 ± 18 ka), Puntas (1132 ± 16 à 1084 ± 17 ka) et Casitagua (878 ± 13 à 785 ± 16 ka) étaient actifs pendant ce stade, ainsi que le volcan Santa Cruz (702 ± 11 ka). Ces données complètent les volcans déjà datés Chacana (1350 ± 90 à 1580 ± 70 ka, et ~810-726 ka; Bigazzi et al., 1997, 2005; Opdyke et al., 2006; Pilicita, 2013), Atacazo-Ninahuilca (La Carcacha: ~1300 ka; Hidalgo, 2006), Pichincha (El Cinto: 1112 à 910 ka; Rucu Pichincha: ~850 à ~150 ka; Robin et al., 2010), and Cayambe (Viejo Cayambe: ~1100 to 1050 ka; Samaniego et al., 2005). Cette activité plus élevée comprend également deux coulées de lave situées au nord du bassin de Guayllabamba et datées à 1152 ± 30 ka et 1038 ± 87 ka (Pacheco, 2013; Alvarado et al., 2014; Bablon et al., 2020a). Plusieurs kilomètres au nord, l'activité initiale de l'édifice de Cerro Negro (complexe volcanique Chiles-Cerro Negro ; segment de Tulcán ; Fig. 6.15) s'est produite à ~880 ka (Telenchana, 2017; Bablon, 2018). Le volcan Sagoatoa, situé à plusieurs km au sud de Guayllamaba (segment d'Ambato ; Fig. 6.15), a montré une activité entre 826 ± 12 et 799 ± 12 ka (Bablon et al., 2019). Peu de données sont disponibles concernant le volcanisme de l'arrière-arc. Un âge à 1150 ± 10 ka a été publié pour le volcan Pan de Azúcar (Hoffer, 2008), tandis que plusieurs galets d'obsidienne trouvés dans la rivière Cosanga située à proximité ont été datés à 670 ± 6 et 290 ± 20 ka

(Bellot-Gurlet et al., 2008). Ces données suggèrent un volcanisme actif sur la marge est de la Cordillère Orientale, dans le segment de Quito et Machachi (Mothes and Hall, 2008; Hall and Mothes, 2010).

3.3. Stade final (*late stage*) : à partir de ~0.6 Ma

Le troisième stade a montré une notable augmentation du nombre de volcans actifs, avec au moins 50 volcans actifs pendant cette période (Fig. 6.16). Plusieurs groupes volcaniques (*volcanic clusters*), définis par une importante concentration de volcans dans certaines zones de quelques dizaines de kilomètres carrés, se sont formés dans l'arc volcanique. Bien que près de vingt volcans restent peu étudiés (la plupart d'entre eux provenant du segment Tulcán, au nord), il est probable que la plupart de ces volcans correspondent probablement à ce stade de l'arc, ou éventuellement au stade intermédiaire. Les données géochronologiques ne sont disponibles que pour le complexe volcanique Chiles-Cerro (570 à 50 ka; Telenchana, 2017; Bablon, 2018) et l'éruption holocène du volcan Soche (9,6 ka; Beate, 1994). L'histoire éruptive détaillée des segments nord (Ibarra) et sud (Ambato) a été présentée en détail par des études dédiées antérieures (Bablon et al., 2019, 2020a), tandis que celle du segment central (Quito et Machachi) a été présentée dans les chapitres 4 et 5, et résumée dans la section 6.3.1 de cette thése. Les références correspondantes sont fournies dans la section 6.1 ainsi que dans la base de données EVEG (Santamaría, 2017).

Nous fournissons dans ce travail les premiers âges radiométriques du groupe volcanique Machachi, situé au sud du bassin de Guayllamamba (Fig. 6.8). Ces âges K-Ar nous ont permis de décrire l'histoire éruptive du Cotopaxi (stade Barrancas : ~540 ka ; stade Morurco : 340 à 300 ka), Rumiñahui (>400 à ~200 ka), Pasochoa (470 à 420 ka), Iliniza (dôme Pilongo : ~350 ka ; Iliniza Nord : ~120 ka ; Iliniza Sud : 45 à 6 ka), Sincholagua (~310 ka), Almas Santas (~370 ka), Corazón (190 à 90 ka) et Santa Cruz (Loma Saquigua : 80 à 60 ka), ainsi que les volcans Chalupas-Quilindaña (pre-caldera lavas: 460 to 420 ka; Chalupas ignimbrite: 216 ka; Quilindaña edifice: 190 to >44 ka; Hammersley, 2003; Bablon et al., 2020b; Córdova et al., 2020), les volcans Antisana (~400 à 0 ka Hall et al., 2017), Huañuna (~10 ka) and Chaupiloma volcanoes (Clapperton et al., 1997; Hall and Mothes, 2008b; Hall et al., 2017).

4. Perspectives sur la relation entre le volcanisme et la tectonique

Comme discuté dans les Chapitres 4 et 5, le volcanisme quaternaire ne montre pas une migration évidente en fonction de sa distance par rapport à l'arc, c'est-à-dire d'est en ouest ou vice versa. Cependant, le volcanisme le plus ancien à chaque étape semble se situer préférentiellement à la limite de la Cordillère Orientale et de la vallée inter-andine. En revanche, le volcanisme a montré une extension progressive vers le nord et le sud du bassin de Guayllabamba (Fig. 6.16), appelée aussi le segment central de l'arc. Nous n'avons pas trouvé d'indice d'une activité soutenue dans le sud de l'arrière-arc entre le stade initial et le stade final. Les éruptions fissurales plus anciennes et les laves émises près de la ville de Puyo (segment d'Ambato) sont de faible volume, et donc peu significatives à l'échelle de l'arc (Hoffer, 2008; Hoffer et al., 2008; Ball, 2015).

Malgré ces observations générales, la distribution spatiale du volcanisme au cours du temps semble être aléatoire pour chacun des stades de l'histoire éruptive de l'arc équatorien. Cependant, la répartition spatiale finale des volcans semble être principalement influencée par les structures tectoniques héritées de la croûte continentale, tandis que l'activité tectonique du Quaternaire a apparemment joué un rôle secondaire (Fig. 6.18). Plus précisément, les corridors volcaniques N-S décrits précédemment (e.g., Hall, 1977; Hall and Beate, 1991; Litherland and Aspden, 1992) coïncident spatialement avec des zones de failles et de sutures anciennes de la croûte continentale (e.g., Litherland et al., 1994; Hughes and Bermúdez, 1997; Boland et al., 2000; Egüez et al., 2017), tandis que, comparativement, peu de volcans sont situés directement sur les nombreux systèmes de failles quaternaires NE-SW (e.g., Tibaldi et al., 2007; Andrade, 2009; Alvarado et al., 2016; Andrade et al., 2019; Baize et al., 2020). Cependant, cette hypothèse mérite de plus amples investigations, car seules quelques études détaillées sont disponibles sur la relation entre l'activité tectonique quaternaire et le développement des reliefs volcaniques dans l'arc équatorien (Andrade et al., 2019; Baize et al., 2020).

Le Chapitre 5 fournit des informations supplémentaires sur les autres corridors volcaniques et leur relation avec les structures tectoniques héritées et quaternaires de la croûte. Notamment, la partie centrale de l'arc, et son nombre particulièrement élevé de volcans formés à partir de ~2,4 Ma, se

superpose spatialement à la projection vers l'intérieur du continent de la ride de Carnegie (Gutscher et al., 1999) et de l'escarpement de la zone de fracture de Grijalva qui délimite la jeune croûte océanique de Nazca (Fig. 1.10; Yepes et al., 2016). L'histoire éruptive proposée suggère que la subduction de ces structures a contribué au développement et à l'expansion du volcanisme équatorien au cours du temps. Nous proposons que les conditions thermiques de la jeune croûte de Nazca et de la ride de Carnegie ont favorisé la génération de magma depuis le début du Pléistocène, notablement dans les segments d'Ibarra, Quito et Machachi. Cette hypothèse est supportée par la grande variabilité des compositions géochimiques des magmas observée pour cette partie centrale de l'arc, comme développé dans le premier chapitre. En effet, les grandes variations des rapports entre les éléments mobiles et les éléments immobiles (e.g., Ba/Th), la faible teneur en Y et en HREE (terres rares lourdes) observée dans certaines laves jeunes, ainsi que les variations des compositions isotopiques de Pb-Sr-Nb, peuvent d'une certaine manière être liées à la subduction de ces structures majeures (e.g., Gutscher et al., 1999; Garrison et al., 2006; Ancellin et al., 2017; Narvaez et al., 2018; Bellver-Baca et al., 2020; Chiaradia et al., 2021). Les données géochimiques acquises dans le cadre de notre étude reflètent les mêmes caractéristiques des magmas décrits dans ces études. En fait, nos données géochimiques ont été utilisées pour distinguer et mieux définir les unités stratigraphiques des volcans étudiés plutôt que de fournir des arguments supplémentaires sur la compréhension des processus pétrogénétiques associés à la formation de ces magmas.

La présente thèse apporte des contraintes temporelles fortes sur certains volcans qui, avec des études géochimiques ciblées, pourraient contribuer à une meilleure caractérision des processus magmatiques sur des grandes échelles de temps. Par exemple, les analyses géochimiques des isotopes et/ou des inclusions fluides provenant de volcans tels que Chacana-Coturco (~2,4 Ma), Puntas-Pambamarca-Ilaló (~1,2 Ma) et Atacazo-Corazón-Pasochoa (<0,4 Ma) offrent un contexte temporel approprié pour étudier les effets des changements des processus pétrogénétiques des magmas équatoriens. Ces analyses permettront de distinguer si les zonations à travers l'arc et le long de l'arc des éléments traces incompatibles, interprétées comme des reflets du changement de la composante de subduction(e.g., Ancellin et al., 2017; Narvaez et al., 2018), sont dépendantes ou non du temps. Par

ailleurs, il est possible que la signature adakitique globale observée dans les magmas plus jeunes de l'arc, mieux échantillonnés, s'étende égalment aux magmas plus anciens. A titre d'exemple, nous constatons que la lave échantillonnée au sommet du Coturco et les dômes dacitiques du Pambamarca (datés à 1959 ± 28 et à 1292 ± 20 ka, respectivement) présentent un léger appauvrissement en Y et HREE par rapport aux LREE. Cette hypothèse de signatures adakitiques plus anciennes devrait être testée plus en détail dans des études géochimiques spécialisées.

Finalement, les nombreuses données fournies dans cette thèse qui ont permis de proposer un modèle de développement du volcanisme équatorien pourraient être comparées à d'autres segments de l'arc Andin ou à d'autres arcs dans le monde. Par exemple, l'histoire éruptive proposée ici suggère que le développement de l'arc semble être favorisé par la subduction d'une ride océanique (i.e., la ride de Carnegie) avec ses conditions thermiques spécifiques, au lieu d'être inhibé, comme cela a été observé dans les Andes centrales par les rides de Nazca et Juan Fernandez (e.g., Gutscher et al., 2000b; Chen et al., 2001; Porter et al., 2012; Ramos and Folguera, 2009). En conséquence, il pourrait être intéressant de comparer la géochronologie, la géochimie et la tectonique des deux zones afin de mieux comprendre la relation entre le développement des arcs volcaniques et la subduction de telles structures, par exemple.

General introduction

View of the western flank of the Cayambe volcano. In the background on the right, ash column from El Reventador volcano.

General introduction

Located in the northwestern convergence zone of South America, Ecuador's continental territory hosts the southern termination of the Northern Volcanic Zone, a volcanic arc formed over the Andes Mountains as a result of the subduction of the oceanic Nazca plate. Remarkably, the number of Quaternary volcanoes in Ecuador is one of the highest in the Andean region with more than 70 volcanoes identified. Although many of these volcanoes are classified as "extinct or at rest", geological evidence suggests that at least 21 edifices were active during the Holocene. Moreover, five volcanoes erupted during the last two decades causing damage to road and power networks, infrastructure, and extensive agricultural lands, affecting several towns including the capital city, Quito. This particularly high concentration of volcanoes is explained by anomalies in the thermal stage and shape of the subducted slab, both inferred from the composition of the erupted magmas, rheological discontinuities in the oceanic crust, and deep slab seismicity.

Furthermore, the oblique convergence and the subduction of topographic heterogeneities in the Nazca plate (i.e., Carnegie Ridge) induce a transpressive stress field extending towards the interior of the continent, which in turn causes a decoupling and displacement of the western margin of the South American plate. Hence, multiple crustal fault systems were formed along the Andes, explaining the occurrence of violent earthquakes outside the subduction zone. This geodynamic setting seems to play a key role during the Pliocene-Pleistocene reorganization of the deformation zone and tectonics. Given the temporal association with the modern volcanism, it is possible to infer that both phenomena could be correlated. In fact, there are multiple hypotheses on the link between volcanism and changes in slab or crustal geodynamics, but their temporal relationship remains unclear due to the lack of reliable geochronological data. Indeed, the geochronological knowledge of the volcanic arc is mostly restricted

to its active edifices, thus biasing the understanding of the older volcanoes. This gap in knowledge also affects the volcanic risk assessment as data about the overall duration of the volcanic activity is not available.

The objective of this thesis is to reconstruct the eruptive history of the Quaternary volcanism in Ecuador, focusing on the central across-arc segment, in order to elucidate their spatial and temporal evolution. For this purpose, nearly 50 new ages were obtained from 15 volcanoes of this region using the unspiked Cassignol-Gillot K-Ar dating method applied to selected mineralogical phases. New morphological and stratigraphic analyses, combined with numerical reconstructions of the paleotopography and geochemical analyses, complement the geochronological data to provide a complete overview of the arc's evolution. This project also includes a more detailed study focused on the eruptive history of Iliniza, a double-peaked compound volcano located in the central segment of the arc. In fact, morphological and stratigraphic evidence suggest a non-confirmed Holocene activity related to the South Iliniza edifice. Finally, the data acquired during this project was combined with those previously obtained in collaboration between the GEOPS laboratory of the Université Paris-Saclay, the Institut de Recherche pour le Développement (IRD) and the Instituto Geofísico de la Escuela Politécnica Nacional (IG-EPN). In this way, this research proposes an evolutionary model of the Ecuadorian arc and explores the potential links between volcanism and the geodynamic setting.

Chapter 1

Sunrise from the summit of Pichincha volcano overlooking southern Quito, the capital of Ecuador. From left to right the summits of Antisana, Sincholagua, Pasochoa, Cotopaxi and Rumiñahui volcanoes.

Chapter 1

Ecuadorian volcanic arc: geologic and tectonic setting

Contents

1.1 Segmentation of the Andean margin 19

1.2 Ecuadorian geodynamic setting 25

1.2.1 Guiana Shield Realm (Guiana Shield and Oriente Foreland Basin) 28

1.2.2 Central Tectonic Realm (Para-autochthonous Terrains and Cretaceous Volcanic Arc Fragments) 29

1.2.2.1 Triassic to Lower Cretaceous Evolution of the Continental Margin 30

1.2.3 Western Tectonic Realm (Western Cordillera and Coastal Forearc) 33

1.2.3.1 Upper Cretaceous to Neogene Events Related to the Accreted Western Terranes 35

1.2.4 Nazca Plate Domain 39

1.2.4.1 Rupture of an ancient oceanic plate 39

1.2.4.2 Nazca Slab Geometry 41

1.2.5 Geodynamics of The North Andean Sliver 44

1.3 Ecuadorian volcanic arc 46

1.3.1 Previous stages: the Neogene volcanism 46

1.3.2 Distribution of volcanic edifices 50

1.3.3 Geochronology of the volcanic arc 54

1.3.4 Geochemical characterization and petrogenetic models 56

1.1 Segmentation of the Andean margin

The Andes is a continuous mountain range extending 8500 km along the western margin of South America. Its average height is 3500 meters above sea level, although it reaches over 6000 meters at numerous locations (Sobolev and Babeyko, 2005; Flores and Pizarro-Araya, 2006). The rise of the Andes is the result of the interaction between the subducting Nazca and Antarctic plates under the South American plate in an orogenic process that began in the Cenozoic era and continues presently (Isacks, 1988; Kennan et al., 1997; Lamb and Davis, 2003; Elger et al., 2005; Arriagada et al., 2008). The Andean orogeny is relatively young considering that oceanic subduction beneath the western margin of the South American plate has been continuous since the Jurassic period (Coira et al., 1982; Rossel et al., 2013; Cochrane et al., 2014; Spikings et al., 2016). The explanation probably lies in convergence rates and relative plate motions changes between the South American plate and the Farallon (actual Cocos and Nazca plates) and Antarctic subducting plates, which coincide with the large extensional and compressional periods observed along the continental active margin (Pardo-Casas and Molnar, 1987; Espurt et al., 2008; Somoza and Ghidella, 2012; Jones et al., 2014). According to Jaillard & Soler (1996), crustal thickening occurred during three major compressive discrete pulses: (1) the Peruvian phase, occurred during the Upper Cretaceous, followed by (2) the Incaic phase in the Eocene and (3) the modern Quechua phase that began in the Neogene.

The Andes exhibit significant latitudinal variations in their mean elevation, width, internal structure, basin distribution and active volcanism that cannot be explained solely by plate kinematics (e.g., Barazangi and Isacks, 1976; Jordan et al., 1983; Gutscher, 2002; Jacques, 2003; Stern, 2004; Espurt et al., 2008). In fact, the convergence rate has been almost similar longwise the South American margin during the Neogene despite a noticeable deceleration on recent times (Norabuena et al., 1999; Kendrick et al., 2003; Quinteros and Sobolev, 2013). As Martinod et al. (2010, 2013, 2016) propose, the oceanic crust heterogeneities and the variations in the geometry of subducting slab might be the cause of the Andean segmentation. Notably, the formation of large flat-slab segments associated with the subduction of buoyant ridges is a predominant phenomenon in the growth of the Andes, and that has even affected plate kinematics (Fig. 1.1a).

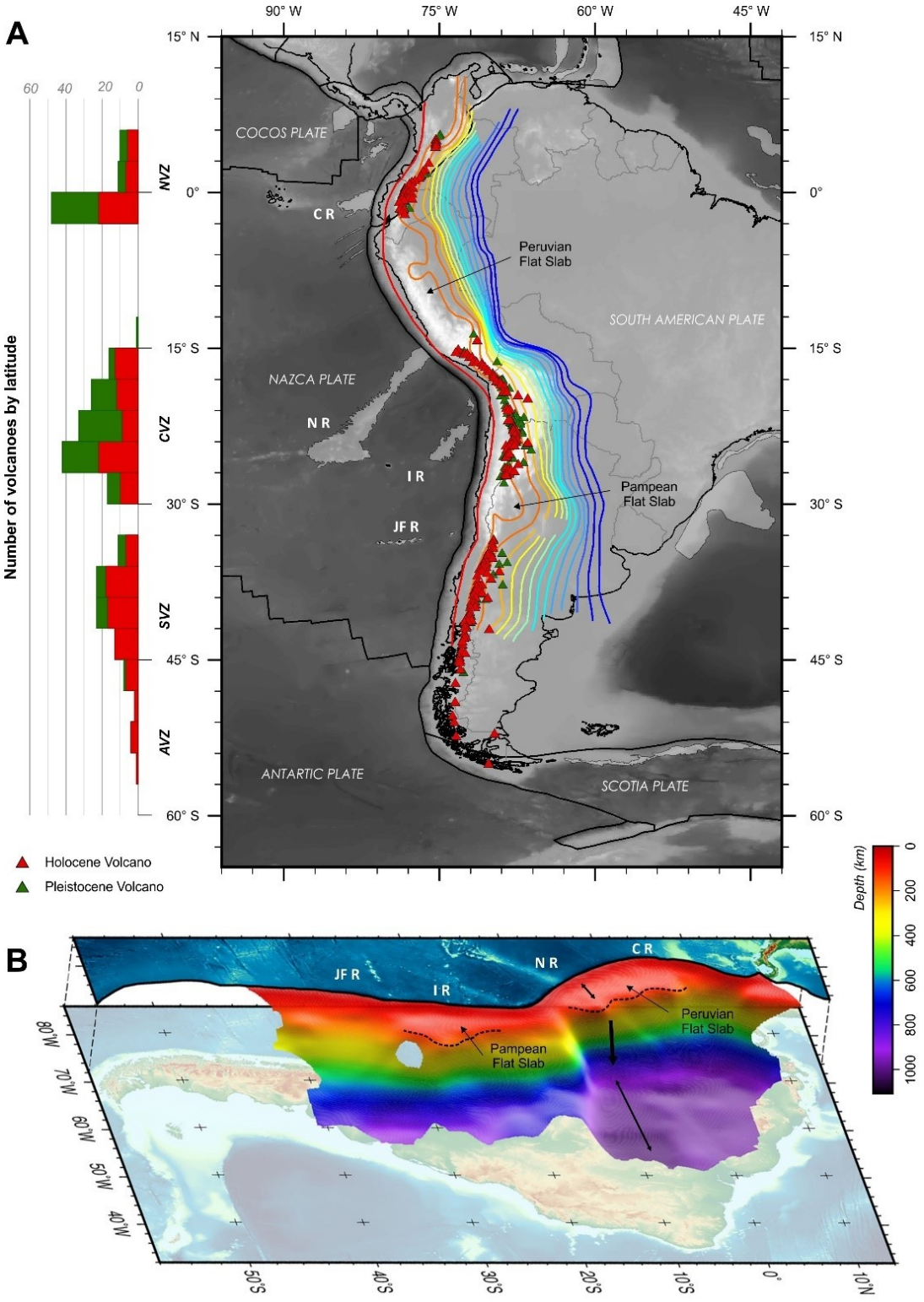

Figure 1.1. *South America tectonic setting and distribution of Quaternary volcanoes by latitude (modified from Portner et al., 2020).* ***a)*** *Schematic map of South America showing Holocene volcanoes as red triangles; and Pleistocene volcanoes as green triangles (Siebert et al., 2011). Nazca slab contours each 50 km. C R: Carnegie; N R: Nazca; I R Iquique; and JF R: Juan Fernandez Ocean Ridges.* ***b)*** *Equivalent Nazca slab model in 3D (Portner et al., 2020).*

The examination of the spatial distribution of earthquake hypocenters showed the geometry of the Wadati-Benioff zone beneath South America, revealing the existence of two major flat subduction segments located in Peru (lat. 3°S to 15°S) and central Chile (lat. 27°S to 33°) (Figure 1.1b; Barazangi and Isacks, 1976; Hanuš and Vaněk, 1978; Gutscher et al., 2000b; Ramos and Folguera, 2009; Portner et al., 2020). In these areas, the subducting plate has generally a steep angle (around 30°) until reaching 100-120 km depth. Then, the slab continues almost horizontally for several hundred kilometers before increasing its subduction angle again (Gutscher et al., 2000b).

The decrease in the average density of the oceanic plate, with the consequent increase in its buoyancy, is the most widely accepted cause to explain the formation of flat slabs. However, an open debate exists about the characterization of the process that causes this phenomenon. The subduction of buoyant structures such as aseismic ridges or oceanic plateaus (Pilger, 1981; Nur and Ben-Avraham, 1983; Gutscher et al., 2000b; Anderson et al., 2007), and hydration processes of the upper mantle (Kopp et al., 2004; Skinner and Clayton, 2011; Porter et al., 2012; Liu and Currie, 2016) are the mechanisms involved in the formation of flat slabs. According to Skinner & Clayton (2013), the numerical reconstructions of the South American margin and the potential bathymetric anomalies of the oceanic crust are not very well correlated with the historical development of flat slabs, therefore they cannot be the exclusive cause of its formation. In contrast, Espurt et al. (2008) suggest that development of flat slabs can result of the forced subduction of large buoyant structures after having subducted for ~700 km. South American flat slabs appeared ~7 Ma after the beginning of the Inca Plateau subduction in Peru, and the Nazca Ridge and Juan Fernández Ridge subduction in Chile. Conversely, in Ecuador and northern Chile where steep slabs are observed, the flat slab formation process may be not complete due to the recent and/or short-range subduction of Carnegie and Iquique ridges respectively.

The slab geometry also influences the arrangement of active volcanism, where its discontinuous distribution along the South American margin is a remarkable feature of the Andean segmentation (Figure 1.1a). The low subducting angle hinders the formation of an asthenospheric wedge between the slab and the continental plate, causing the lack of active volcanism (Gutscher et al., 2000a; Chen et al., 2001; Porter et al., 2012). Consequently, large spatial gaps are observed within the Andean volcanic arc

segmenting its quaternary activity into four regions (Thorpe, 1984; McGeary et al., 1985; Ramos, 1999; Stern, 2004):

- **The Northern Volcanic Zone (NVZ):** which begins in central Colombia (lat 5°N) and continues to Ecuador (lat. 2°S),
- **The Central Volcanic Zone (CVZ):** which includes the volcanoes of southern Peru (lat 15°S), Bolivia and Northern Chile (lat. 27°S),
- **The Southern Volcanic Zone (SVZ):** which occupies the center and south of Chile-Argentina (from lat. 33°S to 47°S), and
- **The Austral Volcanic Zone (AVZ):** which extends through the southernmost tip of Chile (from lat. 48°S to 54°S).

According to the volcanoes database of the Global Volcanism Program of the Smithsonian Institution (Siebert et al., 2011), the Northern Volcanic Zone (NVZ) has the highest concentration of volcanoes active during the Holocene (even back to the Pleistocene; Fig. 1.1a). Furthermore, recent studies carried out in the region have revealed the existence of additional recent eruptive centers that were not included in the global database (e.g., Núñez et al., 2001; Robertson et al., 2002; Duque-Trujillo et al., 2016; Bablon et al., 2019; Murcia et al., 2019), turning the density of volcanoes even higher than previously described. Gómez Tapias (2005) and Marín-Cerón et al. (2019) reviews offer a more exhaustive list of the NVZ eruptive centers that, after a more detailed bibliographic analysis, describe the distribution of volcanoes as four north-south segments (Fig. 1.2) as previously proposed by other authors (e.g., Hall and Wood, 1985; Stern, 2004; Pedraza Garcia et al., 2007).

Segment A - Northern Colombia. Volcanoes in this area form a narrow arc located on the Cordillera Central. This distribution could be related to a steep subducting slab (~45° dip; Pedraza Garcia et al., 2007). The volcanoes in this segment are San Diego, Escondido, Romeral, Cerro Bravo, Nevado del Ruiz, Paramillo del Cisne, Santa Isabel, Santa Rosa, Nevado del Quindio, Nevado del Tolima, Cerro Machin, Guacharacos and El Tambor.

Segment B - Central Colombia. It is located mainly in the highlands of the Cordillera Central, 190 km south of the northern segment after a volcanic gap between the Cerro Machin and Huila volcanoes. A second 80 km-long gap is observed within this segment between the Huila and Puracé volcanoes. Although the large stratovolcanoes form a narrow arc, the presence of the eastern San Agustin monogenetic field and the deep seismicity distribution suggest the slab is subducting at a lower angle than in the northern segment (~30° dip; Pedraza Garcia et al., 2007). The volcanoes from this segment are Huila, Puracé (Coconucos Volcanic complex), Yerbabuena, Merenberg, Sotará Volcanic complex (Sotará, Sucubún, Cerro Gordo, Cerro Azafatudo, Cerro Negro), San Agustin, Cutanga, Petacas, Animas and Doña Juana

Segment C - Southern Colombia. Volcanoes in this segment define a wider arc as they are also located in the Cauca-Patia depression and in the Cordillera Occidental. The monogenetic volcanism observed in the Sibundoy valley would be the southern continuation of the San Agustin field. The slab geometry is similar to that of segment B. The volcanoes in this segment are Morasuco, Bordoncillo, Galeras, Campanero, Sibundoy, Mujundinoy, Azufral, Guayapungo, Cumbal and Chiles-Cerro Negro Volcanic complex. This area can extend to the south including part of the volcanoes from northern Ecuador which share a common geometry in the subducting slab.

Segment D – Ecuador. This is the area with the highest concentration of volcanoes in the NVZ. Volcanoes are located over the Cordillera Real (southern continuation of the Cordillera Central) and Occidental, as well as in the Inter-Andean Valley and the Sub-Andean zone (back-arc zone). Several slab-geometry models have been proposed for this segment due to the lack of intermediate-depth seismicity and the presence of the Carnegie Ridge (see discussion provided in Section 1.2.4.2). The 78 volcanoes that form this Segment D are presented in Figure 1.14.

The processes involved in the formation of the NVZ magmas include not only the geometry of the subducting slab, but also the structural configuration of the South American crust which influences the location, vent arrangement, and size of the volcanic edifices (Marín-Cerón et al., 2019). These processes can be evidenced by the geochemical variations of the volcanic products as they are influenced by the slab fluids input, the heterogeneous melting of mantle wedge, and crust assimilation

processes (Ancellin et al., 2017). Therefore, in order to understand the unique configuration of the Ecuadorian volcanic arc (Segment D of the NVZ), it is essential to review the geological domains involved in its formation, the geochemical characteristics of the volcanic products emitted, and the evolution of these characteristics through time.

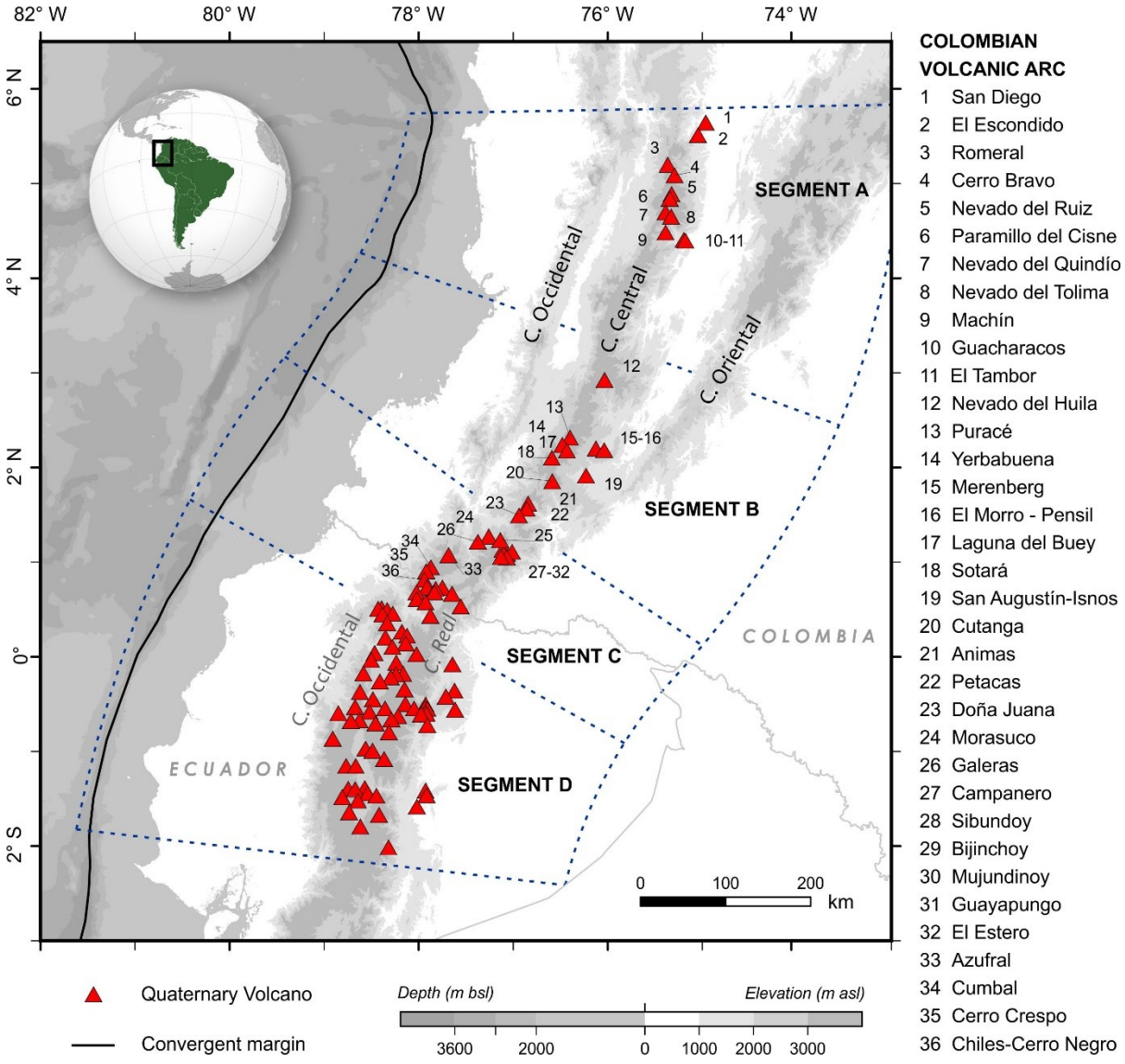

Figure 1.2. *Schematic map of the Northern Volcanic Zone of the Andes in relation to the Nazca-slab segmentation described by Pedraza et al. (2007). The boundary between segments C and D was modified following the results of Yepes et al. (2016). The list of Ecuadorian volcanoes is provided in Figure 1.14.*

1.2 Ecuadorian geodynamic setting

The northwest of the South American plate, where the NVZ is located, is a highly complex area which forms a converging margin with the Nazca and Caribbean plates. Moreover, its northwest edge is composed by a series of accreted terrains that are compressed by the South American craton to the east and by the subducting Nazca plate to the west (Cediel et al., 2003). Therefore, the North Andean segment forms an upper plate "sliver" showing an NE-ward movement "escaping" such compression (Witt et al., 2006; Alvarado et al., 2016). Although the terms "block" and "microplate" are commonly used to refer to this domain (e.g., Gutscher et al., 1999; Potts et al., 2005; Egbue and Kellogg, 2010; Pousse-Beltran et al., 2017), the term North Andean "Sliver" (NAS) is preferred because of: (1) the size of the domain compared to the South American plate, (2) the incorporation into the movement of certain arc and back-arc sections and (3) the internal deformation shown by this domain (Alvarado et al., 2016).

Cediel et al. (2003; 2019) summarized the tectonic assembly of the NAS in terms of its "lithotectonic" units, which were generated in a particular tectonic environment or deformed by a particular tectonic event, and "morphostructural" units, which correspond to physiographic regions that have a topographic expression controlled by faults, folds, and geological discordances. The integration of the regional tectonic assembly allows to distinguish major "tectonic realms" where lithotectonic and morphostructural component units responded altogether to regional tectonics over time (Figure 1.3). This approach allows to describe the complexity of the NAS in terms of its lithological and structural components. Conversely, the traditional approach mainly uses major physiographic structures (like mountain ranges or depressions) as individual entities representing single geological units or events.

Ecuador is physiographically formed *sensu lato* by the Coastal (forearc) and the Oriente (back-arc) basins which are separated by the Western Cordillera and Cordillera Real (Eastern Cordillera). Both mountain ranges form an intra-arc basin called the Inter-Andean Valley (Figure 1.4). In terms of its lithotectonic units, Ecuador is constituted by the Western Tectonic Realm (Western Cordillera and Coastal forearc), the Central Tectonic Realm (Cordillera Real) and the Guiana Shield Realm (Oriente back-arc) to which the Nazca Plate domain is added.

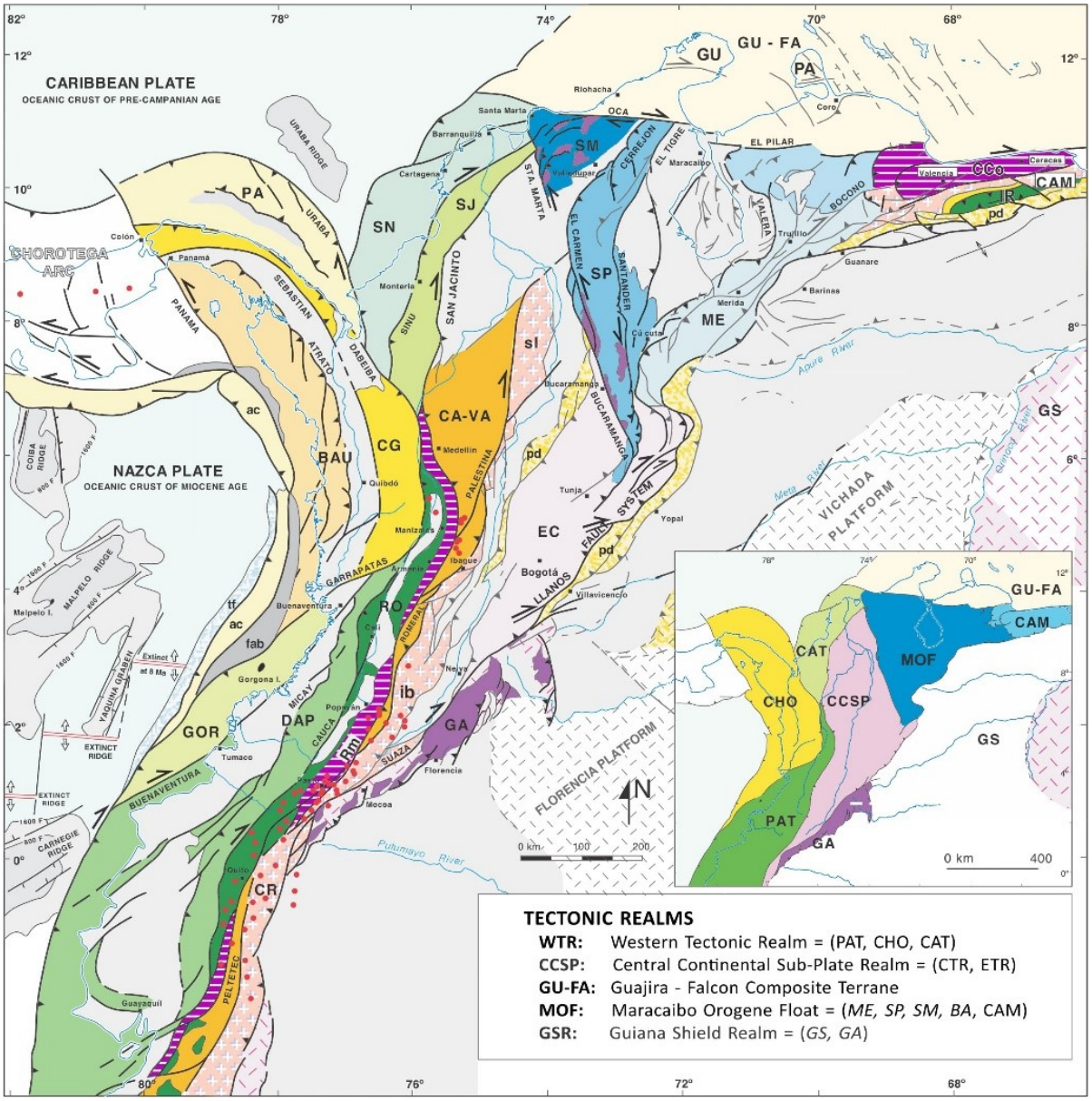

Pacific Terranes (PAT)
(Western Cordillera, s.l.)
GOR = Gorgona
DAP = Dagua-Piñon
Rm = Romeral Melange
RO = Romeral

Choco-Panama Arc (CHO)
BAU = Baudo Mountain
PA = Panama Arc
CG = Cañadas Gordas Litho-Unit

Pacific Colombian Trench
fab = fore arc basin
ac = accretionary prism
tf = trench fill

Western Caribbean (CAT)
SJ = San Jacinto Fault Belt
SN = Sinu Fault Belt

Central Tectonic Realm (CTR)
(Central Cordillera, s.l.)
CA-VA = Cajamarca-Valdivia Litho-Unit
sl = San Lucas Block
Ib = Ibague Block
CR = Cordillera Real

Eastern Tectonic Realm (ETR)
(Eastern Cordillera)
EC = Eastern Cordillera
pd = Piedmonte

Guajira-Falcon Composite Terrane, GU-FA
GU = Guajira Amalgamated Structure
PA = Paraguana Amalgamated Structure

Maracaibo Orogene Float, MOF
ME = Sierra de Merida
SP = Santander Massif-Serrania de Perija
SM = Sierra Nevada de Santa Marta
BA = Baragua and San Luis Range

Eastern Caribbean (CAM)
CCo = Cordillera de la Costa
IR = Interior Range

Guiana Shield Realm, GSR
GS = Guiana Shield
GA = Garson Massif

Figure 1.3. *Lithotectonic and morphostructural map of northwestern South America (modified from Cediel et al., 2003; Cediel, 2019). Quaternary volcanoes represented as red dots.*

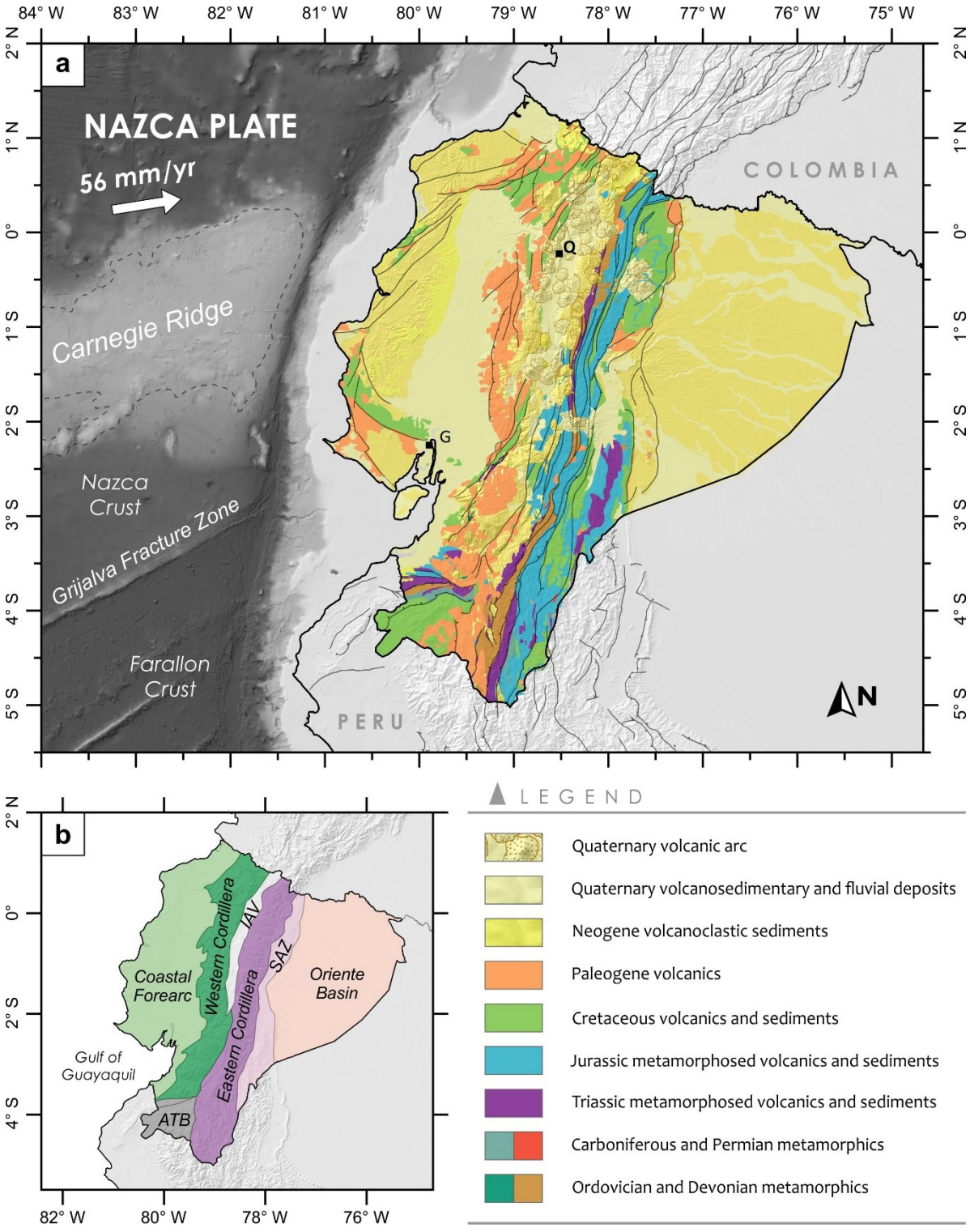

Figure 1.4. a) *Simplified geological map of Ecuador (modified from Egüez et al., 2017). Fault systems and sutures according to Gómez et al. (2019). Main cities are represented with solid squares. Q: Quito; G: Guayaquil. White arrow indicate the direction of the Nazca plate motion relative to South America according to DeMets et al. (2010). b) Schematic map of the Principal geomorphological/geological zones of Ecuador (modified from Aspden et al., 1992b). ATB: Amotape-Tahuín Block; IAV: Inter-Andean Valley; SAV: Sub-Andean Zone.*

1.2.1 Guiana Shield Realm (Guiana Shield and Oriente Foreland Basin)

The Guiana Shield Realm is comprised of the autochthonous units of the Precambrian Guiana Shield overlaid by the sediments of the Oriente foreland Basin (Figure 1.4b). Although the Guiana Shield sequences are not exposed at the surface in Ecuador, lithological columns obtained from exploratory boreholes and seismic sections show that this granite and/or metamorphic basement extends throughout the basin (Díaz et al., 2004), and was dated by Rb-Sr at about 1600 Ma (Litherland et al., 1994). In the southern part of the basin, within the Zamora intrusive complex, there are large 'rafts' of orthogneiss with nematoblastic-migantic texture and quartzites intruded by micro-diorite and pegmatite dikes interpreted as metamorphic roof pendants possibly belonging to the Guiana Shield (Litherland et al., 1994; INIGEMM, 2017).

The Oriente basin recorded several tectonic and sedimentary cycles in the form of a 3 to 5 km thick sequence. The oldest deposits correspond to the metamorphosed and faulted gray shales and quartz sandstones of the Pumboiza Formation (Late Silurian-Lower Devonian), the bioclastic limestones and dolomites of the Macuma Formation (Upper Carboniferous), and the organic matter-rich shales, sandstones and calcites rift deposits of the Santiago Formation (Upper Triassic-Lower Jurassic) (Tschopp, 1953; Díaz et al., 2004; Gaibor et al., 2008). The sequence continues with the Misahuallí Formation (Lower Jurassic-Lower Cretaceous) described as an accumulation of basaltic to rhyolitic lava and pyroclastic deposits which correspond to the effusive expression of the Abitagua and Zamora Jurassic batholiths of the Cordillera Real (Aspden and Litherland, 1992; Romeuf et al., 1995). The Chapiza Formation, a succession of clastic deposits with interspersed dolomites and evaporites to conglomerates in the uppermost levels, is interpreted as the lateral equivalent of the Misahuallí Formation (Jaillard, 1997; Gaibor et al., 2008).

After an intensive period of uplift and erosion, the deposition of the Cretaceous mega sequence began. The Hollín (Aptian-Albian) and Napo (Upper Cretaceous) formations make a thick sequence of sandstones, shales and limestones that represents a succession of several transgression and regression periods in a foreland basin (Barragán et al., 2004). The onset of the Andean orogeny is recorded in the red shales and siltstones of the Tena Formation (Maastrichtian-Paleocene) followed by the fluvial

sediments and conglomerates deposits produced by erosion of the mountain range rise, which are the Tiyuyacu (Eocene), Orteguaza (Oligocene), and the subsequent Neogene formations (Christophoul et al., 2004; Vallejo et al., 2009; Baby et al., 2013). Finally, Neogene tectonics drove the development of the sub-Andean zone (Napo and Cutucú Uplifts), as a back-arc fold-thrust belt located in the western margin of the Oriente Basin (Baby et al., 1999; Gaibor et al., 2008).

1.2.2 Central Tectonic Realm (Para-autochthonous Terrains and Cretaceous Volcanic Arc Fragments)

Litherland et al. (1994) describe the Cordillera Real (CR), as a sequence of Paleozoic-Cretaceous metamorphic rocks that form a series of N-S tectonostratigraphic belts each defined by their homogeneity and stratigraphic continuity (Figure 1.4a).

The Guamote terrain (Lower Jurassic - Cretaceous) is located on the west flank of the CR and is formed by a metasedimentary sequence composed of low-grade quartzites, phyllites and shales (Litherland et al., 1994). To the east, the Alao Terrain conforms a belt of meta-volcanic rocks, such as high-grade greenstones and greenschists (Alao-Paute Unit), and metasedimentary rocks, such as turbidites (Maguazo Unit) and graphite schists (El Pan Unit), interpreted as a Lower Cretaceous volcanic arc (Litherland et al., 1994; Spikings et al., 2015). The western margin of the Alao Terrain is defined by a series of steeply dipping, anastomosed blocks of peridotite, olivine gabbros, spilitised dolerites, basalt and volcanoclastic rocks (Peltetec Unit) that define the Peltetec fault zone (Spikings et al., 2015). Villares et al. (2020) assign this metamorphosed unit to the Upper Triassic.

The Loja terrain forms the central belt of the Cordillera Real. This metamorphic complex includes the pelitic metasediments of the Chigüinda and Agoyán Units (Paleozoic), the S-type granites of the Tres Lagunas Unit (Triasic), the migmatites of the Sabanilla Unit (Triasic) and the amphibolites of the Monte Olivo Unit (Triasic) (Litherland et al., 1994; Spikings et al., 2015, 2000). The same sequence of rocks is observed in the Amotape-Tahuín Block in southwestern Ecuador, with their equivalents being the Tahuín (metasediments), Moromoro (granites and migmatites), and Piedras

(amphibolites) groups (Figure 1.4a). Remarkably, this complex is rotated ~65° clockwise relative to the Cordillera Real (Aspden et al., 1995; Riel et al., 2013; Spikings et al., 2015). The Guamote Terrain and the Peltetec Unit are also present as part of the Mélange Palenque Division and the Raspas Ophiolitic Complex respectively (Aspden et al., 1995).

Lastly, the Salado terrain forms the eastern part of the Cordillera Real. It comprises a folded marginal basin series composed by meta-turbidites and meta-andesites assigned to the Upano unit, pelitic schist of the Cuyuja unit, and marbles and slates of the Cerro Hermoso unit (Lower Cretaceous). The terrain includes the metamorphosed and foliated plutonic rocks of the Azafran and Chingual batholiths (Lower Cretaceous) (Litherland et al., 1994; Spikings et al., 2015). The Cosanga-Méndez Fault separates the terrains of the Cordillera Real from those of the Oriente Basin, where notably, the Cretaceous batholiths remain unfoliated (Litherland et al., 1994).

1.2.2.1 Triassic to Lower Cretaceous Evolution of the Continental Margin

There is general agreement that the rocks of the Loja-Amotape terrain represent a rifting anatexis event that occurred on the northeastern margin of South America (i.e., the Guiana Shield Realm) between 240 and 216 Ma (Figure 1.5; Aspden et al., 1992a; Litherland et al., 1994; Cochrane et al., 2014; Spikings et al., 2015). These non-dismantled sections form the “Loja” and “Amotape” Para-autochthonous Terrains of the Central Tectonic Realm (Cediel et al., 2003; Kennan and Pindell, 2009). The associated marine shelf remained stable until the beginning of the east-dipping subduction of the Farallon plate, which caused the formation of a I- type arc magmatism at about 209 Ma (i.e., Misahuallí arc and Abitagua batholite). The axis of the arc migrated eastward ~190 Ma forming a new volcanic arc that remained active until ~144 Ma (Figure 1.6a). The Salado Terrain sediments were deposited in a marginal basin with sedimentary inputs from the Loja Terraine granitoids and the Misahuallí volcanic arc during Jurassic (Litherland et al., 1994). Nonetheless, data from Spikings et al. (2015) suggest that this basin was formed in a more recent extension stage which also involved the syn-tectonic intrusions of the Azafrán granites during Lower Cretaceous.

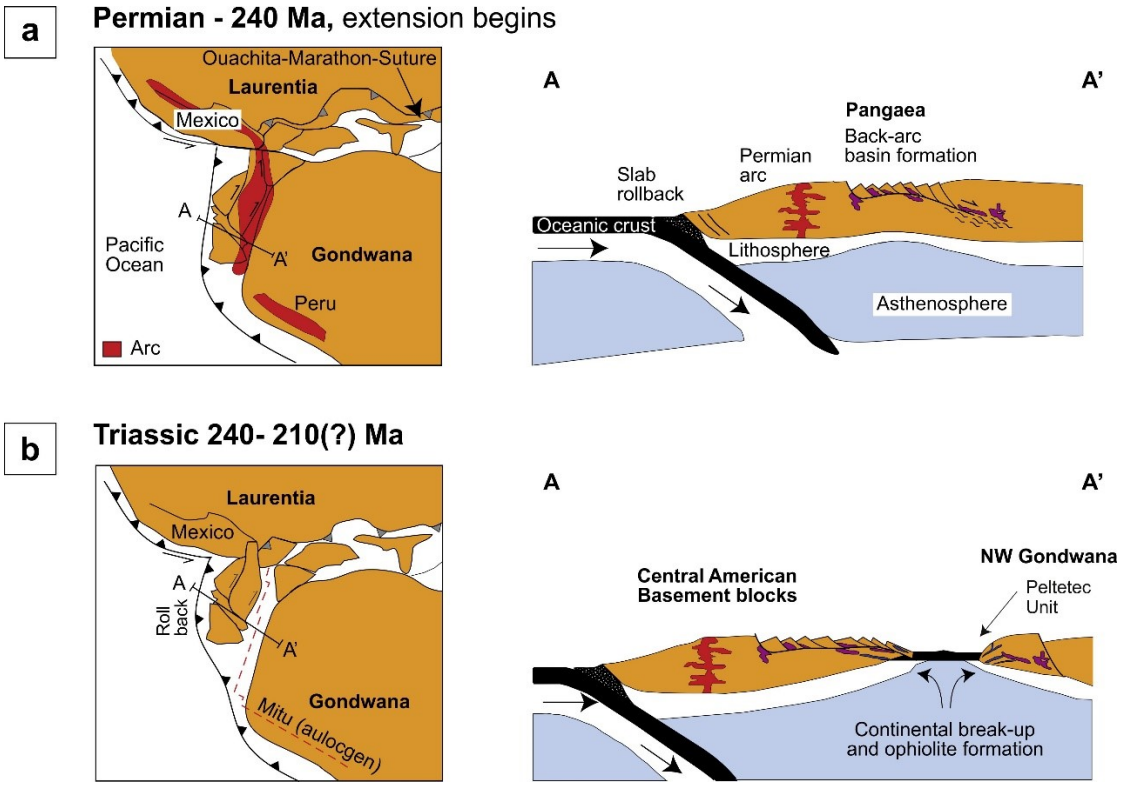

Figure 1.5. *Schematic reconstruction and cross sections for northwestern South America within western Pangaea (modified from Spikings et al., 2015).* ***a)*** *Permian arc and beginning of the Triassic rift.* ***b)*** *Triassic continental break-up.*

The origin of the Alao terrain and its relationship to the Guamote sequence and the Peltetec unit are widely discussed in the literature (e.g., Litherland et al., 1994; Spikings et al., 2015; Villares et al., 2020). It is clear that interpretation depends on answering whether the Peltetec sequence is the result of "in situ" deformation and fragmentation of an accretionary prism, in which the observed eclogites and glaucophane schists have been exhumed during subsequent Andean orogenic events, or if this *mélange* is composed of "allochthonous" fragments generated in an intra-oceanic subduction zone (Kennan and Pindell, 2009). For Litherland et al. (1994), the Alao Terrain defines an allochthonous island arc sequence where the Peltetec unit is interpreted as a subduction complex. This terrain was compressed during the collision/accretion of the allochthonous Chaucha plate where the Guamote sequence is interpreted as a passive margin basin. However, several authors propose that the Alao arc was formed on thin para-allochthonous continental crust during the Early Cretaceous within a marine environment (e.g., Pratt et al., 2005; Villagómez et al., 2011; Spikings et al., 2015). Such hypothesis includes a unique eastward subduction, which, by its rapid extension caused by oceanic trench rollback, may have

rifted some narrow continental slivers thus justifying the position of the Guamote sequence and the origin of the Peltetec unit (Figure 1.6b). Villares et al. (2020) argue that the Peltetec unit is a dismembered ophiolite that was formed earlier during the Upper Triassic rifting (Zircon U-Pb age; ~228 Ma) from a continental back-arc. All these proposals agree about the existence of a compressional episode (i.e., Peltetec Event) that occurred ~ 115 Ma ago (Spikings and Crowhurst, 2004), including the formation of the proto-cordillera, the separation and rotation of the Amotape-Tahuín Block, and the obduction of the Raspas group (Figure 1.6c).

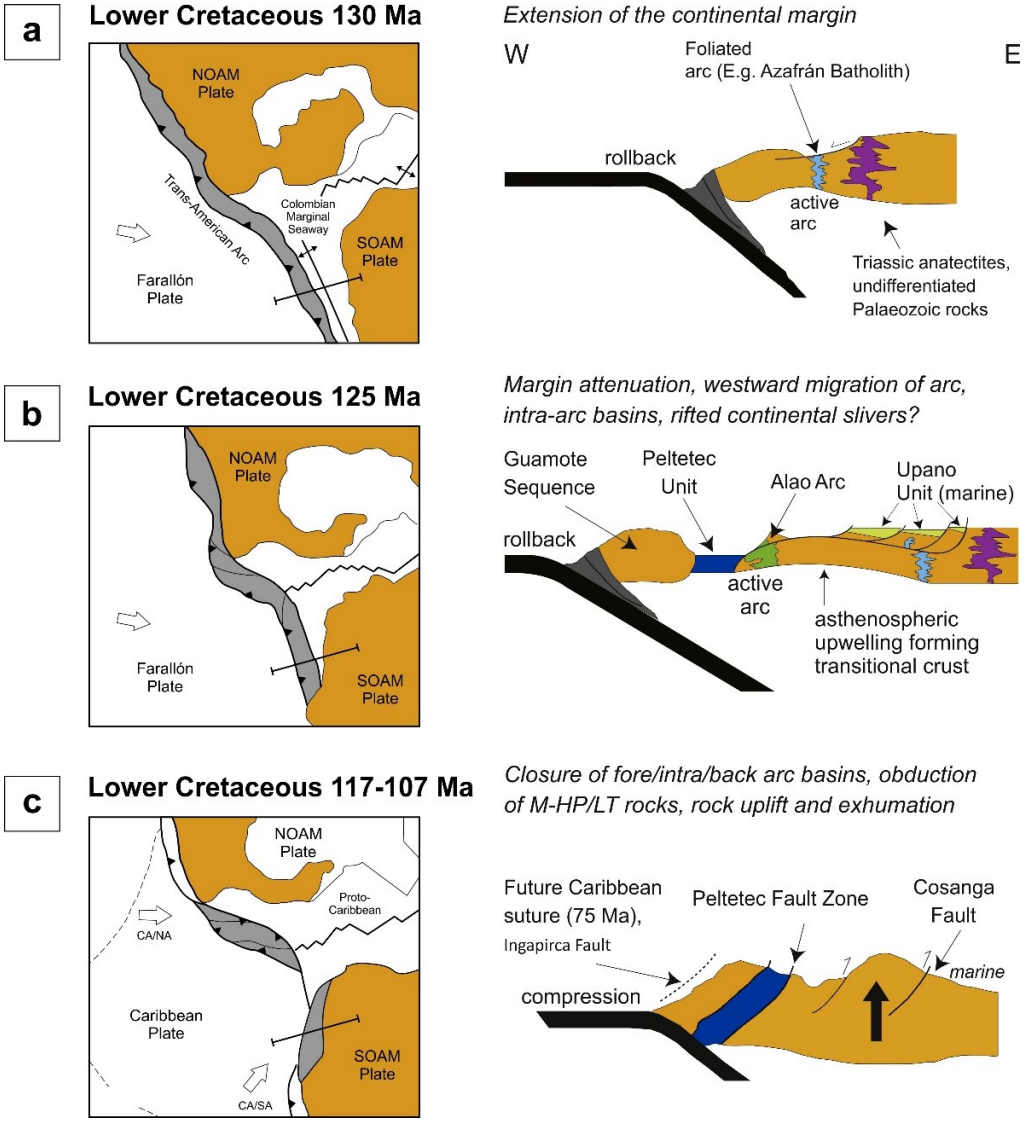

Figure 1.6. *Cretaceous tectonic reconstruction for northwestern South America and schematic cross sections (modified from Villagómez et al., 2011; Spikings et al., 2015). The Early Cretaceous Trans-American Arc is shown as dark gray. NOAM: North American Plate; SOAM: South America. Relative convergence direction: CA/NA: Caribbean Plate/North America; CA/SA: Caribbean Plate/South America.*

1.2.3 Western Tectonic Realm (Western Cordillera and Coastal Forearc)

The Western Tectonic Realm (WTR; Fig. 1.3) includes fragments of oceanic plateaus, aseismic ridges, island arcs and/or ophiolites developed within and/or upon oceanic basement which include the so-called Romeral and Dagua-Piñon Pacific Terraines in the Ecuadorian region (Cediel, 2019). The Romeral terrane contains mafic-ultramafic complexes, ophiolite sequences, and oceanic sediments of probable Late Jurassic (?) and Early Cretaceous age (Cediel et al., 2003) which includes the Peltetec Unit, the Raspas Complex, the Guamote Terrain and the Palenque Mélange. These assemblages are rather related to a marginal mafic basin whose current dispersion may be the result of the strike-slip segmentation of several rifted continental slivers during the accretion of the Caribbean Igneous Province at ~ 75 Ma (Spikings et al., 2015). Therefore, the present study considers the Romeral Terrain as part of the Para-autochthonous Terrains of the Central Tectonic Realm in Ecuador, despite the discussed allochthonous origin of some of its components, and its relationship with the formation/collision of the Caribbean plate (Kennan and Pindell, 2009; Villagómez et al., 2011).

The Dagua-Piñon terrain is formed by basaltic rocks of tholeiitic MORB-type affinity covered by sequences of marine and volcanic arc deposits that morphologically correspond to the Western Cordillera and the Coastal Forearc. The mafic and ultramafic rocks of the Western Cordillera and the overlying volcanic-sedimentary successions form the Pallatanga Block. The Calacalí-Pujili fault system constitutes the eastern limit of the block prior to the Inter-Andean Valley depression (Hughes and Pilatasig, 2002). The Western Cordillera basement is composed of submarine basaltic lavas and dolerites assigned to the Pallatanga Formation, which is interspersed by gabbros, peridotites and dunites from the San Juan unit (Hughes and Bermúdez, 1997; Boland et al., 2000). These rocks are interpreted as an oceanic plateau (geochemically related to the Caribbean Plateau) with its intrusive components (Kerr et al., 2002; Mamberti et al., 2004). A U-Pb crystallitation age of 87.1 ± 1.7 Ma is reported for this ensemble (Vallejo et al., 2006). The overlying sequence begins with the group of volcanic and volcanoclastic rocks of the Rio Cala intra-oceanic arc (Natividad, Rio Cala, Mulaute, and Pilaton units) that were probably formed between the Santonian and Maastrichtian (Vallejo, 2007; Vallejo et al., 2009). On the eastern border of the Western Cordillera, the Yunguilla formation (Campanian -

Maastrichtian), composed of a turbiditic succession of shales and sandstones, is interpreted as a continental forearc basin (Hughes and Pilatasig, 2002).

A second series of Late Maastrichtian-Paleocene marine deposits with important volcanic inputs is reported above the Yunguilla Formation. This volcanic sequence was previously assigned to the Tandapi Unit (Kehrer and van der Kaaden, 1980; Egüez, 1986; Vallejo et al., 2019) and/or in association with the Silante Formation (Vallejo, 2007); however, Vallejo et al. (2019, 2020) reinterpreted this sequence and renames it "Pilalo Unit" which would be correlated with the Sacapalca southern Arc. The overlying Angamarca Group composes a Paleocene-Oligocene turbidite-dominated sedimentary sequence formed by sandstones, conglomerates, and limestone intervals. Together, their component units form a coarsening-upward basin fill sequence, which shows a progradation from submarine fan to fan-delta with continental inputs (Hughes and Pilatasig, 2002). The end of the sequence is composed by a third series of volcanic deposits related to the Saraguro - San Juan Lachas Arc (Oligocene), where its erosion sediments are identified as the Silante Formation (Oligocene-Miocene) (McCourt et al., 1997; Dunkley and Gaibor, 1997; Pratt et al., 1997; Boland et al., 2000; Vallejo, 2007; Vallejo et al., 2020). The Neogene - Quaternary volcanism (discussed in section 1.3) covers the Miocene deposits.

To the east, the Coastal Forearc (Fig. 1.3) contains a sequence of marine deposits that were formed over a basement made up of tholeiitic basaltic and basalt-andesitic lavas assigned to the Piñon Formation (Jaillard et al., 1995). Geochemical data suggest that the Piñon Formation has an oceanic plateau origin and that it is probably related to the Pallatanga Unit (Kerr et al., 2002; Luzieux et al., 2006). Furthermore, Luzieux et al. (2006) propose that both units derive from a common oceanic block extruded above a mantle plume between 90 and 87 Ma at an equatorial latitude (i.e., Caribbean Large Igneous Province). The U-Pb zircon ages obtained from crosscutting intrusions (98.4 ± 1.7 Ma to 90 ± 1.6 Ma) suggest that the Piñón Formation is probably older and therefore corresponds to one of the oldest phases of the Caribbean Plateau (Vallejo et al., 2019). The $^{40}Ar/^{39}Ar$ ages and geochemical data from the submarine Beata Ridge, located in the modern central Caribbean Plate, support the idea that the Galapagos mantle plume was responsible for the formation of the Caribbean Large Igneous Province

(Dürkefälden et al., 2019). This ridge was created during a main extrusive magmatic activity stage from 95 to 83 Ma followed by a less voluminous mainly intrusive stage from 81 to 71 Ma (Révillon et al., 2000; Dürkefälden et al., 2019).

Over the basement basalts lies an association of intra-oceanic island arc rocks of Campanian age that include basaltic flows, hyaloclastites, pillow lavas, and dikes (San Lorenzo and Las Orquideas Formations) conjugated with debris flow and volcanoclastic turbidites series (Cayo and Calentura Formations) (Jaillard et al., 1995; Reynaud et al., 1999; Luzieux et al., 2006). Over them, the basin was filled from Maastrichtian to Eocene by turbidic deposits such as limestones, lutites, siltstones, sandstones, and conglomerates (i.e., Guayaquil, Azúcar, San Eduardo and Ancón formations). The Zapotal Formation (Oligocene) marks the transition from the accretionary and post-accretionary system to the forearc basin depocenter. Subsequently, the Miocene formations constitute forearc sediment series that pass from shallow water environments to littoral facies (Luzieux et al., 2006; Witt et al., 2006).

Lastly, the Macuchi volcanic rocks form the western border of the Western Cordillera next to the coastal basin. The unit is composed of pillow lavas, hyaloclastites, volcanic breccias, and turbidites of basaltic to andesitic composition that form a succession of at least 2000 m in thickness which are separated from the Angamarca Group to the east by the Chimbo-Toachi fault (Aguirre and Atherton, 1987; Hughes and Bermúdez, 1997; Hughes and Pilatasig, 2002; Kerr et al., 2002). The age of this succession is interpreted as Paleocene(?)-Eocene (Egüez, 1986; Hughes and Pilatasig, 2002; Vallejo, 2007).

1.2.3.1 Upper Cretaceous to Neogene Events Related to the Accreted Western Terranes

Lorcan Kennan & Pindell (2009) express that only a simple model can adequately explain the conjugation of terrains and volcanic arcs found in the Northern Andes without assuming the existence of multiple intra-oceanic plate boundaries (e.g., Lebras et al., 1987; Hughes and Pilatasig, 2002; Kerr et al., 2002; Kerr and Tarney, 2005). This unique model suggests the interaction of only three plates

(South America, Caribbean and Farallon) and two volcanic arcs (at the leading and trailing edges of the Caribbean Plate) during the Late Cretaceous to Middle Cenozoic (Fig. 1.7).

The proposal by Villagómez et al. (2011) describes the initial stages of the interaction between the Farallon and the South American plates during the formation of the para-autochthonous terrains of the Central Tectonic Realm, prior to the development of the Caribbean Plate (see section 1.2.2.1). These terrains were compressed/accreted during the Peltetec event (117-107 Ma) coinciding with the opening of the South Atlantic Ocean, which drove rapid westward displacement of the South American Plate (Figure 1.6c).

Stratigraphic, geochemical and geochronological evidence demonstrates that the Pallatanga and Piñon blocks have a common origin on the Caribbean Oceanic Plateau formed from 100 to 90 Ma (Luzieux et al., 2006). The volcanic deposits lying above the basaltic basement of the WTR show the presence of an intra-oceanic island arc between 98 Ma and 85 Ma (i.e., Rio Cala-San Lorenzo Arc) (Vallejo et al., 2019). In contrast, Eastern Cordillera plutons and detrital zircon U-Pb ages suggest the presence of a synchronic volcanic arc formed along the continental margin between 90 to 70 Ma (Aspden et al., 1992b; Vallejo et al., 2019). This oceanic-continental arc association is also described in the Western Cordillera of Colombia. Therefore, Villagómez et al. (2011) propose the existence of a double divergent subduction system between the South American margin and the converging Caribbean Plateau which consumed the oceanic crust located between them. The collision of the Caribbean Large Igneous Province took place between 75 and 70 Ma according to sedimentological and thermochronometric data that record (1) the exhumation of the continental margin (Spikings et al., 2010), (2) the arrival of continental detritic materials to the coastal basins (Luzieux et al., 2006; Witt et al., 2006), and (3) the appearance of red beds in the Oriente Basin (Barragán et al., 2004). Luzieux et al. (2006) argue that the fragmentation of the oceanic plateau during the collision resulted in the formation of the distinct structural blocks of western Ecuador, Colombia, and Venezuela (Fig. 1.7).

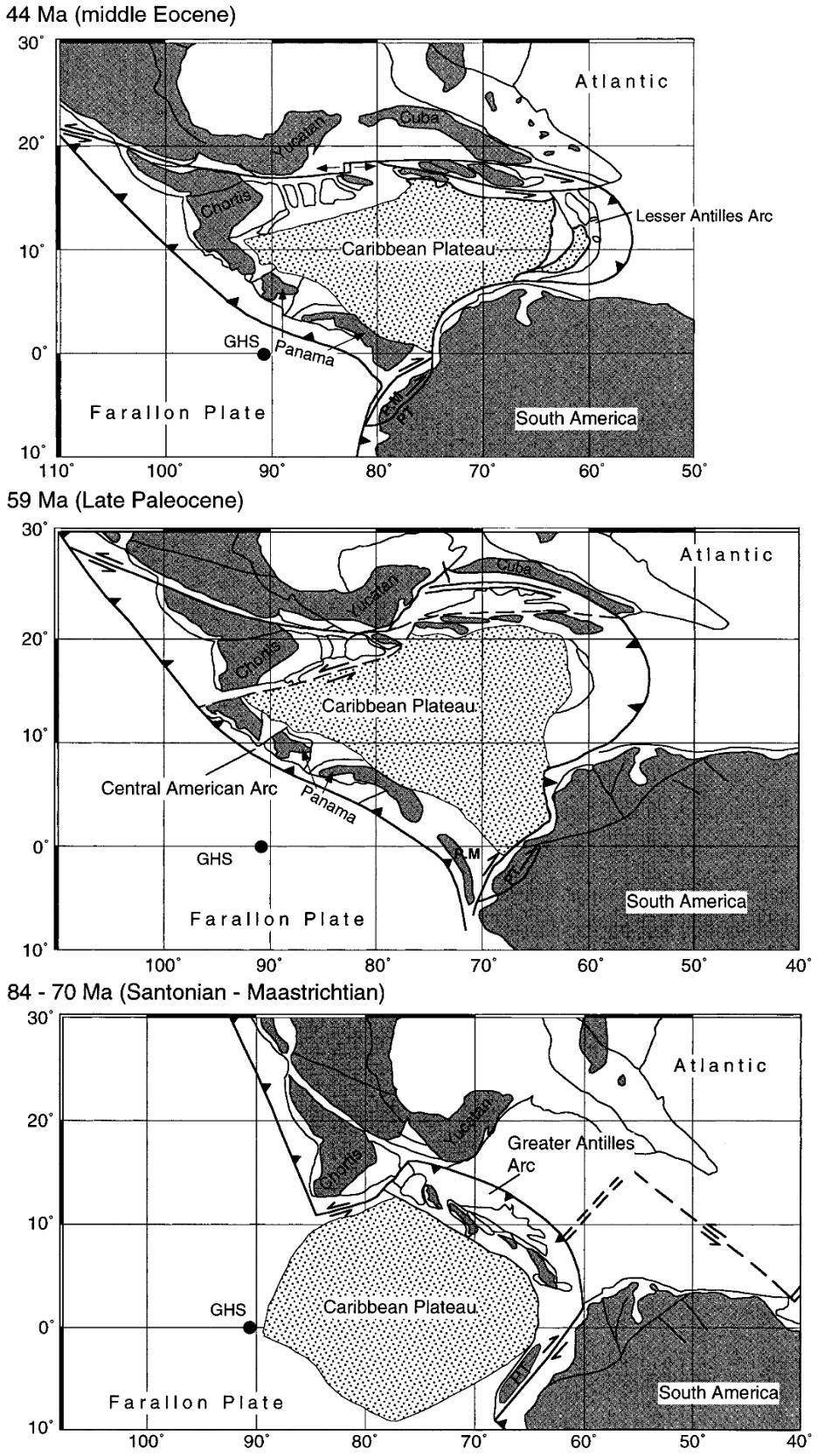

Figure 1.7. *Reconstruction of the Caribbean Plateau from 84 to 44 Ma (Spikings et al., 2001). GHS: Galapagos Hot Spot; PM: Piñon - Macuchi Block; PT: Pallatanga Terrane.*

Finally, subduction below the accreted terrains of the Caribbean Igneous Province led to the formation of the Tandapi (Paleocene), Macuchi (Eocene), San Juan Lachas-Saraguro (Oligocene), and Zumbagua (Neogene) volcanic arcs (Figure 1.8). The created sediments gradually filled the Coastal Forearc, changing progressively from deep turbidic platform environments to shallow water ones and then to littoral facies (Witt et al., 2006, 2019). Strike-slip movement along the suture zones led to the creation of pull-apart basins in the Western Cordillera until the Eocene when a process of exhumation of the mountain range is registered (Toro, 2007; Spikings et al., 2010). Simultaneously, important sequences of fluvial sediments and conglomerates derived from the Andean uplift were deposited near the new mountain range in Oriente and Coastal Basins (Christophoul et al., 2004; Baby et al., 2013).

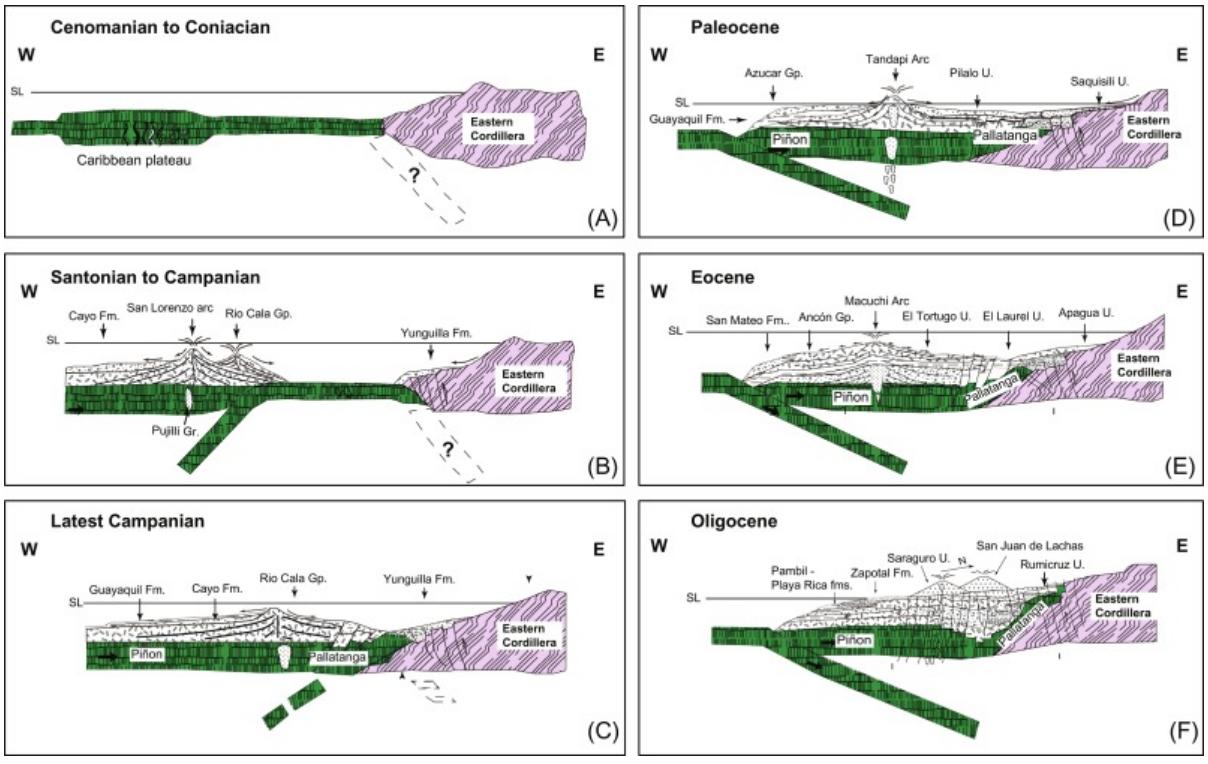

Figure 1.8. *paleogeographic reconstruction showing Late Cretaceous to Oligocene evolution of the Coastal, Western Cordillera, and Eastern Cordillera regions (Vallejo et al., 2019). a) Extrusion of the Caribbean Plateau in the Pacific region. b) Westward subduction below the Caribbean Plateau and formation of Island arc sequences. c) Accretion of the Caribbean Plateau. d) Establishment of the Tandapi volcanic arc of the Western Cordillera. e) The Macuchi arc formed on top of the accreted oceanic plateau. f) Oligocene upward shallowing and establishment of the Saraguro and San Juan de Lachas volcanic arcs.*

1.2.4 Nazca Plate Domain

1.2.4.1 Rupture of an ancient oceanic plate

The Cocos and Nazca plates were created after the fragmentation of the Farallon plate: an ancient lithospheric fragment formed along the eastern margin of the East Pacific Rise (EPR) (Mayes et al., 1990). Magnetic profiles and multibeam bathymetry swaths show that the rupture zone started in the EPR and extended 3000 km along the Farallon plate passing close to the Galapagos hotspot, during a process that occurred at ~22.7 Ma (Chron 6B) (Lonsdale, 2005; Meschede and Barckhausen, 2001). The volcanic activity along the early rupture zones created ridges of 1-2 km high (e.g., Alvarado and Sarmiento Ridges) that later formed the conjugated margins of the new Cocos and Nazca plates as the rift zone progressed (i.e., Hernando and Grijalva Scarps). This fragmentation episode is considered a major plate reorganization that took place during the first 1-2 Ma prior to the final rupture (Lonsdale, 2005; Barckhausen et al., 2008). As a consequence, the northeastern absolute motion vector of the Farallon plate was decomposed into a North vector for the Cocos plate and an East vector for the Nazca plate (Somoza, 1998; Meschede and Barckhausen, 2001; LaFemina et al., 2009; Seton et al., 2012), as is reflected in the reorientation of the Nazca plate hotspot tracks (e.g., Bello-González et al., 2018). The rupture was probably related to the divergent slab-pull stresses originated by the disjunction in the subduction zones of Central America and South America, and to the weakening of the older parts of the plate by the Galapagos hotspot trail (Lonsdale, 2005; Barckhausen et al., 2008).

The breakup of the Farallon plate led to the formation of a complex spreading zone in the opening area (Hey, 1977). The paleogeographic reconstructions shown in Figure 1.9 suggest the presence of at least three spreading systems (Meschede and Barckhausen, 2001) formed (1) at the beginning of the rift opening at ~23 Ma, (2) at the end of a major plate reorganization period at ~19.5 Ma (Lonsdale, 2005; Barckhausen et al., 2008), and (3) at the beginning of a minor plate reorganization period occurring at 14.7 Ma and that culminated in the capture of the northeastern Panama basin (Marpelo microplate) by the Nazca plate at ~9 Ma ago (Morell, 2015). The interaction of these spreading systems with the northern side of the Galapagos hotspot resulted in the formation of the Marpelo-Coiba

(~10-18 Ma) and Cocos (~10 Ma - present) ridges, while the Carnegie ridge (~18 – present) was formed to the south (Werner et al., 2003; Marcaillou et al., 2006; O'Connor et al., 2007; Morell, 2015).

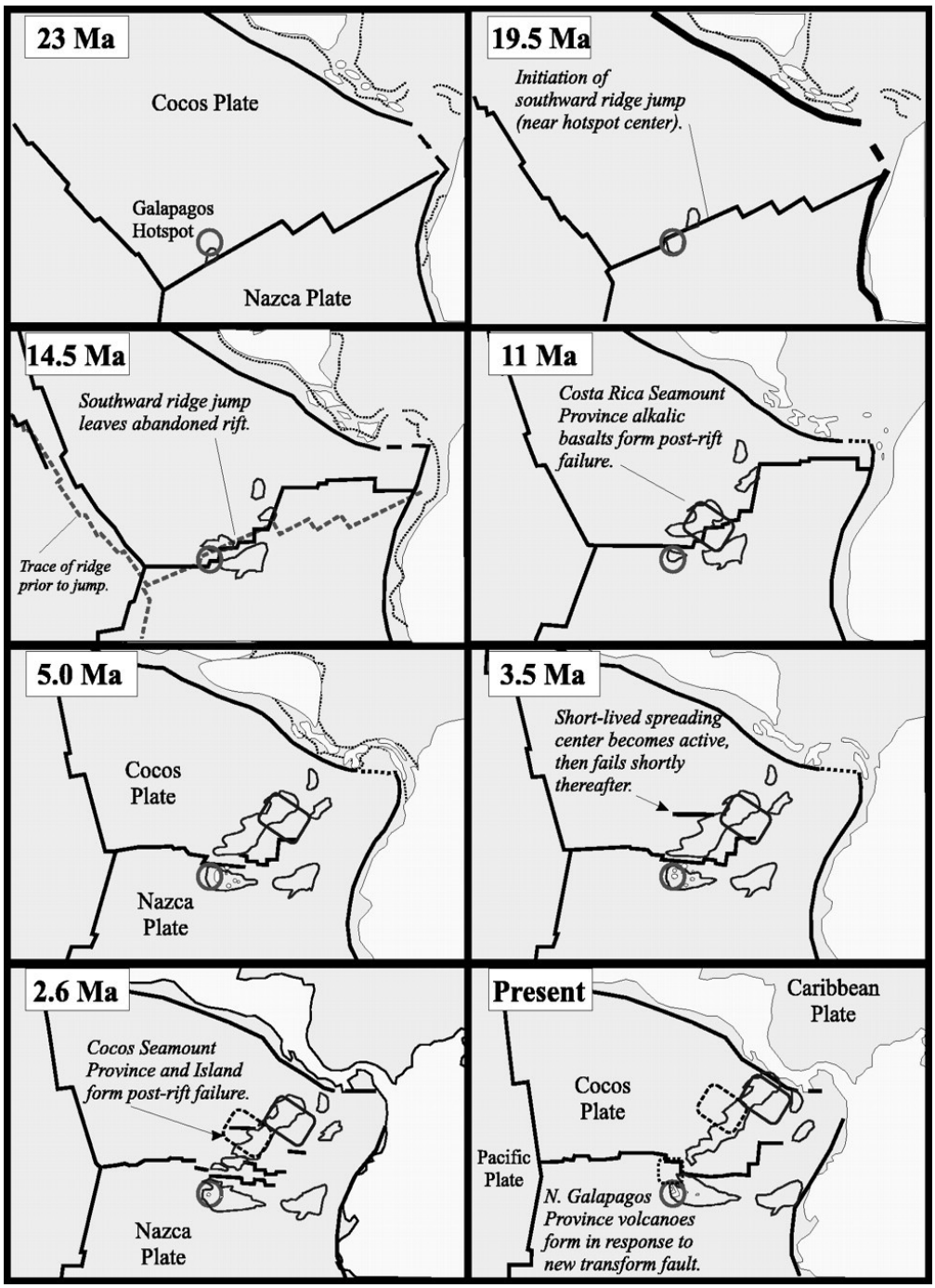

Figure 1.9. *Paleogeographic reconstructions of the plate tectonic evolution of the Cocos and Nazca plates according to Meschede and Barckhausen (2000), modified by Harpp et al., (2005).*

1.2.4.2 Nazca Slab Geometry

Nowadays, the northwestern boundary of the Nazca plate is constituted to the south by the older crust of the Farallon plate (> 30 Ma), and to the north by the younger crust created by the Cocos-Nazca spreading centers (10-23 Ma) overlaid by the 2000 m high Carnegie Ridge. Both sections are separated by the 2000 m high Grijalva Scarp (Fig. 1.10; Lonsdale, 2005). Such configuration of the Nazca plate results in a significant contrast in density, buoyancy, thickness and temperature between both crusts (Yepes et al., 2016).

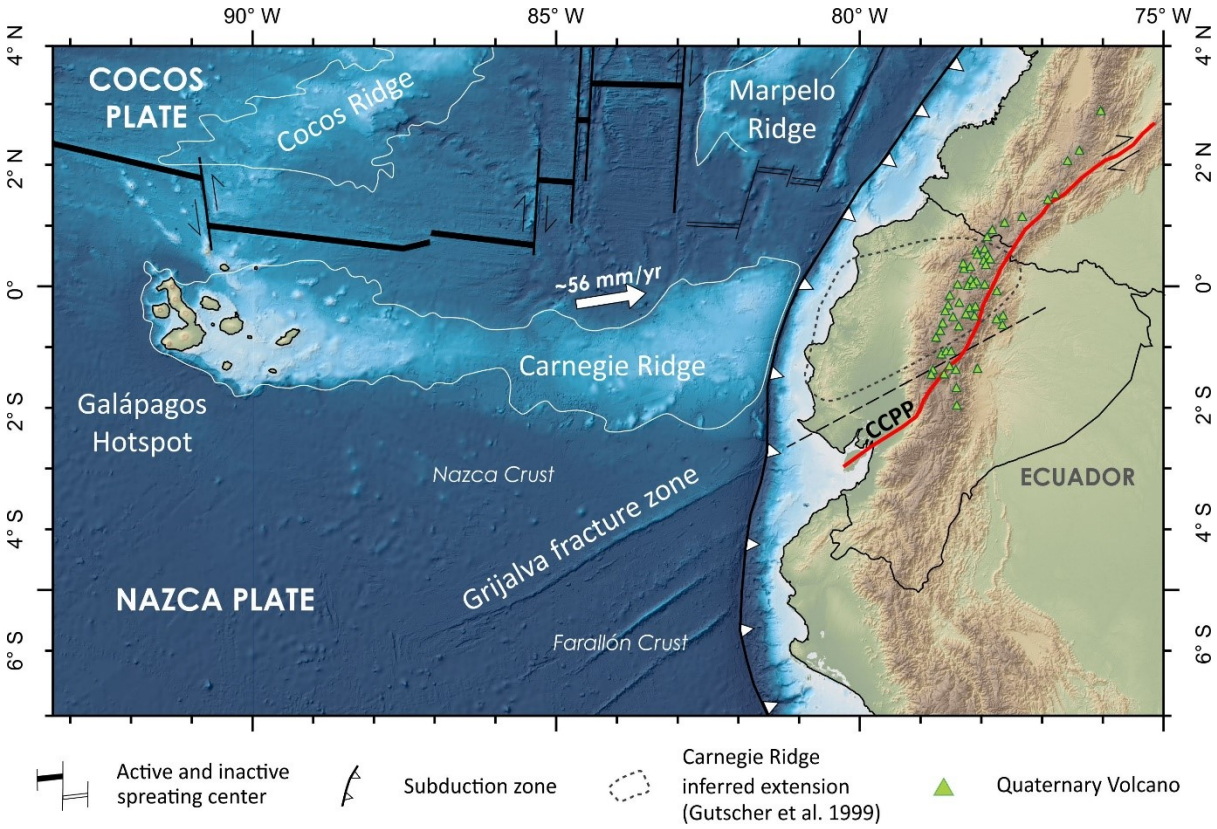

Figure 1.10. *Ecuadorian geodynamic setting (Modified from Gutscher et al., 1999). Bold arrow indicates the direction of the Nazca plate motion relative to South America according to DeMets et al. (2010). CCPP: Chingual-Cosanga-Pallatanga-Puná Fault System*

After entering into subduction, the Nazca plate describes a complex seismicity zone leading to multiple geometry shapes at depth (Portner et al., 2020). In short, the high intermediate-depth seismicity generated by the older Farallon crust defines a shallow flat slab, while northern earthquake epicenters become deeper near the projection of the Grijalva scarp until almost disappearing north of it (Gutscher

et al., 2000b; Tavera and Buforn, 2001; Yepes et al., 2016). Intermediate-depth seismicity reappears faintly north of latitude 2°N, where the younger Nazca crust subducts at 30°-40° (Taboada et al., 2000; Pedraza Garcia et al., 2007; Vargas and Mann, 2013).

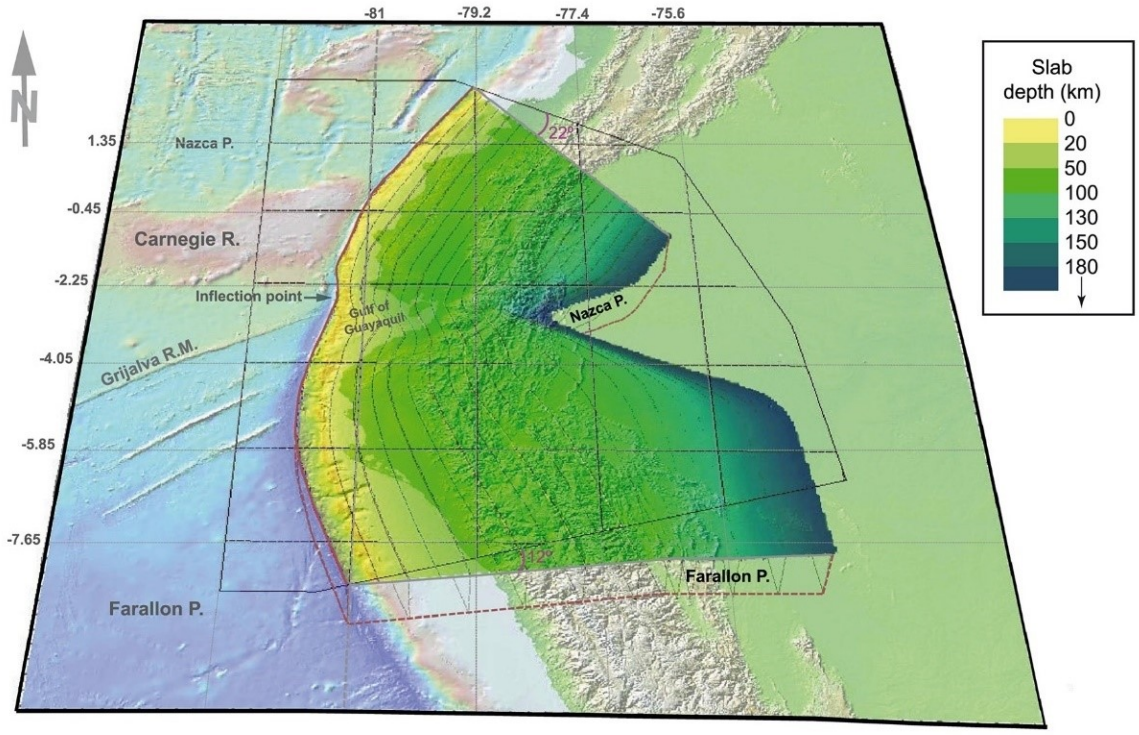

Figure 1.11. *South to north perspective showing the different dipping angles of Farallon and Nazca plates according to Yepes et al. (2016). Slab bending represented as a hypothetical contorted surface. Present-day position of the Grijalva rifted margin at the trench coincides with a noticeable inflection point of the trench axis.*

The absence of intermediate-depth seismicity in Ecuador was previously justified by the existence of a flat slab bounded by tears on its northern and southern flanks (Gutscher et al., 1999). A detailed review of local seismicity disagreed with this hypothesis and demonstrated the existence of a coherent slab subducting at 25°-35° forming a continuous Wadati-Benioff plane up to 300 km landward from the trench (Guillier et al., 2001; Manchuel et al., 2011). Moreover, the presence of tears is not required to justify the steep REE patterns observed in differentiated volcanic rocks of the Ecuadorian arc (Kay et al., 2009; Michaud et al., 2009). Thus, the transition between the flat-slab and steep-slab segments, coincident with the prolongation of the Grijalva scarp, may be defined by a contortion or flexure zone of a coherent slab where the focal point is defined by the curvature of the continental

margin as shown in Figure 1.11 (Yepes et al., 2016; Portner et al., 2020). The convergence vector between the Nazca and South American plates at equatorial latitude (N83°, 56 mm yr^{-1}; Kendrick et al., 2003) does not exhibit significant variations since the Pliocene (Quinteros and Sobolev, 2013; Bello-González et al., 2018). Moreover, the Grijalva Scarp shows an apparent southward migration due to the difference in its orientation (N60°) with respect to the trench (N15-20°) (Collot et al., 2009).

As referred to in previous sections, the presence of seismic ridges has been interpreted as a contributing factor to the formation of long-lived flat slabs; however, the Carnegie Ridge extension at depth may still be insufficient to affect the slab geometry (Espurt et al., 2008). The length of the Galapagos hotspot trail is widely debated due to the lack of conclusive evidence to reconstruct the precise paleogeography of the spreading zone between 20 and 25 Ma (Michaud et al., 2009). However, the coincidence of the rupture zone and the hot spot locations, combined with the change in absolute movement of the Nazca plate from northeastward to eastward direction occurring after the separation of the Farallon plate, implies that 1) the Carnegie Ridge probably does not extend more than 400 km eastward of the current subduction zone, and that 2) the hotspot trace remained close to the margin of the new spreading center (Lonsdale, 2005). Kinematic reconstructions suggest that the Carnegie Ridge and the Grijalva Fracture Zone have been entered into subduction at 4-5 Ma penetrating between 300-400 km onshore (Gutscher et al., 1999; Lonsdale, 2005; Collot et al., 2009; Michaud et al., 2009). Nevertheless, the high-temperature flow environment that created the ridge and the young age of the underlaying crust could explain the lack of intermediate-depth seismicity. Effectively, higher temperatures increase the ductility of the ocean crust thus reducing its potential to generate earthquakes at high depths (Syracuse et al., 2010; Yepes et al., 2016).

1.2.5 Geodynamics of The North Andean Sliver

In Ecuador, the multiple episodes of fragmentation and accretion of terrains created several suture-fault zones that separate the lithotectonic units belonging to the discussed realms. In particular, the Cosanga-Mendez, Peltetec, Calacalí-Pujilí and Chimbo-Toachi fault systems are identified as main suture zones due to the high contrast between the lithological groups located at their boundaries (Fig. 1.12). Such differences allowed the development of the evolutionary models previously described (see Sections 1.2.2.1 and 1.2.3.1). More recently, the plate reorganization process occurred at the beginning of the Miocene resulted in a change in the stress regime at the continental margin causing, for example, the rapid exhumation and deformation of the Cordillera Real (Spikings et al., 2000, 2001, 2010), the development of the Napo and Cutucu Uplifts (Baby et al., 1999; Bès de Berc et al., 2005; Gaibor et al., 2008), and the formation of transpressive structures in the Western Tectonic Realm (Alvarado et al., 2016). The initial deformation systems resulted in the creation of NE trending dextral faults as well as the synchronous uplift of both mountain ranges at the end of the Miocene. The deformation zone progressively migrated eastwards abandoning the structures located in the west. The arrangement of the resulting fault systems seems not to have systematically reactivated the suture zones created prior to the Miocene. In fact, it tended to form new structures affecting several lithotectonic units as they adjusted the stresses generated by the transpressive regime (Alvarado et al., 2016). The opening of the Gulf of Guayaquil, a Pleistocene pull-apart basin located near the stress deflection point of the continental margin, is interpreted as the result of the northeastern migration of the North Andean Sliver given its progressive decoupling from the stable South American Plate (Witt and Bourgois, 2010).

The arrangement of the active fault systems (Fig. 1.12), the analysis of their seismicity and motion, and GPS data show that the boundary of the North Andean Sliver is currently formed by the Chingual-Cosanga-Pallatanga-Puna fault system (CCPP) which extends to Colombia by the Afiladores-Sibundoy-Algeciras system. The Quito-Latacunga fault system, located to the west of the CCPP, creates a microblock mostly integrated by the Inter-Andean valley. The origin of this fault system would correspond to a previous evolutionary stage whose deformation is being transferred along its eastern

border. Finally, GPS data present the NAS as a quasi-rigid continental sliver moving northeast at 8-10 mm yr^{-1} (Alvarado et al., 2016).

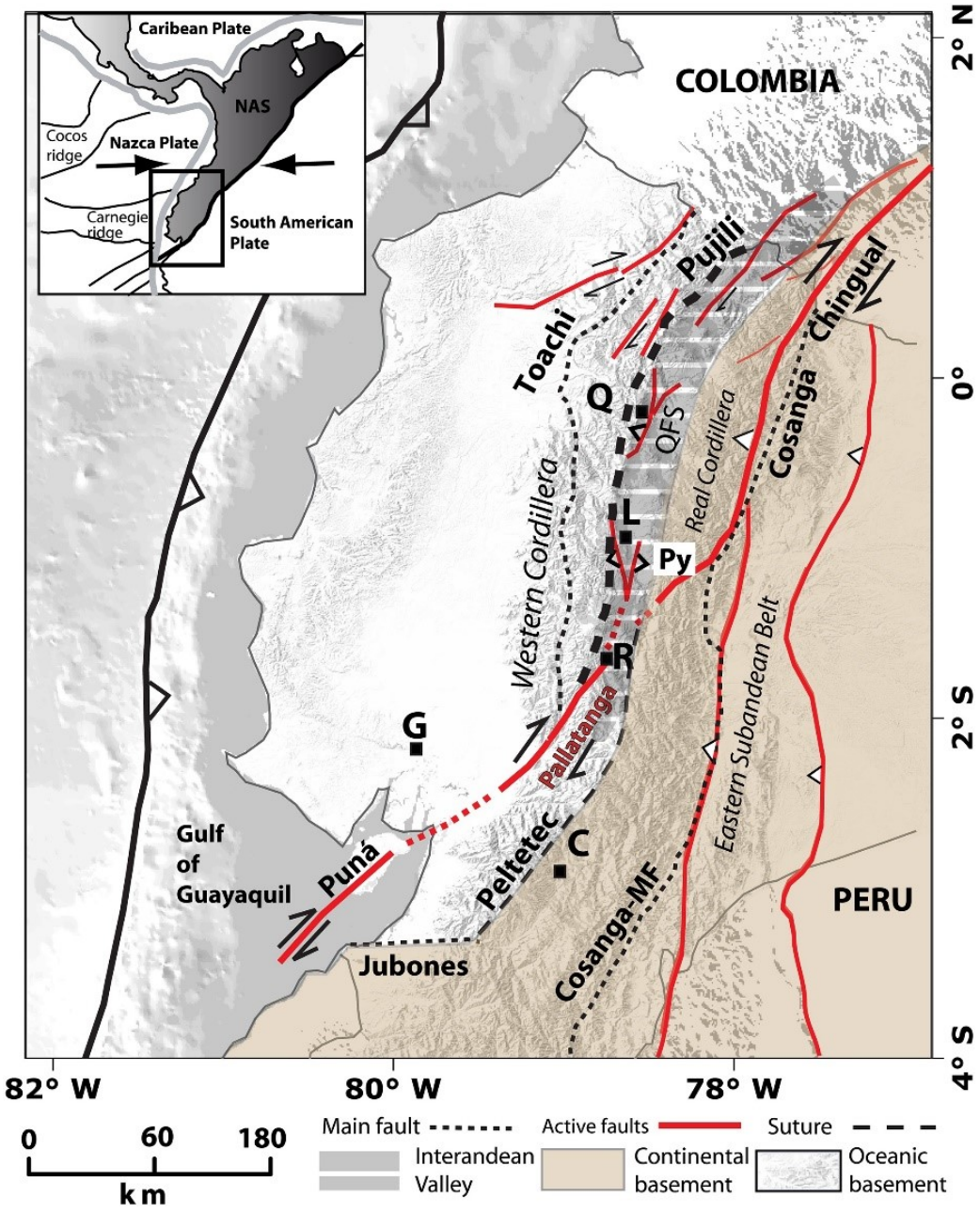

Figure 1.12. *Tectonic map of Ecuador according to Alvarado et al. (2016). Major fault segments are represented in continuous red lines. Principal sutures zones are illustrated in black dotted lines. Cosanga-MF; Peltetec suture: Peltetec; Pujilí Melange Suture: Pujili; Jubones Fault: Jubones; Toachi shear zone: Toachi; Py: Pisayambo zone. QFS: Quito active Fault System. Cities: Q: Quito; L: Latacunga; C: Cuenca; R: Riobamba; G: Guayaquil.*

1.3 Ecuadorian volcanic arc

1.3.1 Previous stages: the Neogene volcanism

Following the accretion of the oceanic terrains of the Western Tectonic Realm (Fig. 1.3), a new continental margin became active with an uninterrupted subduction process. Consequently, several Neogene intrusive systems, volcanic units, and volcanoclastic sediments were formed in the Ecuadorian Andes (Fig. 1.13). A summary of the Neogene volcanism is presented bellow using a chronological approach, although their stratigraphic correlations and timing are still debated.

The oldest Neogene volcanic stages (34-30 Ma and 26-19 Ma) belong to the Loma Blanca (40-29 Ma) and Saraguro (30-19 Ma) formations, described in southern Ecuador, and San Juan de Lachas (36-20 Ma) to the north. These volcano-sedimentary deposits are associated to a common volcanic arc (Hungerbühler et al., 2002; Vallejo et al., 2019). The Silante Formation (Early Miocene) lies in discordance in the east of the north-central Western Cordillera and was probably formed by large fluvial fans with important volcanic inputs from the San Juan de Lachas arc (Vallejo et al., 2020, 2019). Zircon Fission Track (ZFT) ages between 25 and 16 Ma are reported for the Silante Formation (Spikings et al., 2005; Vallejo et al., 2020).

Sporadic radiometric ages from different minor volcanic groups suggest the presence of a second stage that occurred at 17-14 Ma. In particular: the lowest section of Santa Isabel formation (ZFT: 18.8 ± 2.2 to 15.9 ± 1.6 Ma) composed of andesite lava flows and breccias located in the Girón–Santa Isabel area (Hungerbühler et al., 2002), the Quinara formation (ZFT: 15.1 ± 1.6 to 14.2 ± 3.4 Ma) interpreted as the remains of a local volcanic vent located in the Malacatos-Vilcabamba area (Hungerbühler et al., 2002), the Paccha-Cordoncillo granitoid intrusion (K-Ar: 16.89 ± 0.16 Ma) (Pratt et al., 1997) and the oldest portions of the Chaucha batholith (K-Ar: 13.3 ± 0.5 to 12.0 ± 0.6 Ma, and ZFT: 14.84 ± 0.07 Ma) exposed adjacent to the Calacalí–Pujili–Pallatanga fault zone (Schütte et al., 2010), all of them in southern Ecuador; El Corazon granite pluton (K-Ar: 16.1 ± 0.2 to 14.1 ± 0.3 Ma) located in south-central Western Cordillera; and the Apuela batholih (K-Ar: 16.5 ± 1.1 to 13.0 ± 0.6 Ma, and ZFT: 12.87 ± 0.08 Ma) located in northernmost Ecuador (Boland et al., 2000; Schütte et al., 2010).

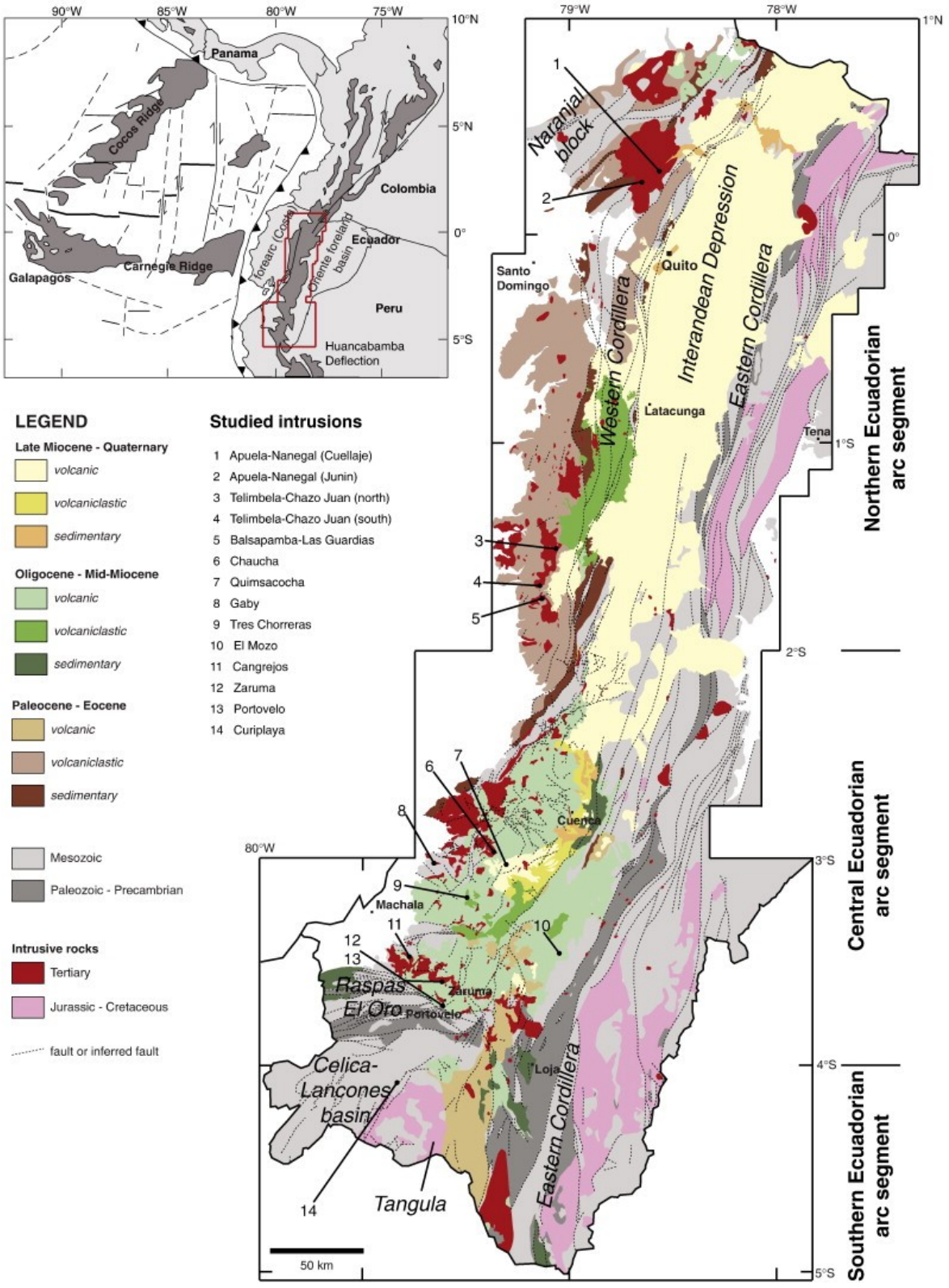

Figure 1.13. *Simplified geological map of the Andean region of Ecuador, focusing on Cenozoic arc magmatic units according to Schütte et al., (2010).*

Several lacustrine, alluvial, and fluvial units with important volcanic-clastic inputs lie in discordance over the volcanic deposits of the earliest stages. In southern Ecuador, these units constitute the intra-mountain basin deposits of Malacatos, Loja, Nabón, Girón-Santa Isabel and Cuenca areas (e.g., Bristow, 1973; Steinmann et al., 1999; Hungerbühler et al., 2002). Schütte et al. (2010) interpret these sequences as resulting from an extensional subsidence in the southern Inter-Andean region (occurred between 15 Ma and 10 Ma) which caused an ingression of shallow seas into the Cuenca and Loja Embayments. Then, a period of compression and tectonic inversion took place around 10-9 Ma when several isolated intra-mountain basins were formed and filled in up to 5 Ma. In central Ecuador, the Zumbagua Group forms a very extensive volcanic and volcanic-sedimentary sequence located on the eastern margin of the Western Cordillera. These sequences were mainly formed in intra-mountainous lacustrine and fluvial basins (Hughes and Bermúdez, 1997; McCourt et al., 1997). The Zumbahua Group was dated by zircon fission-tracks from 15.5 ± 1.2 to 8.4 ± 1.2 Ma (Hughes and Bermúdez, 1997); nonetheless, new data obtained by Vallejo et al. (2019) suggest that the group could be formed at 12-6 Ma. The lack of pre-Miocene grains in the analyzed Zumbahua samples indicates a dominance of magmatic arc sources. Further north, a diorite intrusive located east of Corazón volcano yielded a ZFT of 8.7 ± 0.7 Ma (Spikings et al., 2005). To the north of Cotacachi volcano, andesitic and dacitic lavas belonging to the Pulumbura sequences were dated by $^{40}Ar/^{39}Ar$ at 12.16 ± 1.86 and 11.55 ± 0.22 Ma (Chiaradia et al., 2021).

The third volcanic stage occurred at ca. 8-5 Ma. The Tarqui formation (ZFT: 6.8 ± 0.8 to 5.1 ± 0.6 Ma) covers large areas of southern Ecuador and is formed by andesitic to dacitic breccias, ash flows, ignimbrites, and pyroclastic flows (Bristow, 1973; Steinmann, 1997; Hungerbühler et al., 2002). Similar ages were obtained for the diorite intrusive of Cojitambo (K-Ar: 7.1 ± 0.3 to 5.2 ± 0.2 Ma, and ZFT: 7.8 ± 0.8 Ma) (Barberi et al., 1988; Lavenu et al., 1992; Steinmann et al., 1999) and for the early phase-3 stages of the Quimsacocha Caldera (ZFT: 5.2 ± 0.3 to 4.9 ± 0.3 Ma, and Z-TIMS: 7.13 ± 0.23 Ma) (Beate et al., 2001; Schütte et al., 2010), both located in the Cuenca area. Remarkably, there are no younger volcanic deposits reporter in southern Ecuador. The Cisarán formation, also identified as Alausí formation, covers the south-central part of Ecuador (K-Ar: 8.12 ± 0.10 to 7.15 ±

0.38 Ma, and ZFT: 6.9 ± 0.7 to 6.8 ± 0.8 Ma). It corresponds to a sequence of andesitic to dacitic lavas covered by breccias and pyroclastic deposits (Barberi et al., 1988; Lavenu et al., 1996; Dunkley and Gaibor, 1997; Steinmann, 1997). In the north-central region, a microtonalite intrusive in the Zumbahua Group was dated at 6.27 ± 0.17 Ma (K-Ar) (Hughes and Bermúdez, 1997) together with other volcanic deposits from the same group dated at 6.5 ± 0.4 Ma (ZFT) (Vallejo et al., 2019) and 6.1 ± 0.6 Ma (K-Ar) (Barberi et al., 1988). Lastly in the north, the Angochagua (K-Ar: 6.30 ± 0.06 and 6.31 ± 0.10 Ma) and Pugarán (ZFT: 5.0 ± 2.9 Ma) volcanic groups cover the Real and Western Cordilleras (Barberi et al., 1988; Boland et al., 2000), whereas the volcanoclastic Peñas Coloradas formation (ZFT: 5.4 ± 0.4 Ma) is recognized as an early stage of the Chota Basin (Winkler et al., 2005). Barberi et al. (1988) have also reported a K-Ar age of 4.78 ± 0.50 Ma for the volcanic deposits bellow Chiles volcano, to the south of the Colombian border.

Following an extension period in northern Ecuador, when the Chota basin was formed (Barragán et al., 1996; Winkler et al., 2005), the fourth volcanic stage started at 4-3 Ma. This penultimate volcanic phase is represented in the south-central area by the caldera-filling felsic domes of Quimsacocha (ZFT: 3.6 ± 0.3 Ma; Beate et al., 2001), and the Sicalpa formation (K-Ar: 3.59 ± 0.28 Ma to 2.65 ± 0.21 Ma) characterized by volcanic and volcaoclastic rock of fluvial and lacustrine origin (Lavenu et al., 1992; Winkler et al., 2005). To the north, this stage is represented by the andesitic phases of Yanahurco de Piñan ($^{40}Ar/^{39}Ar$: 3.58 ± 0.03 Ma) (Béguelin et al., 2015), the late volcanic products of the Angochahua formation (K-Ar: 3.46 ± 0.10 to 2.60 ± 0.06 Ma; Barberi et al., 1988; Boland et al., 2000), and the intrusive bodies in the Chota basin (K-Ar: 3.65 ± 0.07 Ma, and AFT: 3.7 ± 1.7 Ma; Barberi et al., 1988; Winkler et al., 2005).

The Pisayambo formation corresponds to the Pliocene pyroclastic deposits, andesitic lava flows, and volcanoclastic sediments located in the heights of the central Cordillera Real. Originally defined by Kennerley (1971) and Baldock (1982), the Pisayambo formation also included other Pliocene volcanic deposits from central Ecuador (e.g., Zumbahua group, Alausí Formation), which were dissociated and reclassified as independent units in more recent studies. Consequently, the K-Ar ages obtained by Lavenu et al. (1992) at 7.9 ± 0.4 Ma in Alausi area and 10.0 ± 1.3 Ma in Zumbahua area,

and by Barberi et al. (1988) at 6.1 ± 0.6 Ma in Zumbahua area, correspond to other geological units and not to Pisayambo itself. Therefore, the precise activity period of the Pisayambo volcanism remains uncertain, nonetheless it may be related to one or several of the previously described stages.

Finally, several fluvial and lacustrine formations appear in the Inter-Andean Valley following the decrease of the fourth stage's volcanic activity. The thickest sequences are observed in the Latacunga and Guayllabamba basins, ranging from 3 Ma to 1 Ma. However, their stratigraphic relationships, formation ambience and ages are still discussed (e.g., Villagómez, 2003; Winkler et al., 2005; Fiorini and Tibaldi, 2012).

1.3.2 Distribution of volcanic edifices

At least 77 quaternary volcanoes are distributed over a 300 km long and 130 km wide area in the central and northern Ecuadorian Andes (Fig. 1.14; Hall, 1977; Hall and Wood, 1985; Barberi et al., 1988; Hall and Beate, 1991; Bernard and Andrade, 2011; Hall et al., 2008; Santamaría, 2017). Five of these volcanoes have erupted since 1999 and, presently, two other showed signals of magmatic unrest. The Reventador eruption in 2002 was the most explosive for the last century. More than fifteen additional volcanoes have been active during the Holocene and are categorized as “potentially active”. Their activity included highly explosive eruptions, which repeatedly affected the inter-Andean valley. This particularly high number of volcanoes and their constant activity represent then a permanent threat for the populations from the Ecuadorian Andes. Large cities such as Quito, Ecuador's capital city, as well as Ibarra, Latacunga, Ambato and Riobamba are vulnerable to volcanic hazards, which also affect large agrarian zones (Fig. 1.14).

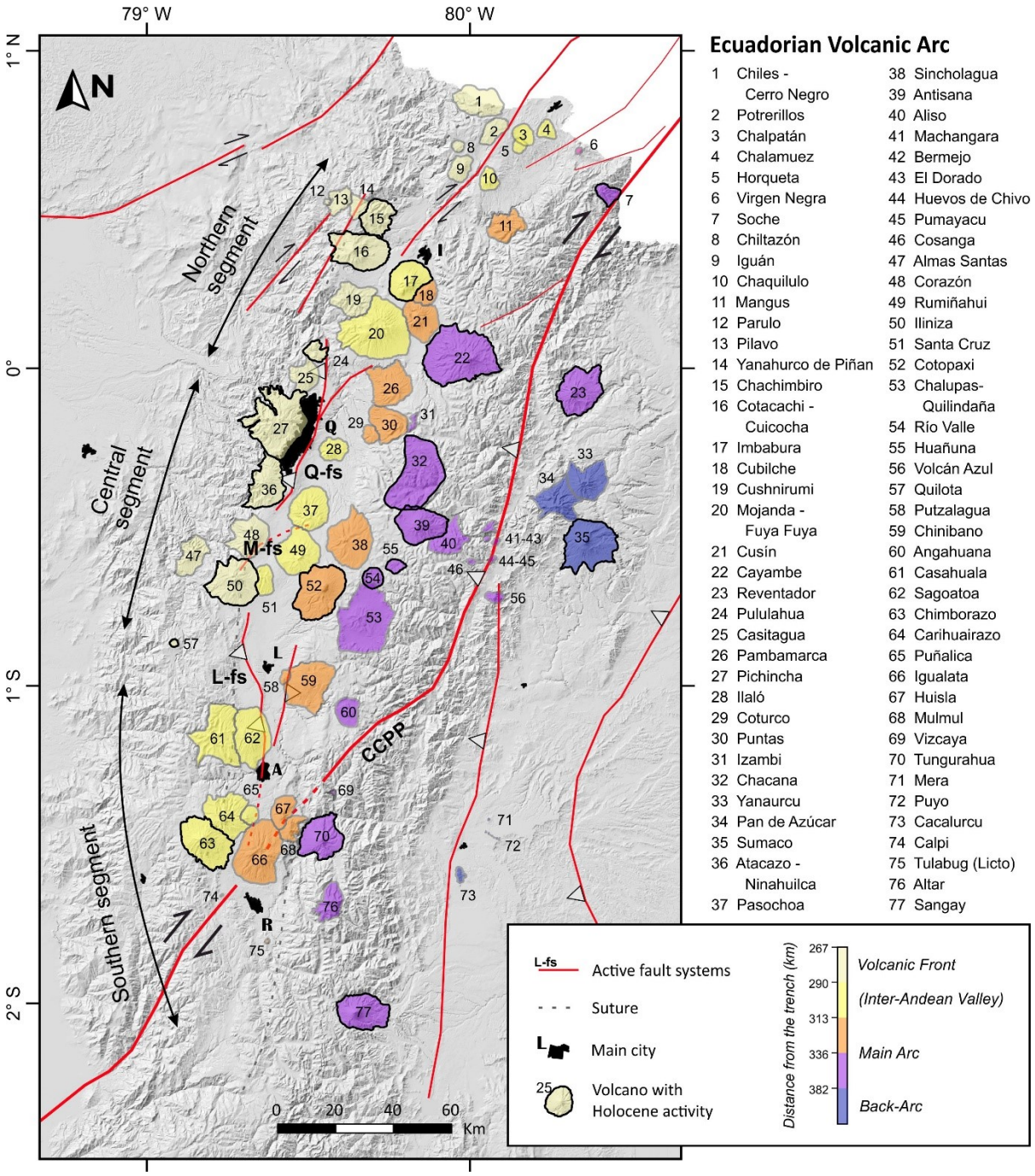

Figure 1.14. *Ecuadorian volcanic arc (Modified from Bernard and Andrade, 2011; Santamaría, 2017). Volcanoes are colored according to their distance from the trench comprising the along-arc corridors of the Volcanic Front (Western Cordillera), Inter-Andean Valley, Main Arc (Eastern Cordillera), and Back-Arc. The variability in the number of volcanic centers is represented by the northern, central, and southern across-arc segments. Active fault systems are represented with red lines according to Alvarado et al. (2016). CCPP: Chingual-Cosanga-Pallatanga-Puná Fault System; Q-fs: Quito Fault System; M-fs: Machachi Fault System; L-fs: Latacunga Fault System. Main cities are represented in black. I: Ibarra; Q: Quito, capital city; L: Latacunga; A: Ambato; R: Riobamba.*

The Ecuadorian arc is often presented as four volcanic corridors based on their distance to the trench which coincide with the north-south alignments of the Western Cordillera (Volcanic Front), the Inter-Andean Valley, the Cordillera Real (Main Arc), and the Sub-Andean Uplift (Back Arc) (e.g., Hall, 1977; Hall and Beate, 1991; Hall et al., 2008). These linear groupings exhibit distinctive petrological and geochemical characteristics that influenced their morphology and eruptive styles (Hall et al., 2008). 1) The characteristic morphology of the edifices from of the Volcanic Front is that of a 15-20 km-wide composite cone created after successive vent and/or conduit migrations (e.g., Chiles-Cerro Negro, Pichincha, Chimborazo volcanoes). Dome complexes are frequently formed during their terminal stages following a progressive evolution of the magmatic composition from high-silica andesites to dacites (e.g., Chachimbiro, Pichincha, Atacazo, Iliniza volcanoes). The volcanic front also includes two 2-3 km wide calderas (Cuicocha and Quilotoa) that were formed after highly explosive eruptions that occurred at the end of the Holocene. 2) In contrast, the Main Arc is dominated by conical edifices that were constructed by successions of low- to high-silica andesite lava flows and scoriaceous pyroclasts (e.g., El Reventador, Cotopaxi, Tungurahua, Sangay). Several of them have repeatedly erupted during historical times generating extensive ash falls, pyroclastic flows, and significant lahars (e.g., Cotopaxi's 1877 eruption). The Main Arc central region contains several rhyolitic centers that formed two 20 km wide calderas (i.e., Chalupas, Chachana) as well as multiple dome complexes and obsidian flows (e.g., Huañuna, Rio Valle, Pumayacu). 3) The edifices of the Inter-Andean valley combine the characteristics of both chains by forming prominent stratovolcanoes (e.g., Pasochoa, Rumiñahui) with terminal dome complexes (e.g., Imbabura, Mojanda - Fuya Fuya), and minor scoria cones (e.g., Calpi, Licto, Vizcaya). These volcanoes are mainly concentrated in three clusters to the north, center and south of the arc. Finally, 4) the back-arc corridor is constituted by less prominent stratovolcanoes (e.g., Pan de Azucar, Sumaco) and scoria cones (e.g., Puyo) mainly composed of basanites and tephrites.

Nevertheless, the Ecuadorian eruptive centers are not uniformly distributed along in the arc and tend to form wide across-arc volcanic clusters (VC) separated by areas with a lower number of volcanoes (LNV). To the north, the Ecuadorian arc begins with the Tulcán VC segment that includes the volcanos located between the Colombian border and the Chota basin (e.g., Chiles-Cerro Negro,

Chalpatán, Soche). No quaternary centers are reported in the Chota basin, which thus makes a 25-35 km long gap to the north of the first VC. The Ibarra VC includes the edifices located between Yanahurcu de Piñan and Cayambe volcanoes (e.g., Chachimbiro, Imbabura, Mojanda-Fuya Fuya). They form a northwest-southeast alignment that extends eastward to El Reventador volcano. The Quito LNV segment is located immediately to the south. Here, the eruptive centers surround the Guayllabamba basin (e.g., Pichincha, Atacazo, Pambamarca, Chacana), except for Ilaló volcano which lies within the inter-Andean valley. The Machachi VC coincides with the widest segment of the arc and contains the edifices located between Almas Santas volcano, and extends eastward to Sumaco volcano (e.g., Ilinizas, Pasochoa, Cotopaxi, Antisana). Remarkably, the axis of the Machachi VC intersect the axis of the Ibarra VC near the Sumaco and Pan de Azúcar volcanoes in the Sub-Andean zone. A second decrease in the number of volcanoes is observed in the Latacunga LNV segment in which the edifices are concentrated in both Cordilleras (e.g., Sagoatoa, Putzalagua, Chinibano). Here, a 50-km long gap is observed in the Western Cordillera where Quilotoa Caldera is the unique volcano in the Zumbahua area (Western Cordillera). Lastly, the Riobamba VC includes the edifices between Chimborazo and Tungurahua volcanoes in an alignment that extends eastward to the Puyo cones in the Oriente basin. To the south, the group includes El Altar volcano and the scoria cones of Calpi and Licto. After a final 45 km long gap, the Ecuadorian Arc ends with the Sangay volcano to the south of the Main Arc (Fig. 1.14).

It is important to note that the volcanic clusters described above seem to coincide with the projection of the topographic reliefs observed on the Nazca plate. For instance, the Machachi and Ibarra VCs are situated in front of the Carnegie Ridge subduction, and the Riobamba VC coincides with the projection of the Grijalva fracture zone (Figure 1.4c). Therefore, a strong relationship has been inferred between the rheological and morphological variations of the subducting Nazca slab, the volcanic arc configuration, and the fluctuations in the composition of their magmas (e.g., Gutscher et al., 1999; Yepes et al., 2016; Ancellin et al., 2017a). A further discussion is provided in section 1.3.4.

1.3.3 Geochronology of the volcanic arc

Based on the pioner studies carried out in the early 20th century, Hall (1977) provided the first descriptions of the "young" volcanism in Ecuador. His work recognized the extensive volcanic units of southern Ecuador (e.g., the Tarqui Formation), and dissociated them from those related to the Quaternary volcanic arc, which developed north of latitude 2°30'S. Hall (1977) also described the distribution of the Quaternary edifices forming the north-south corridors described in section 1.3.2, naming the historically active centers (from AD 1550) as "active volcanoes".

Several studies conducted on a regional scale provided the first geochronological data for the volcanic sequences reported to the north and south of Ecuador. As discussed in section 1.3.1, volcanism was widespread throughout the Ecuadorian Andes until the Miocene, and progressively became restricted to the central and northern areas since the Pliocene. Barberi et al. (1988) and Lavenu et al. (1992) provided several K-Ar ages of the Quaternary volcanoes and their basement volcaniclastic deposits. These authors described a volcanic arc formed as early as ~1.5-1.0 Ma. However, the quality of their data has been questioned because of the use of whole-rock, without the removal of crystalline phases from the groundmass before K-Ar dating. This is a key factor considering that the inherited radiogenic argon present in phenocrysts could cause a significant age bias (e.g., Singer et al., 1998; Samper et al., 2008; Renne et al., 2012). A further discussion is provided in Chapter 2. More recently, Bigazzi et al. (1997, 2005) have reported several fission-track ages obtained from obsidians collected at the Chacana caldera, located in the Cordillera Real. These authors showed that this rhyolitic center was active since at least ~1.3 Ma.

Between 1999 and 2002, the onset of the new eruptive periods of Tungurahua, Pichincha and Reventador volcanoes highlighted the necessity to improve the knowledge of the Ecuadorian arc. Consequently, several stratigraphic, geochronological, geochemical, and geophysical studies were carried out during the last two decades focusing on the volcanoes classified as active and potentially active (e.g., Samaniego et al., 2005, 2012; Robin et al., 2010; Le Pennec et al., 2011). The geochronological study of the older evolutive stages was carried out using new radiometric ages mostly acquired by the $^{40}Ar/^{39}Ar$ dating method applied to the groundmass and to separated crystalline phases.

The younger stages were better constrained using stratigraphic relationships, and samples of intra-deposit coals or inter-layered soils dated by the radiocarbon dating method (e.g., Barba et al., 2008; Hall and Mothes, 2008a; Le Pennec et al., 2008). A compilation of the available geochronological data and a synthesis of the activity periods of each volcano were presented by Santamaria (2017). This study has highlighted that, despite numerous scientific studies, the oldest evolutionary stages of these volcanoes remain poorly constrained, and that information on volcanoes classified as "extinct or in rest" is scarce. Figure 1.15 presents a summary of the geochronological knowledge of the Ecuadorian arc (Santamaría, 2017).

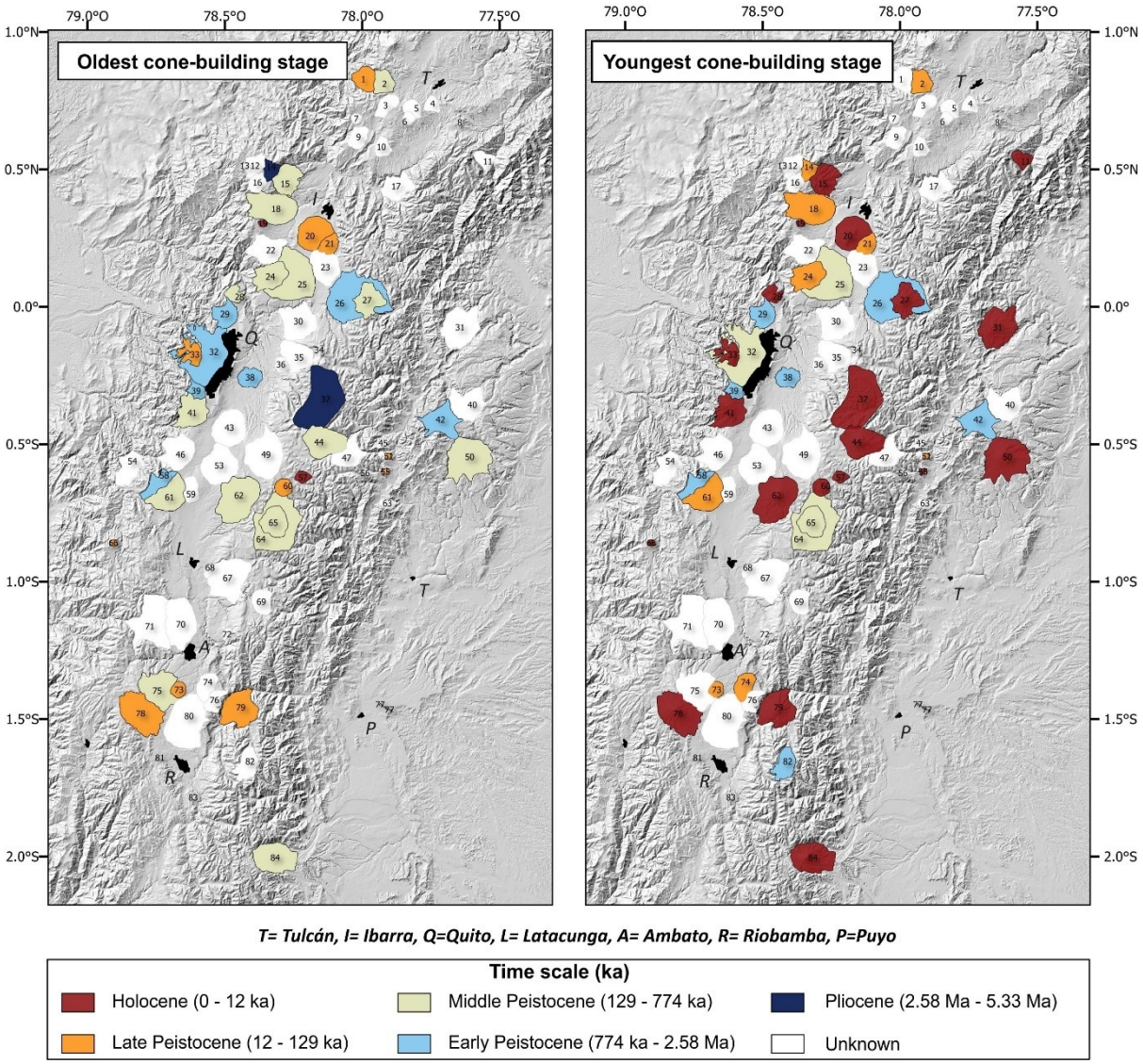

Figure 1.15. *Oldest cone-building stage of the Ecuadorian volcanoes as well as their last known eruption. Modified from Santamaría (2017).*

More recently, the cooperation between the GEOPS laboratory of the *Université Paris-Saclay*, the *Institut de Recherche pour le Développement* (IRD) and the *Instituto Geofísico* of the *Escuela Politécnica Nacional* (IG-EPN), allowed the acquisition of almost a hundred new groundmass K-Ar ages representing more than twenty volcanoes (i.e., Alvarado et al., 2014; Bablon et al., 2018, 2019, 2020a, 2020b). These geochronological data allowed to outline the evolution of both active and extinct volcanoes. Notably, these new K-Ar ages were consistent with the $^{40}Ar/^{39}Ar$, and radiocarbon ages published in the more recent studies, and questioned the accuracy of the K-Ar ages previously acquired on whole-rock samples. A detailed discussion of these data is presented in Chapter 5.

1.3.4 Geochemical characterization and petrogenetic models

Overall, most of the whole-rock geochemical analyses conducted on volcanic samples taken from the Ecuadorian volcanic arc belong to the medium-K calc-alkaline series, with a minor fraction falling in the high-K field (Fig. 1.16). These rocks are mostly classified as basaltic andesites to dacites (52-70 wt.% SiO_2) and scare rhyolites. Conversely, the volcanic products of the Sub-Andean zone belong to the Shoshonitic series and are classified as alkaline basalts and basaltic andesites (42-56 wt.% SiO_2). Figure 1.16a shows that, the Ecuadorian magmas display multiple compositional trends where the edifices belonging to the Volcanic Front have the lowest K_2O concentrations. For similar silica contents, the Main Arc exhibits slightly higher K_2O concentrations. In contrast, the Back Arc presents more depleted SiO_2 values compared to the volcanoes of the Andean range but displays a remarkable K_2O enrichment. The spider diagrams of incompatible elements normalized to the primitive mantle and Rare Earth Elements (REE) normalized to chondrites show a gradual increase of these elements as a function of the distance from the trench (Figures 1.16b and 1.16c).

Likewise, the concentrations of elements considered as fluid-mobile (e.g., Ba, Pb, Cs, Li, B) tents to decrease relative to fluid-immobile elements (e.g., Be, Nb, Th, La) away from the trench (Fig. 1.17). This effect is explained by the gradual decrease in the quantity of fluids liberated by the subducting slab as it goes away from the trench, leading to a lower degree of partial melting of the

mantle wedge (e.g., Barragan et al., 1998; Bourdon et al., 2003; Chiaradia et al., 2009; Hidalgo et al., 2012). Moreover, the elevated quantity of incompatible elements and the increased rates of fluid-mobile to fluid-immobile elements in the Frontal Arc could be related to a massive dehydration of the slab beneath the Western Cordillera (Ancellin et al., 2017a).

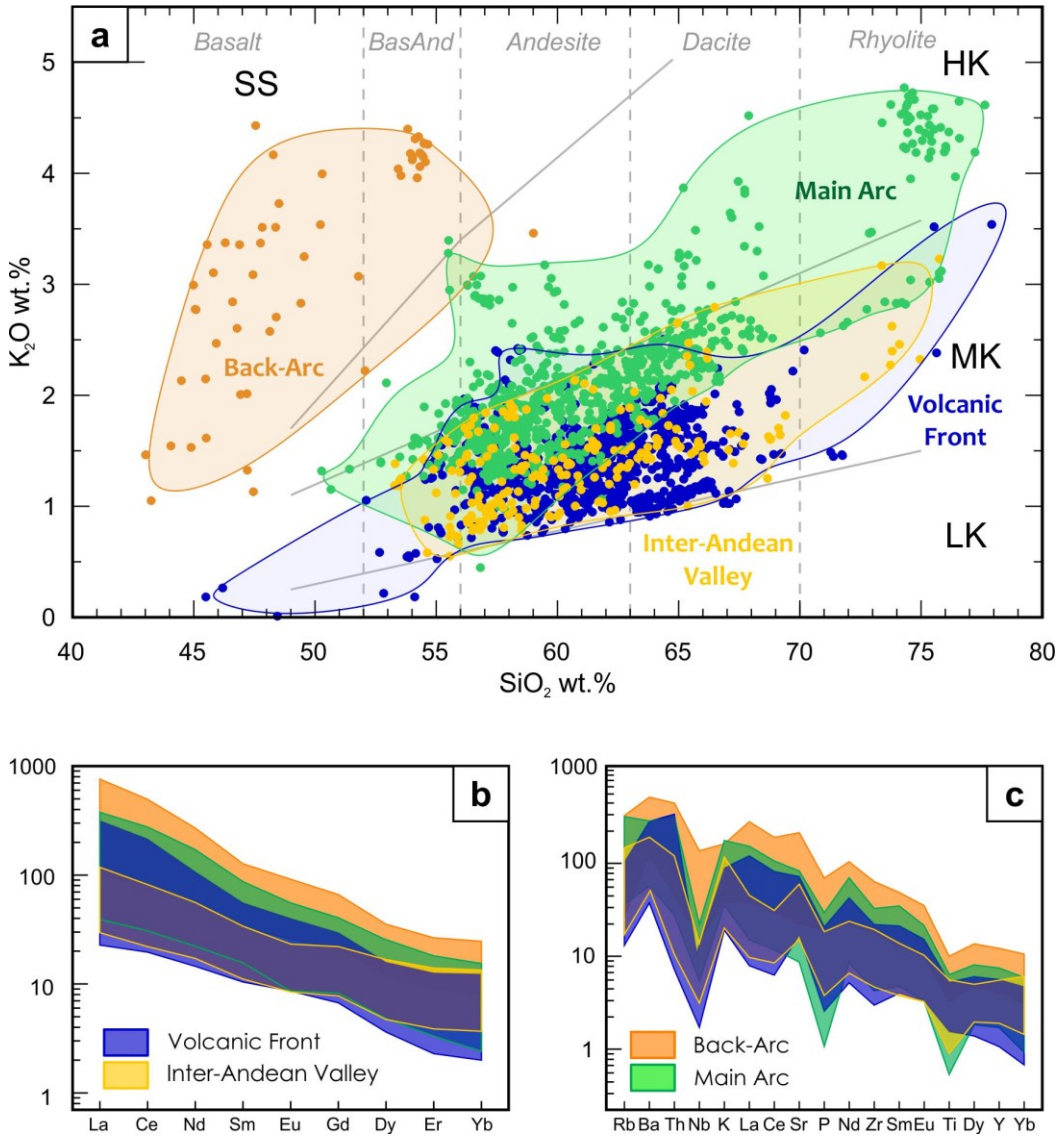

Figure 1.16. a) *K_2O vs SiO_2 diagram (Peccerillo and Taylor, 1976) for eruptive products of the Ecuadorian Arc. SS: Shoshoshonite series; HK: Hight-K, MK: medium-K, and LK: low-K calc-alkaline series. Whole-rock data obtained from the Georoc database.* ***b)*** *Rare Earth Elements normalized to chondrites and* ***c)*** *Incompatible trace elements normalized to primitive mantle spider diagrams (Sun and McDonough, 1989) for the same arrangements.*

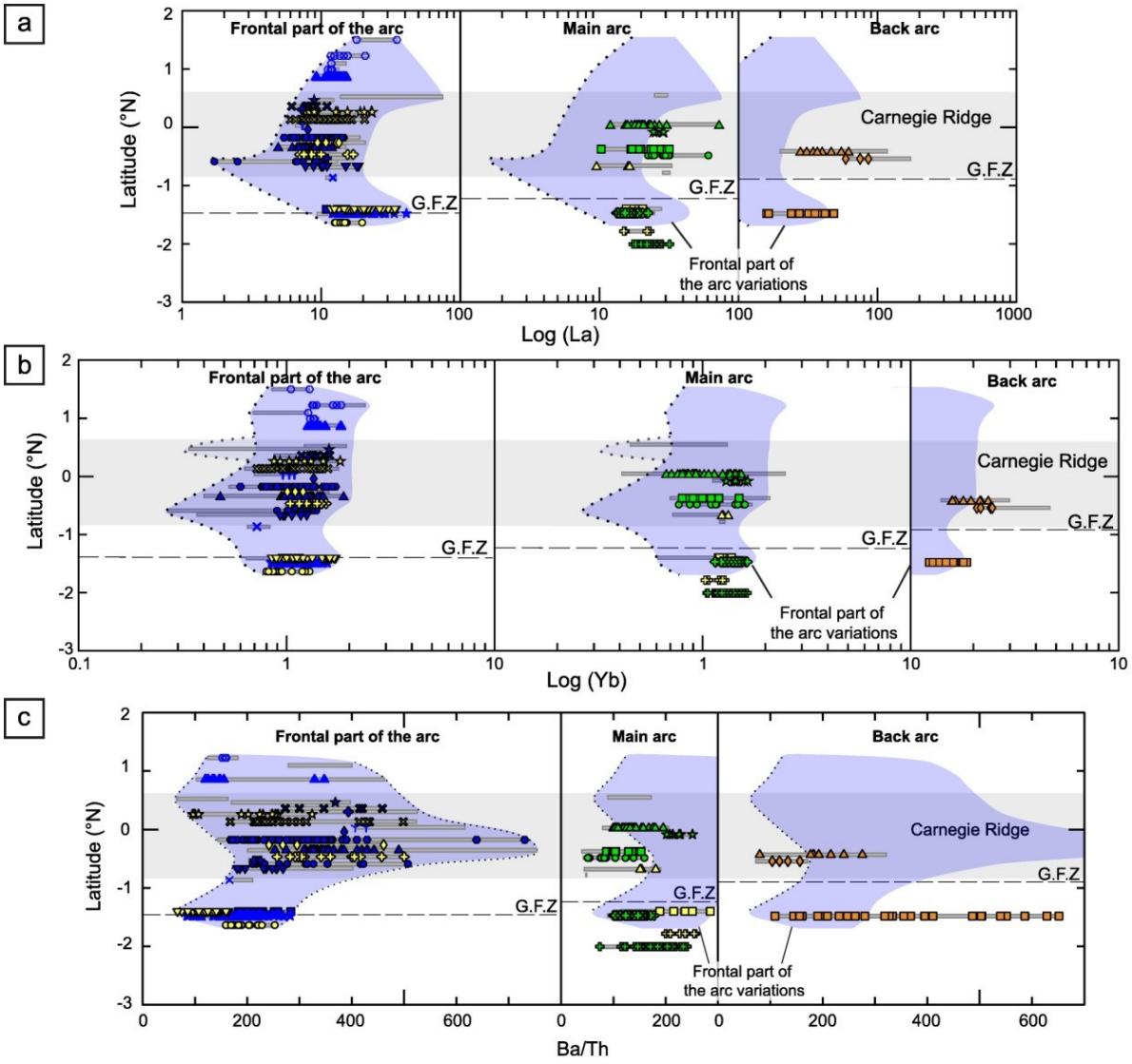

Figure 1.17. *Trace element content and ratio evolutions with latitude according to Ancellin et al. (2017a). Samples arranged according to basement type: from left to right, volcanoes located on oceanic crust (Volcanic Front), continental crust (Main Arc) and sub-Andean zone. The blue-shaded area corresponds to geochemical variations in the Volcanic Front and the gray field marks the inferred position of the Carnegie Ridge beneath the Ecuadorian arc. The dashed line corresponds to the inferred position of the Grijalva Fracture Zone (GFZ) beneath the arc.*

Fluctuations in trace element contents also appear along the arc (Fig. 1.17.). Volcanoes located in the central segment (lat. 0.7°S to 0.2°N) show the lowest minimum concentrations of incompatible trace elements of the arc, which increases away from this area. Notably, the highest concentrations are found at the same latitudinal range in the Sub-Andean area (e.g. Sumaco and Pan de Azúcar volcanoes). Also, the rates of fluid-mobile compared to fluid-immobile elements (e.g., Ba/Th) reach the highest

minimum and maximum values in the central segment of the Volcanic Front (Fig. 1.17c), while the values exhibited by the Main Arc are lower than those of the Volcanic Front. Therefore, the volcanoes from the central segment show the widest ranges of incompatible element contents in the Ecuadorian arc. Conversely, the southern segment (latitude >0.7°S) shows narrower and generally comparable content ranges between the different long-arc alignments (Ancellin et al., 2017a).

Geographical variations were also identified for Sr and Nd isotope ratios (Fig. 1.18; Ancellin et al., 2017a). The lowest values of $^{143}Nd/^{144}Nd$ and the highest values of $^{87}Sr/^{86}Sr$ were detected in the Main Arc volcanoes. Although the range of values shown by the Main Arc is generally homogeneous, this is not the case for the Volcanic Front. Specifically, the northern Volcanic Front present higher values of $^{87}Sr/^{86}Sr$ and lower values of $^{143}Nd/^{144}Nd$ compared to those measured for the southern volcanoes. Most of this variability is explained as resulting from the interaction of magmas with the upper crust through crustal melting and assimilation processes (e.g., Barragan et al., 1998; Samaniego et al., 2005; Hidalgo et al., 2012; Ancellin et al., 2017a; Chiaradia et al., 2021). As presented in section 1.1, the Volcanic Front is built on a basaltic basement of oceanic origin (Western Tectonic Realm), while the Main Arc overlies metamorphic rocks of continental affinity (Guiana Shield Realm).

Likewise, lead isotopic ratios reflect variations along and across the volcanic arc (Ancellin et al., 2017a; Chiaradia et al., 2021). In particular, the $^{207}Pb/^{204}Pb$ ratios are lower in the northern Volcanic Front, while the $^{206}Pb/^{204}Pb$ ratios are higher in the central segment. The $^{207}Pb/^{204}Pb$ range is generally homogeneous in the Main Arc showing the highest values of the arc, while the $^{206}Pb/^{204}Pb$ ratio is usually lower northward. The volcanoes of the Sub-Andean zone present similar features than volcanoes from the Volcanic Front, with lower $^{206}Pb/^{204}Pb$ values to the north and higher values to the south. Notably, the lead isotopic signatures are similar in the Main Arc and the southern Volcanic Front, although the nature of the crust is different. For Ancellin et al. (2017), these signatures reflect the grade of lower crustal assimilation, which appears to be higher in those areas. Consequently, the high $^{206}Pb/^{204}Pb$ ratio observed in the central and northern Volcanic Front have been related to changes in the magma source.

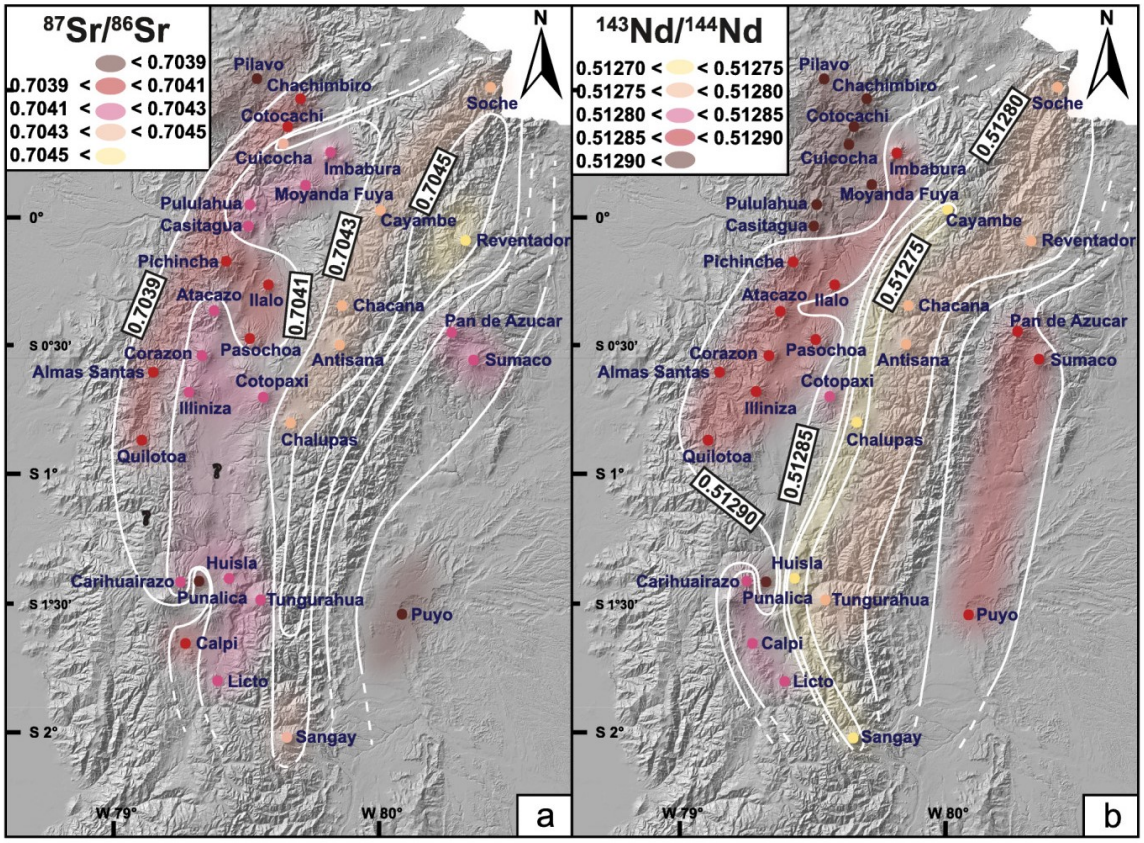

Figure 1.18. *Schematic map showing the distribution of (a) $^{87}Sr/^{86}Sr$ and (b) $^{143}Nd/^{144}Nd$ compositions in Ecuador according to Ancellin et al. (2017a).*

Considering that Ba is a mobile element in most fluids and Th is only mobile in silicate melts, the Ba/Th ratio is a useful indicator of the involvement of aqueous fluids versus silicate melts in magma genesis (Grove et al., 2002, 2012; Kessel et al., 2005). This ratio reaches the highest values in the central and northern segment of the Volcanic Front and is commonly lower and less variable both to the east and south of the arc. Coupling this indicator with the lead isotopic signature observed in the northwest of the volcanic arc, it is possible to infer the nature of the slab-derived fluids. Indeed, the increased $^{206}Pb/^{204}Pb$ signature could be generated by siliceous melts originating from the slab (Ancellin et al., 2017a). Considering that this high lead ratios are also observed in the Galapagos Islands (White et al., 1993; Werner et al., 2003), it is reasonable to suggest then the influence of the Carnegie ridge basalts which are subducted at the same latitude. Alternatively, the rheology of the subducting slab is also a factor to consider. As discussed in Section 1.1, the nature of the slab north of the Grijalva fracture zone is more susceptible to partial melting due to its young age and the high temperature environment to

which it was exposed as it intersected the Galapagos hotspot. Thus, this could favor the production of siliceous melts and the generation of the isotopic signatures described above (Ancellin et al., 2017a).

Finally, several authors pointed out the occurrence of rare calc-alkaline magmas enriched in Sr and light REE (LREE) and depleted in Y and heavy REE (HREE). Such magmas mostly occur in the northern and central segment of the volcanic arc. Using a geochemical modeling approach, several authors highlighted the impossibility of explaining the genesis of these magmas solely from pure fractional crystallization processes from calc-alkaline magmas (e.g., Hidalgo et al., 2007; Schiano et al., 2010; Bellver-Baca et al., 2020). These authors rather proposed that an additional silica-rich melt generated by major fractionation of mineral assemblages including garnet and/or hornblende is required. The petrogenetic processes related to this so called "adakite-like" member has largely been discussed. Such processes would involve partial melting of the subducted slab in the eclogite facies and the subsequent interaction of the derived silicate melts with the mantle wedge (Bourdon et al., 2003; Samaniego et al., 2005, 2010; Hidalgo et al., 2007, 2012), partial melting of the lower crust basalts (Garrison and Davidson, 2003; Garrison et al., 2006), and high-pressure intra-crustal fractionation of amphibole and/or garnet (Bryant et al., 2006; Chiaradia et al., 2009, 2021; Bellver-Baca et al., 2020). According to Tolstykh et al. (2017), the rare occurrence of adakitic melts in melt inclusion studies, and the presence of dakite-like rocks in multiple geodynamic settings illustrate that this type of magma associations do not necessarily derive from adakitic melts. Therefore, adakite-like signatures cannot be used as indicators of a particular geodynamic setting. As previously discussed, the genesis of magmas in the Ecuadorian arc includes complex petrogenetic processes from heterogeneous sources and the interaction of different types of crustal rocks (Egüez et al., 2017; Koch et al., 2021).

Chapter 2

Sampling process of a lava flow in the northern flank of the Iliniza volcano. From left to right: Santiago Santamaria, Pablo Samaniego and Silvana Hidalgo.

Chapter 2

Methodology

Contents

2.1 Sampling strategy and fieldtrips 65
2.2 Potassium–argon radiometric dating 67
2.2.1 Dating principles 67
2.2.2 Sample preparation protocol 69
2.2.3 The K-Ar method 71
2.2.3.1 Potassium measurement protocol 71
2.2.3.2 Argon measurement protocol 72
2.2.3.3 Calculation of radiometric ages and uncertainties 75
2.2.4 The $^{40}Ar/^{39}Ar$ method 76
2.2.5 Dating method limits 80
2.3 Volcanic Surface Modeling 82
2.3.1 Principles 82
2.3.2 Extraction of the representative points of the paleotopography 84
2.3.3 Modeling of paleotopography 86
2.3.3.1 First approach: Kriging interpolation 86
2.3.3.2 Second approach: ShapeVolc interpolation 88
2.3.3.3 Interpolation of the basement surface 88
2.3.4 Calculation of volumes, and construction and erosion rates 89

2.1 Sampling strategy and fieldtrips

Field work and sampling for the present study were carried out in 2019 and 2020 in the central segment of the Ecuadorian arc with the purpose to identify and describe the main volcanic units, to establish their stratigraphic relationships, and to collect new fresh rock samples for K-Ar dating and whole-rock geochemical analyses (Fig. 2.1). With the aim of covering the maximum number of cone-building stages, whenever possible, we sampled the units located at the summit, at mid-elevation, and at the base of the studied volcanoes. Depending on the arrangement of the access routes and pathways, our sampling was performed on several flanks of the volcanoes, ensuring an adequate spatial data distribution. Samples collected exclusively for geochemical analysis followed the same sampling protocols, although with less severe selection criteria in the field.

Samples were dated by applying the K-Ar method on groundmass, using the unspiked Cassignol-Gillot technique (Cassignol and Gillot, 1982). Samples were prepared following the protocols detailed below. Potassium and argon isotopic measurements were carried out at the GEOPS laboratory in Orsay (Paris-Saclay University, France). Whole-rock contents of major and trace elements were measured from agate-grinded powders at the Laboratoire Géosciences Océan, University of Bretagne Occidental (Brest, France) via Inductively Coupled Plasma-Atomic Emission Spectrometry (ICP-AES), following the procedure described by Cotten et al. (1995).

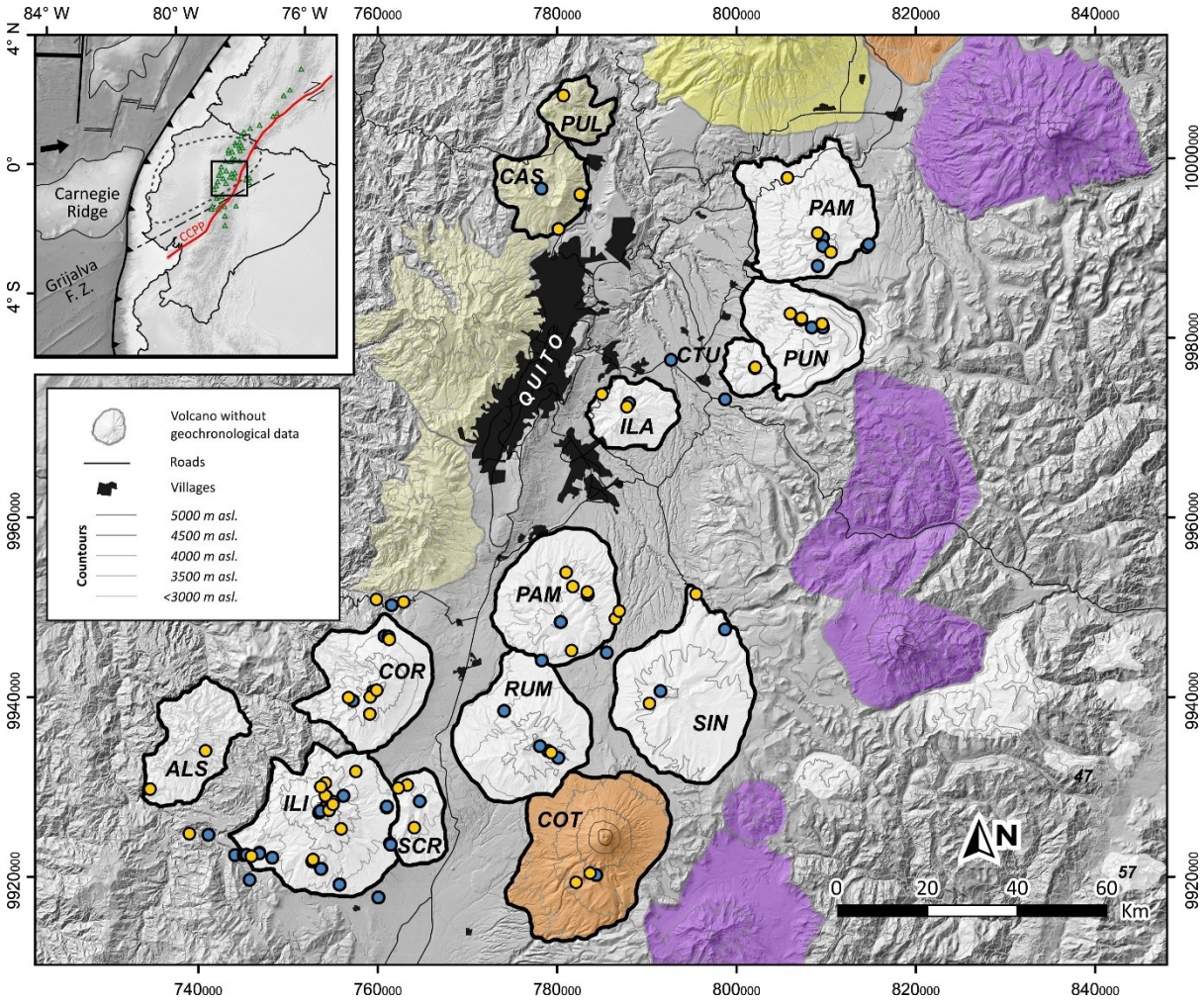

Figure 2.1. *Hill-shaded digital surface model of the central across-arc segment showing the locations of samples collected in this study. K-Ar dated samples are represented with blue dots. Sampled volcanoes showed with solid black outlines. ASL: Almas Santas; CAS: Casitagua; CTU: Coturco; COR: Corazón; COT: Cotopaxi; ILA: Ilaló; ILI: Iliniza; PAS: Pasochoa; PUL: Pululahua; PAM: Pambamarca; PUN: Puntas; RUM: Rumiñahui; SCR: Santa Cruz; SIN: Sincholagua. Non studied volcanoes numbered and colored as in Figure 1.13. Location of Sumaco volcano sample is not showed in this map.*

2.2 Potassium–argon radiometric dating

2.2.1 Dating principles

Potassium (K) is one of the most abundant elements in Earth's crustal rocks, contributing about 2 wt.% (Taylor and McLennan, 1985). Due to its incompatible behavior, potassium tends to accumulate in magmas resulting from low degree partial melting processes, and in liquid residues derived from fractional crystallization processes. Potassium naturally occurs in three isotopes: ^{39}K (93.258%), ^{40}K (0.0117%) and ^{41}K (6.730%), with only ^{39}K and ^{41}K as stable isotopes (Garner et al., 1975). In turn, ^{40}K is a radioactive isotope which naturally decays to argon-40 (^{40}Ar*) and calcium-40 (^{40}Ca*) with a combined half-life of 1.248 Ga (Fig. 2.2; Steiger and Jäger, 1977). Conversion to ^{40}Ca occurs with the emission of a beta particle (β^- decay) for 89.28% of cases, and to ^{40}Ar by electron capture (EC) with the emission of a neutrino and then a gamma ray (γ) for 10.72% of cases. About only 0.001% of ^{40}K atoms decay to ^{40}Ar by emission of a positron (β+; Pradler et al., 2013).

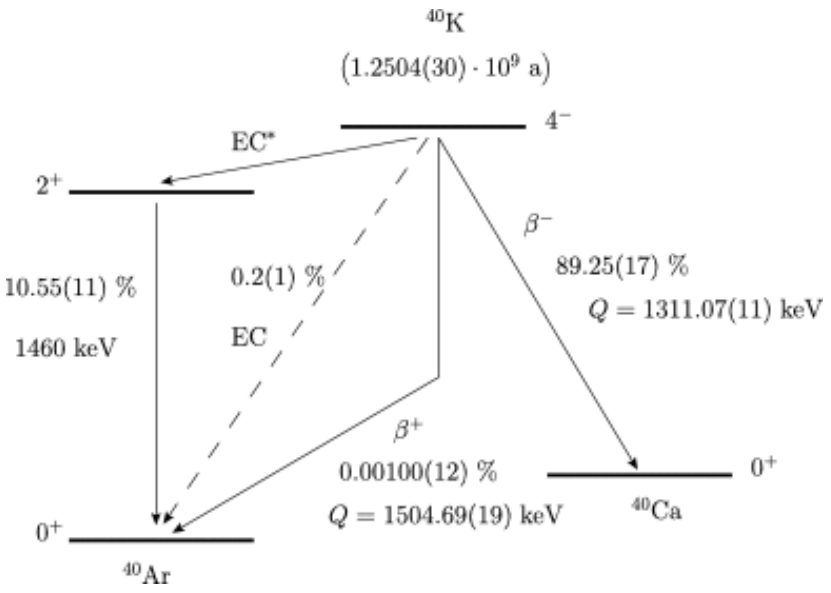

Figure 2.2. *Decay scheme of ^{40}K according to Pradler et al. (2013). The dashed line depicts the direct decay to the ground state of ^{40}Ar.*

Although calcium-40 is the prevalent daughter isotope of ^{40}K radioactive decay, this element is rarely used in dating methods. In fact, the calcium portion in crust of roughly 4 wt.% (Taylor and McLennan, 1985) and the abundance of ^{40}Ca close to 96.94% of the total calcium isotopes prevent the accurate determination of $^{40}Ca^*$ added to the ^{40}Ca already present in the analyzed rock. In contrast, argon is a minor element in rocks that occurs in nature as three isotopes: ^{40}Ar (99.60%), ^{38}Ar (0.063%) and ^{36}Ar (0.336%), where ^{40}Ar is derived solely from the decay of potassium-40. The abundance of argon-40 in atmosphere ($^{40}Ar_{atm}$) is expressed with the $^{40}Ar/^{36}Ar$ isotopic ratio with the value of 295.56 ± 0.31 (Nier, 1950). By being a noble gas, argon does not combine with the other geochemical elements and does not bind to the crystal lattice. Moreover, the size of the ^{40}Ar atom prevents its escape through the spaces left by ^{40}K in the crystal lattice, thus resulting in the accumulation of $^{40}Ar^*$ inside the mineral through time. In igneous rocks, magmatic liquids are initially argon-free as they allow diffusion and subsequent escape of argon. When pressure and temperature conditions allow the crystal formation process, the ^{40}Ar formed from the ^{40}K decay start to be locked up in the crystal lattice (Fig. 2.3). Then, by measuring the ratio of remaining ^{40}K and newly produced ^{40}Ar, it is possible to calculate the age of crystal formation. Nevertheless, post-crystallization changes in pressure and temperature could allow ^{40}Ar to leak out, biasing the calculated sample age.

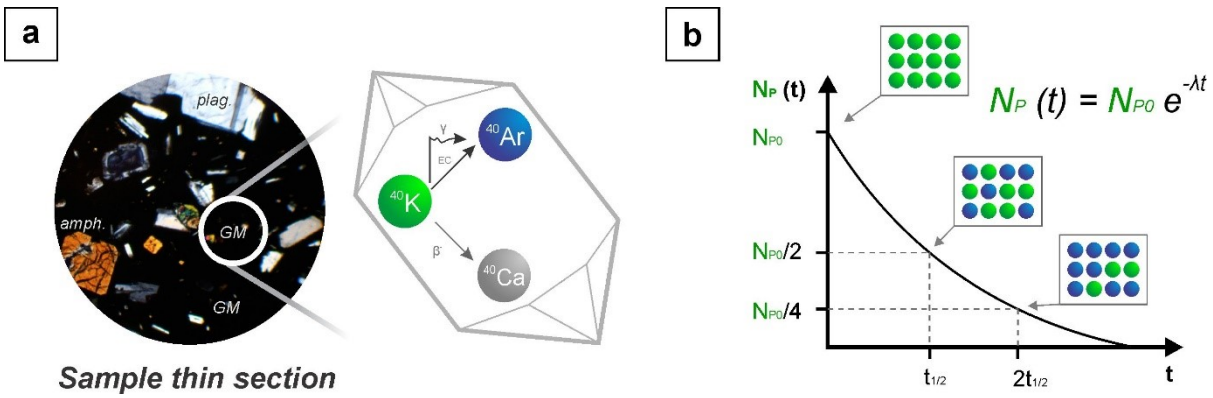

Figure 2.3. *Sketch of the process of accumulation of ^{40}Ar (daughter isotope; blue spheres) by radioactive decay of ^{40}K (parent isotope; green spheres).* ***a)*** *Magma cooling, crystallization, and closure of the crystal lattice. GM: Groundmass.* ***b)*** *Radioactive decay diagram where the number of remaining atoms of the parent isotope (N_P) is function of the initial N_P content (N_{P0}), the radioactive disintegration constant (λ), and the elapsed time since the closure of the crystal lattice (t).*

2.2.2 Sample preparation protocol

It is generally known that the mineral constituents of igneous rocks are formed at different temperature and pressure conditions. Thus, for a given temperature, certain mineral species allow the diffusion of parent or daughter isotopes, while others already have their crystalline lattices "blocked" for diffusion (Dodson, 1973). Once magmas reach the surface, they allow the exchange of isotopes with the atmosphere and reach an isotopic equilibrium. Therefore, those constituent species formed at low temperatures or after rapid cooling, such as groundmass cryptocrysts and volcanic glass, will effectively reflect the eruption age without $^{40}Ar^*$ biases inherited from older crystals.

Another advantage of using groundmass as a dating candidate versus other mineral species is its higher K content, given that K has an incompatible behavior and tends to remain in the magma liquid phase. However, the detection of $^{40}Ar^*$ above the $^{40}Ar_{atm}$ in groundmass could be problematic due to biases in the $^{40}Ar_{atm}$ content caused by weathering, fluid circulation, high vesicle quantity or high glass content. Moreover, the amount of accumulated $^{40}Ar^*$ could be insufficient in young volcanic products to be successfully distinguished above the atmosphere concentration. For these reasons, the use of groundmass was preferred in this study to obtain values close to the real ages of the eruptive events. In cases where measurements were performed on mineral phases, such as plagioclase, the results are interpreted as lower bounds of the true age of formation due to the possible presence of $^{40}Ar^*$ products (e.g., Singer et al., 1998; Harford et al., 2002; Renne et al., 2012; Lahitte et al., 2019).

To ensure optimal results, only volcanic rocks without apparent weathering and with low levels of vesicularity were meticulously selected and sampled in field (Fig. 2.4a-b). A further selection was carried out in the laboratory after meticulous thin section examination (Fig. 2.4c). During this latter step, we also selected the optimum grain size range in which the groundmass could be separated from the phenocrysts, ensuring maximum recovery and petrographic homogeneity in the separated size-fraction. Samples were crushed by hand and sieved in size ranges of 63-80 μm, 80-125 μm or 125-250 μm (Fig. 2.4d). The highest sieve range was used for porphyritic samples with large intergranular spacing, while the smaller sieve range was used for those samples with minor intergranular spacing. The separated material was washed with distilled water in order to remove residual dust from crushing,

and then it was ultrasonically cleaned in a 10% nitric acid solution to remove clays and traces of secondary mineralization such as zeolites, if any.

Figure 2.4. *Illustrative photographs of sample collection and preparation process. See text for details*

A first magnetic separation allowed to separate the groundmass grains, which are generally magnetic due to the presence of iron oxide microcrystals; the poorly magnetic mixed grains of groundmass containing traces of phenocrysts; and the free non-magnetic phenocrysts (Fig. 2.4e). Then, the groundmass grains are subjected to a heavy-liquid separation process to extract the residual heavy crystals ($d>2.85$ g/cm^3) and the remaining mixed grains from the previous process (Fig. 2.4f). This heavy-liquids separation allowed removal of weathered or vesiculated groundmass grains that are typically lighter than the mean groundmass value. The process consists of immersing a small sample

fraction (~200 ml) in bromoform (d=2.88 g/cm^3). The density is then adjusted in successive steps by adding ethanol (d=0.8 g/cm^3) causing the lighter grains to float while the heavier grains fall to the bottom. The heavy fraction is collected with a paper filter, then washed with ethanol and dried at 60°C. Using this process, a pure and homogeneous groundmass fraction is obtained with a small density range which, for the samples analyzed in this study, falls between 2.7 and 2.5 g/cm^3 (Fig. 2.4g). A second magnetic separation ensures the quality of the sample by eliminating possible occurrences of remaining pure crystals. The above-described process was also applied to separate the plagioclase phenocrysts (d 2.6-2.8 g/cm^3) from the heavier pyroxene, amphibole, or biotite crystals. Finally, we have also performed a K-Ar age from an obsidian sample by measuring the glass. This sample was prepared following the same process as above.

2.2.3 The K-Ar method

The ages reported in this study were acquired by the K-Ar method applying the unspiked Cassignol-Gillot technique (Cassignol and Gillot, 1982). This technique is particularly suitable to detect small amounts of ^{40}Ar* diluted in atmospheric ^{40}Ar, which characterize the low-K and/or young-aged volcanic rocks such as those of the Ecuadorian volcanic arc (e.g., Alvarado et al., 2014; Bablon et al., 2019, 2020a). The independent measurements of both potassium and argon contents were performed at the GEOPS laboratory of the Université Paris-Saclay.

2.2.3.1 Potassium measurement protocol

The potassium content is measured by flame absorption spectrometry. For this purpose, a portion of the previously prepared sample is dissolved through an acid etching for 4 hours at room temperature (~25°C), followed by a ten-hour period at 180°C. The acid etching mixture contains 10 ml of nitric acid (HNO_3), 10 ml of hydrofluoric acid (HF), and 2 ml of perchloric acid ($HClO_4$). In this way, the crystal lattice is dismantled, and the potassium is released. Subsequently, the samples are rinsed with distilled water, then dissolved with hydrochloric acid and diluted in a known volume of distilled

water. The volume is adjusted to ensure that the resulting solution contains a potassium concentration compatible with the calibration curve. This curve is obtained by preparing several solutions with known amounts of potassium, usually between 1 and 2 ppm at 0.2 ppm intervals, from a 1 g/l potassium standard solution. This set is subsequently measured by flame absorption spectrometry, in which the diluted samples are compared to the calibration curve to determine their apparent potassium concentration based on the measured absorption. The potassium concentration is calculated by multiplying the apparent concentration by the volume in which it was diluted and then dividing by the mass of sample dissolved. Samples are measured together with the MDO-G (K=3.510 %; Gillot et al., 1992) and the BCR-2 (K=1.481%; Raczek et al., 2001) standards, and blank vessels for comparison and correction. The potassium concentration is measured at least twice in independent series, the mean value is used to calculate the sample age. The value is considered valid when the standard deviation of the different replicates is less than 1%. The relative uncertainty of the potassium measurement process is 1%, representing the uncertainty obtained from repetitive measurements of the standards used, and including the uncertainty on their absolute value. The number of ^{40}K atoms is calculated using the constant isotopic abundance of ^{40}K in nature of 0.01167 atom% (Steiger and Jäger, 1977), and the whole K content in the sample obtained from the previously described procedure.

2.2.3.2 Argon measurement protocol

The argon content is measured following the procedure described by Cassignol and Gillot (1982), using a 180° sector multi-collector mass spectrometer connected to a measuring line operated at pressures below $2x10^{-7}$ Torr (Fig. 2.5a). A known mass of sample wrapped with pure a copper foil and placed in a molybdenum crucible (on the order of 1 g of sample in this study) is progressively heated to ~1500°C using a high-frequency induction furnace (Fig. 2.5c-f). As the sample melts, its volatile components are released in the form of gas (e.g., H_2O, CO_2, hydrocarbons,), which is then purified by exposure to titanium foam grains heated to ~800°C. The gas purification process is completed by lowering the temperature of the titanium foam to room temperature (about 22°C), whereby most of the remaining gases, such as hydrogen, are consumed. Noble gases, including argon,

are inert and do not react with hot metal. The attraction process by cooling with liquid nitrogen allows argon to be separated from helium. Other noble gases (neon, krypton) occur in low concentrations in nature, so they do not represent a measurement issue.

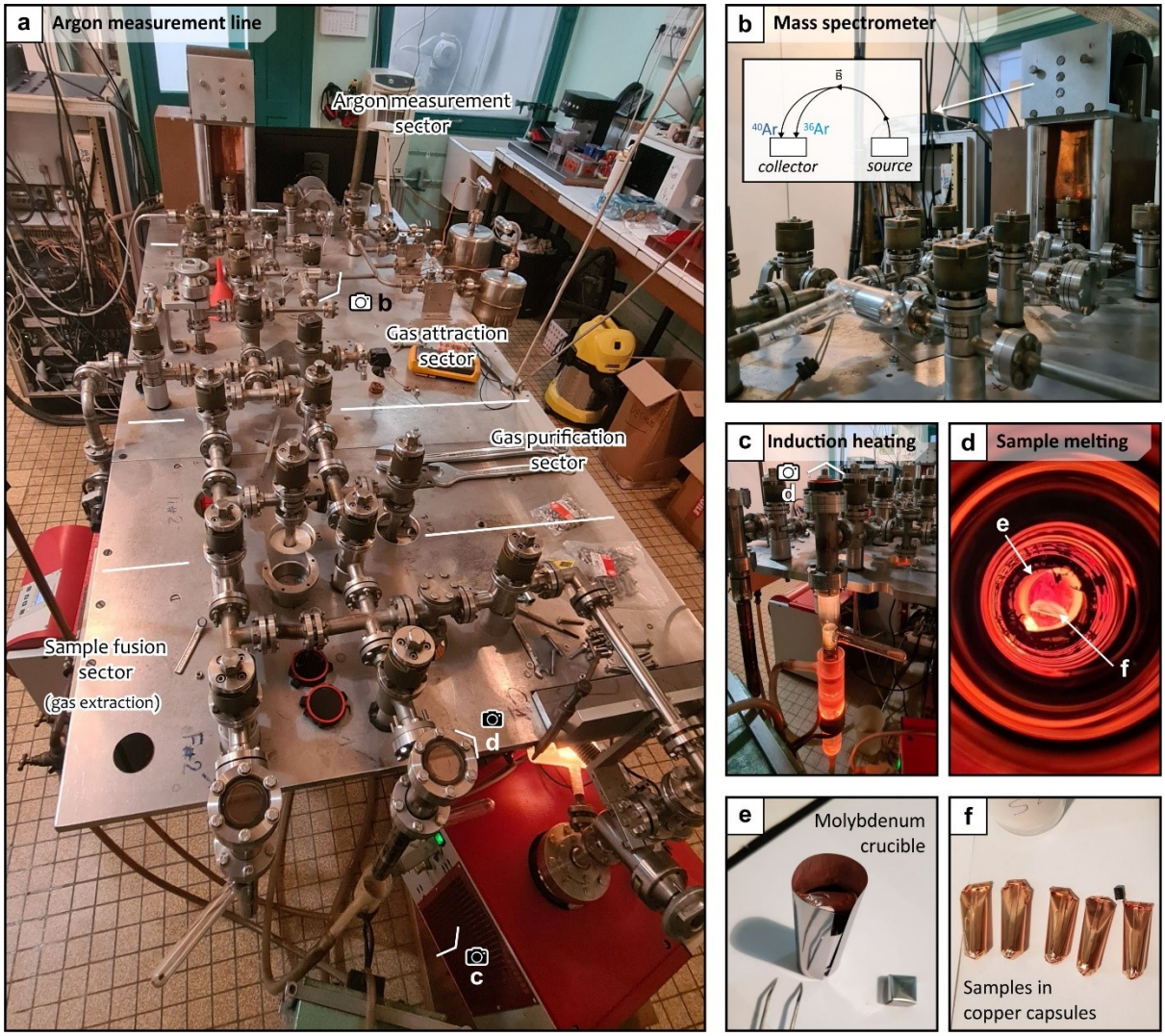

Figure 2.5. *Illustrative photographs of the argon measurement line at GEOPS laboratory, Université Paris Saclay. See text for details.*

In the measurement process, the argon contained in a known volume (PV) of the line is expanded into the mass spectrometer where it is ionized and then accelerated by a high potential difference of about 520v. A magnetic field deviates the trajectories of Ar ions with an arc of 180° whith

different radius depending on their mass of about 0.3T (Fig. 2.5b). Two Faraday cups present at the end of the 180° arc release an electron for each arrival of ions of mass 36 and 40, respectively. It then produces an electrical signal proportional to the number of ^{36}Ar and ^{40}Ar atoms present in the mass spectrometer. Prior to the sample measurement, a Calibrated Dose (*Dose Calibrée*; DC) corresponding to 0.1 cm^3 of atmospheric argon introduced into the known PV volume is measured. This step allows to convert the electrical signal measured into with a number of ^{40}Ar atoms. This value is checked by periodically measuring and comparing the ^{40}Ar signal of the DC with that of the HD-B1 standard (24.18 ± 0.09 Ma; Schwarz and Trieloff, 2007). Following the DC measurement, the purified sample is conducted into the measurement sector by vacuum attraction using activated carbon externally cooled with liquid nitrogen. The sample argon measurement is performed after expansion in the same volume as the DC and under identical conditions.

Unlike traditional measurement techniques, the K-Ar Cassignol-Gillot technique does not require the measurement of a ^{38}Ar spike to quantify the ratios of ^{40}Ar, ^{38}Ar, and ^{36}Ar to estimate the amount of $^{40}Ar_{atm}$ and ^{40}Ar*. The K-Ar dating is based on the hypothesis that the sample crystalized in isotopic equilibrium with the atmosphere and the crystalline lattice remained closed since its cooling. However, the electrical signal obtained from ^{40}Ar over ^{36}Ar in an undisturbed sample (R_{sam}) is expected to be higher than the atmospheric ^{40}Ar/^{36}Ar ratio due to the accumulation of ^{40}Ar*. In order to quantify this atmospheric contamination, following the sample's argon measurement, a second measurement of atmospheric air is performed by adjusting its volume to replicate the sample's ^{40}Ar signal, under analogous conditions inside the mass spectrometer (Fig. 2.6). In this way, the ^{40}Ar* content is calculated by comparing the ^{40}Ar/^{36}Ar ratios of the sample (R_{sam}) and its atmospheric equivalent (R_{atm-eq}), as follows:

$$^{40}Ar^{*}(\%) = \left(1 - \frac{\mathrm{R}_{atm-eq}}{\mathrm{R}_{sam}}\right)$$

The number of ^{40}Ar* atoms is calculated by multiplying the ^{40}Ar*(%) by the sample mass, and the number of argon-40 atoms is determined as a function of the electrical signal detected.

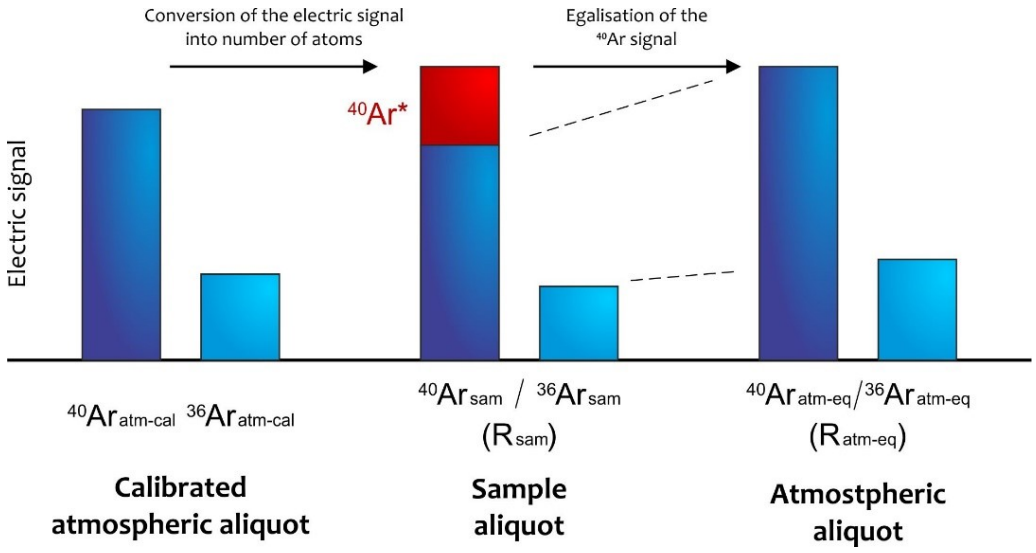

Figure 2.6. *Principle of the K-Ar dating method by the unspiked Cassignol-Gillot technique.*

The systematic measurement of the ISH-G standard of zero age (AD 1301-1302; Gillot et al., 1992), groundmass sample separated from a trachyte lava from the Isle of Ischia (Gulf of Naples, Italy), guarantees that the $^{40}Ar/^{36}Ar$ ratio measurement is identical within uncertainties to the atmospheric one, and validates the initial hypothesis of the Cassignol-Gillot technique. Note that sample mass analysed is adjusted in order to obtain an adequate electrical signal to precisely determine the difference of $^{40}Ar/^{36}Ar$ ratios of the sample and the atmosphere. The detection limit of $^{40}Ar^*$ is 0.1 % of the total ^{40}Ar measured (Quidelleur et al., 2001). Indeed, this detection limit allows to date samples as young as a few thousand years (e.g., Bablon et al., 2019, 2020a) with uncertainties depending on their potassium content (Gillot et al., 2006).

2.2.3.3 Calculation of radiometric ages and uncertainties

Given that the $^{40}Ar^*/^{40}K$ ratio is directly proportional to the time elapsed since the closure of the sample's crystalline system, the age is calculated using the radioactive decay law under the equation:

$$t = \frac{1}{\lambda}\ln\left(1 + \frac{\lambda}{\lambda_\varepsilon + \lambda_{\varepsilon'}} \times \frac{^{40}Ar^*}{^{40}K}\right),$$

where t is the sample age (in yr); λ is the decay constant of ^{40}K in ^{40}Ca* and ^{40}Ar* (5.543×10^{-10} yr^{-1}); λ_ε is the decay constant of ^{40}K in ^{40}Ar* by EC and γ ($0.572\ 543 \times 10^{-10}$ yr^{-1}); and $\lambda_{\varepsilon'}$ is the decay constant of ^{40}K in ^{40}Ar* by β^+ (0.009543×10^{-10} yr^{-1}). Decay constant values according to Steiger and Jäger (1977).

The total relative uncertainty is calculated as follow:

$$\sigma = \sqrt{{\sigma_K}^2 + {\sigma_{^{40}Ar_{cal}}}^2 + {\sigma_{^{40}Ar^*}}^2},$$

where σ_K is the analytical uncertainty of potassium measurements (1%; Gillot et al., 2006); $\sigma^{40}Ar_{cal}$ is the uncertainty in the ^{40}Ar calibration (1%; mostly due to calibration standards uncertainties); and σ ^{40}Ar* is the uncertainty in the determination of ^{40}Ar* content. The latter is calculated using:

$$\sigma_{^{40}Ar^*} = \frac{0.1}{\%^{40}Ar^*} \times 100$$

The age determination is performed at least twice to verify its reproducibility under an uncertainty range of 1-σ. The final age corresponds to the mean of the independent measurements weighted to their ^{40}Ar* content. The age of samples close to the ^{40}Ar* detection limit (when ^{40}Ar* < 0.5%) corresponds to the arithmetic mean of the independent ages.

2.2.4 The ^{40}Ar/^{39}Ar method

The ^{40}Ar/^{39}Ar method was developed in order to measure the isotopic ratio ^{40}K/^{40}Ar* directly in a single mass spectrometer, and thus facilitating the traditional K-Ar measurement by eliminating the K content determination using wet chemistry. For this purpose, the sample is first irradiated in a fast neutron nuclear reactor to transform the potassium-39 atoms into argon-39 atoms ($^{39}Ar_K$) by neutron activation. Since the ^{39}Ar/^{40}Ar ratio is constant in nature, the ^{40}Ar*/$^{39}Ar_K$ ratio becomes proportional to the ^{40}Ar*/^{40}K ratio, and thus proportional to the sample age. This transformation is dependent on the neutron flux at the reactor and the duration of irradiation. To estimate the neutron flux, a J-factor is determined by calculating the age of previously-known-age standards intercalated with the irradiated

samples (Merrihue and Turner, 1966). The irradiation parameter that quantifies the neutron flux received by the sample is calculated, as follows:

$$J = \frac{e^{\lambda \cdot t_{std}} - 1}{{}^{40}Ar^{*}{}_{std}/{}^{39}Ar{}_{std}},$$

where λ is the total ^{40}K decay constant, and t_{std} is the age of the standard. Nevertheless, the neutron flux also interacts with the calcium, potassium, argon, and chlorine atoms creating among others the argon isotopes 36, 37, 38, 39 and 40 (Fig. 2.7; e.g., Mitchell, 1968; Turner, 1971; McDougall and Harrison, 1999). The correction of these values requires the measurement of the ^{38}Ar, ^{37}Ar and ^{36}Ar contents, in addition to the ^{40}Ar and ^{39}Ar. Correction ratios for the interferences are obtained by irradiating pure calcium (CaF_2) and potassium (K_2SO_4) salts simultaneously with the samples (e.g.; Wijbrans et al., 1995; Renne et al., 1998).

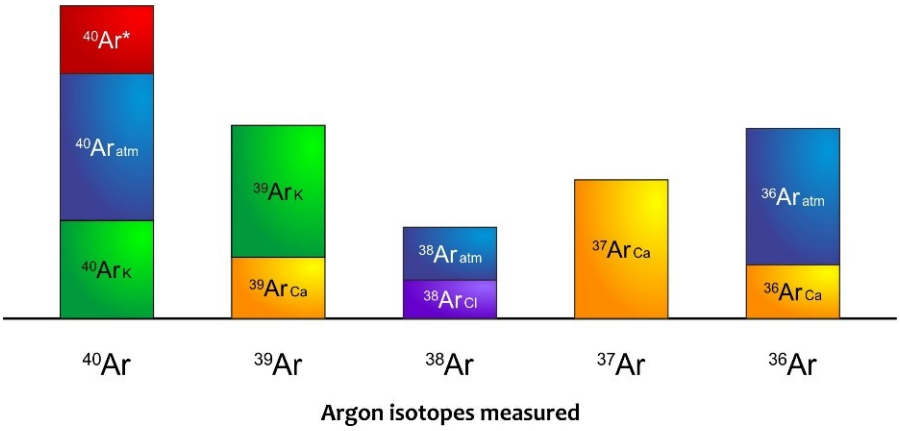

Figure 2.7. *Composition of argon isotopes measured by $^{40}Ar/^{39}Ar$ method. Radiogenic argon ($^{40}Ar^*$); atmosphere argon isotopes (Ar_{atm}); and argon isotopes produced by interaction of neutrons with calcium (Ar_{Ca}), potassium (Ar_K), and chlorine (Ar_{Cl}).*

After the irradiation process, the sample is usually heated until melting in several increasing temperature steps in a high-vacuum line (typically under 10^{-8} Torr). The extracted gas is purified and analyzed in a single mass spectrometer to determine the relative abundances of the argon isotopes ^{40}Ar, ^{39}Ar, ^{38}Ar, ^{37}Ar and ^{36}Ar. After correction for interference reactions, the $^{40}Ar^*/^{39}Ar_K$ ratio is calculated for each step assuming a given initial $^{40}Ar/^{36}Ar$ ratio equivalent to the atmospheric one, as follows:

$$t = \frac{1}{\lambda}\ln\left(1 + J\frac{^{40}Ar^*}{^{39}Ar_K}\right).$$

Note that the $^{40}Ar/^{36}Ar$ atmospheric ratio is still debated. A value of 295.5 (Steiger and Jäger, 1977) has been used for decades, but a more recent determination of 298.56 ± 0.31 has been proposed (Lee et al., 2006). We emphasize that this theoretical value of the $^{40}Ar/^{36}Ar$ atmospheric ratio has no relevance in the K/Ar Cassignol-Gillot dating method, given that the atmospheric ratio is immediately measured and compared with the sample $^{40}Ar/^{36}Ar$ ratio under analogous conditions.

The step-heating measurements are plotted in an apparent age diagram as a function of the cumulative percentage of ^{39}Ar released (Turner et al., 1966). For a closed and/or undisturbed crystalline system, the ^{40}Ar* release during the different increasing temperature steps remains constant. Thus, the values of the ages obtained will define a single and well-defined plateau. For disturbed samples, the different steps will display a disturbed pattern (Fig. 2.8). When present, the plateau age corresponds to the mean of the individual apparent ages of each step included in the plateau, weighted by the inverse of their variance. A well-defined plateau must satisfy minimum criteria (e.g., Dallmeyer and Lecorche, 1990; McDougall and Harrison, 1999; Baksi, 2007; Schaen et al., 2020), such as: it consists of a part of the age spectra constituted by at least three continuous gas fractions which collectively represents more than 70% of the total released ^{39}Ar, with all ages included do not differ by more than 95% of the confidence level (2-σ). In addition, each fraction should represent at least 4% of the total ^{39}Ar whose K/Ca ratios are similar. The single-variable mean standard weighted deviation (MSWD) parameter is used to verify the data dispersion and thus can be used to accept or reject the age obtained (Schaen et al., 2020).

The isochron age is calculated from an inverse correlation diagram in which the $^{36}Ar/^{40}Ar$ ratio is shown in correlation to the $^{39}Ar/^{40}Ar$ ratio for all steps (Fleck et al., 1977; Berger and York, 1981). The linear regression of the plotted data (isochron) enables the determination of the initial $^{39}Ar/^{40}Ar$ ratio for the calculation of the sample age, and the initial atmospheric $^{36}Ar/^{40}Ar$ ratio. Using this approach, it is not required to assume an initial value of $^{36}Ar/^{40}Ar$ to calculate the age of the assemblage. However, the $^{36}Ar/^{40}Ar$ ratio obtained should not differ significantly from ~0.00338 (i.e., 1/295.5).

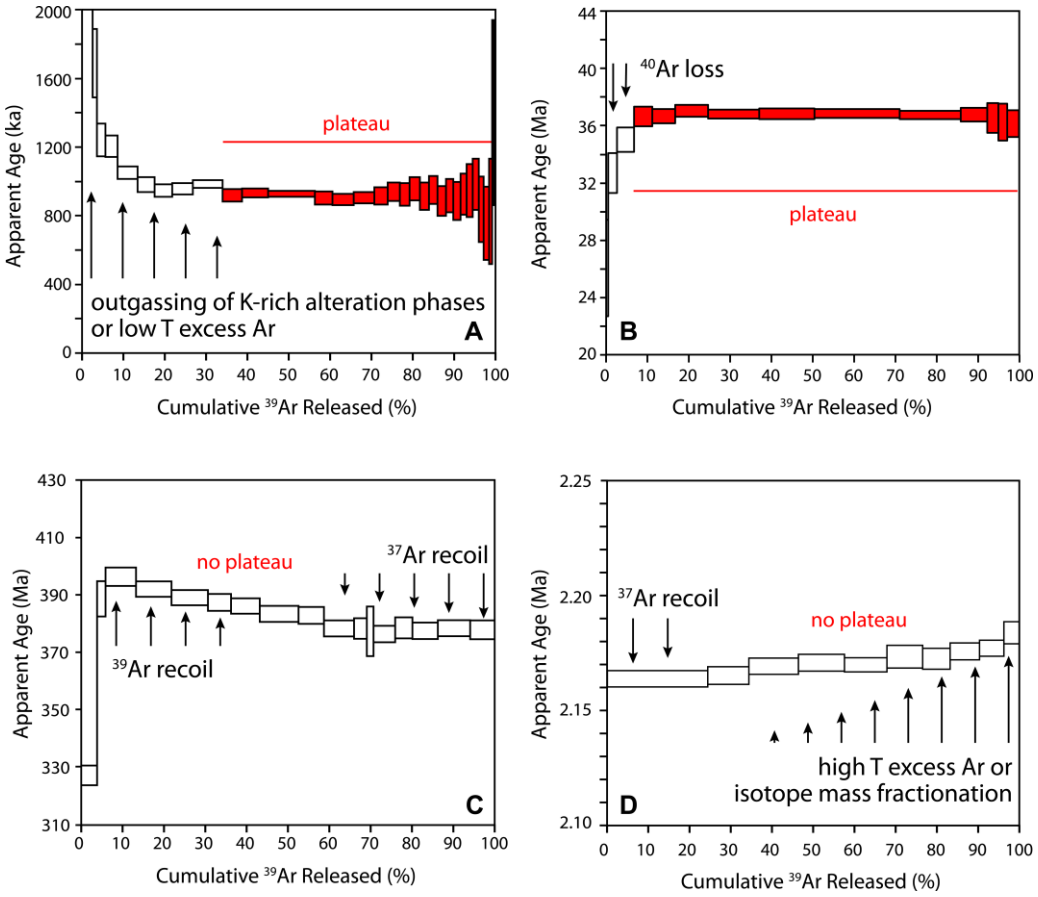

Figure 2.8. *^{40}Ar/^{39}Ar incremental heating experiments showing possible complications in age spectra according to Schaen et al. (2020).*

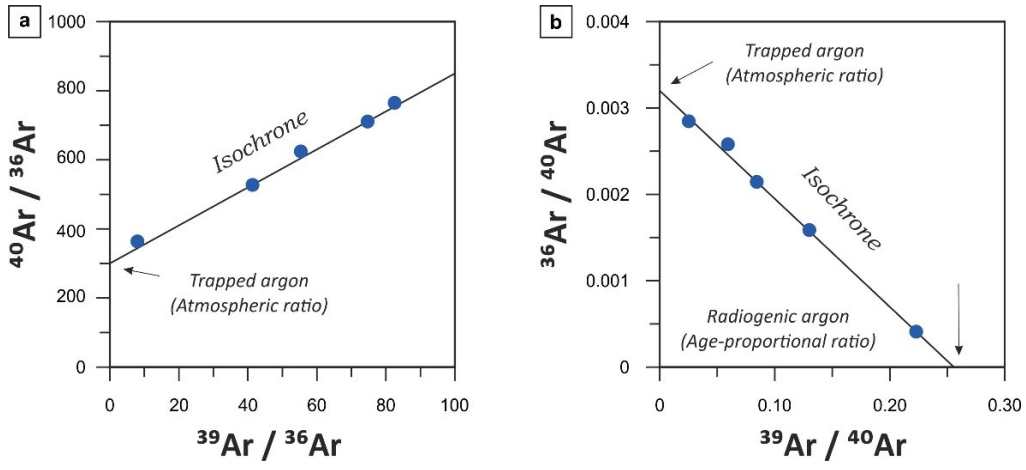

Figure 2.8. *Correlation diagrams of argon isotope ratios (modified from Dalrymple et al., 1988; Kuiper, 2002).* ***a)*** *^{40}Ar/^{36}Ar vs. ^{39}Ar/^{36}Ar diagram representing an isochrone, here the sample age is proportional to the correlation line slope.* ***b)*** *^{36}Ar/^{40}Ar vs. ^{39}Ar/^{40}Ar diagram representing an inverse isochrone, the intersections with the axes correspond to the atmospheric argon trapped in the crystal lattice and the radiogenic argon.*

2.2.5 Dating method limits

As described in section 1.2.1, the potassium-argon radiometric dating measures the time elapsed after crystal lattice closure of an analyzed sample. Most often, such closure occurs either during magma crystallization, or during later thermal events (e.g., re-heating or metamorphism) which re-open the system. For young volcanic rocks, regional metamorphism events affecting the crystal lattice are improbable. Nevertheless, re-heating events may occur when new lava bodies are emplaced on top of pre-existing ones, raising the temperature, and allowing argon diffusion. In this context, the ages of the pre-existing lava bodies could be biased towards more recent values. On the other hand, weathering processes may lead to potassium loss, which is a highly mobile element, and/or induce high atmospheric contamination, that could affect the sample age. Age biases are also produced by the presence of xenoliths, micro-granular enclaves, and/or phenocryst cumulates that potentially carry inherited $^{40}Ar^*$ locked in their crystal lattices during earlier magmatic stages prior to the final cooling and crystallization (e.g., Singer et al., 1998; Harford et al., 2002; Renne et al., 2012; Lahitte et al., 2019). Likewise, the analysis of intrusive bodies, such as dykes, could lead to important biases since the argon isotopic equilibrium with the atmosphere could be incomplete as these bodies crystallized before being exposed at the surface. To avoid these possible age biases, a severe examination and selection at the sampling site is essential. An additional control is carried out during the thin section analysis and hand crushing steps.

Note that magma mixing processes do not create biases in volcanic rock ages, as cooling and crystallization occurs in isotopic equilibrium with the atmosphere. Nevertheless, early crystals formed at depth and carried up to the surface during the eruption may contain inherited $^{40}Ar^*$ if they did not stay long enough in the new magma batch. Therefore, analysis of the groundmass is preferred as it is the last crystallizing phase following a sub-aerial eruption. A meticulous sample preparation process can remove most of the previously described biasing elements.

The K-Ar Cassignol-Gillot dating technique allows the quantification of small amounts of $^{40}Ar^*$ in young volcanic rock samples. This technique has been successfully applied in the Pleistocene volcanic arc of Ecuador (Alvarado et al., 2014; Bablon et al., 2018, 2019, 2020b, 2020a; Almeida et al.,

2019; Telenchana et al., 2019; Baize et al., 2020a), at the Andean range (e.g., Germa et al., 2010; Pallares et al., 2016, 2019; Grosse et al., 2018, 2020), and worldwide (e.g., Germa et al., 2011; Hildenbrand et al., 2018; Dibacto et al., 2020). The results obtained by the K/Ar method were consistent with those obtained by the $^{40}Ar/^{39}Ar$ method within their uncertainty ranges (e.g., Quidelleur et al., 2003). Moreover, the Cassignol-Gillot method is especially suitable for $^{40}Ar^*$ measurements on groundmasses of low-K calc-alkaline lavas, while the high Ca content of such rocks might limit the use of the $^{40}Ar/^{39}Ar$ technique. On the other hand, the $^{40}Ar/^{39}Ar$ technique allows detecting possible perturbations in the $^{40}Ar^*$ content with the step heating approach, and to check that the initial $^{40}Ar/^{36}Ar$ ratio is similar to the atmospheric one. Another advantage of this technique is that the amount of sample needed is significantly reduced. However, the K-Ar Cassignol-Gillot technique does not require the measurement of additional isotopes to correct the bias caused nuclear interferences occurring during irradiation, which is a strong issue in low-K and/or high-Ca lavas such as those found in the Ecuadorian arc. Furthermore, the uncertainty of the $^{40}Ar/^{39}Ar$ age is mainly due to the systematic uncertainties on the standard ages (or flux monitors), in addition to those of the decay constants.

In summary, the use of the K-Ar technique is suitable for recent, fresh, and fast cooling rocks, such as Quaternary sub-aerial lavas. We emphasize that the sampling protocol, selection of the crystalline phase (phenocrysts vs groundmass), and sample preparation are crucial in reducing the age bias factors for both K-Ar and $^{40}Ar/^{39}Ar$ methods.

2.3 Volcanic Surface Modeling

2.3.1 Principles

The use of geographic information system software allows the integration of multiple spatial data such as digital elevation models (DEM), geological maps, satellite photography, orthophotography, as well as maps of geochemical and geochronological data distribution. DEMs provide elevation data in a regular grid of points, also called pixels, allowing the extraction of information related to the terrain morphology for a given area. Within a volcanic context, DEMs allow to characterize the relief of volcanic edifices through the description of their morphology and geometry, the definition of their contours, and the detection of structures created by fault traces, lava flows, sectorial collapses, superposition of edifices, and erosion features (e.g., Székely and Karátson, 2004).

Primary volcanic landforms are structures created during eruptive events and possibly affected by syn-eruptive erosion (Hampton and Cole, 2009; de Silva and Lindsay, 2015). Although these structures range in size and shape (like cinder cones of a few tens of meters in diameter, to shield volcanoes of several hundred kilometers in diameter), this work focuses on the morphologies created by composite volcanoes which are typical in the Ecuadorian arc. During the construction stages of such volcanoes, several eruptive products are emitted predominantly from a central vent. The successive accumulation of lava flows, pyroclastic density current (PDC) deposits, and proximal fallout deposits create volcanic cones of a few kilometers in diameter, with flanks formed by roughly flat surfaces called *planèzes* (e.g., Cotopaxi volcano, Fig. 2.9; Allaby, 2020). Conversely, erosion processes tend to create shallow water courses that intersect the flank planèzes of the volcano. Once the eruptive activity stops, the removal of the eroded material results in the widening and deepening of these valleys, which are then bounded by remnant plains and/or ridges (e.g., Rumiñahui volcano, Fig. 2.9). Erosion processes are intensified in high altitude areas, where the formation, advance and retreat of glacial masses displace large amounts of material, rapidly dismantling the volcanic edifice (e.g., Hampton and Cole, 2009; Conway et al., 2015; Pure et al., 2020).

Numerical reconstructions of paleotopography provide a first order approximation of the original shape of a volcano, by eluding the morphologies created by intense erosion processes (e.g., Lahitte et al., 2012). Moreover, they allow to recognize irregularities in the geometry of the edifice, which can be used to identify changes in the arrangement of the volcanic vents or the presence of satellite structures. In addition, digital models are a suitable tool for quantifying the volume of material accumulated during the construction stages (v_{cs}), and the material removed during the quiescence stages (erosion volume; v_{es}). An adequate knowledge of the eruptive history of a volcano enables the identification of the construction phases and their associated features, reduces the uncertainty in the applied models, and allows the calculation of the output (R_o) and erosion rates (R_e) through time.

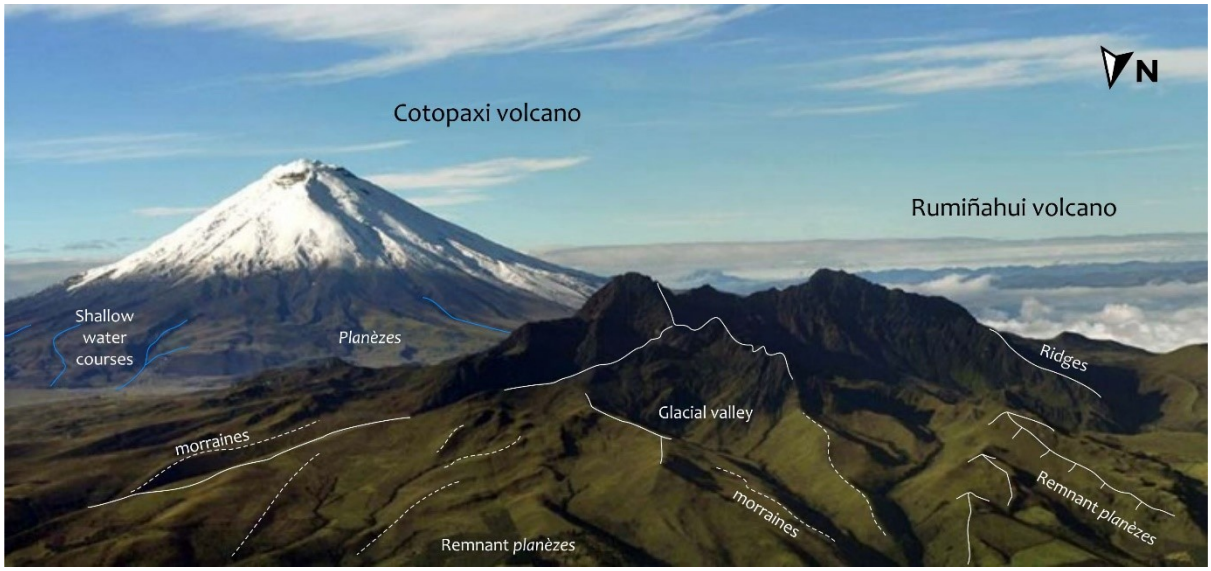

Figure 2.9. *Primary volcanic landforms observed at Cotopaxi volcano (Holocene), compared with the eroded morphology shown by Rumiñahui volcano (Pleistocene). Photography by Kuoda Travel (https://www.kuodatravel.com/).*

2.3.2 Extraction of the representative points of the paleotopography

This work uses the DEM developed by the Sigtierras program of the Ministerio de Agricultura y Ambiente of Ecuador (http://geoportal.agricultura.gob.ec). This DEM's 4-m spatial resolution allows to accurately identify the primary landforms of the Ecuadorian volcanoes (Fig. 2.10). To facilitate the calculation prosses, a regular 30-m point cloud was extracted. We followed the methodology described by Germa et al. (2015) and Dibacto et al. (2020), as summarized below.

The points (or pixels) selection process uses criteria based on both the spatial position of each point and its relationship to the surrounding topography. Within the first category, points located in wide valleys and/or at distances less than 100 m from stream channels are discarded, while points located at distances less than 100 m from the drainage divides are preserved. The second category considers topographic criteria such as slope gradients between 10 and 35°, as well as profile and planform curvature values for points preservation. To identify un-eroded *planèzes*, points with profile and planform curvature values close to 0 were retained, while the identification of ridges considers higher negative values of planform curvature. The combination of the retained points of *planèzes* and ridges then represents the unweathered terrain surface to be modeled, where the parameter values can be modified to adjust the dispersion and density of the final point cloud. Finally, the point set is manually revised by displaying the preserved points in three dimensions to eliminate those points with lower elevation compared to their close neighbors.

ArcGis software was used for the point selection process, the calculation of slope, profile, and planform curvature maps, and the identification of drainage networks and drainage divides (Fig. 2.10). The interpolation of the point set, to reproduce the surface formed after the last cone-building stage (S_{t1}), is performed using an equation which describes the shape of the cone flanks. Here, the elevation at each point is considered as a function of its distance from a vertical symmetry axis. Two interpolation approaches were used in the reconstruction of the S_{t1} surfaces. The first approach interpolates the non-eroded points using a simple exponential model, while the second one uses the ShapeVolc algorithm (Lahitte et al., 2012) that allows to achieve more complex and adjusted surface models.

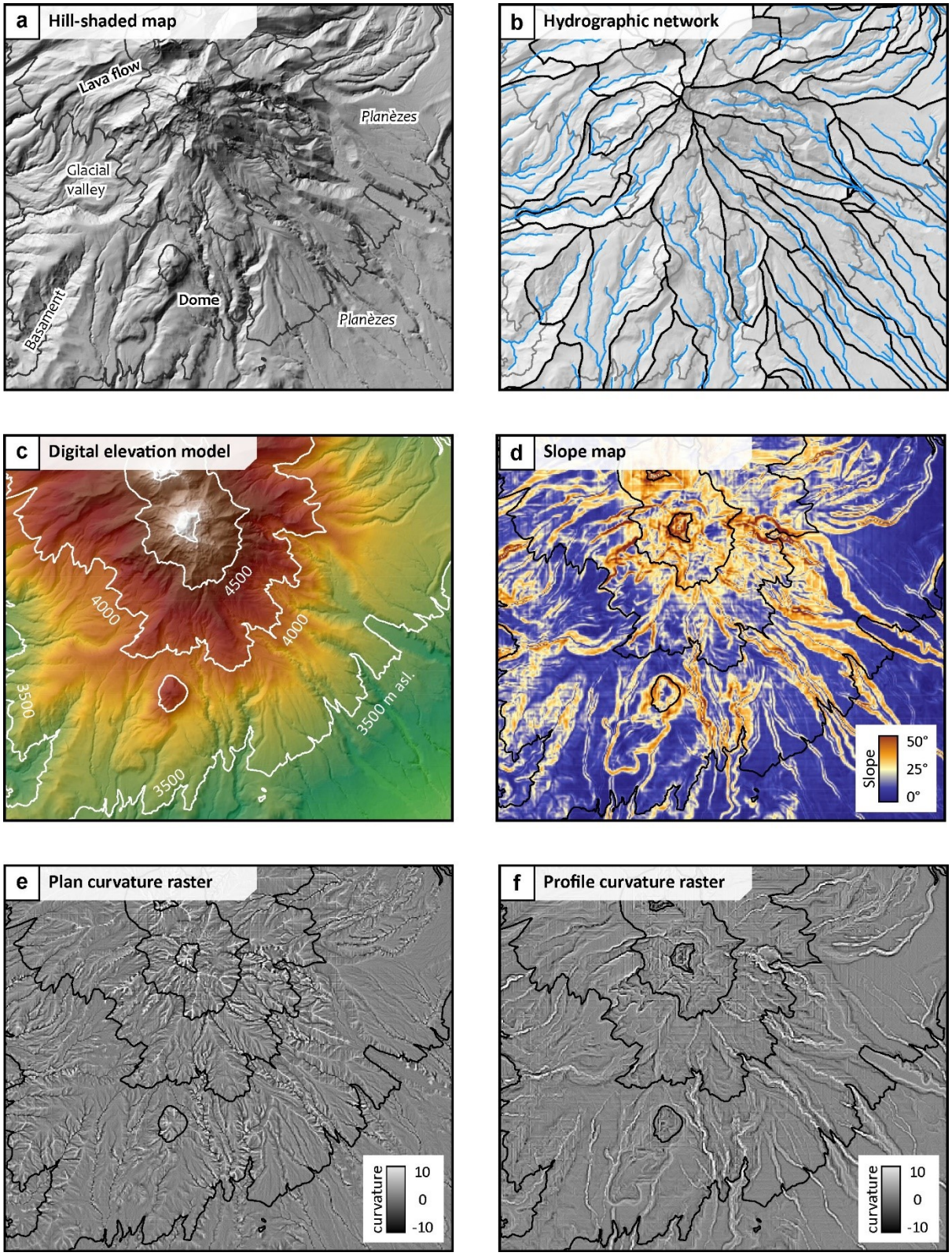

Figure 2.10. *Examples of maps and data obtained from the 4-m Digital Elevation Model of South Iliniza volcano (Western Cordillera, Central Segment).*

2.3.3 Modeling of paleotopography

2.3.3.1 First approach: Kriging interpolation

This approach assumes that the volcanic edifice has a regular conical shape, with a circular base and convex flanks. Also, the model presumes that the axis of the cone under modeling is equivalent to that of the volcanic edifice. The approximate location of the cone axis is obtained by plotting concentric circles concordant with the contour lines at each 200 or 500 m asl (Fig. 2.11b). The common geometric center of these circles represents the spatial position of the cone axis under modeling. Next, the elevations of the points extracted during the selection process (d_E) are plotted as a function of their horizontal distance to the cone axis (d_H). An exponential trendline describing the shape of the cone is obtained using a linear regression process (Fig. 2.11c). The trendline equation uses the form:

$$d_{E-i} = f(d_{H-i}) = c_{se} \cdot \mathrm{e}^{a \cdot d_H},$$

where c_{se} is the cone summit elevation in m. asl., and a is a constant value. This equation is fitted to the points with the highest elevation as a function of their distance from the axis, excluding the most dispersed points with vertical variations greater than ~50 m. Therefore, a point cloud is obtained that accurately represents the low eroded areas of the edifice. A complementary radial point cloud, with center on the cone axis and elevations calculated according to the exponential equation obtained, fills the areas with scarce control points (Fig. 2.11b).

Finally, the point cloud is transferred to ArcGis to compute the surface S_{t1} (Fig. 2.11d). We chose an ordinary kriging surface interpolation method, using the elevation of the points while minimizing the variance. This method also produces a prediction standard error map which is used to calculate the uncertainty derived from the spatial dispersion of the control points σ_{sd-i} (Fig. 2.11e). Uncertainty at each point is defined by $\sigma_{St1-i} = \sqrt{{\sigma_{mod}}^2 + {\sigma_{sd-i}}^2}$, where σ_{mod} is the elevation uncertainty of the modeled surface equivalent to $\sigma_{f(d_{H-i})}$.

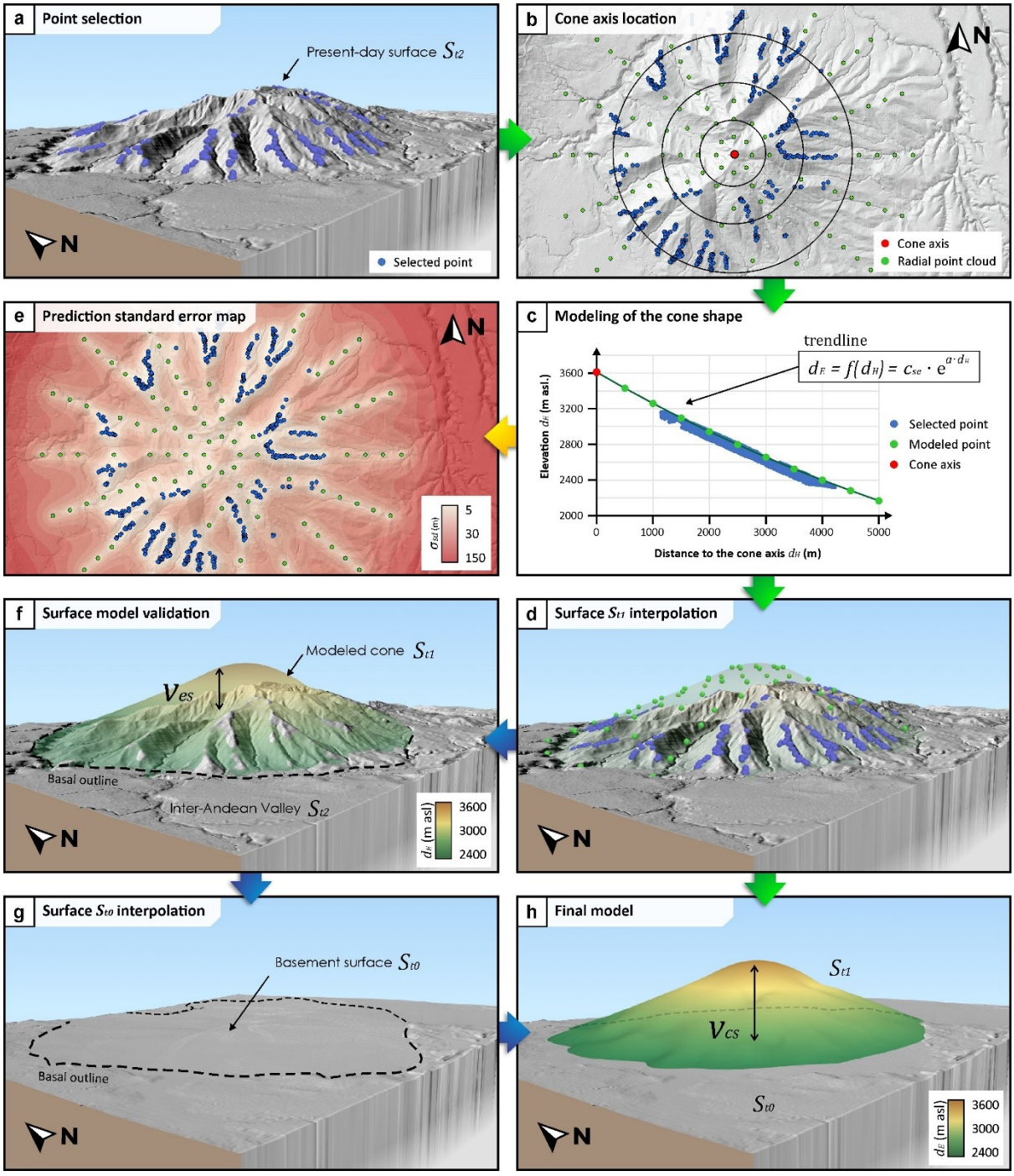

Figure 2.11. *Surface modeling and volume calculation process applied to Ilaló volcano (Inter-Andean Valley, Central Segment), using the Kriging interpolation approach. See text for details. The ShapeVolc interpolation approach (Lahitte et al., 2012) condenses steps b, c, and d into a single algorithm.*

2.3.3.2 Second approach: ShapeVolc interpolation

The ShapeVolc interpolation method developed by Lahitte et al. (2012) adapts the Kriging interpolation method to reduce the problems linked to the heterogeneous distribution of control points. First, the ShapeVolc algorithm generates a global surface model which best fits the elevation of the control points through modification of the location of the cone axis. This software also allows the selection of an elliptical-base cone, as well as several flank-equation models with sector and/or d_H distance weighting. By modifying the model parameters in ShapeVolc, it is possible to improve the adjustment to the control points and obtain more complex morphologies in relation to the regular cone interpolation method. Finally, the ShapeVolc software generates a local surface model, which adapts the regular surface of the calculated cone model to the roughness of the control points, thus producing the S_{t1} surface. The uncertainty at each point σ_{St1-i} is calculated using the same procedure as for the kriging interpolation method.

2.3.3.3 Interpolation of the basement surface

The modeling of the surface on which the volcanic edifice was constructed (basement surface; S_{t0}) employs the ordinary kriging interpolation method. Unlike the S_{t1} surface, the basement lacks sufficient surface exposures to provide useful information about its elevation and geometry. However, its geometry can be inferred by analyzing the configuration of the surrounding topography. For example, it is reasonable to assume that the basement of the Inter-Andean valley volcanoes has a planar geometry (Fig. 2.11f), while the basement of the volcanoes located in the Andean range has a rougher topography. In the latter case, the presence of north-south ridges covered by recent volcanic deposits is plausible, thus increasing the uncertainty in total volume determination. The kriging method interpolates the basement surface using the points along the basal outline of the edifices, which is suitable for volcanoes in the inter-Andean valley (Fig. 2.11g). Conversely, the method requires additional points in rougher areas, such as the Andean range or where the basement correspond to older volcanic structures. These points are obtained by tracing idealized topographic profiles that model the

geometry of the basement based on auxiliary topographic profiles (see Chapter 3). Then, the surface S_{t0} is the result of the ordinary kriging interpolation of the basal outline points combined with those obtained from the idealized topographic profiles. The uncertainty for each point σ_{St0-i} is provided by the prediction standard error map.

2.3.4 Calculation of volumes, and construction and erosion rates

The construction stage volume v_{cs} corresponds to the space enclosed by the basement surfaces S_{t0} and the modeled cone S_{t1} (Fig. 2.11h). Considering that the present-day surface S_{t2} results from the weathering effects on the surface S_{t1}, the erosion stage volume v_{es} corresponds to the empty space between the surfaces S_{t1} and S_{t2} (Fig. 2.11f). To calculate these volumes, the elevation values of the modeled surfaces are extracted at each cell of the original regular 30-m point cloud, followed by the calculation of the difference in elevation between the concerned surfaces. The calculated volume corresponds to the integration of the absolute elevation difference at each point, multiplied by the area covered by each pixel. Volume uncertainty σ_v is given by the combination of the height uncertainties of each point σ_{e-i} multiplied by the pixel area, where $\sigma_{e-i} = \sqrt{{\sigma_{Stf-i}}^2 + {\sigma_{Sti-i}}^2}$. We emphasize that volcanic edifices are formed by different types of materials with different degrees of vesicularity and spatial dispersion, therefore the calculated values are presented as bulk volumes and not as Dense Rock Equivalents (DRE). On the other hand, factors such as syn-eruptive erosion and the strong mobilization of unconsolidated volcanic materials (e.g., fallouts and PDC) result in the dispersion of part of the erupted materials. Consequently, the volume accumulated in the edifices does not represent the total amount of material emitted, so the values presented in this study should be considered as minimum volumes. Nonetheless, the rough quantification of the fallouts and distal PDC volumes emitted by Cotopaxi-IIb volcano suggests that the volume dispersed is below the uncertainty range of our calculations. A further discussion is provided in Chapter 4.

Output (R_o) and erosion (R_e) rates and are obtained by dividing the v_{cs} and v_{es} volumes by the eruptive ΔT_{cs} and quiescent ΔT_{es} period durations, respectively. The absolute uncertainty of each rate is defined by $\sigma_{Ri} = \sqrt{\left(\frac{\sigma_{vi}}{vi}\right)^2 + \left(\frac{\sigma_{Ti}}{\Delta T_i}\right)^2}$, where σ_{Ti} is the uncertainty of the period under analyzed (ΔT_i). In addition to the above-mentioned concerns on volume representativeness, output and erosion rates are susceptible to temporal biases. For example, if the construction periods are not well constrained, usually due to sampling bias in older stratigraphic units, the construction rates may be overestimated and the erosion rates underestimated. On the other hand, events of high material removal, such as sectoral collapses or glacial periods, lead to an underestimation of the construction and/or erosion volumes during such periods. Given the difficulty in accurately assessing such biases, we prefer not to provide new R_o and R_e rates determination for the Ecuadorian arc in this study.

Chapter 3

Iliniza volcano research group. From left to right: Santiago Santamaria, Pablo Samaniego, Silvana Hidalgo and Xavier Quidelleur.

Chapter 3

Geochronological evolution of the potentially active Iliniza Volcano

Journal of Volcanology and Geothermal Research (Accepted, 2022)

Contents

ABSTRACT 96
1. INTRODUCTION 97
2. GEOLOGICAL CONTEXT 99
3. METHODS 100
3.1. Sampling strategy 100
3.2. K-Ar dating 102
3.3. Geochemical analyses 103
3.4. Geomorphological reconstructions 105
4. RESULTS 106
4.1. Morphology 106
4.2. Eruptive Chronology 108
4.2.1. Santa Cruz Volcano 111
4.2.2. Iliniza Volcano 111
4.3. Reconstructed morphology for volume estimations 120
4.3.1. Basement surface reconstruction 120
4.3.2. Iliniza volcano paleosurface reconstruction and volume calculations 120
4.4. Geochemical characterization 123
5. DISCUSSION 127
5.1. Iliniza and Santa Cruz geochronological evolution 127
5.2. The Jatuncama explosive phase 130
5.3. Growth and erosion patterns in Iliniza Volcano 132
5.4. Overall geochemical nature 134
5.5. Exploring the implications for the hazard assessment 136

6. CONCLUSIONS 137
Acknowledgments 138
REFERENCES 139
Appendix A. 150
Appendix B 157
Appendix C 161
Appendix D 162

Geochronological evolution of the potentially active Iliniza Volcano (Ecuador) based on new K-Ar ages

Santiago Santamaria [a]*, Xavier Quidelleur [a], Silvana Hidalgo [b], Pablo Samaniego [c], Jean-Luc Le Pennec [d, e], Céline Liorzou [d], Pierre Lahitte [a], Marco Córdova [b], Pedro Espín [b]

[a] GEOPS, Université Paris-Saclay, CNRS, Rue du Belvédère, 91405 Orsay, France

[b] Instituto Geofísico, Escuela Politécnica Nacional, Ap. 17-01-2759, Quito, Ecuador

[c] Laboratoire Magmas et Volcans, Université Clermont Auvergne, CNRS, IRD, OPGC, F-63000 Clermont-Ferrand, France

[d] Geo-Ocean, Institut Universitaire Européen de la Mer, Université de Bretagne Occidentale, CNRS-UBO-Ifremer-UBS, Rue Dumont d'Urville, 29280 Plouzané, France

[e] IRD – Délégation Ouest, Technopôle Brest-Iroise, CS10070, 29280 Plouzané, France

*Corresponding author. santiago.santamaria@universite-paris-saclay.fr, sdsantiagof@gmail.com

Keywords:

- Iliniza volcano
- Ecuador
- K-Ar dating
- Geomorphology
- Volcanic hazards

Highlights:

- Iliniza volcano is formed by two late-Pleistocene edifices and their satellite vents.
- The North Iliniza edifice started growing at ~123 ka and ended at ~116 ka.
- The South Iliniza edifice was built from ~46 to ~25 ka and produced a VEI 5 event.
- Effusive eruptions took place during the Holocene from 2 southern satellite vents.
- Iliniza volcano should be considered as a potentially active volcano.

ABSTRACT

The youngest volcanism of the Ecuadorian Volcanic Front (Western Cordillera) is mainly dominated by highly explosive events, including the growth and violent destruction of lava domes, and the formation of thick pyroclastic sequences. Deposits associated with such eruptive dynamics have been identified at Iliniza, a compound volcano located in the Western Cordillera with a poorly defined evolutionary history. We present the first K-Ar ages of Iliniza volcano combined with stratigraphic data, numerical reconstructions, and geochemical analyses, providing a new perspective on its evolution. Our results show that Iliniza volcano is much younger than previously proposed. The Iliniza twin-peaked shape is the result of the superposition of two andesitic to dacitic stratovolcanoes. (1) The North Iliniza (NI) edifice was constructed by two lava successions and an intermediate satellite vent, showing a short range of mainly effusive activity between 123 ± 6 and 116 ± 2 ka. (2) The South Iliniza (SI) edifice began its construction through the Lower SI stage when massive lavas dated at ~45 ka formed a basal cone. During the Upper SI stage, the uppermost part of this edifice was destroyed by the highly explosive Jatuncama phase (VEI 5) leaving a 30-40 m-thick ignimbrite sequence. The subsequent extrusion of several dacitic lava domes reconstructed the South Iliniza summit at around 35 ka. The Terminal SI stage corresponds to the emission of several andesitic lavas between 31 ± 4 and 25 ± 3 ka. The Iliniza eruptive activity extended into the Late Pleistocene and Holocene with the extrusion of the Tishigcuchi lava dome, and the emission of the Pongo lava flow dated at 6 ± 4 ka. Based on the proposed eruptive history, we suggest that a revised volcanic hazard assessment of the potentially active Iliniza volcano is required.

1. INTRODUCTION

Magmatism in subduction zones archetypically creates volcanic arcs formed by large composite volcanoes whose erupted volumes reaches several tens of cubic kilometers (de Silva and Lindsay, 2015). After several geochronological studies, it seems that arc volcanoes grow in "spurts", i.e., relatively short-term construction stages separated by long-term quiescence periods. Inside these constructional periods, there are frequent "instantaneous" destruction events, such as sector collapses and caldera-forming eruptions (e.g., Esser et al., 2004; Hildreth, 2007; Conway et al., 2016; Pure et al., 2020). Indeed, several case studies worldwide attest the potential for eruptive activity to occur even after long-term quiescence periods (e.g., García-Palomo et al., 2002; Hora et al., 2007; Mariño et al., 2021). The study of the temporal, morphological and compositional records during the growth of a volcano provides insights into magmatic processes and eruptive behavior at various time scales, and thus represents a key issue for hazard assessment (Gamble et al., 2003; Capra et al., 2008; Brenna et al., 2012).

Although several suitable examples are found in the North and South American arcs, for instance, most studies are focused on recent time scales, leaving the oldest eruptive history poorly studied. Along the Ecuadorian Andes, at least 84 Quaternary volcanoes have been identified (Bernard and Andrade, 2011). These volcanic centers are arranged in north-south alignments, described from east to west as the Volcanic Front, the Main Arc, and the Back-Arc (Fig. 1; Hall and Beate, 1991; Hall et al., 2008). Each alignment shows distinctive characteristics in terms of magma composition, volcanic edifice morphology and eruptive dynamics. In particular, the Volcanic Front includes the edifices located on the Western Cordillera, with 15-20 km-wide composite volcanoes which showed several cone-building stages and major sector collapses (e.g., Pichincha volcanic complex; Robin et al., 2010). The formation of lava dome complexes is also recurrent, and often appears during the final eruptive stages following the transition from high-silica andesites to dacites (e.g., Hidalgo, 2006; Robin et al., 2010; Almeida et al., 2019; Bellver-Baca et al., 2020). Moreover, these stages also involve highly explosive eruptions (e.g., Hidalgo et al., 2008; Robin et al., 2008; Andrade et al., 2021), directed blast events (e.g., Bernard et al., 2014), and the formation of two 3 km-wide calderas (i.e., Cuicocha and

Quilotoa calderas; von Hillebrandt, 1989; Mothes and Hall, 2008; Sierra et al., 2020). Notably, large explosive eruptions occurred during the Holocene in the northern and central segments of the Volcanic Front (Fig. 1), where large urban areas such as Quito (Ecuador's capital city) are nowadays surrounded by a high number of volcanoes.

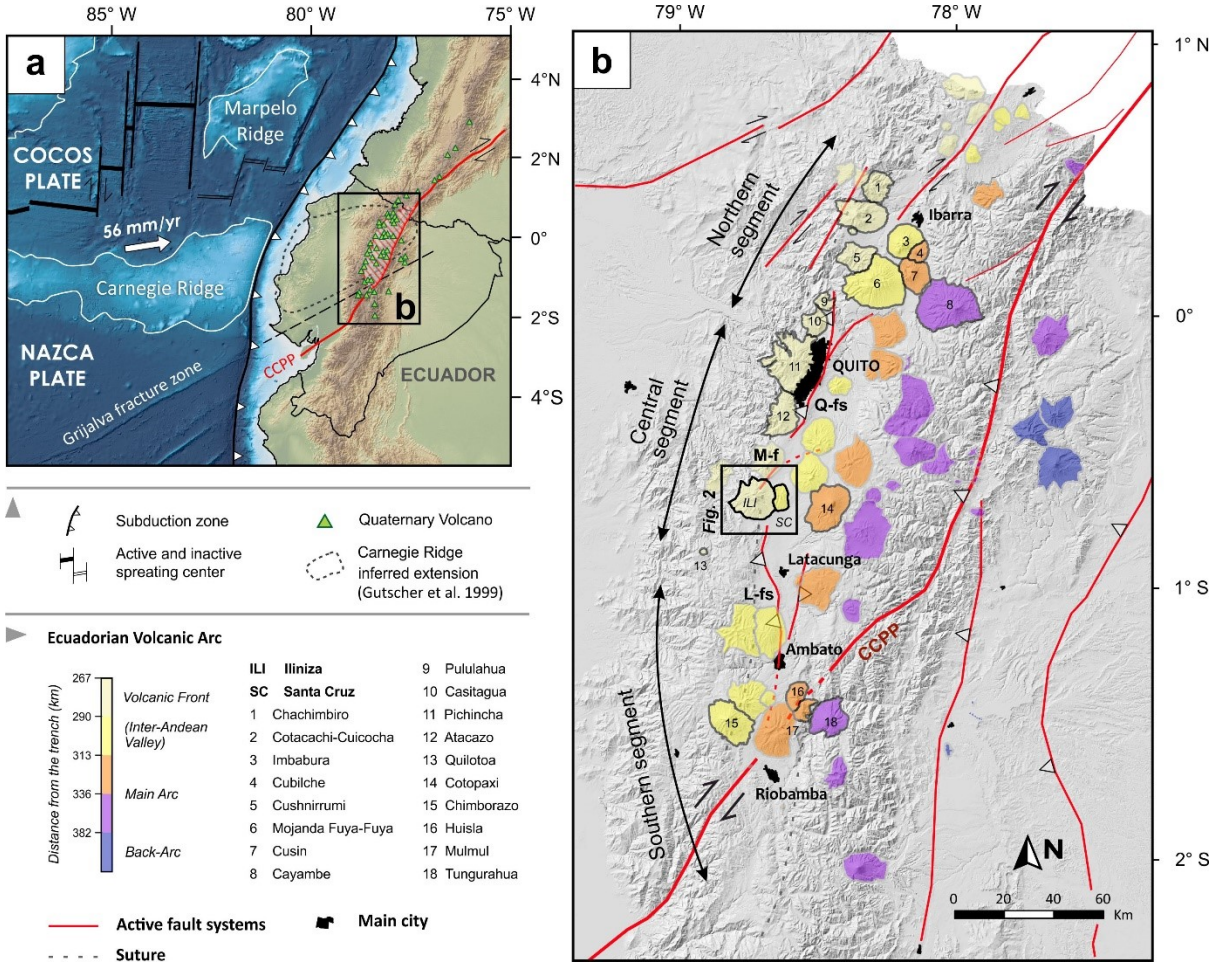

Figure 1. a) *Geodynamic setting of the Ecuadorian arc (Modified from Gutscher et al., 1999). Arrows indicate the direction of the Nazca plate motion relative to the South American continental margin according to DeMets et al. (2010).* ***b)*** *Schematic map of the Ecuadorian volcanic arc. Volcanoes are colored according to their distance from the trench comprising the N-S alignments of the Volcanic Front (Western Cordillera), Inter-Andean Valley, Main Arc (Eastern Cordillera), and Back-Arc. Variability in the number of volcanic centers is represented by the northern, central, and southern across-arc segments. Iliniza (ILI) and Santa Cruz (SC) volcanoes, as well as those mentioned in the text, are outlined with black and grey borders, respectively. Active fault systems are represented with red lines according to Alvarado et al. (2016). CCPP: Chingual-Cosanga-Pallatanga-Puná Fault System; Q-fs: Quito Fault System; M-f: Machachi Fault; L-fs: Latacunga Fault System.*

Iliniza is a twin-peaked compound volcano (5125 m asl) located 50 km south of Quito, in the central segment of the Ecuadorian Volcanic Front (Fig. 1a). Iliniza volcano exhibits volcanological characteristics that are similar to other Volcanic Front edifices, including the presence of dacite lava domes and a thick pyroclastic density current (PDC) deposit, both associated with its late eruptive stages (Hidalgo et al., 2007). Although the geochemistry of the Iliniza volcano's magmas was previously investigated (e.g., Hidalgo et al., 2007, 2012; Schiano et al., 2010; Georgatou et al., 2018), its eruptive chronology remained uncertain due to the lack of radioisotopic ages. Based on erosional geomorphology compared to other volcanoes in the Ecuadorian arc, Hidalgo et al. (2007) suggested that the earliest Iliniza activity might be as old as ~1 Ma, and Hall and Beate (1991) inferred an Holocene age for the Tishigcuchi satellite lava dome. Despite the lack of reliable chronological data, Iliniza volcano was classified as potentially active (Bernard and Andrade, 2011). If confirmed, a relatively young activity would increase the probability of a future reactivation and, consequently, increase the threat that this volcano may represent for the populations living in the Inter-Andean valley.

Here, we define the main geomorphologic and volcanological units of Iliniza volcano and present its first geochronological data, combined with new field observations and geomorphological reconstructions. We aim to constrain the eruptive stages of Iliniza volcano through time, as well as its growth and erosion patterns. In addition, geochemical data are used to describe the compositional evolution of its eruptive products over time. Our results show that the construction period of Iliniza volcano is shorter and younger than expected.

2. GEOLOGICAL CONTEXT

Iliniza volcano is part of the Northern Andean Volcanic Zone, which results from the subduction of the Nazca plate beneath the South American plate (Fig. 1a). The tectonic processes related to the active margin in Ecuador caused the formation of two N-S mountain ranges separated by a tectonic depression known as the Inter-Andean Valley (e.g., Tibaldi and Ferrari, 1992; Spikings et al., 2005; Winkler et al., 2005; Alvarado et al., 2016). Iliniza volcano (0°39.8’S, 78°43.0’W) is constructed

on the boundary between the Western Cordillera and the Inter-Andean Valley. The Western Cordillera mainly consists of deformed oceanic mafic rocks accreted to the continental margin during the Late Cretaceous to Paleocene, which are covered by Paleogene sedimentary and volcano-sedimentary sequences (Jaillard et al., 2004; Vallejo et al., 2009, 2019). These units are in turn overlain by the Silante Formation, which is exposed to the northwest of Iliniza volcano. It is composed of volcanoclastic sandstones, conglomerates and red mudstones derived from the erosion of the San Juan de Lachas volcanic island arc, of Early Miocene age (Boland et al., 2000; Vallejo, 2007; Vallejo et al., 2020). Towards the southwest, the Zumbahua Formation constitutes an extensive volcanic and volcano-sedimentary sequence deposited in lacustrine and fluvial basins during the Late Miocene-Pliocene (Barberi et al., 1988; Hughes and Bermúdez, 1997; Vallejo et al., 2019). Although no radioisotopic ages are reported, a Pliocene age is inferred for the volcanoclastic series forming the plains gullied by the Jatuncama River, to the west of Iliniza (Hughes and Bermúdez, 1997).

The northern Andean geodynamics are dominated by the northeastward decoupling of the North Andean Sliver from the continental margin of South America (Freymueller et al., 1993; Witt et al., 2006; Egbue and Kellogg, 2010; Nocquet et al., 2014). Alvarado et al. (2016) observed that deformation in Ecuador has progressively migrated eastward to its current location on the Chingual-Cosanga-Pallatanga-Puna (CCPP) fault system creating the Quito-Latacunga Microblock (QL-M). Iliniza volcano is located along the NE-SW alignment created by the Machachi right-lateral strike-slip fault (M-f; Soulas et al., 1991; Egüez et al., 2003), and is close to the northern extension of the Latacunga reverse Fault System (Lavenu et al., 1995; Egüez et al., 2003). The M-fs is considered part of the Quito-Latacunga fault system which delineates the western boundary of the QL-M (Alvarado et al., 2016).

3. METHODS

3.1. Sampling strategy

Field work and sampling were carried out in 2019 and 2020 with the purpose to identify and describe the main volcanic units, to establish their stratigraphic relationships, and to collect new fresh

rock samples for K-Ar dating and whole-rock geochemical analyses. In addition, in order to gather a comprehensive stratigraphic record, we used previous field data, petrographic descriptions, and samples from Hidalgo (2001, 2006) and Hidalgo et al. (2007).As a result, we completed a dataset of 113 whole-rock analyses that cover the entire stratigraphic succession Sample locations are shown in Figure 2. All maps and locations are projected using the Universal Transverse Mercator (UTM) coordinate system (Zone 17).

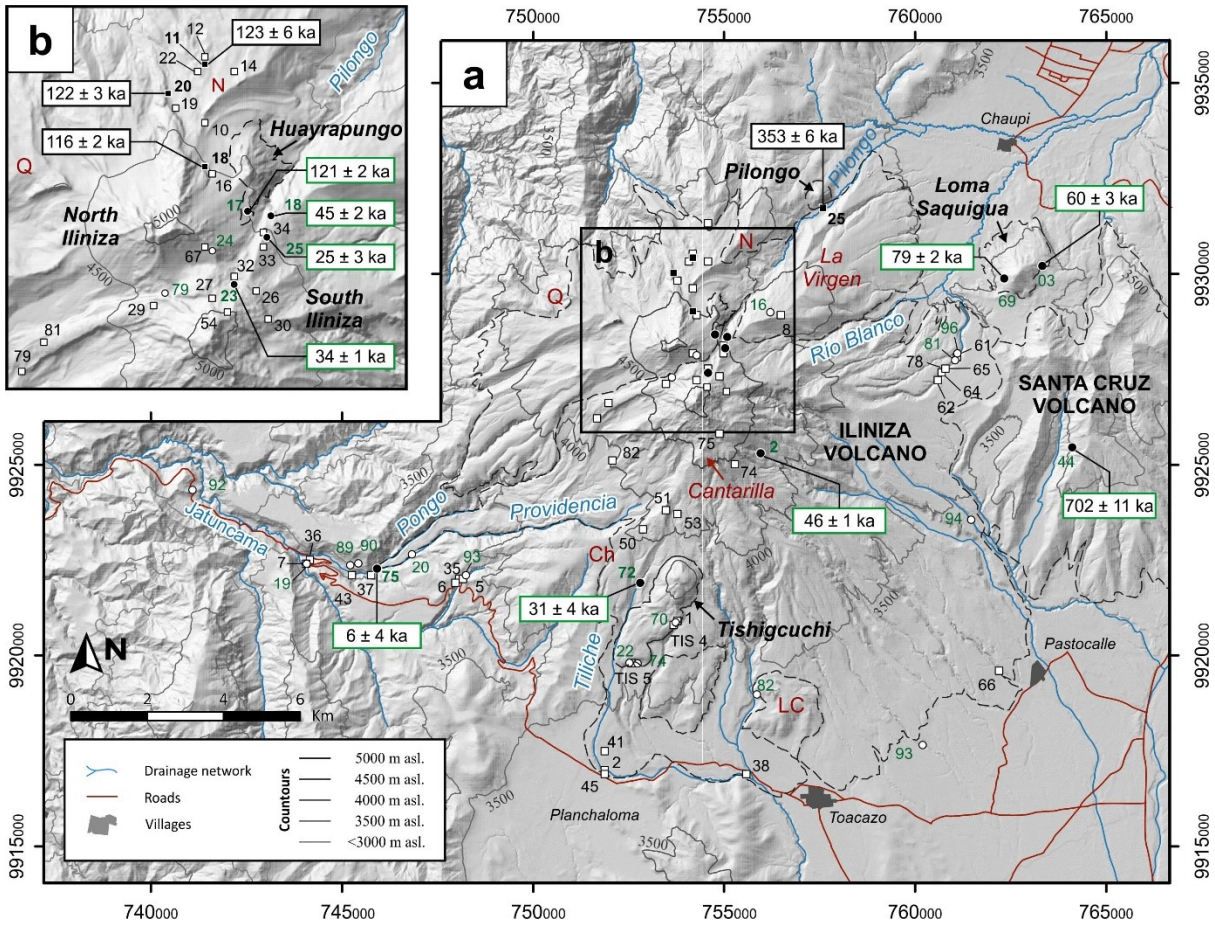

Figure 2. *Hill-shaded digital surface model of Iliniza volcano showing the locations of new samples (circles; green numbers) and those from Hidalgo et al. (2007) (squares; black numbers). K-Ar dated samples are represented with solid symbols. Volcanic peaks shown as black letters. Ridges and hills shown as red letters. Ch: Chilcapamba; LC: Loma La Cruz; N: Ninarrumi; Q: Quillotoro. Rivers and valleys are labelled with blue letters.*

158 From the whole dataset, a total of nineteen new samples were selected for K-Ar dating from
159 lava flows, monolithological breccias, and juvenile blocks from PDC deposits. Six samples belong to
160 the North Iliniza edifice, of which two correspond to monolithological breccias located at the base of
161 the northern flank (ILI 11, ILI 20), three to intermediate height lavas (ILI 16B, ILI 18, 19EQ17), and
162 one to a summit lava (19EQ24). Four lavas of South Iliniza edifice were sampled from the northern
163 (19EQ18, 19EQ25), eastern (19EQ02), southern (20EQ72) and southwestern (19EQ20, 20EQ75)
164 flanks, as along with a lava dome sample (19EQ23b) and a massive lava block (ILI 29A, 20EQ79b)
165 from the summit area. Three juvenile blocks were sampled from PDC's deposits on the northern flank
166 of Iliniza (19EQ16), Jatuncama river valley (19EQ19a) and Santa Rosa area (20EQ81a). Lastly, four
167 dacitic blocks were collected from the Pilongo (ILI 25) and Tishigcuchi (19EQ22, 19EQ70, 20EQ74)
168 satellite lava domes. In addition, three samples of the nearby Santa Cruz volcano were taken from its
169 southern (19EQ44) and northern (19EQ03, 20EQ69) flanks.

170

171 ## 3.2.K-Ar dating

172 Eighteen samples were carefully selected based on their low weathering appraised from thin
173 section examination (Appendix A). High groundmass abundance (relative to phenocrysts content), and
174 low vesicle content were also considered. Samples were dated by applying the K-Ar method on
175 groundmass, using the unspiked Cassignol-Gillot technique (Cassignol and Gillot, 1982). The latter
176 relies on the detection of tiny quantities of radiogenic argon (^{40}Ar*) diluted by ^{40}Ar from atmospheric
177 contamination. The mass spectrometer is used to measure the ^{40}Ar and ^{36}Ar electrical signals extracted
178 from a sample, and to compare them with an aliquot of pure air measured under the same analytical
179 conditions. This approach renders the knowledge of the atmospheric ^{40}Ar/^{36}Ar ratio unnecessary for our
180 technique. The difference of the ^{40}Ar/^{36}Ar isotopic ratios acquired from the sample and the atmosphere
181 is used to quantify the amount of ^{40}Ar* produced by the ^{40}K radioactive decay since the closure of the
182 isotopic system. Thus, the independent measurement of K-content, the ^{40}K relative isotopic abundance
183 in nature and its decay constant (Steiger and Jäger, 1977; Min et al., 2000) allow to calculate the age of
184 the sample. The Cassignol-Gillot technique is adequate to date young calk-alkaline volcanic products

that typically exhibit low $^{40}Ar^*$ contents (Gillot et al., 2006). This technique was successfully applied to the Quaternary Ecuadorian volcanic arc (Alvarado et al., 2014; Bablon et al., 2018, 2019, 2020), in the Andes (e.g., Germa et al., 2010; Samaniego et al., 2016; Grosse et al., 2018, 2020; Pallares et al., 2019; Mariño et al., 2021), and worldwide (e.g., Germa et al., 2011; Hildenbrand et al., 2018; Dibacto et al., 2020). Groundmass fraction is preferred for dating since it is the potassium-enriched phase that crystallizes last following the eruption, and thus incorporated the initial argon with atmospheric isotopic ratio. Furthermore, the use of groundmass avoids the possible contamination by inherited $^{40}Ar^*$ contained in phenocrysts, which could skew ages in young volcanic products (e.g., Singer et al., 1998; Harford et al., 2002; Renne et al., 2012; Lahitte et al., 2019). Samples were prepared following the protocols detailed in Bablon et al. (2018), where analytical procedures, standards used, and uncertainty calculations are also supplied. Potassium and argon isotopic measurements were carried out at the GEOPS laboratory in Orsay (Paris-Saclay University, France). The reproducibility under 1-σ confidence level was checked by performing the measurements at least twice. Fourteen new K-Ar ages were acquired from the previous selected samples and are presented in Table 1.

3.3.Geochemical analyses

Nineteen additional samples were collected for geochemical analyses, following the sampling strategy previously described, to provide a dataset of 40 new analyses presented in Appendix B. Whole-rock contents of major and trace elements were measured from agate-grinded powders at the GEO-OCEAN laboratory, University of Bretagne Occidental (Brest, France) via Inductively Coupled Plasma-Atomic Emission Spectrometry (ICP-AES), following the procedure described by Cotten et al. (1995). Relative standard deviations are <1% for SiO_2, <2 % for the other major elements, and < 5 % for trace elements. To provide a complete dataset covering as much of the volcanic history as possible, we included 73 analyses from Iliniza volcano obtained in the same laboratory and published by Hidalgo et al. (2007).

211 ***Table 1.*** *(Caption provided below)*

Sample	Location and Unit	Longitude (m)	Latitude (m)	K (%)	^{40}Ar* (%)	^{40}Ar* (10^{11} at/g)	Age ± 1σ (ka)	Mean age (ka)
ILINIZA VOLCANO								
Pilongo lava dome								
ILI 25	Lava dome, Pilongo valley	757550	9931731	1.641	10.0%	6.0596	354 ± 6	**353 ± 6**
					16.4%	6.0422	352 ± 5	
North Iliniza edifice								
ILI 11	Monolithological breccia, N flank, *NI-Ls*	754150	9930434	2.404	2.0%	3.0594	122 ± 6	**123 ± 6**
					2.1%	3.1022	124 ± 6	
ILI 20	Monolithological breccia, N flank, *NI-Ls*	753648	9930031	2.148	5.5%	2.7666	123 ± 3	**122 ± 3**
					5.0%	2.6825	120 ± 3	
19EQ17	Lava flow, Huayrapungo peak, *NI-Hs*	754734	9928425	2.226	7.3%	2.8472	122 ± 2	**121 ± 2**
					6.8%	2.7715	119 ± 2	
ILI 18	Lava flow, N flank, *NI-Us*	754151	9929036	1.878	8.6%	2.2906	117 ± 2	**116 ± 2**
					8.7%	2.2671	116 ± 2	
South Iliniza edifice								
19EQ02	Lava flow, E flank, *SI-Ls*	755922	9925321	1.728	3.7%	0.8557	47 ± 1	**46 ± 1**
					3.1%	0.8006	44 ± 2	
19EQ18	Lava flow, N flank, *SI-Ls*	755052	9928362	1.667	1.9%	0.7908	45 ± 2	**45 ± 2**
					1.9%	0.7826	45 ± 2	
19EQ23b	Lava dome, summit area, *SI-U_{SDC}*	754550	9927424	2.302	3.1%	0.8144	34 ± 1	**34 ± 1**
					3.1%	0.8078	34 ± 1	
20EQ72	Lava flow, S flank (Tiliche river), *SI-T_A*	752778	9921934	1.206	0.8%	0.3788	30 ± 4	**31 ± 4**
					0.9%	0.3921	31 ± 4	
19EQ25	Monolithological breccia, N flank, *SI-T_A*	754997	9928069	1.311	0.9%	0.3273	24 ± 3	**25 ± 3**
					0.9%	0.3631	27 ± 3	
Pongo lava flow								
20EQ75	Lava flow, Pongo valley	745904	9922305	1.534	0.2%	0.0922	6 ± 4	**6 ± 4**
					0.2%	0.1017	6 ± 4	
SANTA CRUZ VOLCANO								
19EQ44	Lava flow, S flank, *SC*	764061	9925476	1.096	14.7%	7.9746	697 ± 11	**702 ± 11**
					15.4%	8.0858	706 ± 11	
Loma Saquigua								
20EQ69	Lava dome, *LS-d*	762285	9929891	1.480	5.8%	1.2233	79 ± 2	**79 ± 2**
					6.8%	1.2283	79 ± 2	
19EQ03	Lava flow, N flank, *LS-a*	763281	9930218	1.417	1.8%	0.8927	60 ± 3	**60 ± 3**
					2.2%	0.8868	60 ± 3	

212

Table 1. *K-Ar ages obtained in this study for Iliniza and Santa Cruz volcanoes listed in decreasing order from oldest to youngest. Column headings indicate sample name, outcrop and relative location, volcanological unit (abbreviations as in Figure 4), sample coordinates, potassium (K) content in percent, radiogenic argon content ($^{40}Ar^*$) in percent and in 10^{11} atoms per gram, age obtained for each measurement, and weighted mean age in ka given with a 1-σ uncertainty.*

3.4.Geomorphological reconstructions

Numerical methods allow to model the primary geomorphology of a volcanic edifice despite the presence of intense erosive features. They are used to calculate the bulk volume of an edifice at the end of each construction stage, as well as the volume removed by erosion. The morpho-structural analyses were carried out using field observations, Google Earth® satellite images, orthophotography, and a 4-m spatial resolution digital elevation model (DEM) developed by the Sigtierras program from the Ministry of Agriculture and Livestock of Ecuador (http://geoportal.agricultura.gob.ec). A regular 30-m resolution point cloud was extracted from it to facilitate numerical calculations. We followed the method developed in Lahitte et al. (2012) according to the descriptions provided by Germa et al. (2015) and Dibacto et al. (2020), which are summarized below. The above-mentioned papers yield further methodological details and comparisons with other numerical techniques.

The surface preceding the Iliniza construction (S_{t0}) was calculated using an ordinary kriging interpolation method. Our approach uses the external points extracted from the basal outline of the edifice, and theorized profiles of the paleo-topography. The elevation uncertainty at each point is provided by the prediction standard error map resulting from ordinary kriging. We employed the ShapeVolc software (Lahitte et al., 2012) to model the post-cone-building surfaces S_{t1} based on control points extracted from reliable present-day remnants of pre-erosion topography such as the radial crests and *planèzes*. Uncertainty at each point is defined by $\sigma_{St1-i} = \sqrt{{\sigma_{mod}}^2 + {\sigma_{ed-i}}^2}$, where σ_{mod} is the elevation uncertainty of the modeled surface, and σ_{ed-i} is that derived from the spatial dispersion of the control points determined by a prediction standard error map.

The construction stage volume v_{cs} corresponds to the integration of the elevation difference between S_{t0} and S_{t1} surfaces multiplied by the pixel area, while the erosion stage volume v_{es} uses S_{t1} and present-day S_{t2} surfaces. Volume uncertainty σ_v is given by the combination of the height uncertainties of each point σ_{e-i} multiplied by the pixel area, where $\sigma_{e-i} = \sqrt{{\sigma_{Stf-i}}^2 + {\sigma_{Sti-i}}^2}$. Output ($R_o$) and erosion ($R_e$) rates are obtained by dividing the v_{cs} and v_{es} volumes by the eruptive ΔT_{cs} and quiescent ΔT_{es} period durations, respectively. Rate absolute uncertainty is defined by $\sigma_{Ri} = \sqrt{\left(\frac{\sigma_v}{v}\right)^2 + \left(\frac{\sigma_T}{\Delta T}\right)^2}$, where σ_T is the uncertainty of the period duration ΔT.

4. RESULTS

4.1.Morphology

The twin peaks of Iliniza volcano correspond to two prominent superimposed stratovolcanoes (Fig. 2). The **North Iliniza edifice** (5125 m asl), also called Tioniza (Hidalgo, 2001), stands on the eastern edge of the Western Cordillera at 4000 m asl. This volcano has an elongated basal shape with a radius ranging from 4 km over the Western Cordillera side to 6 km in the Inter-Andean Valley side. The summit's southeastern flank is not preserved. Only a narrow and steep amphitheater (750 m wide and slope angle > 40°), probably formed by glacial erosion, remains in place (Fig. 2b). The North Iliniza lavas partially cover the *Huayrapungo peak* (4585 m asl), a narrow pinnacle located 2.5 km northeast from the summit (Fig. 2b). The **South Iliniza edifice** (5248 m asl) covers the southeast flank of the North Iliniza edifice. This stratovolcano has a well-defined semicircular shape of 7 km of radius, whose summit is located 1.5 km to the southeast of North Iliniza's summit. The base of the volcano ranges from 3300 m asl to 3600 m asl in the inter-Andean valley. Lastly, the **Pilongo** and **Tishigcuchi** satellite lava domes are located at the northern and southern flanks of Iliniza volcano, about 5.2 km from its highest summit.

The late Pleistocene glaciations strongly modified the morphology of Iliniza volcano (Hidalgo, 2001), as shown by the different stages of glacial erosion exhibited by its two edifices. The northern edifice is dissected by wide U-shaped valleys creating a steep central horn surrounded by a low-sloping *plateau* situated between 4100 and 4200 m asl, where its lowest points extend down to 3780 m asl. Several well-defined ridges radiate from the central horn and separate each glacial valley (Fig. 3a). A succession of moraines a few tens of meters thick is observable inside the main glacial valleys at elevations ranging from 4100 m asl to 4500 m asl. The northwestern flank of the Huayrapungo peak is contoured by a succession of lateral moraines that form a glacial fan at the base of this structure, i.e., at about 4100 m asl at the head of the Pilongo Valley (Fig. 3b). In contrast, the South Iliniza glacial valleys are narrow and less incised preserving the conical shape of the edifice. The lowest frontal and lateral moraines are recognizable at the base of the cone at about 3700 m asl on the eastern flank and 3800 m asl on the northern and southern flanks. Heine (2011) presented a summary of evidences describing several glacial cycles in the Ecuadorian Andes (e.g., Clapperton, 1986, 1987; Heine, 1995, 2000). The author inferred that the non-studied moraine sequences of the Iliniza, Cayambe and Antisana volcanoes could include deposits from the Last Glacial Maximum (LGM; ~35-20 ka) and even from older cycles. This hypothesis is supported by the moraine associations identified at Rucu Pichincha volcano, where LGM and Younger Dryas (~12.5-10.2 ka) moraine series were recognized via radiocarbon dating in the interior of pre-existing wide glacial valleys between 4000 and 3800 m.asl. (Heine, 1995). Observed at similar elevations, the moraine sequences described at Chimborazo volcano and in the Papallacta valley (Chacana caldera; Fig. 1) have been attributed to the LGM and others possibly to previous glacial cycles (Clapperton, 1987, 1990; Heine, 1995). Comparing the moraine elevations in the Ecuadorian Andes, we also consider that those observed at Iliniza volcano were emplaced during the LGM (and possibly during earlier glacial cycles), where its northern edifice suffered a more extended erosion, thus explaining its more conspicuous erosional morphology. Nonetheless, further documentation is required to confirm the ages of these glacial deposits.

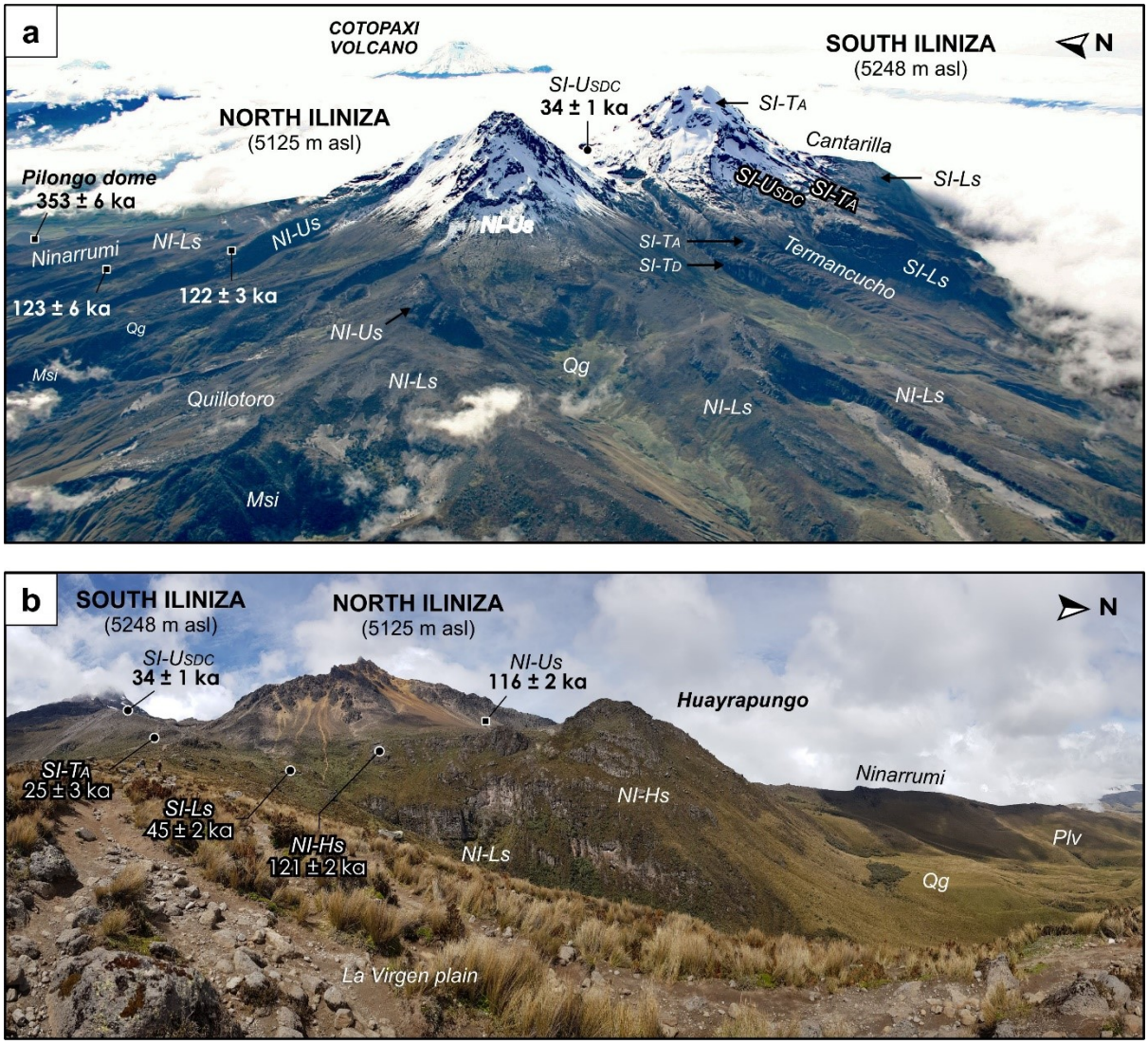

Figure 3. a) *Aerial view of Iliniza volcano, looking east (photography by Patricio Ramon, IG-EPN).* ***b)*** *Panoramic view of the North Iliniza edifice, looking west from La Virgen plain. Geological unit abbreviations as in Figure 4.*

4.2.Eruptive Chronology

The evolution stages of Iliniza volcano and its relationship with the nearby Santa Cruz volcano are presented below, together with a simplified geological map shown in Figure 4. Volcanic units description is based on the previous studies of Hidalgo *(2001, 2002)* and Hidalgo et al. *(2007)*, and our new morphologic, stratigraphic, and geochronological data summarized in Table 2.

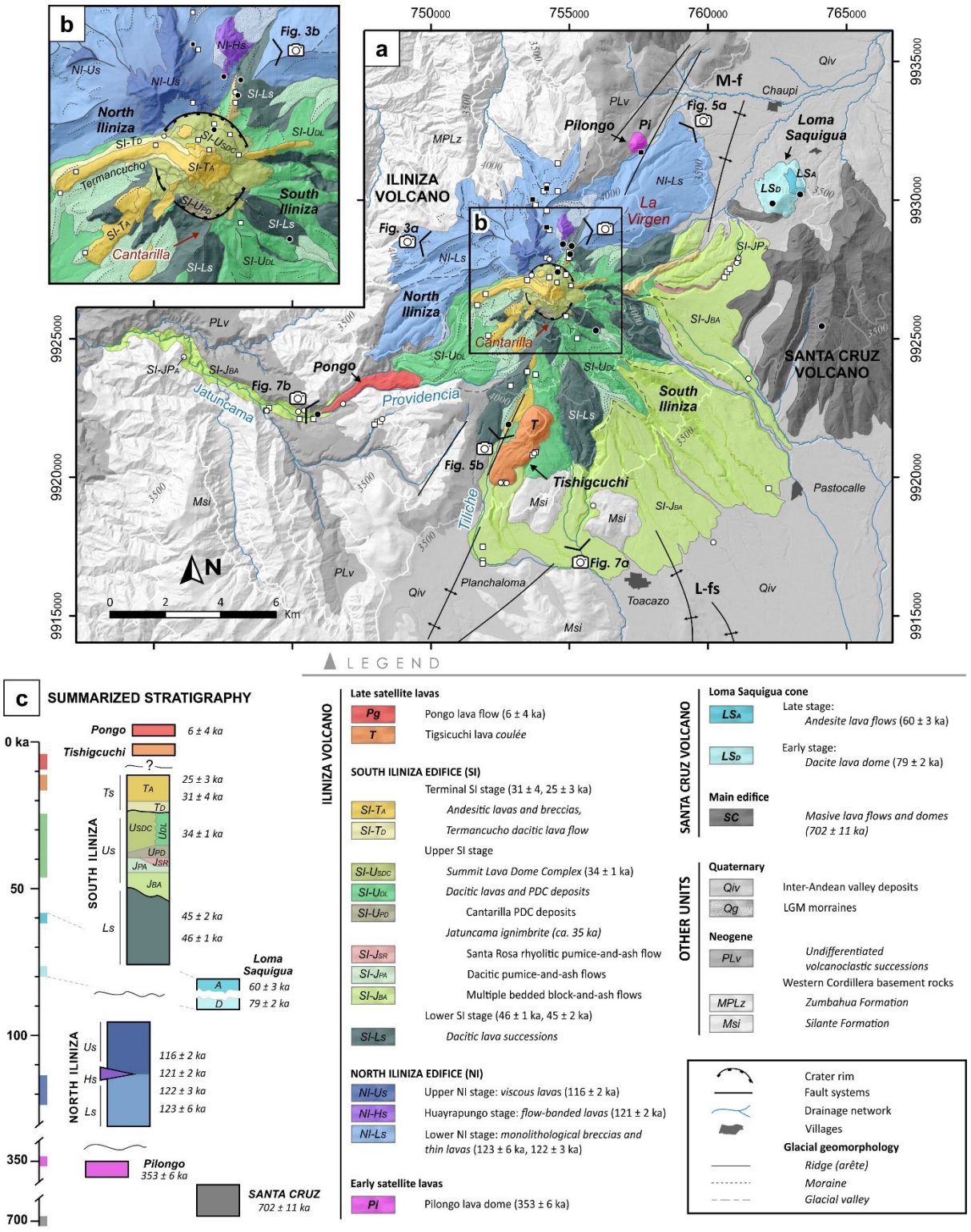

Figure 4. *Simplified geological map of Iliniza volcano after considering our new ages (Table 1) and field observations, as well as those from Hidalgo (2001) and Hidalgo et al. (2007). Sample sites are shown according to figure 2 caption. Local fault systems are symbolized with black lines. M-f: Machachi Fault; L-fs: northern segment of Latacunga Fault System.*

303 ***Table 2.*** *Generalized chronostratigraphy showing the main stages of the Iliniza volcano.*

Edifice	Cone-building stage/Unit		Age (ka)	Volcanology	Petrography
Late satellite lavas	Pongo lava flow		6 ± 4 ka	Effusive eruption: voluminous lava flow	Aphanitic andesite (59 wt.% SiO_2): pl, opx and cpx, ± pl
	Tishigcuchi lava dome		>20 and <8 ka	Lava dome-forming eruption	Andesite (62-63 wt.% SiO_2): pl, amp, opx, ± cpx
South Iliniza	Terminal stage		31 ± 4 to 25 ± 3 ka	Mainly effusive activity: voluminous lava flows and related pyroclastic deposits	Mostly andesites (61–63 wt.% SiO_2): pl, opx, cpx, ± amp
	Upper stage	Summit lava dome complex	34 ± 1 ka	Lava dome-forming eruptions and related PDC	Dacites (64–67 wt.% SiO_2): pl, amp, ± Fe–Ti oxides, ± cpx
		Jatuncama explosive phase	~35 ka	Explosive dome-forming eruption followed by a pumiceous phase: - Dacitic and rhyolitic pumice-and-ash flows - Multiple bedded block-and-ash flows	- Scarce rhyolites (71-72 wt.% SiO_2): pl, ± cpx (aegirine), ± Fe-Ti oxides - Dacites (63-67 wt.% SiO_2): pl, amp, ± cpx
	Cantarilla unconformity				
	Lower stage		45 ± 2 to 46 ± 1 ka	Mainly effusive activity: basal edifice construction	Dacites (62-65 wt. % SiO_2): pl, amp, cpx, ± opx, ± Fe-oxides
North Iliniza	Terminal stage		116 ± 2 ka	Mainly effusive activity: viscous lava flows	Acid-andesites to dacites (62-65 wt.% SiO_2): pl, cpx, opx, ± Fe-Ti oxides, ± amp
	Huayrapungo stage		121 ± 2 ka	Mainly effusive activity: voluminous flow-banded lava flow	Andesites (62 wt.% SiO_2): pl, opx, and scarce cpx, ± Fe-Ti oxides
	Lower stage		122 ± 6 to 123 ± 6 ka	Mainly effusive activity: thin lava flows	Acid-andesites to dacites (62-64 wt.% SiO_2): pl, opx, cpx, ± amp, ± Fe-Ti oxides
Early satellite lavas	Pilongo lava dome		353 ± 6 ka	Lava dome-forming eruption	Porphyritic rhyodacite (68-69 wt.% SiO_2): pl, amp, opx, ± cpx, ± Fe-Ti oxides

304 Abbreviations: pl=plagioclase, amp=amphibole, cpx =clinopyroxene, opx=orthopyroxene.

305

4.2.1. Santa Cruz Volcano

Santa Cruz (SC), is a highly eroded stratovolcano (3978 m asl) mainly comprising successions of andesitic lava flows (e.g., 19EQ44: 56.4 wt.% SiO_2). It is located in the Inter-Andean valley, 10 km east of the South Iliniza edifice (Fig. 2). Only the southern flank of the volcano is exposed, where the preserved gently dipping slopes (8-14°) are dissected by wide and deep valleys. Highly weathered and altered dacitic lava domes are found in the summit area (e.g., 19EQ04: 65.6 wt.% SiO_2). The northern flank, where preserved, is covered by the Inter-Andean valley deposits (Qiv), which are 300 m higher compared to the *Qiv* average elevation at the base of the southern flank. A K-Ar age of 702 ± 11 ka is obtained from an andesitic lava flow of the southern ridge (19EQ44), representing an intermediate age of the Santa Cruz edifice.

Loma Saquigua (**LS)** is an isolated summit peak (3839 m asl) of Santa Cruz volcano. The base of Loma Saquigua is formed by a dacite lava dome (LS_D; 63.7 wt.% SiO_2). A block taken in its eastern flank (20EQ69) yields a relatively young K-Ar age of 79 ± 2 ka. The upper structure of Loma Saquigua consists of andesitic lava flows (LS_A; 57.8 wt.% SiO_2) dated at 60 ± 3 ka (19EQ03). The Santa Cruz volcanic products, including those of Loma Saquigua, show a mineral assemblage composed of plagioclase, orthopyroxene, clinopyroxene, and Fe-Ti oxides, whereas amphibole is more common in the dacitic lavas.

4.2.2. Iliniza Volcano

4.2.2.1. Early satellite lavas

The Pilongo lava dome (Pi) is located on the lower north-western flank of Iliniza volcano, along the western edge of the homonymous valley (Fig. 2). This satellite lava dome is 600 m in basal diameter and reaches a height of 3935 m asl., i.e., 250 m above the valley floor. Due to its low elevation and location, the lava dome does not show evidence of substantial glacial erosion. Erosion caused by fluvial processes created steep slopes on its eastern and southern flank. The northern and western flanks are surrounded by a gently sloping plain consistent in elevation and dip with the northern flank of

Iliniza. The Pilongo lava dome is formed by porphyritic rhyodacites (68-69 wt. % SiO_2; Table 2). A sample taken from the southern base of the lava dome (ILI25) yields an age of 353 ± 6 ka.

4.2.2.2. North Iliniza edifice (NI)

This edifice is formed by two thick sequences of andesitic to dacitic (62-65 wt.% SiO_2) lava flows, monolithological breccias and scarce proximal pyroclastic deposits (Fig. 4; Table 2). The highest portion of the edifice is characterized by widespread hydrothermal alteration. In addition, the lavas sourced from the Huayrapungo satellite peak appear interspersed between the two above-mentioned sequences of North Iliniza.

The Lower NI stage (NI-Ls) is defined by a sequence of monolithological breccias,5-30 m-thick lava flows, and scare pyroclastic successions, displaying andesite to dacite compositions (62-64 wt.% SiO_2). This sequence is well exposed in the glacial ridges around the North Iliniza edifice specially on the Western Cordillera side (e.g., Quillotoro and Ninarrumi hills; Fig. 3a). The NI-Ls maximum thickness is estimated at 200-300 m in the Western Cordillera side, and 700-800 m in the Inter-Andean Valley side. The NI-Ls succession overlies the Mio-Pliocene volcano-sedimentary sequences of the Western Cordillera (i.e., Silante and Zumbahua Formations). Two blocks taken from two monolithological breccia layers (ILI20, ILI11) in the northern flank give ages of 122 ± 6 and 123 ± 6 ka.

The Huayrapungo stage (NI-Hs) is represented by an eroded peak formed by voluminous andesitic lavas (62 wt.% SiO_2) cropping out in the northern NI flank. Huayrapungo lavas exhibit meter-scaled flow banding textures, well-exposed in the southern flank of the peak (Fig. 4b), whereas flow foliation and subvertical columnar jointing are common close to the summit areas. Although field relationships are unclear, it seems that Huayrapungo lavas, of at least 250 m in thickness, overly a pyroclastic succession probably related to the Lower NI stage clearly observed in the southern flank of the Huayrapungo peak. Based on the morphological and structural characteristics of Huayrapungo and

its stratigraphic position, we consider this peak as a satellite vent of the NI edifice. A sample (19EQ17) collected south of the Huayrapungo peak is dated at 121 ± 2 ka.

The Upper NI stage (NI-Us) consist of a 600–700 m-thick pile of viscous lava flows (30-60 m in thickness) that shape the upper structure of the North Iliniza edifice above 4400 m asl (Fig. 4a). This lava succession is andesite to dacite in composition (62-65 wt.% SiO_2). A notable feature is a voluminous 100 m-thick lava exposed in the summit area which flowed down 1500 m northwestwards (Fig. 3a). Erosion reveals the flow foliation structure and fractures associated with a secondary summit vent located at 4800 m asl. A sample collected at the base of this massive lava yields an age of 116 ± 2 ka (ILI18). Another 90 m-thick lava is located on the western flank in the Quillotoro hill, overlying the NI-Ls succession. It is cut by a glacial valley on its highest portion. We suggest an emplacement age similar to that of the ILI18 lava flow.

4.2.2.3. South Iliniza edifice (SI)

This edifice corresponds to a compound volcano formed by a basal stratovolcano discordantly overlain by a summit lava dome complex and massive lava flows (Fig. 5). These successions define the three cone-building stages of the South Iliniza edifice (Table 2). The lower flanks of the edifice are covered by a thick pyroclastic succession associated with the second stage.

The Lower SI stage (SI-Ls) corresponds to an early cone constructed on top of the NI successions and the remnants of the Santa Cruz volcano. It consists of a 1100 m-thick succession of dacitic (62-65 wt. % SiO_2) massive lavas, sparse inter-layered breccias, and semi-consolidated PDC deposits. Outcrops near the center of the edifice show moderated hydrothermal alteration. Two consistent ages of 45 ± 2 ka and 46 ± 1 ka are obtained from lavas located on the northern (19EQ18) and eastern (19EQ02) flanks, respectively. Glacial striations preserved on the northern lava flow confirm its pre-LGM age (roughly 35-20 ka; Clapperton, 1986; Heine, 2011). This basal stratovolcano is disrupted above 4700 m asl where the radial slope decreases top-down from 35° to less than 10° forming a truncated cone. The change in slope is especially noticeable on the southern flank where a

383 saddle shape structure, called the Cantarilla height (Fig. 3a), marks a structural unconformity (Fig. 4a
384 and 5b).

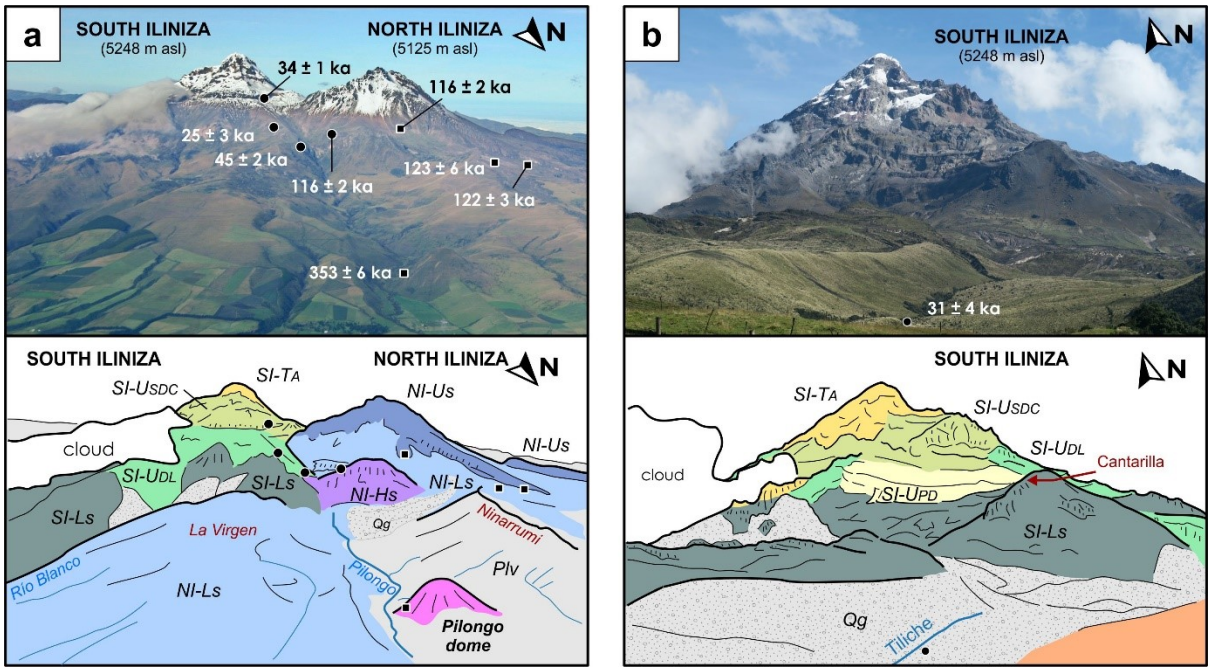

385

386 ***Figure 5.*** *View of* ***a)*** *Iliniza volcano, looking south (photography by Patricio Ramon, IG-EPN), and* ***b)***
387 *South Iliniza edifice, looking north, showing the relationships between the main stratigraphic units*
388 *represented according to Figure 4.*

389

390 **The Upper SI stage (SI-Us)** incorporates a pyroclastic succession surrounding the lower flanks
391 of the basal cone, and the summit lava domes located above the Cantarilla unconformity (Table 2).

392 *The Jatuncama ignimbrite (SI-Ji)* is a widespread PDC succession that crops out at the lower
393 flanks of the South Iliniza edifice (Fig. 6). Widespread outcrops occur in the Jatuncama valley, to the
394 southwest of Iliniza volcano (Fig: 4). The Jatuncama pyroclastic deposits overlie semi-consolidated
395 pyroclastic deposits ascribed to the Lower SI stage to the east, and inorganic consolidated soils to the
396 south of the SI edifice. The Jatuncama ignimbrite consists of a thick multiple bedded *block-and-ash*
397 *PDC sequence* (SI-J_{BA}) overlaid by *pumice-and-ash flow deposits* (SI-J_{PA}). The SI-J_{BA} deposits are
398 continuous, typically normal graded to massive, poorly sorted, slightly consolidated, and gray to pinkish
399 in color. No interlayered paleosoils are observed in the Jatuncama sequence. Degassing pipes are

commonly observed in the upper beds (Fig. 6b). The SI-J_{BA} deposits are constituted by poorly vesiculated juvenile dacite blocks (63-67 wt.% SiO_2; Table 2) showing radial and prismatical-jointed structures, and varying amounts of pumice lapilli. Both clast types are supported in a fine-grained ash-matrix bearing glass shards and free crystals of plagioclase, amphibole, and scarce pyroxene. Low-density pumice lapilli are generally scarce in the lower beds of the SI-J_{BA} deposit, whereas clasts with textural banding of glassy and high-density pumice are common (Fig. 6c). The SI-J_{BA} average thickness is ~30-40 m with a maximum of 120 m in the Jatuncama valley. The reconstructed area covered by the SI-J_{BA} deposits reaches ~60 km^2 with an average thickness of 35 m, yielding an estimated volume of 2.1 km^3. These values suggest an eruptive phase with a volcanic explosivity index (VEI) of at least 5. We should stress that no tephra fallout deposits have been observed, thus the estimated volume should be considered as a minimum. The high-density pumice sample (19EQ19a) collected from an intermediate bed of the SI-J_{BA} in the Jatuncama valley exhibit high atmospheric contamination preventing K-Ar dating.

Two 7-10 m-thick pumice-and-ash PDC units (SI-J_{PA}) overlie the SI-J_{BA} deposits at the Jatuncama valley (site 20EQ92; Fig. 6d) and the northeastern SI flank (site 20EQ96). The SI-J_{PA} units are massive, poorly consolidated, and light gray to beige in color. They are composed of fibrous dacite pumice lapilli (65-67 wt.% SiO_2) and occasional high-density dacite blocks up to 10 cm in diameter (Fig. 6e), supported in a matrix formed by fine glass shards and crystals of plagioclase, amphibole, and pyroxene. In addition, a 25 cm-thick rhyolite pumice-and-ash flow PDC deposit (71-72 wt.% SiO_2) crops out on the northeastern SI flank was described as the *Santa Rosa pumice-and-ash PDC (SI-J_{SR})* by Hidalgo et al. (2007). We identified a ~1-2 m-thick matrix-supported deposit (site 20EQ81), with a poorly-sorted texture, outcropping on top of the northern SI-J_{PA} (site 20EQ96). The collected samples reveal a mixture of rhyolitic pumiceous blocks (20EQ81a) and poorly vesiculated dacite blocks (20EQ81b, c) all ranging from 10-30 cm in diameter, suggesting a probable reworking of the primary deposit described by Hidalgo et al. (2007).

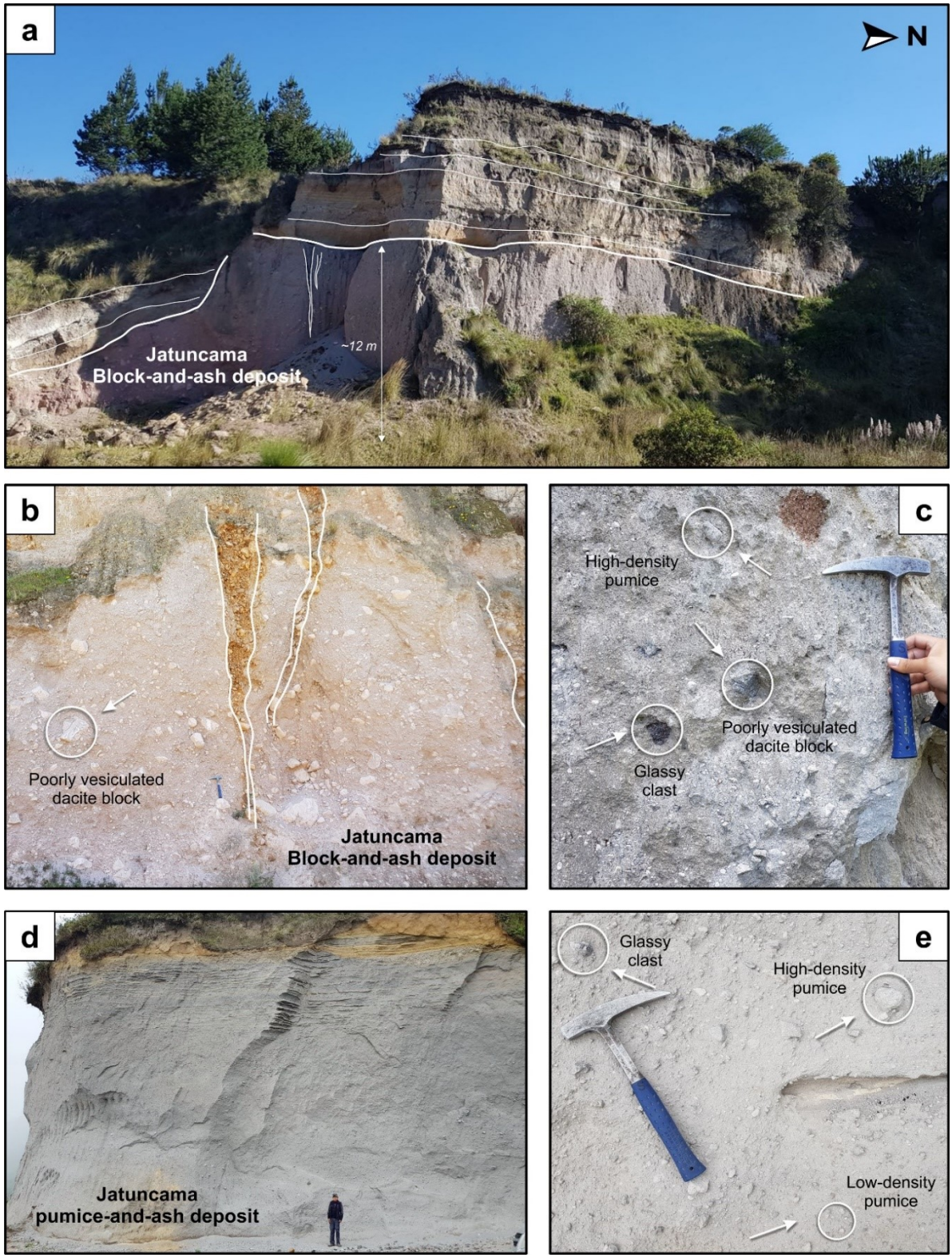

425

426 ***Figure 6. a)*** *Jatuncama ignimbrite deposit at Planchaloma (site ILI 2), and* ***b)*** *detailed view of its*
427 *degassing pipes structures. The deposit is discordantly overlain by lahars, Cotopaxi tephra fallouts,*
428 *and soils.* ***c)*** *Types of clasts observed in a lower section of the ignimbrite deposit at the Jatuncama*
429 *valley (site 19EQ19).* ***d)*** *Pumice-and-ash flow observed at Jatuncama valley (site 20EQ92), and* ***e)***
430 *detailed view of its clastic components.*

The Jatuncama ignimbrite sequence is preserved as a gently sloping surface (4-12°) intersected by shallow fluvial channels. The heads of these streams are commonly covered by moraines or intersected by glacial valleys at elevations above ~3750 m asl, i.e., above the LGM limit observed in other volcanoes of the region (Clapperton, 1986, 1990; Heine, 2000, 2011). The Jatuncama succession is overlain by a thick sequence of paleosoils, tephra fallout deposits from Cotopaxi, and other reworked materials of broadly Holocene age (Fig. 5a). Notably, the Cotopaxi F2 and F4 rhyolitic tephra fall deposits (7770 ± 70 to 5830 ± 80 ^{14}C yr BP; Hall and Mothes, 2008) were identified in the Planchaloma and Pastocalle areas (Fig. 4). Minor landslide scarps affecting these shallow deposits are recognizable on the eastern and southeastern SI flanks.

Two *consolidated PDC deposits (SI-U_{CP})* crop out east of the Cantarilla height, on the southwestern flank of the cone (Fig. 4b). These deposits, which are ~100 m-thick each, overlie the Lower SI sequence forming the conspicuous Cantarilla angular unconformity. The summit lava domes and its related deposits overlie this pyroclastic sequence. Unfortunately, no samples could be collected due to the terrain roughness.

The Summit Lava Dome Complex (SI-U_{SDC}) is located on top of the remnants of the Lower SI edifice (Fig. 5b), between 4710 and 5060 m asl, reaching a basal diameter of ~1.7 km. The SI-U_{SDC} vent, inferred as the geometrical center of the structure, occurs 250 m to the north with respect to that of the basal cone. As a result of the erosion, only the main core of the summit lava domes has been preserved. Multiple lava lobes and remnants of the SI-U_{SDC} talus are exposed in the summit southern flank, forming a sequence of thinner strata lying unconformably upon the older cone in the Cantarilla height (Fig 5b). The summit lava domes are dacitic in composition (64–67 wt.% SiO_2) and. A sample taken at the northern base of the SI-U_{SDC} (19EQ23b) yields an age of 34 ± 1 ka. The higher sections of the South Iliniza edifice are covered by *undifferentiated dacitic breccias (SI-U_{DL})* interpreted as reworked PDC deposits related to the SI-U_{SDC} dome-forming eruptive activity.

The Terminal SI stage (SI-Ts) is represented by several massive lava flows and monolithological breccias that overlie the SI-U_{SDC} deposits and descend mainly along the western flank into the Providencia valley (Fig. 4b and 5). This lava succession shapes the SI edifice summit above

458 5000 m asl, reaching a thickness of ~250 m. The SI-Ts lavas are mostly andesitic in composition (SI-
459 T_A; 61–63 wt.% SiO_2). Two voluminous lava flows, called the Termancucho lavas (Hidalgo, 2001),
460 outcrop on the summit's western flank and can be traced 3 km downslope into the upper Providencia
461 valley (Fig. 3a and 4b). The lower 70 m-thick lava flow (20EQ79) is composed by a porphyritic dacite
462 (SI-T_D; ~67 wt.% SiO_2), whereas the upper 50 m-thick lava flow (ILI 29) has an andesitic composition
463 (~62 wt.% SiO_2) consistent with the overlying SI-T_A series (Table 2). A sample collected from the lower
464 Termancucho lava (20EQ79a) was discarded for K-Ar measurements due to its high phenocryst and
465 low groundmass contents. Another andesitic lava flow outcrops on the southern SI flank at the
466 headwaters of the Tiliche river (site 20EQ72; Fig. 4), is partially overlaid by a LGM moraine. The
467 upstream trace of the Tiliche lava flow is intersected by the Providencia valley, hiding the source of this
468 flow. Nevertheless, we relate this lava flow to the summit's terminal lavas given their similar
469 petrological characteristics and stratigraphic position (Table 2). A sample taken from the base of the
470 Tiliche lava flow (20EQ72) yields an age of 31 ± 4 ka. A comparable, albeit younger, age of 25 ± 3 ka
471 was obtained from an andesitic block (19EQ25) collected from a monolithological breccia on the
472 northern SI flank.

473

474 **4.2.2.4. Late satellite lavas**

475 **Tishigcuchi (T)**, also called Rasuyacu (Hall and Beate, 1991), is a satellite dome *coulée* located
476 on the southern flank of the South Iliniza edifice (Fig. 7a). It is composed of a 1100 m-wide lava dome
477 (4185 m asl), and at least 3 viscous lava flows reaching 90 m-thick and 1800 m-long. The lava SI-J_{BA}
478 was constructed over a 7° slope at 3850 m asl formed by the SI-J_{BA} and the Tiliche lava flow (Fig. 4).
479 The Tishigcuchi lava *coulée* is andesitic in composition (62-63 wt.% SiO_2). No collapse or explosion
480 crater structures are observed, and no pyroclastic deposits related to the Tishigcuchi lava dome are
481 found in our study. The dome shows no evidence of glacial erosion and is covered by soils intercalated
482 with Cotopaxi's rhyolitic Holocene lapilli and ash fall deposits. Attempts to obtain a K-Ar age from the
483 selected samples (19EQ22, 20EQ74) were unsuccessful due to the high atmospheric contamination
484 exhibited by the groundmass.

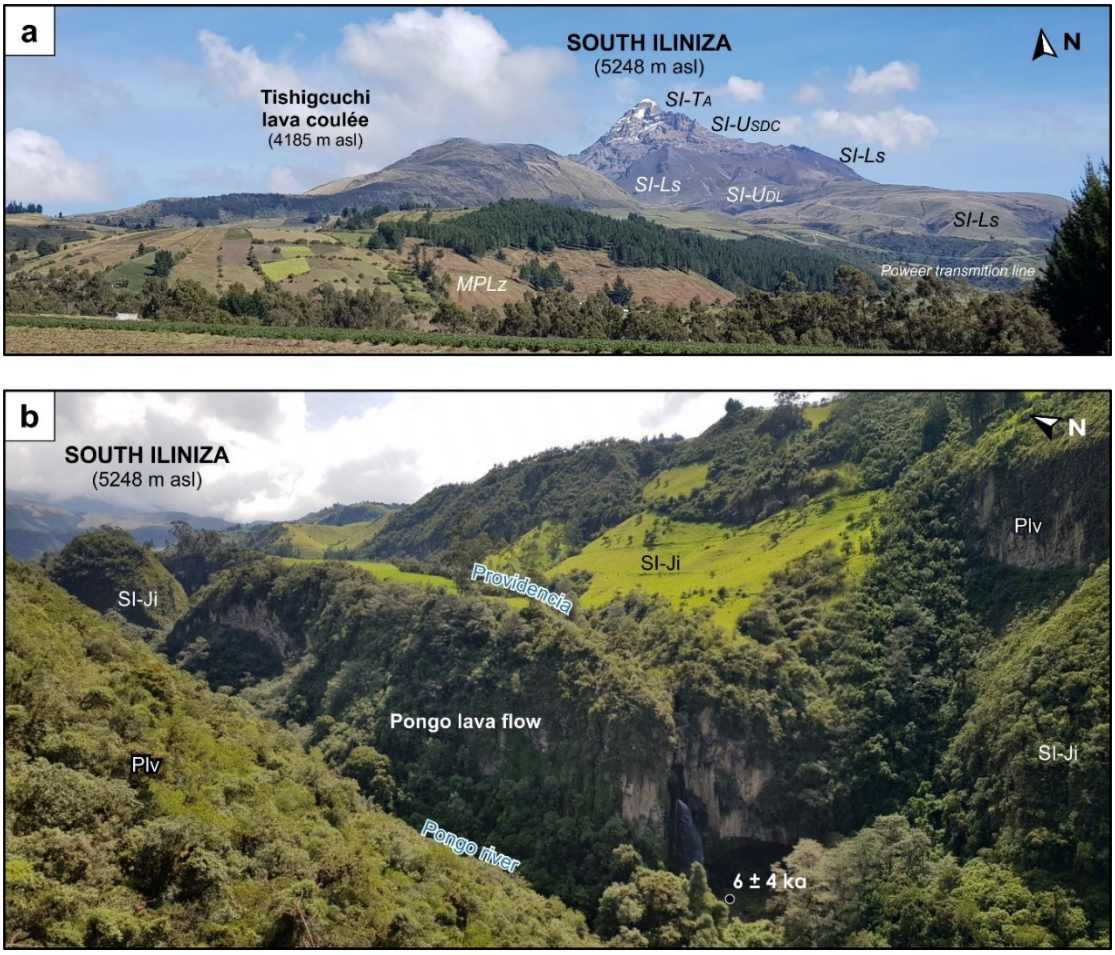

Figure 7. a) *Panoramic view of the Tishigcuchi lava dome and the South Iliniza, looking north.* ***b)*** *View of the Pongo lava flow from the Jatuncama valley. Volcanological unit abbreviations as in Figure 4.*

Pongo (Pg) is a voluminous lava forming a 4 km-long terrace between the Pongo and Providencia rivers, in the Jatuncama valley (Fig. 7b). The erosion caused by the Pongo river has exposed a 60-m-high cliff with columnar jointing at the southwestern edge of the lava. Exposures of the Jatuncama ignimbrite are observed on the valley walls next to the Pongo lava. The Pongo lava is composed by aphanitic andesites (59 wt.% SiO_2). Although the sample collected at the Providencia River (19EQ20) is highly contaminated by atmosphere, a second sample taken at the base of the columnar jointing exposures (20EQ75) provides an age of 6 ± 4 ka. The source of the lava flow cannot be clearly identified upstream into the glacially carved Providencia valley. Given the size of the Pongo lava and its Holocene age, its upper parts should be still observable as they could not have been completely eroded or covered by younger deposits. Thus, an origin from a satellite vent located at the southwestern base of Iliniza volcano is suspected.

4.3.Reconstructed morphology for volume estimations

4.3.1. Basement surface reconstruction

Defining the substratum morphology is an essential step for volume calculations, as minor changes in the basement morphology could lead to volume errors greater than 50% in stratovolcanoes (e.g., Ceboruco volcano; Frey et al., 2004; Tungurahua volcano; Bablon et al., 2018). The basement shape of Iliniza volcano (S_{I-t0} surface) was reconstructed using a theorized topographic profile modeled from four parallel auxiliary profiles located to the north and to the south of the volcano. The auxiliary profiles intersect the hills of Ninarrumi and Quillotoro to the north, and Chilcapamba to the south of the Iliniza volcano (Fig. 2 and 8a), which form the northwestern-southeastern ridge of the Western Cordillera. Further to the east, at the eastern and southeastern foothills of the South Iliniza edifice, the auxiliary profiles intersect a slight elevation of the Santa Cruz volcano and the Loma La Cruz ridge (Fig. 8a).

4.3.2. Iliniza volcano paleosurface reconstruction and volume calculations

The total reconstructed area for Iliniza volcano is 127 km^2, which corresponds to a present-day bulk volume of 34 ± 14 km^3. This volume represents the amount of volcanic products preserved between the present-day topography and the modeled basement surface S_{I-t0}. Considering an activity range of 98 ± 7 kyr, corresponding to the growth of the North and South Iliniza edifices between 123 ± 6 ka and 25 ± 3 ka, an apparent bulk output rate of 0.35 ± 0.14 km^3/kyr was determined. Nevertheless, our results have shown that the eruptive activity of Iliniza volcano was seemingly interrupted by long-term quiescence periods between each construction stage. Therefore, volume calculations, and growth or output rates, require to be adjusted for each construction and erosion stages (Table 3). Appendix C provides several topographic profiles comparing the modeled cones of the Iliniza edifices, the modeled basement surface, and the present-day surface.

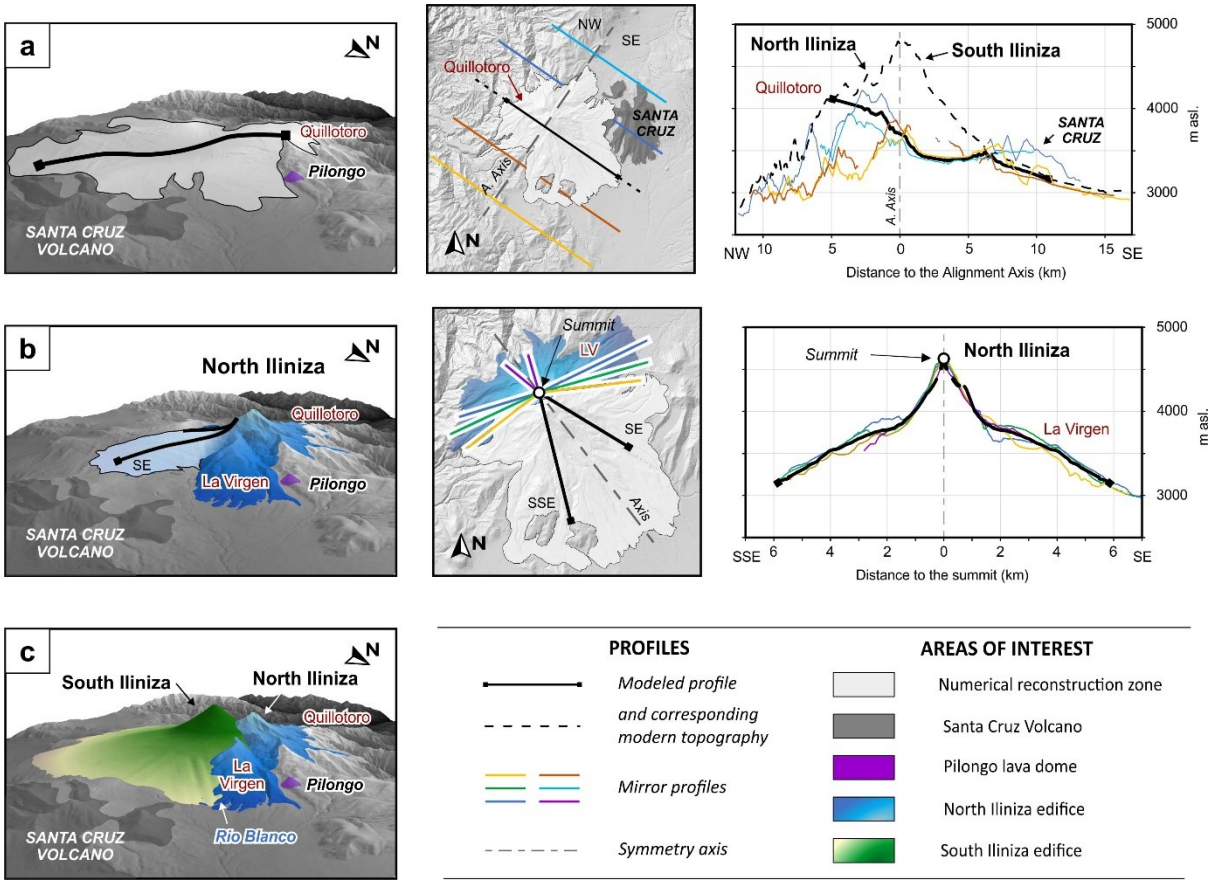

Figure 8. *Model topographic profiles used for the reconstruction of the basement surface area of* ***a)*** *North Iliniza and* ***b)*** *South Iliniza edifices. Figures correspond, from left to right, to perspective and plan views of the reconstructed area, and to the mirror profiles used to create the modeled profile.* ***c)*** *Aerial view of the South Iliniza modeled cone fitted next to the partially eroded North Iliniza edifice.*

The first construction stage of the Iliniza volcano corresponds to the extrusion of the Pilongo lava dome, which has a present-day volume of 18 ± 5 × 10^{-3} km^3. The next stage corresponds to the construction of the North Iliniza edifice. The modeled cone S_{NI-t1} has a semicircular base with a concave profile that reached 5200 m asl. The symmetry axis is located 200 m southwest of the present-day summit and is coincident with the narrow amphitheater of the eastern flank. The volume of the modeled cone v_{NI-cs} is 28 ± 9 km^3, a relatively small value compared to the volcano's heigh of ~1700 m above the Inter-Andean Valley. This value is explained by the presence of the Western Cordillera basement, which makes its base level ~400 m higher than the Inter-Andean valley. Considering a period of activity occurring between 124 ± 5 ka and 116 ± 2 ka, the output rate obtained R_{NI-o} is 3.5 ± 2.6 km^3/kyr.

539 ***Table 3.*** *Construction and erosion volumes calculated based on numerical reconstructions together*
540 *with their corresponding rates. Numerical results given with a 1-σ uncertainty (see text for details).*

Unit	Volume (km^3)	Period (ka)	Duration (kyr)	Output rate (km^3 kyr^{-1})	Volume (km^3)	Period (ka)	Duration (kyr)	Erosion rate (km^3 kyr^{-1})
Iliniza edifices								
North Iliniza	28 ± 9	124 - 116	8 ± 5	**3.5 ± 2.6**	6 ± 2			
Western flank					3 ± 1	116 - 0	116 ± 2	**0.03 ± 0.01**
South Iliniza	18 ± 6	46 - 25	21 ± 4	**0.8 ± 0.3**	6 ± 2	25 - 0	25 ± 3	**0.24 ± 0.09**
Satellite Vents								
Pilongo lava dome	$18 \pm 5 \times 10^{-3}$							
Tishigcuchi lava dome	$339 \pm 41 \times 10^{-3}$							
Pongo lava flow	$73 \pm 18 \times 10^{-3}$							
Present-day whole volcano	34 ± 14	123 - 25	98 ± 7	**0.3 ± 0.1**				

541

542 La Virgen plain (LV), located northeast of Iliniza volcano (Fig. 2 and 5), was originally
543 interpreted as part of the South Iliniza edifice (Hidalgo et al., 2007). However, a detailed analysis of its
544 geometry reveals that the slope gradient direction of La Virgen points to a source located to the west,
545 coinciding with the location of the North Iliniza edifice. We support this hypothesis by the discordant
546 position of the northern lava flow from the SI-Ls stage (19EQ18, ILI 34). This lava flowed into the
547 Pilongo valley between La Virgen plain and the Huayrapungo peak (Fig. 4), implying a pre-South
548 Iliniza construction for the northeastern sector. Overlapping of other products of the South Iliniza
549 edifice is not excluded during the formation of La Virgen plain.

550 The reconstruction of the eastern sector of the North Iliniza edifice at ~45 ka (i.e., before South
551 Iliniza construction) was not straightforward given that this area is covered by the South Iliniza deposits.
552 This area completes the surface S_{NI-t2} corresponding to the relief at the end of the quiescence period
553 between growth of both edifices. We used two auxiliary topographic profiles based on radial sections
554 of the present-day northeastern sector La Virgen and the southwestern sector Pongo alto (Fig. 8b) to
555 compute the surface S_{NI-t2}. The eroded volume v_{NI-es}, calculated between the modeled cone S_{NI-t1}
556 and the eroded surface S_{NI-t2}, is 6 ± 2 km^3. Only the western sector was exposed to non-stop weathering
557 during the ~116 kyr quiescence of North Iliniza. Then, the eroded volume in the western sector v_{es-W}
558 is 3 ± 1 km^3, implying an erosion rate R_{NI-e-W} of 0.03 ± 0.01 km^3/kyr.

559 The construction of the South Iliniza edifice comprises the lower cone-building, the upper cone-
560 building, and the terminal effusive stages. The former two cones were modeled independently as a first
561 approach, but we selected a simpler geometry involving a single cone given the poor geometric
562 constrains. A volume v_{SI-cs} of 18 ± 6 km^3 was obtained for the modeled cone S_{SI-t1}. As in the case of
563 the North edifice, this volume appears to be rather small given the volcano height of ~1850 m measured
564 from the Inter-Andean valley bottom. The modeled paleo-summit is located 250 m east of the current
565 summit and reaches 5300 m asl. Considering a 21 ± 3 kyr-long cone-building period (from 46 ± 1 to 25
566 ± 3 ka), the South Iliniza edifice yields an output rate R_{SI-o} of 0.8 ± 0.3 km^3/kyr. The volume difference
567 between the present-day surface S_{SI-t2} and the reconstructed cone S_{SI-t1} gives an eroded volume v_{SI-es}
568 of 6 ± 2 km^3 implying an erosion rate R_{SI-e} of 0.24 ± 0.09 km^3/kyr. Figure 8c shows that the northern
569 contact between the South Iliniza modeled cone and the partially eroded North Iliniza edifice occurs
570 along the Rio Blanco valley in the northern sector and along the Pongo Alto valley in the southern sector
571 (see also Fig. 11c-f). Lastly, the Tishigcuchi lava dome yields a present-day volume of 339 ± 41 × 10^{-3}
572 km^3, whereas the Pongo lava flow reaches a volume of 73 ± 18 × 10^{-3} km^3.

573

574 4.4.Geochemical characterization

575 The Iliniza volcanic products are classified in the SiO_2 vs. K_2O diagram (Fig. 9a; Peccerillo and
576 Taylor, 1976) as medium-K andesites and dacites, which are similar to those observed in other Volcanic
577 Front edifices (VF, Fig. 1b). Some scarce andesites and rhyolites, corresponding to the Pongo and Santa
578 Rosa units, fall outside the VF field. Each construction stage shows narrow silica content ranges.
579 Negative correlations are observed in Harker diagrams including MgO, Fe_2O_3*, CaO, TiO_2 and Al_2O_3
580 *versus* silica, used as differentiation index, while K_2O and Na_2O show positive correlations (Fig. D.1).
581 The North Iliniza and South Iliniza eruptive products typically form well-defined trends. Samples from
582 the Pilongo and Santa Rosa units plots along or near the prolongation of the Iliniza trend. In contrast,
583 the eruptive products of Tishigcuchi and Pongo show K_2O enrichment and Na_2O depletion compared
584 to the andesitic lavas of the Terminal SI stage (SI-T_A).

585 Variations in trace element contents in relation to silica increase for the North and South Iliniza
586 tend to form well-correlated trends (Fig. D.2). Some transition metals (e.g., V, Sc) show a marked
587 compatible behavior as well as Heavy Rare-Earth Elements (HREE; e.g., Yb) and Y. However, the
588 Large-Ion Lithophile Elements contents (LILE; e.g., Rb, Ba) remain relatively constant, except for
589 South Iliniza edifice which shows an overall incompatible behavior with the andesitic SI-Ts values
590 being the lowest. High contents of Light Rare-Earth Elements (LREE; e.g., La, Ce), Th and Sr are
591 observed in the products of Santa Rosa, Tishigcuchi and Pongo. Cr and Ni are also high for these
592 samples, as well as in the andesitic SI-Ts lavas. Only a few samples are available for lower South Iliniza
593 edifice, making its geochemical signature poorly constrained. Its northern lava flow (19EQ18, ILI 34)
594 exhibits unusually high LREE, Th and Sr contents.

595 Incompatible elements and Rare-Earth Elements (REE) spider diagrams normalized to
596 primitive mantle/chondrites (Sun and McDonough, 1989) are shown in Figure 9b-e. Overall, the
597 chondrite-normalized REE diagram for North and South Iliniza dacites exhibit similar, slightly
598 fractionated patterns with LREE enrichment and HREE depletion, and no Eu anomaly. The South
599 Iliniza samples present an overall, albeit slight, REE depletion relative to North Iliniza, except for the
600 northern Lower SI stage lava flow (19EQ18, ILI 34) which has a strong LREE enrichment. The highest
601 HREE depletions are observed for the most evolved products of Iliniza volcano, i.e., the dacitic
602 Termancucho lava (dacitic SI-Ts), Pilongo and Santa Rosa units. The primitive mantle-normalized plot
603 reveals a similar pattern for all samples with positive Ba, K and Rb anomalies and negative Nb and P.
604 Lower Ti, Dy, Y and Yb signatures characterize the dacitic SI-Ts, Pilongo and Santa Rosa units. The
605 low HREE (e.g., Yb<0.61 ppm) and Y (<7.8 ppm) concentrations observed in the Pilongo and Santa
606 Rosa units, coupled with the high LREE (e.g., La>12 ppm) contents, result in elevated La/Yb ratios
607 compared to other units (Fig 10e). Conversely, samples from the Tishigcuchi and Pongo eruptive
608 products show similar ratios but also higher mafic signatures (e.g., SiO_2<63 wt.%, Mg#>50). Overall,
609 the La/Yb ratio show a slight increase over time (excluding Pilongo), whereas fluid-mobile to fluid-
610 immobile ratios (e.g., Ba/Th) decrease (Fig. 10b, d). Further detailed descriptions regarding the

geochemistry and petrography of Iliniza volcano are provided in Hidalgo (2001, 2002) and Hidalgo et al. (2007).

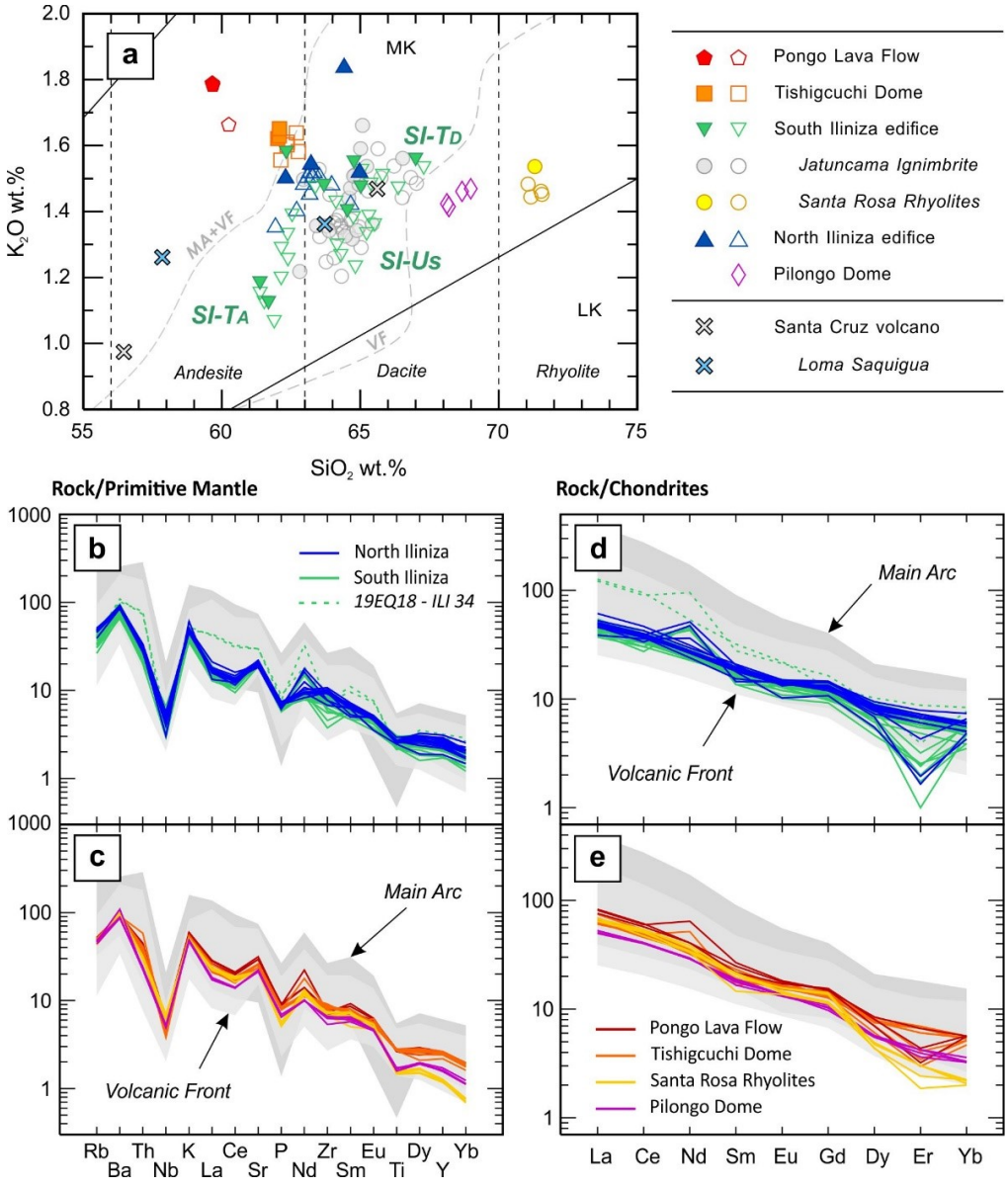

Figure 9. a) *K_2O vs SiO_2 diagram (Peccerillo and Taylor, 1976) for eruptive products of Iliniza and Santa Cruz volcanoes. MK: medium-K, and LK: low-K calc-alkaline series. The late evolutionary stages of the South Iliniza edifice are shown with green symbols. Volcanological unit abbreviations as in Figure 4. Gray dashed lines indicate the composition fields created by the Volcanic Front (VF) and Main Arc (MA) whole-rock data obtained from the Georoc database. Open symbols are for data from Hidalgo et al. (2007).* ***b-c)*** *Incompatible trace elements normalized to primitive mantle spider diagrams (Sun and McDonough, 1989) for North and South Iliniza edifices, and Iliniza satellite lavas and the SI-J_{SR} units, respectively.* ***d-e)*** *Rare Earth Elements normalized to chondrites diagram (Sun and McDonough, 1989) for the same arrangements. Dark grey and light grey areas represent the composition fields depicted by the Volcanic Front and Main Arc whole-rock data, respectively.*

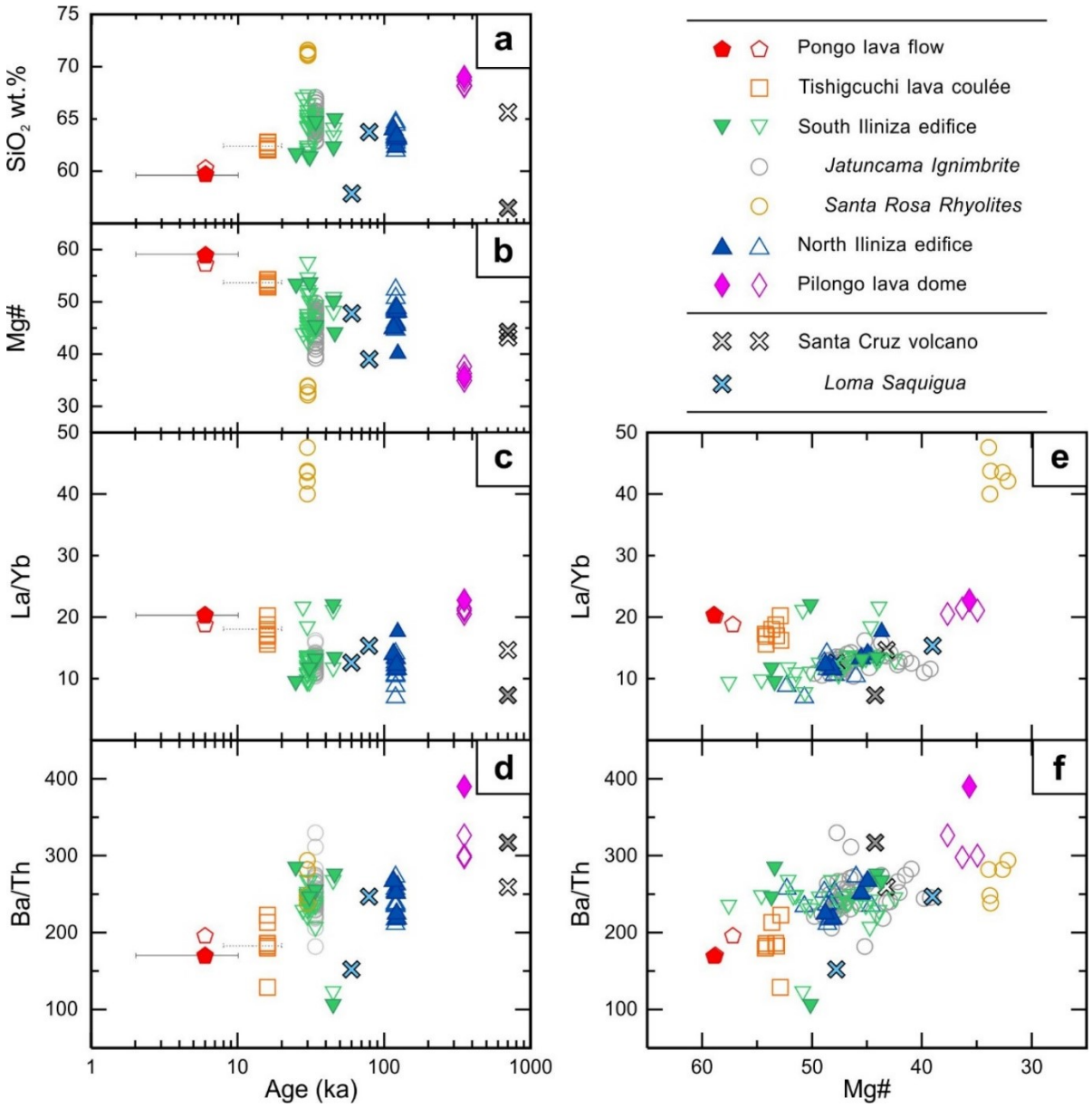

624

625 ***Figure 10.*** *Temporal variations of* ***a)*** *Mg# (=100∗Mg/(Mg+Fe^{2+})),* ***b)*** *SiO_2 (wt.%), and* ***c)*** *La/Yb and*
626 ***d)*** *Ba/Th ratios. Horizontal axis represents the timeline (ka) in logarithmic scale.* ***e)*** *La/Yb and* ***f)***
627 *Ba/Th ratios plotted against Mg#. Filled symbols are for dated samples (Table 1). The 1σ age*
628 *uncertainty is shown with a solid line for Pongo lava flow, while the age estimation range is shown as*
629 *a dashed line for Tishigcuchi lava coulée.*

630

5. DISCUSSION

5.1.Iliniza and Santa Cruz geochronological evolution

Although a rather limited number of ages have been obtained here, their key stratigraphic position allows us to propose a complete geochronological evolution of Iliniza and Santa Cruz volcanoes. Our stratigraphic, geochronological, and geochemical data suggest that the Iliniza volcano had a relatively short lifetime span. We propose that Iliniza volcano was constructed in short eruptive intervals separated by long repose periods throughout late Pleistocene (from ~350 ka to the Holocene) as summarized below. Prior to the construction of the Iliniza volcano, the Santa Cruz volcano was constructed in the Inter-Andean valley. The predominantly effusive activity of the Santa Cruz volcano, dated at 702 ± 11 ka, is represented by the thick lavas exposed on its southern flank and the dacitic lava domes present in the summit area. We found no other evidence of volcanic activity in this area until the extrusion of the Pilongo lava dome, the earliest stage of Iliniza volcano, which took place close to the Machachi fault (Fig. 3) at 353 ± 6 ka.

After an apparent quiescence period of ~230 kyr, the North Iliniza volcano started the construction of a ~1600 m-high edifice, in the southern prolongation of the Machachi fault (Fig. 11a). Two lava successions characterize the effusive activity occurring between 123 ± 6 and 116 ± 2 ka (Table 1), after the Penultimate Glacial Maximum (Shackleton et al., 2003). Nevertheless, we interpret this age range with caution as no basal lava could be sampled. Based on morphological and stratigraphic evidence, we attribute the formation of the Huayrapungo peak to a satellite vent contemporary with the lower lava sequence. Later, the erosion caused by Pleistocene glaciations, presumably from pre-LGM glacial cycles (>49 ka; Heine, 2011), shaped the wide radial glacial valleys around the North Iliniza summit, and incised the Pilongo and Providencia-Pongo paleo-valleys (Fig. 4). After an apparent ~620 kyr-long quiescence period, activity resumed on the Santa Cruz volcano when the dacitic lava dome of Loma Saquigua was extruded at 79 ± 2 ka, followed by the emission of andesitic lavas at 60 ± 3 ka (Fig. 11b).

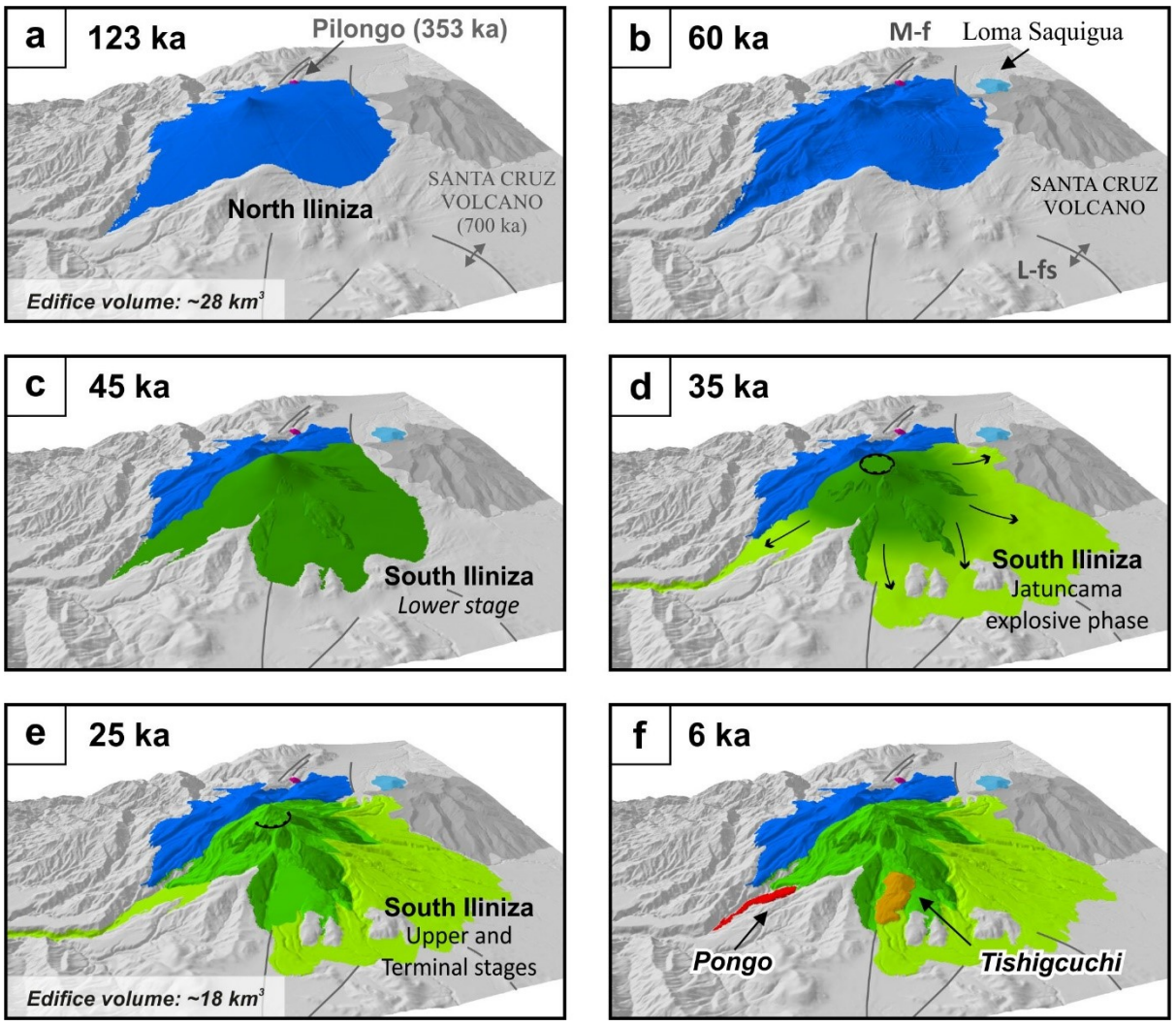

656

657 ***Figure 11.*** *Synthetic charts showing the evolution of Iliniza and Santa Cruz volcanoes through time*
658 *based on our numerical reconstructions.* ***a)*** *North Iliniza edifice construction;* ***b)*** *Santa Cruz volcano*
659 *reactivation with the Loma Saquigua lavas emission;* ***c)*** *South Iliniza Lower Cone construction;* ***d)*** *the*
660 *Jatuncama highly explosive eruptive phase creating a thick pyroclastic deposit;* ***e)*** *South Iliniza*
661 *Upper cone construction and terminal lavas emission; and* ***f)*** *Holocene Tishigcuchi lava coulée and*
662 *Pongo lava flow. Note that illustrations of phases c and d are mostly schematic, see text for details.*
663 *Local fault systems are symbolized with black lines. M-f: Machachi Fault; L-fs: northern segment of*
664 *Latacunga Fault System.*

665 The South Iliniza edifice was constructed on top of the partially eroded North Iliniza. A
666 conspicuous structural unconformity marks the two growth phases of this edifice. The earliest phase
667 corresponds to the emplacement of the Lower SI stage eruptive products, which are constituted by thick
668 lavas and pyroclastic successions dated at about 45 ka, forming a basal edifice (Fig. 11c). Remnants of
669 this edifice are exposed in the southern flank and in the center of the South Iliniza edifice. According

to the stratigraphic position of the Jatuncama ignimbrite deposits covered by LGM moraines, and its radial distribution fanning away from the South Iliniza edifice, we propose that this unit represents an explosive phase prior to the second growth phase of this edifice (Fig. 11d). As discussed below, the geochemistry of the dacitic components of the Jatuncama ignimbrite is comparable to the SI summit lava domes (SI-U_{SDC} unit), thus supporting our hypothesis. During the second growth phase, a summit lava dome complex and its related pyroclastic deposits subsequently filled the depression caused by the Jatuncama eruption (crater rim, Fig. 4) and reconstructed the volcanic cone since 34 ± 1 ka. Then, a final mostly effusive stage involved the emission of several andesitic lavas covering the uppermost parts of the volcanic cone (Fig. 11e). Our K-Ar ages suggest that this activity extended up to 25 ± 3 ka.

The Tishigcuchi lava dome coulée and Pongo lava flow extrusions represent the youngest eruptive stages of the Iliniza volcano (Fig. 11f), as previously suggested (Hall and Beate, 1991). The Tishigcuchi lava dome was extruded on the southern flank of the volcano along the southern prolongation of the Machachi fault. Although no radiometric age could be obtained, a stratigraphic age between 20 to 8 ka can be proposed due to the presence of the underlying Tiliche lava flow dated at 31 ± 4 ka, the lack of LGM glacial erosion or associated deposits (maximum extents reached at 34.8-27.9 ka and 19.2 ka; Heine, 2011), and the overlying Cotopaxi F2 and F4 fallout deposits (~8.5 and ~6.7 cal ka; Hall and Mothes, 2008). Finally, the age obtained from the Pongo lava flow (6 ± 4 ka) demonstrates that Iliniza volcano was still active during the Holocene.

The available ages in the central part of the Ecuadorian arc point to the existence of two types of volcanism based on the extent of their eruptive chronology. The long-lived volcanic complexes, which exhibit multiple edifices and cone-building stages as old as 1 Ma, extending their activity to more recent times even up to the Holocene (e.g., Pichincha and Cayambe volcanic complexes; Samaniego et al., 2005; Robin et al., 2010), and the short-lived compound volcanoes, which were rather formed in briefer cone-building stages of few tens of ka and were mostly emplaced in relatively recent times (e.g., Cotacachi and Imbabura volcanoes; Le Pennec et al., 2011; Almeida et al., 2019). Our new K-Ar ages reveal that the age and extent of Iliniza volcanic activity is in good agreement with this group of young short-lived volcanoes, whereas Santa Cruz could be considered as a long-lived volcano.

5.2.The Jatuncama explosive phase

The Jatuncama ignimbrite samples exhibit a dacitic composition similar to that of the South Iliniza upper stage (Fig. 12). However, the compositional dispersion of the SI-J_{BA} points to a more intricate deposit, as indicated by the SiO_2 content ranging between 63 and 67 wt.%. Figures 12a and 12b show the geochemical distribution of the SI-J_{BA} dacitic juvenile clasts compared to the South Iliniza units. For similar SiO_2 and Mg# values, the low-density pumices are slightly enriched in K_2O compared to the high-density pumices and dacites. Furthermore, the high-density pumices generally fall within the SI-U_{SDC} field, while low-density pumices are more correlated with the SI-T_D pole. The few glassy juvenile clasts available are relatively scattered without any clear relationship. The SI-J_{BA} composition also shows slight variations according to the location of the sampling site (Fig. 12d). A relatively higher dispersion degree is observed in the Jatuncama valley and on the southern flank (sites 7-9) compared to the southeastern flank where low K_2O samples seem to be absent (sites 3-5). This difference may be explained by the fact that the lower SI-J_{BA} beds, with higher participation of high-density pumices and dacites, are not well exposed on the southeastern flank. In addition, the plots of the SI-J_{PA} units (20EQ92, 20EQ96) fall in the fields of slightly K_2O enriched clasts. Therefore, on the basis of this geochemical evidence, the petrographic descriptions provided above, and the fact that neither discordances, nor interlayered paleosoils are observed in the Jactuncama succession, we argue that the Jatuncama ignimbrite units correspond to an intricate deposit formed during an explosive dome-forming eruption followed by a pumiceous phase both associated with the upper SI stage, as suggested by Hidalgo et al. (2007). The Jatuncama eruption was followed by the extrusion of the Summit Lava Dome Complex (SI-U_{SDC}). Based on the estimated volume of the Jatuncama deposits, we infer the formation of a 1.5-2 km-wide crater (Figures 4 and 11d) related to the Jatuncama explosive phase (minimum VEI ~5), which agrees with the top surface diameter of the truncated basal cone (i.e., SI-Ls). The Cantarilla discordance marks the inferred crater rim created during the Jatuncama explosive phase (Fig. 11d).

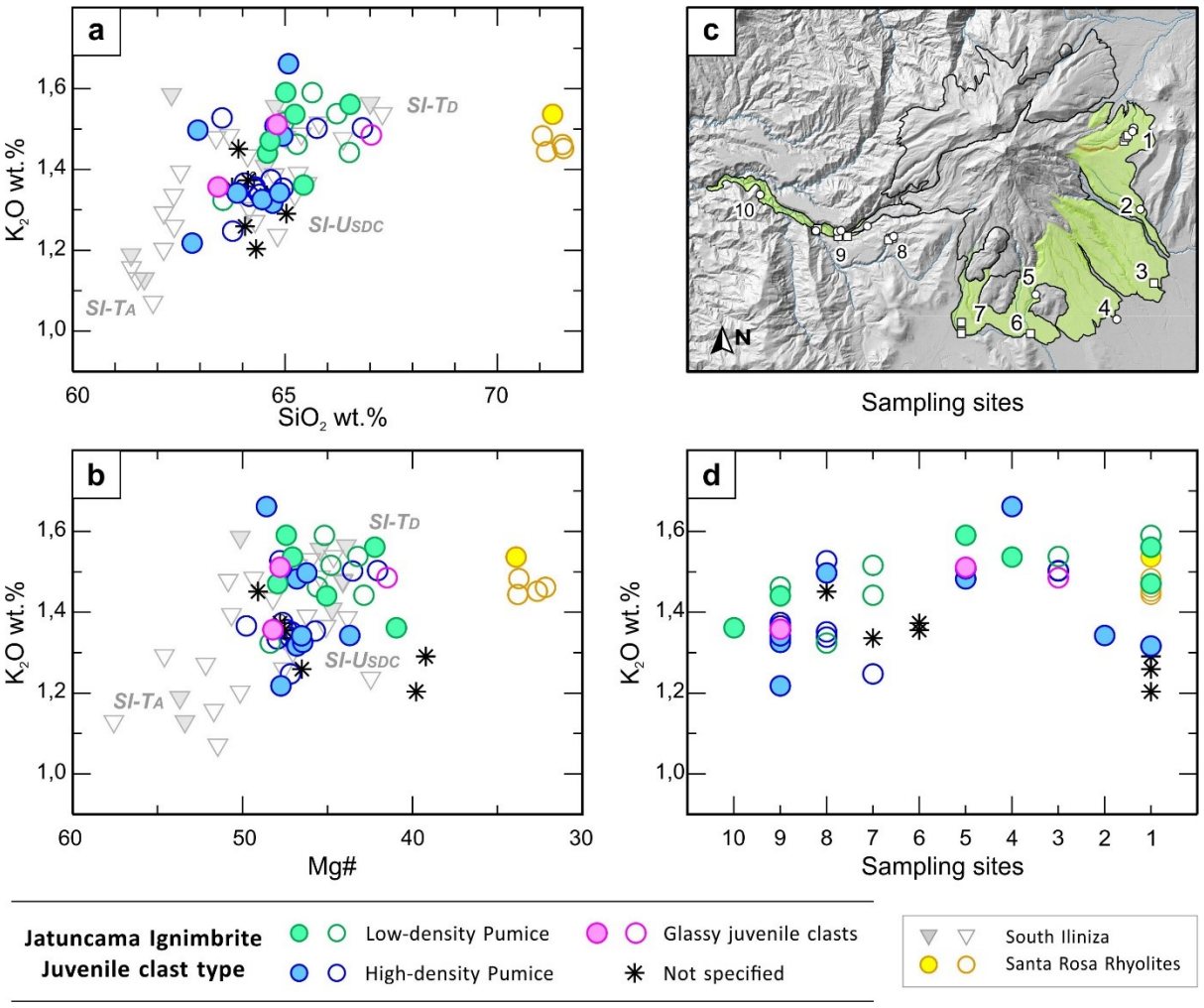

721

722 ***Figure 12.*** *Geochemical diagrams for Jatuncama pyroclastic samples classified by clast type. K_2O*
723 *versus* ***a)*** *SiO_2 and* ***b)*** *Mg# (=100∗Mg/(Mg+Fe^{2+})) diagrams. SI-U_{SDC}: South Iliniza upper cone; SI-*
724 *T_D: Dacite Terminal Lavas; SI-T_A: Andesite Terminal Lavas.* ***C)*** *Geographical distribution of*
725 *sampling sites around the base of South Iliniza and* ***d)*** *their variation in K_2O content. Open symbols*
726 *are for data from Hidalgo et al. (2007).*

727 In the lack of direct measurement, geomorphological, stratigraphic, and geochemical data can
728 provide an approximate age for the Jatuncama ignimbrite. Considering that the SI-Ji sequence overlies
729 the SI-Ls deposits and its distribution around the basal SI edifice, a lower bound is defined by the Lower
730 SI stage at 45 ± 2 ka. The overlaying Tiliche lava flow (20EQ72) constrains the upper bound at 31 ± 1
731 ka. Such pre-LGM age is supported by the glacial morphology affecting the highest sections of the
732 ignimbrite deposit, and by the thick Holocene tephra fallout sequence. Finally, considering the
733 geochemical affinity with the SI-U_{SDC} unit, we propose that the Jatuncama explosive phase, and the

734 formation of the SI-Ji pyroclastic sequence, occurred shortly before the extrusion of the summit lava
735 domes dated at 34 ± 1 ka (19EQ23b).

736

737 ## 5.3.Growth and erosion patterns in Iliniza Volcano

738 Volcanic edifices are composed of a wide variety of eruptive products including lava flows,
739 lava domes, PDC successions, and fallout deposits accumulated around a central vent. The destruction
740 of part of the volcanic edifice during highly explosive events and/or sector collapses, and the re-
741 mobilization of unconsolidated materials are other factors to consider during or in between the growth
742 phases. Therefore, the bulk volume of the main edifice does not represent the entire volcanic products
743 emitted and thus the calculated values should be considered as minima. Nevertheless, volumes obtained
744 in numerical reconstructions provide a first-order approximation, allowing recognition of fluctuations
745 in its spatial and temporal output patterns, and allowing comparison with other eruptive centers, as
746 discussed below.

747 According to our numerical reconstructions both Iliniza edifices reached similar heights and
748 volumes. The combined v_{cs} volumes of the Iliniza edifices and satellite lava domes reaches a total bulk
749 volume of 46 ± 15 km^3 of accumulated material (Table 2). This value includes the volume of material
750 removed by erosion during the quiescence periods (v_{es}). About 61 vol.% of this volume belongs to the
751 North Iliniza edifice, 38 vol.%. to the South Iliniza edifice, and the remaining 1 vol.% to the satellite
752 lavas. Due to the complex topography of the Iliniza basement, our results exhibit a relatively high
753 uncertainty of ~35 vol.%. The volume of the SI-Ji deposits is implicitly included in our calculations as
754 its estimated value is within the volume uncertainty range.

755 The bulk volume of Iliniza volcano is similar to those reported for the other compound
756 volcanoes located at the Ecuadorian northern cross-arc segment, e.g., Cushnirumi, Cusin, Fuya-Fuya
757 and Imbabura, which range from 31 ± 19 km^3 to 61 ± 24 km^3 (Bablon et al., 2020). Large volcanic
758 complex such as Pichincha, Cayambe and Mojanda accumulated larger volumes ranging from 115 ± 5
759 to ~160 km^3 (Robin et al., 2010; Samaniego et al., 2005; Bablon et al., 2020), which is not the case of

760 Iliniza volcano. In contrast, Antisana has a bulk volume of ~61 km^3, but has a lifespan longer than 400
761 ka (Hall et al., 2017b). Volcanoes with volumes similar to those of Iliniza volcano are also found in the
762 southern cross-arc segment. Effectively, each Iliniza edifice is comparable in volume to the Mulmul or
763 Huisla stratovolcanoes, which show values of 22 ± 7 and 25 ± 11 km^3 (Bablon et al., 2018, 2020).
764 Nevertheless, Iliniza volcano has a smaller volume relative to Chimborazo (Samaniego et al., 2012) and
765 the whole Tungurahua (Bablon et al., 2018) volcanoes. Compared to other worldwide volcanoes, Iliniza
766 could be considered as a medium-size compound volcano, whose volume and shape are typical of
767 continental arcs (Grosse et al., 2009). Similar bulk volumes to Iliniza are found in volcanoes such as
768 Parinacota (Hora et al., 2007), Ampato-Sabancaya (Samaniego et al., 2016), Yucamane-Calientes
769 (Rivera et al., 2020), Ceboruco (Frey et al., 2004), or Katmai (Hildreth et al., 2003b) volcanoes.
770 Nonetheless, the lifespans of these volcanoes differ by several tens of thousands of years.

771 The output rates calculated for the North Iliniza (3.5 ± 2.6 km^3/kyr) and South Iliniza (0.8 ± 0.3
772 km^3/kyr) edifices are quite variable, although both structures show comparable volumes and shapes.
773 The higher growth rate of North Iliniza is explained by the short range of activity displayed by our
774 radiometric ages. The lack of outcrops and/or sampling of the lower units might have biased the activity
775 range towards the late-stage ages, then, the impact on output rates can be significant. Nevertheless, the
776 sampling distribution and the small age range observed do not exclude a short-term (few tens of ka)
777 construction of the North Iliniza edifice. In fact, high growth rates have also been documented for
778 several Ecuadorian volcanoes such as Cubilche, Cusin, Imbabura (Bablon et al., 2020), Tungurahua III
779 (Bablon et al., 2018), Cotopaxi (Hall and Mothes, 2008), and Guagua Pichincha (Robin et al., 2010)
780 volcanoes, with R_o values ranging from 2.0 ± 1.5 to 3.6 ± 2.1 km^3/kyr. In contrast, the South Iliniza
781 growth rate is comparable to those of other Ecuadorian arc volcanoes. R_o values between 0.6 ± 0.3 and
782 0.8 ± 0.2 km^3/kyr were reported for volcanoes such as Pichincha (Robin et al., 2010), Tungurahua I and
783 II (Bablon et al., 2018), Mulmul (Bablon et al., 2019), and Chimborazo (Samaniego et al., 2012). Similar
784 output rates were reported for other Andean volcanoes such as Misti (Thouret et al., 2001), Parinacota
785 (Hora et al., 2007), and Ampato-Sabancaya (Samaniego et al., 2016); although they are comparatively
786 higher than in other continental arc systems such as the Cascades Range, Central Andes, Mexico, Japan,

787 or Alaska (e.g., Crisp, 1984; Hildreth et al., 2003a, 2003b; Frey et al., 2004; Ownby et al., 2007). Output
788 rate comparisons should be taken with caution as R_o values (> 1-2 km^3/kyr) are typical of short-term
789 growth episodes (of few ka), whereas low values are typical of bulk eruptive rates (i.e., long periods
790 including the quiescensde periods; Bablon et al., 2020).

791 The eruptive history of the Iliniza edifices developed separately in time, in contrast to other
792 twin-peaked volcanoes such as Mojada-Fuya Fuya (Robin et al., 2009) in the Ecuadorian arc, or
793 Yucamane-Calientes (Rivera et al., 2020) in the Peruvian arc. In fact, the evolution of Iliniza and Santa
794 Cruz volcanoes included long-lasting quiescence periods, which is also the case for other volcanoes in
795 the Ecuadorian Andes such as Cotopaxi (Hall and Mothes, 2008), Pichincha (Robin et al., 2010),
796 Atacazo-Ninahuilca (Hidalgo, 2006), and Tungurahua (Bablon et al., 2018). Long resting periods
797 (several tens of thousands of years) are also reported in other twin volcanoes and compound volcanoes
798 in the region and worldwide such as San Pedro-San Pablo (Bertin and Amigo, 2015; González-Maurel
799 et al., 2019), Ampato-Sabancaya (Samaniego et al., 2016), Yucamane-Calientes (Rivera et al., 2020),
800 and Colima (Robin et al., 1987; Cortés et al., 2010). These observations suggest that eruptive hiatuses
801 are also common in this type of compound volcanoes from volcanic arcs, contrasting with models of
802 sustained eruptive activity throughout their lifetimes (e.g., Conway et al., 2016; Pure et al., 2020), while
803 increasing the potential for reactivation in present-day dormant volcanoes.

804

805 ## 5.4.Overall geochemical nature

806 Overall, samples from the North and South Iliniza (NS-I) edifices exhibit rather little
807 geochemical variability along a single evolutive trends (Fig. A.1) suggesting neither a change in
808 magmatic sources nor in the magmatic process active at crustal levels. In contrast, important differences
809 rise when NS-I trace element contents are compared to the early and late satellite lavas and the Santa
810 Rosa rhyolites, in which HREE depletions and LREE enrichments were identified. Notably, the Iliniza
811 rocks do not show a continuous increase in SiO_2 or decrease in Mg# over time (Fig. 10a) as observed

812 at other volcanoes from the central segment of the arc (e.g., Pichincha volcano; Robin et al., 2010). The
813 silica-poor units (i.e., SI-T_A, T and Pg units) occur during the late evolutionary stages of Iliniza.

814 As presented in Table 2, the common mineral assemblages exhibit by the North Iliniza lavas
815 include plagioclase, orthopyroxene, clinopyroxene, Fe-Ti oxides and scarce amphibole, whereas the
816 South Iliniza eruptive products include plagioclase, amphibole, clinopyroxene, Fe-oxides and rare
817 orthopyroxene. Based on a geochemical modelling approach, Hidalgo et al. (2007) and Schiano et al.
818 (2010) proposed that the NS-I magmatic series could result from an amphibole-dominated fractional
819 crystallization process of typical calc alkaline arc magmas. Their models also showed that the silica-
820 rich products of Pilongo and Santa Rosa units require more complex petrogenetical models. In fact, the
821 trace element contents of these units were unable to be reconciled with a parental melt with NS-I
822 composition through a single fractional crystallization process, thus, implying the occurrence of an
823 additional parental melt and a mixing process involving both magmas. The petrogenetic processes
824 related to the origin of such silica-rich magmas are widely discussed as they could be produced by
825 several processes including partial melting of the subducted slab and the metasomatism of the mantle
826 wedge caused by the derived silicate melts (e.g., Bourdon et al., 2003; Samaniego et al., 2005, 2010;
827 Hidalgo et al., 2007, 2012), crustal melting and/or assimilation of the lower crust (Garrison and
828 Davidson, 2003; Garrison et al., 2006; Sainlot et al., 2020), and intra-crustal fractionation of the required
829 high-pressure assemblages (e.g., Bryant et al., 2006; Chiaradia et al., 2009; Bellver-Baca et al., 2020).
830 However, a comprehensive analysis of these petrogenetic processes and their temporal behavior is
831 beyond the scope of this paper. Nonetheless, the whole Iliniza magmatic series could be thus explained
832 by a fractional crystallization process coupled with magma mixing between mafic and silica-rich end-
833 members (Hidalgo et al., 2007; Schiano et al., 2010); where the geochemical signatures of both end-
834 members seem to occur throughout the geochronological evolution of Iliniza volcano, rather than being
835 restricted to its final stages.

836

5.5.Exploring the implications for the hazard assessment

Unlike other active and potentially active volcanoes from the Volcanic Front (e.g., Pululahua, Guagua Pichincha, Ninahuilca), whose eruptions involved dacitic magmas and dome-forming eruptive dynamics, the Holocene activity of Iliniza mainly released andesitic lavas. Based on the proposed eruptive chronology, we infer that the most probable eruptive scenario could be dominated by the emission of lava flows and/or the formation of low-viscosity lava domes, whose subsequent collapse may produce PDCs and regional tephra fallout deposits. The apparent migration of the active vents through time, from northern to southern locations, favors an eruptive scenario possibly taking place on the southern flank of Iliniza volcano. However, an active vent located in higher areas close to the summit cannot be discarded. In such case, an eruption in these steeper slope areas would favor the destabilization of the newly emitted lavas increasing the risk of PDC formation, potentially accompanied by explosive phases and widespread tephra fallouts (Voight et al., 2002; Harnett et al., 2018). Such events could affect the 200,000 inhabitants living within 20 km of the volcano (INEC, 2010), including the populations of Chaupi, Pastocalle and Toacazo (Fig. 2).

Although a high explosive phase was identified at Iliniza volcano, this event was unique throughout its eruptive history and are absent in the Holocene eruptive chronology. Therefore, we expect that a scenario involving a highly explosive eruption (e.g., VEI 5), such as the Jatuncama event, is less probable in the short term. In addition, the Iliniza eruptive history does not include any major flank collapse, as no avalanche deposits or morphological remains suggesting a collapse amphitheater were identified. However, the occurrence of the Iliniza volcano above an active strike-slip fault system, the potential weakening of its flanks caused by weathering and hydrothermal alteration, and the steeply inclined slopes of its uppermost areas increase the risk of a potential collapse promoted by a tectonic event.

Finally, the Cotopaxi fallout deposits covering the Iliniza volcano slopes is an additional hazard to consider, although it is not intrinsically related to the Iliniza activity. The Holocene tephra layers deposited on the flanks of Iliniza could be easily remobilized, especially during the rainy season (December to April), forming secondary lahars that flow into the ravines of the volcano. The Cotopaxi

tephra sequence, reaching up to 10 m in thickness, may slide due to the low cohesion of the lower and thicker tephra layers. This hazard is supported by the multiple landslide deposits observed on the southern flank of the Santa Cruz volcano (Hall et al., 2017a), and by the small scarps observed on the east and southeast slopes of the South Iliniza edifice.

6. CONCLUSIONS

This work provides the first geochronological data for the Iliniza volcano and allows to establish a comprehensive overview of its development over time. The first volcanic manifestations in the area correspond to the adjacent Santa Cruz volcano dated at 702 ± 11 ka. After a long quiescent period, its activity resumed at 79 ± 2 ka and 60 ± 3 ka forming the small-volume Loma Saquigua lava dome.

Iliniza shows a young episodic activity that began with the extrusion of the rhyodacite Pilongo lava dome occurring at 353 ± 6 ka. The Iliniza compound volcano (46 ± 15 km^3) comprises two andesitic to dacitic edifices formed in several cone-building stages. The older North Iliniza edifice (28 ± 19 km^3) was first constructed by a succession of thin lavas and breccias during the Lower NI stage at 123-122 ka, followed by the formation of the Huayrapungo satellite peak at 121 ± 2 ka. Then, thick viscous lava sequence dated at 116 ± 2 ka built the higher portion of the edifice through the Upper NI stage. The North Iliniza edifice showed a relatively high output rate of 3.5 ± 2.6 km^3/kyr.

After a ~70 kyr quiescence period, the South Iliniza edifice (18 ± 6 km^3) grew over the remnants of the North Iliniza edifice in three main cone-building stages, with an output rate of 0.8 ± 0.3 km^3/kyr. A basal edifice was constructed during the Lower SI stage by a series of massive lavas of dacitic composition, dated between 46 ± 1 and 45 ± 2 ka. The Upper SI stage started with the Jatuncama explosive phase, in which the uppermost portion of the basal stratovolcano was destroyed and a 30-40 m-thick dacitic pyroclastic succession was deposited. The estimated minimum bulk volume of the Jatuncama ignimbrite deposits is 2.1 km^3, corresponding to a VEI ~5 eruption. The subsequent eruptive activity rebuilt the South Iliniza edifice with the emplacement of a summit lava dome complex and its related PDC deposits. The Terminal SI stage corresponds to the emission of several lava flows of

andesitic composition dated between 31 ± 4 and 25 ± 3 ka. Finally, higher K andesite magmas were emitted from satellite vents located to the south of Iliniza forming the Tishigcuchi lava dome probably in the Holocene, and the Pongo lava flow dated at 6 ± 4 ka. Contrary to other volcanoes of the volcanic front, the Iliniza magmas show a compositional transition from dacites (63-67 wt.% SiO_2) to andesites (60-63 wt.% SiO_2) in the later eruptive stages. Based on these lines of geological and geochronological evidences, we support the hypothesis that the Iliniza volcano must be considered as a potentially active volcanic center.

Acknowledgments

The authors wish to thank Brad Singer and Georges Boudon, and an anonymous reviewer, for their detailed reviews, constructive comments, and suggestions, which helped us to improve this manuscript. The authors are grateful to the "Reserva Ecológica Ilinizas" members for sampling authorization and logistics. We also thank Patricio Ramon for useful discussions and for authorizing the use of his aerial photographic material, as well as Pablo Grosse for useful discussions and remarks, and Valérie Godard for having manufactured all the thin sections. This work is part of an Ecuadorian-French cooperation program carried out between the Instituto Geofísico, Escuela Politécnica Nacional (IGEPN), Quito, Ecuador, and the French Institut de Recherche pour le Développement (IRD), thought the Laboratoire Mixte International "Séismes et Volcans dans les Andes du Nord" (LMI-SVAN) program. This work was supported by the CNRS/INSU TelluS and the LMI-SVAN programs. The first author's PhD grant was funded by the "Secretaria Nacional de Educación Superior, Ciencia, Tecnología e Innovación" (SENESCYT), Ecuador. This is Laboratoire de Géochronologie Multi-Techniques (LGMT) contribution number 169 and Laboratory of Excellence ClerVolc contribution number XXX.

REFERENCES

Almeida, M., Bablon, M., Andrade, D., Hidalgo, S., Quidelleur, X., Samaniego, P., 2019. New constraints on the geological and chronological evolution of the Cotacachi-Cuicocha Volcanic Complex (Ecuador). Presented at the 8th International Symposium on Andean Geodynamics (ISAG), Quito, Ecuador.

Alvarado, A., Audin, L., Nocquet, J.M., Jaillard, E., Mothes, P., Jarrín, P., Segovia, M., Rolandone, F., Cisneros, D., 2016. Partitioning of oblique convergence in the Northern Andes subduction zone: Migration history and the present-day boundary of the North Andean Sliver in Ecuador. Tectonics 35, 1048–1065. https://doi.org/10.1002/2016TC004117

Alvarado, A., Audin, L., Nocquet, J.M., Lagreulet, S., Segovia, M., Font, Y., Lamarque, G., Yepes, H., Mothes, P., Rolandone, F., Jarrín, P., Quidelleur, X., 2014. Active tectonics in Quito, Ecuador, assessed by geomorphological studies, GPS data, and crustal seismicity. Tectonics 33, 67–83. https://doi.org/10.1002/2012TC003224

Andrade, S.D., Müller, A.V., Vasconez, F.J., Beate, B., Aguilar, J., Santamaría, S., 2021. Pululahua dome complex, Ecuador: eruptive history, total magma output and potential hazards. Journal of South American Earth Sciences 106, 103046. https://doi.org/10.1016/j.jsames.2020.103046

Bablon, M., Quidelleur, X., Samaniego, P., Le Pennec, J.-L., Audin, L., Jomard, H., Baize, S., Liorzou, C., Hidalgo, S., Alvarado, A., 2019. Interactions between volcanism and geodynamics in the southern termination of the Ecuadorian arc. Tectonophysics 751, 54–72. https://doi.org/10.1016/j.tecto.2018.12.010

Bablon, M., Quidelleur, X., Samaniego, P., Le Pennec, J.-L., Lahitte, P., Liorzou, C., Bustillos, J.E., Hidalgo, S., 2018. Eruptive chronology of Tungurahua volcano (Ecuador) revisited based on new K-Ar ages and geomorphological reconstructions. Journal of Volcanology and Geothermal Research 357, 378–398. https://doi.org/10.1016/j.jvolgeores.2018.05.007

Bablon, M., Quidelleur, X., Samaniego, P., Le Pennec, J.-L., Santamaría, S., Liorzou, C., Hidalgo, S., Eschbach, B., 2020. Volcanic history reconstruction in northern Ecuador: insights for eruptive and erosion rates on the whole Ecuadorian arc. Bull Volcanol 82, 11. https://doi.org/10.1007/s00445-019-1346-1

Barberi, F., Coltelli, M., Ferrara, G., Innocenti, F., Navarro, J.M., Santacroce, R., 1988. Plio-quaternary volcanism in Ecuador. Geological Magazine 125, 1–14.

Bellver-Baca, M.T., Chiaradia, M., Beate, B., Beguelin, P., Deriaz, B., Mendez-Chazarra, N., Villagómez, D., 2020. Geochemical evolution of the Quaternary Chachimbiro Volcanic Complex (frontal volcanic arc of Ecuador). Lithos 356–357, 105237. https://doi.org/10.1016/j.lithos.2019.105237

947 Bernard, B., Andrade, D., 2011. Volcanes Cuaternarios del Ecuador Continental. IGEPN Poster
948 Informativo.
949 Bernard, B., Hidalgo, S., Robin, C., Beate, B., Quijozaca, J., 2014. The 3640–3510 BC rhyodacite
950 eruption of Chachimbiro compound volcano, Ecuador: a violent directed blast produced by a
951 satellite dome. Bull Volcanol 76, 1–20. https://doi.org/10.1007/s00445-014-0849-z
952 Bertin, D., Amigo, Á., 2015. Geología y peligros del volcán San Pedro, II Región. Presented at the XIV
953 Congreso Geologico Chileno, La Serena, Chile, pp. 128–131.
954 Boland, M., Ibadango, E., Pilatasig, L.F., McCourt, W., Aspden, J.A., Hughen, R., Beate, B., 2000.
955 Geology of the Cordillera Occidental of Ecuador between 0°00' and 1°00'N (No. 10), Proyecto
956 de Desarrollo Minero y Control Ambiental. Cogidem - Brithis Geological Survey, Quito.
957 Bourdon, E., Eissen, J.-P., Gutscher, M.-A., Monzier, M., Hall, M.L., Cotten, J., 2003. Magmatic
958 response to early aseismic ridge subduction: the Ecuadorian margin case (South America).
959 Earth and Planetary Science Letters 205, 123–138. https://doi.org/10.1016/S0012-
960 821X(02)01024-5
961 Brenna, M., Cronin, S.J., Smith, I.E.M., Sohn, Y.K., Maas, R., 2012. Spatio-temporal evolution of a
962 dispersed magmatic system and its implications for volcano growth, Jeju Island Volcanic Field,
963 Korea. Lithos 148, 337–352. https://doi.org/10.1016/j.lithos.2012.06.021
964 Bryant, J.A., Yogodzinski, G.M., Hall, M.L., Lewicki, J.L., Bailey, D.G., 2006. Geochemical
965 Constraints on the Origin of Volcanic Rocks from the Andean Northern Volcanic Zone,
966 Ecuador. Journal of Petrology 47, 1147–1175. https://doi.org/10.1093/petrology/egl006
967 Capra, L., Norini, G., Groppelli, G., Macías, J.L., Arce, J.L., 2008. Volcanic hazard zonation of the
968 Nevado de Toluca volcano, México. Journal of Volcanology and Geothermal Research 176,
969 469–484. https://doi.org/10.1016/j.jvolgeores.2008.04.016
970 Cassignol, C., Gillot, P.-Y., 1982. Range and effectiveness of unspiked potassium-argon dating:
971 experimental groundwork and applications, in: Odin, G.S. (Ed.), Numerical Dating in
972 Stratigraphy. John Wiley & Sons, pp. 159–179.
973 Chiaradia, M., Müntener, O., Beate, B., Fontignie, D., 2009. Adakite-like volcanism of Ecuador: lower
974 crust magmatic evolution and recycling. Contrib Mineral Petrol 158, 563–588.
975 https://doi.org/10.1007/s00410-009-0397-2
976 Clapperton, C.M., 1990. Glacial and volcanic geomorphology of the Chimborazo-Carihuairazo Massif,
977 Ecuadorian Andes. Earth and Environmental Science Transactions of The Royal Society of
978 Edinburgh 81, 91–116. https://doi.org/10.1017/S0263593300005174
979 Clapperton, C.M., 1987. Maximal extent of late Wisconsin glaciation in the Ecuadorian Andes.
980 Quaternary of South America and Antarctic Peninsula 5, 165–179.
981 Clapperton, C.M., 1986. Glacial geomorphology, Quaternary glacial sequence and palaeoclimatic
982 inferences in the Ecuadorian Andes, in: Gardiner, V. (Ed.), International Geomorphology, Part
983 II. Wiley, London, pp. 843–870.

984 Conway, C.E., Leonard, G.S., Townsend, D.B., Calvert, A.T., Wilson, C.J.N., Gamble, J.A., Eaves,
985 S.R., 2016. A high-resolution 40Ar/39Ar lava chronology and edifice construction history for
986 Ruapehu volcano, New Zealand. Journal of Volcanology and Geothermal Research 327, 152–
987 179. https://doi.org/10.1016/j.jvolgeores.2016.07.006
988 Cortés, A., Garduño Monroy, V., Macías, J., Navarro-Ochoa, C., Komorowski, J.-C., Saucedo, R.,
989 Gavilanes Ruiz, J., 2010. Geologic mapping of the Colima volcanic complex (Mexico) and
990 implications for hazard assessment. Special Paper of the Geological Society of America 464,
991 249–264. https://doi.org/10.1130/2010.2464(12)
992 Cotten, J., Le Dez, A., Bau, M., Caroff, M., Maury, R.C., Dulski, P., Fourcade, S., Bohn, M., Brousse,
993 R., 1995. Origin of anomalous rare-earth element and yttrium enrichments in subaerially
994 exposed basalts: Evidence from French Polynesia. Chemical Geology 119, 115–138.
995 https://doi.org/10.1016/0009-2541(94)00102-E
996 Crisp, J.A., 1984. Rates of magma emplacement and volcanic output. Journal of Volcanology and
997 Geothermal Research 20, 177–211. https://doi.org/10.1016/0377-0273(84)90039-8
998 de Silva, S., Lindsay, J.M., 2015. Chapter 15 - Primary Volcanic Landforms, in: Sigurdsson, H. (Ed.),
999 The Encyclopedia of Volcanoes (Second Edition). Academic Press, Amsterdam, pp. 273–297.
1000 https://doi.org/10.1016/B978-0-12-385938-9.00015-8
1001 DeMets, C., Gordon, R.G., Argus, D.F., 2010. Geologically current plate motions. Geophysical Journal
1002 International 181, 1–80. https://doi.org/10.1111/j.1365-246X.2009.04491.x
1003 Dibacto, S., Lahitte, P., Karátson, D., Hencz, M., Szakács, A., Biró, T., Kovács, I., Veres, D., 2020.
1004 Growth and erosion rates of the East Carpathians volcanoes constrained by numerical models:
1005 Tectonic and climatic implications. Geomorphology 368, 107352.
1006 https://doi.org/10.1016/j.geomorph.2020.107352
1007 Egbue, O., Kellogg, J., 2010. Pleistocene to Present North Andean "escape." Tectonophysics 489, 248–
1008 257. https://doi.org/10.1016/j.tecto.2010.04.021
1009 Egüez, A., Alvarado, A., Yepes, H., Machette, M.N., Costa, C., Dart, R.L., 2003. Database and map of
1010 Quaternary faults and folds of Ecuador and its offshore regions. US Geological Survey Open-
1011 File Report 03-289 71. https://doi.org/10.3133/ofr03289
1012 Esser, R.P., Kyle, P.R., McIntosh, W.C., 2004. 40Ar/39Ar dating of the eruptive history of Mount
1013 Erebus, Antarctica: volcano evolution. Bull Volcanol 66, 671–686.
1014 https://doi.org/10.1007/s00445-004-0354-x
1015 Frey, H.M., Lange, R.A., Hall, C.M., Delgado-Granados, H., 2004. Magma eruption rates constrained
1016 by 40Ar/39Ar chronology and GIS for the Ceboruco–San Pedro volcanic field, western Mexico.
1017 GSA Bulletin 116, 259–276. https://doi.org/10.1130/B25321.1
1018 Freymueller, J.T., Kellogg, J.N., Vega, V., 1993. Plate Motions in the north Andean region. Journal of
1019 Geophysical Research: Solid Earth 98, 21853–21863. https://doi.org/10.1029/93JB00520

1020 Gamble, J.A., Price, R.C., Smith, I.E.M., McIntosh, W.C., Dunbar, N.W., 2003. 40Ar/39Ar
1021 geochronology of magmatic activity, magma flux and hazards at Ruapehu volcano, Taupo
1022 Volcanic Zone, New Zealand. Journal of Volcanology and Geothermal Research 120, 271–287.
1023 https://doi.org/10.1016/S0377-0273(02)00407-9
1024 García-Palomo, A., Macías, J.L., Arce, J.L., Capra, L., Garduño, V.H., Espíndola, J.M., 2002. Geology
1025 of Nevado de Toluca Volcano and surrounding areas, central Mexico. Geological Society of
1026 America Map and Chart Series, MCH089 26.
1027 Garrison, J., Davidson, J., Reid, M., Turner, S., 2006. Source versus differentiation controls on U-series
1028 disequilibria: Insights from Cotopaxi Volcano, Ecuador. Earth and Planetary Science Letters
1029 244, 548–565. https://doi.org/10.1016/j.epsl.2006.02.013
1030 Garrison, J.M., Davidson, J.P., 2003. Dubious case for slab melting in the Northern volcanic zone of
1031 the Andes. Geology 31, 565–568. https://doi.org/10.1130/0091-
1032 7613(2003)031<0565:DCFSMI>2.0.CO;2
1033 Georgatou, A., Chiaradia, M., Rezeau, H., Wälle, M., 2018. Magmatic sulphides in Quaternary
1034 Ecuadorian arc magmas. Lithos 296–299, 580–599.
1035 https://doi.org/10.1016/j.lithos.2017.11.019
1036 Germa, A., Lahitte, P., Quidelleur, X., 2015. Construction and destruction of Mont Pelée volcano:
1037 Volumes and rates constrained from a geomorphological model of evolution. Journal of
1038 Geophysical Research: Earth Surface 120, 1206–1226. https://doi.org/10.1002/2014JF003355
1039 Germa, A., Quidelleur, X., Gillot, P.Y., Tchilinguirian, P., 2010. Volcanic evolution of the back-arc
1040 Pleistocene Payun Matru volcanic field (Argentina). Journal of South American Earth Sciences
1041 29, 717–730. https://doi.org/10.1016/j.jsames.2010.01.002
1042 Germa, A., Quidelleur, X., Lahitte, P., Labanieh, S., Chauvel, C., 2011. The K–Ar Cassignol–Gillot
1043 technique applied to western Martinique lavas: A record of Lesser Antilles arc activity from
1044 2Ma to Mount Pelée volcanism. Quaternary Geochronology 6, 341–355.
1045 https://doi.org/10.1016/j.quageo.2011.02.001
1046 Gillot, P.Y., Hildenbrand, A., Lefèvre, J.C., Albore-Livadie, C., 2006. The K/Ar dating method:
1047 principle, analytical techniques, and application to Holocene volcanic eruptions in Southern
1048 Italy. Acta Vulcanologica 18, 55–66.
1049 González-Maurel, O., Godoy, B., le Roux, P., Rodríguez, I., Marín, C., Menzies, A., Bertin, D., Morata,
1050 D., Vargas, M., 2019. Magmatic differentiation at La Poruña scoria cone, Central Andes,
1051 northern Chile: Evidence for assimilation during turbulent ascent processes, and genetic links
1052 with mafic eruptions at adjacent San Pedro volcano. Lithos 338–339, 128–140.
1053 https://doi.org/10.1016/j.lithos.2019.03.033
1054 Grosse, P., Ochi Ramacciotti, M.L., Escalante Fochi, F., Guzmán, S., Orihashi, Y., Sumino, H., 2020.
1055 Geomorphology, morphometry, spatial distribution and ages of mafic monogenetic volcanoes
1056 of the Peinado and Incahuasi fields, southernmost Central Volcanic Zone of the Andes. Journal

of Volcanology and Geothermal Research 401, 106966. https://doi.org/10.1016/j.jvolgeores.2020.106966

Grosse, P., Orihashi, Y., Guzmán, S.R., Sumino, H., Nagao, K., 2018. Eruptive history of Incahuasi, Falso Azufre and El Cóndor Quaternary composite volcanoes, southern Central Andes. Bull Volcanol 80, 1–26. https://doi.org/10.1007/s00445-018-1221-5

Grosse, P., Vries, B. van W. de, Petrinovic, I.A., Euillades, P.A., Alvarado, G.E., 2009. Morphometry and evolution of arc volcanoes. Geology 37, 651–654. https://doi.org/10.1130/G25734A.1

Gutscher, M.-A., Malavieille, J., Lallemand, S., Collot, J.-Y., 1999. Tectonic segmentation of the North Andean margin: impact of the Carnegie Ridge collision. Earth and Planetary Science Letters 168, 255–270. https://doi.org/10.1016/S0012-821X(99)00060-6

Hall, M.L., Beate, B., 1991. El volcanismo plio cuaternario en los Andes del Ecuador, in: El paisaje volcánico de la sierra ecuatoriana: geomorfología, fenómenos volcánicos y recursos asociados, Estudios de Geografia. Corporación Editora Nacional, Quito, pp. 5–17.

Hall, M.L., Mothes, P., 2008. The rhyolitic–andesitic eruptive history of Cotopaxi volcano, Ecuador. Bull Volcanol 70, 675–702. https://doi.org/10.1007/s00445-007-0161-2

Hall, M.L., Mothes, P., Vallance, J., Alvarado, A., 2017a. Deslizamientos del Yacupungo, in: Cabero, A., Zúñiga, M.A., Le Pennec, J.-L., Narváez, D., Hernández, M.J., Nocquet, J.M., Gómez, F.V. (Eds.), Memorias VIII Jornadas En Ciencias de La Tierra. Presented at the VIII Jornadas en Ciencas de la Tierra, EPN Editorial, Quito, Ecuador, pp. 85–87.

Hall, M.L., Mothes, P.A., Samaniego, P., Militzer, A., Beate, B., Ramón, P., Robin, C., 2017b. Antisana volcano: A representative andesitic volcano of the eastern cordillera of Ecuador: Petrography, chemistry, tephra and glacial stratigraphy. Journal of South American Earth Sciences 73, 50–64. https://doi.org/10.1016/j.jsames.2016.11.005

Hall, M.L., Samaniego, P., Le Pennec, J.L., Johnson, J.B., 2008. Ecuadorian Andes volcanism: A review of Late Pliocene to present activity. Journal of Volcanology and Geothermal Research, Recent and active volcanism in the Ecuadorian Andes 176, 1–6. https://doi.org/10.1016/j.jvolgeores.2008.06.012

Harford, C.L., Pringle, M.S., Sparks, R.S.J., Young, S.R., 2002. The volcanic evolution of Montserrat using 40Ar/39Ar geochronology. Geological Society, London, Memoirs 21, 93–113. https://doi.org/10.1144/GSL.MEM.2002.021.01.05

Harnett, C.E., Thomas, M.E., Purvance, M.D., Neuberg, J., 2018. Using a discrete element approach to model lava dome emplacement and collapse. Journal of Volcanology and Geothermal Research 359, 68–77. https://doi.org/10.1016/j.jvolgeores.2018.06.017

Heine, K., 2011. Chapter 57 - Late Quaternary Glaciations of Ecuador, in: Ehlers, J., Gibbard, P.L., Hughes, P.D. (Eds.), Developments in Quaternary Sciences, Quaternary Glaciations - Extent and Chronology. Elsevier, pp. 803–813. https://doi.org/10.1016/B978-0-444-53447-7.00057-X

1094 Heine, K., 2000. Tropical South America during the Last Glacial Maximum: evidence from glacial,
1095 periglacial and fluvial records. Quaternary International, Quaternary palaeohydorlogy of South
1096 America 72, 7–21. https://doi.org/10.1016/S1040-6182(00)00017-3
1097 Heine, K., 1995. Late Quaternary glacier advances in the Ecuadorian Andes: a preliminary report.
1098 Quaternary of South America and Antarctic Peninsula 9, 1–22.
1099 Hidalgo, S., 2006. Les intéractions entre magmas calco-alcalins "classiques" et adakitiques: exemple
1100 du complexe volcanique Atacazo-Ninahuilca (Equateur) (Ph.D. thesis). Université Blaise
1101 Pascal - Clermont-Ferrand II, Clermont-Ferrand, France.
1102 Hidalgo, S., 2002. Géochimie du complexe volcanique des Iliniza: pétrogenèse de séries à affinité
1103 adakitique de l'arc équatorien (DEA Report). Université Blaise Pascal, Clermont-Ferrand.
1104 Hidalgo, S., 2001. Estudio geovolcanológico del complejo volcánico Iliniza (Engineer memoir).
1105 Escuela Politécnica Nacional, Quito.
1106 Hidalgo, S., Gerbe, M.C., Martin, H., Samaniego, P., Bourdon, E., 2012. Role of crustal and slab
1107 components in the Northern Volcanic Zone of the Andes (Ecuador) constrained by Sr–Nd–O
1108 isotopes. Lithos 132–133, 180–192. https://doi.org/10.1016/j.lithos.2011.11.019
1109 Hidalgo, S., Monzier, M., Almeida, E., Chazot, G., Eissen, J.-P., van der Plicht, J., Hall, M.L., 2008.
1110 Late Pleistocene and Holocene activity of the Atacazo–Ninahuilca Volcanic Complex
1111 (Ecuador). Journal of Volcanology and Geothermal Research 176, 16–26.
1112 https://doi.org/10.1016/j.jvolgeores.2008.05.017
1113 Hidalgo, S., Monzier, M., Martin, H., Chazot, G., Eissen, J.-P., Cotten, J., 2007. Adakitic magmas in
1114 the Ecuadorian Volcanic Front: Petrogenesis of the Iliniza Volcanic Complex (Ecuador).
1115 Journal of Volcanology and Geothermal Research 159, 366–392.
1116 https://doi.org/10.1016/j.jvolgeores.2006.07.007
1117 Hildenbrand, A., Marques, F.O., Catalão, J., 2018. Large-scale mass wasting on small volcanic islands
1118 revealed by the study of Flores Island (Azores). Scientific Reports 8, 13898.
1119 https://doi.org/10.1038/s41598-018-32253-0
1120 Hildreth, W., 2007. Quaternary Magmatism in the Cascades: Geologic Perspectives. U.S. Geological
1121 Survey.
1122 Hildreth, W., Fierstein, J., Lanphere, M., 2003a. Eruptive history and geochronology of the Mount
1123 Baker volcanic field, Washington. GSA Bulletin 115, 729–764. https://doi.org/10.1130/0016-
1124 7606(2003)115<0729:EHAGOT>2.0.CO;2
1125 Hildreth, W., Lanphere, M.A., Fierstein, J., 2003b. Geochronology and eruptive history of the Katmai
1126 volcanic cluster, Alaska Peninsula. Earth and Planetary Science Letters 214, 93–114.
1127 https://doi.org/10.1016/S0012-821X(03)00321-2
1128 Hora, J.M., Singer, B.S., Wörner, G., 2007. Volcano evolution and eruptive flux on the thick crust of
1129 the Andean Central Volcanic Zone: 40Ar/39Ar constraints from Volcán Parinacota, Chile. GSA
1130 Bulletin 119, 343–362. https://doi.org/10.1130/B25954.1

Hughes, R.A., Bermúdez, R., 1997. Geology of the Cordillera Occidental of Ecuador between 0°00' and 1°00'S (No. 4), Proyecto de Desarrollo Minero y Control Ambiental. Cogidem - Brithis Geological Survey, Quito.

INEC, 2010. Censo de Población y Vivienda 2010 [WWW Document]. Instituto Nacional de Estadística y Censos, Ecuador. URL https://www.ecuadorencifras.gob.ec/base-de-datos-censo-de-poblacion-y-vivienda-2010/ (accessed 5.20.20).

Jaillard, E., Ordoñez, M., Suárez, J., Toro, J., Iza, D., Lugo, W., 2004. Stratigraphy of the late Cretaceous–Paleogene deposits of the cordillera occidental of central ecuador: geodynamic implications. Journal of South American Earth Sciences 17, 49–58. https://doi.org/10.1016/j.jsames.2004.05.003

Lahitte, P., Dibacto, S., Karátson, D., Gertisser, R., Veres, D., 2019. Eruptive history of the Late Quaternary Ciomadul (Csomád) volcano, East Carpathians, part I: timing of lava dome activity. Bull Volcanol 81, 27. https://doi.org/10.1007/s00445-019-1286-9

Lahitte, P., Samper, A., Quidelleur, X., 2012. DEM-based reconstruction of southern Basse-Terre volcanoes (Guadeloupe archipelago, FWI): Contribution to the Lesser Antilles Arc construction rates and magma production. Geomorphology, Volcano Geomorphology: landforms, processes and hazards 136, 148–164. https://doi.org/10.1016/j.geomorph.2011.04.008

Lavenu, A., Winter, T., Dávila, F., 1995. A Pliocene–Quaternary compressional basin in the Interandean Depression, Central Ecuador. Geophysical Journal International 121, 279–300. https://doi.org/10.1111/j.1365-246X.1995.tb03527.x

Le Pennec, J.L., Ruiz, A.G., Eissen, J.P., Hall, M.L., Fornari, M., 2011. Identifying potentially active volcanoes in the Andes: Radiometric evidence for late Pleistocene-early Holocene eruptions at Volcán Imbabura, Ecuador. Journal of Volcanology and Geothermal Research 206, 121–135. https://doi.org/10.1016/j.jvolgeores.2011.06.002

Mariño, J., Samaniego, P., Manrique, N., Valderrama, P., Roche, O., van Wyk de Vries, B., Guillou, H., Zerathe, S., Arias, C., Liorzou, C., 2021. The Tutupaca volcanic complex (Southern Peru): Eruptive chronology and successive destabilization of a dacitic dome complex. Journal of South American Earth Sciences 109, 103227. https://doi.org/10.1016/j.jsames.2021.103227

Min, K., Mundil, R., Renne, P.R., Ludwig, K.R., 2000. A test for systematic errors in 40Ar/39Ar geochronology through comparison with U/Pb analysis of a 1.1-Ga rhyolite. Geochimica et Cosmochimica Acta 64, 73–98. https://doi.org/10.1016/S0016-7037(99)00204-5

Mothes, P.A., Hall, M.L., 2008. The plinian fallout associated with Quilotoa's 800 yr BP eruption, Ecuadorian Andes. Journal of Volcanology and Geothermal Research, Recent and active volcanism in the Ecuadorian Andes 176, 56–69. https://doi.org/10.1016/j.jvolgeores.2008.05.018

Nocquet, J.-M., Villegas-Lanza, J.C., Chlieh, M., Mothes, P.A., Rolandone, F., Jarrin, P., Cisneros, D., Alvarado, A., Audin, L., Bondoux, F., Martin, X., Font, Y., Régnier, M., Vallée, M., Tran, T.,

1168 Beauval, C., Mendoza, J.M.M., Martinez, W., Tavera, H., Yepes, H., 2014. Motion of
1169 continental slivers and creeping subduction in the northern Andes. Nature Geoscience 7, 287–
1170 291. https://doi.org/10.1038/ngeo2099
1171 Ownby, S., Delgado Granados, H., Lange, R.A., Hall, C.M., 2007. Volcán Tancítaro, Michoacán,
1172 Mexico, 40Ar/39Ar constraints on its history of sector collapse. Journal of Volcanology and
1173 Geothermal Research 161, 1–14. https://doi.org/10.1016/j.jvolgeores.2006.10.009
1174 Pallares, C., Quidelleur, X., Debreil, J.A., Antoine, C., Sarda, P., Tchilinguirian, P., Delpech, G., Gillot,
1175 P.-Y., 2019. Quaternary evolution of the El Tromen volcanic system, Argentina, based on new
1176 K-Ar and geochemical data: Insights for temporal evolution of magmatic processes between
1177 arc and back-arc settings. Journal of South American Earth Sciences 90, 338–354.
1178 https://doi.org/10.1016/j.jsames.2018.12.022
1179 Peccerillo, A., Taylor, S.R., 1976. Geochemistry of eocene calc-alkaline volcanic rocks from the
1180 Kastamonu area, Northern Turkey. Contr. Mineral. and Petrol. 58, 63–81.
1181 https://doi.org/10.1007/BF00384745
1182 Pure, L.R., Leonard, G.S., Townsend, D.B., Wilson, C.J.N., Calvert, A.T., Cole, R.P., Conway, C.E.,
1183 Gamble, J.A., Smith, T. 'Bubs,' 2020. A high resolution 40Ar/39Ar lava chronology and edifice
1184 construction history for Tongariro volcano, New Zealand. Journal of Volcanology and
1185 Geothermal Research 403, 106993. https://doi.org/10.1016/j.jvolgeores.2020.106993
1186 Renne, P.R., Mulcahy, S.R., Cassata, W.S., Morgan, L.E., Kelley, S.P., Hlusko, L.J., Njau, J.K., 2012.
1187 Retention of inherited Ar by alkali feldspar xenocrysts in a magma: Kinetic constraints from
1188 Ba zoning profiles. Geochimica et Cosmochimica Acta 93, 129–142.
1189 https://doi.org/10.1016/j.gca.2012.06.029
1190 Rivera, M., Samaniego, P., Vela, J., Le Pennec, J.-L., Guillou, H., Paquette, J.-L., Liorzou, C., 2020.
1191 The eruptive chronology of the Yucamane-Calientes compound volcano: A potentially active
1192 edifice of the Central Andes (southern Peru). Journal of Volcanology and Geothermal Research
1193 393, 106787. https://doi.org/10.1016/j.jvolgeores.2020.106787
1194 Robin, C., Eissen, J.-P., Samaniego, P., Martin, H., Hall, M., Cotten, J., 2009. Evolution of the late
1195 Pleistocene Mojanda–Fuya Fuya volcanic complex (Ecuador), by progressive adakitic
1196 involvement in mantle magma sources. Bulletin of Volcanology 71, 233–258.
1197 https://doi.org/10.1007/s00445-008-0219-9
1198 Robin, C., Mossand, P., Camus, G., Cantagrel, J.-M., Gourgaud, A., Vincent, P.M., 1987. Eruptive
1199 history of the Colima volcanic complex (Mexico). Journal of Volcanology and Geothermal
1200 Research 31, 99–113. https://doi.org/10.1016/0377-0273(87)90008-4
1201 Robin, C., Samaniego, P., Le Pennec, J.-L., Fornari, M., Mothes, P., van der Plicht, J., 2010. New
1202 radiometric and petrological constraints on the evolution of the Pichincha volcanic complex
1203 (Ecuador). Bull Volcanol 72, 1109–1129. https://doi.org/10.1007/s00445-010-0389-0

1204 Robin, C., Samaniego, P., Le Pennec, J.-L., Mothes, P., van der Plicht, J., 2008. Late Holocene phases
1205 of dome growth and Plinian activity at Guagua Pichincha volcano (Ecuador). Journal of
1206 Volcanology and Geothermal Research, Recent and active volcanism in the Ecuadorian Andes
1207 176, 7–15. https://doi.org/10.1016/j.jvolgeores.2007.10.008
1208 Sainlot, N., Vlastélic, I., Nauret, F., Moune, S., Aguilera, F., 2020. Sr–Pb isotopes signature of Lascar
1209 volcano (Chile): Insight into contamination of arc magmas ascending through a thick
1210 continental crust. Journal of South American Earth Sciences 101, 102599.
1211 https://doi.org/10.1016/j.jsames.2020.102599
1212 Samaniego, P., Barba, D., Robin, C., Fornari, M., Bernard, B., 2012. Eruptive history of Chimborazo
1213 volcano (Ecuador): A large, ice-capped and hazardous compound volcano in the Northern
1214 Andes. Journal of Volcanology and Geothermal Research 221–222, 33–51.
1215 https://doi.org/10.1016/j.jvolgeores.2012.01.014
1216 Samaniego, P., Martin, H., Monzier, M., Robin, C., Fornari, M., Eissen, J.-P., Cotten, J., 2005.
1217 Temporal Evolution of Magmatism in the Northern Volcanic Zone of the Andes: The Geology
1218 and Petrology of Cayambe Volcanic Complex (Ecuador). Journal of Petrology 46, 2225–2252.
1219 https://doi.org/10.1093/petrology/egi053
1220 Samaniego, P., Rivera, M., Mariño, J., Guillou, H., Liorzou, C., Zerathe, S., Delgado, R., Valderrama,
1221 P., Scao, V., 2016. The eruptive chronology of the Ampato–Sabancaya volcanic complex
1222 (Southern Peru). Journal of Volcanology and Geothermal Research 323, 110–128.
1223 https://doi.org/10.1016/j.jvolgeores.2016.04.038
1224 Samaniego, P., Robin, C., Chazot, G., Bourdon, E., Cotten, J., 2010. Evolving metasomatic agent in the
1225 Northern Andean subduction zone, deduced from magma composition of the long-lived
1226 Pichincha volcanic complex (Ecuador). Contrib Mineral Petrol 160, 239–260.
1227 https://doi.org/10.1007/s00410-009-0475-5
1228 Schiano, P., Monzier, M., Eissen, J.-P., Martin, H., Koga, K.T., 2010. Simple mixing as the major
1229 control of the evolution of volcanic suites in the Ecuadorian Andes. Contrib Mineral Petrol 160,
1230 297–312. https://doi.org/10.1007/s00410-009-0478-2
1231 Shackleton, N.J., Sánchez-Goñi, M.F., Pailler, D., Lancelot, Y., 2003. Marine Isotope Substage 5e and
1232 the Eemian Interglacial. Global and Planetary Change, THE EEMIAN INTERGLACIAL: A
1233 GLOBAL PERSPECTIVE 36, 151–155. https://doi.org/10.1016/S0921-8181(02)00181-9
1234 Sierra, D., Hidalgo, S., Almeida, M., Vigide, N., Lamberti, M.C., Proaño, A., Narváez, D.F., 2020.
1235 Temporal and spatial variations of CO2 diffuse volcanic degassing on Cuicocha Caldera Lake
1236 – Ecuador. Journal of Volcanology and Geothermal Research 107145.
1237 https://doi.org/10.1016/j.jvolgeores.2020.107145
1238 Singer, B.S., Wijbrans, J.R., Nelson, S.T., Pringle, M.S., Feeley, T.C., Dungan, M.A., 1998. Inherited
1239 argon in a Pleistocene andesite lava: 40Ar/39Ar incremental-heating and laser-fusion analyses

of plagioclase. Geology 26, 427–430. https://doi.org/10.1130/0091-7613(1998)026<0427:IAIAPA>2.3.CO;2

Soulas, J.-P., Eguez, A., Yepes, Hugo, Perez, H., 1991. Tectónica activa y riesgo sísmico en los Andes Ecuatorianos y el extremo sur de Colombia. Bol. Geol. Ecuat. 2, 3–11.

Spikings, R., Winkler, W., Hughes, R.A., Handler, R., 2005. Thermochronology of allochthonous terranes in Ecuador: Unravelling the accretionary and post-accretionary history of the Northern Andes. Tectonophysics, Andean Geodynamics: 399, 195–220. https://doi.org/10.1016/j.tecto.2004.12.023

Steiger, R.H., Jäger, E., 1977. Subcommission on geochronology: Convention on the use of decay constants in geo- and cosmochronology. Earth and Planetary Science Letters 36, 359–362. https://doi.org/10.1016/0012-821X(77)90060-7

Sun, S.-S., McDonough, W.F., 1989. Chemical and isotopic systematics of oceanic basalts: implications for mantle composition and processes. Geol. Soc. Lond. Spec. Publ. 42, 313–345. https://doi.org/10.1144/GSL.SP.1989.042.01.19

Thouret, J.-C., Finizola, A., Fornari, M., Legeley-Padovani, A., Suni, J., Frechen, M., 2001. Geology of El Misti volcano near the city of Arequipa, Peru. GSA Bulletin 113, 1593–1610. https://doi.org/10.1130/0016-7606(2001)113<1593:GOEMVN>2.0.CO;2

Tibaldi, A., Ferrari, L., 1992. From latest miocene thrusting to quaternary transpression and transtension in the Interandean Valley, Ecuador. Journal of Geodynamics 15, 59–83. https://doi.org/10.1016/0264-3707(92)90006-E

Vallejo, C., 2007. Evolution of the Western Cordillera in the Andes of Ecuador (Late Cretaceous-Paleogene) (Ph.D. thesis). University of Aberdeen, Zürich.

Vallejo, C., Almagor, S., Romero, C., Herrera, J.L., Escobar, V., Spikings, R., Winkler, W., Vermeesch, P., 2020. Sedimentology, Provenance and Radiometric Dating of the Silante Formation: Implications for the Cenozoic Evolution of the Western Andes of Ecuador. Minerals 10, 929. https://doi.org/10.3390/min10100929

Vallejo, C., Spikings, R., Horton, B.K., Luzieux, L., Romero, C., Winkler, W., Thomsen, T.B., 2019. Chapter 8 - Late cretaceous to miocene stratigraphy and provenance of the coastal forearc and Western Cordillera of Ecuador: Evidence for accretion of a single oceanic plateau fragment, in: Horton, B.K., Folguera, A. (Eds.), Andean Tectonics. Elsevier, pp. 209–236. https://doi.org/10.1016/B978-0-12-816009-1.00010-1

Vallejo, C., Winkler, W., Spikings, R., Luzieux, L., Heller, F., Bussy, F., 2009. Mode and timing of terrane accretion in the forearc of the Andes in Ecuador. Geological Society of America Memoirs 204, 197–216. https://doi.org/10.1130/2009.1204(09)

Voight, B., Komorowski, J.-C., Norton, G.E., Belousov, A.B., Belousova, M., Boudon, G., Francis, P.W., Franz, W., Heinrich, P., Sparks, R.S.J., Young, S.R., 2002. The 26 December (Boxing Day) 1997 sector collapse and debris avalanche at Soufrière Hills Volcano, Montserrat.

1277 Geological Society, London, Memoirs 21, 363–407.
1278 https://doi.org/10.1144/GSL.MEM.2002.021.01.17
1279 von Hillebrandt, C., 1989. Estudio geovolcanológico del complejo volcánico Cuicocha-Cotacachi y sus
1280 aplicaciones, Provincia de Imbabura (Master's thesis). Escuela Politécnica Nacional, Quito,
1281 Ecuador.
1282 Winkler, W., Villagómez, D., Spikings, R., Abegglen, P., Tobler, St., Egüez, A., 2005. The Chota basin
1283 and its significance for the inception and tectonic setting of the inter-Andean depression in
1284 Ecuador. Journal of South American Earth Sciences, Cenozoic Andean Basin Evolution 19, 5–
1285 19. https://doi.org/10.1016/j.jsames.2004.06.006
1286 Witt, C., Bourgois, J., Michaud, F., Ordoñez, M., Jiménez, N., Sosson, M., 2006. Development of the
1287 Gulf of Guayaquil (Ecuador) during the Quaternary as an effect of the North Andean block
1288 tectonic escape. Tectonics 25. https://doi.org/10.1029/2004TC001723
1289

Appendix A.

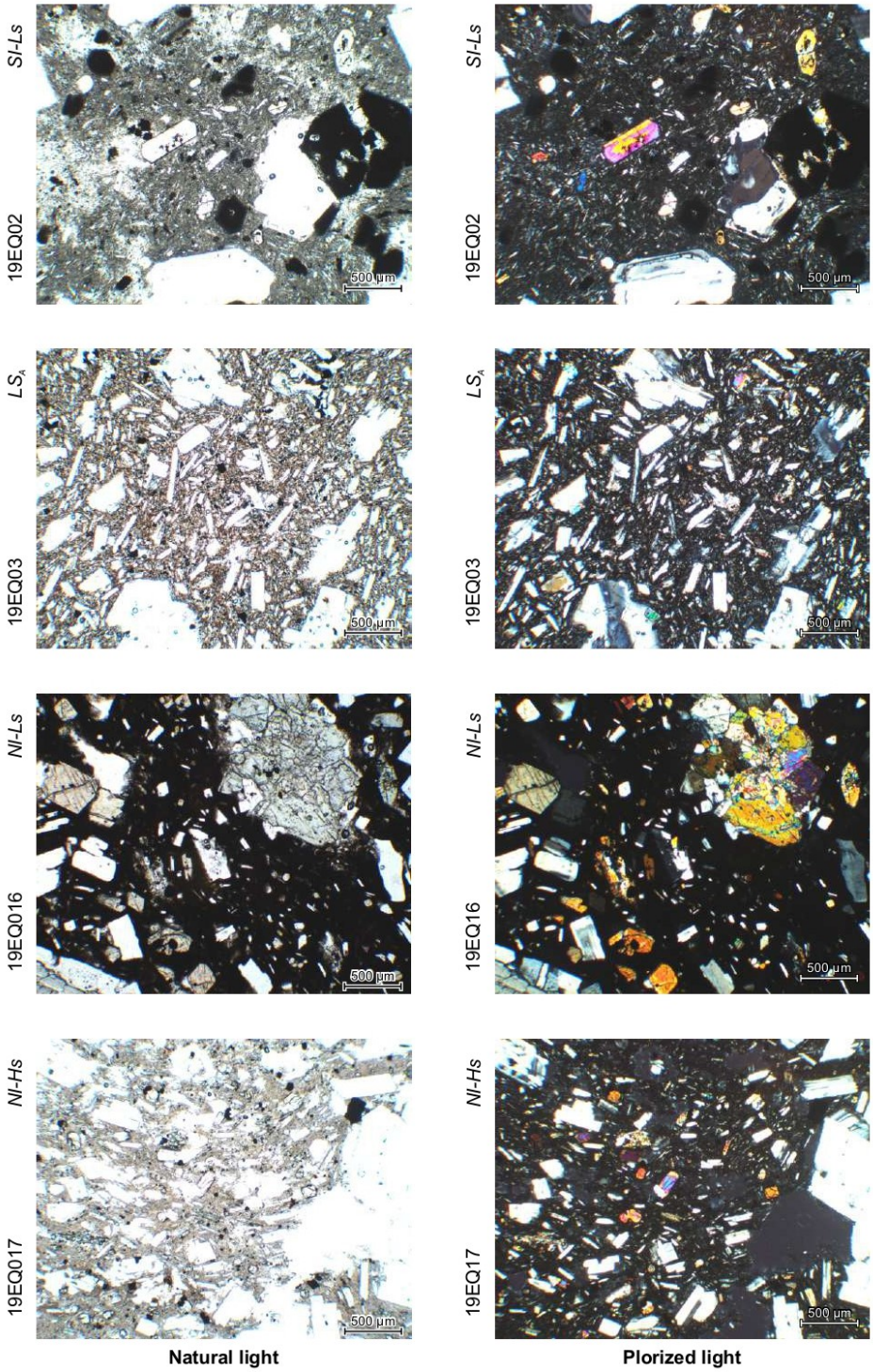
SI-Ls
19EQ02
LS$_A$
19EQ03
NI-Ls
19EQ016
NI-Hs
19EQ017
SI-Ls
19EQ02
LS$_A$
19EQ03
NI-Ls
19EQ16
NI-Hs
19EQ17
500 µm
Natural light
Plorized light

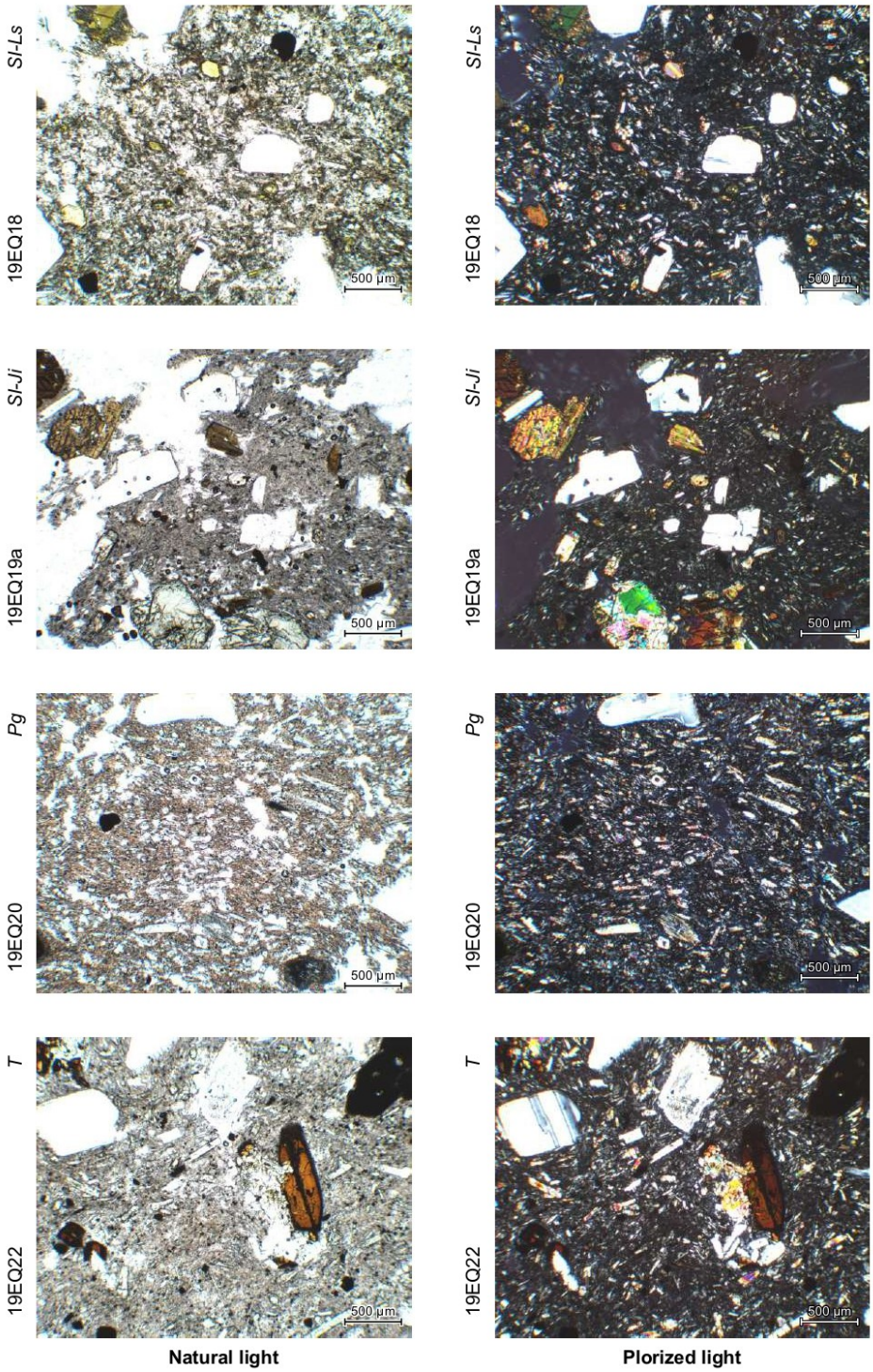
Sl-Ls
19EQ18
Sl-Ji
19EQ19a
Pg
19EQ20
T
19EQ22
500 µm
Natural light
Plorized light

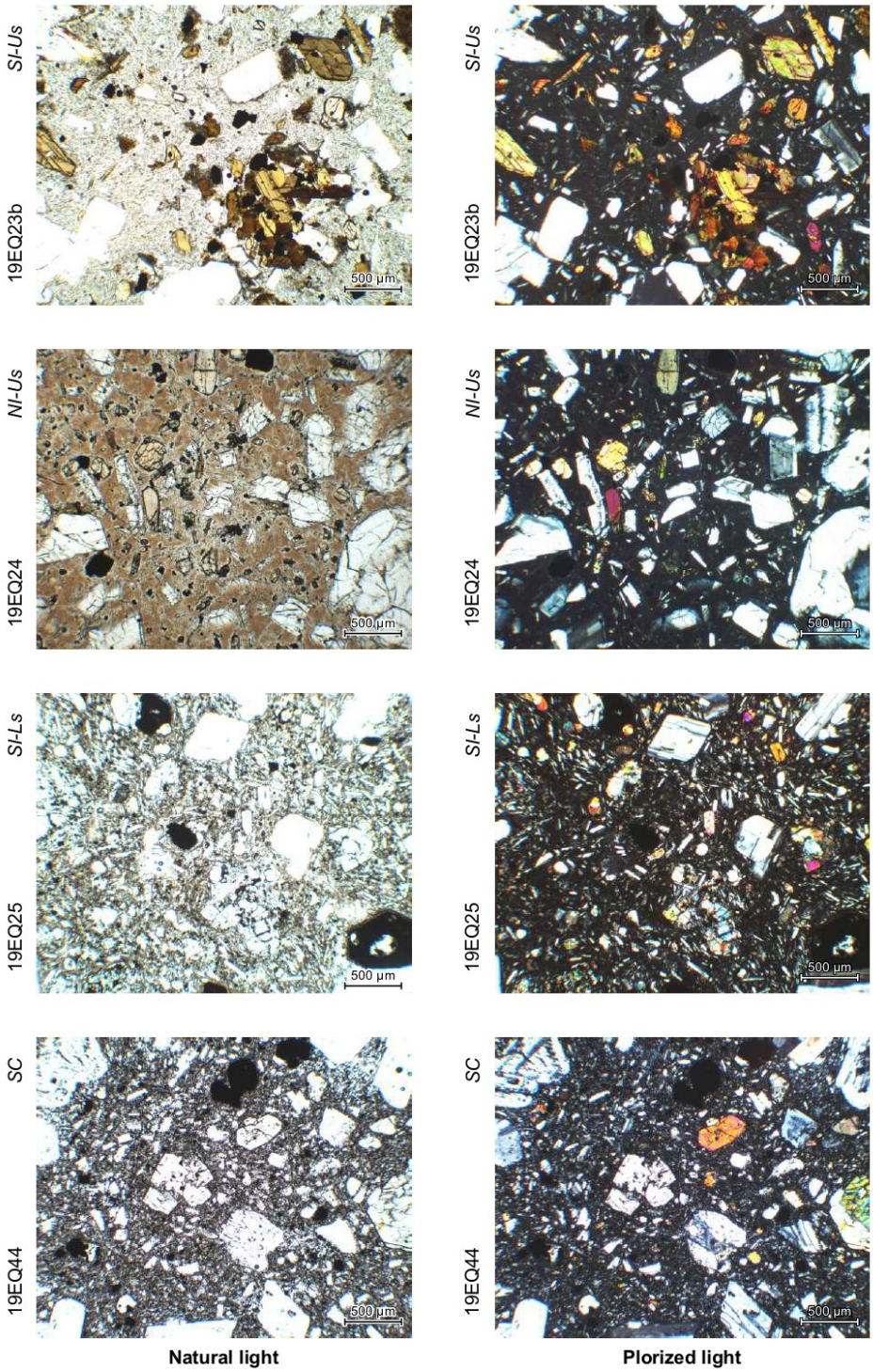
SI-Us
19EQ23b
NI-Us
19EQ24
SI-Ls
19EQ25
SC
19EQ44
500 µm
Natural light
Plorized light

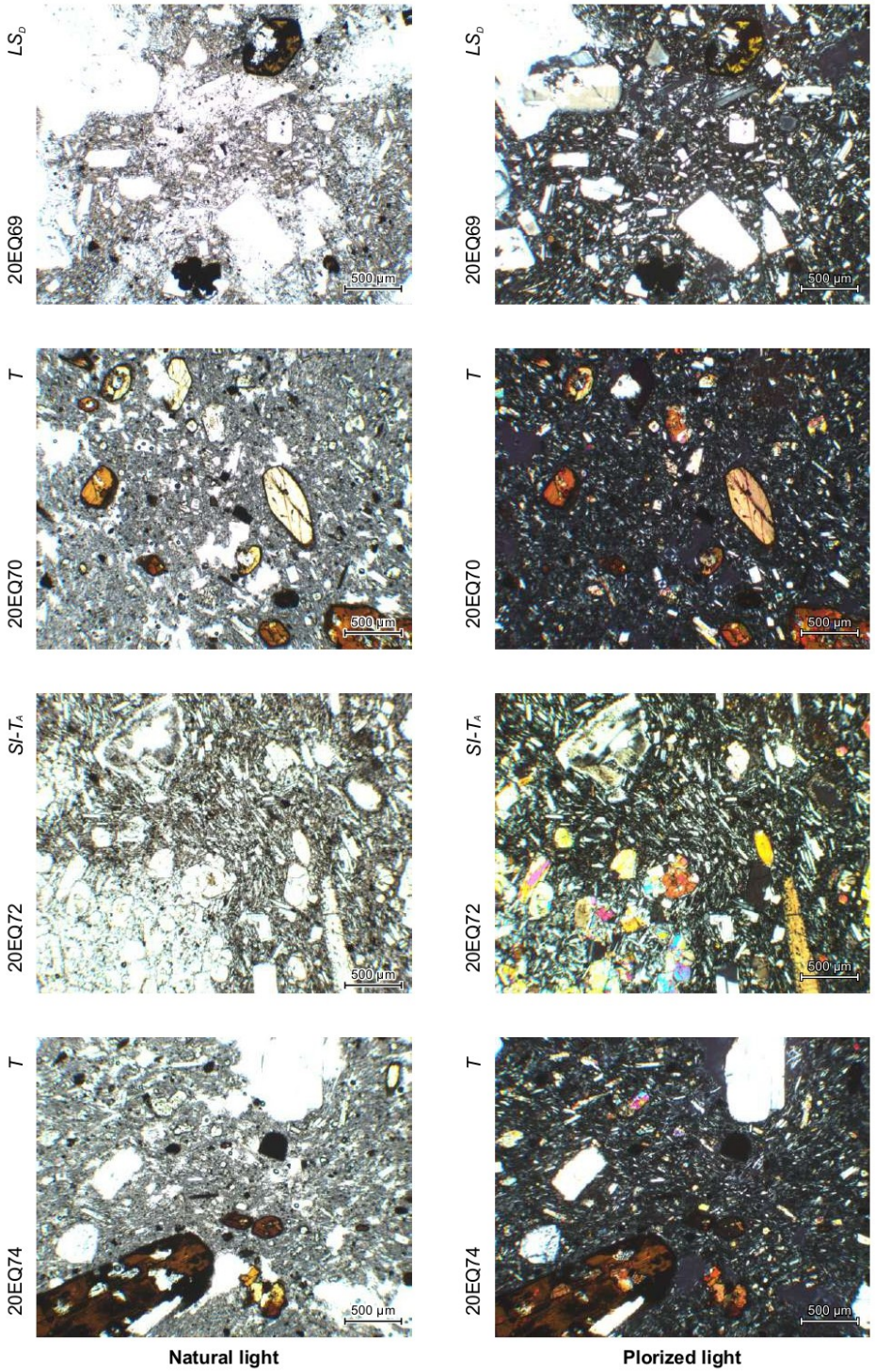
LSD
20EQ69
T
20EQ70
SI-TA
20EQ72
T
20EQ74
500 µm
Natural light
Plorized light

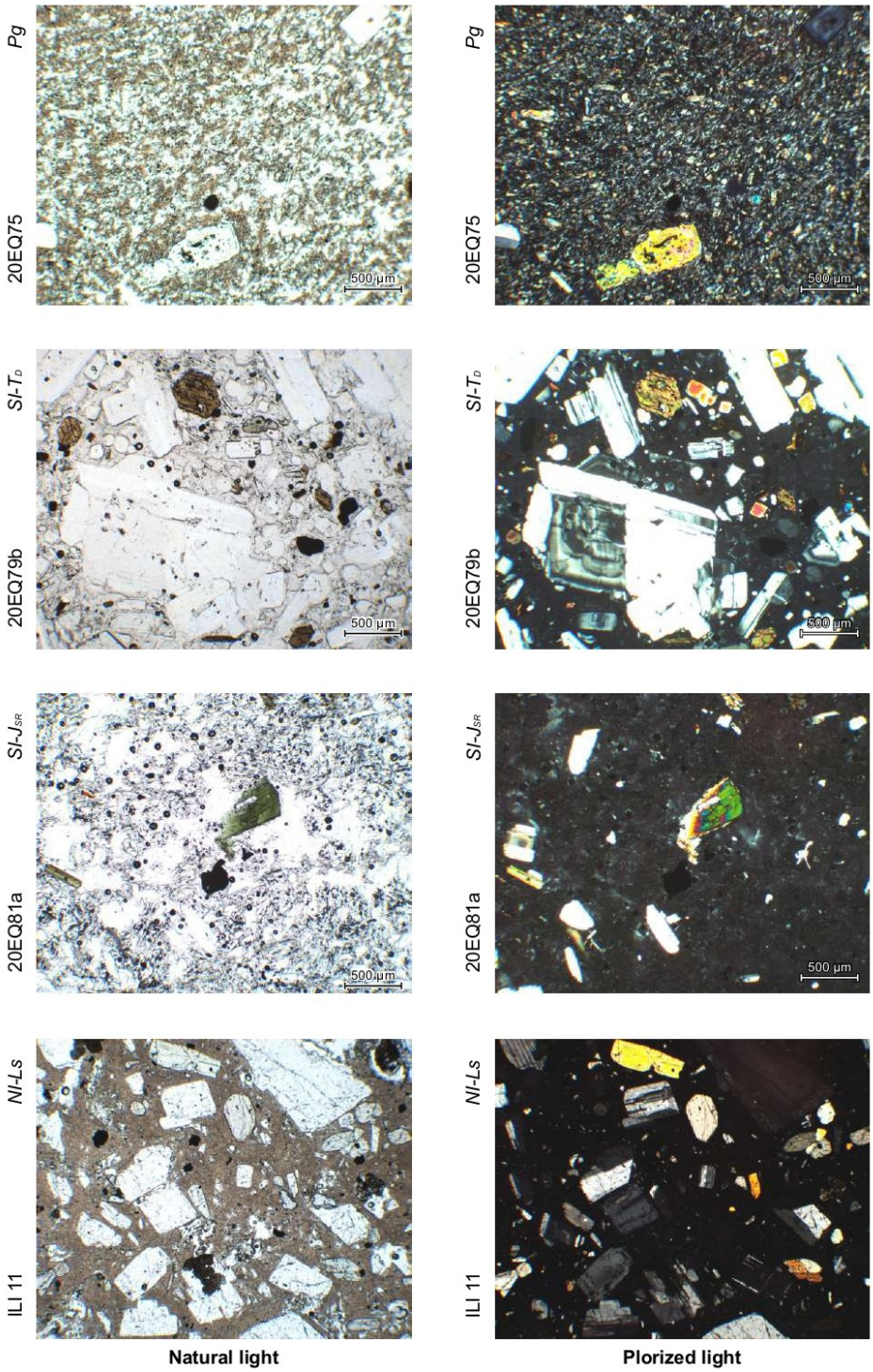
Pg
20EQ75
500 µm
Pg
20EQ75
500 µm
Sl-T$_D$
20EQ79b
500 µm
Sl-T$_D$
20EQ79b
500 µm
Sl-J$_{SR}$
20EQ81a
500 µm
Sl-J$_{SR}$
20EQ81a
500 µm
Nl-Ls
Ill 11
Nl-Ls
Ill 11
Natural light
Plorized light

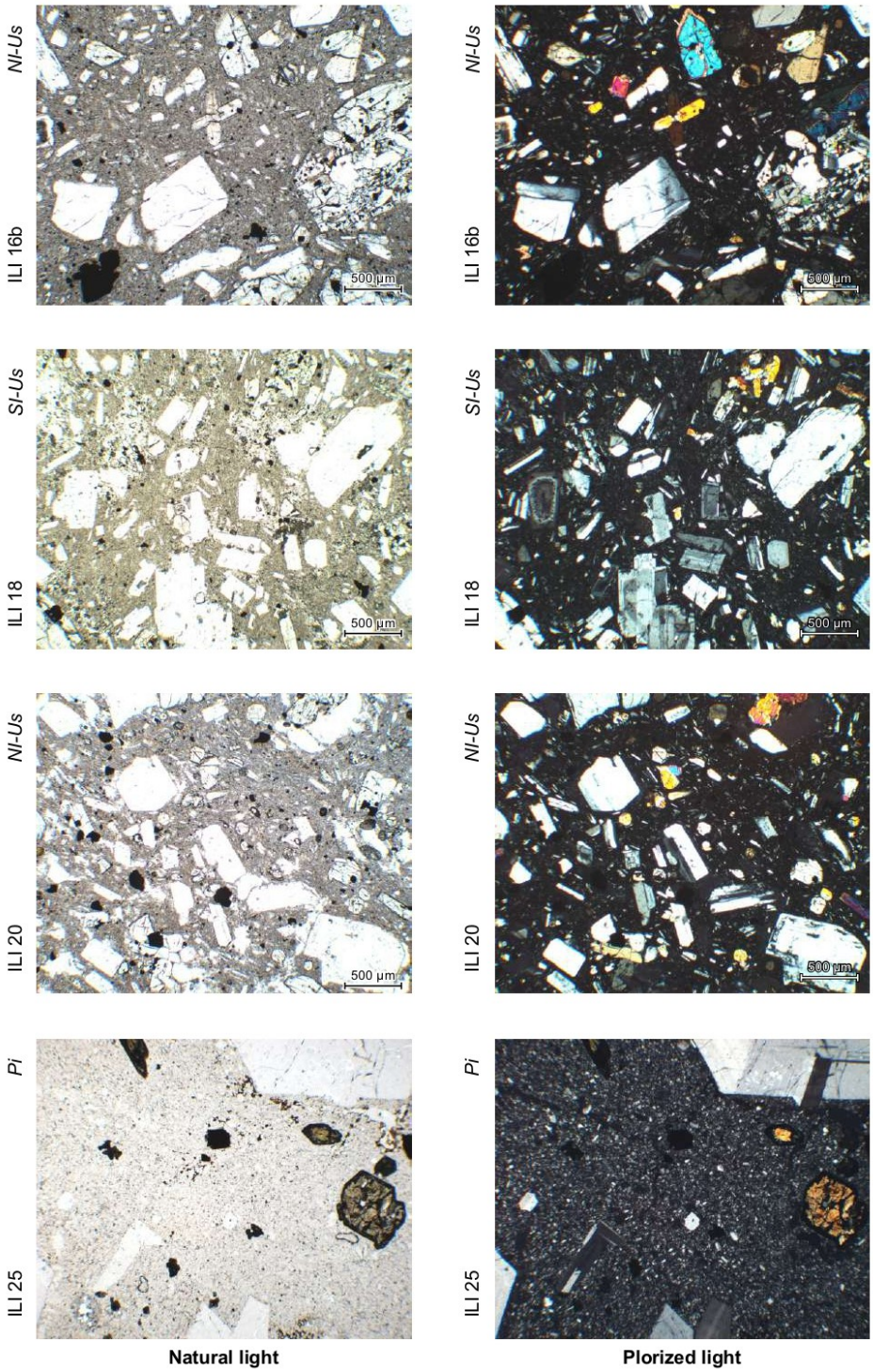
NI-Us
ILI 16b
500 µm
NI-Us
ILI 16b
500 µm
SI-Us
ILI 18
500 µm
SI-Us
ILI 18
500 µm
NI-Us
ILI 20
500 µm
NI-Us
ILI 20
500 µm
Pi
ILI 25
Pi
ILI 25
Natural light
Plorized light

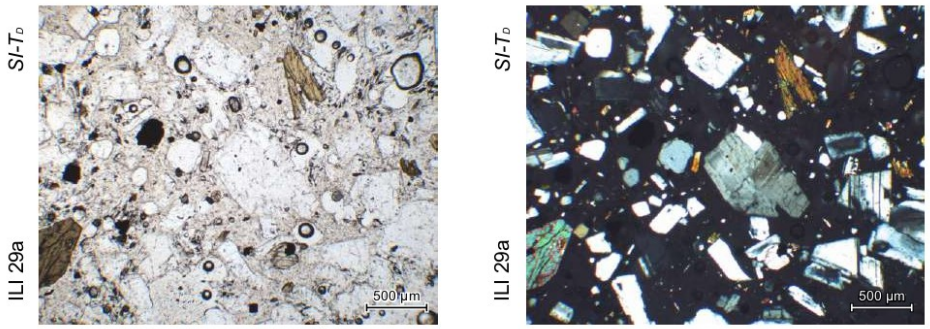
SI-T0
ILI 29a
500 µm
Natural light
SI-T0
ILI 29a
500 µm
Plorized light

Appendix B

Major and trace element composition of whole-rock samples. All major data were brought down to a total of 100%. *(Santamaría et al.)*

	North Iliniza			South Iliniza						
Sample	19EQ16	19EQ17	19EQ24	19EQ02	19EQ18	20EQ94b	19EQ19a	19EQ19B	19EQ21	20EQ81b
Unit	NI-Ls	NI-H	NI-Us	SI-Ls	SI-Ls	SI-Ls	SI-J_{BA}	SI-J_{BA}	SI-J_{BA}	SI-J_{BA}
wt.%										
SiO_2	63.23	62.31	64.42	65.02	62.33	63.70	63.43	64.59	62.82	64.71
TiO_2	0.55	0.57	0.53	0.49	0.51	0.53	0.53	0.52	0.56	0.44
Al_2O_3	16.54	17.36	16.78	16.81	16.39	16.33	16.49	16.41	16.75	17.01
Fe_2O_3	5.99	5.91	4.96	5.06	5.93	5.51	5.67	5.38	5.98	4.63
MnO	0.10	0.09	0.08	0.08	0.10	0.09	0.09	0.08	0.09	0.08
MgO	2.57	2.49	2.39	2.02	3.01	2.71	2.66	2.23	2.76	2.05
CaO	5.34	5.61	5.12	4.70	6.03	5.42	5.43	5.06	5.56	5.34
Na_2O	4.00	4.02	3.74	4.23	3.96	4.10	4.20	4.17	4.12	4.30
K_2O	1.54	1.50	1.84	1.48	1.59	1.48	1.36	1.44	1.22	1.32
P_2O_5	0.13	0.14	0.14	0.13	0.17	0.13	0.14	0.13	0.14	0.12
L.O.I.	0.07	1.49	2.32	0.61	0.45	0.63	1.18	3.59	0.46	0.62
ppm										
Sc	12.44	11.38	11.42	10.36	17.07	11.93	10.85	9.59	12.38	10.50
V	119.44	123.96	102.45	101.99	132.00	117.26	106.12	102.02	121.18	93.21
Cr	29.89	17.47	36.37	37.42	67.56	60.15	54.68	38.29	65.37	34.21
Co	13.77	13.47	12.02	10.37	15.08	14.22	13.21	12.52	15.82	11.25
Ni	10.49	7.20	7.19	10.32	10.08	16.03	17.66	13.24	23.93	9.43
Rb	30.19	24.86	32.45	27.65	26.70	28.16	26.18	30.62	22.31	24.37
Sr	386.26	445.70	410.32	425.45	627.37	430.32	401.72	411.34	440.40	450.04
Y	13.09	10.69	8.47	8.03	13.09	11.29	9.98	9.73	10.24	10.13
Zr	103.49	86.75	86.00	65.81	83.56	87.23	78.83	80.56	88.07	74.29
Nb	2.85	2.80	2.14	2.91	2.20	2.09	3.52	3.90	3.88	2.70
Ba	648.28	596.55	599.74	598.86	713.62	614.36	496.00	557.65	603.83	571.48
La	11.58	10.98	9.17	9.75	28.82	10.36	10.43	10.91	10.49	10.31
Ce	23.78	20.48	21.88	18.53	55.02	21.92	21.62	21.52	24.86	19.48
Nd	23.93	22.04	16.96	21.29	44.57	10.43	20.00	11.60	11.35	9.89
Sm	3.13	2.20	2.72	2.08	4.24	2.61	2.28	2.67	2.33	2.07
Eu	0.77	0.84	0.59	0.59	1.23	0.71	0.70	0.83	0.92	0.73
Gd	2.98	2.57	2.21	1.89	3.37	2.78	2.07	2.16	2.11	2.30
Dy	2.02	1.74	1.40	1.18	2.26	1.68	1.64	1.59	1.66	1.64
Er	0.71	0.27	0.32	0.41	0.65	0.69	0.17	0.48	0.72	0.52
Yb	1.12	0.83	0.73	0.72	1.31	0.83	0.80	0.80	0.88	0.78
Th	2.38	2.37	2.37	2.17	6.68	2.49	2.41	2.13	1.83	2.26

	South Iliniza									
Sample	20EQ81c	20EQ82a	20EQ82b	20EQ82c	20EQ82d	20EQ89	20EQ90	20EQ93a	20EQ93b	20EQ94a
Unit	SI-J_{BA}	SI-J_{BA}	SI-J_{BA}	SI-J_{BA}	SI-J_{BA}	SI-J_{BA}	SI-J_{BA}	SI-J_{BA}	SI-J_{BA}	SI-J_{BA}
wt.%										
SiO_2	64.65	65.02	64.82	64.95	64.76	64.46	63.88	65.23	65.08	64.87
TiO_2	0.51	0.48	0.47	0.47	0.49	0.53	0.55	0.49	0.49	0.40
Al_2O_3	16.61	15.88	16.40	16.18	16.24	16.09	16.16	15.94	15.95	17.49
Fe_2O_3	5.09	5.25	5.00	5.09	5.16	5.50	5.76	5.18	5.05	4.29
MnO	0.08	0.10	0.08	0.08	0.09	0.08	0.09	0.08	0.08	0.07
MgO	2.36	2.39	2.31	2.26	2.37	2.41	2.53	2.32	2.41	1.68
CaO	5.06	4.95	5.13	5.10	5.06	5.24	5.39	4.94	5.06	5.26
Na_2O	4.04	4.21	4.16	4.26	4.19	4.24	4.18	4.14	4.08	4.48
K_2O	1.47	1.59	1.51	1.48	1.51	1.33	1.34	1.54	1.66	1.34
P_2O_5	0.13	0.14	0.12	0.12	0.12	0.13	0.13	0.13	0.13	0.11
L.O.I.	2.38	1.71	0.61	0.01	1.16	0.01	1.20	1.30	0.82	0.08
ppm										
Sc	11.27	10.98	10.89	10.82	11.12	10.93	11.79	10.67	11.12	8.51
V	100.96	106.63	104.35	106.37	105.79	117.91	118.79	106.38	106.32	86.20
Cr	48.15	55.96	52.43	47.04	53.28	61.69	54.06	49.03	62.79	20.74
Co	12.81	13.46	12.88	12.62	12.66	14.66	14.59	12.27	12.27	9.37
Ni	12.82	13.65	13.42	11.30	11.16	17.37	15.92	11.76	14.40	8.58
Rb	29.15	31.26	30.51	30.23	28.07	26.77	24.27	33.49	35.57	26.08
Sr	401.81	378.75	441.54	437.90	432.70	421.82	425.00	390.09	407.56	471.61
Y	10.59	10.64	11.26	11.18	11.41	10.69	10.71	10.00	11.10	8.60
Zr	89.34	92.05	89.83	91.20	89.44	76.89	76.16	88.08	85.91	56.73
Nb	2.05	3.53	2.66	2.17	2.62	3.17	2.74	2.24	2.05	2.35
Ba	572.65	594.92	645.36	646.23	638.24	592.98	546.13	590.31	612.98	557.65
La	10.47	11.26	10.66	11.06	10.73	9.97	10.01	10.71	10.23	9.67
Ce	19.93	22.25	20.48	18.47	20.93	20.38	19.75	20.01	20.41	20.15
Nd	10.53	10.90	10.54	10.63	10.82	10.54	11.82	10.42	10.60	9.02
Sm	2.26	2.00	2.72	2.37	2.12	1.89	2.43	2.75	2.38	2.34
Eu	0.68	0.68	0.62	0.73	0.68	0.70	0.67	0.66	0.64	0.67
Gd	2.25	2.23	1.86	2.16	2.21	2.29	2.52	2.06	1.90	1.73
Dy	1.72	1.74	1.61	1.64	1.78	1.69	1.87	1.69	1.66	1.39
Er	0.68	0.68	0.75	0.61	0.97	0.92	0.85	1.13	0.70	0.73
Yb	0.83	0.83	0.79	0.79	0.82	0.70	0.78	0.82	0.79	0.61
Th	2.50	2.70	2.71	2.51	2.66	1.91	2.02	2.51	2.33	2.03

	South Iliniza								
Sample	20EQ98	20EQ92	20EQ96b	20EQ81a	19EQ23a	19EQ23b	19EQ25	20EQ72	20EQ79b
Unit	SI-J_{BA}	SI-J_{PA}	SI-J_{PA}	SI-J_{SR}	SI-U_{SDC}	SI-U_{SDC}	SI-T_A	SI-T_A	SI-T_D
wt.%									
SiO_2	62.95	65.44	66.53	71.30	64.54	64.77	61.69	61.38	67.00
TiO_2	0.56	0.48	0.47	0.32	0.53	0.52	0.53	0.63	0.48
Al_2O_3	16.45	16.35	15.66	15.23	16.31	16.34	16.37	16.34	15.74
Fe_2O_3	6.12	5.19	5.15	2.80	5.51	5.22	6.36	6.39	4.50
MnO	0.09	0.08	0.09	0.05	0.08	0.08	0.10	0.09	0.06
MgO	2.65	1.81	1.90	0.72	2.25	2.19	3.67	3.74	1.77
CaO	5.54	4.80	4.51	3.13	4.99	4.93	6.04	6.12	4.34
Na_2O	4.00	4.35	3.99	4.80	4.26	4.24	3.99	3.99	4.41
K_2O	1.50	1.36	1.56	1.54	1.41	1.56	1.13	1.19	1.56
P_2O_5	0.13	0.14	0.13	0.11	0.14	0.14	0.13	0.13	0.13
L.O.I.	0.66	1.03	3.27	1.66	1.12	1.18	0.34	-0.16	1.07
ppm									
Sc	12.68	8.77	9.24	2.39	9.68	10.20	13.71	14.74	7.68
V	127.54	90.67	96.56	32.99	107.02	102.75	134.26	149.23	87.38
Cr	40.48	16.47	20.75	5.40	35.21	33.31	136.81	151.55	35.95
Co	15.36	10.80	15.82	4.42	13.26	12.19	20.53	18.65	9.81
Ni	12.48	5.92	6.05	1.58	15.62	12.70	47.13	40.67	13.31
Rb	50.63	24.44	28.85	27.64	29.86	29.82	16.71	20.68	29.47
Sr	396.24	425.48	373.68	454.35	420.65	411.11	394.48	439.29	408.97
Y	13.29	10.92	10.70	5.78	10.05	9.45	10.96	11.37	8.18
Zr	100.28	89.82	74.44	75.01	80.57	76.33	70.47	81.56	42.02
Nb	3.38	2.92	2.54	4.09	2.79	2.50	2.06	4.65	2.72
Ba	566.54	545.56	612.08	706.59	570.02	573.02	485.08	504.08	640.09
La	10.52	10.65	10.75	16.13	11.17	10.68	9.56	10.91	12.90
Ce	22.05	22.53	20.62	28.76	23.82	22.79	16.74	20.27	23.59
Nd	11.87	11.81	10.99	15.60	12.13	20.79	22.36	11.54	11.85
Sm	3.02	2.59	2.39	2.23	2.58	2.65	2.08	2.73	2.50
Eu	0.74	0.84	0.65	0.79	0.74	0.76	0.76	0.74	0.69
Gd	2.57	2.33	2.09	2.31	2.39	2.22	2.58	2.64	2.18
Dy	2.12	1.78	1.77	1.12	1.76	1.65	1.72	1.92	1.35
Er	1.12	0.83	0.40	0.31	1.07	0.33	0.04	0.53	0.42
Yb	1.01	0.85	0.88	0.34	0.81	0.81	1.00	0.93	0.60
Th	2.08	1.93	2.30	2.51	2.75	2.24	1.70	2.04	2.79

	Tishigcuchi			Pongo		Santa Cruz volcano			
Sample	19EQ22	20EQ70	20EQ74	19EQ20	20EQ75	19EQ04	19EQ44	19EQ03	20EQ69
Unit	T	T	T	Pg	Pg	SC	SC	LS_A	LS_D
wt.%									
SiO_2	62.02	62.08	62.09	59.66	59.68	65.62	56.47	57.85	63.73
TiO_2	0.59	0.59	0.59	0.57	0.58	0.49	0.72	0.78	0.52
Al_2O_3	15.78	15.83	15.81	15.41	15.45	17.35	19.76	17.62	17.47
Fe_2O_3	6.23	6.21	6.13	6.74	6.68	4.20	7.26	7.69	5.30
MnO	0.10	0.09	0.09	0.11	0.11	0.04	0.11	0.12	0.10
MgO	3.64	3.52	3.53	4.85	4.83	1.61	2.91	3.55	1.71
CaO	5.94	5.93	5.98	6.92	6.92	4.83	7.25	6.93	4.97
Na_2O	3.91	3.95	3.96	3.76	3.78	4.34	4.35	4.00	4.64
K_2O	1.62	1.63	1.65	1.79	1.78	1.47	0.97	1.26	1.36
P_2O_5	0.17	0.17	0.17	0.19	0.19	0.06	0.19	0.21	0.21
L.O.I.	0.64	0.32	0.43	0.38	0.57	0.73	0.52	0.72	0.28
ppm									
Sc	13.55	14.75	14.51	17.68	18.87	7.42	14.80	16.29	6.82
V	132.86	139.25	134.99	145.03	156.48	91.90	167.28	176.77	83.65
Cr	93.13	103.24	105.59	135.86	150.97	18.33	40.36	51.78	11.65
Co	18.46	18.76	18.00	20.20	22.47	6.81	21.78	20.7	10.48
Ni	31.03	32.22	33.03	48.07	50.63	9.89	26.22	21.55	4.63
Rb	27.41	30.49	30.87	32.84	30.52	32.95	15.12	23.45	23.86
Sr	499.39	547.97	545.99	617.93	663.59	534.03	582.89	548.98	538.25
Y	9.93	11.51	11.43	11.86	11.96	10.82	16.22	13.57	12.47
Zr	88.72	92.49	88.88	81.84	78.85	91.83	98.60	107.77	112.81
Nb	2.69	3.16	2.84	3.27	4.42	3.54	2.33	3.99	5.29
Ba	618.9	637.50	630.35	648.12	622.64	673.51	440.62	495.44	601.10
La	14.32	17.67	16.30	19.24	19.65	13.90	11.31	13.52	14.88
Ce	29.92	32.85	30.06	36.61	37.39	27.37	22.03	25.47	31.80
Nd	24.13	16.01	15.38	30.04	18.99	15.04	20.98	23.26	14.44
Sm	2.53	3.26	2.87	4.10	3.32	2.61	3.20	3.62	3.08
Eu	1.04	0.90	0.88	1.06	0.99	0.95	0.97	0.94	0.86
Gd	2.65	2.75	2.76	3.09	3.18	2.97	2.91	3.32	2.70
Dy	1.55	2.07	1.79	1.77	2.04	1.91	2.72	2.30	2.20
Er	0.49	0.67	0.57	0.53	0.72	0.87	1.33	0.85	1.22
Yb	0.80	0.87	0.87	0.96	0.96	0.95	1.55	1.08	0.97
Th	2.90	4.95	3.39	3.81	3.69	2.60	1.39	3.26	2.44

Appendix C

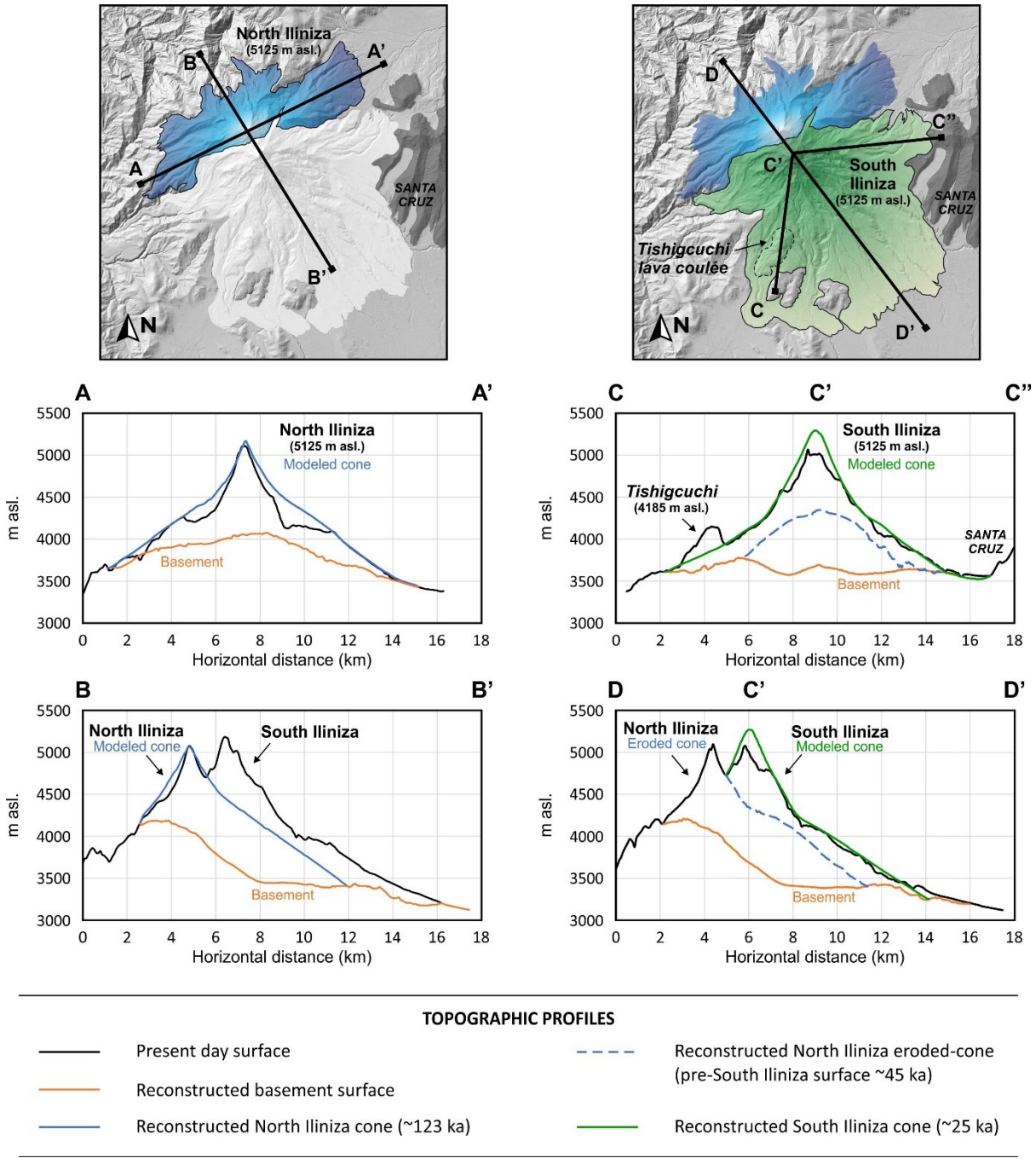

Figure C.1. Comparative topographic profiles between the modeled cones of the North and South Iliniza edifices (S_{NI-t1} and S_{SI-t1}, respectively), eastern sector of the eroded North Iliniza edifice (S_{NI-t2}), the modeled basement surface, and the present-day surface.

Appendix D

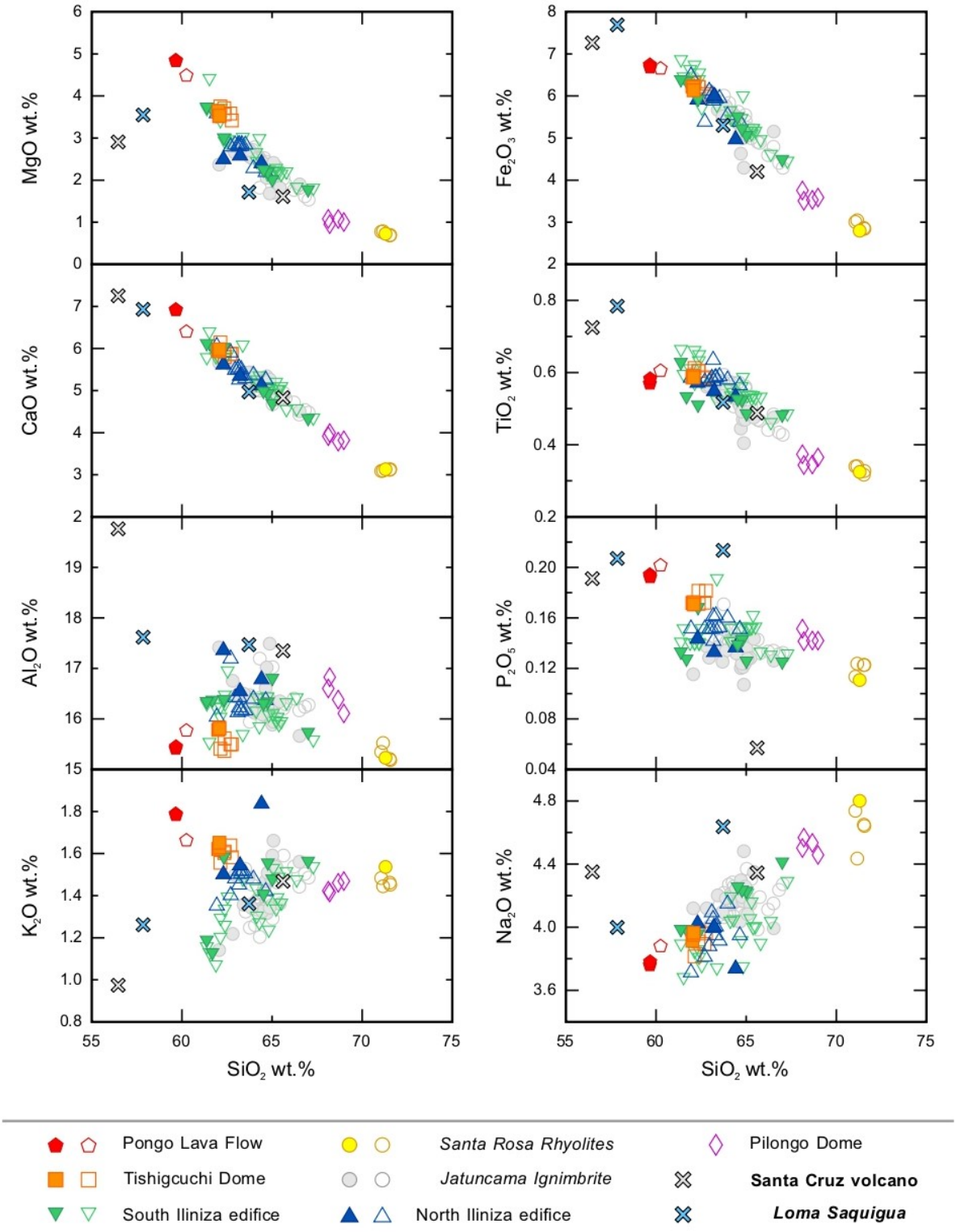

Figure D.1. Major elements (wt.%) vs SiO2 (wt.%) diagrams for eruptive products of Iliniza and Santa Cruz volcanoes. Open symbols are for data from Hidalgo et al. (2007).

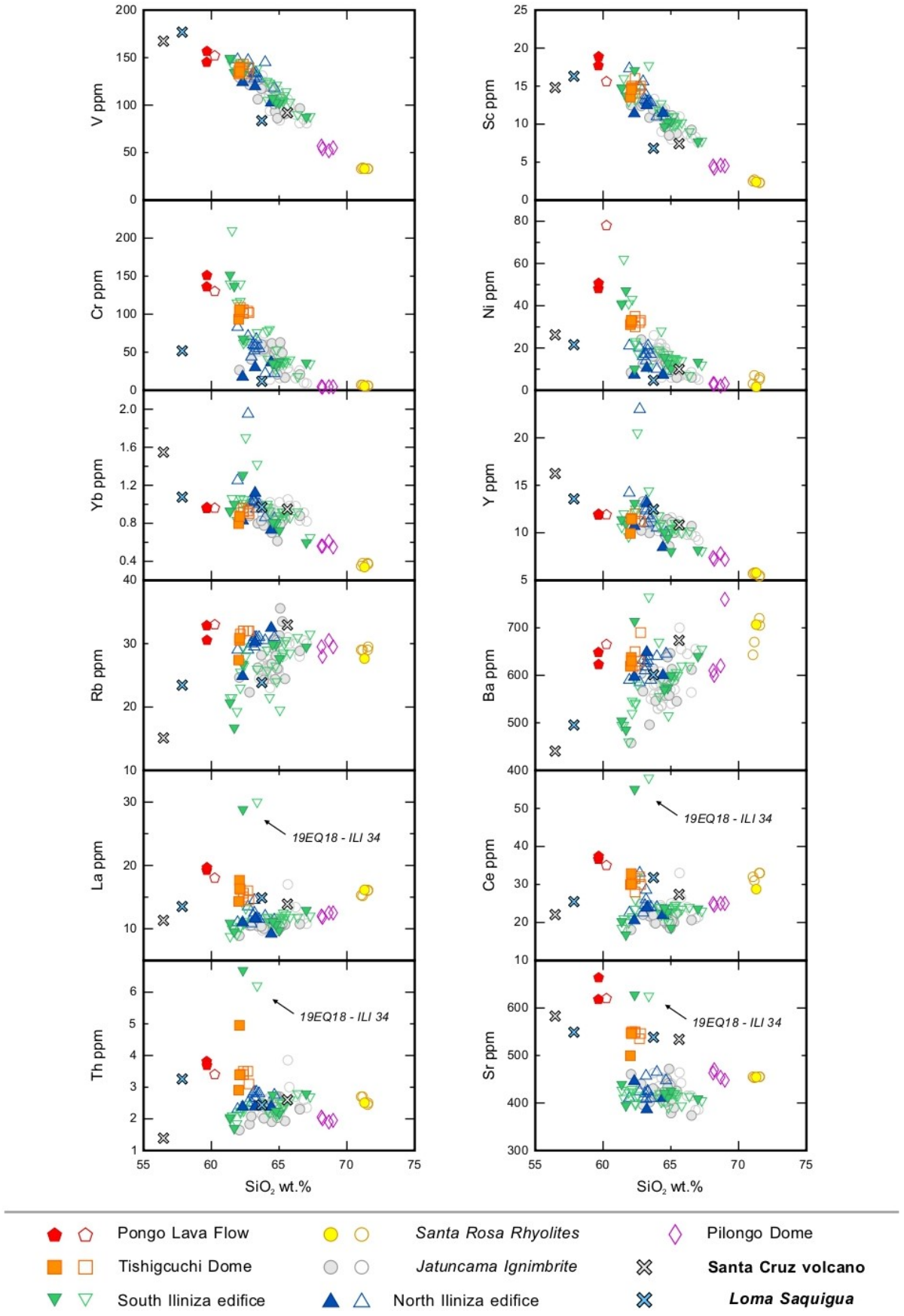

Figure D.2. Trace elements (ppt) vs SiO2 (wt.%) diagrams for eruptive products of Iliniza and Santa Cruz volcanoes. Open symbols are for data from Hidalgo et al. (2007).

Chapter 4

Cotopaxi volcano and the Morurco peak, Eastern Cordillera.

Chapter 4

Timing of Pleistocene volcanism and its relationship with geodynamics in the central segment of the Ecuadorian Andes

Article project

Contents

ABSTRACT 170

1. INTRODUCTION 171

2. GEOLOGICAL CONTEXT 173

2.1. Ecuadorian geological setting 173

2.2. Volcanism from the central segment 174

3. METHODS 177

3.1. Sampling strategy 177

3.2. K-Ar dating 179

3.3. Whole-rock geochemical analyses 180

3.4. Numerical reconstructions of paleotopographies for volume calculations 181

4. RESULTS 182

4.1. K-Ar dating 182

4.2. Construction and erosion volumes of the central segment volcanoes 185

4.3. Geochemical characterization 187

5. DISCUSSION 190

5.1. Comparison with previous geochronological data 190

5.2. Eruptive history of the central segment 191

5.3. Temporal and spatial arrangement of the central segment volcanoes 198

5.3.1. Spatial arrangement of volcanoes over pre-Quaternary crust structures 198

5.3.2. Possible influences of Quaternary tectonics in the central segment volcanic landforms 200

6. CONCLUSIONS 202

REFERENCES 203
Appendix A. 213
Appendix B 218
Appendix C 222

Timing of Pleistocene volcanism and its relationship with geodynamics in the central segment of the Ecuadorian Andes

Santiago Santamaria [a], Xavier Quidelleur [a], Pablo Samaniego [b], Laurence Audin [c], Jean-Luc Le Pennec [b], Silvana Hidalgo [d], Céline Liorzou [e]

[a] GEOPS, Université Paris-Saclay, CNRS, Rue du Belvédère, 91405 Orsay, France

[b] Laboratoire Magmas et Volcans, Université Clermont Auvergne, CNRS, IRD, OPGC, F-63000 Clermont-Ferrand, France

[c] Institut des Sciences de la Terre, IRD: UR219, Université Joseph Fourier–Grenoble I–INSU–OSUG, Grenoble, France

[d] Instituto Geofísico, Escuela Politécnica Nacional, Ap. 17-01-2759, Quito, Ecuador

[e] Laboratoire Géosciences Océan, Institut Universitaire Européen de la Mer, Université de Bretagne Occidentale, Rue Dumont d'Urville, 29280 Plouzané, France

Keywords:

- Ecuador
- K-Ar dating
- Geodynamics
- Pleistocene
- Eruptive history

Key Points:

-
-
-

Word count:

- Abstract: 194 words
- Main body: 8152 words

Figures: 8

Tables: 2

ABSTRACT

The unusually high number of volcanoes in the Ecuadorian arc, located in the deformation zone of the continental North Andean Sliver, coincides with the projection of the major rheological anomalies observed in the Nazca plate, such as the Carnegie Ridge and the Grijalva fracture zone. Although the relationship between this tectonic frame and volcanism was largely discussed in the literature, their temporal relationship has not been thoroughly investigated due to the lack of geochronological data. We present here 20 new K-Ar ages obtained for 7 volcanoes of the central segment of the Ecuadorian arc which, together with previous data, showed that volcanism in this area started at 1.3 Ma. A notable increase in volcanic activity occurred at 550 ka, where a dozen volcanoes were formed in a relatively small area of the central segment. While the arrangement of the volcanoes appears to be controlled by crust tectonic structures, the proposed eruptive history suggests that their emplacement in space occurred randomly through time. Finally, we infer that the magmatic productivity rate was roughly constant during the last 550 ka in this area, based on the cumulative bulk volumes calculated for the volcanic edifices over time.

1. INTRODUCTION

The Northern Andean Volcanic Zone results from the subduction of the Nazca plate under the northwestern margin of South America (Figure 1). Unlike the narrow arrangement created by the almost 40 volcanoes in Colombia, more than 80 Pleistocene eruptive centers (21 with Holocene activity) form the Ecuadorian volcanic arc and cover an area up to 130 km wide north of 2°S latitude (Hall and Wood, 1985; Pedraza Garcia et al., 2007). Usually, the volcanoes are classified according to their distribution in along-arc corridors defined by their geographic relationship with the two subparallel mountain ranges forming the Ecuadorian Andes (Western and Eastern Cordilleras), the tectonic depression which separates both ranges (Inter-Andean Valley), and the sub-Andean Amazonian lowlands (e.g., Hall and Beate, 1991; Hall et al., 2008; Ancellin et al., 2017). However, the distribution of volcanoes is not homogeneous along the arc. In fact, numerous edifices are found in areas of a few square kilometers where the distance between its summits ranges between 6-12 km. These volcanic clusters are separated by areas with a much-reduced number of volcanoes. Moreover, the location a considerable number of volcanoes seems to coincide with the subduction of several topographic and rheological anomalies of the Nazca plate (Fig. 1). Most notably (1) the Grijalva Fracture Zone, which currently separates the older Farallon crust (> 30 Ma) from the younger Nazca crust (< 20 Ma), and (2) the Carnegie ridge created by the Nazca plate transition over the Galapagos hotspot (Meschede and Barckhausen, 2000; Lonsdale, 2005; O'Connor et al., 2007). The presence of these structures, together with the convex shape of the continental margin, were interpreted to be responsible for the slab flexure described beneath the Ecuadorian arc (Yepes et al., 2016; Portner et al., 2020). In addition, the oblique convergence of the Nazca plate is associated with the motion of the northwestern margin of South America forming the North Andean Sliver. This displacement occurs through the Chingual-Cosanga-Pallatanga-Puná (CCPP) fault system (Fig. 1c) which traverses the Ecuadorian Andes and propagates northward into Colombia (Witt and Bourgois, 2010; Alvarado et al., 2014; Nocquet et al., 2014).

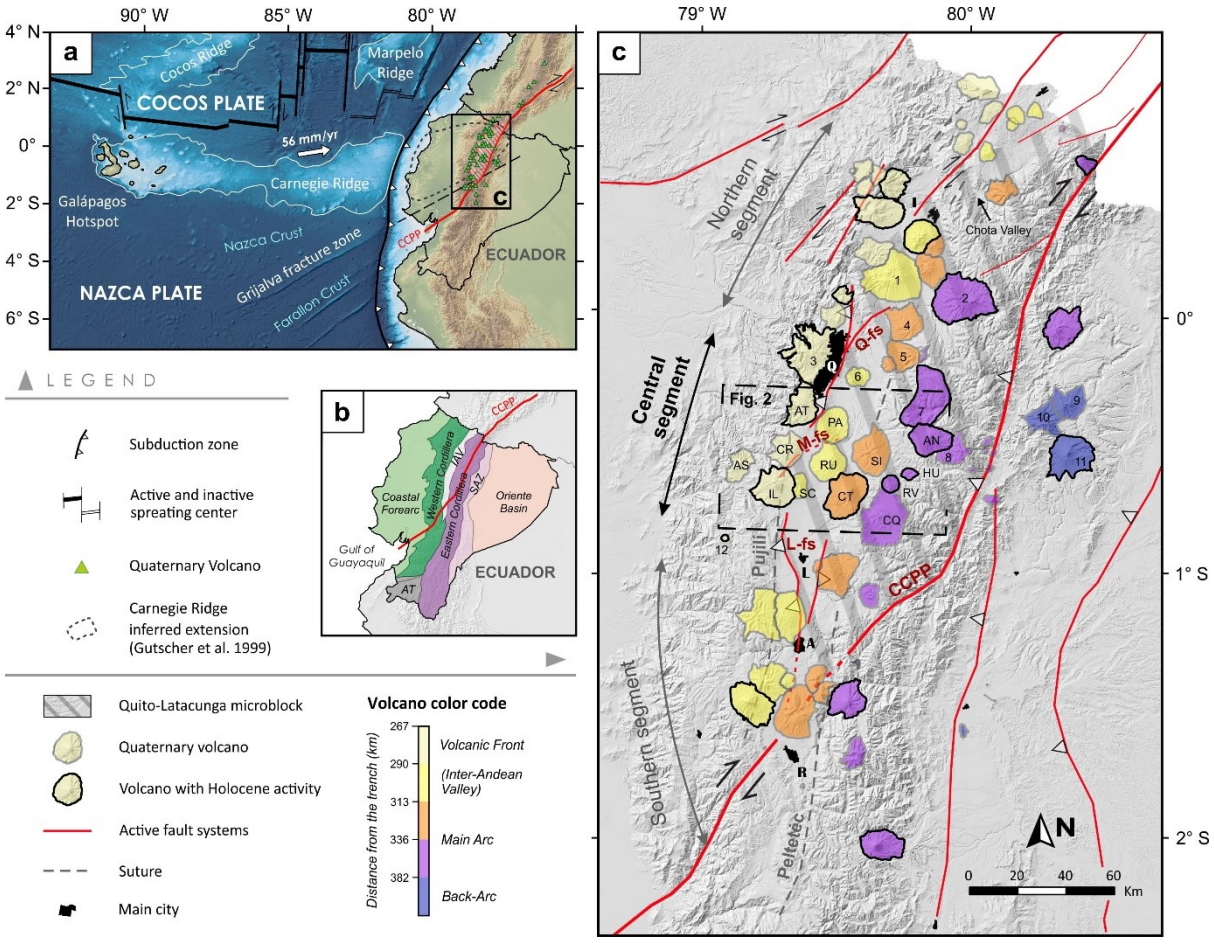

Figure 1. a) *Regional Geodynamic setting of the Ecuadorian margin. White arrow indicate the direction of the Nazca plate motion relative to South America (DeMets et al., 2010). Topography and bathymetry from the GEBCO 2020 program.* ***b)*** *Major geomorphological provinces of Ecuador (modified from Aspden et al., 1992). AT: Amotape-Tahuín; IAV: Inter-Andean Valley; SAZ: Sub-Andean Zone.* ***c)*** *Schematic map of the Ecuadorian volcanic arc. Volcanoes are colored according to their distance from the trench comprising the N-S alignments of the Volcanic Front (Western Cordillera), Inter-Andean Valley, Main Arc (Eastern Cordillera), and Back-Arc. Variability in the number of volcanic centers is represented by the northern, central, and southern across-arc segments. Volcanoes of the central segment: Antisana (AN), Almas Santas (AS), Atacazo-Ninahuica (AT), Chalupas-Quilindaña (CQ), Corazón (CR), Cotopaxi (CT), Huañuna (HU), Iliniza (IL), Pasochoa (PA), Rumiñahui (RU), Rio Valle (RV), Santa Cruz (SC), Sincholagua (SI). Other volcanoes referred in the text are: Mojanda – Fuya Fuya (1), Cayambe (2), Pichincha (3), Pambamarca (4), Puntas (5), Ilaló (6), Chacana (7), Aliso (8), Yanahurco (9), Pan de Azúcar (10), Sumaco (11), Quilotoa (12). Active fault systems represented with red lines according to Alvarado et al. (2016). CCPP: Chingual-Cosanga-Pallatanga-Puná Fault System; Q-fs: Quito Fault System; M-fs: Machachi Fault System; L-fs: Latacunga Fault System. Main cities are represented in black. I: Ibarra; Q: Quito, capital city; L: Latacunga; A: Ambato; R: Riobamba.*

Twenty km to the south of Quito, Ecuador's capital city, more than a dozen of volcanoes are placed in a 70 km wide (E-W) and 40 km long (N-S) area defining the central across-arc segment of the Ecuadorian arc. This segment is located above the Carnegie ridge projection in the younger Nazca crust (Figure 1c). Although several studies were conducted on the slab structure (e.g., Gutscher et al., 1999; Michaud et al., 2009; Yepes et al., 2016) and the kinematics along crustal faults (e.g., Fiorini and Tibaldi, 2012; Alvarado et al., 2014, 2016; Jomard et al., 2021), their relationship with the volcanism is not yet established. Notwithstanding, the volcanoes from the central segment have been investigated individually and at a regional scale for geochemistry and stratigraphy (e.g., Chemin, 2004; Hall et al., 2017; Hidalgo et al., 2007; Hall and Mothes, 2008a; Ancellin et al., 2017; Chiaradia et al., 2020; Santamaría et al., submitted). However, the geochronological data remain scarce particularly on the oldest edifices.

This study presents new geochronological data together with new field observations for the volcanoes of the central segment of Ecuador, in order to investigate the temporal link between volcanism and its geodynamic setting. By combining the available ages for the well-studied Holocene active volcanoes, we describe for the first time the Pleistocene eruptive history of this segment. Furthermore, this work aims to explore the relationship between ancient and recent tectonics and the development of volcanism in this area.

2. GEOLOGICAL CONTEXT

2.1. Ecuadorian geological setting

The Ecuadorian continental margin consists of a series of allochthonous and para-autochthonous terrains containing several fault systems and sutures roughly parallel to the trench. The Oriente Foreland Basin (Fig. 1b) corresponds to a sedimentary sequence, formed since the Mesozoic, which is overlaying the Precambrian Guyanese craton (Vallejo et al., 2021). To the East, the Eastern Cordillera is formed by Paleozoic to Jurassic metamorphic belts of sedimentary and igneous origin (Litherland et al., 1994; Spikings et al., 2015). This association of terrains is interpreted as the South

American Triassic anatexis zone that gave rise to the separation of several terrains and macroblocks, followed by episodes of collision/accretion of this para-autochthonous terrains combined with arc magmatism (Villagómez et al., 2011; Spikings et al., 2015; Villares et al., 2020). The Cretaceous compressional phase formed the Peltetec suture which marks the western edge of the Eastern Cordillera terranes (John et al., 2010; Spikings et al., 2015).

The Western Cordillera is composed of deformed Cretaceous mafic and ultramafic rocks which are overlain by sequences of marine sediments and volcanic deposits (Vallejo et al., 2019). Further east, the Coastal Forearc consists of several Mesozoic to Cenozoic sedimentary basins formed above the ultramafic basement (Luzieux et al., 2006; Witt et al., 2006; Vallejo et al., 2019). These occurrences are interpreted as the remnants of an oceanic plateau accreted to the continental margin during the Late Cretaceous-Paleogene (Jaillard et al., 2004; Spikings et al., 2010; Vallejo et al., 2019). The Pujilí suture was formed after this accretionary event. The transition between the Western and Eastern Cordillera terrains is masked by the Inter-Andean Valley, an intramountainous basin containing a thick sequence of Miocene-Pleistocene volcanic sediments which overlies a tectonic *mélange* composed of continental and oceanic units (e.g., Aspden et al., 1995; Lavenu et al., 1995; Hungerbühler et al., 2002; Winkler et al., 2005). The Quaternary volcanic arc overlies Miocene-Pliocene volcanic sequences which are located over both Cordilleras. In particular, the volcanoes of the central segment were built above the Silante (late Oligocene - middle Miocene) and Zumbahua (middle Miocene) formations in the Western Cordillera (Vallejo et al., 2019, 2020), and the Pisayambo volcanics (possibly Miocene) in the Eastern Cordillera (Barberi et al., 1988; Lavenu et al., 1995; Egüez et al., 2017).

2.2. Volcanism from the central segment

The central across-arc segment roughly corresponds to the volcanism occurred approximately between latitudes 0.3°S and 0.7°S (Fig. 1c). Although this distinction primarily includes the volcanism of the Chacana caldera (Hall and Mothes, 2008b) and the group of edifices situated in the Sub-Andean zone (e.g., Hoffer, 2008; Mothes and Hall, 2008; Salgado et al., 2021), this present study focuses on the

volcanic cluster located between the Eastern and Western Cordilleras. A summary of the geological background for these volcanoes is provided below.

Almas Santas volcano (3786 m asl.; Lat. 0°35'S; Long. 78°51'W), located in the western side of the Western Cordillera, is one of the closest volcanic centers to the trench of the entire Ecuadorian arc. This volcano is formed by a basal andesitic edifice constructed during a mostly effusive stage followed by the emplacement of dacitic to rhyolitic domes (or a dacitic to rhyolitic dome complex), such as Cerro Azul, a satellite dome located on its eastern flank. A sector collapse towards the NW partially destroyed the volcanic edifice probably at the end of its eruptive history (Chemin, 2004). No geochronological data are available for Almas Santas, a Middle Pleistocene age was suggested based on its highly eroded morphology (Chemin, 2004).

Eastwards, four volcanoes are present on the eastern edge of the Western Cordillera, next to the Inter-Andean valley. La Carcacha (3880 m asl.; Lat. 0°19'S; Long. 78°36'W) is a ~1.29 Ma edifice associated to the **Atacazo-Ninahuilca volcanic complex** located on the southern periphery of Quito (Hidalgo, 2006). The Atacazo edifice (4455 m asl.; Lat. 0°21'S; Long. 78°37'W), formed between ~220 ka and ~83 ka, partially covered La Carcacha edifice and experienced a major sector collapse followed by the extrusion of several satellite domes around 70 ka (Hidalgo, 2006). At least six Plinian eruptive phases related to the Ninahuilca dome complex occurred during the Holocene (Hidalgo et al., 2008). Southward, **El Corazón** volcano (4784 m asl.; Lat. 0°32'S; Long. 78°40'W) was formed by andesite lava sequences and exhibit a conspicuous sector collapse amphitheater open to the west. Cerro Bomboli and La Moya satellite domes are placed on the northern and eastern flanks of the volcano, respectively. Further south, **Iliniza** volcano (5248 m asl.; Lat. 0°40'S; Long. 78°43'W) is made up of two superimposed stratovolcanoes formed between ~124-116 ka and ~45-25 ka, respectively. The twin-peaked volcano is surrounded by the Pilongo (~353 ka) and Tishigcuchi (probably Holocene) domes. The Pongo lava flow (~6 ka) represents its most recent activity (Hidalgo et al., 2007; Santamaría et al., submitted).

Three highly eroded volcanoes are situated in the Inter-Andean valley. East of El Corazón, **Pasochoa** volcano (4199 m asl.; Lat. 0°28'S; Long. 78°29'W) is made up of voluminous basaltic

andesite lava sequences. A groundmass $^{40}Ar/^{39}Ar$ age of 1.33 ± 0.30 Ma was obtained from a southwestern lava flow (Opdyke et al., 2006). Adjacent to the south of Pasochoa, **Rumiñahui** volcano (4722 m asl.; Lat. 0°35'S; Long. 78°30'W) is formed by two lava sequences showing mid- to high-potassium andesite compositions, respectively (Starr, 1984). Both volcanoes exhibit eroded collapse amphitheaters on their western flanks. To the southwest, **Santa Cruz** volcano (3978 m asl.; Lat. 0°39'S; Long. 78°38'W) is composed of andesitic lavas and dacitic domes dated at about 700 ka. Recent data suggest a renewed activity between ~79-60 ka forming the Loma Saquigua dome (Santamaría et al., submitted). Together, Rumiñahui and Santa Cruz volcanoes make the Tiopullo plateau (3500 m asl.), a topographic upland that divides the basins of Machachi-Guayllabamba to the north and Latacunga to the south. The Tiopullo plateau has a NW-SE elongated shape approximately 10 km wide and 5 km long, and reaches a height of 230 m above the inter-Andean valley.

Located to the east of Pasochoa, on the western edge on the Eastern Cordillera, **Sincholagua** volcano (4873 m asl.; Lat. 0°32'S; Long. 78°22'W) is an eroded lacking geochronological and geochemical data. Further south, **Cotopaxi** (5897 m asl.; Lat. 0°41'S; Long. 78°26'W) is an active volcano whose Holocene activity has been studied thoroughly (e.g., Hall and Mothes, 2008a; Pistolesi et al., 2013; Tsunematsu and Bonadonna, 2015; Vezzoli et al., 2017; Sierra et al., 2019). Its eruptive history started with an ancient rhyolite caldera (CT-I Barrancas stage), whose explosive and effusive deposits are preserved on Cotopaxi's present-day southern flank. The Cotopaxi-I caldera is overlain by a sequence of andesitic lavas and breccias associated with the Morurcu peak (CT-I Morurco stage), a remnant volcanic neck located at the southern caldera rim. A voluminous andesite lava, which flowed ~40 km northward in the Pita river valley, is associated to this stage (Hall and Mothes, 2008a). The ages of the rhyolite and andesite sequences are not well constrained. Two fission track ages of 0.56 ± 0.04 and 0.54 ± 0.05 Ma were obtained from biotite-rich obsidians (Bigazzi et al., 1997), unfortunately sampling sites were not provided. The Cotopaxi-I series and the Sincholagua southern flank are covered by a thick ignimbrite deposit created by the **Chalupas** caldera-forming eruption, which occurred to the southeast of Cotopaxi (Lat. 0°47'S; Long. 78°20'W). The ignimbrite eruption dated at 216 ± 5 ka (Bablon et al., 2020b) was followed by the construction of the **Quilindaña** andesite edifice (4876 m

194 asl.) taking place between ~184 and ~169 ka (Hammersley, 2003; Córdova et al., 2020). Several tephra
195 fall deposits dated at ~43 ka represent its youngest resurgent activity (Córdova et al., 2020). The
196 **Huañuña** (4197 m asl.; Lat. 0°37'S; Long. 78°14'W) and **Chaupiloma** (also called Rio Valle; 4126 m
197 asl.; Lat. 0°40'S; Long. 78°16'W) are rhyolitic domes located to the north of Chalupas caldera. Based
198 on stratigraphic evidence, a Holocene age was assigned to these volcanic centers (Mothes and Hall,
199 2008; Hall et al., 2017). Northeast of Sincholagua and Huañuña, **Antisana** volcano (5758 m asl.; Lat.
200 0°29'S; Long. 78°08'W) is made up of three successive andesite edifices constructed from ~400 ka
201 (Hall et al., 2017), including the voluminous Cuyuja lava sequence dated at 0.21 ± 0.03 Ma (Opdyke et
202 al., 2006). Stratigraphic evidence suggest that the latest activity at Antisana occurred prior to 800 yr BP
203 (Hall et al., 2017).

204

205 3. METHODS

206 3.1. Sampling strategy

207 Field work was conducted in several field trips between 2016 and 2020 to collect fresh rock
208 samples for K-Ar dating and whole-rock geochemical analyses. Due to the scarce information on the
209 stratigraphy of some of the central segment volcanoes, we sampled the summit and basal areas of the
210 edifices, when possible, in order to cover their whole eruptive history (Figure 2).

211 At Almas Santas volcano, one sample was recovered from the Tangan massive lava flow
212 (southern flank; 19EQ36) and from an andesitic block located at the base of Cerro Azul satellite cone
213 (eastern flank; 19EQ43). A total of thirteen samples were additionally collected from Corazón volcano.
214 Eight lavas were sampled from the northern (19EQ13) and southern (19EQ07, 19EQ05, 19EQ10)
215 flanks, as well as from the summit area (19EQ08, 20EQ83, 20EQ84). One of them belonging to the
216 lava sequence found at the base of the Bómboli satellite cone (19EQ11). An andesitic block was
217 recovered from a monolithological breccia at the base of the summit pyramid (19EQ09). A juvenile
218 block was collected from a pyroclastic density current deposit (PDC; 19EQ14a), and two samples were

taken from fallout layers in the northern flank (19EQ15a, 19EQ15b). Additionally, one block was collected from an avalanche deposit on the northwestern flank (20EQ50).

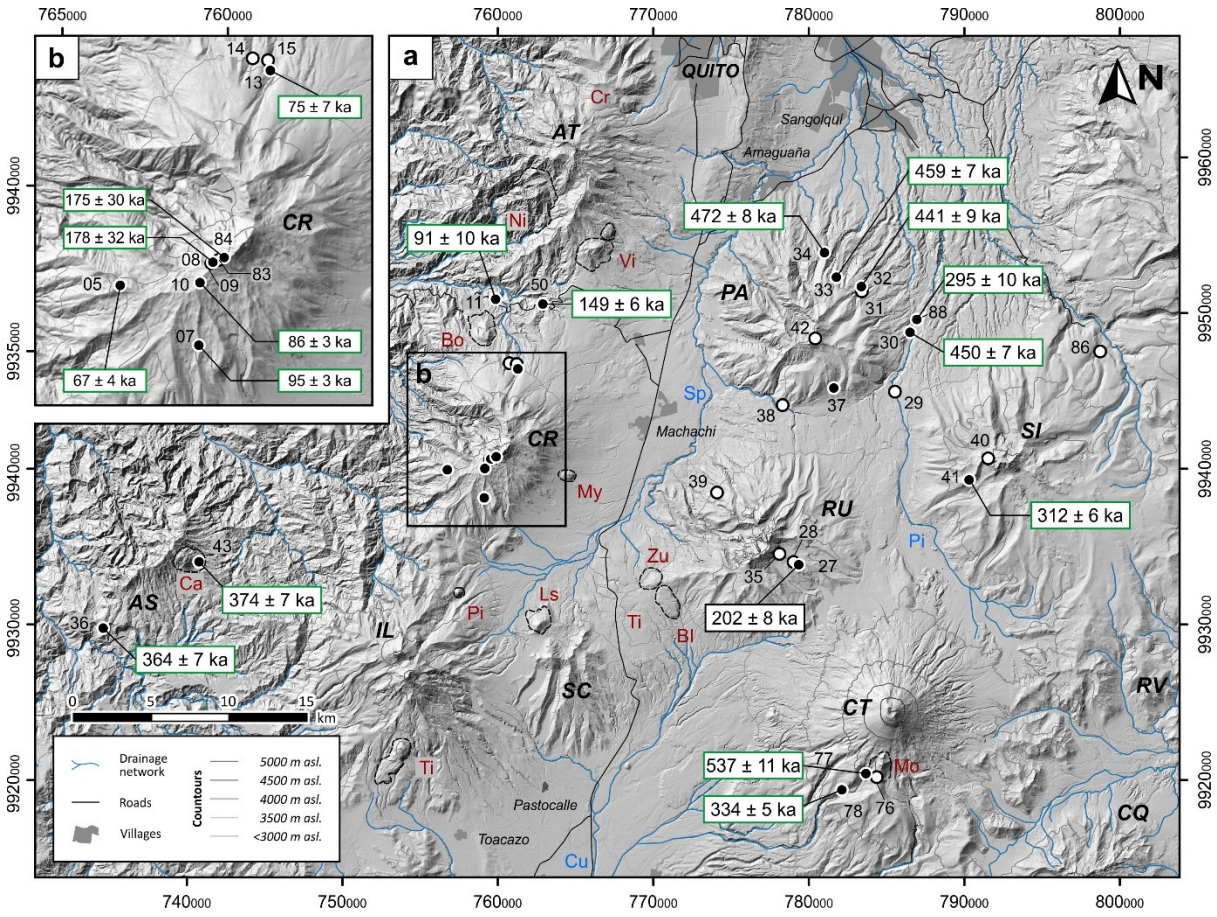

Figure 2. *Hill-shaded digital surface model of the Central Segment showing the sampling locations and geochronological results. Numbers correspond to the last two digits of sample name (19EQxx or 20EQxx according to the recollection year). K-Ar dated samples are represented with solid symbols. Topography from the Sigtierras program. Volcanic peaks shown as black letters (see Fig. 1 caption). Satellite domes and cones shown as red letters. Bl: Boliche; Bo: Bomboli; Ca: Cerro Azul; Cr: Carcacha; Ls: Loma Saquigua; Vi: La Viudita; Mo: Morurco; My: Moya; Ni: Ninahuilca; Ti: Tiopullo; Pi: Pilongo; Zu: Zunfana. Rivers and valleys represented as blue letters. Cu: Cutuchi; Pi: Pita; Sp: San Pedro. Coordinates are in Universal Transverse Mercator (UTM) zone 17.*

Seven lava samples were obtained from Pasochoa volcano. Four are from the northern flank (19EQ31, 19EQ32, 19EQ34, 19EQ37), one from the eastern flank (19EQ30) and two from the southern flank (19EQ37, 19EQ38). Sparse exposures of massive lavas in the summit area precluded sampling, but we collected one dyke sample for geochemical analysis (19EQ42b). Likewise, the outcrops of the Rumiñahui volcano were mostly composed of weathered monolithic breccias and lava flows. Thus, only

three lava samples were recovered from this volcano (19EQ27, 19EQ28, 19EQ39), together with one block taken from a breccia near the upper part of the central peak (19EQ35).

The limited access paths to Sincholagua volcano prevented adequate sampling of this volcano. Only two lavas were recovered from the northeast (20EQ86) and west (19EQ41) flanks, apart from the summit area (19EQ40). Following the description of Hall et al. (2008), we collected five samples from the older stages of Cotopaxi volcano. One sample from the base of Morurco peak belongs to a massive mica-rich obsidian flow (Cotopaxi I - Barrancas stage; 20EQ77), and two samples correspond to the overlying sequence composed of andesitic lavas (Cotopaxi I - Morurco stage; 20EQ76, 20EQ78) and monolithological breccias. Finally, two samples of the upper massive lava flows were recovered in the Pita River valley (Cotopaxi I B - Morurco stage; 19EQ29, 20EQ77).

3.2. K-Ar dating

Twenty-one unaltered samples from the central segment volcanoes were carefully selected after examination of thin sections (Appendix A), for dating by the K-Ar method using the unspiked Cassignol-Gillot technique (Cassignol and Gillot, 1982). This technique was successfully applied to date young volcanic rocks, typically with low radiogenic argon content, in the Ecuadorian volcanic arc (Alvarado et al., 2014; Bablon et al., 2018, 2019, 2020b; Santamaría et al., submitted), as well as in other arc segments of the Andes (e.g., Germa et al., 2010; Pallares et al., 2016, 2019; Grosse et al., 2018, 2020), and worldwide (e.g., Germa et al., 2011; Hildenbrand et al., 2018; Dibacto et al., 2020). Samples were manually crushed and sieved to 63–80, 80–125 or 125–250 μm, according to the phenocrysts over groundmass ratio. Then, magnetic separation and heavy liquids (bromoform) were used to extract the groundmass in a narrow density range, removing the phenocrysts and any undetected weathered fraction. The Cassignol-Gillot technique was preferentially applied to the groundmass as it is the latest phase to crystallize in isotopic equilibrium with the atmosphere, and thus provides the emplacement age of a volcanic deposit. Early formed crystalline phases (e.g., plagioclase phenocrysts)

could carry inherited ^{40}Ar biasing the obtained age. Thus, such values are only interpreted as older bounds of the real eruption age.

The Cassignol-Gillot technique is suitable for detecting tiny quantities of radiogenic argon ($^{40}Ar^*$) produced by radioactive decay of ^{40}K, which could have been diluted in ^{40}Ar derived from atmospheric contamination. The electrical signal difference of the $^{40}Ar/^{36}Ar$ ratio obtained from the sample and from an air aliquot, measured under identical conditions using a 180° sector multi-collector mass spectrometer, allows to quantify the $^{40}Ar^*$ content (%). The mass spectrometer detection limit, close to 0.1% for $^{40}Ar^*$ (Quidelleur et al., 2001), allows dating volcanic products even of Holocene age with a relatively small uncertainty (Gillot et al., 2006). The ^{40}Ar signal is regularly calibrated with systematic measurements of the HD-B1 standard with an age of 24.18 ± 0.09 Ma (Schwarz and Trieloff, 2007). The potassium (K) concentration was measured by flame absorption spectroscopy, in conjunction with the standards MDO-G (Gillot et al., 1992) and BCR2 (Raczek et al., 2001) for comparison and correction. Then, the $^{40}K/K$ ratio in nature and the ^{40}K decay constant (Steiger and Jäger, 1977) allow to calculate the sample age. Both potassium and argon measurements were carried out at the GEOPS laboratory (Paris-Saclay University, France), and were performed at least twice to verify their reproducibility within 1-σ uncertainty range. See Bablon et al. (2018) for a full description of sample preparation, analytical procedures, and age and uncertainty calculations.

3.3. Whole-rock geochemical analyses

Whole-rock major and trace element contents were measured for all dated samples as well as for 12 additional samples specifically collected for geochemical analyses, completing a dataset of 35 new analyse. Agate-crushed powders were analyzed by Inductively Coupled Plasma-Atomic Emission Spectrometry (ICP-AES), at the Laboratoire Géosciences Océan, Université de Bretagne Occidental (Brest, France), following the analytical procedure described in Cotten et al. (1995). Relative uncertainties are lower than 1% for SiO_2, and 2% for the other major elements, and 5% for trace

elements. Major element concentrations were recalculated to a total of 100% on a water free-basis and are presented in Appendix B.

3.4. Numerical reconstructions of paleotopographies for volume calculations

Numerical reconstructions of paleotopography provide a useful tool in the comprehension of the size reached by a volcanic edifice while eluding its erosion features (e.g., Grosse et al., 2009, 2020; Lahitte et al., 2012; Germa et al., 2015). Here, we employed the numerical reconstructions as a first approximation of the volume of material accumulated by the volcanic edifice at the end of its construction stage, as well as the amount of material removed since the end of the volcanic activity. For this purpose, we used a 4-m resolution digital elevation model (DEM) developed by the Sigtierras program from the Ministerio de Agricultura y Ambiente of Ecuador. The structural features of the volcanoes, and their relationships with local and regional fault systems, were mapped using a slope map obtained from this DEM, as well as field observations, Google Earth satellite images and orthophotography.

We chose a simple procedure for the reconstruction of the volcanic edifices due to the limited stratigraphic constraints, following the method described by Germa et al. (2015), Bablon et al. (2018, 2020a), and Santamaria et al. (submitted), and summarized as follows. The basement surface S_{t0} was modelled using an ordinary Kriging interpolation of the ArcGIS software, starting from the basal outline of the edifice. A regular 100 m point cloud was extracted from the Sigtierras DEM for each volcanic edifice, where points located in high erosion areas, such as deep glacial and fluvial valleys, were discarded. Thus, the points preserved in crests or smooth plateaus were interpreted as low erosion surfaces. Based on previous results from other volcanoes in the region (Bablon et al., 2018, 2020a; Santamaría et al., submitted), we selected a conical model with a circular base and a concave profile shape which corresponds to the surface reached at the end of the construction stage S_{t1}. Such profile corresponds to the exponential trend line created by plotting the elevation of the preserved points versus their distance from a symmetry axis which was shifted to obtain the best adjustment. The surface

311 uncertainty at each point σ_{St-i} is provided by the prediction standard error map resulting from ordinary
312 kriging. The present-day topography S_{t2} is interpreted as the result of the erosion of the modeled cone
313 S_{t1} after the quiescence period. The construction stage volume v_{cs} and the erosion stage volume v_{es}
314 were calculated by the integration of the elevation difference between S_{t0} - S_{t1}, and S_{t1} - S_{t2} surfaces
315 multiplied by the pixel area, respectively. Volume uncertainty σ_v corresponds to the combination of the
316 elevation uncertainties of each point σ_{e-i} multiplied by the pixel area, where $\sigma_{e-i} =$
317 $\sqrt{{\sigma_{Stf-i}}^2 + {\sigma_{Sti-i}}^2}$.

318

319 4. RESULTS

320 4.1. K-Ar dating

321 Twenty new K-Ar ages are presented in Table 1 and shown in Figure 2. Overall, the analyzed
322 samples have porphyritic textures with variable amounts of phenocrysts such as plagioclase,
323 orthopyroxene, clinopyroxene, amphibole and rare biotite. The groundmass commonly consists of
324 plagioclase, pyroxene, and scarce Fe-Ti oxides microlites contained in a glassy matrix. All analyses
325 were performed on groundmass, except one on plagioclase phenocrysts (19EQ27) and one on obsidian
326 shards (20EQ77). The K content ranges between 0.76 and 1.75 wt.% for groundmass, reaching a
327 minimum of 0.51 wt.% in plagioclase and a maximum of 2.4 wt.% in obsidian fractions. The radiogenic
328 argon content ranges between 0.5% and 28.9%, with a maximum of 47.7% for plagioclase.

329 The samples taken from the eastern and southern flanks of Almas Santas volcano yielded
330 similar ages of 374 ± 7 ka (19EQ43) and 364 ± 7 ka (19EQ36), respectively. Considering the sampling
331 bias toward the upper exposed sections of the edifice, this narrow age range probably represents the end
332 of the latest cone-building stage of the volcano.

333

334 ***Table 1.*** *K-Ar ages obtained in this study for central segment volcanoes. Column headings indicate*
335 *sample name, outcrop nature and relative location, sample coordinates projected using the Universal*
336 *Transverse Mercator (UTM) coordinate system (Zone 17), potassium (K) content in percent, radiogenic*
337 *argon content (^{40}Ar*) in percent and in 10^{11} atoms per gram, age obtained for each measurement, and*
338 *weighted mean age in ka given with a 1-σ uncertainty. All measurements were performed on*
339 *groundmass, except for one sample measured on plagioclase phenocrysts (**) and one on volcanic*
340 *glass (***).*

Sample	Location and Unit	Longitude (m)	Latitude (m)	K (%)	^{40}Ar* (%)	^{40}Ar* (10^{11} at/g)	Age ± 1σ (ka)	Mean age (ka)
Almas Santas volcano								
19EQ43	Lava flow, Cerro Azul	740786	9934033	0.992	8.4%	3.8562	372 ± 7	**374 ± 7**
					8.1%	3.8998	377 ± 7	
19EQ36	Lava flow, Tangan	734605	9929768	0.756	8.2%	2.8759	364 ± 7	**364 ± 7**
					7.4%	2.8822	365 ± 7	
Corazón volcano								
19EQ08	Lava flow, summit pyramid	759536	9940634	1.579	0.6%	2.9028	176 ± 28	**178 ± 32**
					0.5%	2.9836	181 ± 38	
20EQ84	Lava flow, summit pyramid	759883	9940775	0.972	0.6%	1.7824	176 ± 30	**175 ± 30**
					0.6%	1.7798	175 ± 29	
19EQ07	Lava flow, S flank	759112	9938136	1.334	3.9%	1.3350	96 ± 3	**95 ± 3**
					3.6%	1.2996	93 ± 3	
19EQ11	Lava flow, Cerro Bómboli	759847	9950892	1.323	0.9%	1.2223	88 ± 10	**91 ± 10**
					1.0%	1.3013	94 ± 10	
19EQ10	Lava flow, S flank	759148	9940026	1.057	2.8%	0.9700	88 ± 3	**86 ± 3**
					2.7%	0.9196	83 ± 3	
19EQ13	Lava flow, N flank	761280	9946424	1.279	1.1%	1.0225	77 ± 7	**75 ± 7**
					1.1%	0.9799	73 ± 6	
19EQ05	Lava flow, SW flank	756746	9939943	0.966	2.0%	0.7031	70 ± 4	**67 ± 4**
					1.9%	0.6539	65 ± 4	
Atacazo avalanche								
20EQ50	Dacite block, S avalanche	762881	9950592	1.279	2.5%	1.9833	148 ± 6	**149 ± 6**
					2.8%	2.0019	150 ± 6	
Pasochoa volcano								
19EQ34	Lava flow, N flank	780987	9953901	0.856	12.0%	4.1969	469 ± 8	**472 ± 8**
					12.4%	4.2349	474 ± 8	
19EQ33	Lava flow, N flank	781758	9952313	1.807	26.5%	8.6492	458 ± 7	**459 ± 7**
					28.9%	8.6627	459 ± 7	
19EQ30	Lava flow, E flank	786494	9948763	1.080	11.5%	5.1295	455 ± 8	**450 ± 7**
					13.3%	5.0254	446 ± 7	
19EQ32	Lava flow, NW flank	783362	9951701	1.093	6.9%	5.0002	438 ± 9	**441 ± 9**
					7.1%	5.0665	444 ± 9	
19EQ37	Lava flow, S flank	781599	9945191	1.086	5.2%	4.7482	419 ± 10	**423 ± 10**
					5.1%	4.8376	427 ± 10	

Sample	Location and Unit	Longitude (m)	Latitude (m)	K (%)	^{40}Ar* (%)	^{40}Ar* (10^{11} at/g)	Age ± 1σ (ka)	Mean age (ka)
Rumiñahui volcano								
19EQ27**	Lava flow, E flank	779336	9933840	0.523	47.7%	1.0812	198 ± 8	**202 ± 8**
					43.4%	1.1254	206 ± 8	
Sincholagua volcano								
19EQ41	Lava flow, summit pyramid	790298	9939301	1.739	9.0%	5.6975	314 ± 6	**312 ± 6**
					9.2%	5.6261	310 ± 6	
Cotopaxi volcano								
20EQ77***	Obsidian flow, Morurco	783660	9920417	2.430	6.2%	13.5144	532 ± 11	**537 ± 11**
					6.4%	13.7703	542 ± 11	
20EQ78	Lava flow, S flank	782119	9919377	1.743	13.0%	6.1003	335 ± 5	**334 ± 5**
					12.7%	6.0550	333 ± 5	
20EQ88	Lava flow, Tanipamba (Pita valley)	786939	9949596	1.746	3.0%	5.3977	296 ± 11	**295 ± 10**
					3.9%	5.3573	294 ± 9	

Further east, Corazón volcano exhibits a wide range of ages between 178 ± 32 and 67 ± 4 ka. Notably, the sample 19EQ08 taken from the summit pyramid was dated at 178 ± 32 ka and represents the oldest phase of the volcano. A second sample taken from an upper section of the same sequence and dated at 175 ± 30 ka supports this result. However, we take both ages with caution due to their high atmospheric contamination and low radiogenic argon content reflected in their large uncertainty range. An age at 149 ± 6 ka was obtained for a dacitic block (17EQ59) collected from a debris avalanche deposit at the base of the northern flank. Lastly, the ages obtained from the lavas sampled on the northern and southern flanks range from 95 ± 3 to 67 ± 4 ka, the latter being the youngest age obtained in this study.

In the inter-Andean valley, the ages obtained for Pasochoa volcano exhibit a narrow range between 472 ± 8 and 423 ± 20 ka. This includes a voluminous lava flow in the Pita valley, on the east flank of Pasochoa volcano, dated at 450 ± 7 ka (19EQ30). Further south, the highly weathered state of the Rumiñahui volcanic products precluded groundmass analyses. We thus analyzed plagioclase phenocrysts separated from the less weathered sample 19EQ27, yielding an age of 207 ± 9 ka. Given

the possible existence of inherited radiogenic argon, this result is considered as a maximum value for the true eruption age.

Similar than Rumiñahui, the **Sincholagua** lavas exhibit high weathering for most outcrops. Nevertheless, a fresh lava sampled on the eastern flank (19EQ41) yielded a groundmass K-Ar age of 316 ± 6 ka. Regarding **Cotopaxi-I** volcano, the sampled obsidian flow at the base of the Morurco peak yielded an age of 537 ± 11 ka (20EQ77), corresponding to the oldest value obtained in this study. Finally, a lava flow exposed south of Morurco (20EQ78), and the voluminous Pita lava flow (20EQ88) yielded close ages of 334 ± 5 and 295 ± 10 ka, respectively.

4.2. Construction and erosion volumes of the central segment volcanoes

The numerical reconstructions allowed us to calculate the bulk volume of the volcanic edifices within the central segment, as well as the volume of the material removed by erosion. Note that the surface models applied disregard the amount of material lost during the construction stage due to erosion or possible sectorial collapses. Therefore, the volumes obtained here are considered as minimum values. On the other hand, the heterogeneity of volcanic materials prevents us from expressing our values as dense rock equivalent (DRE) volumes, and therefore they are reported as bulk volumes. The obtained values are presented in Table 2, together with volumes and estimations made by other authors. Our calculations showed that the most voluminous edifice is the Almas Santas volcano with a bulk value of 90 ± 14 km^3, while the smallest one corresponds to La Carcacha volcano with a value of 8 ± 1 km^3. Altogether, the average volume reached by the volcanoes of the central segment is 43 ± 12 km^3. The minimum uncertainty in volumetric calculations is 10 vol.%, with a maximum of 24 vol.%. The present-day volume of dismantled material is of at least 24% of the initial volume. Notably, the Almas Santas, Corazon and Sincholagua volcanoes exhibit the highest erosion percentages, up to 74 vol.%.

Note that output and erosion rates were not investigated here given the multiplicity of factors controlling these processes, and which are beyond the scope of this research. For instance, factors such as the heterogeneity of the constituent eruptive products in a volcanic edifice, their distribution around

382 the main vent, and their mechanical resistance to erosion could cause noticeable discrepancies in the
383 volume reached at the end of the construction periods (e.g., Hora et al., 2007; Zernack et al., 2009;
384 Yamamoto et al., 2018). On the other hand, external factors could influence the rate of syn-eruptive
385 erosion, which in turn biases the output rates. Examples of such factors include the edifice elevation
386 and geographical setting, which influence the precipitation range and/or the extent of glacial cover to
387 which volcanic edifices are exposed through time (Brook et al., 2011; Conway et al., 2016; Pure et al.,
388 2020). At the same time, the tectonic activity could influence both the geometry of the volcanic edifice
389 cone and its dismantling degree (Lagmay et al., 2000; Mathieu et al., 2011; Mathieu and van Wyk de
390 Vries, 2011).

391 ***Table 2.*** *Construction and erosion volumes calculated based on numerical reconstructions together*
392 *with their corresponding rates. Numerical results given with a 1-σ uncertainty (see text for details).*

Volcano	Construction Volume (km^3)	Uncertainty percentage	Erosion Volume (km^3)	Erosion percentage	Reference
Almas Santas	90 ± 14	15%	67 ± 3	74%	This study
Atacazo	61 ± 7	12%	36 ± 1	60%	This study
- Carcacha	8 ± 1	12%	3 ± 0	41%	This study
Corazon	31 ± 7	21%	22 ± 0	71%	This study
Pasochoa	63 ± 6	10%	19 ± 1	30%	This study
Rumiñahui	43 ± 10	24%	21 ± 1	49%	This study
Santa Cruz	21 ± 3	15%	5 ± 0	24%	This study
Sincholagua	42 ± 7	16%	31 ± 2	74%	This study
Cotopaxi II	32 ± 3	9%			This study
Quilindaña	25 ± 3	18%	16 ± 1	63%	This study
Iliniza (whole)	46 ± 15	32%	12 ± 4	26%	Santamaría et al. (submitted)
- North Iliniza	28 ± 9	32%	6 ± 2	21%	Santamaría et al. (submitted)
- South Iliniza	18 ± 6	33%	6 ± 2	33%	Santamaría et al. (submitted)
Cotopaxi I – Caldera stage	~32				Hall and Mothes (2008a)
Cotopaxi I – Morurco stage	~4				Hall and Mothes (2008a)
Cotopaxi II	~51				Hall and Mothes (2008a)
Antisana	~50				Hall et al. (2017)
Chalupas (bulk)	230 ± 30	8%			Bablon et al.(2020b)
Chalupas (DRE)	~100				Hall and Mothes (2008a), Crosweller et al. (2012)

393

394

395

4.3. Geochemical characterization

As shown in Figure 3a (Peccerillo and Taylor, 1976), most of the samples from this study are classified as medium-K basaltic andesites to low-silica dacites, with SiO_2 contents ranging between 53 wt.% and 64 wt.%. The Cotopaxi-I obsidian (20EQ77) is the unique rhyolite of the group with a concentration of SiO_2 around 74 wt.%. The K_2O contents vary between 0.7 wt.% and 2.7 wt.%, which also almost corresponds to the range exhibited by the Rumiñahui samples. Notably, samples 19EQ37 and 19EQ39, collected from Rumiñahui volcano, plots in the limit between the medium and high-K calc-alkaline series (Fig. 3a). Our data is consistent with previous studies carried out on other volcanoes from the central segment (Figure 3). For instance, the sampled lavas from Almas Santas volcano (19EQ36, 19EQ43) fall in the field shaped by the andesitic series defined by Chemin (2004). Likewise, the lavas and breccias of Corazón volcano display a low-silica andesite field compared to those available in Schiano et al. (2010), which were collected around Cerro Bomboli. The andesitic lavas of Pasochoa are consistent with the field defined by the same authors. Curiously, only two dacite lavas were found in both volcanoes: 19EQ14a and 19EQ33, respectively. The samples collected from Rumiñahui volcano belong to the two sequences described by Starr (1984) where samples 19EQ39 and the dated 19EQ27 belongs to the high-K series. Finally, the Cotopaxi-I samples are consistent with available geochemical data (Bryant et al., 2006; Garrison et al., 2006, 2011). In particular, the obsidian 20EQ77 shows silica and potassium contents like those reported by Bellot-Gurlet et al. (2008) (samples CTX45 and CTX 46 from Bigazzi et al., 1992). Considering the analogous mineralogical composition described by these authors, we can argue that our sample corresponds to the same obsidian flow. Also, samples collected from the Cotopaxi-I southern flank (20EQ76 and 20EQ78) are consistent with the Morurco andesitic series (Garrison et al., 2006). Although the Pita lava flow (19EQ29, 20EQ88) exhibits a lower silica content, falling close to the field described by the Pasochoa and Rumiñahui lavas, the Cotopaxi-I samples plot along a single trend. Note that the geochemical data available for Cotopaxi-I are scarce, and thus its compositional field is poorly defined.

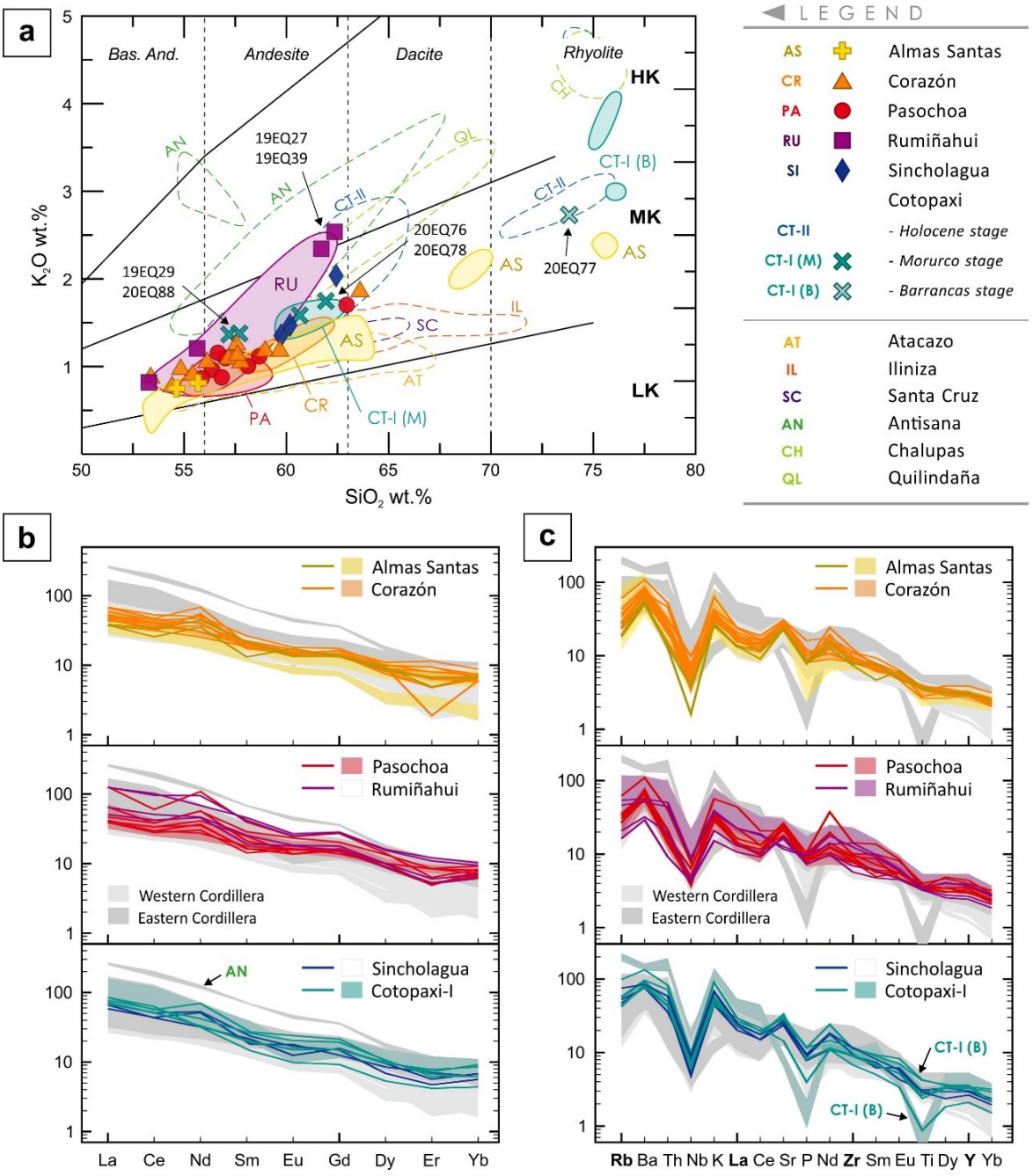

Figure 3. a) *K_2O vs SiO_2 diagram (Peccerillo and Taylor, 1976) for eruptive products of the Central Segment volcanoes. HK: Hight-K, MK: medium-K, and LK: low-K calc-alkaline series. Shaded areas represent the composition fields of the volcanoes from this study, while dashed areas are for other volcanoes based on the Georoc database and other studies (Starr, 1984; Chemin, 2004; Garrison et al., 2006; Bellot-Gurlet et al., 2008; Schiano et al., 2010; Ancellin et al., 2017; Hall et al., 2017; Bablon et al., 2020b; Chiaradia et al., 2020; Córdova et al., 2020; Santamaría et al., submitted).* ***b)*** *Rare Earth Elements normalized to chondrites, and* ***c)*** *Incompatible trace elements normalized to the primitive mantle diagrams (Sun and McDonough, 1989) for the same arrangements. The sampled volcanoes were organized according to their position in the Western Cordillera (yellow and orange lines), Inter-Andean Valley (red and purple lines), and Eastern Cordillera (blue and turquoise lines). Shaded areas represent the composition fields created by bibliographic data.*

Rare-Earth Elements (REE) Chondrite-normalized plots (Figure 3b; Sun and McDonough, 1989) show slightly fractionation patterns between Light REE (LREE; La, Ce, Nd) and Heavy REE (HREE; Dy, Er, Yb), without significant Eu anomaly. Samples from the volcanoes in the Western Cordillera (e.g., Cotopaxi, Sincholagua) exhibit a slight REE enrichment compared to those of the Inter-Andean Valley (e.g., Pasochoa, Rumiñahui), reaching stronger HREE depletions in the Eastern Cordillera (e.g., Almas Santas, Corazón). Variations in REE content are also observed for each volcano. For instance, the andesite lavas from Almas Santas (19EQ36, 19EQ43) present a slight HREE enrichment compared with the rhyodacite-rhyolite series (Chemin, 2004). Likewise, the HK andesites from Rumiñahui volcano (e.g., 19EQ27, 19EQ39) and the dacitic 19EQ33 sample from Pasochoa volcano shows the highest LREE enrichments in the Inter-Andean valley volcanoes. Trace Elements normalized to Primitive mantle diagrams (Figure 3c; Sun and McDonough, 1989) display an overall enrichment of Large-Ion Lithophile Elements (LILE; Rb, Ba, and K) and Sr, as well as depletion of Nd, P, and slight Ti. The Cotopaxi-I obsidians (20EQ77) shows the highest P and Ti negative anomalies.

The geochemical evolution of the magmas in the central segment is strongly influenced by fractional crystallization processes, as suggested by the negative correlation between the compatible elements and the SiO_2 contents, as well as by several petrogenetic models conducted in the volcanoes of the area (Barragan et al., 1998; Bourdon et al., 2003; Bryant et al., 2006; Chiaradia et al., 2009; Hidalgo et al., 2012; Ancellin et al., 2017). These models support fractionation of variable amounts of plagioclase, pyroxene, amphibole, and olivine. However, the occurrence of certain lavas with strong Y and HREE depletions observed in volcanoes such as Ilinizas, Almas Santas and Cotopaxi, were explained by more complex petrogenetic processes leading to higher amphibole and garnet fractionations (e.g., Chemin, 2004; Garrison et al., 2006; Hidalgo et al., 2007). Such processes seem to be related to changes in the subducting slab inputs that metasomatize the mantle wedge, and/or to processes of fractional crystallization and magma mixing occurring in the lower crust (e.g., Garrison et al., 2006; Hidalgo et al., 2007, 2012; Chiaradia et al., 2009, 2020; Schiano et al., 2010; Bellver-Baca et al., 2020). Our data reflect the same general processes related to magma evolution in a subduction context, rather than contribute to the comprehension of the more detailed processes which are beyond

the scope of this paper. Therefore, we recommend consulting the referenced sources for a more detailed discussion.

5. DISCUSSION

5.1. Comparison with previous geochronological data

Overall, the new radiometric ages acquired in this study are consistent with those reported for other volcanoes in the central segment. An unpublished $^{40}Ar/^{39}Ar$ age obtained at the Laboratoire Geoazur (Côte d'Azur University, Nice, France) was obtained for the Corazón volcano (M. Fornari pers. com.). Hand-picked groundmass fragments from the sample BOM-5, collected north of the Bomboli cone, yielded a plateau age of 190 ± 10 ka, and a consistent inverse isochron age of 188 ± 10 ka. These values are significantly older than our K-Ar age of 91 ± 10 ka obtained from a nearby lava flow (19EQ11) outcropping near the Bomboli cone. Considering the lower stratigraphic position of the BOM-5 sampling site, the occurrence of two lava sequences of different ages is plausible. Indeed, the BOM-5 age falls in the range described by our geochronological data for the early cone-building stage of Corazón volcano, dated at 175 ± 30 ka (20EQ84) and 178 ± 32 ka (19EQ08), whereas the 19EQ11 age is consistent with the late stage occurred between 67 ± 4 ka (19EQ05) and 95 ± 3 ka (19EQ07). Nevertheless, we note that the groundmass separation method used in BOM-5 does not prevent the occurrence of phenocrysts or weathered phases, which could have biased the resulting age. Unfortunately, the lack of detailed data and age spectrum nor isochron prevents us from any further investigation.

The paleomagenetic study of Opdyke et al. (2006) provided a $^{40}Ar/^{39}Ar$ age of 1.33 ± 0.30 Ma (three steps only plateau age) for a normal polarity lava flow (EC-47) sampled on the eastern flank of Pasochoa. The corresponding isochron yielded an age of 1.93 ± 2.88 Ma with a $^{40}Ar/^{36}Ar$ initial ratio of 271 ± 116, suggesting a high contamination by atmosphere. The low precision of this age precludes comparison with the geomagnetic polarity time scale; nonetheless, we note that the geomagnetic field was dominantly reverse during the Matuyama Chron (i.e., 0.77 to 2.58 Ma; Cohen and Gibbard, 2019). Conversely, we provide a K-Ar age of 450 ± 7 ka obtained from a nearby lava flow (19EQ30) belonging

to the same unit. Our age is in good agreement not only with the normal polarity reported by Opdyke et al. (2006), but also with the all other new ages of Pasochoa volcano which range from 423 ± 10 to 472 ± 8 ka (Table 1).

Two obsidian blocks belonging to the Cotopaxi-I rhyolitic stage were previously dated at 0.54 ± 0.05 Ma (CTX 46) and 0.56 ± 0.04 Ma (CTX 45) using the fission-track method (Bigazzi et al., 1997). By applying the K-Ar method for dating an obsidian flow (20EQ77), we obtained a consistent and better-defined age of 537 ± 11 ka. The geochemical and petrographic similarities observed between our samples and those of Bigazzi et al. (1997), including the occurrence of biotite and scarce quartz, suggest that we have successfully dated obsidian samples from the same sequence by applying two different techniques.

5.2. Eruptive history of the central segment

Based on our new K-Ar ages, and stratigraphic and morphological data, as well as on the previous studies carried out in the Central Segment volcanoes, we present the eruptive history for this area of the Ecuadorian arc as follows (Figure 4).

The oldest eruptive activity took place in the Carcacha volcano (Western Cordillera) at about 1.30 Ma (Hidalgo, 2006). After a period of apparent quiescence, the volcanic activity resumed southwards forming the Santa Cruz volcano in the Inter-Andean Valley around 702 ± 11 ka (Santamaría et al., submitted). From ~550 ka, the volcanic activity seems to increase in the Central Segment (Fig. 5). The Cotopaxi-I caldera (Eastern Cordillera) showed highly explosive eruptions and effusive activity of rhyolitic affinity dated at 537 ± 11 ka (20EQ77). About 65 kyr later, the construction of the andesitic Pasochoa volcano occurred in the Inter-Andean Valley between 472 ± 8 ka (19EQ34) and 423 ± 10 ka (19EQ37), as well as the emplacement of massive dacitic lava flows and PDC deposits corresponding to the pre-caldera Chalupas volcanic system (Eastern Cordillera) between 459 ± 9 and 418 ± 10 ka (plagioclase $^{40}Ar/^{39}Ar$ plateau ages) (Hammersley, 2003).

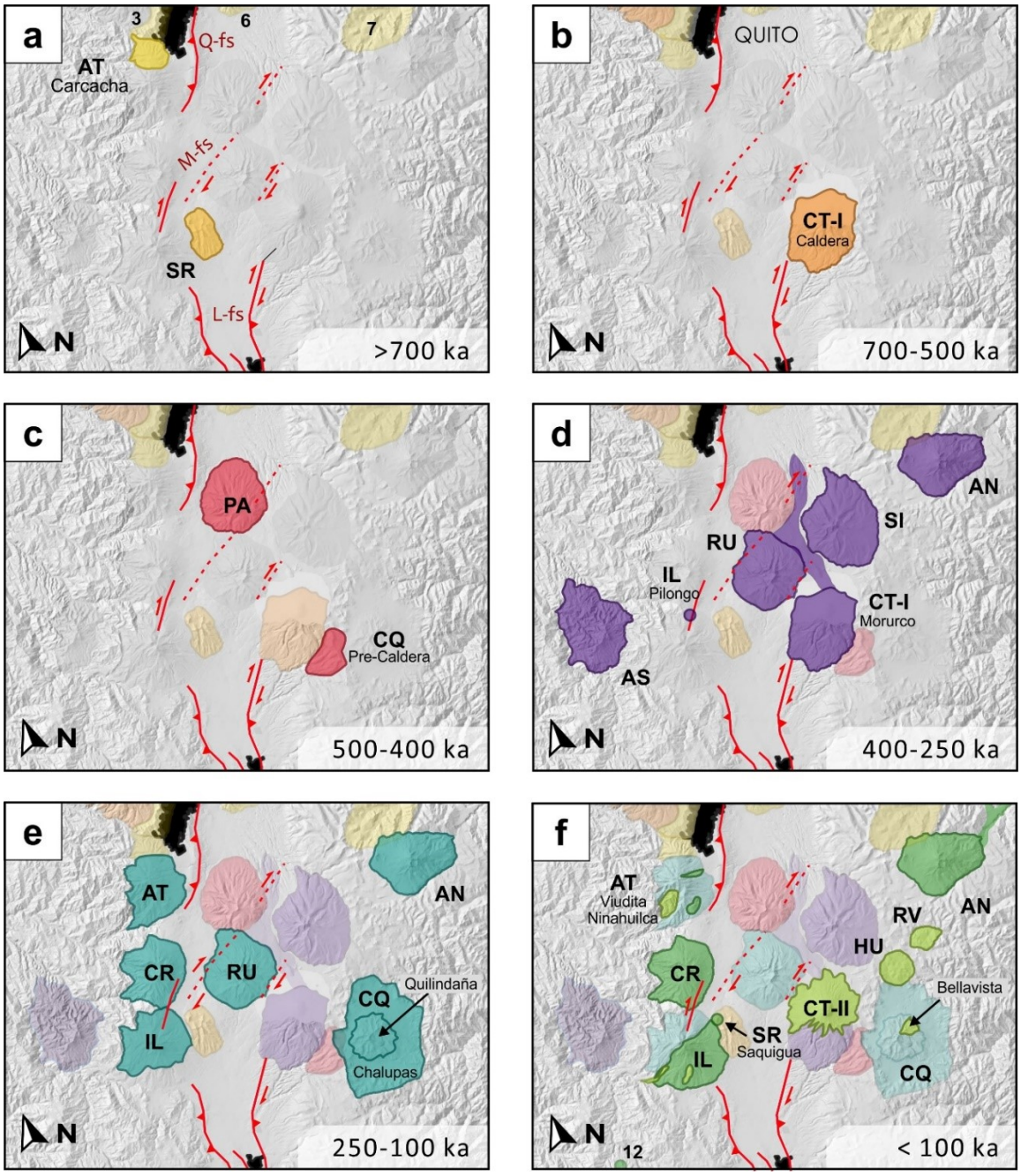

Figure 4. *Synthesis cartoons of the eruptive history of the Ecuadorian central arc segment.* ***a)*** *Early stage of the Quaternary volcanic arc. Construction of the volcanoes AT: Carcacha (1.3 Ma) and SC: Santa Cruz (700 ka); as well as other coeval edifices outside the study area: El Cinto (3), Ilaló (6), Chacana (7).* ***b)*** *Early construction of the volcano cluster. CT-I: Cotopaxi-I Barrancas stage at 550 ka.* ***c)*** *PA: Pasochoa; CQ: Chalupas pre-caldera deposits.* ***d)*** *AN: Antisana-I; AS: Almas Santas; CT-I: Cotopaxi-I Morurco stage; IL: Pilongo dome of Iliniza; RU: early stage of Rumiñahui; and SI: Sincholagua. The distal flows of the Morurco cone represented as a purple field north of CT-I.* ***e)*** *AN: Antisana; AT: Atacazo; CQ: Chalupas caldera-forming eruption (216 ± 5 ka), and construction of the post-caldera Quilindaña edifice; CR: Corazón; IL: North Iliniza edifice; RU: Rumiñahui late stage.*

Figure 4 (continuation of caption). f) *Modern stage of the volcano cluster (dark green) and its Holocene activity (light green). AN: Antisana II and III; AT: Atacazo satellite domes, and Ninahuilca dome complex. CR: Corazón; CT-II: Cotopaxi-II edifice; CQ: Bellavista dome; HU: Huañuna dome; IL: South Iliniza edifice, and its satellite domes; RV: Rio Valle dome; and Quilotoa caldera (12). Active fault systems shown for all charts as red lines according to Alvarado et al. (2016) and this study. Charts are rotated to coincide with the lineament orientation of the Volcanic Front.*

The volcanic activity spread along the central segment between ~400 and ~300 ka, with the onset of Almas Santas volcano (dated at 374 ± 7 and 364 ± 7 ka) and the extrusion of the Pilongo dome (353 ± 6 ka, Iliniza volcano; Santamaría et al., submitted) in the Western Cordillera, together with the construction of Antisana (from 378 ± 38 ka; Hall et al., 2017), Cotopaxi-I Morurco (around 334 ± 5 ka), and Sincholagua (around 312 ± 6 ka) volcanoes in the Eastern Cordillera. We propose that emplacement of the older Rumiñahui volcano occurred during this last evolutionary stage of the Central Segment as suggested by (1) the long-term erosion phase deduced from the widespread dike exposures in the summit area, (2) the upper bound provided by the 207 ± 9 ka age (19EQ27) related to its late andesitic series, and (3) the required presence of a prominent edifice at the location of Rumiñahui volcano for channeling the Pita lava flows (295 ± 10 ka) northward from the Morurco cone to the south (Cotopaxi-I volcano) to its terminal position east of Pasochoa volcano to the north.

The slope direction of the summit area of the Tiopullo plateau is consistent with a source near the SW ridge of Rumiñahui (Fig. 5a). Accordingly, we suspect that Tiopullo was probably formed by a succession of lava flows derived from fissure eruptions occurred near the SW flank of Rumiñahui, thereby explaining the lack of a prominent cone at the Tiopullo summit, the plateau size, and its gentle slope. This hypothesis is further supported by the presence of the Zunfana cone (3703 m asl.; 140 m above the plateau level) and the Boliche dome *coulée* (70 m thick) which are located near the inferred Tiopullo source (Fig 5c-d). Although Zunfana and Boliche appear to be younger than the Tiopullo plateau because of their comparatively lower degree of erosion, they could be considered as evidence of volcanic activity at the Tiopullo emission site. However, a more detailed study is required to establish the origin of these structures and their relationship with Tiopullo and the Rumiñahui volcano.

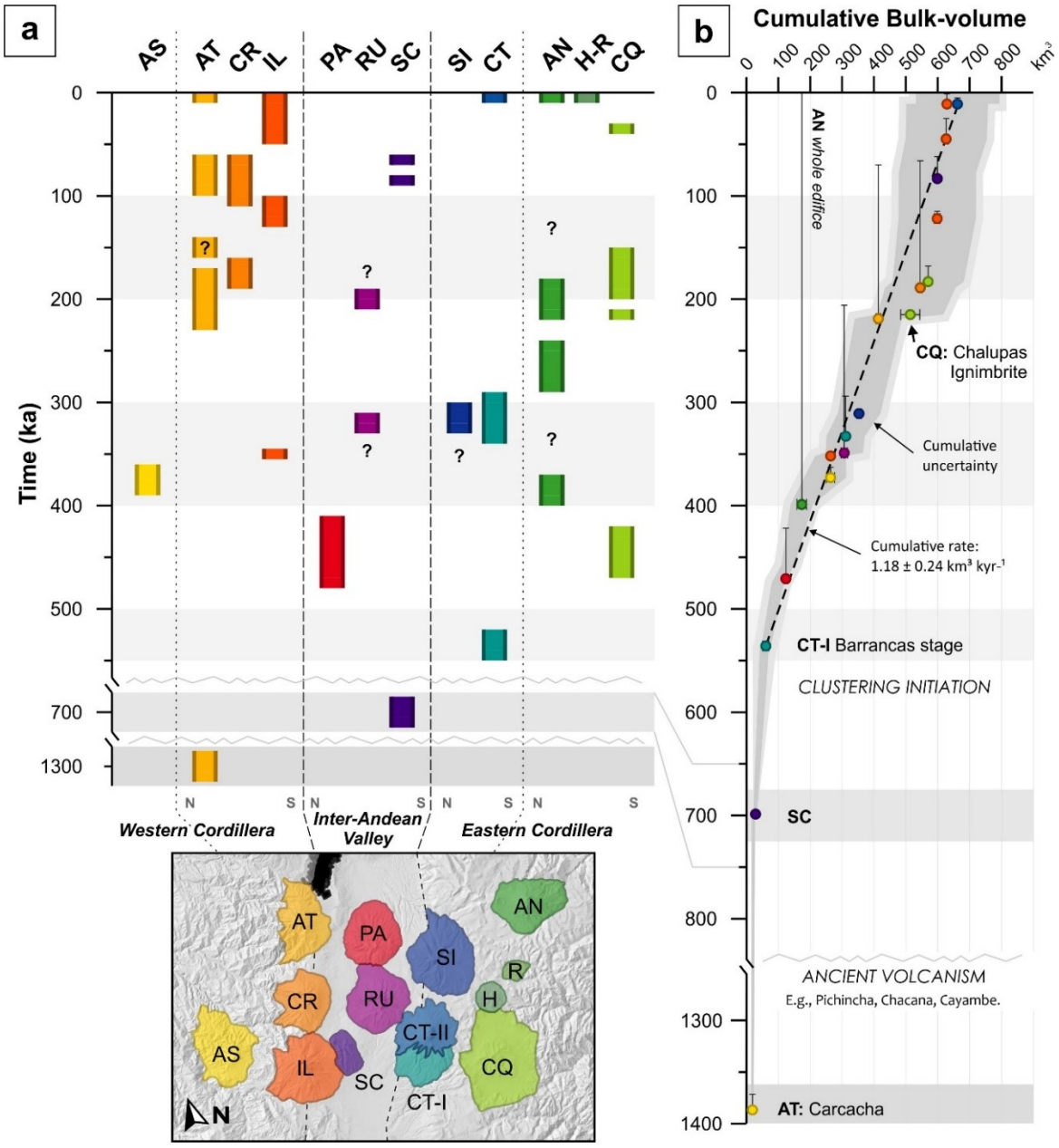

Figure 5. *Temporal evolution of volcanism in the central segment.* ***a)*** *Schematic diagram of the individual cone-building stages over time. See text for details.* ***b)*** *Cumulative bulk volume (km^3) of all volcanoes in the central segment over time. Uncertainty bars show the extent of the considered construction periods in ka according to Table 2. The bulk volumes of Antisana, Rumiñahui, Corazón and Atacazo volcanoes do not distinguish the different cone-building stages due to the lack of detailed stratigraphic data. Dashed line symbolizes the cumulative volume rate over the last ~550 ka, whereas the shaded field represents the cumulative volumetric uncertainty range. Abbreviations of volcano names as in Figure 1.*

559 The apparent quiescence period in the Western Cordillera since ~300 ka ended when the
560 volcanic activity resumed south of Carcacha volcano forming the basal edifice of Atacazo volcano. This
561 early cone was dated at 222 ± 9 and 195 ± 10 ka (groundmass $^{40}Ar/^{39}Ar$ ages; Hidalgo, 2006). Then, the
562 emplacement of the lower Corazon series occurred to the south of Atacazo around 178 ± 32 ka
563 (19EQ08). The block (17EQ59) collected from an avalanche deposit between Corazón and Atacazo
564 volcanoes yielded a K-Ar age of 149 ± 6 ka. The Sr and Th contents compared to LILE (e.g., Ba) and
565 LREE (e.g., La) of this sample (Fig. B1.1) are consistent with those observed in Atacazo volcano (Fig
566 C1), suggesting that this sample could be associated with Atacazo instead of Corazón. This suggests a
567 possible extension of the Atacazo volcanic activity up to ~150 ka.

568 In the Inter-Andean Valley, the activity resumed at Rumiñahui volcano at 207 ± 9 ka (19EQ27)
569 as is suggested by the plagioclase K-Ar age obtained from its terminal andesitic series. Nonetheless, as
570 this age could be biased towards too old values by inherited argon, it is possible that Rumiñahui volcano
571 could have been active in more recent times. Synchronously in the Eastern Cordillera, the emission of
572 the voluminous Cuyuja lava flow (11 km^3) took place from a fissure located to the southeast of Antisana
573 volcano at 210 ± 30 ka (groundmass $^{40}Ar/^{39}Ar$ plateau age (Opdyke et al., 2006; Hall et al., 2017).
574 Further south, the Chalupas ignimbrite eruption (VEI 7) took place to the southeast of Cotopaxi-I
575 volcano at 216 ± 5 ka, forming a ~17 km-wide caldera and a widespread ignimbrite deposit which
576 covered the Inter-Andean valley (Mothes and Hall, 2008; Bablon et al., 2020b). The early cone-building
577 stages of Quilindaña volcano, an intra-caldera stratovolcano, followed the Chalupas eruption between
578 184 ± 3 ka (Buenavista dome; groundmass $^{40}Ar/^{39}Ar$ age; (Córdova et al., 2020) and 169 ± 1 ka
579 (plagioclase $^{40}Ar/^{39}Ar$ age; Hammersley, 2003).

580 Finally, the volcanic activity appeared restricted to both cordilleras during the last 100 kyr. In
581 the Western Cordillera, Atacazo and Corazón volcanoes were active until at least ~70 ka (Hidalgo,
582 2006). Simultaneously, the construction of Iliniza volcano occurred to the south of the Pilongo dome
583 starting with its northern edifice at 123-116 ka. It was followed by the onset of its southern edifice at
584 46-25 ka. The growth of the Loma Saquigua cone (79-60 ka) in Santa Cruz volcano is the unique
585 eruptive activity documented in the inter-Andean valley during this period (Santamaría et al.,

586 submitted). Despite the lack of radiometric dates, stratigraphic and morphological evidence suggests
587 that the Antisana volcano was also active in this interval (Hall et al., 2017). During the Holocene, the
588 explosive activity of the Ninahuilca dome complex followed the sector collapse of Atacazo Volcano
589 (Hidalgo et al., 2008) while mainly effusive activity occurred at Iliniza volcano (Santamaría et al.,
590 submitted). In the Eastern Cordillera, several explosive rhyolitic eruptions preceded the construction of
591 the andesitic cone of Cotopaxi II (Hall and Mothes, 2008a). The fallout stratigraphic relationships
592 observed in the Eastern Cordillera suggest that the activity of the Huañuna and Rio Valle rhyolitic
593 centers apparently occurred during the Holocene (Mothes and Hall, 2008; Hall et al., 2017), as well as
594 that of Antisana volcano and Buenavista dome (Quilindaña volcano; Córdova et al., 2020).

595 Volumetric calculations indicate that the central segment volcanoes grew to roughly
596 homogeneous sizes (Table 2), reaching bulk volumes of 43 ± 12 km^3. These volumes provide a first-
597 order estimate of the amount of erupted material, despite factors such as type, distribution and
598 vesicularity of the volcanic deposits, and their syn-eruptive erosion, which are not accounted for. The
599 tephra dispersion outside the volcanic edifice is an additional factor to consider. For instance, the bulk
600 volume of fallout deposits of the Cotopaxi Holocene (< 4.5 ka) andesitic series is estimated between 4
601 and 9 km^3 (DRE volume ~1.5-3.5 km^3; Hall and Mothes, 2008a), whereas the calculated bulk volume
602 of the Cotopaxi edifice is 32 ± 3 km^3. We emphasize that all our calculated values should be considered
603 as representative for each volcano as more detailed stratigraphic studies are required to improve our
604 estimations. Figure 6b plots the accumulated bulk-volume of the central segment edifices over time.
605 The bulk volume of the Chalupas ignimbrite of 230 ± 30 km^3 (Bablon et al., 2020b) was replaced with
606 its Dense Rock Equivalent (DRE) of ~100 km^3 (Hall and Mothes, 2008a; Crosweller et al., 2012) given
607 that the higher vesicularity of this unit induces a bias in the accumulated volume. This change was
608 introduced only for comparative purposes with other volcanoes in the region. Despite the above
609 limitations, we note that the cumulative cone-building volume in the central segment has a roughly
610 stable rate of 1.18 ± 0.24 km^3/kyr since ~550 ka. Then, we deduce an overall stable magmatic production
611 in the region assuming that the cone-building volumes are proportional to the erupted volumes. This

assumption does not rule out large variations in growth or magmatic production rates throughout the eruptive history of each volcano.

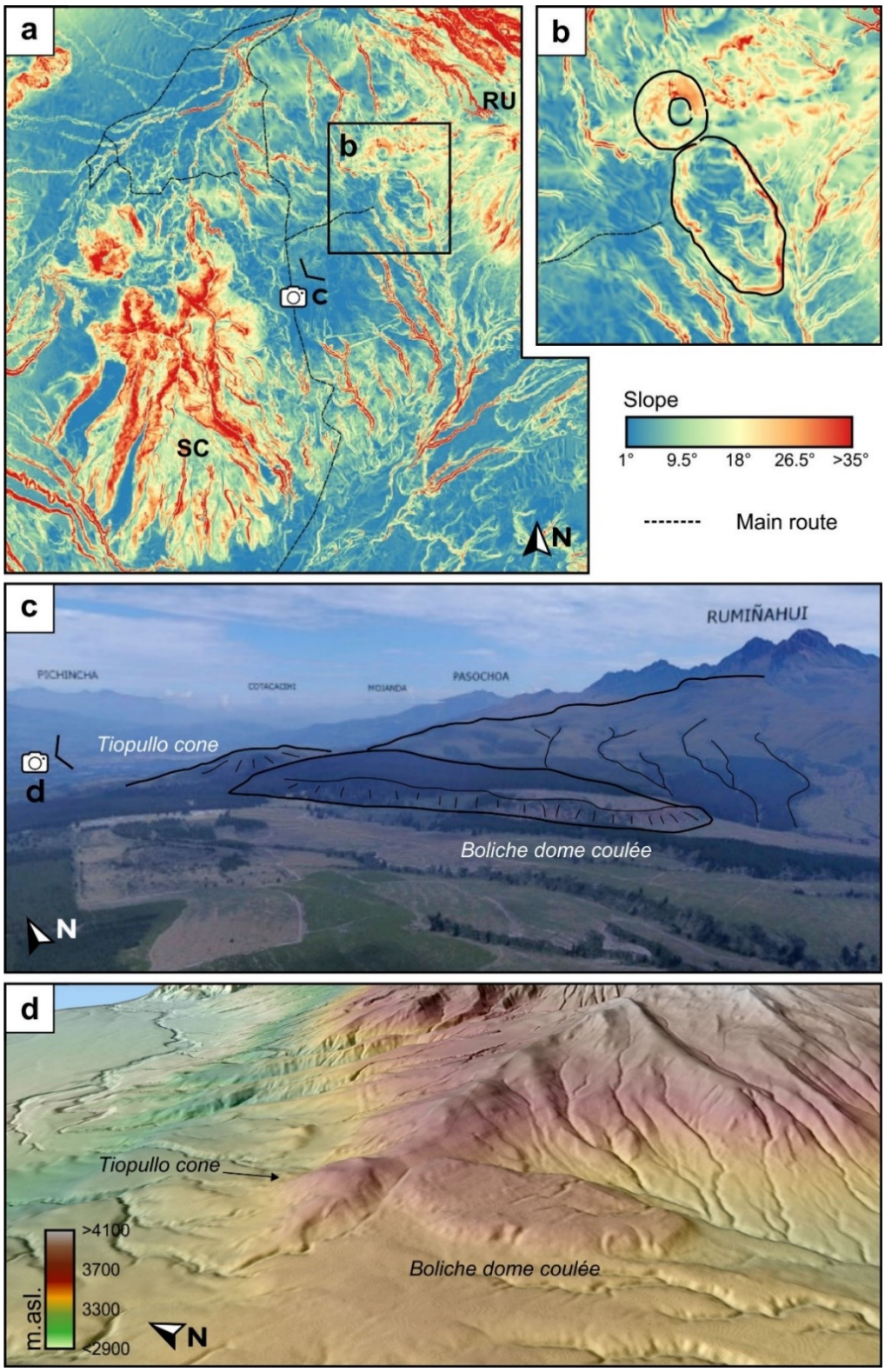

Figure 6. *Volcanic landforms observed in the Tiopullo plateau.* ***a)*** *Slope map showing the gently sloping and slightly eroded surface of the Tiopullo plateau compared to the more eroded morphology of the adjacent Santa Cruz (SC) and Rumiñahui (RM) volcanoes.* ***b)*** *Detailed view of the Tiopullo cone and the Boliche dome coulee (photography by Benjamin Bernard, IG-EPN).* ***c)*** *Photography and* ***d)*** *topographic model of the same volcanic landforms.*

5.3. Temporal and spatial arrangement of the central segment volcanoes

The most common volcanic landforms in the central segment are represented by composite stratovolcanoes, lava domes and calderas which are distributed in NE-SW alignments following the volcano corridors of the Ecuadorian arc (Fig. 1 and 2). Notably, the position of Almas Santas volcano, located 15 km east of the Volcanic Front, makes the central segment one of the widest in the Ecuadorian Andes. This location geographically closer to the trench is also shared by Quilotoa, a 3 km-wide caldera located 30 km to the south of Almas Santas. Notwithstanding this remarkable arrangement, the overall correlation between the temporal evolution and geographical position of these volcanoes is puzzling. Indeed, Figure 4 shows that although volcanic activity was permanent in each corridor for the last ~550 ka, it was unevenly distributed. This observation contrasts with the dynamics of the northern and southern segments for which Bablon et al. (2019, 2020a) described a relative migration to the northwest and south, respectively. Nevertheless, the occurrence of edifices older than 1 Ma to the north of the central segment (e.g., Cayambe, Samaniego et al., 2005; Chacana caldera, Opdyke et al., 2006; Ruco Pichincha, Robin et al., 2010; Pre-Mojanda lavas, Bablon et al., 2020a) suggests an overall southward extension of Ecuadorian volcanism (Bablon et al., 2019). From the above considerations, the central segment appears as a key area to better understand the formation of the Ecuadorian arc, and the factors that controlled the emplacement of those volcanoes placed in the central segment.

5.3.1. Spatial arrangement of volcanoes over pre-Quaternary crust structures

As previously highlighted by Litterland and Aspen (1992), the volcano distribution in the Ecuadorian arc seems to be influenced by the major tectonic structures of the continental crust formed prior to the Quaternary (Fig. 7). In the central segment, Almas Santas volcano and the Atacazo-Corazón-

Iliniza association occur above ancient N-S oriented fault systems which separate the Cretaceous oceanic plateau basalts and ophiolites units in the Western Cordillera (Hughes and Bermúdez, 1997; Hughes and Pilatasig, 2002), i.e, the Toachi and Pujilí faults. To the east, the tectonic structures of the Eastern Cordillera are covered by thick Neogene volcanic sequences. Nevertheless, the position of the Peltetec fault, for instance, is inferred based on the change in slope of the western edge of the Eastern Cordillera which coincides with the exposures of the Peltetec fault to the north in the Chota Valley and to the south in the Pizayambo area (Litherland et al., 1994; Winkler et al., 2005). The Main Arc volcanoes form N-S lignements roughly coincident with the orientation and position of these structures. The arrangement of the ancient structures of the inter-Andean valley remains unclear due to the scarce basement exposures. However, the position of the Pasochoa and Rumiñahui volcanoes, and Ilaló further north, suggests the existence of a N-S element in this area of the Inter-Andean valley.

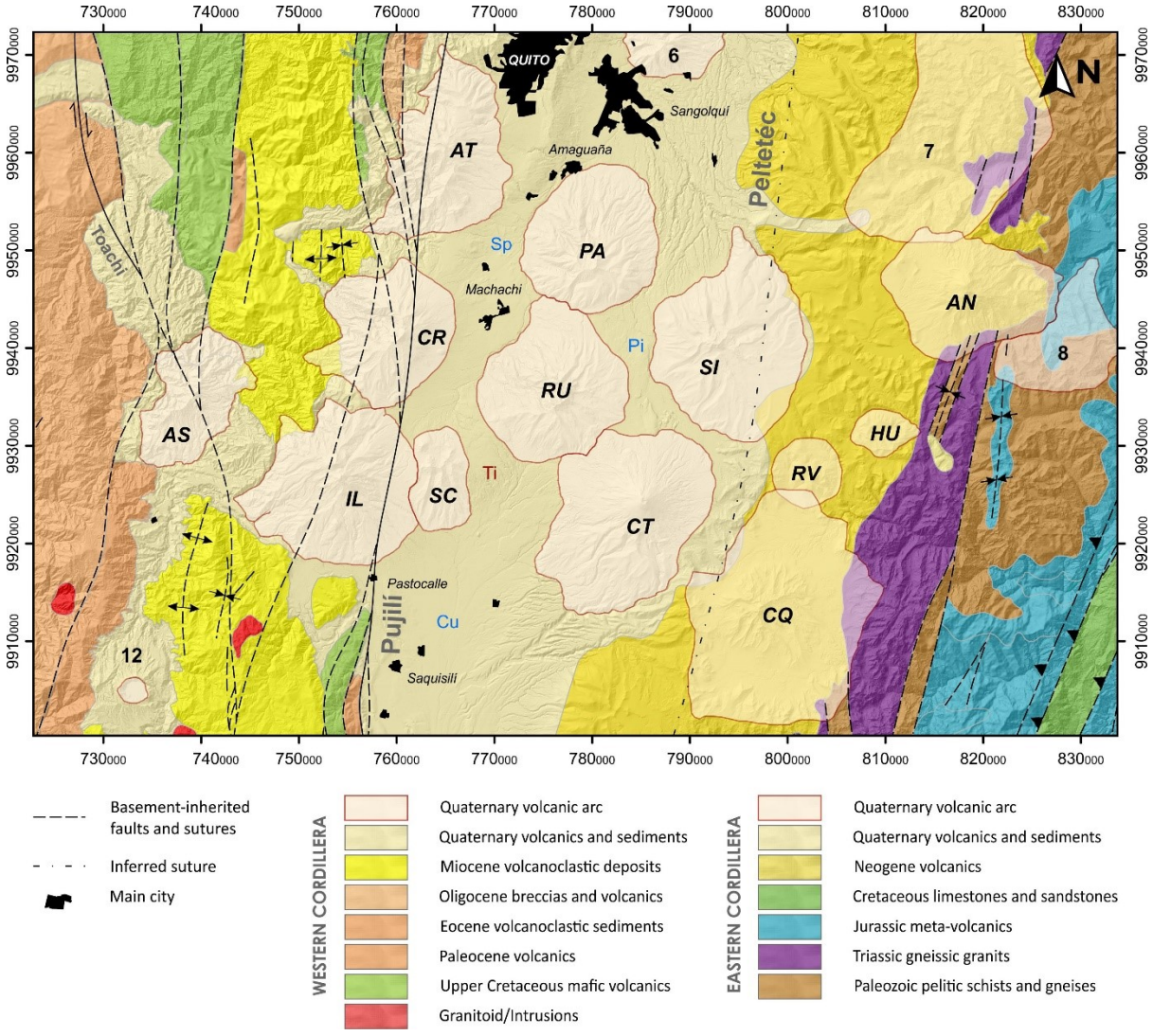

Figure 7. *Geological map of the central segment basement (Modified from Litherland et al., 1994; Hughes and Bermúdez, 1997; Egüez et al., 2017; Vallejo et al., 2020). Dashed lines show the tectonic structures inherited from basement. Pujilí suture drawn as a continuous line, and inferred location of the Peltetec suture as a dotted line. Abbreviations of volcano names as in Figure 1.*

5.3.2. Possible influences of Quaternary tectonics in the central segment volcanic landforms

Regarding Quaternary tectonics, the central segment is located in the interaction zone between the Quito and Latacunga reverse fault systems which are expressed to the north and south of the segment as parallel strands of folds located above major west dipping, blind, en echelon thrust faults (Figure 8; Fiorini and Tibaldi, 2012; Alvarado et al., 2014, 2016). These structures affect the volcano-sedimentary deposits of the eastern margin of the Inter-Andean Valley, probably converging towards the ancient Pujilí fault (Western Cordillera; Alvarado et al., 2016) below the Iliniza and Corazón volcanoes, thus affecting their volcanic structures. For instance, the Iliniza volcano exhibited a progressive migration of its activity to the south, following a NE-SW axis (Santamaría et al., submitted) consistent with the projection of the Pujilí suture, while the preserved areas of the western flank of Corazón volcano present NE-SW faults which possibly contributed to its destabilization and sector collapse. Accordingly, Figure 8 illustrates that shallow seismicity is present in this area of the Western Cordillera, following the outline of the volcanic and tectonic structures described above. Additionally, we noticed a N-S reverse fault with few meters of detachment on the east flank of the Corazón volcano, based on the systematic deflection of the small springs descending from the volcano. This fault was also described by Egüez and Yepes (1994) as the Aloag fault (Fig. 8).

To the east of Iliniza, the right-lateral strike-slip Machachi fault continues across the Inter-Andean Valley extending along the NW flank of Rumiñahui volcano toward the SE of Pasochoa volcano (Egüez and Yepes, 1994; Soulas et al., 1991). This fault affects both Pleistocene and Holocene deposits (Egüez and Yepes, 1994). We did not find strong morphological evidence of the Machachi fault trace. Nevertheless, its orientation is compatible with the strike-slip focal mechanisms observed south of Iliniza volcano (Pastocalle seismic zone; Basualto and Troncoso, 2003) and south of Pasochoa

volcano (Pita valley seismic zone; Hernández et al., 2020). Furthermore, the occurrence of intense historical earthquakes in those zones (Beauval et al., 2010) suggests a potentially higher degree of fault coupling. North of Cotopaxi volcano, Fiorini and Tibaldi (2012) described several minor strike-slip faults with NNE-SSW orientation in the Pita River valley. For these authors, the Cotopaxi volcano zone acts as a fault transfer zone that accommodates the higher shortening observed in the Latacunga basin compared to the Guayllabamba basin.

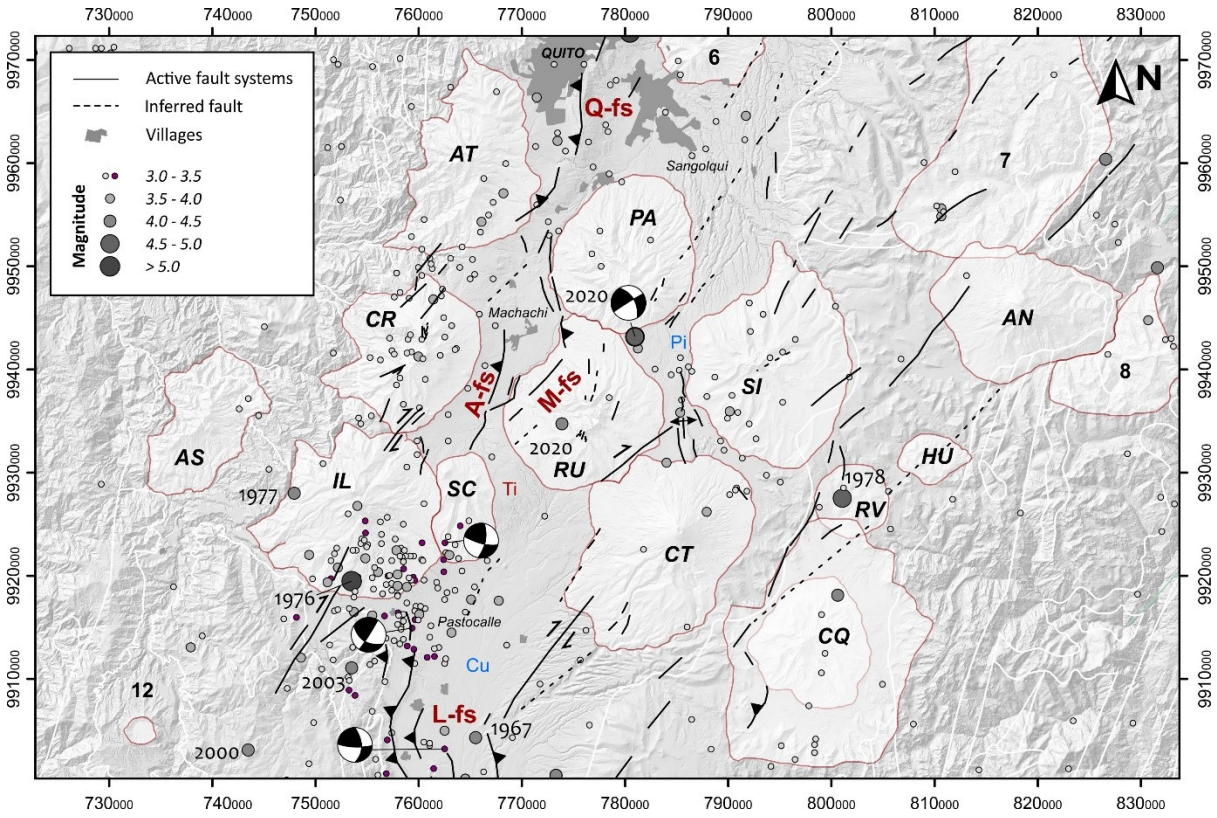

Figure 8. *Schematic map of the Quaternary fault systems of the central segment focused in the Inter-Andean Valley (Egüez and Yepes, 1994; Alvarado, 2012; Alvarado et al., 2014; Fiorini and Tibaldi, 2012; and this study). A-fs: Aloag fault-system; Q-fs: Quito fault-system; L-fs: Latacunga fault-system; M-fs: Machachi fault-system. Locations of the historical earthquakes according to the "Catalogo Homogenizado 1587 – 2011" of the IG-EPN, with hypocenter depths less than 40 km. The AD 2020 earthquake location according to Hernández et al. (2020). Moment tensor solutions from Basualto and Troncoso (2003), and Hernández et al. (2020). Abbreviations of volcano names and valleys as in Figure 1.*

Although the morphological evidence regarding the interaction between the stratovolcanoes and the strike-slip faults arrangement in the inter-Andean valley is unclear, we suggest that these faults

had an important role in the magma migration during the Pleistocene. For instance, the concurrence between the location of this transfer zone with the position of the Tiopullo plateau and its surrounding volcanic structures (e.g., Boliche and Zunfana vents), suggests that the fault arrangement could contribute to the formation of the plateau. Furthermore, minor reverse faults were identified in the inter-Andean valley to the north and south of the Tiopullo plateau (Alvarado, 2012), but no significant deformation was noticed in the Cotopaxi fallout deposits overlying the plateau.

6. CONCLUSIONS

The 20 new radiometric ages presented in this work provide the first geochronological data for the volcanoes of the central segment of Ecuador. Despite the significant erosion experienced by some volcanoes, most of the edifices were constructed during the Late Pleistocene. The volcanic activity started between ~1.3 Ma and ~700 ka with the onset of Carcacha and Santa Cruz edifices (Hidalgo, 2006; Santamaría et al., submitted). From ~550 ka onwards, the volcanic activity increased in the region with the gradual formation of a volcanic cluster composed of at least a dozen of stratovolcanoes and some smaller volcanic cones and domes, spread over a 70 km wide (E-W) and 40 km long (N-S) area. These volcanic features seem to have been randomly constructed over, or near, basement-inherited fault systems and sutures. Although Pleistocene reverse and dextral strike-slip fault systems has been observed, mainly based on structural features and shallow seismicity distribution (e.g., Soulas et al., 1991; Egüez and Yepes, 1994; Alvarado, 2012; Fiorini and Tibaldi, 2012), the minor deformation associated with such systems suggest that they probably had a secondary role in the volcanoes arrangement. Numerical reconstructions showed that the volcanic edifices from the studied area reached typical volumes between 31 and 56 km^3. Based on the proposed evolutionary history and, assuming that the petrographic heterogeneities in the volcanoes constituent materials, as well as their syn-eruptive dispersion, we suggest that the overall rate of magmatic production was roughly stable in the region during the last 550 ka. However, we do not exclude the occurrence of sporadic magmatic pulses and short periods of quiescence that could affect this rate over time.

REFERENCES

Alvarado, A., 2012. Néotectonique et cinématique de la déformation continentale en Equateur (Ph.D. thesis). Université de Grenoble, Grenoble, France.

Alvarado, A., Audin, L., Nocquet, J.M., Jaillard, E., Mothes, P., Jarrín, P., Segovia, M., Rolandone, F., Cisneros, D., 2016. Partitioning of oblique convergence in the Northern Andes subduction zone: Migration history and the present-day boundary of the North Andean Sliver in Ecuador. Tectonics 35, 1048–1065. https://doi.org/10.1002/2016TC004117

Alvarado, A., Audin, L., Nocquet, J.M., Lagreulet, S., Segovia, M., Font, Y., Lamarque, G., Yepes, H., Mothes, P., Rolandone, F., Jarrín, P., Quidelleur, X., 2014. Active tectonics in Quito, Ecuador, assessed by geomorphological studies, GPS data, and crustal seismicity. Tectonics 33, 67–83. https://doi.org/10.1002/2012TC003224

Ancellin, M.-A., Samaniego, P., Vlastélic, I., Nauret, F., Gannoun, A., Hidalgo, S., 2017. Across-arc versus along-arc Sr-Nd-Pb isotope variations in the Ecuadorian volcanic arc. Geochem. Geophys. Geosyst. 18, 1163–1188. https://doi.org/10.1002/2016GC006679

Aspden, J.A., Bonilla, W., Duque, P., 1995. The El Oro metamorphic complex, Ecuador: geology and economic mineral deposits, Overseas geology and mineral resources. British Geological Survey, Keyworth, Nottingham.

Aspden, J.A., Harrison, S.H., Rundle, C.C., 1992. New geochronological control for the tectono-magmatic evolution of the metamorphic basement, Cordillera Real and El Oro Province of Ecuador. Journal of South American Earth Sciences 6, 77–96. https://doi.org/10.1016/0895-9811(92)90019-U

Bablon, M., Quidelleur, X., Samaniego, P., Le Pennec, J.-L., Audin, L., Jomard, H., Baize, S., Liorzou, C., Hidalgo, S., Alvarado, A., 2019. Interactions between volcanism and geodynamics in the southern termination of the Ecuadorian arc. Tectonophysics 751, 54–72. https://doi.org/10.1016/j.tecto.2018.12.010

Bablon, M., Quidelleur, X., Samaniego, P., Le Pennec, J.-L., Lahitte, P., Liorzou, C., Bustillos, J.E., Hidalgo, S., 2018. Eruptive chronology of Tungurahua volcano (Ecuador) revisited based on new K-Ar ages and geomorphological reconstructions. Journal of Volcanology and Geothermal Research 357, 378–398. https://doi.org/10.1016/j.jvolgeores.2018.05.007

Bablon, M., Quidelleur, X., Samaniego, P., Le Pennec, J.-L., Santamaría, S., Liorzou, C., Hidalgo, S., Eschbach, B., 2020a. Volcanic history reconstruction in northern Ecuador: insights for eruptive and erosion rates on the whole Ecuadorian arc. Bull Volcanol 82, 11. https://doi.org/10.1007/s00445-019-1346-1

Bablon, M., Quidelleur, X., Siani, G., Samaniego, P., Le Pennec, J.-L., Nouet, J., Liorzou, C., Santamaría, S., Hidalgo, S., 2020b. Glass shard K-Ar dating of the Chalupas caldera major eruption: Main Pleistocene stratigraphic marker of the Ecuadorian volcanic arc. Quaternary Geochronology 57, 101053. https://doi.org/10.1016/j.quageo.2020.101053

Barberi, F., Coltelli, M., Ferrara, G., Innocenti, F., Navarro, J.M., Santacroce, R., 1988. Plio-quaternary volcanism in Ecuador. Geological Magazine 125, 1–14.

763 Barragan, R., Geist, D., Hall, M., Larson, P., Mark Kurz, 1998. Subduction controls on the compositions
764 of lavas from the Ecuadorian Andes. Earth and Planetary Science Letters 154, 153–166.
765 https://doi.org/10.1016/S0012-821X(97)00141-6

766 Basualto, D., Troncoso, L., 2003. Evidencias de sismicidad en la zona de Pastocalle y una eventual
767 actividad anómala del volcán Cotopaxi. Presented at the 10° Congreso Geológico Chileno,
768 Universidad de Concepción, Concepcion, Chile.

769 Beauval, C., Yepes, H., Bakun, W.H., Egred, J., Alvarado, A., Singaucho, J.-C., 2010. Locations and
770 magnitudes of historical earthquakes in the Sierra of Ecuador (1587–1996). Geophys J Int 181,
771 1613–1633. https://doi.org/10.1111/j.1365-246X.2010.04569.x

772 Bellot-Gurlet, L., Dorighel, O., Poupeau, G., 2008. Obsidian provenance studies in Colombia and
773 Ecuador: obsidian sources revisited. Journal of Archaeological Science 35, 272–289.
774 https://doi.org/10.1016/j.jas.2007.03.008

775 Bellver-Baca, M.T., Chiaradia, M., Beate, B., Beguelin, P., Deriaz, B., Mendez-Chazarra, N.,
776 Villagómez, D., 2020. Geochemical evolution of the Quaternary Chachimbiro Volcanic
777 Complex (frontal volcanic arc of Ecuador). Lithos 356–357, 105237.
778 https://doi.org/10.1016/j.lithos.2019.105237

779 Bigazzi, G., Coltelli, M., Hadler, N.J.C., Araya, A.M.O., Oddone, M., Salazar, E., 1992. Obsidian-
780 bearing lava flows and pre-Columbian artifacts from the Ecuadorian Andes: First new
781 multidisciplinary data. Journal of South American Earth Sciences 6, 21–32.
782 https://doi.org/10.1016/0895-9811(92)90014-P

783 Bigazzi, G., Coltelli, M., Halder, J., Osorio, A.M., 1997. Provenance studies of obsidian artefacts using
784 fission track analyses in South America: an overview. Presented at the Congreso Internacional
785 del Americanistas (ICA), Quito, Ecuador, pp. 1–16.

786 Bourdon, E., Eissen, J.-P., Gutscher, M.-A., Monzier, M., Hall, M.L., Cotten, J., 2003. Magmatic
787 response to early aseismic ridge subduction: the Ecuadorian margin case (South America).
788 Earth and Planetary Science Letters 205, 123–138. https://doi.org/10.1016/S0012-
789 821X(02)01024-5

790 Brook, M.S., Neall, V.E., Stewart, R.B., Dykes, R.C., Birks, D.L., 2011. Recognition and paleoclimatic
791 implications of late-Holocene glaciation on Mt Taranaki, North Island, New Zealand. The
792 Holocene 21, 1151–1158. https://doi.org/10.1177/0959683611400468

793 Bryant, J.A., Yogodzinski, G.M., Hall, M.L., Lewicki, J.L., Bailey, D.G., 2006. Geochemical
794 Constraints on the Origin of Volcanic Rocks from the Andean Northern Volcanic Zone,
795 Ecuador. Journal of Petrology 47, 1147–1175. https://doi.org/10.1093/petrology/egl006

796 Cassignol, C., Gillot, P.-Y., 1982. Range and effectiveness of unspiked potassium-argon dating:
797 experimental groundwork and applications, in: Odin, G.S. (Ed.), Numerical Dating in
798 Stratigraphy. John Wiley & Sons, pp. 159–179.

799 Chemin, S., 2004. Le volcan quaternaire Almas Santas (Cordillère occidentale, Equateur). Etude
800 volcanologique, minéralogique et géochimique (Master's thesis). Université de Lausanne,
801 Lausanne, Suisse.

Chiaradia, M., Müntener, O., Beate, B., 2020. Effects of aseismic ridge subduction on the geochemistry of frontal arc magmas. Earth and Planetary Science Letters 531, 115984. https://doi.org/10.1016/j.epsl.2019.115984

Chiaradia, M., Müntener, O., Beate, B., Fontignie, D., 2009. Adakite-like volcanism of Ecuador: lower crust magmatic evolution and recycling. Contrib Mineral Petrol 158, 563–588. https://doi.org/10.1007/s00410-009-0397-2

Cohen, K.M., Gibbard, P.L., 2019. Global chronostratigraphical correlation table for the last 2.7 million years, version 2019 QI-500. Quaternary International, SI: Quaternary International 500 500, 20–31. https://doi.org/10.1016/j.quaint.2019.03.009

Conway, C.E., Leonard, G.S., Townsend, D.B., Calvert, A.T., Wilson, C.J.N., Gamble, J.A., Eaves, S.R., 2016. A high-resolution 40Ar/39Ar lava chronology and edifice construction history for Ruapehu volcano, New Zealand. Journal of Volcanology and Geothermal Research 327, 152–179. https://doi.org/10.1016/j.jvolgeores.2016.07.006

Córdova, M.D., Mothes, P.A., Gaunt, H.E., Salgado, J., 2020. Post-Caldera Eruptions at Chalupas Caldera, Ecuador: Determining the Timing of Lava Dome Collapse, Hummock Emplacement and Dome Rejuvenation. Front. Earth Sci. 8. https://doi.org/10.3389/feart.2020.548251

Cotten, J., Le Dez, A., Bau, M., Caroff, M., Maury, R.C., Dulski, P., Fourcade, S., Bohn, M., Brousse, R., 1995. Origin of anomalous rare-earth element and yttrium enrichments in subaerially exposed basalts: Evidence from French Polynesia. Chemical Geology 119, 115–138. https://doi.org/10.1016/0009-2541(94)00102-E

Crosweller, H.S., Arora, B., Brown, S.K., Cottrell, E., Deligne, N.I., Guerrero, N.O., Hobbs, L., Kiyosugi, K., Loughlin, S.C., Lowndes, J., Nayembil, M., Siebert, L., Sparks, R.S.J., Takarada, S., Venzke, E., 2012. Global database on large magnitude explosive volcanic eruptions (LaMEVE). Journal of Applied Volcanology 1, 4. https://doi.org/10.1186/2191-5040-1-4

DeMets, C., Gordon, R.G., Argus, D.F., 2010. Geologically current plate motions. Geophysical Journal International 181, 1–80. https://doi.org/10.1111/j.1365-246X.2009.04491.x

Dibacto, S., Lahitte, P., Karátson, D., Hencz, M., Szakács, A., Biró, T., Kovács, I., Veres, D., 2020. Growth and erosion rates of the East Carpathians volcanoes constrained by numerical models: Tectonic and climatic implications. Geomorphology 368, 107352. https://doi.org/10.1016/j.geomorph.2020.107352

Egüez, A., Gaona, M., Albán, A., 2017. Mapa Geológico de la República del Ecuador.

Egüez, A., Yepes, H., 1994. Estudio neotectonico y de peligro sismico para el Proyecto Hidroelectrico Toachi. Instituto Ecuatoriano de Electrificacion - INECEL, Quito, Ecuador.

Fiorini, E., Tibaldi, A., 2012. Quaternary tectonics in the central Interandean Valley, Ecuador: Fault-propagation folds, transfer faults and the Cotopaxi Volcano. Global and Planetary Change, Coupled deep Earth and surface processes in System Earth: monitoring, reconstruction and process modeling 90–91, 87–103. https://doi.org/10.1016/j.gloplacha.2011.06.002

Garrison, J., Davidson, J., Reid, M., Turner, S., 2006. Source versus differentiation controls on U-series disequilibria: Insights from Cotopaxi Volcano, Ecuador. Earth and Planetary Science Letters 244, 548–565. https://doi.org/10.1016/j.epsl.2006.02.013

842 Garrison, J.M., Davidson, J.P., Hall, M., Mothes, P., 2011. Geochemistry and Petrology of the Most
843 Recent Deposits from Cotopaxi Volcano, Northern Volcanic Zone, Ecuador. Journal of
844 Petrology 52, 1641–1678. https://doi.org/10.1093/petrology/egr023

845 Germa, A., Lahitte, P., Quidelleur, X., 2015. Construction and destruction of Mont Pelée volcano:
846 Volumes and rates constrained from a geomorphological model of evolution. Journal of
847 Geophysical Research: Earth Surface 120, 1206–1226. https://doi.org/10.1002/2014JF003355

848 Germa, A., Quidelleur, X., Gillot, P.Y., Tchilinguirian, P., 2010. Volcanic evolution of the back-arc
849 Pleistocene Payun Matru volcanic field (Argentina). Journal of South American Earth Sciences
850 29, 717–730. https://doi.org/10.1016/j.jsames.2010.01.002

851 Germa, A., Quidelleur, X., Lahitte, P., Labanieh, S., Chauvel, C., 2011. The K–Ar Cassignol–Gillot
852 technique applied to western Martinique lavas: A record of Lesser Antilles arc activity from
853 2Ma to Mount Pelée volcanism. Quaternary Geochronology 6, 341–355.
854 https://doi.org/10.1016/j.quageo.2011.02.001

855 Gillot, P.-Y., Cornette, Y., Max, N., Floris, B., 1992. Two reference materials, Trachytes MDO-G and
856 ISH-G, for Argon Dating (K-Ar and 40Ar/39Ar) of Pleistocene and Holocene rocks.
857 Geostandards Newsletter 16, 55–60. https://doi.org/10.1111/j.1751-908X.1992.tb00487.x

858 Gillot, P.Y., Hildenbrand, A., Lefèvre, J.C., Albore-Livadie, C., 2006. The K/Ar dating method:
859 principle, analytical techniques, and application to Holocene volcanic eruptions in Southern
860 Italy. Acta Vulcanologica 18, 55–66.

861 Grosse, P., Ochi Ramacciotti, M.L., Escalante Fochi, F., Guzmán, S., Orihashi, Y., Sumino, H., 2020.
862 Geomorphology, morphometry, spatial distribution and ages of mafic monogenetic volcanoes
863 of the Peinado and Incahuasi fields, southernmost Central Volcanic Zone of the Andes. Journal
864 of Volcanology and Geothermal Research 401, 106966.
865 https://doi.org/10.1016/j.jvolgeores.2020.106966

866 Grosse, P., Orihashi, Y., Guzmán, S.R., Sumino, H., Nagao, K., 2018. Eruptive history of Incahuasi,
867 Falso Azufre and El Cóndor Quaternary composite volcanoes, southern Central Andes. Bull
868 Volcanol 80, 1–26. https://doi.org/10.1007/s00445-018-1221-5

869 Grosse, P., Vries, B. van W. de, Petrinovic, I.A., Euillades, P.A., Alvarado, G.E., 2009. Morphometry
870 and evolution of arc volcanoes. Geology 37, 651–654. https://doi.org/10.1130/G25734A.1

871 Gutscher, M.-A., Malavieille, J., Lallemand, S., Collot, J.-Y., 1999. Tectonic segmentation of the North
872 Andean margin: impact of the Carnegie Ridge collision. Earth and Planetary Science Letters
873 168, 255–270. https://doi.org/10.1016/S0012-821X(99)00060-6

874 Hall, M.L., Beate, B., 1991. El volcanismo plio cuaternario en los Andes del Ecuador, in: El paisaje
875 volcánico de la sierra ecuatoriana: geomorfología, fenómenos volcánicos y recursos asociados,
876 Estudios de Geografia. Corporación Editora Nacional, Quito, pp. 5–17.

877 Hall, M.L., Mothes, P., 2008a. The rhyolitic–andesitic eruptive history of Cotopaxi volcano, Ecuador.
878 Bull Volcanol 70, 675–702. https://doi.org/10.1007/s00445-007-0161-2

879 Hall, M.L., Mothes, P.A., 2008b. The Chacana caldera complex in Ecuador, in: Volume 3: Collapse
880 Calderas Workshop. Presented at the IOP Conference Series: Earth and Environmental Science
881 (EES), IOP Publishing, Querétaro, Mexico. https://doi.org/10.1088/1755-1307/3/1/012004

Hall, M.L., Mothes, P.A., Samaniego, P., Militzer, A., Beate, B., Ramón, P., Robin, C., 2017. Antisana volcano: A representative andesitic volcano of the eastern cordillera of Ecuador: Petrography, chemistry, tephra and glacial stratigraphy. Journal of South American Earth Sciences 73, 50–64. https://doi.org/10.1016/j.jsames.2016.11.005

Hall, M.L., Samaniego, P., Le Pennec, J.L., Johnson, J.B., 2008. Ecuadorian Andes volcanism: A review of Late Pliocene to present activity. Journal of Volcanology and Geothermal Research, Recent and active volcanism in the Ecuadorian Andes 176, 1–6. https://doi.org/10.1016/j.jvolgeores.2008.06.012

Hall, M.L., Wood, C.A., 1985. Volcano-tectonic segmentation of the northern Andes. Geology 13, 203–207. https://doi.org/10.1130/0091-7613(1985)13<203:VSOTNA>2.0.CO;2

Hammersley, L.C., 2003. Isotopic evidence for the relative roles of fractional crystallization, crustal assimilation and magma supply in the generation of large volume rhyolitic eruptions (Ph.D. thesis). University of California, Berkeley, CA.

Hernández, S., Acosta, E., Barros, J., Acero, W., 2020. Sismos en Ecuador - Pichincha (Informe Sísmico Especial No. 2020– 009). Instituto Geofísico, Escuela Politécnica Nacional, Quito, Ecuador.

Hidalgo, S., 2006. Les intéractions entre magmas calco-alcalins “classiques” et adakitiques: exemple du complexe volcanique Atacazo-Ninahuilca (Equateur) (Ph.D. thesis). Université Blaise Pascal - Clermont-Ferrand II, Clermont-Ferrand, France.

Hidalgo, S., Gerbe, M.C., Martin, H., Samaniego, P., Bourdon, E., 2012. Role of crustal and slab components in the Northern Volcanic Zone of the Andes (Ecuador) constrained by Sr–Nd–O isotopes. Lithos 132–133, 180–192. https://doi.org/10.1016/j.lithos.2011.11.019

Hidalgo, S., Monzier, M., Almeida, E., Chazot, G., Eissen, J.-P., van der Plicht, J., Hall, M.L., 2008. Late Pleistocene and Holocene activity of the Atacazo–Ninahuilca Volcanic Complex (Ecuador). Journal of Volcanology and Geothermal Research, Recent and active volcanism in the Ecuadorian Andes 176, 16–26. https://doi.org/10.1016/j.jvolgeores.2008.05.017

Hidalgo, S., Monzier, M., Martin, H., Chazot, G., Eissen, J.-P., Cotten, J., 2007. Adakitic magmas in the Ecuadorian Volcanic Front: Petrogenesis of the Iliniza Volcanic Complex (Ecuador). Journal of Volcanology and Geothermal Research 159, 366–392. https://doi.org/10.1016/j.jvolgeores.2006.07.007

Hildenbrand, A., Marques, F.O., Catalão, J., 2018. Large-scale mass wasting on small volcanic islands revealed by the study of Flores Island (Azores). Scientific Reports 8, 13898. https://doi.org/10.1038/s41598-018-32253-0

Hoffer, G., 2008. Fusion partielle d’un manteau métasomatisé par un liquide adakitique : approches géochimique et expérimentale de la genèse et de l’évolution des magmas de l’arrière-arc équatorien (Ph.D. thesis). Université Blaise Pascal - Clermont-Ferrand II, Clermont-Ferrand, France.

Hora, J.M., Singer, B.S., Wörner, G., 2007. Volcano evolution and eruptive flux on the thick crust of the Andean Central Volcanic Zone: 40Ar/39Ar constraints from Volcán Parinacota, Chile. GSA Bulletin 119, 343–362. https://doi.org/10.1130/B25954.1

Hughes, R.A., Bermúdez, R., 1997. Geology of the Cordillera Occidental of Ecuador between 0°00' and 1°00'S (No. 4), Proyecto de Desarrollo Minero y Control Ambiental. Cogidem - Brithis Geological Survey, Quito.

Hughes, R.A., Pilatasig, L.F., 2002. Cretaceous and Tertiary terrane accretion in the Cordillera Occidental of the Andes of Ecuador. Tectonophysics, Andean Geodynamics ISAG 4 345, 29–48. https://doi.org/10.1016/S0040-1951(01)00205-0

Hungerbühler, D., Steinmann, M., Winkler, W., Seward, D., Egüez, A., Peterson, D.E., Helg, U., Hammer, C., 2002. Neogene stratigraphy and Andean geodynamics of southern Ecuador. Earth-Science Reviews 57, 75–124. https://doi.org/10.1016/S0012-8252(01)00071-X

Jaillard, E., Ordoñez, M., Suárez, J., Toro, J., Iza, D., Lugo, W., 2004. Stratigraphy of the late Cretaceous–Paleogene deposits of the cordillera occidental of central ecuador: geodynamic implications. Journal of South American Earth Sciences 17, 49–58. https://doi.org/10.1016/j.jsames.2004.05.003

John, T., Scherer, E.E., Schenk, V., Herms, P., Halama, R., Garbe-Schönberg, D., 2010. Subducted seamounts in an eclogite-facies ophiolite sequence: the Andean Raspas Complex, SW Ecuador. Contrib Mineral Petrol 159, 265–284. https://doi.org/10.1007/s00410-009-0427-0

Jomard, H., Saqui, D., Baize, S., Alvarado, A., Bernard, B., Audin, L., Hidalgo, S., Pacheco, D., Ruiz, M., Segovia, M., 2021. Interactions between active tectonics and gravitational deformation along the Billecocha fault system (Northern Ecuador): Insights from morphological and paleoseismological investigations. Journal of South American Earth Sciences 111, 103406. https://doi.org/10.1016/j.jsames.2021.103406

Lagmay, A.M.F., van Wyk de Vries, B., Kerle, N., Pyle, D.M., 2000. Volcano instability induced by strike-slip faulting. Bull Volcanol 62, 331–346. https://doi.org/10.1007/s004450000103

Lahitte, P., Samper, A., Quidelleur, X., 2012. DEM-based reconstruction of southern Basse-Terre volcanoes (Guadeloupe archipelago, FWI): Contribution to the Lesser Antilles Arc construction rates and magma production. Geomorphology, Volcano Geomorphology: landforms, processes and hazards 136, 148–164. https://doi.org/10.1016/j.geomorph.2011.04.008

Lavenu, A., Winter, T., Dávila, F., 1995. A Pliocene–Quaternary compressional basin in the Interandean Depression, Central Ecuador. Geophysical Journal International 121, 279–300. https://doi.org/10.1111/j.1365-246X.1995.tb03527.x

Litherland, M., Aspden, J.A., 1992. Terrane-boundary reactivation: A control on the evolution of the Northern Andes. Journal of South American Earth Sciences 5, 71–76. https://doi.org/10.1016/0895-9811(92)90060-C

Litherland, M., Aspden, J.A., Jemielita, R.A., 1994. The metamorphic belts of Ecuador, Overseas Memoir Institute of Geological Sciences. British Geological Survey, Keyworth, Nottingham.

Lonsdale, P., 2005. Creation of the Cocos and Nazca plates by fission of the Farallon plate. Tectonophysics 404, 237–264. https://doi.org/10.1016/j.tecto.2005.05.011

Luzieux, L.D.A., Heller, F., Spikings, R., Vallejo, C.F., Winkler, W., 2006. Origin and Cretaceous tectonic history of the coastal Ecuadorian forearc between 1°N and 3°S: Paleomagnetic, radiometric and fossil evidence. Earth and Planetary Science Letters 249, 400–414. https://doi.org/10.1016/j.epsl.2006.07.008

962 Mathieu, L., van Wyk de Vries, B., 2011. The impact of strike-slip, transtensional and transpressional
963 fault zones on volcanoes. Part 1: Scaled experiments. Journal of Structural Geology 33, 907–
964 917. https://doi.org/10.1016/j.jsg.2011.03.002

965 Mathieu, L., van Wyk de Vries, B., Pilato, M., Troll, V.R., 2011. The interaction between volcanoes
966 and strike-slip, transtensional and transpressional fault zones: Analogue models and natural
967 examples. Journal of Structural Geology 33, 898–906.
968 https://doi.org/10.1016/j.jsg.2011.03.003

969 Meschede, M., Barckhausen, U., 2000. Plate Tectonic Evolution of the Cocos-Nazca Spreading Center.
970 Proc. ODP, Sci. Results, Fluid, Mass, and Thermal Fluxes in the Pacific Margin of Costa Rica
971 170, 1–10. https://doi.org/doi:10.2973/odp.proc.sr.170.009.2000

972 Michaud, F., Witt, C., Royer, J.-Y., 2009. Influence of the subduction of the Carnegie volcanic ridge
973 on Ecuadorian geology: Reality and fiction, in: Ramos, V.A., Dickinson, W.R., Kay, S.M.
974 (Eds.), Backbone of the Americas: Shallow Subduction, Plateau Uplift, and Ridge and Terrane
975 Collision, Memoir - Geological Society of America. The Geological Society of America, pp.
976 217–228. https://doi.org/10.1130/2009.1204(10)

977 Mothes, P.A., Hall, M.L., 2008. Rhyolitic calderas and centers clustered within the active andesitic belt
978 of Ecuador's Eastern Cordillera, in: Volume 3: Collapse Calderas Workshop. Presented at the
979 IOP Conference Series: Earth and Environmental Science, IOP Publishing, Querétaro, Mexico,
980 p. 012007. https://doi.org/10.1088/1755-1307/3/1/012007

981 Nocquet, J.-M., Villegas-Lanza, J.C., Chlieh, M., Mothes, P.A., Rolandone, F., Jarrin, P., Cisneros, D.,
982 Alvarado, A., Audin, L., Bondoux, F., Martin, X., Font, Y., Régnier, M., Vallée, M., Tran, T.,
983 Beauval, C., Mendoza, J.M.M., Martinez, W., Tavera, H., Yepes, H., 2014. Motion of
984 continental slivers and creeping subduction in the northern Andes. Nature Geoscience 7, 287–
985 291. https://doi.org/10.1038/ngeo2099

986 O'Connor, J.M., Stoffers, P., Wijbrans, Jan.R., Worthington, T.J., 2007. Migration of widespread long-
987 lived volcanism across the Galápagos Volcanic Province: Evidence for a broad hotspot melting
988 anomaly? Earth and Planetary Science Letters 263, 339–354.
989 https://doi.org/10.1016/j.epsl.2007.09.007

990 Opdyke, N.D., Hall, M., Mejia, V., Huang, K., Foster, D.A., 2006. Time-averaged field at the equator:
991 Results from Ecuador. Geochemistry, Geophysics, Geosystems 7.
992 https://doi.org/10.1029/2005GC001221

993 Pallares, C., Quidelleur, X., Debreil, J.A., Antoine, C., Sarda, P., Tchilinguirian, P., Delpech, G., Gillot,
994 P.-Y., 2019. Quaternary evolution of the El Tromen volcanic system, Argentina, based on new
995 K-Ar and geochemical data: Insights for temporal evolution of magmatic processes between
996 arc and back-arc settings. Journal of South American Earth Sciences 90, 338–354.
997 https://doi.org/10.1016/j.jsames.2018.12.022

998 Pallares, C., Quidelleur, X., Gillot, P.-Y., Kluska, J.-M., Tchilinguirian, P., Sarda, P., 2016. The
999 temporal evolution of back-arc magmas from the Auca Mahuida shield volcano (Payenia
1000 Volcanic Province, Argentina). Journal of Volcanology and Geothermal Research 323, 19–37.
1001 https://doi.org/10.1016/j.jvolgeores.2016.04.043

Peccerillo, A., Taylor, S.R., 1976. Geochemistry of eocene calc-alkaline volcanic rocks from the Kastamonu area, Northern Turkey. Contr. Mineral. and Petrol. 58, 63–81. https://doi.org/10.1007/BF00384745

Pedraza Garcia, P., Vargas, C.A., Monsalve J., H., 2007. Geometric model of the Nazca plate subduction in southwest Colombia. Earth Sciences Research Journal 11, 124–134.

Pistolesi, M., Cioni, R., Rosi, M., Cashman, K.V., Rossotti, A., Aguilera, E., 2013. Evidence for lahar-triggering mechanisms in complex stratigraphic sequences: the post-twelfth century eruptive activity of Cotopaxi Volcano, Ecuador. Bull Volcanol 75, 1–18. https://doi.org/10.1007/s00445-013-0698-1

Portner, D.E., Rodríguez, E.E., Beck, S., Zandt, G., Scire, A., Rocha, M.P., Bianchi, M.B., Ruiz, M., França, G.S., Condori, C., Alvarado, P., 2020. Detailed Structure of the Subducted Nazca Slab into the Lower Mantle Derived From Continent-Scale Teleseismic P Wave Tomography. Journal of Geophysical Research: Solid Earth 125, e2019JB017884. https://doi.org/10.1029/2019JB017884

Pure, L.R., Leonard, G.S., Townsend, D.B., Wilson, C.J.N., Calvert, A.T., Cole, R.P., Conway, C.E., Gamble, J.A., Smith, T. 'Bubs,' 2020. A high resolution 40Ar/39Ar lava chronology and edifice construction history for Tongariro volcano, New Zealand. Journal of Volcanology and Geothermal Research 403, 106993. https://doi.org/10.1016/j.jvolgeores.2020.106993

Quidelleur, X., Gillot, P.-Y., Soler, V., Lefèvre, J.-C., 2001. K/Ar dating extended into the last millennium: Application to the youngest effusive episode of the Teide Volcano (Spain). Geophysical Research Letters 28, 3067–3070. https://doi.org/10.1029/2000GL012821

Raczek, I., Stoll, B., Hofmann, A.W., Peter Jochum, K., 2001. High-Precision Trace Element Data for the USGS Reference Materials BCR-1, BCR-2, BHVO-1, BHVO-2, AGV-1, AGV-2, DTS-1, DTS-2, GSP-1 and GSP-2 by ID-TIMS and MIC-SSMS. Geostandards Newsletter 25, 77–86. https://doi.org/10.1111/j.1751-908X.2001.tb00789.x

Robin, C., Samaniego, P., Le Pennec, J.-L., Fornari, M., Mothes, P., van der Plicht, J., 2010. New radiometric and petrological constraints on the evolution of the Pichincha volcanic complex (Ecuador). Bull Volcanol 72, 1109–1129. https://doi.org/10.1007/s00445-010-0389-0

Salgado, J.A., Mothes, P.A., Córdova, M.D., 2021. New observations on the recent eruptive activity of Sumaco Volcano (Ecuador), based on geochronology, stratigraphy and petrography. Journal of South American Earth Sciences 112, 103568. https://doi.org/10.1016/j.jsames.2021.103568

Samaniego, P., Martin, H., Monzier, M., Robin, C., Fornari, M., Eissen, J.-P., Cotten, J., 2005. Temporal Evolution of Magmatism in the Northern Volcanic Zone of the Andes: The Geology and Petrology of Cayambe Volcanic Complex (Ecuador). Journal of Petrology 46, 2225–2252. https://doi.org/10.1093/petrology/egi053

Santamaría, S., Quidelleur, X., Hidalgo, S., Samaniego, P., Le Pennec, J.-L., Liorzou, C., Lahitte, P., Córdova, M., Espin, P., submitted. Geochronological evolution of the potentially active Iliniza Volcano (Ecuador) based on new K-Ar ages. Journal of Volcanology and Geothermal Research.

Schiano, P., Monzier, M., Eissen, J.-P., Martin, H., Koga, K.T., 2010. Simple mixing as the major control of the evolution of volcanic suites in the Ecuadorian Andes. Contrib Mineral Petrol 160, 297–312. https://doi.org/10.1007/s00410-009-0478-2

Schwarz, W.H., Trieloff, M., 2007. Intercalibration of 40Ar–39Ar age standards NL-25, HB3gr hornblende, GA1550, SB-3, HD-B1 biotite and BMus/2 muscovite. Chemical Geology 242, 218–231. https://doi.org/10.1016/j.chemgeo.2007.03.016

Sierra, D., Vasconez, F., Andrade, S.D., Almeida, M., Mothes, P., 2019. Historical Distal Lahar Deposits on the Remote Eastern-Drainage of Cotopaxi Volcano, Ecuador. Journal of South American Earth Sciences 95, 102251. https://doi.org/10.1016/j.jsames.2019.102251

Soulas, J.-P., Eguez, A., Yepes, Hugo, Perez, H., 1991. Tectónica activa y riesgo sísmico en los Andes Ecuatorianos y el extremo sur de Colombia. Bol. Geol. Ecuat. 2, 3–11.

Spikings, R., Cochrane, R., Villagomez, D., Van der Lelij, R., Vallejo, C., Winkler, W., Beate, B., 2015. The geological history of northwestern South America: from Pangaea to the early collision of the Caribbean Large Igneous Province (290–75Ma). Gondwana Research 27, 95–139. https://doi.org/10.1016/j.gr.2014.06.004

Spikings, R., Crowhurst, P.V., Winkler, W., Villagomez, D., 2010. Syn- and post-accretionary cooling history of the Ecuadorian Andes constrained by their in-situ and detrital thermochronometric record. Journal of South American Earth Sciences 30, 121–133. https://doi.org/10.1016/j.jsames.2010.04.002

Starr, J.P., 1984. Geology and petrology of Rumiñahui volcano, Ecuador (Master's thesis). Departament of Geology of the University the Oregon, Oregon, USA.

Steiger, R.H., Jäger, E., 1977. Subcommission on geochronology: Convention on the use of decay constants in geo- and cosmochronology. Earth and Planetary Science Letters 36, 359–362. https://doi.org/10.1016/0012-821X(77)90060-7

Sun, S.-S., McDonough, W.F., 1989. Chemical and isotopic systematics of oceanic basalts: implications for mantle composition and processes. Geol. Soc. Lond. Spec. Publ. 42, 313–345. https://doi.org/10.1144/GSL.SP.1989.042.01.19

Tsunematsu, K., Bonadonna, C., 2015. Grain-size features of two large eruptions from Cotopaxi volcano (Ecuador) and implications for the calculation of the total grain-size distribution. Bull Volcanol 77, 1–12. https://doi.org/10.1007/s00445-015-0949-4

Vallejo, C., Almagor, S., Romero, C., Herrera, J.L., Escobar, V., Spikings, R., Winkler, W., Vermeesch, P., 2020. Sedimentology, Provenance and Radiometric Dating of the Silante Formation: Implications for the Cenozoic Evolution of the Western Andes of Ecuador. Minerals 10, 929. https://doi.org/10.3390/min10100929

Vallejo, C., Romero, C., Horton, B.K., Spikings, R.A., Gaibor, J., Winkler, W., Esteban, J.J., Thomsen, T.B., Mariño, E., 2021. Jurassic to Early Paleogene sedimentation in the Amazon region of Ecuador: Implications for the paleogeographic evolution of northwestern South America. Global and Planetary Change 204, 103555. https://doi.org/10.1016/j.gloplacha.2021.103555

Vallejo, C., Spikings, R., Horton, B.K., Luzieux, L., Romero, C., Winkler, W., Thomsen, T.B., 2019. Chapter 8 - Late cretaceous to miocene stratigraphy and provenance of the coastal forearc and Western Cordillera of Ecuador: Evidence for accretion of a single oceanic plateau fragment, in: Horton, B.K., Folguera, A. (Eds.), Andean Tectonics. Elsevier, pp. 209–236. https://doi.org/10.1016/B978-0-12-816009-1.00010-1

Vezzoli, L., Apuani, T., Corazzato, C., Uttini, A., 2017. Geological and geotechnical characterization of the debris avalanche and pyroclastic deposits of Cotopaxi Volcano (Ecuador). A contribute to instability-related hazard studies. Journal of Volcanology and Geothermal Research 332, 51–70. https://doi.org/10.1016/j.jvolgeores.2017.01.004

Villagómez, D., Spikings, R., Magna, T., Kammer, A., Winkler, W., Beltrán, A., 2011. Geochronology, geochemistry and tectonic evolution of the Western and Central cordilleras of Colombia. Lithos 125, 875–896. https://doi.org/10.1016/j.lithos.2011.05.003

Villares, F., Garcia-Casco, A., Blanco-Quintero, I.F., Montes, C., Reyes, P.S., Cardona, A., 2020. The Peltetec ophiolitic belt (Ecuador): a window to the tectonic evolution of the Triassic margin of western Gondwana. International Geology Review 0, 1–25. https://doi.org/10.1080/00206814.2020.1830313

Winkler, W., Villagómez, D., Spikings, R., Abegglen, P., Tobler, St., Egüez, A., 2005. The Chota basin and its significance for the inception and tectonic setting of the inter-Andean depression in Ecuador. Journal of South American Earth Sciences, Cenozoic Andean Basin Evolution 19, 5–19. https://doi.org/10.1016/j.jsames.2004.06.006

Witt, C., Bourgois, J., 2010. Forearc basin formation in the tectonic wake of a collision-driven, coastwise migrating crustal block: The example of the North Andean block and the extensional Gulf of Guayaquil-Tumbes Basin (Ecuador-Peru border area). GSA Bulletin 122, 89–108. https://doi.org/10.1130/B26386.1

Witt, C., Bourgois, J., Michaud, F., Ordoñez, M., Jiménez, N., Sosson, M., 2006. Development of the Gulf of Guayaquil (Ecuador) during the Quaternary as an effect of the North Andean block tectonic escape. Tectonics 25. https://doi.org/10.1029/2004TC001723

Yamamoto, T., Kudo, T., Isizuka, O., 2018. Temporal variations in volumetric magma eruption rates of Quaternary volcanoes in Japan. Earth Planets Space 70, 1–12. https://doi.org/10.1186/s40623-018-0849-x

Yepes, H., Audin, L., Alvarado, A., Beauval, C., Aguilar, J., Font, Y., Cotton, F., 2016. A new view for the geodynamics of Ecuador: Implication in seismogenic source definition and seismic hazard assessment. Tectonics 35, 1249–1279. https://doi.org/10.1002/2015TC003941

Zernack, A.V., Procter, J.N., Cronin, S.J., 2009. Sedimentary signatures of cyclic growth and destruction of stratovolcanoes: A case study from Mt. Taranaki, New Zealand. Sedimentary Geology, Source to sink 220, 288–305. https://doi.org/10.1016/j.sedgeo.2009.04.024

Appendix A.

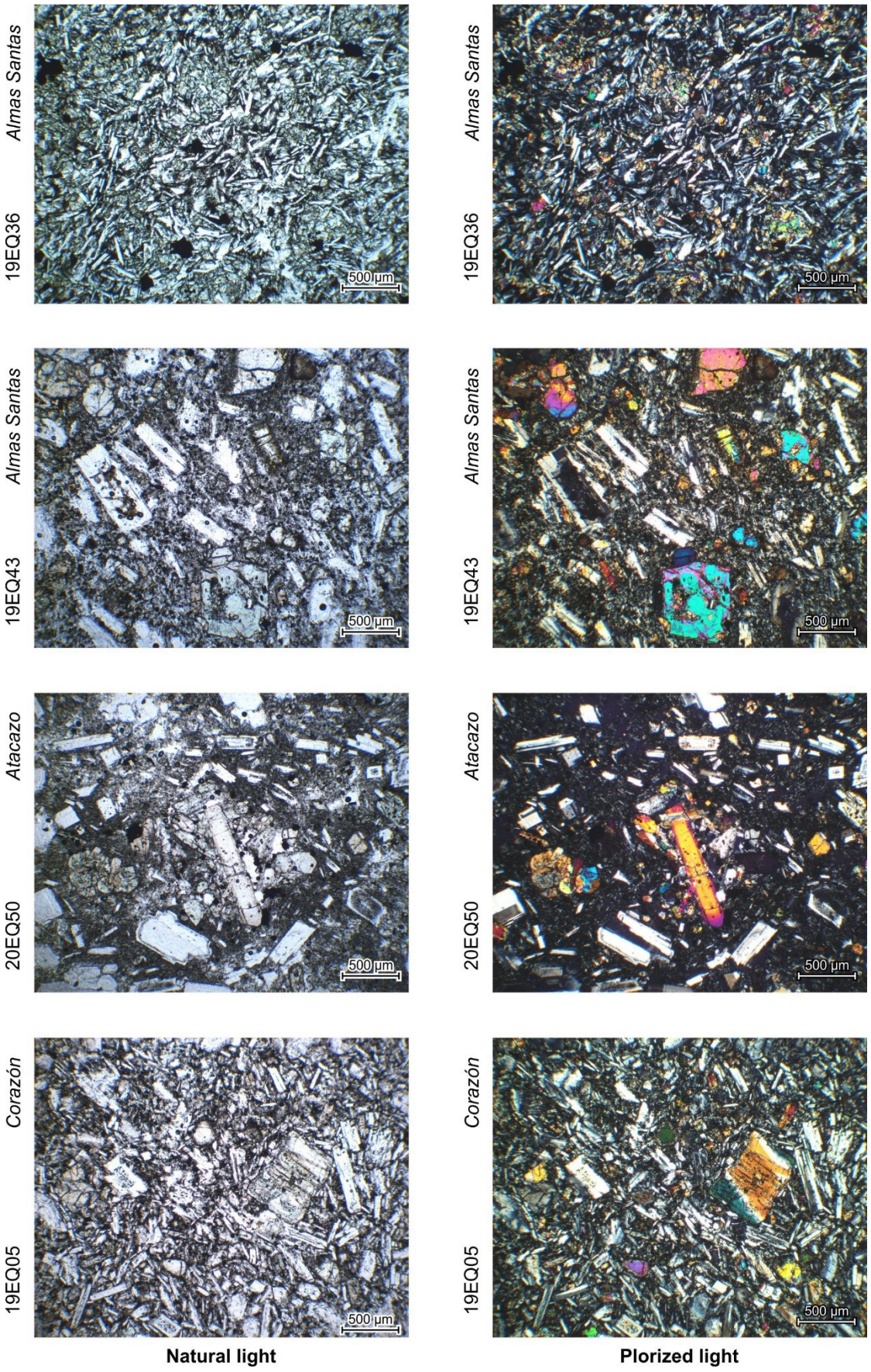
Almas Santas
19EQ36
500 µm
Almas Santas
19EQ36
500 µm
Almas Santas
19EQ43
500 µm
Almas Santas
19EQ43
500 µm
Atacazo
20EQ50
500 µm
Atacazo
20EQ50
500 µm
Corazón
19EQ05
500 µm
Corazón
19EQ05
500 µm
Natural light
Plorized light

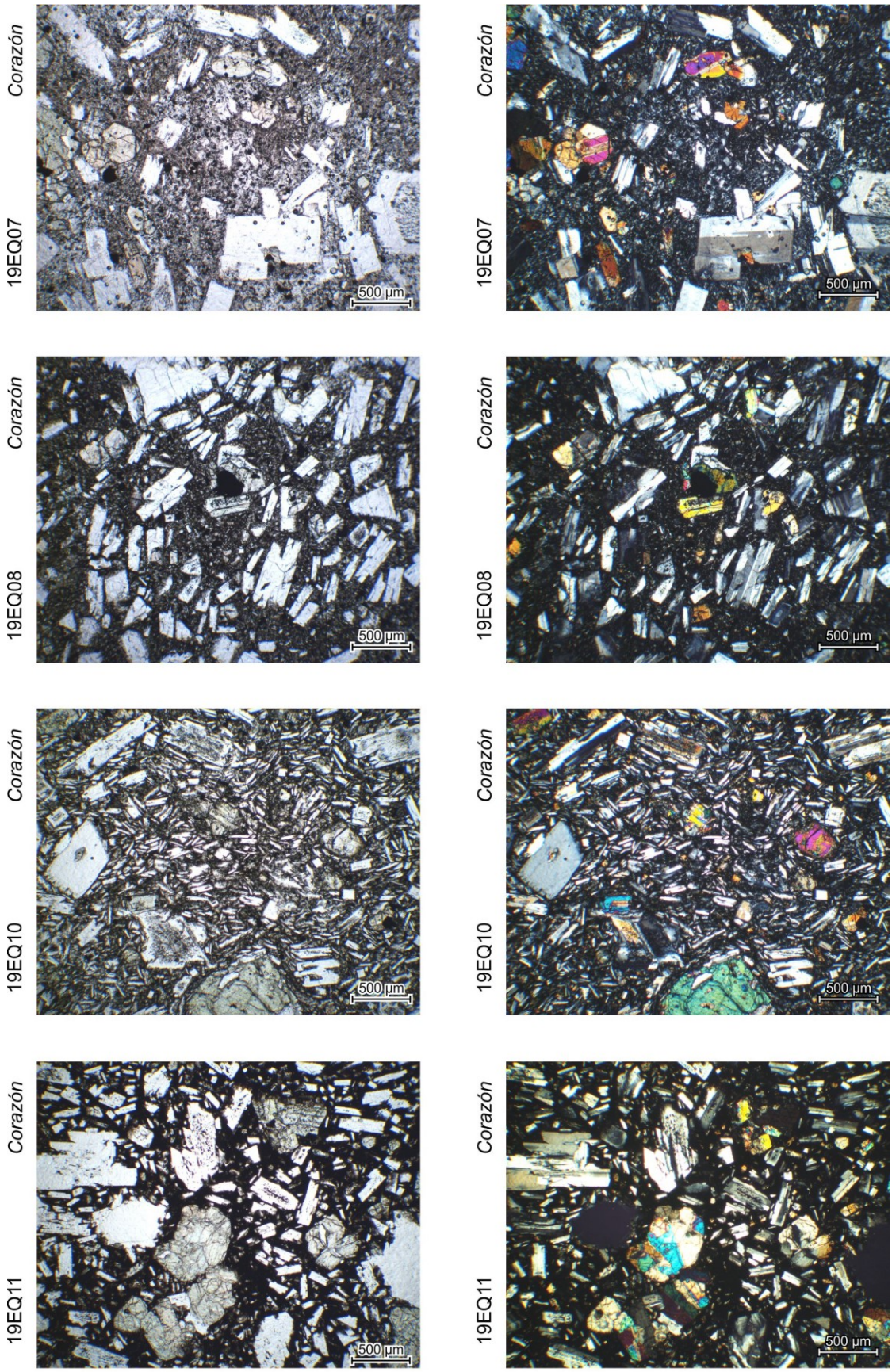
Corazón
19EQ07
500 µm
Corazón
19EQ07
500 µm
Corazón
19EQ08
500 µm
Corazón
19EQ08
500 µm
Corazón
19EQ10
500 µm
Corazón
19EQ10
500 µm
Corazón
19EQ11
500 µm
Corazón
19EQ11
500 µm
Natural light
Plorized light

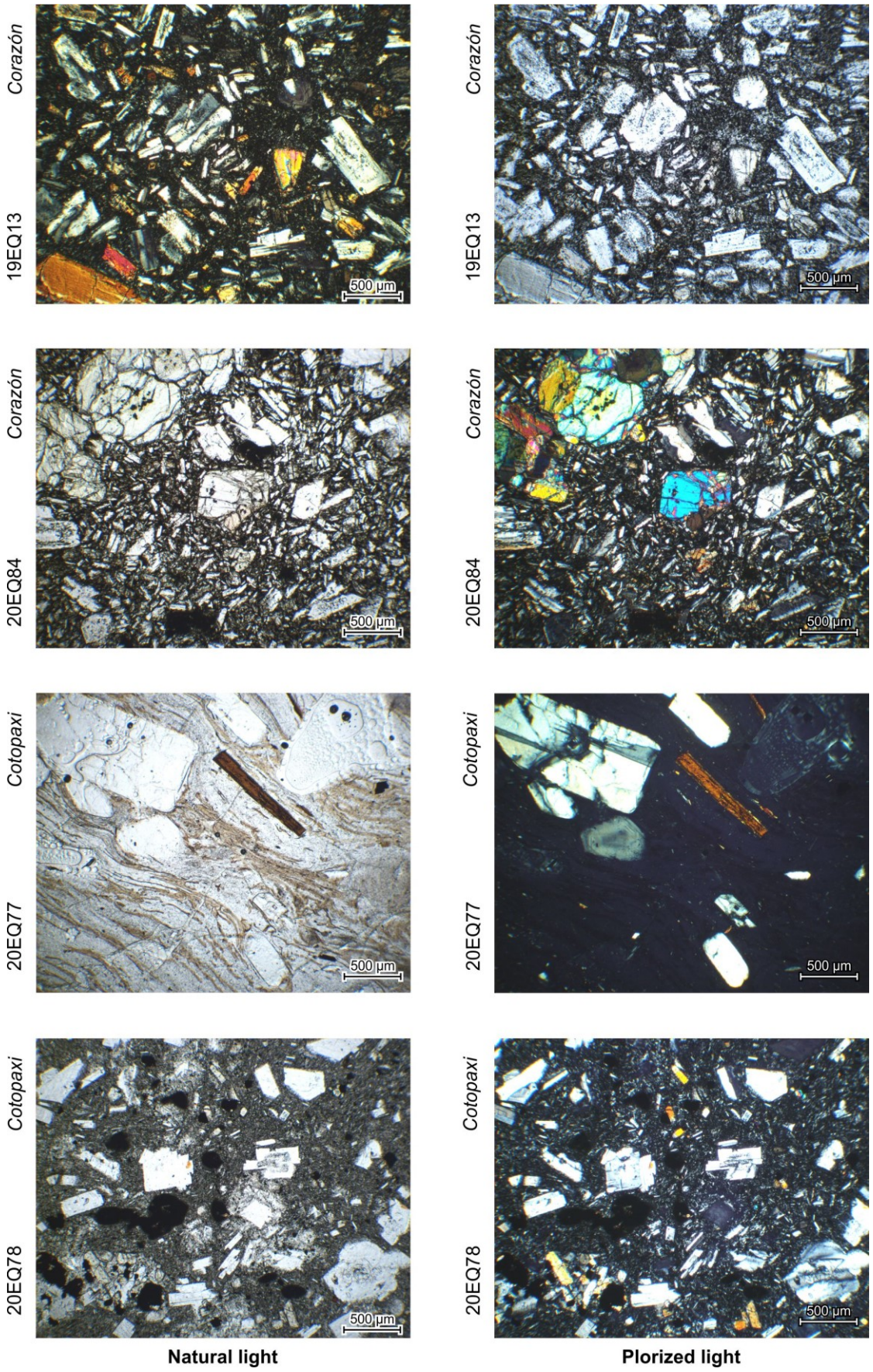
Corazón
19EQ13
500 µm
Corazón
19EQ13
500 µm
Corazón
20EQ84
500 µm
Corazón
20EQ84
500 µm
Cotopaxi
20EQ77
500 µm
Cotopaxi
20EQ77
500 µm
Cotopaxi
20EQ78
500 µm
Cotopaxi
20EQ78
500 µm
Natural light
Plorized light

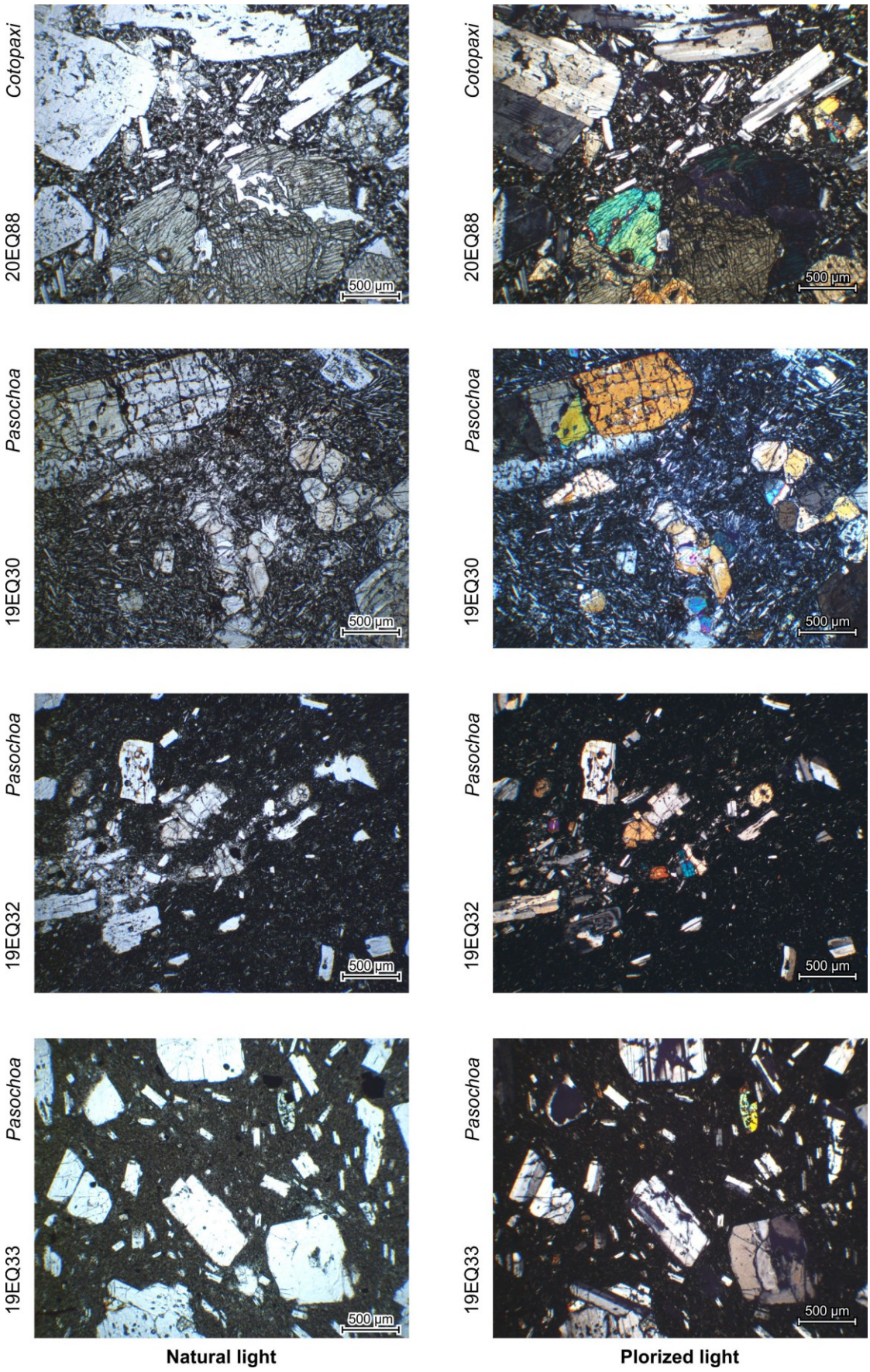
Cotopaxi
20EQ88
Pasochoa
19EQ30
Pasochoa
19EQ32
Pasochoa
19EQ33
500 µm
Natural light
Plorized light

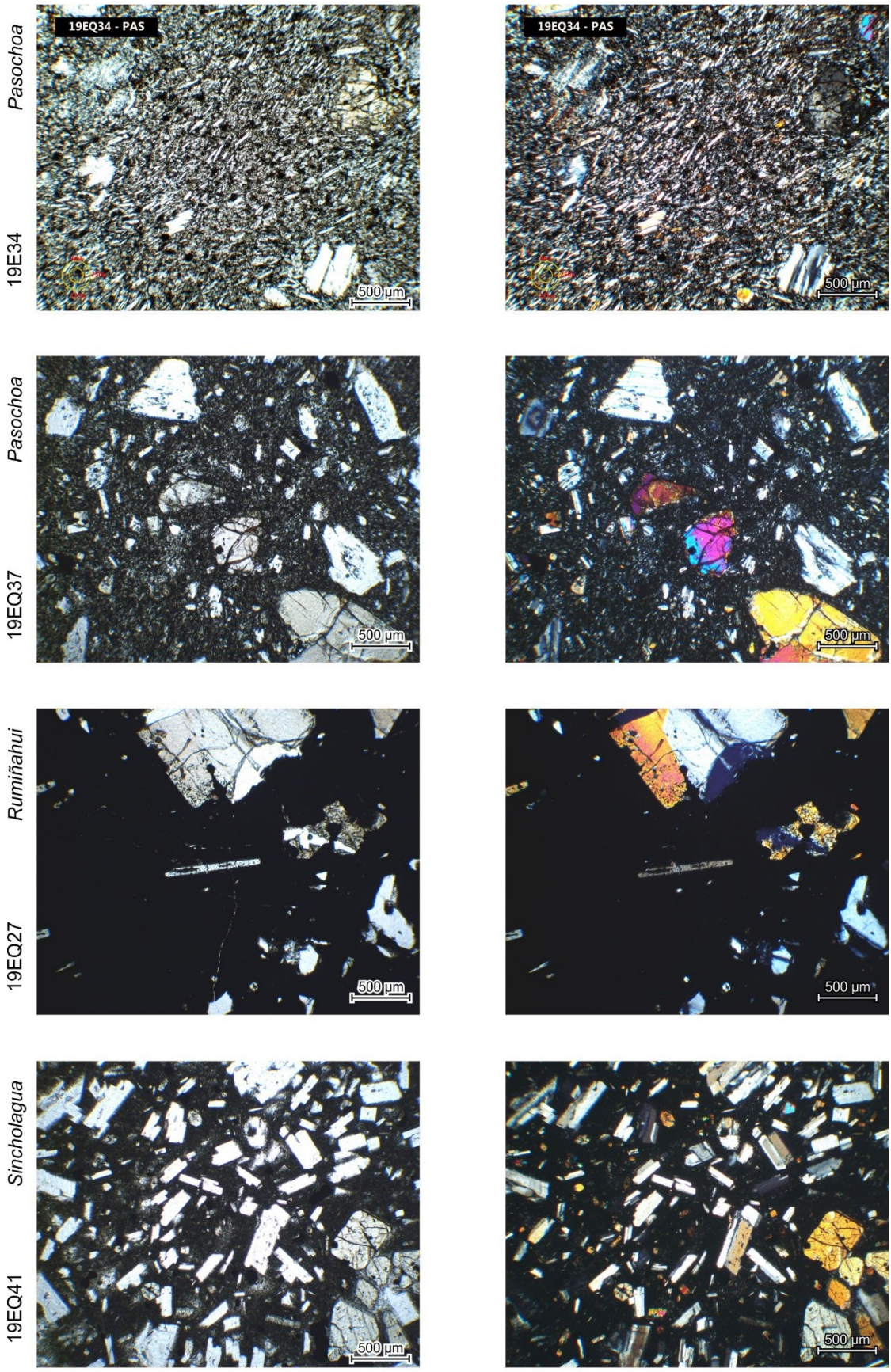
Pasochoa
19E34
19EQ34 - PAS
500 µm
Pasochoa
19EQ37
500 µm
Rumiñahui
19EQ27
500 µm
Sincholagua
19EQ41
500 µm
Natural light
Plorized light

Appendix B

Major and trace element composition of whole-rock samples. All major data were brought down to a total of 100%. *(Santamaría et al.)*

	Almas Santas		Corazón						
Sample	19EQ36	19EQ43	20EQ50	19EQ05	19EQ07	19EQ08	19EQ09	19EQ10	19EQ11
wt.%									
SiO_2	54.64	55.69	62.28	54.84	58.97	57.56	56.13	57.18	57.77
TiO_2	0.78	0.73	0.56	0.84	0.73	0.80	0.72	0.73	0.75
Al_2O_3	16.41	16.79	16.27	16.79	17.53	17.30	17.13	17.56	16.64
Fe_2O_3	8.92	8.44	6.06	8.63	7.42	7.71	8.21	7.89	7.78
MnO	0.13	0.13	0.09	0.13	0.11	0.11	0.14	0.12	0.11
MgO	6.57	6.37	2.62	5.63	3.15	3.93	4.52	4.11	4.56
CaO	8.00	7.17	5.48	8.15	6.57	6.74	8.12	7.16	7.25
Na_2O	3.61	3.70	3.96	3.81	4.18	4.27	3.82	3.98	3.91
K_2O	0.75	0.81	1.48	0.97	1.17	1.25	1.04	1.09	1.04
P_2O_5	0.17	0.17	0.13	0.21	0.18	0.34	0.16	0.18	0.18
L.O.I.	-0.17	0.76	0.66	-0.34	-0.09	0.87	1.36	-0.12	0.24
ppm									
Sc	21.09	23.12	12.68	22.29	13.83	13.90	21.44	16.83	19.20
V	204.02	200.10	127.54	206.89	164.77	164.56	199.07	180.67	179.02
Cr	291.67	297.97	40.48	159.10	25.59	66.60	73.01	69.03	135.18
Co	34.12	32.32	15.36	29.68	18.84	21.29	25.98	22.78	25.05
Ni	102.59	113.00	12.48	54.26	14.03	29.93	41.67	30.84	46.95
Rb	11.30	14.41	50.63	16.73	23.00	20.91	17.45	17.52	16.92
Sr	490.76	479.61	396.24	582.44	476.74	629.47	463.71	500.54	513.33
Y	13.23	13.76	13.29	12.53	13.2	13.88	17.23	13.87	12.51
Zr	83.93	80.4	100.28	90.89	104.84	122.16	87.13	95.14	96.16
Nb	2.69	1.13	3.38	4.01	3.29	6.84	2.41	3.99	3.03
Ba	341.38	382.64	566.54	441.73	510.25	559.71	457.70	494.23	441.96
La	9.21	8.99	10.52	12.17	10.50	16.17	12.76	13.86	10.27
Ce	20.62	15.67	22.05	27.78	21.21	32.52	19.49	27.48	25.15
Nd	20.68	16.52	11.87	21.93	24.24	23.40	25.67	19.18	18.95
Sm	3.31	2.01	3.02	3.32	3.13	4.04	2.75	2.65	2.99
Eu	0.79	1.01	0.74	0.82	0.86	1.05	0.81	0.85	0.78
Gd	2.76	2.77	2.57	3.05	2.83	3.58	3.38	2.95	2.76
Dy	2.19	2.34	2.12	2.26	2.37	2.54	2.79	2.51	2.08
Er	1.11	0.81	1.12	1.08	1.06	1.57	1.90	1.56	0.79
Yb	1.15	1.17	1.01	1.07	1.10	1.10	1.50	1.24	1.10
Th	1.12	1.05	2.08	1.93	2.16	2.58	1.91	3.81	2.05

	Corazón						Cotopaxi		
Sample	19EQ13	19EQ14a	19EQ15A	19EQ15B	20EQ83	20EQ84	19EQ29	20EQ76	20EQ77
wt.%									
SiO_2	57.61	63.59	54.42	59.68	53.37	55.42	57.20	61.93	73.83
TiO_2	0.72	0.56	0.82	0.59	0.84	0.82	0.92	0.52	0.19
Al_2O_3	17.18	16.43	16.65	17.87	16.07	16.57	16.85	17.57	14.77
Fe_2O_3	7.77	5.54	9.08	6.83	8.40	8.51	8.30	5.92	1.52
MnO	0.11	0.09	0.13	0.11	0.12	0.12	0.11	0.09	0.08
MgO	4.22	2.48	6.10	2.73	5.93	5.78	4.20	2.20	0.39
CaO	7.00	5.08	8.25	6.32	7.96	7.77	6.78	5.81	1.73
Na_2O	4.08	4.20	3.54	3.99	3.74	3.87	4.03	4.04	4.68
K_2O	1.13	1.85	0.77	1.17	0.87	0.90	1.36	1.75	2.73
P_2O_5	0.18	0.18	0.17	0.19	0.26	0.24	0.25	0.18	0.09
L.O.I.	-0.09	1.01	-0.04	1.11	1.06	0.64	0.26	0.85	2.76
ppm									
Sc	16.52	9.81	22.70	12.35	19.39	17.54	15.58	12.85	1.56
V	179.15	108.36	212.33	128.36	202.91	199.10	184.77	121.92	8.13
Cr	130.87	35.45	223.59	31.23	245.13	229.59	107.45	9.77	4.07
Co	24.94	13.88	30.46	16.95	30.92	29.14	25.95	12.75	0.14
Ni	41.85	15.03	67.78	16.78	83.78	87.05	49.76	6.44	0.00
Rb	14.54	37.20	14.74	26.42	11.79	15.47	28.26	36.49	62.61
Sr	537.35	454.28	506.20	537.13	611.36	565.71	611.70	703.48	302.77
Y	12.4	12.82	14.1	14.32	14.65	12.78	16.34	14.92	9.56
Zr	100.09	134.53	88.93	119.54	88.75	89.68	125.58	104.47	75.83
Nb	4.26	4.97	3.31	4.26	5.46	4.52	4.91	4.42	6.84
Ba	485.88	735.84	344.94	573.12	405.20	382.24	547.22	672.36	931.60
La	10.86	15.93	8.76	11.87	11.20	12.64	20.09	16.83	20.09
Ce	19.97	28.80	19.36	22.66	25.72	24.61	34.51	31.27	38.45
Nd	17.61	31.93	11.89	14.21	13.99	14.19	32.62	15.53	14.82
Sm	3.28	3.10	2.82	3.44	3.01	3.38	4.14	3.05	2.23
Eu	0.91	0.77	0.85	0.98	0.90	0.87	1.39	0.87	0.57
Gd	2.81	2.87	2.96	2.81	2.96	3.31	4.39	3.12	1.90
Dy	2.07	1.90	2.58	2.27	2.34	2.34	2.64	2.42	1.35
Er	1.08	0.80	1.31	1.33	1.06	0.31	1.11	1.29	0.69
Yb	0.98	1.07	1.22	1.28	0.99	1.02	1.04	1.45	0.75
Th	1.91	4.33	1.26	2.24	1.68	1.76	3.59	6.07	6.99

	Cotopaxi		Pasochoa							
Sample	20EQ78	20EQ88	19EQ30	19EQ31	19EQ32	19EQ33	19EQ34	19EQ37	19EQ38	19EQ42b
wt.%										
SiO_2	60.66	57.71	56.37	58.68	57.03	62.94	55.86	58.13	56.85	56.66
TiO_2	0.57	0.91	0.74	0.74	0.87	0.76	0.75	0.76	0.83	0.77
Al_2O_3	17.87	16.84	15.30	16.62	18.49	17.86	16.93	17.83	18.56	17.95
Fe_2O_3	6.35	7.91	8.84	7.68	7.72	5.88	8.58	7.72	8.34	8.11
MnO	0.11	0.10	0.13	0.11	0.10	0.08	0.13	0.11	0.11	0.13
MgO	2.58	3.98	6.54	4.16	2.80	1.28	5.22	3.19	3.22	3.64
CaO	5.98	6.86	7.55	6.87	7.29	4.96	7.74	6.98	7.71	7.54
Na_2O	4.12	4.06	3.39	3.85	4.38	4.30	3.76	4.11	4.15	3.88
K_2O	1.58	1.38	0.96	1.11	1.10	1.70	0.86	1.00	0.87	1.15
P_2O_5	0.18	0.26	0.18	0.18	0.22	0.23	0.17	0.17	0.18	0.19
L.O.I.	0.24	0.15	-0.15	0.48	-0.07	1.30	-0.07	0.12	0.02	0.64
ppm										
Sc	13.32	15.14	23.45	18.18	14.55	8.68	22.42	15.10	15.49	17.73
V	132.19	186.47	194.50	177.90	186.26	125.26	199.34	187.68	199.24	192.06
Cr	9.40	105.75	316.44	129.97	25.10	4.92	138.37	55.32	48.12	49.06
Co	15.42	25.29	32.28	25.44	21.73	13.27	30.82	22.70	22.75	25.59
Ni	8.72	49.91	107.24	46.74	23.72	5.61	61.62	30.78	31.71	33.74
Rb	35.52	26.59	21.13	21.21	16.83	39.22	22.32	22.59	17.24	19.34
Sr	665.90	625.37	381.27	456.98	554.50	440.28	473.80	459.44	505.61	537.18
Y	15.6	15.32	16.23	15.05	18.04	19.95	15.91	14.07	13.97	13.39
Zr	99.02	130.68	104.29	109.73	112.3	160.11	92.05	100.44	85.97	88.96
Nb	4.47	5.69	3.28	3.04	4.57	5.54	3.08	2.68	3.53	2.97
Ba	643.17	592.26	379.83	459.94	524.46	766.23	404.03	460.11	388.97	474.10
La	15.99	18.31	9.63	11.14	15.46	30.15	9.57	9.96	9.27	9.28
Ce	31.69	35.28	20.50	23.53	23.50	36.83	20.71	18.04	18.25	17.12
Nd	15.38	19.67	19.28	26.76	26.50	50.67	16.57	17.19	12.83	14.20
Sm	2.95	3.98	3.80	3.23	4.42	6.05	2.51	2.46	2.72	2.19
Eu	0.90	1.18	0.80	0.93	1.36	1.43	0.79	0.94	0.96	0.92
Gd	3.12	3.96	3.39	3.18	4.19	5.58	3.18	3.23	2.84	3.07
Dy	2.52	2.71	2.52	2.23	3.42	3.58	2.57	2.28	2.54	2.29
Er	1.21	1.03	0.81	0.82	1.41	1.05	1.39	0.88	1.40	0.86
Yb	1.56	1.06	1.33	1.19	1.57	1.41	1.36	1.08	1.21	1.15
Th	4.18	3.61	1.43	1.82	1.46	3.44	1.19	1.42	1.26	1.23

	Rumiñahui				Sincholagua		
Sample	19EQ27	19EQ28	19EQ35	19EQ39	19EQ40	19EQ41	20EQ86
wt.%							
SiO_2	61.71	55.64	53.28	62.36	62.43	59.75	60.18
TiO_2	1.01	0.94	0.91	0.95	0.63	0.64	0.67
Al_2O_3	16.05	18.20	17.32	15.65	16.71	17.42	17.93
Fe_2O_3	6.82	7.97	9.06	6.50	5.70	6.85	6.95
MnO	0.09	0.11	0.12	0.08	0.11	0.10	0.10
MgO	2.42	3.92	6.02	2.18	2.79	3.35	2.50
CaO	5.14	7.65	8.58	4.77	5.30	6.08	6.13
Na_2O	4.08	4.12	3.66	3.93	4.10	4.26	3.90
K_2O	2.34	1.20	0.82	2.54	2.04	1.35	1.47
P_2O_5	0.34	0.24	0.24	0.33	0.21	0.19	0.17
L.O.I.	0.24	0.01	2.38	0.36	1.43	-0.01	0.81
ppm							
Sc	11.62	15.47	18.91	11.15	9.80	12.43	12.93
V	173.42	195.92	206.20	155.10	111.39	135.66	144.76
Cr	59.37	129.39	184.59	61.37	60.94	103.35	7.97
Co	16.65	24.65	32.62	16.29	13.99	20.03	16.66
Ni	25.53	54.26	75.33	25.27	27.19	37.87	11.03
Rb	66.04	25.00	18.71	79.98	47.84	33.29	29.90
Sr	456.92	613.32	663.81	413.97	533.82	579.38	500.06
Y	23.49	14.89	13.31	22.1	12.02	13.26	13.74
Zr	237.74	116.24	92.1	277.08	130	106.93	101.43
Nb	9.91	4.51	4.13	9.79	6.19	3.49	5.81
Ba	821.06	466.52	415.03	922.78	588.68	532.53	535.05
La	29.69	15.29	12.03	29.51	17.03	13.84	15.65
Ce	58.83	31.13	25.90	62.35	31.22	26.83	26.47
Nd	44.30	21.84	21.43	32.01	24.78	24.00	14.90
Sm	6.41	3.90	2.93	7.00	3.61	2.76	3.27
Eu	1.45	1.06	1.04	1.56	0.97	1.04	0.72
Gd	5.75	3.68	3.21	5.85	3.07	2.57	3.23
Dy	3.94	2.54	2.30	4.08	1.75	2.16	2.41
Er	1.81	1.00	0.85	2.01	0.78	1.16	0.94
Yb	1.61	1.19	1.04	1.75	0.96	1.05	1.16
Th	8.36	3.14	1.25	9.81	4.96	3.71	3.04

Appendix C

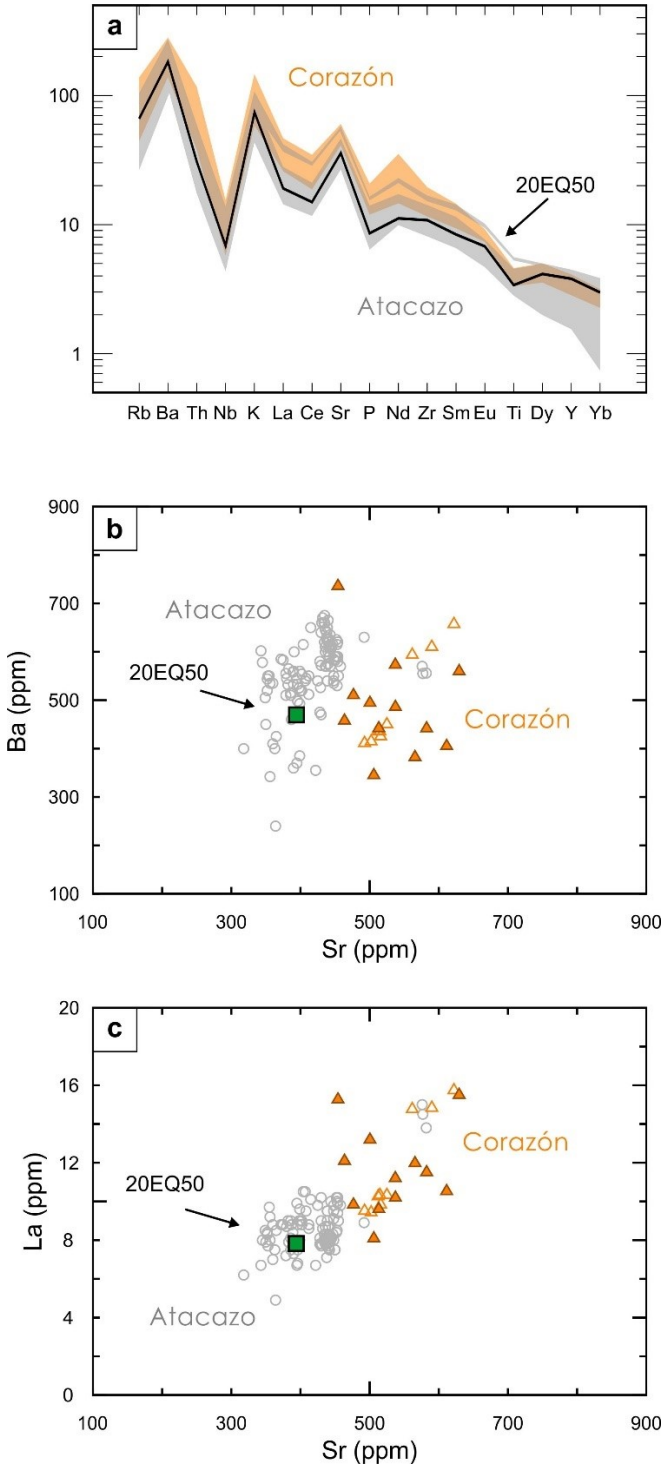

Figure C1. a) Incompatible trace elements normalized to the primitive mantle diagram (Sun and McDonough, 1989) compararing sample 20EQ50 (dark line) with Corazón (orange area) and Atacazo (grey area) volcanoes. **b)** Ba (ppm) and **c)** La (ppm) versus Sr (ppm) plots for the same arrangement. Corazón samples represented as orange triangles, and Atacazo as grey circles. Solid triangles present data from this study. Unfilled symbols represent data from the Georoc database and other studies (Hidalgo, 2006; Hidalgo et al., 2012).

Chapter 5

Eroded summit of Puntas volcano, Eastern Cordillera.

Chapter 5

Evolution of the Pleistocene volcanism in the Ecuadorian Andes

Article project

Contents

ABSTRACT 228

1. INTRODUCTION 229

2. GEOLOGICAL CONTEXT 230

2.1. Ecuadorian geological setting 230

2.2. Overview of the Ecuadorian volcanic arc 232

2.3. Volcanism from the Quito segment 235

3. METHODS 239

3.1. Sampling strategy 239

3.2. K-Ar dating 240

3.3. Whole-rock geochemical analyses 241

4. RESULTS 242

4.1. K-Ar dating 242

4.2. Geochemical characterization 244

5. DISCUSSION 246

5.1. Comparison with previous geochronological data on the Quito segment 246

5.2. Geochronological data compilation of the Ecuadorian volcanic arc 247

5.3. Pleistocene eruptive history 252

5.3.1. Early stage: 2.5 to 1.4 Ma 253

5.3.2. Intermediary stage: 1.4 to 0.6 Ma 255

5.3.3. Late stage: from 600 ka 257

5.4. Geochemical characterization 260

5.5. Relationship between volcanism and tectonics 263

5.6. Relationship between volcanism and the Nazca slab 267

6. CONCLUSIONS 269
REFERENCES 271
Appendix A. 284
Appendix B 287
Appendix C 290

Evolution of the Pleistocene volcanism in the Ecuadorian Andes: a review based on new and recent geochronological data

Santiago Santamaria [a], Mathilde Bablon [a, b], Xavier Quidelleur [a], Pablo Samaniego [c], Jean-Luc Le Pennec [c], Silvana Hidalgo [d], Céline Liorzou [e]

[a] GEOPS, Université Paris-Saclay, CNRS, Rue du Belvédère, 91405 Orsay, France

[b] Géoazur, IRD-CNRS-OCA, Université Côte d'Azur, Sophia Antipolis, France

[c] Laboratoire Magmas et Volcans, Université Clermont Auvergne, CNRS, IRD, OPGC, F-63000 Clermont-Ferrand, France

[d] Instituto Geofísico, Escuela Politécnica Nacional, Ap. 17-01-2759, Quito, Ecuador

e Laboratoire Géosciences Océan, Institut Universitaire Européen de la Mer, Université de Bretagne Occidentale, Rue Dumont d'Urville, 29280 Plouzané, France

Keywords:

- Ecuador
- K-Ar dating
- Geodynamics
-
-

Key Points:

-
-
-

Word count:

- Abstract: 331 words
- Main body: 10198 words

Figures: 11

Tables: 2

ABSTRACT

The Ecuadorian arc is composed of an unusually high number of volcanoes located over a relatively small area. Among them, some volcanoes forms clusters located in the center of the volcanic arc, an area which coincides with the onshore projection of the subducting Carnegie Ridge lying on the <20 Ma Nazca crust. Although several geochronological studies were carried out in the last two decades, the eruptive history of the central zone of the arc remained poorly documented. In this study, we present new K-Ar ages obtained from this area, referred as the Quito segment, the capital of Ecuador. These results were then included in a updated comprehensive geochronological database, allowing us to describe, for the first time, the spatial and temporal development of Quaternary volcanic activity in Ecuador. A total of, 77 Quaternary volcanoes were identified in the Ecuadorian Andes. The volcanic arc developed in three stages marked by increases in the number of active volcanoes. During the early stage, the documented volcanic activity was mostly concentrated in the Eastern Cordillera of the Quito segment starting at ~2.4 Ma. Minor effusive eruptions took place in the southern back-arc during this stage. Since ~1.4 Ma, the activity spread to the surroundings of the Quito segment and new edifices also appeared in the Western Cordillera and the Inter-Andean Valley. Towards the end of this intermediate stage (i.e., ~800 ka), volcanism occurred in isolated areas to the north and south of the Inter-Andean valley. Finally, the late stage was characterized by a remarkable increase in volcanic activity since ~600 ka. Approximately 50 volcanoes were active during this stage. The spatial distribution of the Ecuadorian arc volcanism seems to be guided by old tectonic structures of the crust, rather than those formed during the Quaternary. Nevertheless, we note that the spatial and temporal evolution of volcanism highlights the influence of the Carnegie Ridge and the thermal regime anomaly of the young Nazca crust in order to account for the increase of volcanic activity in Ecuador.

1. INTRODUCTION

The Northern Andean Volcanic Zone results from the subduction of the oceanic Nazca plate beneath the northwestern margin of the continental South American plate (Hall and Wood, 1985). The volcanic activity in Ecuador developed over a large area up to 270 km wide, producing around eighty Quaternary volcanoes (Hall and Beate, 1991; Hall et al., 2008; Bernard and Andrade, 2011). The resent eruptive activity of Tungurahua, Pichincha and Reventador volcanoes during the 2000s highlighted the necessity to improve the knowledge of the Ecuadorian volcanoes and thus the associated volcanic hazard assessment. Therefore, several stratigraphic, geochronological, geochemical, and geophysical studies were carried out in the Ecuadorian Andes (e.g., Hall and Mothes, 2008a; Robin et al., 2010; Le Pennec et al., 2011), mainly focusing on volcanoes that were "active" during the Holocene, or with morphological features suggesting a "potential" Holocene activity (Hall and Beate, 1991). These studies revealed that at least twenty Ecuadorian volcanoes were active during the Holocene (e.g., Samaniego et al., 1998; Barba et al., 2008; Hidalgo et al., 2008; Robin et al., 2008; Bernard et al., 2014). Their activity resulted in the formation of thick volcaniclastic sequences over which heavily populated areas are presently located, including the capital city of Ecuador, Quito (Hall and Mothes, 2008b). Several authors also pointed out a possible link between the spatial distribution of volcanism and its geochemical variability, in relation to crustal tectonics, the slab geometry and the subduction of the Carnegie Ridge (e.g., Litherland and Aspden, 1992; Barberi et al., 1988; Gutscher et al., 1999; Garrison et al., 2006; Chiaradia et al., 2009; Hidalgo et al., 2012). Despite these efforts, the oldest evolutionary stages of these volcanoes remain poorly constrained (Santamaría, 2017).

Recently, several geochronological studies shade light on the development of ancient volcanism with emphasis on the southern termination of the arc, and its central and northern segments (e.g., Alvarado et al., 2014; Bablon et al., 2019, 2020a; Santamaría et al., in preparation). However, the study of several volcanoes of the Quito segment has not been prioritized because of their longevity inferred from their eroded surfaces. We provide here twelve new K-Ar ages of ancient edifices from the Quito segment in order to clarify the eruptive history of volcanoes from this heavily populated area. These data were added to the updated Ecuadorian geochronological database (Santamaría, 2017) allowing us

to present the first summary of the eruptive history the whole volcanic arc. Then, the analysis of the spatial and temporal development of the Ecuadorian volcanoes provides new insights into their relationship with the crustal structures and the slab configuration. We observe that volcanism developed around the Quito segment since at least 2.4 Ma, where the distribution of volcanism seems to be influenced by the ancient tectonic structures of the crust. Throughout the Ecuadorian arc, a remarkable increase in the number of active volcanoes was observed during the Late Pleistocene.

2. GEOLOGICAL CONTEXT

2.1. Ecuadorian geological setting

In terms of its physiography, Ecuador is composed of the Coastal and Oriente basins which are separated by the Andes Mountains. The northern Ecuadorian Andes are divided into two parallel ranges, known as the Eastern and Western Cordilleras, with the Inter-Andean valley in between (Fig. 1a). The basement lithologies and ages in these domains are widely variable (Egüez et al., 2017). For instance, the Coastal basin and the Western Cordillera are formed by Cretaceous MORB-like basalts accreted during the Late Cretaceous-Paleogene, which are overlain by Tertiary marine sediments and volcanoclastic deposits (Jaillard et al., 2004; Witt et al., 2019; Vallejo et al., 2019). Conversely, the Eastern Cordillera consist of Paleozoic to Jurassic metamorphic rocks, mostly of continental affinity, and felsic to mafic igneous rocks (Litherland et al., 1994; Spikings et al., 2015; Villares et al., 2020). The Inter-Andean Valley is composed by Miocene-Pleistocene volcanic sediments which overlies a tectonic *mélange* of continental and oceanic rocks derived from both Cordilleras (Aspden et al., 1995; Lavenu et al., 1995; Winkler et al., 2005). The basement of the Oriente basin corresponds to the Pre-cambrian Guyanese craton which is overlain by a thick Mesozoic to Cenozoic sedimentary sequence (Ibanez-Mejia et al., 2011; Gutiérrez et al., 2019; Vallejo et al., 2021). The Miocene-Pliocene volcanic activity formed thick volcanic sequences (Lavenu et al., 1995; Vallejo et al., 2019, 2020; Chiaradia et al., 2021), presently exposed over both cordilleras, on which part of the Pleistocene-

Holocene volcanic edifices developed. The continental crust thickness is estimated at ~55-60 km in the Western Cordillera, being 60 km thinner in the Eastern Cordillera (Koch et al., 2021).

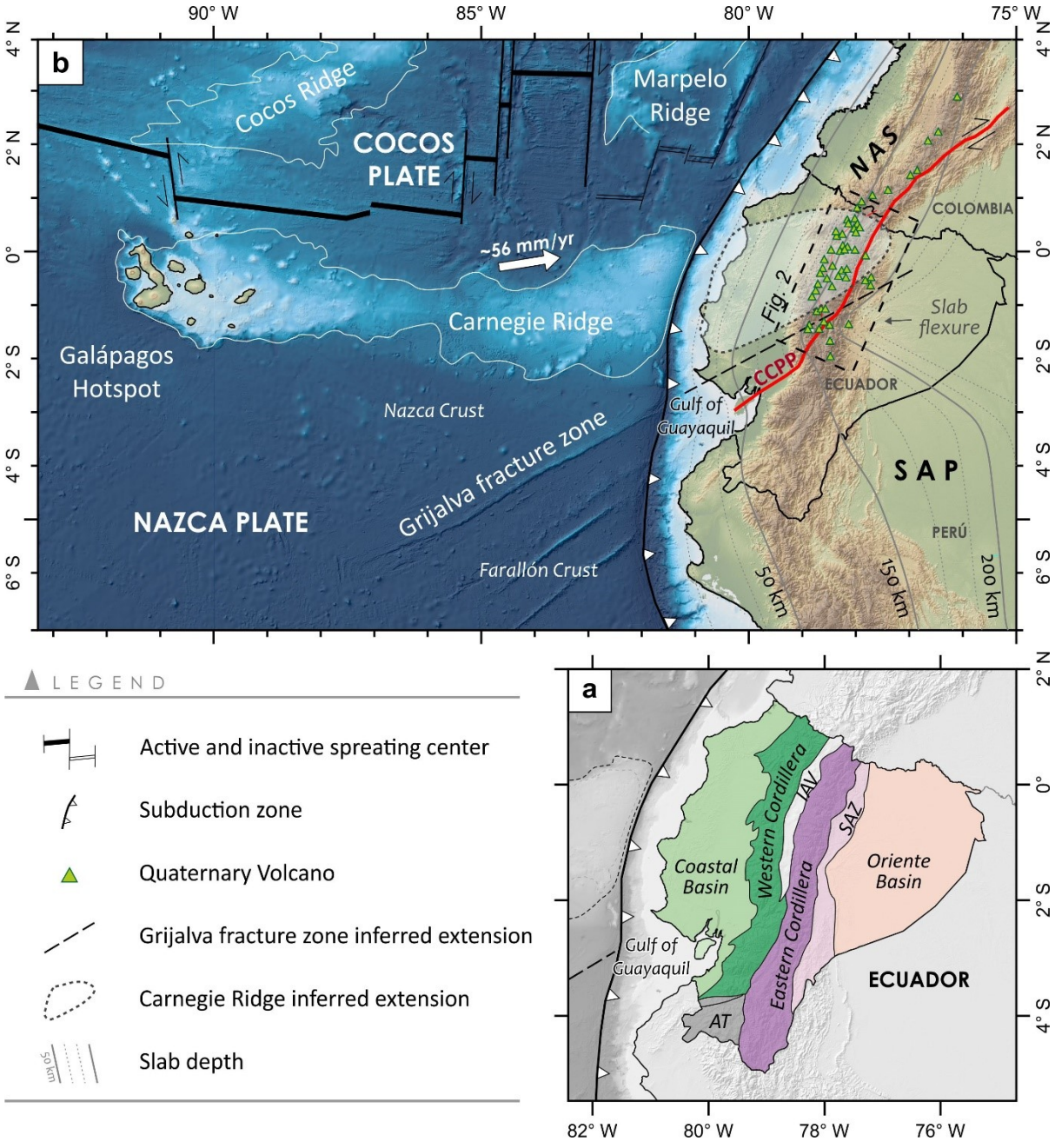

Figure 1. a) *Major geomorphological provinces of Ecuador (modified from Aspden et al., 1992). AT: Amotape-Tahuín; IAV: Inter-Andean Valley; SAZ: Sub-Andean Zone.* ***b)*** *Geodynamic setting of the Ecuadorian margin. White arrow indicate the direction of the Nazca plate motion relative to South America (DeMets et al., 2010). Topography and bathymetry from the GEBCO 2020 program. Slab depth and Carnegie Ridge inferred extension from Yepes et al. (2016) and Gutscher et al., (1999), respectively. CCPP: Chingual-Cosanga-Pallatanga-Puná fault system (Alvarado et al., 2016). NAS: North Andean Sliver; SAP: South American Plate.*

The subduction of the oceanic Nazca plate led to the development of the Ecuadorian volcanic arc (Hall and Wood, 1985). The Nazca plate is tectonically composed by the older Farallon crust (> 30 Ma) to the south and the younger Nazca Crust (< 20 Ma) to the north (Fig. 1b). Both oceanic crusts are separated by the Grijalva Fracture Zone (FZ), which resulted from the fragmentation of the ancient Farallon plate following a major plate reorganization occurred during the Early Miocene (~22.7 Ma). Moreover, the eastward motion of the Nazca plate over the Galapagos hot spot led to the formation of the Carnegie ridge, a 300 km-wide submarine mountain range built upon the younger Nazca crust (Meschede and Barckhausen, 2000; Lonsdale, 2005; O'Connor et al., 2007). This complex structure and thermal state of the Nazca plate affects the buoyancy of the subducted slab, which is then reflected in a change of the dip angle from ~12° for the older crust to >22° for the younger crust. This difference in subduction angles combined with the convex shape of the continental margin has induced a slab flexure beneath the Ecuadorian Andes (Fig. 1b; Yepes et al., 2016; Portner et al., 2020). Furthermore, the oblique convergence of the Nazca Plate caused the motion of the northwestern edge of the South American plate known as the North Andean Sliver (NAS). The southeastern limit of the NAS deformation zone corresponds to the Chingual-Cosanga-Pallatanga-Puná (CCPP) fault system. The CCPP fault system begins in the Gulf of Guyaquil, then intersects the Ecuadorian Andes near the southern termination of the volcanic arc, and continues northwards along the western edge of the Eastern Cordillera (Witt and Bourgois, 2010; Alvarado et al., 2014; Nocquet et al., 2014).

2.2. Overview of the Ecuadorian volcanic arc

The Quaternary volcanism in Ecuador is characterized by a wide diversity of well-preserved volcanic morphologies related to multiple eruptive styles and magmatic compositions. The resulting structures typically corresponds to prominent composite cones of several kilometers in basal diameter, usually larger than 7 km (e.g., Cotopaxi-IIb volcano; Hall and Mothes, 2008a). Successive conduit migrations and/or changes in the eruptive styles caused the superposition of the constructed edifices. Such occurrences created large volcanic complexes or compound volcanoes, which are the most common structures observed in the Ecuadorian Andes (e.g., Pichincha volcanic complex; Robin et al.,

2010). The construction processes of these edifices were also interrupted by sector collapses, separating their eruptive histories into various cone-building stages (e.g., Tungurahua volcano; Hall et al., 1999). Conversely, highly explosive eruptions derived in the formation of negative landforms such as large calderas (e.g., Chalupas caldera; Beate, 1985; Bablon et al., 2020b). Also, less prominent structures such as lava domes (e.g., Pululahua dome complex; Andrade et al., 2021) and monogenetic cones with their corresponding lava flows (e.g., Tulabug cone; Bablon et al., 2019), have been identified.

The Ecuadorian arc is usually described in terms of the geographical distribution of its numerous volcanoes along NW-SE corridors roughly parallel to the trench (e.g., Hall, 1977; Hall and Beate, 1991). These volcanoes built on oceanic basement (Western Cordillera and eastern Inter-Andean valley) constitute the Volcanic Front, while those built on continental basement (Western Inter-Andean valley and Eastern Cordillera) are called the Main Arc. The Back-Arc corridor includes the volcanoes located in the Sub-Andean zone (Fig. 2). The magmas from each corridor show distinctive geochemical and petrographic characteristics that lead to different eruptive styles and volcanic landforms (Hall et al., 2008; Ancellin et al., 2017). Notably, the along-arc distribution of these volcanoes is not uniform. Despite the high concentration of volcanoes in the Ecuadorian arc, various across-arc zones of scarce and profuse volcanic activity occur (Bablon et al., 2019). Figure 2 shows the segmentation of the Ecuadorian arc considering ~50 km-long intervals perpendicular to the Volcanic Front axis. Note that the limits of this segments are roughly coincident with the borders of the Chota, Guayllabamba, Latacunga and Riobamba valleys, where a lower number of volcanoes is observed. The volcanoes located in the Tulcán, Ibarra, Machachi and Ambato segments form “volcanic clusters” including composite stratovolcanoes, lava domes and calderas. In these areas, the distance between the volcanoes summits ranges between ~7 and ~15 km only. These volcanic clusters cover areas of a few hundred square kilometers. We notice that, despite the short distance between volcanoes, their eruptive products show a wide geochemical variability resulting in multiple eruptive styles.

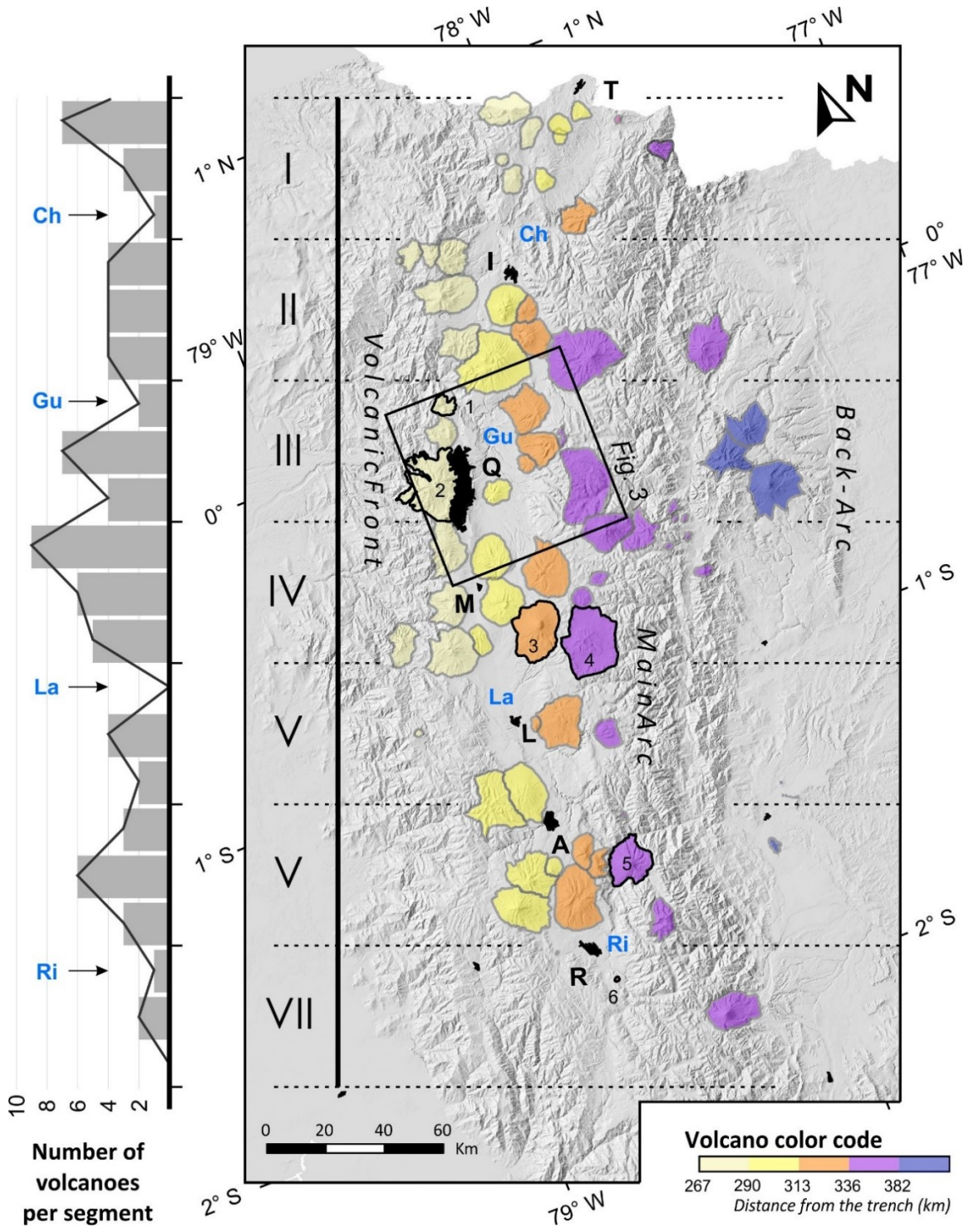

Figure 2. *Segmentation of the Ecuadorian volcanic arc. Ech section is named in function of the main city contained, which are represented in black letters. T: Tulcán, I: Ibarra; Q: Quito (Ecuador's capital city); L: Latacunga; A: Ambato; R: Riobamba. Volcanoes' shapes taken from Bernard and Andrade (2011), and are colored according to their distance from the trench. Examples of volcanic landforms: (1) Pululahua dome complex, (2) Pichincha volcanic complex, (3) Cotopaxi volcano, (4) Chalupas caldera, (5) Tungurahua volcano, (6) Tulabug cone. Main valleys represented as blue letters. Ch: Chota; Gu: Guayllabamba; La: Latacunga; Ri: Riobamba.*

2.3. Volcanism from the Quito segment

The Quito segment includes the volcanoes located approximately between latitudes 0° and 0.4° S (Fig. 2). Our study is focused on the volcanoes from the surroundings of the Guayllabamba valley and which lacks geochronological constrains (Fig. 3). The volcanoes located in the Sub-Andean zone (e.g., Hoffer, 2008; Mothes and Hall, 2008a; Salgado et al., 2021) were excluded due to the limited access roads and rainforest cover which preclude adequate sampling. A summary of the geological background for the Quito segment volcanoes is provided below.

Pululahua (3357 m asl.; Lat. 0°05'N; Long. 78°49'W) is a dacitic dome complex, mostly formed during the Holocene, located on the axis of the eastern edge of the Western Cordillera. The most recent activity of Pululahua (2.3 - 2.6 cal ka BP) included several highly explosive events (VEI 4) which produced a caldera-like crater and culminated with the extrusion of several dacitic domes (Andrade et al., 2021). Southward, the **Casitagua** volcano (3519 m asl.; Lat. 0°33'S; Long. 78°48'W) is formed by a sequence of pyroclastic deposits and andesitic lavas overlayed by the lacustrine sediments of the San Miguel Formation, and the Cangahua Formation which is a type of Upper Pleistocene volcanic paleosol formed by tuffs, ash, and pumice falls (Pacheco et al., 2014). The summit area of Casitagua is presently a caldera-like crater of 5 km-diameter, hosting several dacitic domes. Multiple domes also occur to the east and southwest of Casitagua volcano. The Catequilla and Pacto satellite domes, which intrude the Casitagua volcanic sequences deformed by the Quito fault system, were dated at 833 ± 26 ka and 898 ± 15 ka respectively, using the K-Ar Cassignol-Gillot technique applied to the groundmass and plagioclase phenocrysts (Pacheco, 2013; Alvarado et al., 2014). Note that a poorly defined whole-rock K-Ar age at 1400 ± 1400 ka was provided for the Lulunurcu satellite dome by Geothermica Italiana (1989).

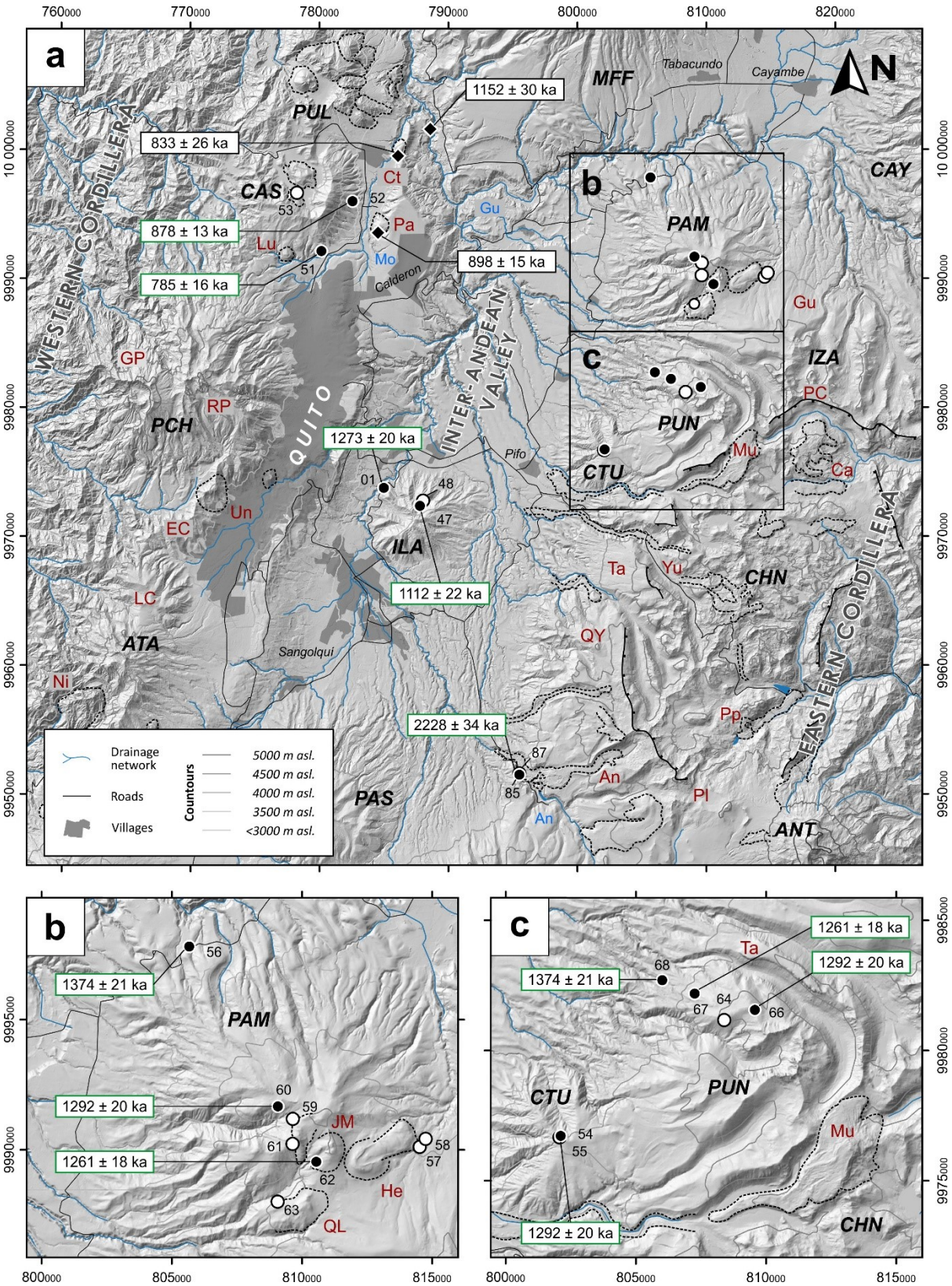

197

198 ***Figure 3.*** *(Caption provided in the next page).*

199

Figure 3. *Hill-shaded digital surface model of the Quito Segment showing the sampling locations and geochronological results. Numbers correspond to the last two digits of sample name (19EQxx or 20EQxx according to the recollection year). K-Ar dated samples are represented with solid symbols. K-Ar ages from Alvarado et al., (2014) Topography from the Sigtierras program. Volcanoes shown as black letters. ANT: Antizana; ATA: Atacazo; CAS: Casitagua; CAY: Cayambe; CHN: Chacana; CTU: Coturco; IZA: Izambi; PAM: Pambamarca; PAS: Pasochoa; PCH: Pichincha; PUL: Pululahua; PUN: Puntas. Volcanic landforms shown as red letters. An: Antisanilla; Ca: Callejones; Ct: Catequilla; EC: El Cinto; GP: Guagua Pichincha; Gu: Gualimburo; He: Herradura; JM: Jambi Machay; LC: La Carcacha; Mu: Mullumica; Ni: Ninahuilca; Pa: Pacpo; PC: Pucará Chico; Pl: Plaza de Armas series; Pp: Papallacta Flow; QL: Quito Loma; QY: Quiscatola-Yanaurcu series; RP: Rucu Pichincha; Ta: Tablones series; Yu: Yuyos flow. Rivers and valleys represented as blue letters. An: Antisanilla; Gu: Guayllabamba; Mo: Monjas. Coordinates are in Universal Transverse Mercator (UTM) zone 17.*

Further south, the **Pichincha volcanic complex** (4776 m asl.; Lat. 0°17'S; Long. 78°60'W) is formed by three superposed edifices (Robin et al., 2010). El Cinto, dated by $^{40}Ar/^{39}Ar$ at 1112 ± 24 ka, represents the oldest edifice of the complex. It was later intruded by the Ungi dome dated at 910 ± 70 ka. The Rucu Pichincha edifice is mainly composed of andesitic lavas and breccias successions formed between ~850 and ~262 ka, partially covering El Cinto edifice. Further west, the Guagua Pichincha edifice, mostly dacitic in composition, rests upon the western side of Rucu Pichincha. Its construction started as early as 52 ± 4 ka, and its most recent activity occurred between AD 1999 and 2001. Notably, several sector collapses occurred during the eruptive history of Pichincha volcano (Robin et al., 2010). South of the El Cinto edifice lies La Carcacha volcano (3880 m asl.; Lat. 0°19'S; Long. 78°36'W), an older edifice (~1290 ka; Hidalgo, 2006) of the **Atacazo-Ninahuilca volcanic complex** (4455 m asl.; Lat. 0°36'S; Long. 78°62'W). The main Atacazo cone-building stages took place between ~220 and ~83 ka, followed by the extrusion of several satellite domes around ~71 ka, and the Holocene high-explosive activity (VEI 4) of the Ninahuilca dome complex. **Ilaló** (3188 m asl.; Lat. 0°26'S; Long. 78°42'W) is the only volcano occurring in the Inter-Andean valley within the study area. This highly eroded volcano is formed by sequences of andesitic lavas (Chiaradia et al., 2009) overlain by the Cangahua Formation. A whole-rock K-Ar age at 1620 ± 160 ka was obtained for a basaltic andesite lava (Barberi et al., 1988), although the location of the sampling site is not provided.

Several highly eroded volcanoes dominate the western edge of the Eastern Cordillera. To the north of the study area, **Pambamarca** volcano (4078 m asl.; Lat. 0°08'S; Long. 78°21'W) is formed by voluminous andesitic lava sequences overlain by a complex of dacitic and rhyolitic domes. Herradura is a dome *coulée* located in the summit area that, unlike most of the structures of Pambabarca volcano, shows scarce signs of erosion. Further south, **Cerro Puntas** (4558 m asl.; Lat. 0°19'S; Long. 78°21'W) is a volcano composed by sequences of monolithological breccias and lavas, surrounded by incised glacial valleys. The southwestern flank of Puntas volcano partially covers the smaller **Coturco** volcano (3572 m asl.; Lat. 0°21'S; Long. 78°28'W), also spelled Cotohurcu or called Leon Dormido (Bernard and Andrade, 2011). To the east, the **Chacana** caldera (4493 m asl.; Lat. 0°21'S; Long. 78°15'W) dominates the Western Cordillera occupying a 32 km long (N-S) and 20 km wide (E-W) area. The oldest volcanic products of Chacana are dated by $^{40}Ar/^{39}Ar$ between 2150 ± 200 and 2710 ± 190 ka (Opdyke et al., 2006). The caldera formation episode included the emission of voluminous ignimbrite flows that spread radially along the caldera flanks forming the Quiscatola-Yanaurcu, and Tablones series. These sequences are dated by obsidian fission-tracks between 1350 ± 90 and 1580 ± 70 ka, and at 810 ± 50 ka, respectively (Bellot-Gurlet et al., 2008). Two $^{40}Ar/^{39}Ar$ ages are provided for the first series at 1670 ± 190 and 1460 ± 50 ka (Opdyke et al., 2006). Alternatively, two glass K-Ar ages of 980 ± 13 and 810 ± 40 ka are consistent with the range of the Tablones series, although the sampling locations are not well defined (Barberi et al., 1988). The *planèzes* created by these deposits surround the Pambamarca, Puntas and Coturco volcanoes. The subsequent Chacana activity phase corresponds to the caldera floor uplift produced by a shallow intracaldera intrusion (post-collapse resurgence stage), followed by a high explosive episode occurring between 18 and 20 ka (fission-track ages) with two 8 m-thick regional pumice-fallouts, and several rhyolitic domes were emitted. More recently, several andesitic and dacitic lava flows were emitted, including the fissure eruptions of Antisanilla (AD 1728) and Papallacta (AD 1773).

A sequence of voluminous andesitic lavas forms the northern flank of the Chacana caldera. These lava flows are associated with the **Izambi** volcano (4325 m asl.; Lat. 0°19'S; Long. 78°17'W), also called Gualimburo (Aguilera et al., 2007). Some authors consider this voluminous sequence as part

of the Chacana series, while assigning the upper lava sequence (Pucará Chico peak) to the Izambi volcano (e.g., Hall and Mothes, 2008c; Bernard and Andrade, 2011). A basaltic andesite lava was dated by whole-rock K-Ar at 1300 ± 200 ka (Barberi et al., 1988). Although the sampling site is not provided, the sample may correspond to the more accessible Gualimburo series. Alternatively, an obsidian block sampled near the Pucará Chico peak yielded a fission track age of 370 ± 60 ka (Bigazzi et al., 2005).

3. METHODS

3.1. Sampling strategy

Sampling work was carried out during a field campaign conducted in 2020. Fresh lavas with low vesicle contents were sampled for K-Ar dating and whole-rock geochemical analyses. Where possible, outcrops located both at the summit and basal areas of the volcanic edifices were targeted (Fig. 3), in other to bracket the whole eruptive history of the studied volcanoes.

At Casitagua volcano, two samples were collected from massive andesitic lava flows located on its southern (20EQ51a) and western (20EQ52a) flanks. Three juvenile blocks (20EQ51b, 20EQ52b, 20EQ52c) were sampled from pyroclastic density current (PDC) deposits overlying the previously sampled lavas for geochemical comparison purposes. A dacitic dome was sampled in the interior of the caldera-like depression (20EQ53). At Ilaló volcano, three massive lava flows located at the base (19EQ01) and in the summit area (19EQ47, 19EQ48) were sampled. The overlying thick Cangahua Formation deposits precludes the exposure of multiple outcrops on these volcanoes, and consequently, prevented additional sampling.

Eight samples were obtained from the Pambamarca volcano. Four samples correspond to andesitic lavas located on the northern flank (20EQ56) and the summit area (20EQ59, 20EQ60, 20EQ61). Four samples were collected from the Herradura (20EQ57, 20EQ58), Jambi Machay (20EQ62), and Quito Loma (20EQ63) summit rhyolitic domes. Only the northern flank of Puntas volcano was sampled due to poor access routes. However, four massive lavas were sampled at different altitudes (20EQ64, 20EQ65, 20EQ67, and 20EQ68). Likewise, only two lavas could be sampled in the

summit area at Coturco volcano (20EQ54, 20EQ55). Finally, a lava from the basal sequence of the southern side of the Antisanilla valley (20EQ85), located on the Chacana caldera southern flank, was sampled together with the AD 1728 Antisanilla lava flow (20EQ87).

3.2. K-Ar dating

Twelve samples were carefully selected for radiometric dating after thin-section examination (Appendix A). We used the K-Ar dating method applying the unspiked Cassignol-Gillot technique, which was successfully applied to in the Ecuadorian volcanic arc (Alvarado et al., 2014; Bablon et al., 2018, 2019, 2020b; Santamaría et al., submitted) and worldwide (e.g., Grosse et al., 2018, 2020; Hildenbrand et al., 2018; Dibacto et al., 2020). The Cassignol-Gillot technique is particularly suitable for dating volcanic rocks with low radiogenic argon (^{40}Ar*) contents diluted in ^{40}Ar derived from atmospheric contamination, such as those young low-K lavas encountered in the Ecuadorian arc. Using a 180° sector multi-collector mass spectrometer, the electrical signals measured for the ^{40}Ar and the ^{36}Ar extracted from a given sample, are compared with those acquired from an air aliquot measured under identical pressure conditions. The resulting electrical difference in the measured ratios allows to determine the ^{40}Ar* produced by radioactive decay of ^{40}K since closure of the sample. The ^{40}Ar signal is calibrated by systematic measurements of the HD-B1 standard (24.18 ± 0.09 Ma; Schwarz and Trieloff, 2007) in order to convert the electrical signals into a certain number of atoms. Thus, the argon measurement process is solely dependent on the sample ^{40}Ar* content, whose electrical signal is optimized by adjusting the initial sample mass. The detection limit of the mass spectrometer close to 0.1% for ^{40}Ar* (Quidelleur et al., 2001) allows to date Holocene volcanic rocks with a relatively small uncertainty (Gillot et al., 2006). The potassium (K) concentration is measured independently by flame absorption spectroscopy. MDO-G (Gillot et al., 1992) and BCR2 (Raczek et al., 2001) standards are measured together with the analyzed samples for sake of comparison and correction purposes. Finally, the age is calculated using the ^{40}K/K ratio in nature, the ^{40}K to ^{40}Ar decay constant, and the measured K and ^{40}Ar* contents. The measuring process was carried out at the GEOPS laboratory of the Université

309 Paris-Saclay (France), where the reproducibility was verified within 1-σ uncertainty range by
310 replicating the whole process at least twice for each sample.

311 We prefer to apply the Cassignol-Gillot technique to the groundmass considering that this is
312 the last phase to crystallize in equilibrium with the atmosphere following a volcanic eruption. Pre-
313 eruption crystallized phases, such as plagioclase phenocrysts, may carry inherited radiogenic argon
314 biasing the calculated ages (e.g., Samper et al., 2008; Renne et al., 2012). Therefore, we consider crystal
315 ages as older bounds of the real eruption date. Groundmass and crystal phases were separated following
316 the protocols described by Bablon et al. (2018), summarized below. The samples were hand crushed
317 and sieved to 63-80, 80-125 or 125-250 μm, according to the space left between the phenocrysts, which
318 is occupied by the groundmass. Subsequently, an acid solution (10% HNO_3) washing, and a magnetic
319 and heavy-liquid (bromoform) separation process ensured that the recovered fraction remains
320 homogeneous within a narrow density range and does not contain undetected weathered fractions.

321

322 **3.3. Whole-rock geochemical analyses**

323 Whole-rock major and trace element contents were measured for all dated samples, including
324 13 additional samples collected for comparison purposes. The whole dataset of 25 analyses is presented
325 in Appendix B where major element concentrations were recalculated to a total of 100% on a water
326 free-basis. Agate-crushed powders were analyzed by Inductively Coupled Plasma-Atomic Emission
327 Spectrometry (ICP-AES) following the analytical procedure described in Cotten et al. (1995). The
328 relative uncertainties are < 1% for SiO_2, < 2% for other major elements, and < 5% for trace elements.
329 The measuring process was caried out at the Laboratoire Géosciences Océan, Université de Bretagne
330 Occidental (France).

331

4. RESULTS

4.1. K-Ar dating

The selected samples showed porphyritic to aphanitic textures with a mineral assemblage composed of plagioclase, orthopyroxene, clinopyroxene, and amphibole (Appendix A). Samples form Pambamarca summit domes 20EQ62 and 20EQ63 presented scarce biotite, whereas sample 20EQ63 showed unusually higher amounts of orthopyroxene, amphibole, and biotite. The groundmass was commonly composed of plagioclase, pyroxene, and scarce Fe-Ti oxides microlites supported in a glassy matrix. Radiometric measurements were performed on groundmass grains only. Except for samples 20EQ62, for which plagioclase phenocrysts were used, and 20EQ54, for which both groundmass and plagioclase phenocrysts were analyzed. The groundmass K content ranges between 0.964% and 1.411%, and between 0.382% and 1.141% for plagioclases. The minimum content of 40Ar* is 6.7%, with a mean value of 21.4%. Note that although the plagioclase fractions showed lower amounts of K, the 40Ar* content is relatively high, allowing an easy determination with the Cassignol-Gillot technique.

Twelve new K-Ar ages are presented in Table 1. Samples collected from Casitagua volcano yield ages of 785 ± 16 ka (20EQ51a) and 878 ± 13 ka (20EQ52a). A narrower age range between 1112 ± 22 ka (19EQ01a) and 1273 ± 20 ka (19EQ47) is obtained from Ilaló volcano. Further east, two andesitic lavas from Pambamarca volcano is dated at 1261 ± 18 ka (20EQ60) and 1374 ± 21 ka (20EQ56). Due to the highly weathered state of the groundmass phases observed in the somite domes samples from Pambamarca volcano, we have analyzed plagioclase phenocrysts and have obtained an age of 1292 ± 20 ka for the Jamby Machay dome (20EQ62). For Puntas volcano, three ages at 1084 ± 17 ka (20EQ67b), 1128 ± 16 ka (20EQ68), and 1132 ± 16 ka (20EQ66) have been obtained. Considering the limited number of samples from Coturco volcano and the slight evidence of weathering, the measurements were performed on both groundmass and plagioclase phenocrysts extracted from the freshest sample 20EQ54. The calculated values were consistent within the 1-sigma uncertainty range, providing an averaged age of 1959 ± 28 ka. Finally, the Antisanilla valley sample 20EQ85 was dated at 2228 ± 34 ka.

359 ***Table 1.*** *K-Ar ages obtained for the volcanoes of the Quito segment. Column headings indicate sample*
360 *name, outcrop nature and relative location, sample coordinates projected using the Universal*
361 *Transverse Mercator (UTM) coordinate system (Zone 17), potassium (K) content in percent, radiogenic*
362 *argon content ($^{40}Ar^*$) in percent and in 10^{11} atoms per gram, age obtained for each measurement, and*
363 *weighted mean age in ka given with a 1-σ uncertainty. All measurements were performed on*
364 *groundmass, except for three analyses performed on plagioclase phenocrysts (**).*

Sample	Location and Unit	Long. (m)	Lat. (m)	K (%)	$^{40}Ar^*$ (%)	$^{40}Ar^*$ (10^{11} at/g)	Age ± 1σ (ka)	Mean age (ka)
Casitagua volcano								
20EQ52a	Lava flow, E flank	782567	9995974	1.329	20.3	12.1227	873 ± 13	878 ± 13
					19.7	12.2556	883 ± 13	
20EQ51a	Lava flow, SE flank	780212	9992204	1.411	7.5	11.6027	787 ± 15	785 ± 16
					6.9	11.5223	782 ± 16	
Ilaló volcano								
19EQ01	Lava flow, E flank	784978	9973735	0.964	14.5	12.7775	1273 ± 20	1273 ± 20
					13.9	12.8238	1274 ± 20	
19EQ47	Lava flow, N flank	787784	9972350	1.133	7.1	12.9692	1096 ± 22	1112 ± 22
					7.1	13.2883	1123 ± 22	
					6.7	13.2122	1116 ± 23	
Pambamarca volcano								
20EQ56	Lava flow, NW flank	805673	9997815	1.241	19.5	17.804	1373 ± 21	1374 ± 21
					21.5	17.8125	1374 ± 20	
20EQ62**	Jamby Machay	810553	9989550	0.382	12.4	5.1262	1285 ± 21	1292 ± 20
20EQ62**	dome, summit area				18.2	5.1773	1297 ± 20	
20EQ60	Lava flow, summit area	809077	9991663	1.586	37.2	20.7881	1254 ± 18	1261 ± 18
					39.2	21.0203	1268 ± 18	
Puntas volcano								
20EQ66	Lava flow, E flank	809562	9981566	1.449	31.7	17.0642	1127 ± 16	1132 ± 16
					33.2	17.2136	1137 ± 16	
20EQ68	Lava flow, E flank	806008	9982702	1.362	30.9	16.0579	1128 ± 16	1128 ± 16
					33.2	16.0570	1128 ± 16	
20EQ67b	Lava flow, E flank	807261	9982195	1.034	14.3	11.6670	1080 ± 17	1084 ± 17
					12.8	11.7687	1089 ± 18	
Coturco volcano								
20EQ54	Lava flow, summit area	802112	9976733	1.610	47.7	33.1602	1971 ± 28	1959 ± 28
20EQ54**				1.141	43.4	23.2191	1948 ± 28	
Chacana Caldera								
20EQ85	Lava flow, Antisanilla valley	795498	9951500	1.319	19.6	30.7537	2232 ± 34	2228 ± 34
					16.4	30.6488	2224 ± 34	

365

366 **4.2. Geochemical characterization**

367 Figures 4a and 4b show the Peccerillo and Taylor (1976) rock classification diagram for the
368 samples collected in this study. Most samples are Low to Medium-K basaltic andesites and andesites
369 with SiO_2 contents ranging from 53 to 63 wt.% and K_2O contents from 0.7 to 2.5 wt.%. Samples taken
370 on the Casitagua volcano plot in the field displayed by the PDC deposits sampled in the Quito fault
371 uplift (Fig. 3b), which is located on the opposite side of the Monjas river valley (Fig. 2). Note that data
372 from the Catequilla dome also plots in the same Casitagua PDC field (Pacheco, 2013). The andesitic
373 lavas of the Ilaló volcano lie in the field described by previous studies (Chiaradia et al., 2009), except
374 sample 20EQ48 which shows lower silica content (Fig. 4b). The sample of the old Chacana series
375 20EQ85 is a basaltic andesite that plots outside the Chacana field (e.g., Chiaradia et al., 2009, 2014;
376 Villares, 2010) although it appears consistent with the overall volcano trend. The samples from the
377 Jambi Machay (20EQ62) and Quito Loma (20EQ63) summit domes of Pambamarca volcano are the
378 only medium-K rhyolites identified in this study (Fig. 3b). The samples from the Herradura dome
379 (20EQ57 and 20EQ58) exhibit an unusual K_2O enrichment at low SiO_2 content, thus are classified as
380 basaltic andesites belonging to the Shoshonitic series, which are rather common in back-arc volcanoes
381 (e.g., Hoffer et al., 2008; Garrison et al., 2017).

382 Spider diagrams of trace elements normalized to the primitive mantle, and Rare-Earth Elements
383 (REE) normalized to chondrites are presented in Figures 4c and 4d, respectively. In summary, these
384 diagrams show fractionation between Light REE (LREE; e.g., La, Ce) and Heavy REE (HREE; e.g.,
385 Yb) with a slightly declining but homogeneous pattern with no Eu anomaly observed for Casitagua,
386 Ilaló, Puntas and Coturco volcanoes. A slight increase in REE concentration is noted between the
387 Volcanic Front (Casitagua), Inter-Andean Valley (Ilaló) and the Main Arc (Puntas, Coturco), indicating
388 a positive correlation between the REE contents and the distance from the trench (Fig. 4c-d). Sample
389 20EQ48 from Ilaló volcano displays the highest REE contents. The Pambamarca volcano lavas exhibit
390 a wide REE content range, where the andesitic samples, the summit rhyolitic domes, and the Herradura
391 dome define compositional fields consistent with those found in the Chacana caldera. In particular, the
392 Herradura dome (20EQ57, 20EQ58) shows the highest REE enrichment of the whole dataset, creating

a pattern remarkably similar to the Yuyos lava flow from Chacana caldera (Fig. 3a; Chiaradia et al., 2014). Other lavas with similar petrographic and geochemical characteristics occur at Cayambe (Cono La Virgen; Samaniego et al., 2005) and Antisana (Cuyuja lavas; Hall et al., 2017) volcanoes. The primitive mantle-normalized trace element patterns reveal an overall enrichment in Large-Ion Lithophile Elements (LILE; e.g., Rb, Ba). A negative Nb anomaly is observable for the whole dataset (Fig. 4d). Only the samples from the Jambi Machay (20EQ62) and Quito Loma (20EQ63) domes show marked negative P and Ti anomalies. These domes also present the highest depletions of Dy, Y and Yb (Fig. 4d).

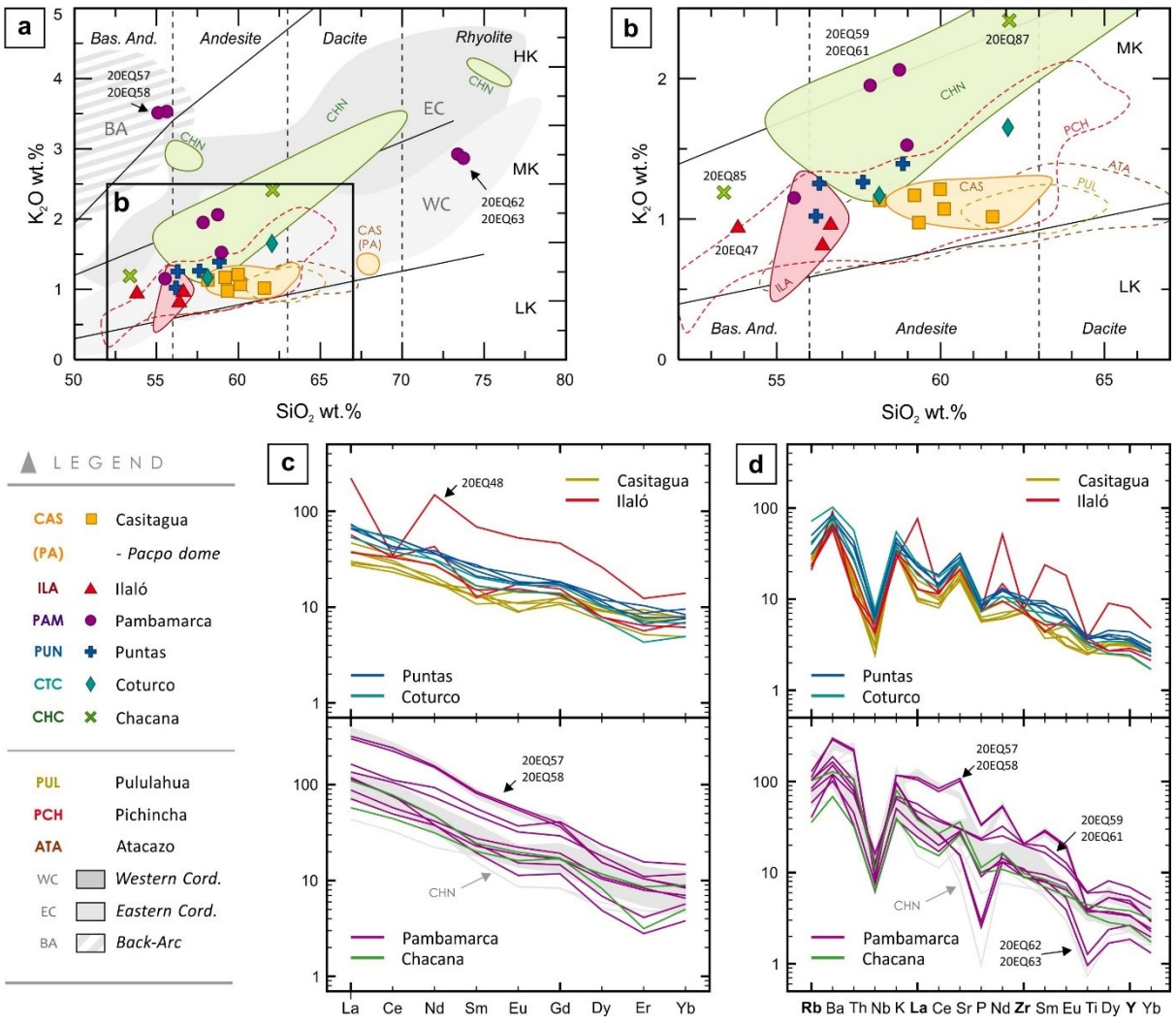

Figure 4. *(Caption provided in the next page).*

Figure 4. a-b) *K_2O vs SiO_2 diagram (Peccerillo and Taylor, 1976) for eruptive products of the Quito segment volcanoes. HK: Hight-K, MK: medium-K, and LK: low-K calc-alkaline series. Colored areas represent the composition fields created by bibliographic data for Casitagua, Chacana, and Ilaló volcanoes (Pacheco, 2013; Chiaradia et al., 2009, 2014). Shaded areas represent the composition fields of the volcanoes from Western Cordillera, Eastern Cordillera, and Back-Arc based on the Georoc database (http://georoc.mpch-mainz.gwdg.de/georoc/).* ***c)*** *Rare Earth Elements normalized to chondrites, and* ***d)*** *Incompatible trace elements normalized to the primitive mantle diagrams (Sun and McDonough, 1989) for the Quito segment. The sampled volcanoes were organized according to their position in the Western Cordillera (yellow lines), Inter-Andean Valley (red lines), and Eastern Cordillera (blue and turquoise lines). Chacana (green lines) and Pambamarca (purple lines) samples showed in separated panels. Shaded area refers to bibliographic data from Chacana (Bryant et al., 2006; Chiaradia et al., 2009, 2014).*

5. DISCUSSION

5.1. Comparison with previous geochronological data on the Quito segment

Overall, our new K-Ar ages presented here are consistent with studies. Samples from the Catequilla and Pacpo satellite domes of Casitagua volcano were previously dated at the GEOPS laboratory using the same methods as our study, providing an age range between 833 ± 26 and 898 ± 15 ka (Fig., 3a; Pacheco, 2013; Alvarado et al., 2014). We dated two andesitic lava flows directly sampled on the flanks of Casitagua volcano obtaining a coherent age range of 785 ± 16 (20EQ51a) and 878 ± 13 (20EQ52a) ka. These new data show that the Casitagua eruptive activity was contemporaneous with the emplacement of the Catequilla and Pacpo satellite domes. Moreover, this eruptive activity range is consistent with the K-Ar age at 1152 ± 30 ka obtained from the underlying basaltic andesite lavas assigned to the Pisque Formation (Fig. 3a; Alvarado et al., 2014). Although the source of these latter lavas is unknown, the thickness of this sequence suggest that they were probably emitted from a proximal eruptive center.

In the inter-Andean valley, our groundmass ages acquired from Ilaló volcano suggets an activity between 1112 ± 18 ka and 1273 ± 20 ka (19EQ47 and 19EQ01, respectively). This range is younger than the whole-rock K-Ar age at 1620 ± 160 ka (EC 76) obtained from an unidentified lava of Ilaló

volcano (Barberi et al., 1988). Although the precise sampling site EC 76 is not reported, the analyzed sample seems to correspond to the lava 19EQ01 located in an easily accessible outcrop on the northern flank of Illaló (Fig. 3a; P. Mothes pers. com.). We interpret the ages difference to the whole-rock analysis resulting in (1) the occurrence of unseparated phenocrysts, which may carry inherited argon; and/or (2) the inclusion of unseparated weathered grains, for which potassium may have been partially leached out (e.g., Samper et al., 2008; Schaen et al., 2020). This bias towards older ages for whole-rock dating has already been noted in other lavas in the Ecuadorian arc dated on whole-rock fractions (e.g., Bablon et al., 2018, 2019) and elsewhere (Quidelleur et al., 1999, 2021; Samper et al., 2008).

5.2. Geochronological data compilation of the Ecuadorian volcanic arc

In order to characterize the Quaternary volcanism in Ecuador, we followed the "volcano-as-eruptive-subsystem" definition of Szakács (2010), in which a volcano corresponds to the shallowest magma reservoir, all magma plumbing pathways, and the volcanic edifice at the surface. Although subsurface studies are desirable to differentiate one eruptive subsystem from another, we focused on the ultimate landforms created by these subsystems, and which can be spatially differentiated from others. In this study, those eruptive subsystems that show a spatial and/or temporal overlap (e.g., Rucu Pichincha and Guagua Pichincha volcanoes; Bernard and Andrade, 2011) were considered as a single identity (e.g., Pichincha volcanic complex; Robin et al., 2010) instead of multiple ones. A thorough bibliographic review combined with new field works led to the identification of 77 individual volcanoes in the Ecuadorian arc (Table 2).

Several studies were conducted on volcanoes with a morphology suggesting a recent activity (e.g., Hall and Beate, 1991; Hidalgo et al., 2008; Robin et al., 2009, 2010; Le Pennec et al., 2011). The eruptive history of these volcanoes was mostly constrained by new $^{40}Ar/^{39}Ar$ (measured on groundmass or separed crystalline phases) and ^{14}C ages, combined with stratigraphic relationships and geochemical analyses. A first compilation of the available geochronological data and a summary of cone-building stages of each volcano was provided by the "Ecuadorian volcanic events and geochronological

459 database" (EVEG; Santamaría, 2017). More recently, almost a hundred of new groundmass K-Ar ages,
460 obtained in the GEOPS laboratory, have constrained the oldest eruptive history of these volcanoes (Fig.
461 5). They completed the poor information previously available for the volcanoes classifies as "extinct or
462 in rest" (Alvarado et al., 2014; Telenchana et al., 2017; Bablon et al., 2018, 2019, 2020a, 2020b;
463 Almeida et al., 2019; Andrade et al., 2021; Santamaría et al., submitted, in preparation; this study).

464 In order to constrain the Pliocene eruptive history of the Ecuadorian arc, we have updated the
465 EVEG database (Santamaría, 2017), by adding the most recent data while removing the low-quality
466 ages. In particular, $^{40}Ar/^{39}Ar$ ages were reviewed on the basis of minimum quality criteria, such as
467 plateau ages calculated with at least three consecutive steps corresponding to at least 50% of the total
468 ^{39}Ar released, and having an associated isochron with an initial $^{40}Ar/^{36}Ar$ ratio indistinguishable from
469 the atmospheric value (e.g., Schaen et al., 2020). Since reliability of the whole-rock K-Ar ages (Barberi
470 et al., 1988; Lavenu et al., 1995) has been questioned (see previous section), we have discarded such
471 records from the EVEG database. Finally, we have shortened the Holocene volcanic records because
472 their extension and accuracy (of a few tens to hundreds of years) are overshadowed by the time scale
473 of the present study (several thousands of years). The updated version of the EVEG database focused
474 on the Pleistocene volcanic activity is presented in Appendix C.

475

476 ***Table 2.*** *Quaternary volcanoes of the Ecuadorian Arc.*

Code	Volcano name	Eruptive classification	Morphological classification	Last known eruption
ALS	**Aliso**	Extinct or at rest	Composite volcano	
ASN	**Almas Santas**	Extinct or at rest	Composite volcano	364 ± 7 ka
ALT	**Altar**	Extinct or at rest	Composite volcano	
ANG	**Angahuana**	Extinct or at rest	Caldera	
ANT	**Antisana**	Potentially active	Compound volcano or complex volcano	< 800 ka
ATA	**Atacazo - Ninahuilca**	Potentially active	Compound volcano or complex volcano	~ 2270 cal yr BP
BMJ	**Bermejo**	Extinct or at rest	Lava dome	
CAC	**Cacalurcu**	Extinct or at rest	Monogenetic cone	2.67 ± 0.06 Ma
CAL	**Calpi cones**	Potentially active	Monogenetic cone	9 ± 3 ka
CRH	**Carihuairazo**	Extinct or at rest	Composite volcano	208 ± 10 ka

Code	Volcano name	Eruptive classification	Morphological classification	Last known eruption
CSL	**Casahuala**	Extinct or at rest	Composite volcano	
CAS	**Casitagua**	Extinct or at rest	Composite volcano	785 ± 16 ka
CAY	**Cayambe**	Active	Compound volcano or complex volcano	AD 1786
CHN	**Chacana**	Active	Caldera	AD 1773
CCB	**Chachimbiro**	Potentially active	Compound volcano or complex volcano	~ 5525 cal yr BP
CPT	**Chalpatán**	Extinct or at rest	Caldera	
CLP	**Chalupas - Quilindaña**	Extinct or at rest	Caldera	~ 43 cal ka BP
CQL	**Chaquilulo**	Extinct or at rest	Composite volcano	
CCN	**Chiles - Cerro Negro**	Potentially active	Compound volcano or complex volcano	Unknown
CTZ	**Chiltazón**	Extinct or at rest	Lava dome complex	
CHB	**Chimborazo**	Potentially active	Compound volcano or complex volcano	~1 320 yr BP
CNB	**Chinibano**	Extinct or at rest	Composite volcano	
CLM	**Chulamuez**	Extinct or at rest	Composite volcano	
COR	**Corazón**	Extinct or at rest	Composite volcano	67 ± 4 ka
COS	**Cosanga**	Extinct or at rest	Composite volcano	290 ± 20 ka
CTC	**Cotacachi - Cuicocha**	Potentially active	Compound volcano or complex volcano	~3 280 cal yr BP
COT	**Cotopaxi**	Active	Composite volcano	AD 2015
CTU	**Coturco**	Extinct or at rest	Composite volcano	1959 ± 28 ka
CUB	**Cubilche**	Extinct or at rest	Compound volcano or complex volcano	~30 cal ka BP
CSH	**Cushnirumi**	Extinct or at rest	Composite volcano	383 ± 6 ka
CUS	**Cusín**	Extinct or at rest	Composite volcano	495 ± 12 ka
DOR	**El Dorado**	Potentially active	Composite volcano	~43.5 cal ka BP
HOR	**Horqueta**	Extinct or at rest	Composite volcano	
HNA	**Huañuna**	Potentially active	Lava dome	
HCH	**Huevos de Chivo**	Potentially active	Lava dome complex	11.58 cal ka BP
HUI	**Huisla**	Extinct or at rest	Composite volcano	492 ± 9 ka
IGL	**Igualata**	Extinct or at rest	Composite volcano	107 ± 11 ka
IGN	**Iguán**	Extinct or at rest	Composite volcano	
ILA	**Ilaló**	Extinct or at rest	Composite volcano	1112 ± 22 ka
ILI	**Iliniza**	Potentially active	Compound volcano or complex volcano	
IMB	**Imbabura**	Potentially active	Compound volcano or complex volcano	~4 cal yr BP
IZA	**Izambi**	Extinct or at rest	Undefined	370 ± 60 ka
MAC	**Machángara**	Extinct or at rest	Undefined	
MAN	**Mangus**	Extinct or at rest	Composite volcano	
MER	**Mera lavas**	Extinct or at rest	D - Fissure vent	1.92 ± 0.10 Ma

Code	Volcano name	Eruptive classification	Morphological classification	Last known eruption
MFF	**MojandFuya Fuya**	Extinct or at rest	Compound volcano or complex volcano	> 28 ± 5 ka
MUL	**Mulmul**	Extinct or at rest	Composite volcano	< 33 cal ka BP
PAM	**Pambamarca**	Extinct or at rest	Composite volcano	< 33 cal ka BP
PDA	**Pan de Azúcar**	Extinct or at rest	Composite volcano	1.15 ± 0.01 Ma
PAR	**Parulo**	Extinct or at rest	Lava dome	< 33 ka
PAS	**Pasochoa**	Extinct or at rest	Composite volcano	
PCH	**Pichincha**	Active	Compound volcano or complex volcano	AD 1999 - 2001
PLV	**Pilavo**	Extinct or at rest	Lava cone	< 33 ka
POT	**Potrerillos**	Extinct or at rest	Composite volcano	
PUL	**Pululahua**	Potentially active	Lava dome complex	~ 2205 cal yr BP
PUM	**Pumayacu**	Potentially active	Lava dome complex	> 2 ka
PUN	**Puntas**	Extinct or at rest	Composite volcano	1084 ± 17 ka
PLC	**Puñalica**	Extinct or at rest	Lava cone	18 ± 3 ka
PUT	**Putzalagua**	Extinct or at rest	Lava dome complex	
PUY	**Puyo cones**	Extinct or at rest	D - Fissure vent	190 ± 70 ka
QLT	**Quilotoa**	Potentially active	Caldera	~750 cal yr BP
REV	**Reventador**	Active (in eruption)	Composite volcano	AD 2002 - Ongoing
RVA	**Río Valle**	Potentially active	Lava dome	> 6.3 ka
RUM	**Rumiñahui**	Extinct or at rest	Composite volcano	<202 ± 8 ka
SAG	**Sagoatoa**	Extinct or at rest	Composite volcano	799 ± ka
SAN	**Sangay**	Active (in eruption)	Composite volcano	Ongoing
SCR	**Santa Cruz**	Extinct or at rest	Composite volcano	60 ± 3 ka
SIN	**Sincholagua**	Extinct or at rest	Composite volcano	312 ± 6 ka
SCH	**Soche**	Potentially active	Compound volcano or complex volcano	~9600 cal yr BP
SUM	**Sumaco**	Active	Composite volcano	< AD 1926
TUL	**Tulabug**	Extinct or at rest	Monogenetic cone	
TUN	**Tungurahua**	Active	Composite volcano	AD 1999 - 2016
VNG	**Virgen Negra**	Extinct or at rest	Lava dome	
VIZ	**Vizcaya cone**	Extinct or at rest	Monogenetic cone	253 ± 5 ka
VAZ	**Volcán Azul**	Extinct or at rest	Undefined	
YNP	**Yanahurcu de Piñan**	Extinct or at rest	Compound volcano or complex volcano	60 ± 20 ka
YNU	**Yanaurcu**	Extinct or at rest	Composite volcano	

477

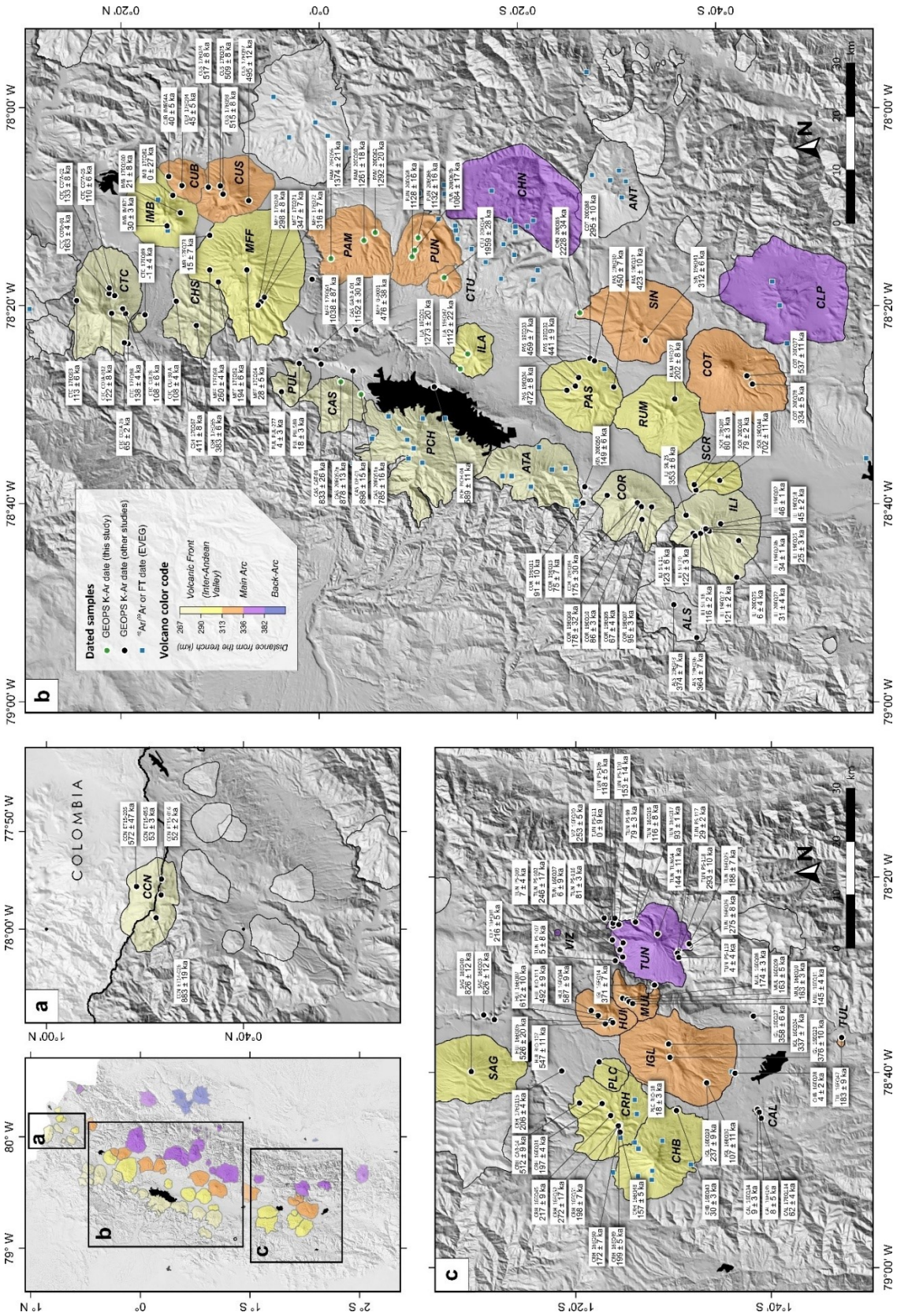

Figure 5. *Summary of the K-Ar ages acquired by the GEOPS laboratory. Samples from this study represented as green dots, and from other studies as solid dots. Sampled volcanoes are colored in function to their distance to the trench. Location of $^{40}Ar/^{39}Ar$ and obsidian Fission Track (FT) dated samples compiled in the EVEG database are shown in blue squares.*

5.3. Pleistocene eruptive history

Figure 6 shows the cone-building stages of the Ecuadorian volcanoes based on the updated EVEG catalog, our new K-Ar ages, and stratigraphic and morphological data. Remarkably, the volcanic activity was not homogeneously distributed in space or in time. Three evolutive stages can be identified based on the number of active volcanoes at ~2.5, ~1.4 and ~0.6 Ma. Accordingly, the summary of the Pleistocene eruptive history of the Ecuadorian arc is presented, for each stage, below.

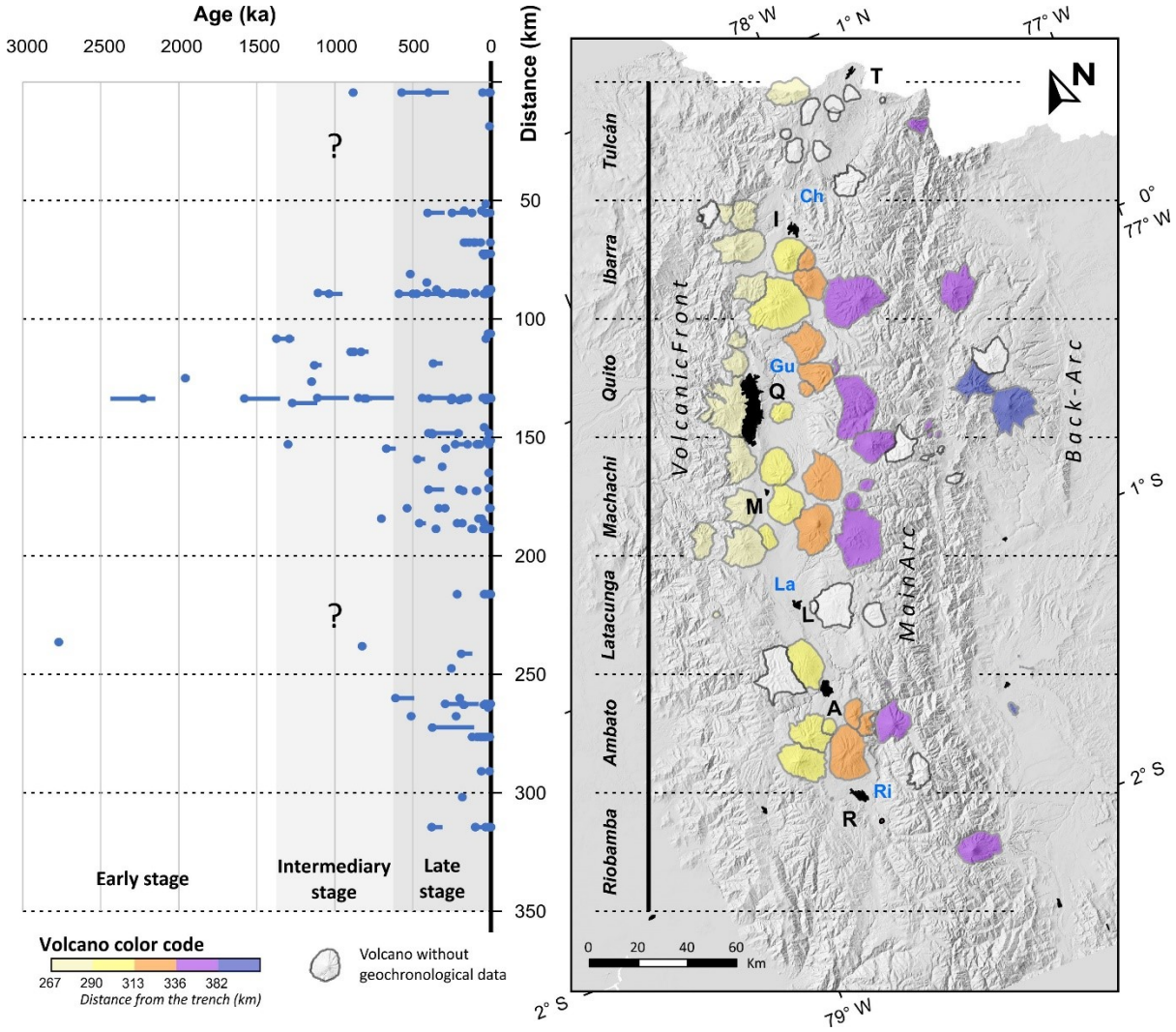

Figure 6. *Stages of eruptive history of the Ecuadorian arc. Individual cone-building stages represented according to the position of each volcano relative to the Volcanic Front axis. The cone-building stages of a lifespan lest than ~100 kyr are represented as solid dots. The oldest stages of the volcanoes in the Tulcán and Latacunga segments remains poorly constrained.*

5.3.1. Early stage: 2.5 to 1.4 Ma

Only limited data mostly concentrated in the Quito and Ambato-Latacunga segments, provide evidence for a volcanic activity occurred during this early stage (Fig. 7). Notwithstanding, the sampling biases towards the most recent units, and the limited studies focused on the Early Pleistocene volcanism, prevent us from ruling out the occurrence of additional activity in other segments.

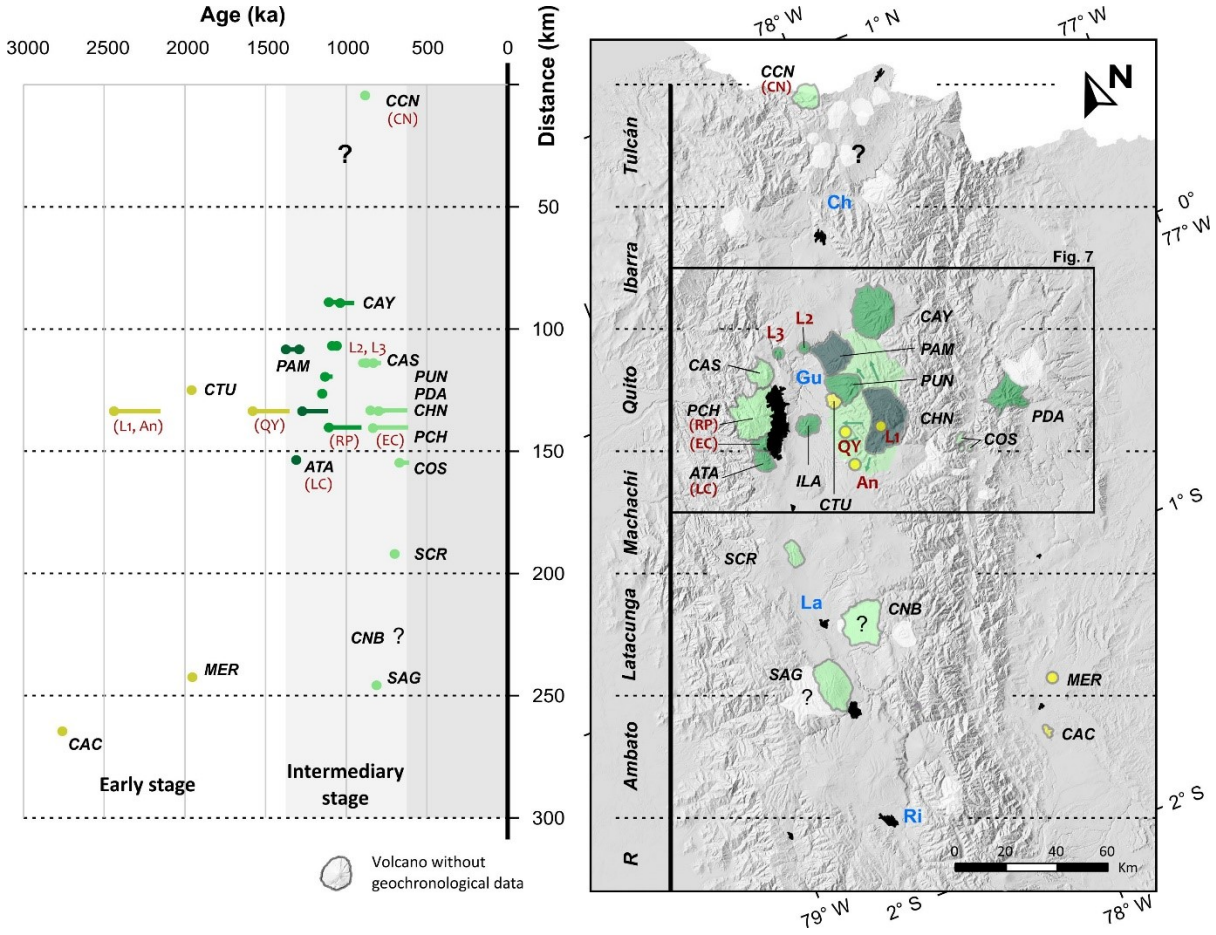

Figure 7. *Sketch of the Early (yellow) and Intermediary (green) stages of eruptive history of the Ecuadorian arc. The structures crated during the Intermediary stage colored by age: 1.4-1.2 Ma (dark green), 1.2-1.0 Ma (green), and 1.0-0.6 Ma (light green). The locations of the Pre-Chacana (L1), Mera (MER), Pre-Mojanda (L2), and Pisque (L3) eruptive centers are undefined, thus they are represented as oversized dots. Volcanoes shown as black letters according to Table 2. Landforms referred in the text shown as red letters as in Figure 3.*

Quito segment

Although many $^{40}Ar/^{39}Ar$ plateau ages provided for the **Chacana** caldera (Western Cordillera) exhibited perturbed age spectra patterns and relatively low precision isochron ages (Opdyke et al., 2006), the best-defined determinations suggest an active volcanism occurred at the center of the present-day Chacana caldera at ~2.4 Ma (Fig. 8). We obtained a more precise K-Ar age for the basal lava sequences forming the southern flank of the caldera at 2228 ± 34 ka (20EQ85; Table 1), thus implying a more widespread volcanism probably related to the Chanana pre-caldera stage. To the east, the construction of **Coturco** volcano seems to be coeval with this Chacana early stage, as suggested by the K-Ar age of 1959 ± 28 ka (20EQ54) acquired from a summit lava. No additional age from this period has been reported for the Western Cordillera or the Sub-Andean zone.

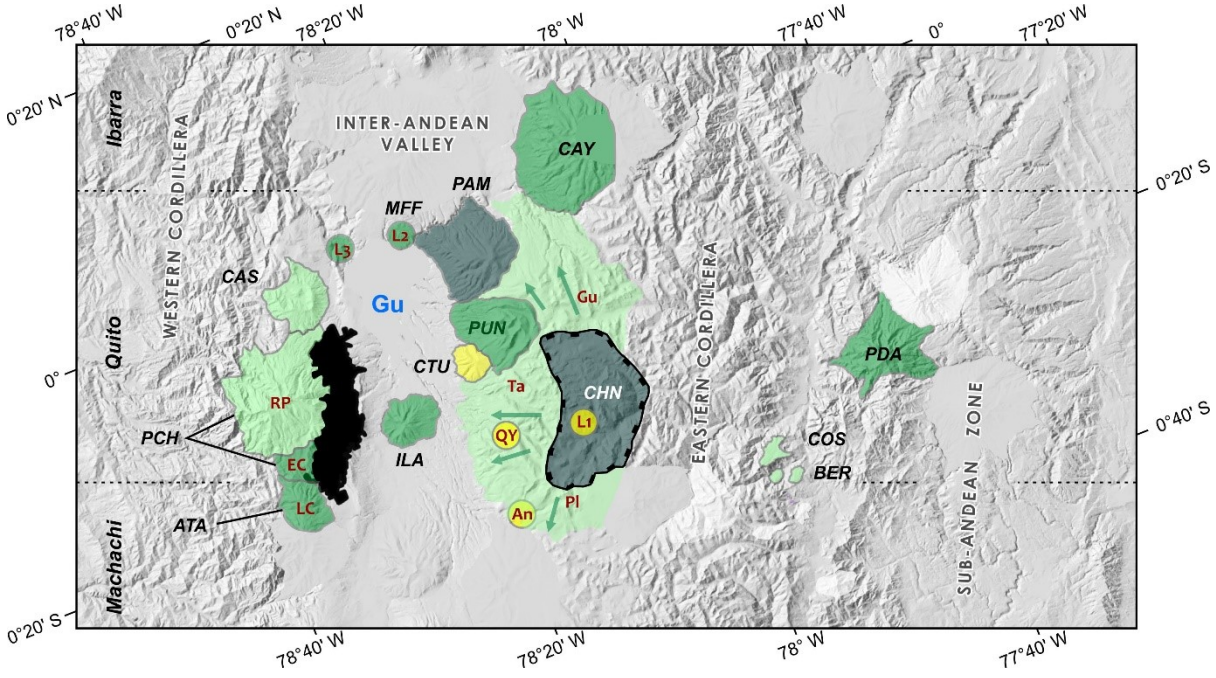

Figure 8. *Sketch of the Quito segment at the end of the Intermediary stage. Volcanic landforms colored as in Figure 6.* ***Early stage events:*** *emission of the pre-Chacana lavas (L1, An, QY) and construction of the Coturco volcano (CTU).* ***Intermediary stage events:*** *formation of the early Chacana series (QY) followed by the construction of the Pambamarca (PAM), Puntas (PUN), and Viejo Cayambe (CAY) edifices. Further east, construction of Ilaló (ILA), El Cinto (EC), and La Carcacha (LC), and emission of the Pre-Mojanda (P2) and Pisque (L3) lavas. Activity of Pan de Azúcar (PDA) volcano occurred in the sub-Andean zone. The last edifices to be constructed were Casitagua (CAS) and Rucu Pichincha (RP). The deposits created by the formation of the Chacana Caldera (Gu, Ta, Pl) partially covered the Pambamarca, Puntas, and Coturco volcanoes.*

529 ***Coeval activity in the Ambato-Latacunga segment (Back-Arc)***

530 The mostly effusive volcanism which occurred in the Sub-Andean zone formed various cone-
531 shaped landforms of a few tens of meters height (Cacalurco and Chuvaurcu cones), as well as thin lava
532 sequences to the south of Puyo city (Hoffer et al., 2008; Ball, 2015). A $^{40}Ar/^{39}Ar$ age of 2670 ± 60 ka
533 was obtained from the northern cone of **Cacalurcu** volcano (Hoffer et al., 2008). Note that intense
534 erosion and scarce exposures prevented accurate mapping in this zone. To the north of Puyo, a lava
535 sequence identified as "**Mera Lavas**" was dated by $^{40}Ar/^{39}Ar$ at 1920 ± 100 ka (Hoffer et al., 2008).
536 The source of this lavas remains unknown.

537

538 **5.3.2. Intermediary stage: 1.4 to 0.6 Ma**

539 During the intermediary stage, several new edifices were constructed in the Quito segment and
540 in the southern area of the Ibarra segment (Fig. 7). By the end of this stage, new volcanic activity
541 occurred in the segments of Tulcán to the north, and Machachi and Ambato to the south, in which only
542 a few new structures appeared (Fig. 8).

543

544 ***Quito segment***

545 In the Western Cordillera, the formation of the **Chacana** caldera is associated with massive
546 lava sequences overlayed by voluminous ignimbrite deposits and obsidian flows (Hall and Mothes,
547 2008c; Beate and Urquizo, 2015). The sequence cropping out on the western caldera flank was dated
548 between 1350 ± 90 and 1580 ± 70 ka (Bigazzi et al., 2005; Opdyke et al., 2006). To the north, the
549 overlaying El Tablon obsidian flow, dated at 810 ± 50 ka (Bigazzi et al., 2005), provides the younger
550 bound for the Chacana caldera formation. Notably, the eastern flank of the oldest Coturco volcano
551 seems to be covered by these sequences, further supporting the new K-Ar age of 1959 ± 28 ka obtained
552 here for this volcano (Table 1).

Further north, the edifices of **Pambamarca** and **Puntas** volcanoes were built on the northwestern and western flanks of Chacana (Fig. 8). The eruptive activity of these andesitic volcanoes occurred during the earliest stage of Chachana caldera-formation, as suggested by our K-Ar ages between 1261 ± 18 and 1374 ± 21 ka for Pambamarca volcano, and from 1084 ± 17 to 1132 ± 16 ka for Puntas volcano (Table 1). The Pambamarca activity finished with the extrusion of the summit rhyolitic dome complex at 1292 ± 20 ka (20EQ68). We propose that the main stage of the Chacana caldera-formation could be more recent or contemporaneous with Pambamarca and Puntas volcanoes, considering that the Chacana ignimbrite series overlies both volcanoes while surrounding their edifices (Hall and Mothes, 2008c). The age of the post-caldera activity of Chacana is defined by the Plaza de Armas lava sequence (southern caldera border; Fig. 3, 7) dated at ~726 ka (Pilicita, 2013), which is roughly coeval to El Tablón obsidian flow (western caldera border) dated at 810 ± 50 ka (Bigazzi et al., 2005).

Volcanic activity in the Western Cordillera seems to have first appear during this stage. In the southern Quito segment (Fig. 8), **La Carcacha** volcano was active at ~1300 ka (Hidalgo, 2006). It was followed to the north by the **El Cinto** volcano dated at 1112 ± 24 ka (Robin et al., 2010). El Cinto edifice was later intruded by the Ungi dome at 910 ± 7 ka (Robin et al., 2010). Further north, the activity of the **Casitagua** volcano built an andesitic main edifice surrounded by several domes between 898 ± 15 and 785 ± 16 ka (Alvarado et al., 2014; this study). Then, the construction of the **Lower Rucu Pichincha** edifice took place between the Casitagua and El Cinto volcanoes. The lava sequences of this volcano were dated between ~850 and ~590 ka (Robin et al., 2010; Alvarado et al., 2014), and thus are coeval to Casitagua volcano.

In the Guayllabamba valley (Inter-Andean valley), the activity of **Ilaló** volcano occurred between 1112 ± 22 and 1273 ± 20 ka forming an edifice composed of andesitic lava sequences. Then, in the northern border of the Guayllabamba valley, the emission of voluminous basaltic andesitic lavas were dated at 1152 ± 30 ka (**Pisque** Formation; Alvarado et al., 2014) and 1038 ± 87 ka **(pre-Mojanda** lavas; Bablon et al., 2020a). Finally, the activity of the **Pan de Azúcar** volcano (sub-Andean zone) occurred during this stage at 1150 ± 10 ka (Hoffer, 2008).

Extension to the Ibarra and Machachi segments

The volcanic activity described in the Quito segment was also present in the Ibarra and Machachi segments (Fig. 8). **Viejo Cayambe** is an ancient edifice formed to the northeast of the Chacana and Pambamarca volcanoes, in the Eastern Cordillera (Ibarra segment). This edifice, dated between 1108 ± 11 and 1050 ± 5 ka, was formed by andesitic to dacitic lava sequences that culminated in a caldera-forming eruption (Samaniego et al., 2005). Further south, the **Santa Cruz** volcano activity occurred in the Inter-Andean valley to the south of La Carcacha volcano (Machachi segment; Fig. 7). This edifice was formed by andesitic lava series dated at 702 ± 11 ka, and several dacitic domes in the summit area (Santamaría et al., submitted). Furthermore, several obsidian pebbles were identified in the Cosanga river, in the Sub-Andean zone between the Quito and Machachi segments. These fragments are related to an unknown source located in the Western Cordillera, probably the **Cosanga** or **Bermejo** centers (Mothes and Hall, 2008a). Two fission-track ages suggest that part of these obsidians was produced from eruptions occurring at 670 ± 6 and 290 ± 20 ka (Bellot-Gurlet et al., 2008).

Coeval activity in other segments

Unpublished data suggest that the lower **Cerro Negro** edifice (Western Cordillera, Tulcan segment) was active at ~880 ka (Fig. 7; Telenchana et al., 2017). However, this volcano remains poorly documented. Conversely, in the Latacunga segment, recent K-Ar groundmass ages show that the **Sagoatoa** volcano (Eastern Cordillera) was active between 826 ± 12 and 799 ± 12 ka. We note that two unreliable ages at 1850 ± 190 and 1850 ± 240 ka (Lavenu et al., 1995; Opdyke et al., 2006) were obtained from a sequence of basaltic andesite lavas north of **Chinibano** volcano (Eastern Cordillera), However, based on the erosional features and by comparison with other eroded volcanoes, we suggest that this volcano could have been constructed during the intermediate stage of the Ecuadorian arc.

5.3.3. Late stage: from 600 ka

During the late stage of the Ecuadorian volcanic arc, a striking increase in the number of active volcanoes can be observed in almost all segments (Fig. 9) with at least 50 volcanoes active during this

606 period. Although nearly twenty volcanoes remain poorly studied (most of them from the Tulcán
607 segment), we suspect that most of these volcanoes probably correspond to the late stage of the arc or
608 possibly to the intermediate stage. As shown in Figure 9, most of the volcanic activity seems to extend
609 through time from the Quito segment to the adjacent segments of Ibarra and Machachi. The eruptive
610 history of the Ibarra, Machachi, Latacunga, Ambato, Riobamba segments was presented in details
611 elsewhere (Bablon et al., 2019, 2020a; Santamaría et al., in preparation). Therefore, we describe below
612 only the detailed eruptive history of the Quito segment.

613

614 ***Quito segment***

615 The volcanic activity of the Quito segment was widespread in both Cordilleras and in the Sub-
616 Andean zone. In the Western Cordillera, the eruptive history of the Rucu Pichincha edifice extended to
617 ~150 ka including the sector collapse of its western flank (Robin et al., 2010). The westward migration
618 of activity caused the formation of the Guagua Pichincha edifice as early as ~60 ka, which included two
619 sectoral collapses and the extrusion of several dacitic domes (Robin et al., 2010). The last eruption of
620 Guagua Pichincha took place in AD 1999-2002. Both edifices make the **Pichincha volcanic complex**.
621 To the north, the highly explosive activity of the **Pululahua dome complex** occurred during the
622 Holocene. In the Eastern Cordillera, several obsidian and lava flows were emitted during the resurgent
623 phase of the **Chacana** caldera. The Mullumica and Callejones flows, dated between 180 and 200 ka,
624 are related to major Plinian eruptions whose pumice fallout deposits, known as the Pifo layers, are
625 important stratigraphic markers of the Guayllabamba basin (Bigazzi et al., 2005; Hall and Mothes,
626 2008c). To the north of the Chacana caldera, the **Izambi** volcanic series were formed at 370 ± 60 ka
627 (Bigazzi et al., 2005), whereas the underlying lava sequences seems to be related to the early stages of
628 Chacana (e.g., Aguilera et al., 2007; Hall and Mothes, 2008c).

629 Unlike the adjacent segments, the volcanic activity in the Inter-Andean valley appears to be
630 absent during this stage. However, thick volcanoclastic sequences from both cordilleras were deposited
631 in the Inter-Andean valley, resulting in the Guayllabamba and Chiche formations lying on top of the

lacustrine deposits of the San Miguel formation (Villagómez, 2003; Pacheco et al., 2014). Further west, multiple rhyolitic eruptions occurred on the western edge of the Cordillera Occidental, to the east of the Chacana caldera (e.g., Cosanga and Bermejo centers; Mothes and Hall, 2008a). Although the eruptive histories of these volcanoes remain poorly documented, radiocarbon dates and stratigraphic relationships suggest that their activity continued into the Holocene (e.g., El Dorado and Pumayacu centers; Hall and Mothes, 2010). Further west, unpublished $^{40}Ar/^{39}Ar$ ages suggest that the **Sumaco** volcano (back-arc) was active between 255 ± 32 and 200 ± 8 ka (M. Fornari pers. com.), while its most recent activity occurred during the 16th century (Salgado et al., 2021).

Holocene volcanism

From the 77 Quaternary volcanoes identified in this study, 25 experienced eruptive activity during the Holocene (Fig. 9). They include Antisana (Hall et al., 2017), Atacazo-Ninahuilca (Hidalgo et al., 2008), Calpi cones (Bablon et al., 2019), Cayambe (Samaniego et al., 1998), Chacana (Hall and Mothes, 2008c), Chachimbiro (Bernard et al., 2014), Chimborazo (Barba et al., 2008), Cotacachi-Cuicocha (Almeida et al., 2019), Cotopaxi (e.g., Hall and Mothes, 2008a; Tsunematsu and Bonadonna, 2015; Vezzoli et al., 2017), Huañuna (Hall et al., 2017), Iliniza (Santamaría et al., submitted), Imbabura (Le Pennec et al., 2011), Pichincha (Robin et al., 2008), Pululahua (Andrade et al., 2021), Quilotoa (Mothes and Hall, 2008b), Reventador (e.g., Naranjo et al., 2016), Sangay (Valverde et al., 2021), Soche (Beate, 1994; Hall and Mothes, 2008b), Sumaco (Salgado et al., 2021), Tungurahua (e.g., Le Pennec et al., 2013, 2016; Bablon et al., 2018), and the volcanoes located of the western side of the Eastern Cordillera El Dorado, Huevos de Chivo, and Pumayacu (Hall and Mothes, 2010). Although there is no clear evidence of significant explosive activity during the Holocene at the Chiles-Cerro Negro volcano (Santamaría et al., 2017), the unrest episode observed in AD 2014 implies that this volcano may still be active (Ebmeier et al., 2016). Finally, due to the lack of exhaustive studies, we do not exclude that other volcanoes may have erupted during the Holocene. For instance, the extrusion of the present-day poorly eroded domes of the Mojanda-Fuya Fuya volcanic complex (e.g., Panecillo dome; Robin et al., 2009) and Pambamarca volcano (i.e. Herradura dome; this study), could have ocurred during the Holocene.

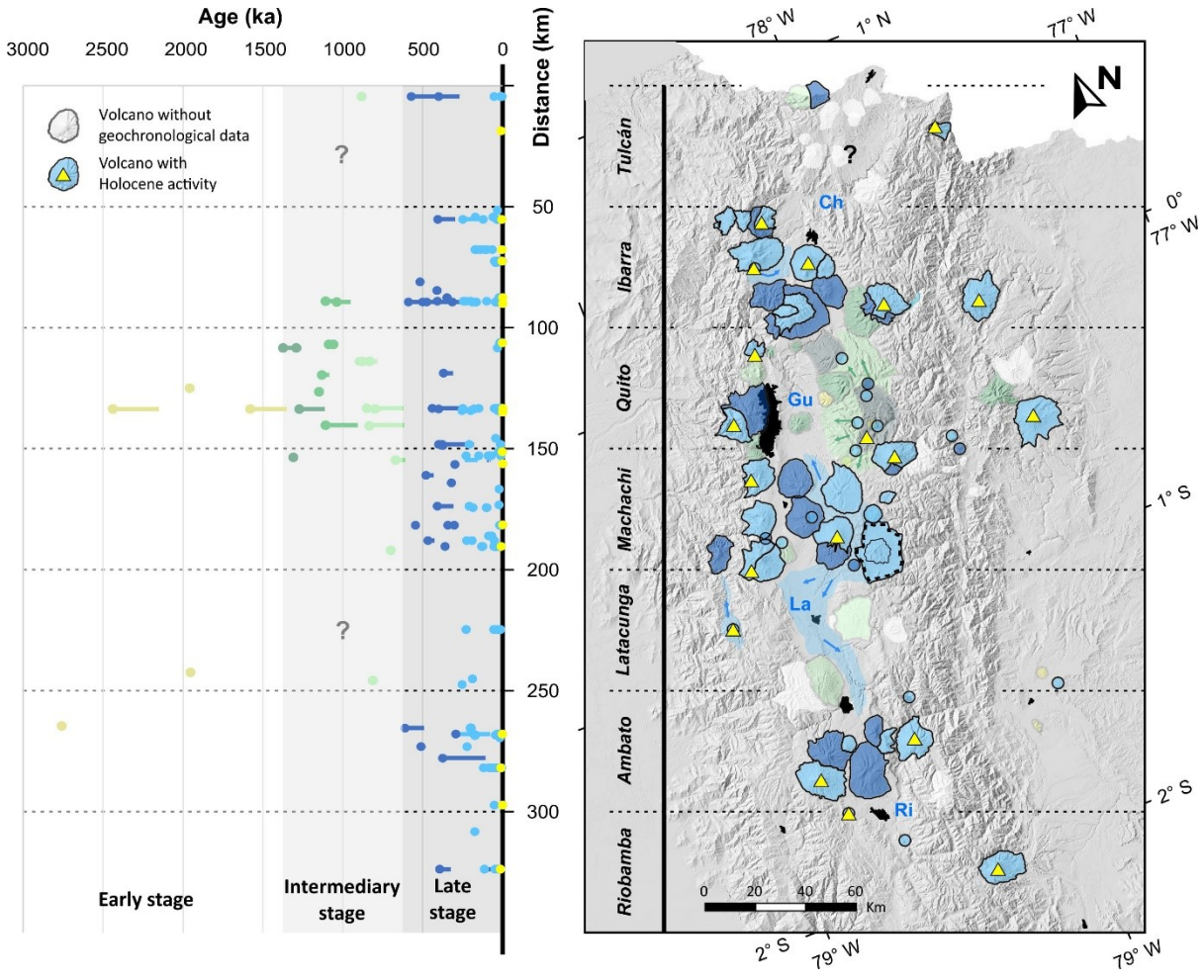

Figure 9. *Sketch of the Late (blue) stage of eruptive history of the Ecuadorian arc. Structures crated during this stage colored by age: 600-300 ka (dark blue) and <300 ka (light blue). Locations of small eruptive centers (<5 km in diameter) represented as oversized dots. Volcanoes with Holocene activity highlighted with yellow triangles. See Appendix D for a detailed view and volcano names.*

5.4. Geochemical characterization

The volcanic products of the Ecuadorian arc have been classified as medium to high potassium calc-alkaline basaltic andesites to rhyolites (e.g., Hall et al., 2008; Hidalgo et al., 2012; Ancellin et al., 2017; Chiaradia et al., 2020), with exceptional occurrences of shoshonitic rocks (e.g., Hoffer et al., 2008; Garrison et al., 2017). Overall, the concentrations of incompatible elements (e.g., K, Rb, Sr, Ba, La, Th) tend to increase farther away from the trench (Fig. 10a-b). Furthermore, a decrease in the concentrations of elements considered as fluid-mobile (e.g., Ba, Pb, Cs, Li, B) relative to fluid-immobile

672 elements (e.g., Be, Nb, Th, La) was observed as the distance from the trench increases. High Ba/Th
673 (Fig. 10c), Ba/La, and Ba/Nb ratios are thus commonly observed in in the volcanoes placed close to the
674 trench, and exceptionally in the Puyo lavas (Ambato segment back-arc). Notably, the widest variability
675 ranges in trace element contents are found in the center of the arc (Ibarra, Quito, and Machachi
676 segments; e.g., Ancellin et al., 2017). For instance, the La content and the Ba/Th ratio remains in a short
677 range of variability in the southern termination of the arc (Latacunga, Ambato, and Riobamba segments)
678 compared to the more variable values observed in the central arc (Fig. 10d-e). These ratios can be used
679 to deduce a gradual decrease in the quantity of fluids liberated by the subducting slab further away from
680 the trench, and then leading to a lower degree of partial melting of the mantle wedge (e.g., Hidalgo et
681 al., 2012; Ancellin et al., 2017). A change in the nature of the slab inputs, from aqueous fluids to
682 siliceous melts, was observed towards the central part of the arc by linking the behavior of the Ba/Th
683 ratio to the $^{206}Pb/^{204}Pb$ isotopic ratio (Samaniego et al., 2010; Ancellin et al., 2017; Narvaez et al., 2018).

684 On the other hand, various studies highlighted the role of fractional crystallization processes in
685 the magmatic evolution of the central and northern segment lavas (e.g., Schiano et al., 2010; Hidalgo et
686 al., 2012; Chiaradia et al., 2020). Their geochemical modeling approach commonly included a
687 metasomatized mantle-derived basaltic melt, and the fractionation of variable amounts of plagioclase,
688 pyroxene, amphibole, and olivine. However, the exceptional strong Y and HREE depletions observed
689 in certain lavas were unable to be justified by simple fractional crystallization models, as they required
690 a more extensive fractionation of amphibole and garnet. Thus, the observed geochemical variation has
691 been related to changes in the deep mantle source and/or crustal processes, coupled with magma mixing
692 and fractional crystallization processes (Garrison et al., 2006; Hidalgo et al., 2007, 2012; Chiaradia et
693 al., 2009, 2020; Schiano et al., 2010; Bellver-Baca et al., 2020). Despite the crustal thickness ranging
694 between 50 and 65 km beneath the volcanic arc (Koch et al., 2021), the estimated amount of upper
695 crustal contamination (between ~1 and 2.4%) is relatively low compared to the imprint of the lower
696 crustal assimilation (ranging from east to west between ~3 and ~27%) as demonstrated by isotopic (Sr-
697 Nd-Pb) and trace elements models (Garrison et al., 2006; Hidalgo et al., 2012; Ancellin et al., 2017).
698 Although minor geochemical variations can be observed through time, our major and trace element

699 analyses reflect the same behavior described by these authors. The detailed identification of the
700 magmatic processes active in this part of the Ecuadorian arc is beyond the scope of this contribution.

701

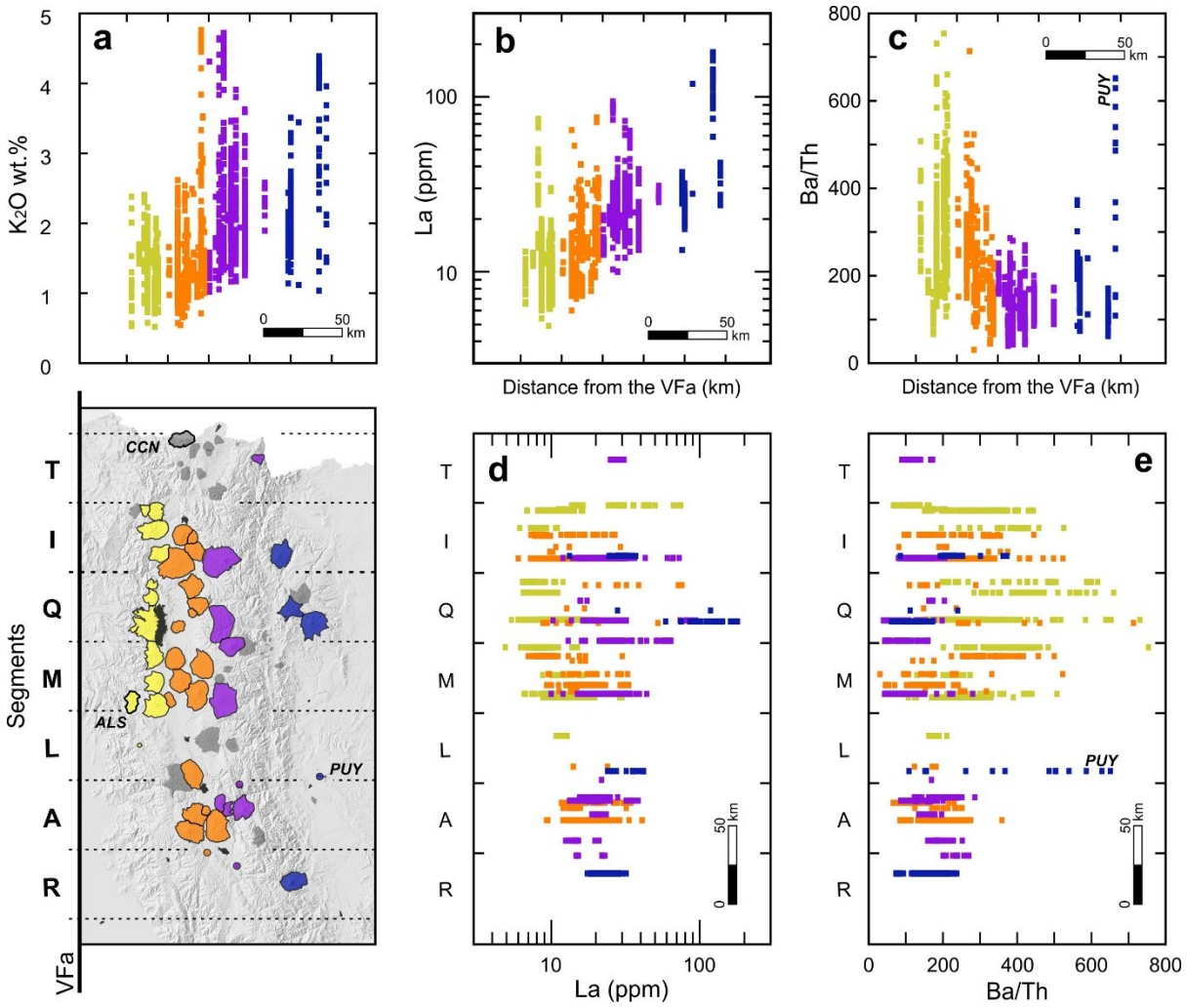

702

703 ***Figure 10.*** *Geochemical variability observed in the Ecuadorian Arc.* ***a)*** *K_2O (wt.%),* ***b)*** *La (ppm), and*
704 ***c)*** *Ba/Th as function of the distance from the Volcanic Front axis (VFa).* ***d)*** *La (ppm), and* ***e)*** *Ba/Th*
705 *variations relative to the arc segmentation. Across-arc and along-arc distances relative to the*
706 *position of Almas Santas (ALS) and Chiles-Cerro Negro (CCN) volcanoes, respectively. PUY: Puyo*
707 *cones. Data obtained from the Georoc database (http://georoc.mpch-mainz.gwdg.de/georoc/)*
708 *complemented with our data and other studies (Pacheco, 2013; Bablon et al., 2020a; Córdova et al.,*
709 *2020; Santamaría et al., submitted).*

710

5.5. Relationship between volcanism and tectonics

The concordance between the ancient NE-SW crustal structures of the Andean Range and the corridors of the Ecuadorian arc is noticeable (Fig. 11a; Litherland and Aspden, 1992). Comparable relationships between the crustal tectonic structures and the arrangement of volcanoes have been also documented in the other Andean volcanic zones (e.g., Acocella et al., 2007; Cembrano and Lara, 2009; González et al., 2009; Salas et al., 2017; Tibaldi et al., 2017) and even worldwide (e.g., Takada, 1994; Tibaldi and Bonali, 2017; Bonali et al., 2018). Indeed, numerous studies revealed that the ascension of magma through the crust is mainly controlled by tectonics (e.g., van Wyk de Vries and van Wyk de Vries, 2018). Whereas diapirism is a dominant process in magma transport at deeper levels within the ductile lower crust, dike propagation is prevalent in the upper brittle crust, which is also more susceptible to tectonics (e.g., Weinberg, 1996; Petford et al., 2000). Thus, multiple authors highlighted the arrangement of eruptive centers and/or dykes as a response to the regional tectonic stress (e.g., Delaney et al., 1986; Cembrano and Lara, 2009; Sychev et al., 2019; Díaz et al., 2020). Moreover, the volcanoes distribution and unrest periods also seem to be affected by local stress regimes and the mechanical properties of the bedrock, which ultimately influence the magma pressure in the conduit (e.g., Gudmundsson, 2006; Gudmundsson and Philipp, 2006; Ebmeier et al., 2016). Following the approach of Cembrano and Lara (2009), we differentiated two volcano-tectonic associations according to their spatial distribution over present-day active and inactive (inherited) crustal structures.

Volcanoes over inherited basement structures

This category includes the eruptive centers located above or close to major tectonic structures of the continental crust formed prior to the Pleistocene. They correspond to mostly inactive fault systems and sutures that could serve as passive pathways for magma ascent (Litherland and Aspden, 1992). In the Western Cordillera, the edifices of the Volcanic Front lie above ancient margin-parallel thrust-belt faults (Fig. 11a). These NNE-SSW oriented fault systems separate the Cretaceous oceanic plateau basalts and ophiolites units (e.g., San Juan, Pallatanga, and Pilatón Formations) to the East,

737 from the Paleogene to Eocene volcanic and volcanoclastic units (e.g., Macuchi Formation) to the West
738 (Hughes and Bermúdez, 1997; Hughes and Pilatasig, 2002; Vallejo et al., 2019). The Chachimbiro-
739 Pichincha-Iliniza and Carihuairazo-Chimborazo volcanoes are placed over the Calacalí-Pujilí-
740 Pallatanga suture zone, whereas Almas Santas, the westernmost volcano of the arc, is placed over the
741 Chimbo-Toachi suture zone (Hughes and Pilatasig, 2002; Vallejo et al., 2019). Although the volcanoes
742 of the Eastern Cordillera are apparently more dispersed than in the Western Cordillera, the N-S
743 Pambamarca-Sincholagua-Cotopaxi, and Cayambe-Antisana-Chalupas associations can be
744 distinguished (Fig. 11a). Despite that the thrust-belt faults structures of the western edge of the Eastern
745 Cordillera are hidden by a thick Pliocene volcanoclastic cover (e.g. Pisayambo and Angamarca
746 Formations), their existence is inferred by the scarce exposures further north in the Chota Valley and in
747 the Pisayambo zone to the south (Litherland et al., 1994; Winkler et al., 2005). These major fault
748 systems separate the metamorphic groups formed during the Triassic anatexis and posterior accretion
749 of the Jurassic para-autochthonous terrains (Litherland et al., 1994; Villagómez et al., 2011; Spikings
750 et al., 2015). For instance, the Pambamarca-Sincholagua-Cotopaxi volcanoes were constructed over the
751 Peltetec suture zone (Litherland et al., 1994; Vallejo et al., 2019). Similarly, although evidence is
752 lacking, the Mojanda-Ilaló-Pasochoa-Rumiñahui alignment suggest the presence of an inherited
753 basement structures beneath the Inter-Andean valley. Nonetheless, exposures of the Inter-Andean
754 valley bedrock are scarce, resulting in an incomplete understanding of the suture architecture created
755 by the accretion of the Western Cordillera terrains (Litherland et al., 1994; Hughes and Pilatasig, 2002).
756 Further east, the back-arc volcanoes are built near the basement-involved thrust belt faults related to the
757 Napo Uplift, which was formed by the eastward thrusting of the Western Cordillera (Bès de Berc et al.,
758 2005; Gutiérrez et al., 2019). Although several of these structures are still active, their extension and
759 behavior are still poorly documented.

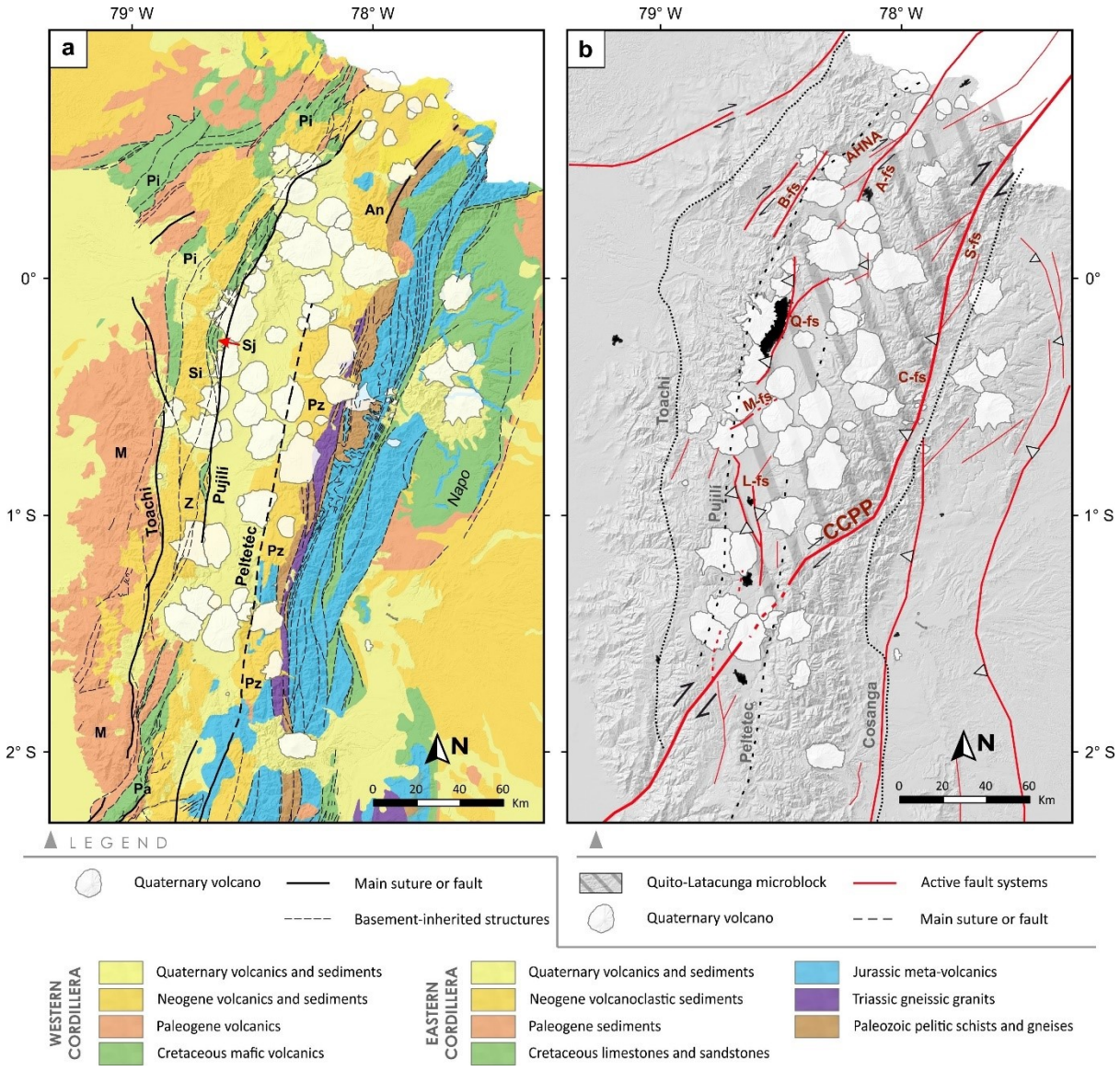

760

761 ***Figure 11. a)*** *Synthetic geological map of the central and northern Ecuadorian Andes showing the*
762 *basement-inherited structures beneath the volcanic arc (Modified from Hughes and Bermúdez, 1997;*
763 *Litherland et al., 1994; Egüez et al., 2017; Vallejo et al., 2019). Geological units mentioned in the*
764 *text represented as black letters. An: Angochagua; M: Macuchi; Pa: Pallatanga; Pi: Pilatón; Pz:*
765 *Pizayambo; Si: Silante; Sj: San Juan; Z: Zumbahua.* ***b)*** *Tectonic map of the same area describing the*
766 *active faults as red lines. A-fs: Ambi; B-fs: Billecocha; C-fs: Cosanga; L-fs: Latacunga; M:*
767 *Machachi; Q-fs: Quito; and S-fs: Salado fault systems as red letters.*

768

Volcanoes over present-day compressional or transpressional tectonics

This category includes volcanoes whose spatial distribution and morphology seem to be controlled by Quaternary fault systems (Fig. 11b). Although several active fault systems (fs) have been identified in the Ecuadorian Andes (e.g., Alvarado et al., 2016), few volcanic landforms could be linked from the motion and spatial arrangement of the Quaternary fault systems (Andrade, 2009). The CCPP-fs is the major tectonic structure in Ecuador connecting several transpresive and reverse subsystems from the Gulf of Guayaquil to the eastern border of the Eastern Cordillera. Surprisingly, only a few volcanoes are found near or over this major system. To the north, the Soche and Reventador volcanoes, as well as the Cosanga volcano cluster, are located next to the Cosanga and Salado subsystems. However, scarce volcanic morphologies seem to be related to the fault motions (Tibaldi et al., 2007; Alvarado et al., 2016). The CCPP-fs intersects the Inter-Andean valley in the Ambato segment, running through the Huisla, Mulmul and Igualata volcanoes, and the Calpi cones. Notably, the Igualata volcano edifice shows a summit graben bordered by sigmoid faults, while its basal outline evidences the lateral displacement of the CCPP-fs (Baize et al., 2020). Nonetheless, the whole Ambato volcanic cluster does not present a clear lignent with the CCPP-fs (i.e. Chimborazo-Tungurahua cluster). Likewise, some components of the El Angel-Huayrapungo-Nanegal-Apuela fault system (AHNA-fs) influenced the shape of some volcanoes in the Ibarra segment to the north. For instance, the Billecocha subsystem apparently influenced the orientation of the Cotacachi sector collapses as well as their subsequent reconstruction patterns (Almeida et al., 2019; Jomard et al., 2021). Farther east, the Alambi subsystem played a key role in the preferential growth patterns of the Imbabura volcano (Andrade et al., 2019). The central part of the arc is located in the interaction zone between the Quito and Latacunga reverse fault systems (QL-fs) which are expressed to the north and south of the segment as parallel strands of folds located above major west dipping, blind, en echelon thrust faults (Fiorini and Tibaldi, 2012; Alvarado et al., 2014, 2016). These structures affect the volcano-sedimentary deposits of the eastern margin of the Inter-Andean Valley, probably converging towards the Pujilí suture zone (Western Cordillera; Alvarado et al., 2016) below the fontal-arc volcanoes. Notably, several segments of the Quito-fs are curved around the volcanic edifices implying that the onset of volcanic activity occurred

prior to tectonic activity (Alvarado et al., 2014). Based on the limited correlation between the active fault system arrangement and the distribution of volcanism, we propose that the basement inherited structures played a predominant role in the magma ascension and distribution of the volcanic edifices, while active tectonics controlled second-order morphological features.

5.6. Relationship between volcanism and the Nazca slab

The spatial distribution of the volcanic clusters without Quaternary tectonic subsystems suggests may be also associated to magmatic anomalies at depth possibly caused by variations in the geometry and/or thermal state of the slab. Yepes et al. (2016) have revealed the geometry of the slab beneath Ecuador as a contorted surface, where the projection of the Grijalva FZ coincides with an inferred slab flexure at depth. For Bablon et al. (2019) the apparent southward migration of the volcanoes in the Ambato segment, placed above the Grijalva FZ, was probably influenced by changes in the slab geometry which were independent of the Grijalva FZ displacement. Below the central and northern parts of the arc, the inslab Nazca plate seismicity is not observable probably due to the slab thermal state created by the younger Nazca crust (Gutscher et al., 1999, 2000; Yepes et al., 2016). Therefore, we are unable to establish an adequate relationship of volcanism and the slab geometry. However, the magma generation conditions place the slab at a depth of roughly 100-120 km and dipping at about 20° only (Yepes et al., 2016; Portner et al., 2020). This position may favor a wide zone of magma generation causing the volcanoes to appear in a wider area. Moreover, the occurrence of the Sub-Andean volcanoes suggest a wide magma generation zone for the whole Ecuadorian arc.

We notice that, despite the scarce geochronological data, an intense volcanism seems to be present in the Quito segment since at least ~2.4 Ma, or even earlier in the back-arc on the Ambato segment (i.e. Cacalurco cones). These oldest volcanic areas are located over key slab structures, i.e., the projection of the Carnegie ridge onto the young Nazca crust, and the Nazca slab flexure, respectively. We speculate that the thermal regime of the young Nazca crust and the Carnegie Ridge favored magma generation since the Early Pleistocene. Moreover, the volcanoes of the Ibarra, Quito and Machachi

822 segments exhibit important variations in the geochemistry of their magmas which may be linked to the
823 subduction of these structures, as previously suggested (e.g., Gutscher et al., 1999; Ancellin et al., 2017;
824 Garrison et al., 2017; Chiaradia et al., 2021).

825 As noted by Bablon et al. (2019), the slab motion bellow the Ecuadorian arc is not sufficient to
826 drive a migration of magmatism though the Late Pleistocene by itself. This observation is consistent
827 with the proposed eruptive history, where the late-stage volcanism shows an apparent random
828 emplacement over time, without remarkable N-S or E-W migrations. Given that the slab displacement
829 is not fast enough to allow the Nazca thermal state transition to cover the whole arc during the Late
830 Pleistocene (Bablon et al., 2019, 2020a), the conditions that caused the spatial prolongation of the
831 magmatic generation zone should be a long-lived phenomenon. Alternatively, the changes that drove
832 the increase in volcanism at 600 ka may be related to variations in the crustal stress field and/or
833 variations in slab geometry somewhat unrelated to its displacement. Indeed, the timing of the increase
834 in the volcanic activity seems to coincide with other regional tectonic events, such as: (1) the cessation
835 of the Late Pliocene WNW–ESE compressional phase registered in the Chota basin (Fig. 1c; northern
836 Ecuadorian Andes) prior to the Late Pleistocene, as was recorded by the deformed dykes and sills (AFT
837 age: 3.7 ± 1.7 Ma) which are unconformably overlaid by the undeformed volcanoclastic rocks (ZFT
838 age: 0.5 ± 0.2 Ma; Barragán et al., 1996; Winkler et al., 2005); (2) the formation the Quito-Latacunga
839 microblock during the Pleistocene as a consequence of the latest transfer stage of the North Andean
840 Sliver deformation zone from the Western Cordillera to the east of the Eastern Cordillera, by creating
841 (or reactivating) and abandoning tectonic structures over time in favor of compatible convergence
842 directions (Fig. 1c; Alvarado et al., 2016); and (3) the Late Pleistocene increase of the subsidence and
843 deposition rates observed in the Gulf of Guayaquil (Fig. 1b) recorded by the pile of sediments up to 4
844 km in thickness, dated by foraminifera chronobiozones and marine transgression-regressive structures,
845 which overlies the thinner Pliocene series (Witt et al., 2006; Witt and Bourgois, 2010; Loayza et al.,
846 2013). This readjustment in the upper crust dynamics during the Pleistocene may reflect changes in slab
847 geometry, as well as changes in the depth, residence time, and ascent rate of magmas in the crust. Thus,
848 volcanoes appear randomly over wider areas at the observed time scales. Nonetheless, a further analysis

849 of the temporal relationship between these tectonic events and the whole arc volcanism should be
850 discussed in a focused survey.

851

852 **6. CONCLUSIONS**

853 After two decades of research conducted on the Ecuadorian Andes volcanism, the
854 geochronological data acquired in numerous studies were compiled into an extensive database. It
855 allowes to define the spatial and temporal evolution of volcanism in the Ecuadorian Andes for the first
856 time. This data compilation demonstrated that the Ecuadorian arc is composed of at least 77 Quaternary
857 volcanoes, was built in three main stages with an overall marked increase in the number of active
858 volcanoes. (1) The new K-Ar ages acquired in this study demonstrated that volcanism started as early
859 as ~2.4 Ma in the central part of the Ecuadorian arc (Quito segment) with the formation of the Chacana
860 and Coturco volcanoes in the Eastern Cordillera. A minor volcanic activity seems to have occurred in
861 the southern back-arc (Ambato segment) with the emission of large volume lava flows (Hoffer et al.,
862 2008). (2) Then, the volcanic activity extended at ~1.4 Ma around the Guayllabamba valley creating
863 the edifices of Cayambe (Samaniego et al., 2005), Pambamarca, Puntas, Casitagua (this study),
864 Pichincha (El Cinto and Rucu Pichincha; Robin et al., 2010), and La Carcacha (Atacazo volcanic
865 complex; Hidalgo, 2006). The construction of Ilaló volcano, and the emission of the Pre-Mojanda
866 (Bablon et al., 2020a) and Pisque lavas (Alvarado et al., 2014) occurred in the Inter-Andean valley.
867 Towards the end of the intermediate stage (i.e., ~900-600 ka), single edifices appeared in the northern
868 (Cerro Negro; Telenchana et al., 2017), south-central (Santa Cruz; Santamaría et al., submitted), and
869 southern (Sagoatoa; Bablon et al., 2019) zones of the Inter-Andean valley. (3) A notable increase in the
870 volcanic activity occurred since ~600 ka, when at least 50 volcanoes were active during this interval.
871 Instead of being homogeneously distributed along the arc, several of these volcanoes were emplaced in
872 areas of a few dozens of square kilometers forming E-W elongated volcanic clusters (e.g., Bablon et
873 al., 2019, 2020a). At least 25 of these volcanoes were still active during the Holocene.

874 The spatial arrangement of the volcanoes seems to be primarily influenced by the tectonic
875 structures inherited from the continental crust, whereas the Quaternary tectonic activity may have
876 played a secondary role in the distribution of the volcanoes. We note that the higher concentration of
877 volcanoes towards the central part of the arc and the long duration of the volcanic activity in this area
878 are spatially coincident with the inland projection of noticeable features in the slab, such as the younger
879 Nazca crust and the Carnegie ridge. Although several non-exclusively petrogenetic models have been
880 proposed to explain the magmatic geochemical variability in the central part of the arc (e.g., Garrison
881 et al., 2006; Chiaradia et al., 2009, 2021; Hidalgo et al., 2012), our data set show that the subduction of
882 these slab features probably drove the increase and expansion of the volcanic activity in the Ecuadorian
883 arc.

884 # REFERENCES

885 Acocella, V., Vezzoli, L., Omarini, R., Matteini, M., Mazzuoli, R., 2007. Kinematic variations across
886 Eastern Cordillera at 24°S (Central Andes): Tectonic and magmatic implications. Tectonophysics
887 434, 81–92. https://doi.org/10.1016/j.tecto.2007.02.001

888 Aguilera, G., Castilla, W., Nasimba, E., León, E., Calero, B., Pilatasig, L., Gordón, D., 2007. Hoja
889 geológica Cangahua.

890 Almeida, M., Bablon, M., Andrade, D., Hidalgo, S., Quidelleur, X., Samaniego, P., 2019. New
891 constraints on the geological and chronological evolution of the Cotacachi-Cuicocha Volcanic
892 Complex (Ecuador). Presented at the 8th International Symposium on Andean Geodynamics
893 (ISAG), Quito, Ecuador.

894 Alvarado, A., Audin, L., Nocquet, J.M., Jaillard, E., Mothes, P., Jarrín, P., Segovia, M., Rolandone, F.,
895 Cisneros, D., 2016. Partitioning of oblique convergence in the Northern Andes subduction zone:
896 Migration history and the present-day boundary of the North Andean Sliver in Ecuador.
897 Tectonics 35, 1048–1065. https://doi.org/10.1002/2016TC004117

898 Alvarado, A., Audin, L., Nocquet, J.M., Lagreulet, S., Segovia, M., Font, Y., Lamarque, G., Yepes, H.,
899 Mothes, P., Rolandone, F., Jarrín, P., Quidelleur, X., 2014. Active tectonics in Quito, Ecuador,
900 assessed by geomorphological studies, GPS data, and crustal seismicity. Tectonics 33, 67–83.
901 https://doi.org/10.1002/2012TC003224

902 Ancellin, M.-A., Samaniego, P., Vlastélic, I., Nauret, F., Gannoun, A., Hidalgo, S., 2017. Across-arc
903 versus along-arc Sr-Nd-Pb isotope variations in the Ecuadorian volcanic arc. Geochem. Geophys.
904 Geosyst. 18, 1163–1188. https://doi.org/10.1002/2016GC006679

905 Andrade, S.D., 2009. The influence of active tectonics on the structural development and flank collapse
906 of Ecuadorian arc volcanoes (Ph.D. thesis). Clermont-Ferrand 2, Clermont-Ferrand, France.

907 Andrade, S.D., Müller, A.V., Vasconez, F.J., Beate, B., Aguilar, J., Santamaría, S., 2021. Pululahua
908 dome complex, Ecuador: eruptive history, total magma output and potential hazards. Journal of
909 South American Earth Sciences 106, 103046. https://doi.org/10.1016/j.jsames.2020.103046

910 Andrade, S.D., van Wyk de Vries, B., Robin, C., 2019. Imbabura volcano (Ecuador): The influence of
911 dipping-substrata on the structural development of composite volcanoes during strike-slip
912 faulting. Journal of Volcanology and Geothermal Research, GEOLOGICAL DATA IN
913 VOLCANOLOGY: COLLECTION, ORGANISATION AND APPLICATIONS 385, 68–80.
914 https://doi.org/10.1016/j.jvolgeores.2018.11.017

915 Aspden, J.A., Bonilla, W., Duque, P., 1995. The El Oro metamorphic complex, Ecuador: geology and
916 economic mineral deposits, Overseas geology and mineral resources. British Geological Survey,
917 Keyworth, Nottingham.

918 Aspden, J.A., Harrison, S.H., Rundle, C.C., 1992. New geochronological control for the tectono-
919 magmatic evolution of the metamorphic basement, Cordillera Real and El Oro Province of
920 Ecuador. Journal of South American Earth Sciences 6, 77–96. https://doi.org/10.1016/0895-
921 9811(92)90019-U

922 Bablon, M., Quidelleur, X., Samaniego, P., Le Pennec, J.-L., Audin, L., Jomard, H., Baize, S., Liorzou,
923 C., Hidalgo, S., Alvarado, A., 2019. Interactions between volcanism and geodynamics in the

924 southern termination of the Ecuadorian arc. Tectonophysics 751, 54–72.
925 https://doi.org/10.1016/j.tecto.2018.12.010

926 Bablon, M., Quidelleur, X., Samaniego, P., Le Pennec, J.-L., Lahitte, P., Liorzou, C., Bustillos, J.E.,
927 Hidalgo, S., 2018. Eruptive chronology of Tungurahua volcano (Ecuador) revisited based on new
928 K-Ar ages and geomorphological reconstructions. Journal of Volcanology and Geothermal
929 Research 357, 378–398. https://doi.org/10.1016/j.jvolgeores.2018.05.007

930 Bablon, M., Quidelleur, X., Samaniego, P., Le Pennec, J.-L., Santamaría, S., Liorzou, C., Hidalgo, S.,
931 Eschbach, B., 2020a. Volcanic history reconstruction in northern Ecuador: insights for eruptive
932 and erosion rates on the whole Ecuadorian arc. Bull Volcanol 82, 11.
933 https://doi.org/10.1007/s00445-019-1346-1

934 Bablon, M., Quidelleur, X., Siani, G., Samaniego, P., Le Pennec, J.-L., Nouet, J., Liorzou, C.,
935 Santamaría, S., Hidalgo, S., 2020b. Glass shard K-Ar dating of the Chalupas caldera major
936 eruption: Main Pleistocene stratigraphic marker of the Ecuadorian volcanic arc. Quaternary
937 Geochronology 57, 101053. https://doi.org/10.1016/j.quageo.2020.101053

938 Baize, S., Audin, L., Alvarado, A., Jomard, H., Bablon, M., Champenois, J., Espin, P., Samaniego, P.,
939 Quidelleur, X., Le Pennec, J.-L., 2020. Active Tectonics and Earthquake Geology Along the
940 Pallatanga Fault, Central Andes of Ecuador. Frontiers in Earth Science 8, 193.
941 https://doi.org/10.3389/feart.2020.00193

942 Ball, P., 2015. Geochemical Analysis of Ecuadorian Back-Arc Lavas (Master's thesis). University of
943 Oxford, Oxford, UK.

944 Barba, D., Robin, C., Samaniego, P., Eissen, J.-P., 2008. Holocene recurrent explosive activity at
945 Chimborazo volcano (Ecuador). Journal of Volcanology and Geothermal Research, Recent and
946 active volcanism in the Ecuadorian Andes 176, 27–35.
947 https://doi.org/10.1016/j.jvolgeores.2008.05.004

948 Barberi, F., Coltelli, M., Ferrara, G., Innocenti, F., Navarro, J.M., Santacroce, R., 1988. Plio-quaternary
949 volcanism in Ecuador. Geological Magazine 125, 1–14.

950 Barragán, R., Baudino, R., Marocco, R., 1996. Geodynamic evolution of the Neogene intermontane
951 Chota basin, Northern Andes of Ecuador. Journal of South American Earth Sciences 9, 309–319.
952 https://doi.org/10.1016/S0895-9811(96)00016-8

953 Beate, B., 1994. El Soche: Un volcán activo en la Provincia de Sucumbíos, Ecuador - primeros datos
954 descriptivos, in: Lachowicz, H. (Ed.), . Presented at the Terceras Jornadas en Ciéncias de la
955 Tierra, Facultad de Geologia, Escuela Politécnica Nacional, Quito, Ecuador, pp. 9–10.

956 Beate, B., 1985. El flujo piroclastico de Chalupas como causante de un desastre natural en el
957 Cuaternario de los Andes Septentrionales del Ecuador, in: Espinosa, T. (Ed.), . Presented at the
958 Primer Simposio Latinoamericano sobre Desastres Naturales, Quito, Ecuador, pp. 21–27.

959 Beate, B., Urquizo, M., 2015. Geothermal Country Update for Ecuador: 2010-2015, in: Proceedings
960 World Geothermal Congress. pp. 19–24.

961 Bellot-Gurlet, L., Dorighel, O., Poupeau, G., 2008. Obsidian provenance studies in Colombia and
962 Ecuador: obsidian sources revisited. Journal of Archaeological Science 35, 272–289.
963 https://doi.org/10.1016/j.jas.2007.03.008

964 Bellver-Baca, M.T., Chiaradia, M., Beate, B., Beguelin, P., Deriaz, B., Mendez-Chazarra, N.,
965 Villagómez, D., 2020. Geochemical evolution of the Quaternary Chachimbiro Volcanic Complex
966 (frontal volcanic arc of Ecuador). Lithos 356–357, 105237.
967 https://doi.org/10.1016/j.lithos.2019.105237

968 Bernard, B., Andrade, D., 2011. Volcanes Cuaternarios del Ecuador Continental. IGEPN Poster
969 Informativo.

970 Bernard, B., Hidalgo, S., Robin, C., Beate, B., Quijozaca, J., 2014. The 3640–3510 BC rhyodacite
971 eruption of Chachimbiro compound volcano, Ecuador: a violent directed blast produced by a
972 satellite dome. Bull Volcanol 76, 849. https://doi.org/10.1007/s00445-014-0849-z

973 Bès de Berc, S., Soula, J.C., Baby, P., Souris, M., Christophoul, F., Rosero, J., 2005. Geomorphic
974 evidence of active deformation and uplift in a modern continental wedge-top–foredeep transition:
975 Example of the eastern Ecuadorian Andes. Tectonophysics, Andean Geodynamics: 399, 351–
976 380. https://doi.org/10.1016/j.tecto.2004.12.030

977 Bigazzi, G., Hadler Neto, J.C., Iunes, P.J., Osório Araya, A.M., 2005. Fission-track dating of South
978 American natural glasses: an overview. Radiation Measurements, Proceedings of the 2nd Latin
979 American Symposium on Nuclear Tracks 39, 585–594.
980 https://doi.org/10.1016/j.radmeas.2004.09.006

981 Bonali, F.L., Tibaldi, A., Pasquaré Mariotto, F., Russo, E., 2018. Interplay between inherited rift faults
982 and strike-slip structures: Insights from analogue models and field data from Iceland. Global and
983 Planetary Change, From the deep Earth to the surface 171, 88–109.
984 https://doi.org/10.1016/j.gloplacha.2018.03.009

985 Bryant, J.A., Yogodzinski, G.M., Hall, M.L., Lewicki, J.L., Bailey, D.G., 2006. Geochemical
986 Constraints on the Origin of Volcanic Rocks from the Andean Northern Volcanic Zone, Ecuador.
987 Journal of Petrology 47, 1147–1175. https://doi.org/10.1093/petrology/egl006

988 Cembrano, J., Lara, L., 2009. The link between volcanism and tectonics in the southern volcanic zone
989 of the Chilean Andes: A review. Tectonophysics, Understanding stress and deformation in active
990 volcanoes 471, 96–113. https://doi.org/10.1016/j.tecto.2009.02.038

991 Chiaradia, M., Bellver-Baca, M.T., Valverde, V., Spikings, R., 2021. Geochemical and isotopic
992 variations in a frontal arc volcanic cluster (Chachimbiro-Pulumbura-Pilavo-Yanaurcu, Ecuador).
993 Chemical Geology 574, 120240. https://doi.org/10.1016/j.chemgeo.2021.120240

994 Chiaradia, M., Müntener, O., Beate, B., 2020. Effects of aseismic ridge subduction on the geochemistry
995 of frontal arc magmas. Earth and Planetary Science Letters 531, 115984.
996 https://doi.org/10.1016/j.epsl.2019.115984

997 Chiaradia, M., Müntener, O., Beate, B., 2014. Quaternary Sanukitoid-like Andesites Generated by
998 Intracrustal Processes (Chacana Caldera Complex, Ecuador): Implications for Archean
999 Sanukitoids. Journal of Petrology 55, 769–802. https://doi.org/10.1093/petrology/egu006

1000 Chiaradia, M., Müntener, O., Beate, B., Fontignie, D., 2009. Adakite-like volcanism of Ecuador: lower
1001 crust magmatic evolution and recycling. Contrib Mineral Petrol 158, 563–588.
1002 https://doi.org/10.1007/s00410-009-0397-2

1003 Córdova, M.D., Mothes, P.A., Gaunt, H.E., Salgado, J., 2020. Post-Caldera Eruptions at Chalupas
1004 Caldera, Ecuador: Determining the Timing of Lava Dome Collapse, Hummock Emplacement
1005 and Dome Rejuvenation. Front. Earth Sci. 8. https://doi.org/10.3389/feart.2020.548251

1006 Cotten, J., Le Dez, A., Bau, M., Caroff, M., Maury, R.C., Dulski, P., Fourcade, S., Bohn, M., Brousse,
1007 R., 1995. Origin of anomalous rare-earth element and yttrium enrichments in subaerially exposed
1008 basalts: Evidence from French Polynesia. Chemical Geology 119, 115–138.
1009 https://doi.org/10.1016/0009-2541(94)00102-E

1010 Delaney, P.T., Pollard, D.D., Ziony, J.I., McKee, E.H., 1986. Field relations between dikes and joints:
1011 Emplacement processes and paleostress analysis. Journal of Geophysical Research: Solid Earth
1012 91, 4920–4938. https://doi.org/10.1029/JB091iB05p04920

1013 DeMets, C., Gordon, R.G., Argus, D.F., 2010. Geologically current plate motions. Geophysical Journal
1014 International 181, 1–80. https://doi.org/10.1111/j.1365-246X.2009.04491.x

1015 Díaz, D., Zúñiga, F., Castruccio, A., 2020. The interaction between active crustal faults and volcanism:
1016 A case study of the Liquiñe-Ofqui Fault Zone and Osorno volcano, Southern Andes, using
1017 magnetotellurics. Journal of Volcanology and Geothermal Research 393, 106806.
1018 https://doi.org/10.1016/j.jvolgeores.2020.106806

1019 Dibacto, S., Lahitte, P., Karátson, D., Hencz, M., Szakács, A., Biró, T., Kovács, I., Veres, D., 2020.
1020 Growth and erosion rates of the East Carpathians volcanoes constrained by numerical models:
1021 Tectonic and climatic implications. Geomorphology 368, 107352.
1022 https://doi.org/10.1016/j.geomorph.2020.107352

1023 Ebmeier, S.K., Elliott, J.R., Nocquet, J.-M., Biggs, J., Mothes, P., Jarrín, P., Yépez, M., Aguaiza, S.,
1024 Lundgren, P., Samsonov, S.V., 2016. Shallow earthquake inhibits unrest near Chiles–Cerro
1025 Negro volcanoes, Ecuador–Colombian border. Earth and Planetary Science Letters 450, 283–
1026 291. https://doi.org/10.1016/j.epsl.2016.06.046

1027 Egüez, A., Gaona, M., Albán, A., 2017. Mapa Geológico de la República del Ecuador.

1028 Fiorini, E., Tibaldi, A., 2012. Quaternary tectonics in the central Interandean Valley, Ecuador: Fault-
1029 propagation folds, transfer faults and the Cotopaxi Volcano. Global and Planetary Change,
1030 Coupled deep Earth and surface processes in System Earth: monitoring, reconstruction and
1031 process modeling 90–91, 87–103. https://doi.org/10.1016/j.gloplacha.2011.06.002

1032 Garrison, J., Davidson, J., Reid, M., Turner, S., 2006. Source versus differentiation controls on U-series
1033 disequilibria: Insights from Cotopaxi Volcano, Ecuador. Earth and Planetary Science Letters 244,
1034 548–565. https://doi.org/10.1016/j.epsl.2006.02.013

1035 Garrison, J.M., Sims, K.W.W., Yogodzinski, G.M., Escobar, R.D., Scott, S., Mothes, P., Hall, M.L.,
1036 Ramon, P., 2017. Shallow-level differentiation of phonolitic lavas from Sumaco Volcano,
1037 Ecuador. Contrib Mineral Petrol 173, 6. https://doi.org/10.1007/s00410-017-1431-4

1038 Geotérmica Italiana, 1989. Mitigación del riesgo volcánico en el área metropolitana de Quito (Informe
1039 final No. 2). INEMIN, DGCS, Pisa, Italy.

1040 Gillot, P.-Y., Cornette, Y., Max, N., Floris, B., 1992. Two reference materials, Trachytes MDO-G and
1041 ISH-G, for Argon Dating (K-Ar and 40Ar/39Ar) of Pleistocene and Holocene rocks.
1042 Geostandards Newsletter 16, 55–60. https://doi.org/10.1111/j.1751-908X.1992.tb00487.x

1043 Gillot, P.Y., Hildenbrand, A., Lefèvre, J.C., Albore-Livadie, C., 2006. The K/Ar dating method:
1044 principle, analytical techniques, and application to Holocene volcanic eruptions in Southern Italy.
1045 Acta Vulcanologica 18, 55–66.

1046 González, G., Cembrano, J., Aron, F., Veloso, E.E., Shyu, J.B.H., 2009. Coeval compressional
1047 deformation and volcanism in the central Andes, case studies from northern Chile (23°S–24°S).
1048 Tectonics 28. https://doi.org/10.1029/2009TC002538

1049 Grosse, P., Ochi Ramacciotti, M.L., Escalante Fochi, F., Guzmán, S., Orihashi, Y., Sumino, H., 2020.
1050 Geomorphology, morphometry, spatial distribution and ages of mafic monogenetic volcanoes of
1051 the Peinado and Incahuasi fields, southernmost Central Volcanic Zone of the Andes. Journal of
1052 Volcanology and Geothermal Research 401, 106966.
1053 https://doi.org/10.1016/j.jvolgeores.2020.106966

1054 Grosse, P., Orihashi, Y., Guzmán, S.R., Sumino, H., Nagao, K., 2018. Eruptive history of Incahuasi,
1055 Falso Azufre and El Cóndor Quaternary composite volcanoes, southern Central Andes. Bull
1056 Volcanol 80, 1–26. https://doi.org/10.1007/s00445-018-1221-5

1057 Gudmundsson, A., 2006. How local stresses control magma-chamber ruptures, dyke injections, and
1058 eruptions in composite volcanoes. Earth-Science Reviews 79, 1–31.
1059 https://doi.org/10.1016/j.earscirev.2006.06.006

1060 Gudmundsson, A., Philipp, S.L., 2006. How local stress fields prevent volcanic eruptions. Journal of
1061 Volcanology and Geothermal Research 158, 257–268.
1062 https://doi.org/10.1016/j.jvolgeores.2006.06.005

1063 Gutiérrez, E.G., Horton, B.K., Vallejo, C., Jackson, L.J., George, S.W.M., 2019. Chapter 9 - Provenance
1064 and geochronological insights into Late Cretaceous-Cenozoic foreland basin development in the
1065 Subandean Zone and Oriente Basin of Ecuador, in: Horton, B.K., Folguera, A. (Eds.), Andean
1066 Tectonics. Elsevier, pp. 237–268. https://doi.org/10.1016/B978-0-12-816009-1.00011-3

1067 Gutscher, M.-A., Malavieille, J., Lallemand, S., Collot, J.-Y., 1999. Tectonic segmentation of the North
1068 Andean margin: impact of the Carnegie Ridge collision. Earth and Planetary Science Letters 168,
1069 255–270. https://doi.org/10.1016/S0012-821X(99)00060-6

1070 Gutscher, M.-A., Spakman, W., Bijwaard, H., Engdahl, E.R., 2000. Geodynamics of flat subduction:
1071 Seismicity and tomographic constraints from the Andean margin. Tectonics 19, 814–833.
1072 https://doi.org/10.1029/1999TC001152

1073 Hall, M.L., 1977. El volcanismo en el Ecuador. Instituto Panamericano de Geografía e Historia, Quito.

1074 Hall, M.L., Beate, B., 1991. El volcanismo plio cuaternario en los Andes del Ecuador, in: El paisaje
1075 volcánico de la sierra ecuatoriana: geomorfología, fenómenos volcánicos y recursos asociados,
1076 Estudios de Geografia. Corporación Editora Nacional, Quito, pp. 5–17.

1077 Hall, M.L., Mothes, P., 2010. New active rhyolitic eruption centers - Eastern foot of the Ecuadorian
1078 Andes, in: Abstracts Volume. Presented at the Cities on Volcanoes 6th, Tenerife, Spain, p. 44.

1079 Hall, M.L., Mothes, P., 2008a. The rhyolitic–andesitic eruptive history of Cotopaxi volcano, Ecuador.
1080 Bull Volcanol 70, 675–702. https://doi.org/10.1007/s00445-007-0161-2

Hall, M.L., Mothes, P., 2008b. Volcanic impediments in the progressive development of pre-Columbian civilizations in the Ecuadorian Andes. Journal of Volcanology and Geothermal Research, Volcanoes and Human History 176, 344–355. https://doi.org/10.1016/j.jvolgeores.2008.01.039

Hall, M.L., Mothes, P.A., 2008c. The Chacana caldera complex in Ecuador, in: Volume 3: Collapse Calderas Workshop. Presented at the IOP Conference Series: Earth and Environmental Science (EES), IOP Publishing, Querétaro, Mexico. https://doi.org/10.1088/1755-1307/3/1/012004

Hall, M.L., Mothes, P.A., Samaniego, P., Militzer, A., Beate, B., Ramón, P., Robin, C., 2017. Antisana volcano: A representative andesitic volcano of the eastern cordillera of Ecuador: Petrography, chemistry, tephra and glacial stratigraphy. Journal of South American Earth Sciences 73, 50–64. https://doi.org/10.1016/j.jsames.2016.11.005

Hall, M.L., Robin, C., Beate, B., Mothes, P., Monzier, M., 1999. Tungurahua Volcano, Ecuador: structure, eruptive history and hazards. Journal of Volcanology and Geothermal Research 91, 1–21. https://doi.org/10.1016/S0377-0273(99)00047-5

Hall, M.L., Samaniego, P., Le Pennec, J.L., Johnson, J.B., 2008. Ecuadorian Andes volcanism: A review of Late Pliocene to present activity. Journal of Volcanology and Geothermal Research, Recent and active volcanism in the Ecuadorian Andes 176, 1–6. https://doi.org/10.1016/j.jvolgeores.2008.06.012

Hall, M.L., Wood, C.A., 1985. Volcano-tectonic segmentation of the northern Andes. Geology 13, 203–207. https://doi.org/10.1130/0091-7613(1985)13<203:VSOTNA>2.0.CO;2

Hidalgo, S., 2006. Les intéractions entre magmas calco-alcalins “classiques” et adakitiques: exemple du complexe volcanique Atacazo-Ninahuilca (Equateur) (Ph.D. thesis). Université Blaise Pascal - Clermont-Ferrand II, Clermont-Ferrand, France.

Hidalgo, S., Gerbe, M.C., Martin, H., Samaniego, P., Bourdon, E., 2012. Role of crustal and slab components in the Northern Volcanic Zone of the Andes (Ecuador) constrained by Sr–Nd–O isotopes. Lithos 132–133, 180–192. https://doi.org/10.1016/j.lithos.2011.11.019

Hidalgo, S., Monzier, M., Almeida, E., Chazot, G., Eissen, J.-P., van der Plicht, J., Hall, M.L., 2008. Late Pleistocene and Holocene activity of the Atacazo–Ninahuilca Volcanic Complex (Ecuador). Journal of Volcanology and Geothermal Research, Recent and active volcanism in the Ecuadorian Andes 176, 16–26. https://doi.org/10.1016/j.jvolgeores.2008.05.017

Hidalgo, S., Monzier, M., Martin, H., Chazot, G., Eissen, J.-P., Cotten, J., 2007. Adakitic magmas in the Ecuadorian Volcanic Front: Petrogenesis of the Iliniza Volcanic Complex (Ecuador). Journal of Volcanology and Geothermal Research 159, 366–392. https://doi.org/10.1016/j.jvolgeores.2006.07.007

Hildenbrand, A., Marques, F.O., Catalão, J., 2018. Large-scale mass wasting on small volcanic islands revealed by the study of Flores Island (Azores). Scientific Reports 8, 13898. https://doi.org/10.1038/s41598-018-32253-0

Hoffer, G., 2008. Fusion partielle d’un manteau métasomatisé par un liquide adakitique : approches géochimique et expérimentale de la genèse et de l’évolution des magmas de l’arrière-arc équatorien (Ph.D. thesis). Université Blaise Pascal - Clermont-Ferrand II, Clermont-Ferrand, France.

1121 Hoffer, G., Eissen, J.-P., Beate, B., Bourdon, E., Fornari, M., Cotten, J., 2008. Geochemical and
1122 petrological constraints on rear-arc magma genesis processes in Ecuador: The Puyo cones and
1123 Mera lavas volcanic formations. Journal of Volcanology and Geothermal Research, Recent and
1124 active volcanism in the Ecuadorian Andes 176, 107–118.
1125 https://doi.org/10.1016/j.jvolgeores.2008.05.023

1126 Hughes, R.A., Bermúdez, R., 1997. Geology of the Cordillera Occidental of Ecuador between 0°00'
1127 and 1°00'S (No. 4), Proyecto de Desarrollo Minero y Control Ambiental. Cogidem - Brithis
1128 Geological Survey, Quito.

1129 Hughes, R.A., Pilatasig, L.F., 2002. Cretaceous and Tertiary terrane accretion in the Cordillera
1130 Occidental of the Andes of Ecuador. Tectonophysics, Andean Geodynamics ISAG 4 345, 29–48.
1131 https://doi.org/10.1016/S0040-1951(01)00205-0

1132 Ibanez-Mejia, M., Ruiz, J., Valencia, V.A., Cardona, A., Gehrels, G.E., Mora, A.R., 2011. The
1133 Putumayo Orogen of Amazonia and its implications for Rodinia reconstructions: New U–Pb
1134 geochronological insights into the Proterozoic tectonic evolution of northwestern South America.
1135 Precambrian Research 191, 58–77. https://doi.org/10.1016/j.precamres.2011.09.005

1136 Jaillard, E., Ordoñez, M., Suárez, J., Toro, J., Iza, D., Lugo, W., 2004. Stratigraphy of the late
1137 Cretaceous–Paleogene deposits of the cordillera occidental of central ecuador: geodynamic
1138 implications. Journal of South American Earth Sciences 17, 49–58.
1139 https://doi.org/10.1016/j.jsames.2004.05.003

1140 Jomard, H., Saqui, D., Baize, S., Alvarado, A., Bernard, B., Audin, L., Hidalgo, S., Pacheco, D., Ruiz,
1141 M., Segovia, M., 2021. Interactions between active tectonics and gravitational deformation along
1142 the Billecocha fault system (Northern Ecuador): Insights from morphological and
1143 paleoseismological investigations. Journal of South American Earth Sciences 111, 103406.
1144 https://doi.org/10.1016/j.jsames.2021.103406

1145 Koch, C.D., Delph, J., Beck, S.L., Lynner, C., Ruiz, M., Hernandez, S., Samaniego, P., Meltzer, A.,
1146 Mothes, P., Hidalgo, S., 2021. Crustal thickness and magma storage beneath the Ecuadorian arc.
1147 Journal of South American Earth Sciences 110, 103331.
1148 https://doi.org/10.1016/j.jsames.2021.103331

1149 Lavenu, A., Winter, T., Dávila, F., 1995. A Pliocene–Quaternary compressional basin in the
1150 Interandean Depression, Central Ecuador. Geophysical Journal International 121, 279–300.
1151 https://doi.org/10.1111/j.1365-246X.1995.tb03527.x

1152 Le Pennec, J.-L., de Saulieu, G., Samaniego, P., Jaya, D., Gailler, L., 2013. A Devastating Plinian
1153 Eruption at Tungurahua Volcano Reveals Formative Occupation at ~1100 cal BC in Central
1154 Ecuador. Radiocarbon 55, 1199–1214. https://doi.org/10.1017/S0033822200048116

1155 Le Pennec, J.-L., Ramón, P., Robin, C., Almeida, E., 2016. Combining historical and 14C data to assess
1156 pyroclastic density current hazards in Baños city near Tungurahua volcano (Ecuador).
1157 Quaternary International, Volcanic Activity and Human Society 394, 98–114.
1158 https://doi.org/10.1016/j.quaint.2015.06.052

1159 Le Pennec, J.L., Ruiz, A.G., Eissen, J.P., Hall, M.L., Fornari, M., 2011. Identifying potentially active
1160 volcanoes in the Andes: Radiometric evidence for late Pleistocene-early Holocene eruptions at
1161 Volcán Imbabura, Ecuador. Journal of Volcanology and Geothermal Research 206, 121–135.
1162 https://doi.org/10.1016/j.jvolgeores.2011.06.002

1163 Litherland, M., Aspden, J.A., 1992. Terrane-boundary reactivation: A control on the evolution of the
1164 Northern Andes. Journal of South American Earth Sciences 5, 71–76.
1165 https://doi.org/10.1016/0895-9811(92)90060-C

1166 Litherland, M., Aspden, J.A., Jemielita, R.A., 1994. The metamorphic belts of Ecuador, Overseas
1167 Memoir Institute of Geological Sciences. British Geological Survey, Keyworth, Nottingham.

1168 Loayza, T.G., Proust, J.-N., Michaud, F., Collot, J.-Y., 2013. Evolution Pléistocène du Système de
1169 canyons du Golfe de Guayaquil (Equateur): Contrôles paléo-climatiques et tectoniques.
1170 Presented at the 14e Congrès Français de Sédimentologie, Paris, Francia.

1171 Lonsdale, P., 2005. Creation of the Cocos and Nazca plates by fission of the Farallon plate.
1172 Tectonophysics 404, 237–264. https://doi.org/10.1016/j.tecto.2005.05.011

1173 Meschede, M., Barckhausen, U., 2000. Plate Tectonic Evolution of the Cocos-Nazca Spreading Center.
1174 Proc. ODP, Sci. Results, Fluid, Mass, and Thermal Fluxes in the Pacific Margin of Costa Rica
1175 170, 1–10. https://doi.org/doi:10.2973/odp.proc.sr.170.009.2000

1176 Mothes, P.A., Hall, M.L., 2008a. Rhyolitic calderas and centers clustered within the active andesitic
1177 belt of Ecuador's Eastern Cordillera, in: Volume 3: Collapse Calderas Workshop. Presented at
1178 the IOP Conference Series: Earth and Environmental Science, IOP Publishing, Querétaro,
1179 Mexico, p. 012007. https://doi.org/10.1088/1755-1307/3/1/012007

1180 Mothes, P.A., Hall, M.L., 2008b. The plinian fallout associated with Quilotoa's 800 yr BP eruption,
1181 Ecuadorian Andes. Journal of Volcanology and Geothermal Research, Recent and active
1182 volcanism in the Ecuadorian Andes 176, 56–69. https://doi.org/10.1016/j.jvolgeores.2008.05.018

1183 Naranjo, M.F., Ebmeier, S.K., Vallejo, S., Ramón, P., Mothes, P., Biggs, J., Herrera, F., 2016. Mapping
1184 and measuring lava volumes from 2002 to 2009 at El Reventador Volcano, Ecuador, from field
1185 measurements and satellite remote sensing. Journal of Applied Volcanology 5, 8.
1186 https://doi.org/10.1186/s13617-016-0048-z

1187 Narvaez, D.F., Rose-Koga, E.F., Samaniego, P., Koga, K.T., Hidalgo, S., 2018. Constraining magma
1188 sources using primitive olivine-hosted melt inclusions from Puñalica and Sangay volcanoes
1189 (Ecuador). Contrib Mineral Petrol 173, 80. https://doi.org/10.1007/s00410-018-1508-8

1190 Nocquet, J.-M., Villegas-Lanza, J.C., Chlieh, M., Mothes, P.A., Rolandone, F., Jarrin, P., Cisneros, D.,
1191 Alvarado, A., Audin, L., Bondoux, F., Martin, X., Font, Y., Régnier, M., Vallée, M., Tran, T.,
1192 Beauval, C., Mendoza, J.M.M., Martinez, W., Tavera, H., Yepes, H., 2014. Motion of continental
1193 slivers and creeping subduction in the northern Andes. Nature Geoscience 7, 287–291.
1194 https://doi.org/10.1038/ngeo2099

1195 O'Connor, J.M., Stoffers, P., Wijbrans, Jan.R., Worthington, T.J., 2007. Migration of widespread long-
1196 lived volcanism across the Galápagos Volcanic Province: Evidence for a broad hotspot melting
1197 anomaly? Earth and Planetary Science Letters 263, 339–354.
1198 https://doi.org/10.1016/j.epsl.2007.09.007

1199 Opdyke, N.D., Hall, M., Mejia, V., Huang, K., Foster, D.A., 2006. Time-averaged field at the equator:
1200 Results from Ecuador. Geochemistry, Geophysics, Geosystems 7.
1201 https://doi.org/10.1029/2005GC001221

1202 Pacheco, D., 2013. Estudio Geológico de las formaciones Cuaternarias en la zona San Antonio de
1203 Pichincha - Pomasqui (Engineer memoir). Escuela Politécnica Nacional, Quito, Ecuador.

Pacheco, D.A., Andrade, D., Alvarado, A., 2014. Estratigrafía de la Cuenca San Antonio de Pichincha. Revista Politécnica 33.

Peccerillo, A., Taylor, S.R., 1976. Geochemistry of eocene calc-alkaline volcanic rocks from the Kastamonu area, Northern Turkey. Contr. Mineral. and Petrol. 58, 63–81. https://doi.org/10.1007/BF00384745

Petford, N., Cruden, A.R., McCaffrey, K.J.W., Vigneresse, J.-L., 2000. Granite magma formation, transport and emplacement in the Earth's crust. Nature 408, 669–673. https://doi.org/10.1038/35047000

Pilicita, B.F., 2013. Estudio de fuentes termales, fallas geológicas, descarga de calor en la Caldera de Chacana y el aprovechamiento actual del recurso geotérmico (Engineer memoir). Escuela Politécnica Nacional, Quito, Ecuador.

Portner, D.E., Rodríguez, E.E., Beck, S., Zandt, G., Scire, A., Rocha, M.P., Bianchi, M.B., Ruiz, M., França, G.S., Condori, C., Alvarado, P., 2020. Detailed Structure of the Subducted Nazca Slab into the Lower Mantle Derived From Continent-Scale Teleseismic P Wave Tomography. Journal of Geophysical Research: Solid Earth 125, e2019JB017884. https://doi.org/10.1029/2019JB017884

Quidelleur, X., Gillot, P.-Y., Carlut, J., Courtillot, V., 1999. Link between excursions and paleointensity inferred from abnormal field directions recorded at La Palma around 600 ka. Earth and Planetary Science Letters 168, 233–242. https://doi.org/10.1016/S0012-821X(99)00061-8

Quidelleur, X., Gillot, P.-Y., Soler, V., Lefèvre, J.-C., 2001. K/Ar dating extended into the last millennium: Application to the youngest effusive episode of the Teide Volcano (Spain). Geophysical Research Letters 28, 3067–3070. https://doi.org/10.1029/2000GL012821

Quidelleur, X., Michon, L., Famin, V., Geffray, M.-C., Danišík, M., Gardiner, N., Rusquet, A., Zakaria, M.G., 2021. Holocene volcanic activity in Anjouan Island (Comoros archipelago) revealed by new Cassignol-Gillot groundmass K–Ar and 14C ages. Quaternary Geochronology 101236. https://doi.org/10.1016/j.quageo.2021.101236

Raczek, I., Stoll, B., Hofmann, A.W., Peter Jochum, K., 2001. High-Precision Trace Element Data for the USGS Reference Materials BCR-1, BCR-2, BHVO-1, BHVO-2, AGV-1, AGV-2, DTS-1, DTS-2, GSP-1 and GSP-2 by ID-TIMS and MIC-SSMS. Geostandards Newsletter 25, 77–86. https://doi.org/10.1111/j.1751-908X.2001.tb00789.x

Renne, P.R., Mulcahy, S.R., Cassata, W.S., Morgan, L.E., Kelley, S.P., Hlusko, L.J., Njau, J.K., 2012. Retention of inherited Ar by alkali feldspar xenocrysts in a magma: Kinetic constraints from Ba zoning profiles. Geochimica et Cosmochimica Acta 93, 129–142. https://doi.org/10.1016/j.gca.2012.06.029

Robin, C., Eissen, J.-P., Samaniego, P., Martin, H., Hall, M., Cotten, J., 2009. Evolution of the late Pleistocene Mojanda–Fuya Fuya volcanic complex (Ecuador), by progressive adakitic involvement in mantle magma sources. Bull Volcanol 71, 233. https://doi.org/10.1007/s00445-008-0219-9

Robin, C., Samaniego, P., Le Pennec, J.-L., Fornari, M., Mothes, P., van der Plicht, J., 2010. New radiometric and petrological constraints on the evolution of the Pichincha volcanic complex (Ecuador). Bull Volcanol 72, 1109–1129. https://doi.org/10.1007/s00445-010-0389-0

Robin, C., Samaniego, P., Le Pennec, J.-L., Mothes, P., van der Plicht, J., 2008. Late Holocene phases of dome growth and Plinian activity at Guagua Pichincha volcano (Ecuador). Journal of Volcanology and Geothermal Research, Recent and active volcanism in the Ecuadorian Andes 176, 7–15. https://doi.org/10.1016/j.jvolgeores.2007.10.008

Salas, P.A., Rabbia, O.M., Hernández, L.B., Ruprecht, P., 2017. Mafic monogenetic vents at the Descabezado Grande volcanic field (35.5°S–70.8°W): the northernmost evidence of regional primitive volcanism in the Southern Volcanic Zone of Chile. Int J Earth Sci (Geol Rundsch) 106, 1107–1121. https://doi.org/10.1007/s00531-016-1357-5

Salgado, J.A., Mothes, P.A., Córdova, M.D., 2021. New observations on the recent eruptive activity of Sumaco Volcano (Ecuador), based on geochronology, stratigraphy and petrography. Journal of South American Earth Sciences 103568. https://doi.org/10.1016/j.jsames.2021.103568

Samaniego, P., Martin, H., Monzier, M., Robin, C., Fornari, M., Eissen, J.-P., Cotten, J., 2005. Temporal Evolution of Magmatism in the Northern Volcanic Zone of the Andes: The Geology and Petrology of Cayambe Volcanic Complex (Ecuador). Journal of Petrology 46, 2225–2252. https://doi.org/10.1093/petrology/egi053

Samaniego, P., Monzier, M., Robin, C., Hall, M.L., 1998. Late Holocene eruptive activity at Nevado Cayambe Volcano, Ecuador. Bull Volcanol 59, 451–459. https://doi.org/10.1007/s004450050203

Samaniego, P., Robin, C., Chazot, G., Bourdon, E., Cotten, J., 2010. Evolving metasomatic agent in the Northern Andean subduction zone, deduced from magma composition of the long-lived Pichincha volcanic complex (Ecuador). Contrib Mineral Petrol 160, 239–260. https://doi.org/10.1007/s00410-009-0475-5

Samper, A., Quidelleur, X., Boudon, G., Le Friant, A., Komorowski, J.C., 2008. Radiometric dating of three large volume flank collapses in the Lesser Antilles Arc. Journal of Volcanology and Geothermal Research 176, 485–492. https://doi.org/10.1016/j.jvolgeores.2008.04.018

Santamaría, S., 2017. Catálogo de eventos volcánicos ocurridos en el Ecuador continental desde el Plioceno y análisis de la frecuencia eruptiva (Engineer memoir). Escuela Politécnica Nacional, Quito, Ecuador.

Santamaría, S., Quidelleur, X., Hidalgo, S., Samaniego, P., Le Pennec, J.-L., Liorzou, C., Lahitte, P., Córdova, M., Espin, P., submitted. Geochronological evolution of the potentially active Iliniza Volcano (Ecuador) based on new K-Ar ages. Journal of Volcanology and Geothermal Research.

Santamaría, S., Quidelleur, X., Samaniego, P., Audin, L., Le Pennec, J.-L., Hidalgo, S., Liorzou, C., in preparation. Timing of Pleistocene volcanism and its relationship with geodynamics in the central segment of the Ecuadorian Andes.

Santamaría, S., Telenchana, E., Bernard, B., Hidalgo, S., Beate, B., Córdova, M., Narváez, D., 2017. Registro de erupciones ocurridas en los Andes del Norte durante el Holoceno: Nuevos resultados obtenidos en la turbera de Potrerillos, Complejo Volcánico Chiles-Cerro Negro. Revista Politécnica 39, 7–16.

Schaen, A.J., Jicha, B.R., Hodges, K.V., Vermeesch, P., Stelten, M.E., Mercer, C.M., Phillips, D., Rivera, T.A., Jourdan, F., Matchan, E.L., Hemming, S.R., Morgan, L.E., Kelley, S.P., Cassata, W.S., Heizler, M.T., Vasconcelos, P.M., Benowitz, J.A., Koppers, A.A.P., Mark, D.F., Niespolo, E.M., Sprain, C.J., Hames, W.E., Kuiper, K.F., Turrin, B.D., Renne, P.R., Ross, J., Nomade, S.,

Guillou, H., Webb, L.E., Cohen, B.A., Calvert, A.T., Joyce, N., Ganerød, M., Wijbrans, J., Ishizuka, O., He, H., Ramirez, A., Pfänder, J.A., Lopez-Martínez, M., Qiu, H., Singer, B.S., 2020. Interpreting and reporting 40Ar/39Ar geochronologic data. GSA Bulletin 133, 461–487. https://doi.org/10.1130/B35560.1

Schiano, P., Monzier, M., Eissen, J.-P., Martin, H., Koga, K.T., 2010. Simple mixing as the major control of the evolution of volcanic suites in the Ecuadorian Andes. Contrib Mineral Petrol 160, 297–312. https://doi.org/10.1007/s00410-009-0478-2

Schwarz, W.H., Trieloff, M., 2007. Intercalibration of 40Ar–39Ar age standards NL-25, HB3gr hornblende, GA1550, SB-3, HD-B1 biotite and BMus/2 muscovite. Chemical Geology 242, 218–231. https://doi.org/10.1016/j.chemgeo.2007.03.016

Spikings, R., Cochrane, R., Villagomez, D., Van der Lelij, R., Vallejo, C., Winkler, W., Beate, B., 2015. The geological history of northwestern South America: from Pangaea to the early collision of the Caribbean Large Igneous Province (290–75Ma). Gondwana Research 27, 95–139. https://doi.org/10.1016/j.gr.2014.06.004

Sun, S.-S., McDonough, W.F., 1989. Chemical and isotopic systematics of oceanic basalts: implications for mantle composition and processes. Geol. Soc. Lond. Spec. Publ. 42, 313–345. https://doi.org/10.1144/GSL.SP.1989.042.01.19

Sychev, I.V., Koulakov, I., Egorushkin, I., Zhuravlev, S., West, M., Khrepy, S.E., Al-Arifi, N., Alajmi, M.S., 2019. Fault-Associated Magma Conduits Beneath Volcán de Colima Revealed by Seismic Velocity and Attenuation Tomography Studies. Journal of Geophysical Research: Solid Earth 124, 8908–8923. https://doi.org/10.1029/2019JB017449

Szakács, A., 2010. From a definition of volcano to conceptual volcanology. https://doi.org/10.1130/2010.2470(05)

Takada, A., 1994. The influence of regional stress and magmatic input on styles of monogenetic and polygenetic volcanism. Journal of Geophysical Research: Solid Earth 99, 13563–13573. https://doi.org/10.1029/94JB00494

Telenchana, E., Bernard, B., Hidalgo, S., Beate, B., 2017. Modelo evolutivo del volcán Chiles, in: Memorias VIII Jornadas En Ciencias de La Tierra. Presented at the 8vas Jornadas en Ciencias de la Tierra, pp. 391–395.

Tibaldi, A., Bonali, F.L., 2017. Intra-arc and back-arc volcano-tectonics: Magma pathways at Holocene Alaska-Aleutian volcanoes. Earth-Science Reviews 167, 1–26. https://doi.org/10.1016/j.earscirev.2017.02.004

Tibaldi, A., Bonali, F.L., Corazzato, C., 2017. Structural control on volcanoes and magma paths from local- to orogen-scale: The central Andes case. Tectonophysics 699, 16–41. https://doi.org/10.1016/j.tecto.2017.01.005

Tibaldi, A., Rovida, A., Corazzato, C., 2007. Late Quaternary kinematics, slip-rate and segmentation of a major Cordillera-parallel transcurrent fault: The Cayambe-Afiladores-Sibundoy system, NW South America. Journal of Structural Geology 29, 664–680. https://doi.org/10.1016/j.jsg.2006.11.008

Tsunematsu, K., Bonadonna, C., 2015. Grain-size features of two large eruptions from Cotopaxi volcano (Ecuador) and implications for the calculation of the total grain-size distribution. Bull Volcanol 77, 1–12. https://doi.org/10.1007/s00445-015-0949-4

Vallejo, C., Almagor, S., Romero, C., Herrera, J.L., Escobar, V., Spikings, R., Winkler, W., Vermeesch, P., 2020. Sedimentology, Provenance and Radiometric Dating of the Silante Formation: Implications for the Cenozoic Evolution of the Western Andes of Ecuador. Minerals 10, 929. https://doi.org/10.3390/min10100929

Vallejo, C., Romero, C., Horton, B.K., Spikings, R.A., Gaibor, J., Winkler, W., Esteban, J.J., Thomsen, T.B., Mariño, E., 2021. Jurassic to Early Paleogene sedimentation in the Amazon region of Ecuador: Implications for the paleogeographic evolution of northwestern South America. Global and Planetary Change 204, 103555. https://doi.org/10.1016/j.gloplacha.2021.103555

Vallejo, C., Spikings, R., Horton, B.K., Luzieux, L., Romero, C., Winkler, W., Thomsen, T.B., 2019. Chapter 8 - Late cretaceous to miocene stratigraphy and provenance of the coastal forearc and Western Cordillera of Ecuador: Evidence for accretion of a single oceanic plateau fragment, in: Horton, B.K., Folguera, A. (Eds.), Andean Tectonics. Elsevier, pp. 209–236. https://doi.org/10.1016/B978-0-12-816009-1.00010-1

Valverde, V., Mothes, P.A., Beate, B., Bernard, J., 2021. Enormous and far-reaching debris avalanche deposits from Sangay volcano (Ecuador): Multidisciplinary study and modeling the 30 ka sector collapse. Journal of Volcanology and Geothermal Research 411, 107172. https://doi.org/10.1016/j.jvolgeores.2021.107172

van Wyk de Vries, B., van Wyk de Vries, M., 2018. Chapter 7 - Tectonics and Volcanic and Igneous Plumbing Systems, in: Burchardt, S. (Ed.), Volcanic and Igneous Plumbing Systems. Elsevier, pp. 167–189. https://doi.org/10.1016/B978-0-12-809749-6.00007-8

Vezzoli, L., Apuani, T., Corazzato, C., Uttini, A., 2017. Geological and geotechnical characterization of the debris avalanche and pyroclastic deposits of Cotopaxi Volcano (Ecuador). A contribute to instability-related hazard studies. Journal of Volcanology and Geothermal Research 332, 51–70. https://doi.org/10.1016/j.jvolgeores.2017.01.004

Villagómez, D., 2003. Evolución geológica Plio cuaternaria del valle Interandino central en Ecuador zona Quito Guayllabamba San Antonio (Engineer memoir). Escuela Politécnica Nacional, Quito, Ecuador.

Villagómez, D., Spikings, R., Magna, T., Kammer, A., Winkler, W., Beltrán, A., 2011. Geochronology, geochemistry and tectonic evolution of the Western and Central cordilleras of Colombia. Lithos 125, 875–896. https://doi.org/10.1016/j.lithos.2011.05.003

Villares, F., 2010. Estudio geovulcanologico de la zona sur de la caldera Chacana, provincias de Napo - Pichincha (Engineer memoir). Escuela Politécnica Nacional, Quito, Ecuador.

Villares, F., Garcia-Casco, A., Blanco-Quintero, I.F., Montes, C., Reyes, P.S., Cardona, A., 2020. The Peltetec ophiolitic belt (Ecuador): a window to the tectonic evolution of the Triassic margin of western Gondwana. International Geology Review 0, 1–25. https://doi.org/10.1080/00206814.2020.1830313

Weinberg, R.F., 1996. Ascent mechanism of felsic magmas: news and views. Earth and Environmental Science Transactions of The Royal Society of Edinburgh 87, 95–103. https://doi.org/10.1017/S0263593300006519

Winkler, W., Villagómez, D., Spikings, R., Abegglen, P., Tobler, St., Egüez, A., 2005. The Chota basin and its significance for the inception and tectonic setting of the inter-Andean depression in Ecuador. Journal of South American Earth Sciences, Cenozoic Andean Basin Evolution 19, 5–19. https://doi.org/10.1016/j.jsames.2004.06.006

Witt, C., Bourgois, J., 2010. Forearc basin formation in the tectonic wake of a collision-driven, coastwise migrating crustal block: The example of the North Andean block and the extensional Gulf of Guayaquil-Tumbes Basin (Ecuador-Peru border area). GSA Bulletin 122, 89–108. https://doi.org/10.1130/B26386.1

Witt, C., Bourgois, J., Michaud, F., Ordoñez, M., Jiménez, N., Sosson, M., 2006. Development of the Gulf of Guayaquil (Ecuador) during the Quaternary as an effect of the North Andean block tectonic escape. Tectonics 25. https://doi.org/10.1029/2004TC001723

Witt, C., Reynaud, J.Y., Barba, D., Poujol, M., Aizprua, C., Rivadeneira, M., Amberg, C., 2019. From accretion to forearc basin initiation: The case of SW Ecuador, Northern Andes. Sedimentary Geology 379, 138–157. https://doi.org/10.1016/j.sedgeo.2018.11.009

Yepes, H., Audin, L., Alvarado, A., Beauval, C., Aguilar, J., Font, Y., Cotton, F., 2016. A new view for the geodynamics of Ecuador: Implication in seismogenic source definition and seismic hazard assessment. Tectonics 35, 1249–1279. https://doi.org/10.1002/2015TC003941

Appendix A.

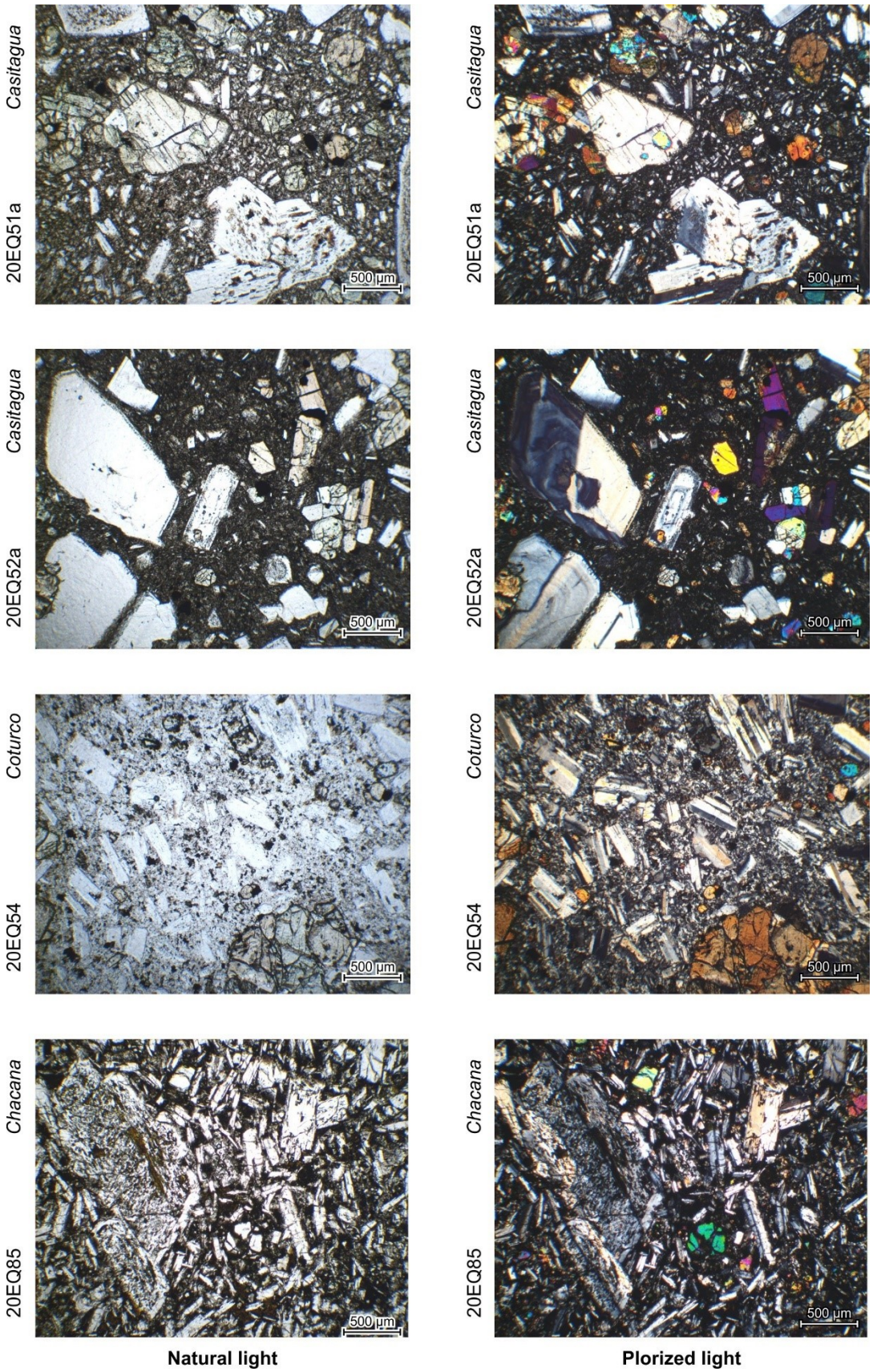
Casitagua
20EQ51a
500 µm
Casitagua
20EQ51a
500 µm
Casitagua
20EQ52a
500 µm
Casitagua
20EQ52a
500 µm
Coturco
20EQ54
500 µm
Coturco
20EQ54
500 µm
Chacana
20EQ85
500 µm
Chacana
20EQ85
500 µm
Natural light
Plorized light

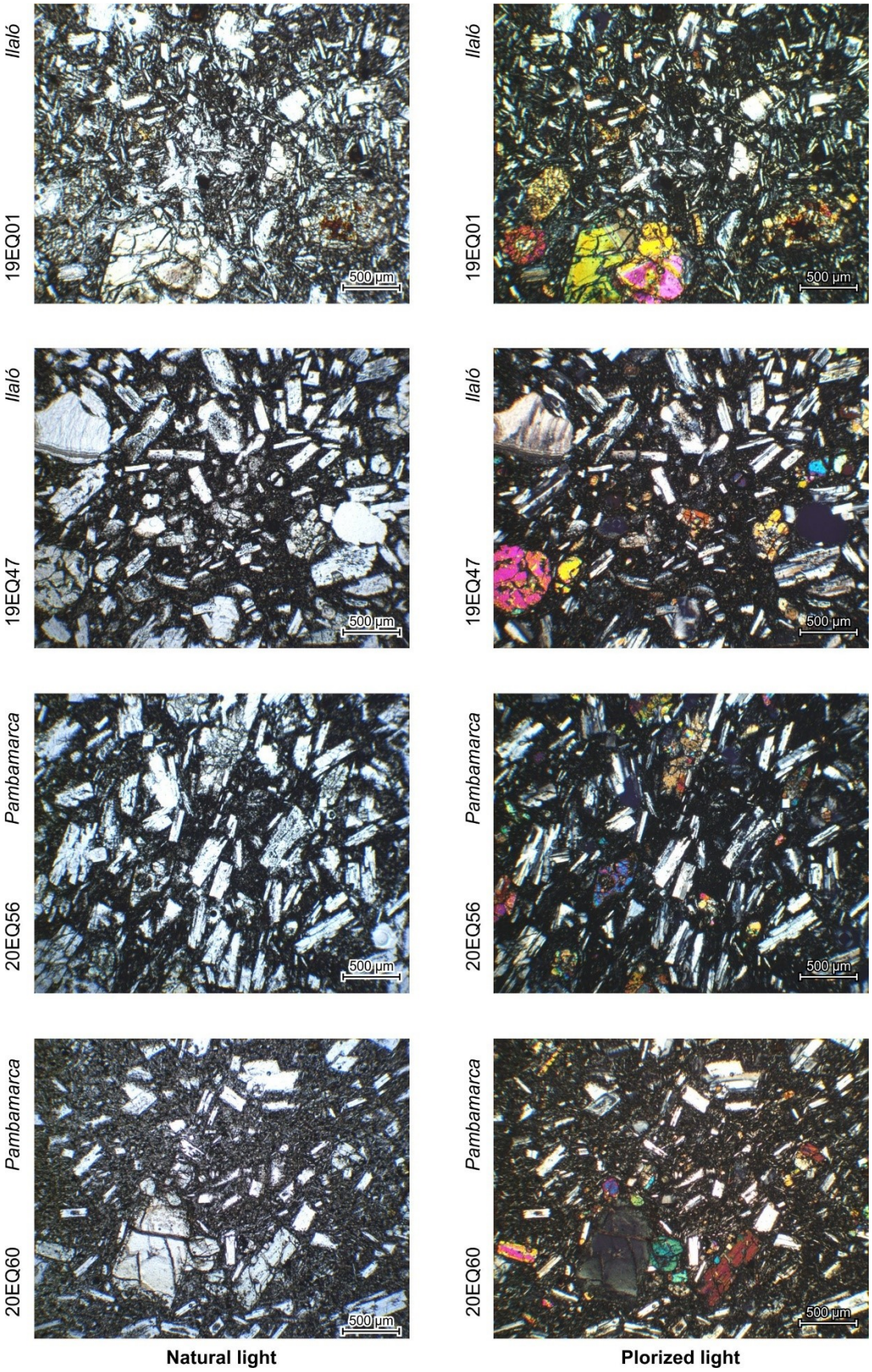
Ilaló
19EQ01
500 µm
Ilaló
19EQ01
500 µm
Ilaló
19EQ47
500 µm
Ilaló
19EQ47
500 µm
Pambamarca
20EQ56
500 µm
Pambamarca
20EQ56
500 µm
Pambamarca
20EQ60
500 µm
Pambamarca
20EQ60
500 µm
Natural light
Plorized light

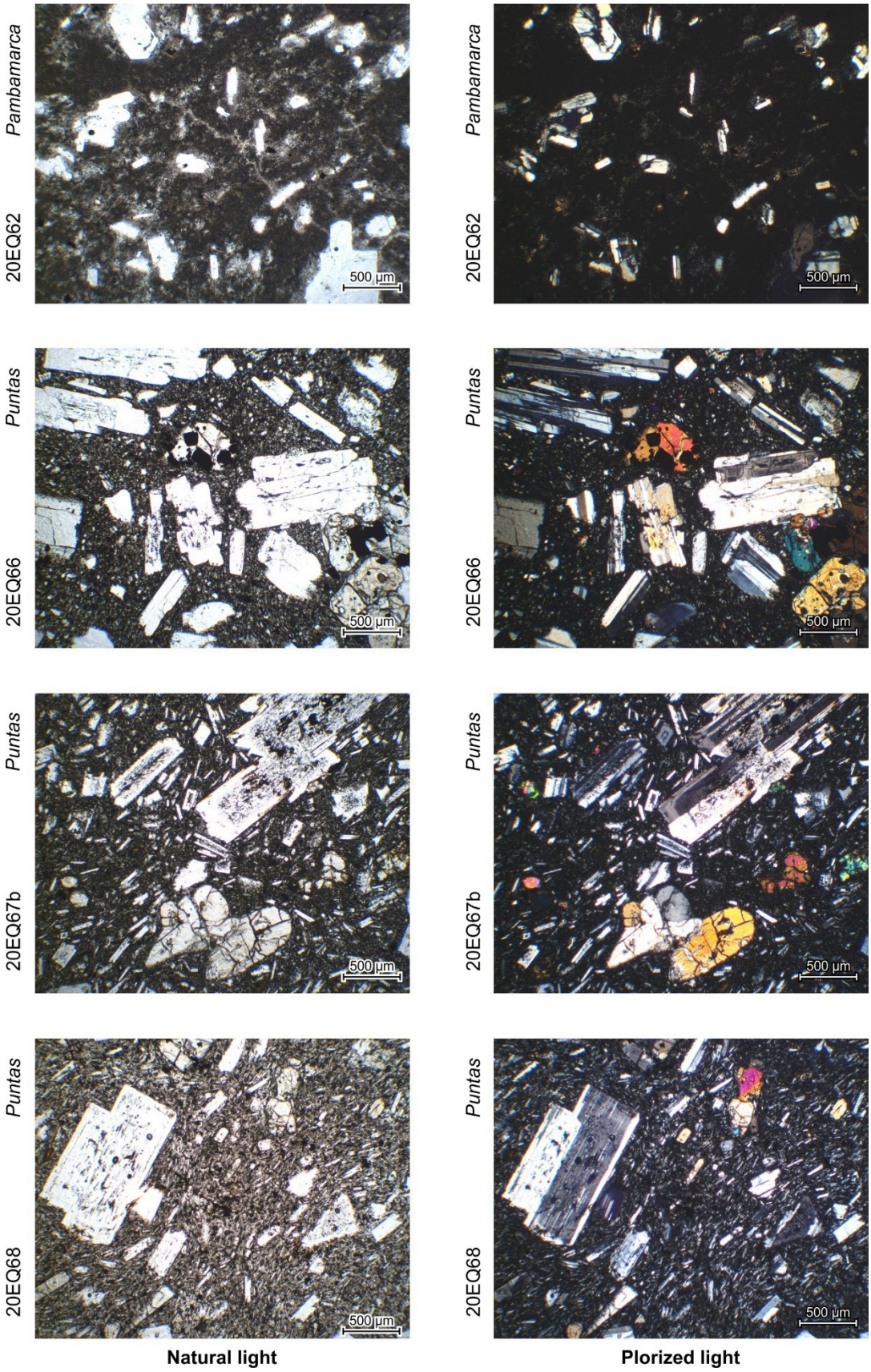
Pambamarca
20EQ62
500 µm
Pambamarca
20EQ62
500 µm
Puntas
20EQ66
500 µm
Puntas
20EQ66
500 µm
Puntas
20EQ67b
500 µm
Puntas
20EQ67b
500 µm
Puntas
20EQ68
500 µm
Puntas
20EQ68
500 µm
Natural light
Plorized light

Appendix B

Major and trace element composition of whole-rock samples. All major data were brought down to a total of 100%. See text for details of sampling locations and stratigraphic units. *(Santamaría et al.)*

	Ilaló volcano			Casitagua volcano					
Sample	19EQ01	19EQ47	19EQ48	20EQ51a	20EQ52a	20EQ53	20EQ51b	20EQ52b	20EQ52c
wt.%									
SiO_2	56.65	53.82	56.40	58.14	60.11	61.59	59.34	59.20	59.99
TiO_2	0.75	0.81	0.82	0.64	0.55	0.60	0.55	0.53	0.57
Al_2O_3	17.24	16.73	17.42	16.47	16.09	17.49	16.25	15.79	15.80
Fe_2O_3	8.11	8.75	8.54	7.54	7.07	6.37	7.22	6.87	6.57
MnO	0.12	0.13	0.11	0.12	0.12	0.11	0.12	0.11	0.09
MgO	5.01	6.78	5.39	4.89	4.20	2.37	4.48	4.20	4.40
CaO	7.15	8.52	6.69	7.09	6.58	5.86	7.04	6.57	6.11
Na_2O	3.86	3.35	3.66	3.84	4.08	4.43	3.89	3.70	3.87
K_2O	0.96	0.94	0.81	1.13	1.07	1.02	0.97	1.17	1.21
P_2O_5	0.16	0.16	0.16	0.14	0.13	0.16	0.12	0.12	0.13
L.O.I.	0.47	0.81	1.88	0.39	0.31	0.62	0.76	0.99	0.82
ppm									
Sc	18.89	20.88	19.27	20.07	19.50	12.40	19.49	18.86	16.35
V	184.15	197.39	181.70	172.30	161.76	127.64	160.58	152.94	144.97
Cr	203.27	307.68	278.51	165.06	159.15	27.44	136.37	144.61	196.40
Co	27.44	37.07	28.10	25.26	23.38	16.38	23.37	21.83	23.59
Ni	71.12	132.90	103.57	56.17	43.55	11.92	37.12	38.96	58.54
Rb	14.45	14.48	13.24	17.04	17.95	19.15	15.49	14.56	15.19
Sr	521.12	520.99	451.32	431.09	354.82	442.20	389.04	336.55	441.48
Y	12.4	13.17	36.54	13.98	14.77	14.9	14.27	14.46	10.7
Zr	86.79	78.12	85.92	86.41	92.5	104.2	79.18	82.09	79.49
Nb	3.27	3.8	3.04	2.17	2.71	3.91	2.29	1.77	1.74
Ba	446.71	404.48	639.63	428.95	479.14	505.84	436.51	456.29	461.88
La	13.46	8.80	52.51	8.99	9.09	11.09	6.52	7.13	6.81
Ce	20.29	20.22	21.22	17.47	18.65	21.58	14.22	15.57	15.78
Nd	20.04	12.92	69.40	9.67	8.81	12.58	8.21	8.30	8.23
Sm	1.96	2.32	10.55	1.90	1.65	2.55	1.99	2.03	2.36
Eu	1.01	0.90	3.06	0.85	0.65	0.83	0.63	0.51	0.53
Gd	3.19	2.74	9.55	2.88	2.54	2.89	2.29	2.59	2.19
Dy	1.99	2.00	6.64	2.31	2.38	2.54	2.29	2.29	1.83
Er	1.06	0.93	2.04	1.27	1.22	1.17	1.56	1.41	0.86
Yb	1.05	1.18	2.38	1.34	1.38	1.29	1.30	1.35	0.83
Th	1.71	0.96	0.90	1.01	1.51	1.19	1.05	1.04	1.32

	Coturco volcano		Pambamarca volcano					
Sample	20EQ54	20EQ55	20EQ56	20EQ58	20EQ59	20EQ60	20EQ61	20EQ62
wt.%								
SiO_2	62.06	58.13	55.53	55.64	57.85	58.97	58.75	73.39
TiO_2	0.69	0.70	0.85	0.86	1.29	0.80	1.32	0.28
Al_2O_3	16.25	16.06	16.55	14.25	17.57	17.23	18.18	15.39
Fe_2O_3	5.94	6.79	8.43	7.13	7.90	7.25	7.24	1.60
MnO	0.07	0.09	0.12	0.12	0.11	0.10	0.07	0.03
MgO	3.36	4.38	5.81	6.66	2.49	3.48	1.47	0.14
CaO	5.65	6.76	7.61	7.89	5.92	6.37	5.85	1.80
Na_2O	4.12	3.86	3.72	3.21	4.41	4.07	4.53	4.39
K_2O	1.65	1.17	1.15	3.53	1.95	1.53	2.06	2.92
P_2O_5	0.21	0.16	0.22	0.73	0.49	0.20	0.52	0.06
L.O.I.	0.81	0.89	0.36	0.85	1.31	0.37	1.60	1.38
ppm								
Sc	13.23	18.70	20.46	20.74	13.55	13.47	13.22	2.06
V	136.41	163.08	199.51	222.33	170.73	160.70	166.83	13.29
Cr	144.91	136.09	257.10	276.06	10.49	66.72	8.89	1.56
Co	18.68	25.29	31.38	27.24	19.38	21.76	15.00	0.71
Ni	43.36	60.84	96.17	106.70	9.00	37.40	10.14	0.37
Rb	45.49	25.10	25.53	70.22	49.56	36.95	53.24	65.84
Sr	558.42	528.87	580.59	2275.79	631.10	602.91	641.80	330.76
Y	11.13	15.35	15.24	20.87	24.86	15.58	31.33	12.06
Zr	107.36	85.62	100.31	229.63	222.83	117.29	232.89	99.73
Nb	5.43	3.92	4.41	5.88	11.36	5.36	11.49	8.43
Ba	714.29	568.76	815.31	2090.36	839.88	708.41	1048.04	1145.75
La	16.72	12.71	16.92	76.08	32.15	20.86	38.89	28.24
Ce	30.90	23.37	30.35	148.90	64.91	35.37	68.51	46.06
Nd	14.45	14.66	17.61	73.19	34.36	19.46	43.62	22.14
Sm	2.55	3.12	3.50	12.97	7.32	4.21	8.64	3.68
Eu	0.85	0.99	1.08	3.33	1.87	1.29	2.15	0.88
Gd	2.85	3.42	3.43	8.11	6.03	3.96	8.43	3.00
Dy	1.87	2.56	2.64	3.93	4.57	2.77	5.99	1.75
Er	0.71	1.17	1.31	1.73	1.83	1.38	2.59	0.68
Yb	0.84	1.15	1.19	1.47	1.98	1.11	2.50	0.97
Th	4.84	2.41	2.83	19.05	6.09	3.83	6.62	7.48

	Pambamarca		Puntas				Chacana	
Sample	20EQ63	20EQ57	20EQ64	20EQ66	20EQ67b	20EQ68	20EQ85	20EQ87
wt.%								
SiO_2	73.74	55.11	58.85	56.31	56.20	57.63	53.39	62.10
TiO_2	0.21	0.84	0.79	0.88	0.81	0.80	0.97	0.76
Al_2O_3	15.20	13.73	19.50	18.39	18.40	18.86	18.08	16.15
Fe_2O_3	1.56	6.98	6.37	7.80	7.99	7.18	8.67	5.80
MnO	0.05	0.11	0.09	0.11	0.12	0.10	0.13	0.09
MgO	0.27	6.52	1.97	3.65	4.03	3.03	5.05	2.83
CaO	1.62	7.58	6.43	7.38	7.33	6.80	8.86	5.31
Na_2O	4.43	3.09	4.41	4.02	3.94	4.14	3.45	4.31
K_2O	2.86	3.51	1.39	1.25	1.02	1.26	1.19	2.41
P_2O_5	0.05	0.72	0.19	0.21	0.18	0.19	0.22	0.25
L.O.I.	1.79	0.90	0.65	0.24	0.41	0.61	1.76	0.04
ppm								
Sc	1.51	20.50	12.34	16.70	19.57	15.80	21.71	10.20
V	9.33	210.66	141.40	197.70	186.63	162.21	218.48	131.19
Cr	1.77	259.74	6.71	51.72	67.08	45.45	116.03	50.05
Co	0.67	26.66	16.67	22.22	26.31	21.55	28.64	16.94
Ni	1.22	116.25	7.69	23.62	34.11	23.36	54.28	24.26
Rb	65.00	81.26	31.66	26.63	19.83	26.29	22.48	64.83
Sr	323.87	2136.64	608.59	673.67	559.37	561.49	553.74	759.90
Y	8.45	22.42	17.44	16.61	19.92	15.87	17.4	11.89
Zr	123.58	233.67	120.13	101.4	99.48	109.85	101.68	109.96
Nb	8.94	6.54	4.71	4.83	4.37	4.75	4.56	7.7
Ba	1311.17	2003.76	595.90	534.09	463.17	548.78	478.55	897.25
La	27.40	71.70	15.68	15.80	17.43	15.64	13.67	26.18
Ce	47.54	137.60	32.83	32.65	24.92	26.34	27.20	47.80
Nd	17.80	70.99	17.12	17.13	18.13	16.71	14.70	22.29
Sm	2.98	12.44	3.23	3.66	4.01	4.22	3.08	3.74
Eu	0.66	3.17	1.04	1.01	1.27	1.07	0.93	1.15
Gd	2.42	7.52	3.74	3.79	3.77	3.55	3.48	3.53
Dy	1.24	3.91	3.03	2.67	3.35	2.90	2.98	2.10
Er	0.46	1.73	1.71	1.29	1.44	1.10	1.43	0.52
Yb	0.65	1.42	1.42	1.33	1.62	1.29	1.52	0.85
Th	8.78	18.20	3.67	3.16	2.27	3.17	2.73	9.10

Appendix C

Updated version of the Ecuadorian Volcanic Events and Geochronological database (EVEG).

Available in:

https://1drv.ms/x/s!AvfZGoXtHCw-ib0-HbqMna3oRHj7wQ?e=bEexAx

Chapter 6

View of the Inter-Andean valley from Santa Cruz volcano to the north. From left to right: Loma Saquigua cone, Corazón volcano and Atacazo-Ninahuilca volcanic complex.

Chapter 6

Summary

Contents

6.1 Geochronological background of the Ecuadorian volcanic arc 294
6.2 Iliniza volcano, a surprisingly young volcano 297
6.2.1 Eruptive history of Iliniza and Santa Cruz volcanoes 297
6.2.1.1 Previous volcanism: Santa Cruz volcano 297
6.2.1.2 Iliniza volcano 299
6.2.2 Implications for the hazard assessment 303
6.3 Geochronological evolution of the Ecuadorian volcanic arc 305
6.3.1 New K-Ar ages obtained for the central segment volcanoes 305
6.3.1.1 Volcanism in the Guayllabamba valley 310
6.3.1.2 The Machachi volcanic cluster 317
6.3.2 Volcanism at the Ecuadorian volcanic arc scale 326
6.3.2.1 Compilation of geochronological data 326
6.3.2.2 Eruptive history of the Ecuadorian volcanic arc 328
6.4 Relationship between volcanism and tectonics 334

6.1 Geochronological background of the Ecuadorian volcanic arc

The eruptive history of the Ecuadorian arc until AD ~2017 was mostly described on the basis of geochronological studies carried out on selected volcanoes. As described in Chapter 2, these studies were mostly focused on defining the most recent cone-building stages of the "active" volcanoes in the region. The volcanoes with eruptive activity documented in historical records (back to the Spanish colonization of Ecuador in AD 1534; Hall, 1977; Hall and Beate, 1991) or with morphological and stratigraphic evidence suggesting a Holocene eruptive activity were prioritized.

Volcanoes with geochronological data include Antisana (Bourdon et al., 2002; Hall et al., 2017b), Atacazo-Ninahuilca (Hidalgo, 2006; Hidalgo et al., 2008), Casitagua (Pacheco, 2013; Alvarado et al., 2014), Cayambe (Samaniego et al., 1998, 2005), Chacana (Bigazzi et al., 1992, 1997, 2005; Opdyke et al., 2006; Hall and Mothes, 2008c; Villares, 2010; Pilicita, 2013; Chiaradia et al., 2014), Chachimbiro (Bernard et al., 2014), Chimborazo (Barba et al., 2008; Samaniego et al., 2012), Cotacachi-Cuicocha (von Hillebrandt, 1989; Almeida, 2016), Cotopaxi (e.g., Hall and Mothes, 2008a; Tsunematsu and Bonadonna, 2015; Vezzoli et al., 2017), Huañuna (Hall et al., 2017b), Iliniza (Hidalgo, 2002, 2001; Hidalgo et al., 2007), Imbabura (Andrade, 2009; Le Pennec et al., 2011), Mojanda-Fuya Fuya (Robin et al., 1997, 2008a), Pan de Azúcar (Hoffer, 2008), Pichincha (Robin et al., 2010, 2008b), Pululahua (Andrade, 2002; Andrade et al., 2014; Vasconez, 2015), Puyo cones and Mera Lavas , Sangay (Monzier et al., 1999; Valverde, 2014; Narvaez et al., 2018), Soche (Beate, 1994; Hall and Mothes, 2008b), Sumaco (Hoffer, 2008; Garrison et al., 2017), Tungurahua (Hall et al., 1999; Le Pennec et al., 2013, 2016), Yanahurcu de Piñan (Béguelin et al., 2015), and the volcanoes located of the western side of the Eastern Cordillera: Cosanga, Bermejo, El Dorado, Huevos de Chivo, and Pumayacu (Mothes and Hall, 2008a; Bellot-Gurlet et al., 2008; Hall and Mothes, 2010). However, the eruptive history of several old edifices, recognized by their advanced stages of erosion, remained poorly defined. Few publications provided geochronologic data on their ancient cone-building stages (e.g., Barberi et al., 1988; Lavenu et al., 1992; Bigazzi et al., 2005; Opdyke et al., 2006; Hoffer et al., 2008). Moreover, the reliability of whole-rock K-Ar ages (Barberi et al., 1988; Lavenu et al., 1992) was recently questioned because of

biases caused by the presence of argon inherited from unseparated phenocrysts and/or the presence of altered mineralogical phases (see Chapter 2).

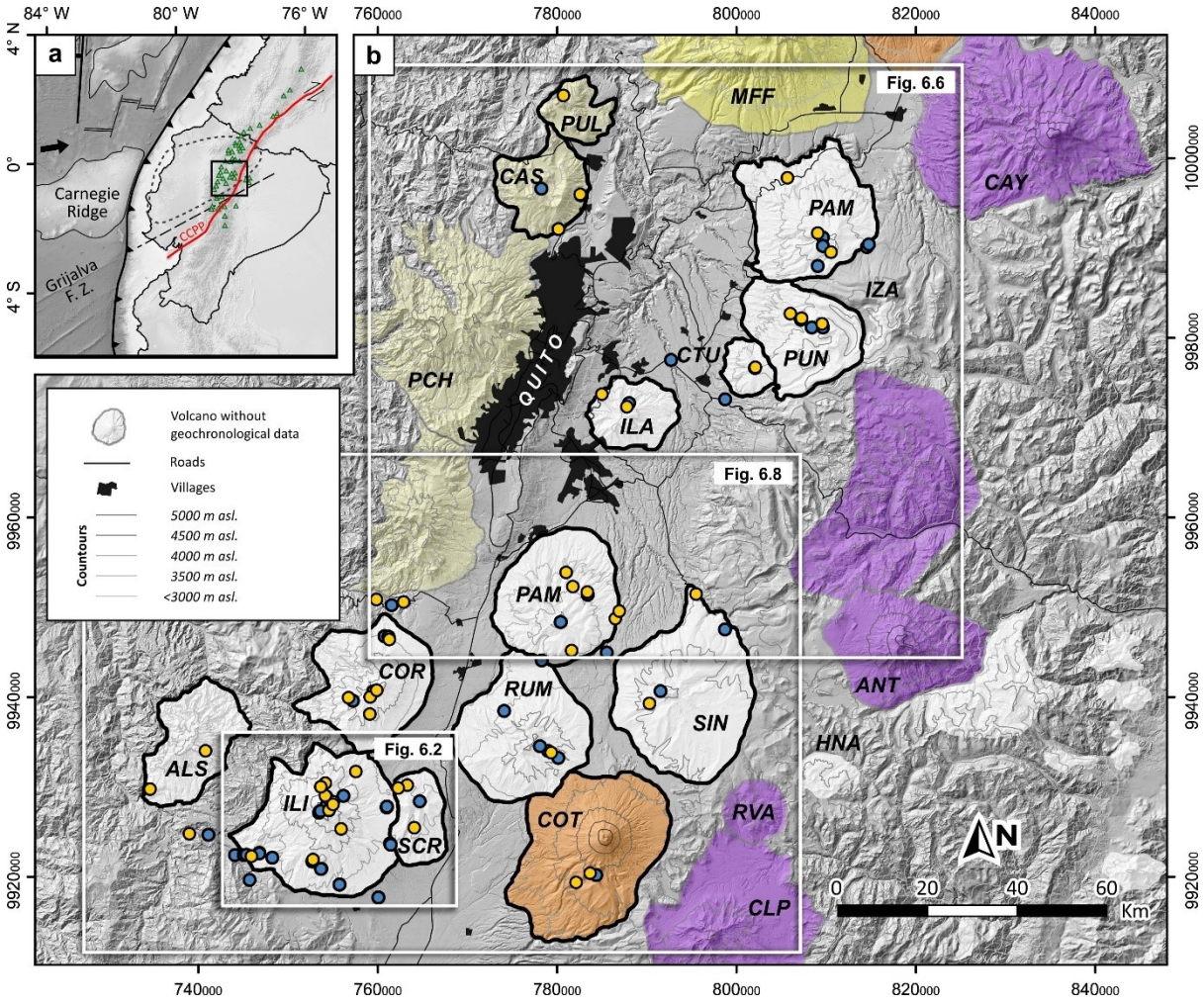

Figure 6.1. *Hill-shaded digital surface model of the central Ecuadorian arc showing the locations of samples collected in this study. K-Ar dated samples are represented with blue dots. Sampled volcanoes showed with solid black outlines. abbreviations of volcano names provided in Table 6.1*

More than a hundred new groundmass K-Ar ages were acquired during the last few years (Alvarado et al., 2014; Almeida, 2016; Almeida et al., 2019; Bablon et al., 2018, 2019, 2020a, 2020b; Telenchana, 2017) thanks to the cooperation between the GEOPS laboratory of the Université Paris-Saclay (France), the Institut de Recherche pour le Développement (IRD, France), and the Instituto Geofísico de la Escuela Politécnica Nacional (IG-EPN, Ecuador). These geochronological data provided a new perspective on the evolution of the northern and southern segments of the arc. The

present Ph.D. thesis provides 49 new K-Ar ages obtained from 15 volcanoes located in the central segment of the Ecuadorian arc (Fig. 6.1), complementing the previous studies of other volcanoes in the region. Coupled with new field observations, stratigraphic correlations, morphological analyses and geochemical data, our new geochronological dataset allows us to describe the eruptive history of the volcanoes from this region, and for the first time, from the whole Ecuadorian arc. This chapter synthesizes the geochronological findings of the central segment, starting with the detailed study on the Iliniza volcano.

Table 6.1. *Names and abbreviations of the volcanoes identified in the Ecuadorian Arc.*

N	Code	Volcano name	N	Code	Volcano name	N	Code	Volcano name
1	***ALI***	Aliso	**27**	***COT***	Cotopaxi	**53**	***PLV***	Pilavo
2	***ALS***	Almas Santas	**28**	***CTU***	Coturco	**54**	***POT***	Potrerillos
3	***ALT***	Altar	**29**	***CUB***	Cubilche	**55**	***PUL***	Pululahua
4	***ANG***	Angahuana	**30**	***CSH***	Cushnirumi	**56**	***PUM***	Pumayacu
5	***ANT***	Antisana	**31**	***CUS***	Cusín	**57**	***PUN***	Puntas
6	***ATA***	Atacazo - Ninahuilca	**32**	***DOR***	El Dorado	**58**	***PLC***	Puñalica
7	***BMJ***	Bermejo	**33**	***HOR***	Horqueta	**59**	***PUT***	Putzalagua
8	***CAC***	Cacalurcu	**34**	***HNA***	Huañuna	**60**	***PUY***	Puyo cones
9	***CAL***	Calpi cones	**35**	***HCH***	Huevos de Chivo	**61**	***QLT***	Quilotoa
10	***CRH***	Carihuairazo	**36**	***HUI***	Huisla	**62**	***REV***	Reventador
11	***CSL***	Casahuala	**37**	***IGL***	Igualata	**63**	***RVA***	Río Valle (Chaupiloma)
12	***CAS***	Casitagua	**38**	***IGN***	Iguán	**64**	***RUM***	Rumiñahui
13	***CAY***	Cayambe	**39**	***ILA***	Ilaló	**65**	***SAG***	Sagoatoa
14	***CHN***	Chacana	**40**	***ILI***	Iliniza	**66**	***SAN***	Sangay
15	***CCB***	Chachimbiro	**41**	***IMB***	Imbabura	**67**	***SCR***	Santa Cruz
16	***CPT***	Chalpatán	**42**	***IZA***	Izambi	**68**	***SIN***	Sincholagua
17	***CLP***	Chalupas - Quilindaña	**43**	***MAC***	Machángara	**69**	***SCH***	Soche
18	***CQL***	Chaquilulo	**44**	***MAN***	Mangus	**70**	***SUM***	Sumaco
19	***CCN***	Chiles - Cerro Negro	**45**	***MER***	Mera lavas	**71**	***TUL***	Tulabug
20	***CTZ***	Chiltazón	**46**	***MFF***	Mojanda - Fuya Fuya	**72**	***TUN***	Tungurahua
21	***CHB***	Chimborazo	**47**	***MUL***	Mulmul	**73**	***VNG***	Virgen Negra
22	***CNB***	Chinibano	**48**	***PAM***	Pambamarca	**74**	***VIZ***	Vizcaya cone
23	***CLM***	Chulamuez	**49**	***PDA***	Pan de Azúcar	**75**	***VAZ***	Volcán Azul
24	***COR***	Corazón	**50**	***PAR***	Parulo	**76**	***YNP***	Yanahurcu de Piñan
25	***COS***	Cosanga	**51**	***PAS***	Pasochoa	**77**	***YNU***	Yanaurcu
26	***CTC***	Cotacachi - Cuicocha	**52**	***PCH***	Pichincha			

6.2 Iliniza volcano, a surprisingly young volcano

Iliniza is a double-peaked volcano located in the central segment of the Ecuadorian arc, 55 km south of Quito. Iliniza stands on the eastern edge of the Western Cordillera, partially overlying the Inter-Andean valley Santa Cruz volcano. The wide glacial valleys present in the highest areas of Iliniza volcano, especially those observed in its northern edifice, suggested by comparison with other eroded volcanoes in the region that the age of this volcano could reach ~1 Ma (Hidalgo et al., 2007). Meanwhile, a formation age close to the Holocene was proposed for a well preserved satellite dome located in the southern flank of Iliniza volcano (Hall and Beate, 1991).

6.2.1 Eruptive history of Iliniza and Santa Cruz volcanoes

Our 14 new K-Ar ages acquired on the Iliniza volcano (Fig. 6.2) allowed us to constrain its formation age, together with that of the adjacent Santa Cruz volcano. We combined the stratigraphic data provided by Hidalgo (2001, 2002) with new field observations and geochemical data to describe the eruptive history of the volcano, summarized below.

6.2.1.1 Previous volcanism: Santa Cruz volcano

The oldest volcanism in the studied area indeed corresponds to the activity of **Santa Cruz volcano (SC)**. Its main edifice was constructed in the Inter-Andean Valley by successions of massive andesitic lavas. An age of 702 ± 11 ka was obtained from a lava flow located in the southern flank of the volcano. Several dacitic domes were extruded in the summit area, presumably at the end of the eruptive history of the basal edifice. Unexpectedly, two samples collected from *Loma Saquigua (LS)*, an isolated peak of the Santa Cruz volcano summit, yielded ages of 79 ± 2 ka and 60 ± 3 ka (Fig. 6.2). This resurgent activity of Santa Cruz was marked by the extrusion of a dacitic dome followed by the emission of andesitic lava flows.

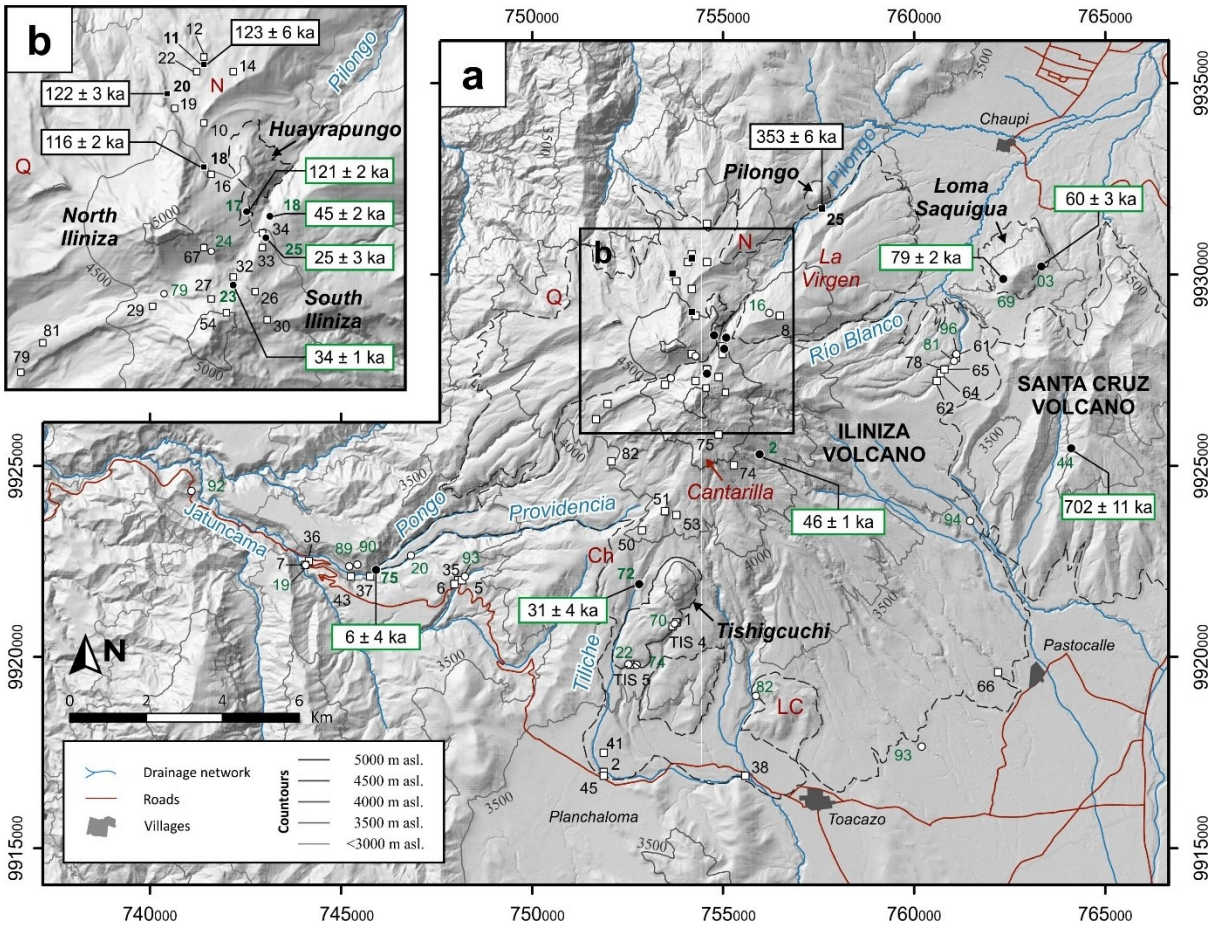

Figure 6.2. *Hill-shaded digital surface model of Iliniza volcano showing the locations of samples recollected in this study (circles; green numbers; Santamaría et al., submitted) and those from Hidalgo et al. (2007) (squares; black numbers). K-Ar dated samples are represented with solid symbols. Ridges and hills shown as red letters. Ch: Chilcapamba; LC: Loma La Cruz; N: Ninarrumi; Q: Quillotoro. Rivers and valleys are labelled with blue letters.*

6.2.1.2 Iliniza volcano

The eruptive history of **Iliniza volcano** begins with the extrusion of the rhyodacitic **Pilongo dome (Pi)**, which is located on the lower north-western flank of the present-day Iliniza volcano (Fig. 6.2). A sample from this dome yielded an age of 353 ± 6 ka. Following this rather small activity, our ages suggest the occurrence of a quiescence period in the area until the construction of the **North Iliniza edifice (NI)**, which is located in the Western Cordillera 5 km southwest of Pilongo and 10 km west of Santa Cruz. The North Iliniza (NI) edifice is formed by several sequences of acid-andesite to dacite monolithological breccias and thin lavas (Fig. 6.3a) erupted during the *Lower NI stage (NI-Ls)*. The northern flank sequences were dated between 122 ± 6 and 123 ± 6 ka. Then, a voluminous andesitic lava peak was formed on the northern flank of North Iliniza during the *Huayrapungo stage (NI-Hs)*. A lava flow showing meter-sized flow banding textures was dated at 121 ± 2 ka (Fig. 6.3b). The construction of the North Iliniza edifice concluded with the emission of voluminous lava flows, acid-andesite to dacite in composition, which shape the upper structure of the cone during the *Upper NI stage (NI-Us)*. A sample collected at the base of the most voluminous lava flow (100 m-thick and 1500 m-long; NI northern flank) yielded an age of 116 ± 2 ka.

The numerical reconstructions of the North Iliniza edifice suggest that this conical landform reached a bulk volume of 28 ± 9 km^3. Although our geochronological results suggest a short formation period ranging from 123 ± 6 ka to 116 ± 2 ka, we emphasize that the geochronological sampling of the oldest units was not exhaustive due to their scarce exposure and limited accessibility. Therefore, it is possible that the onset of activity in the North Iliniza edifice could be older than shown by our data. Nevertheless, we estimate an overall output rate of 3.5 ± 2.6 km^3/kyr based on the calculated bulk volume for the North Iliniza edifice and its estimated lifetime.

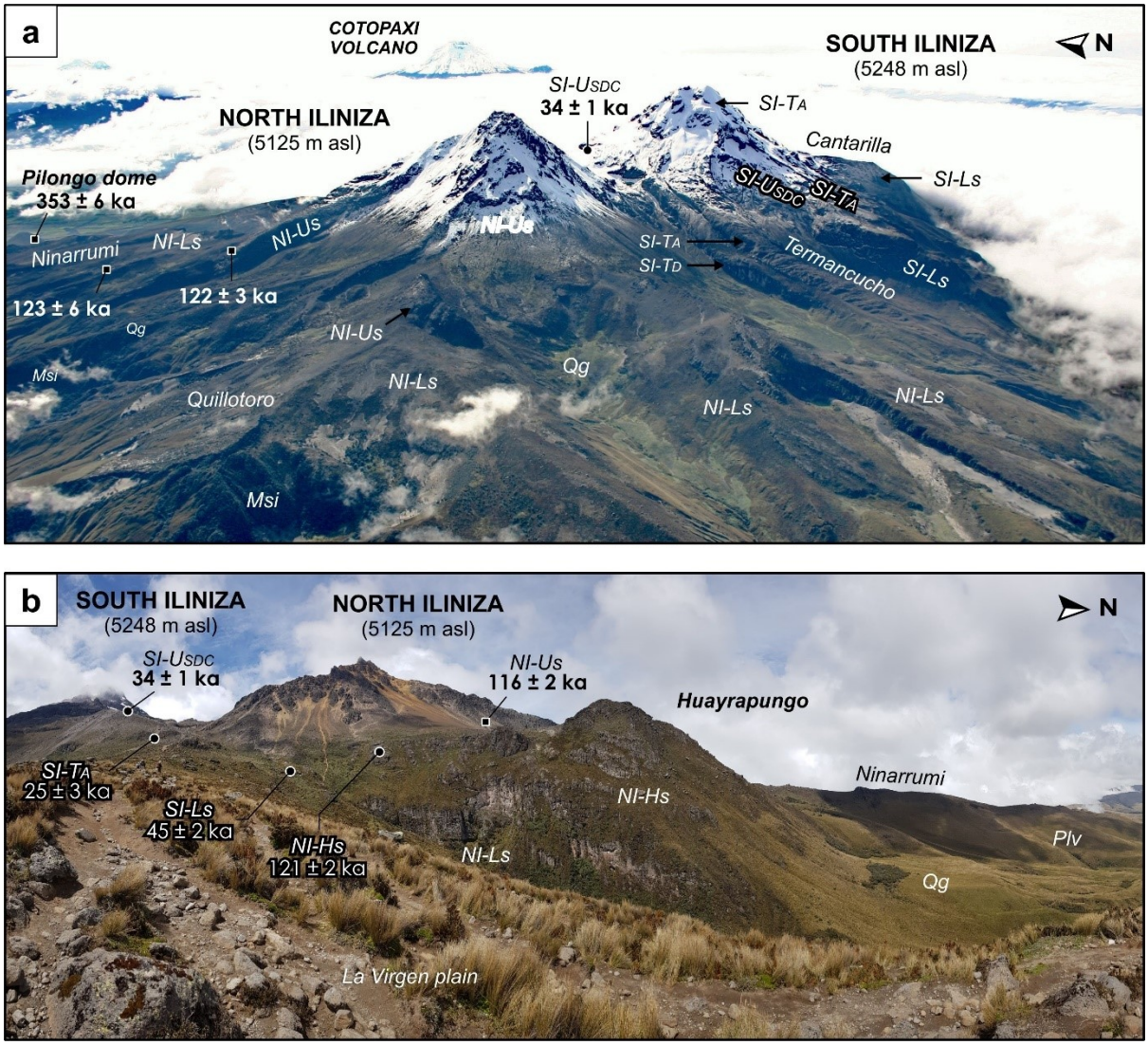

Figure 6.3. a) *Aerial view of Iliniza volcano, looking east (photography by Patricio Ramon, IG-EPN).* ***b)*** *Panoramic view of the North Iliniza edifice, looking west from La Virgen plain. Geological unit abbreviations and relative location of the photographs provided in Figure 6.4.*

After a second period of apparent quiescence, the main emission center of Iliniza migrated ~1.6 km southeast from the summit of the North Iliniza edifice. The subsequent volcanic activity formed the **South Iliniza edifice (SI)** in three cone-building stages (Fig. 6.3). During the *Lower SI stage (SI-Ls)*, a succession of dacitic massive lavas and sparse inter-layered breccias shaped the basal edifice. Two ages of 45 ± 2 ka and 46 ± 1 ka were obtained from dacitic lavas from the uppermost sequences. The South Iliniza deposits partially covered the eroded Santa Cruz volcano, in agreement with our geochronological results.

A noticeable unconformity, spatially coincident with a change in the radial slope of the basal edifice from 35° to 10°, was observed in the uppermost area of the southern side of the South Iliniza edifice (Fig. 6.3a). This unconformity marks a clear separation between the previous stage and the pyroclastic and effusive deposits emitted during the *Upper SI stage (SI-Us)*. In detail, a sequence of two consolidated PDC deposits *(SI-U_{CP})* overlies the SI-Ls deposits forming the Cantarilla unconformity. To the north, a complex of dacitic domes *(SI-U_{SDC})* dated at 34 ± 1 ka constitutes the summit of the South Iliniza edifice (Fig. 6.3). Furthermore, the base of the edifice is covered by a volumetric widespreaded PDC succession called *the Jatuncama ignimbrite* (*SI-Ji*; Fig. 6.4). This succession is composed by a thick multiple bedded block-and-ash flow sequence (SI-J_{BA}) overlaid by pumice-and-ash flow deposits (SI-J_{PA}). The SI-J_{BA} deposits are composed of poorly vesiculated juvenile dacite blocks and varying amounts of pumice lapilli supported in a fine-grained ashy matrix. This sequence covers an area of ~60 km^2 with an average thickness of 30-40 m, equivalent to a bulk volume of ~2.1 km^3. It corresponds to a volcanic explosivity index (VEI) of at least 5. Several 7-10 m-thick pumice-and-ash flow units (SI-J_{PA}) overlie part of the SI-J_{BA} deposits. The rhyolitic Santa Rosa pumice-and-ash flow (SI-J_{SR}) outcrops on the northwest flank of the South Iliniza edifice (Fig. 6.4). The radial distribution of the Jatuncama ignimbrite pointing towards the summit of the South Iliniza edifice, its stratigraphic position overlying the basal SI edifice deposits, and its geochemical and mineralogical affinity with the *SI-U_{SDC}* unit support the occurrence of a high-explosive phase (VEI 5) at the beginning of the Upper SI stage. We suggest that this explosive activity caused the formation of the Jatuncama pyroclastic deposits, while destroying the uppermost portion of the South Iliniza edifice and forming a large 1.5 km-wide crater. Subsequently, the emission of several dacitic domes reconstructed the volcanic cone creating the Cantarilla unconformity at about 34 ± 1 ka. The most recent volcanic activity of the South Iliniza edifice occurred during the *Terminal SI stage (SI-Ts)*, when several massive andesitic lavas were emitted forming the edifice summit (Fig. 6.3a). Two ages at 25 ± 3 ka and 31 ± 4 ka suggest that this less explosive activity of andesitic nature occurred shortly after the Upper SI stage events. The bulk volume of material accumulated by the South Iliniza edifice reached 18 ± 6 km^3. Considering that its eruptive activity extended between 46 ± 1 and 25 ± 3 ka, the corresponding output rate is 0.8 ± 0.3 km^3/kyr.

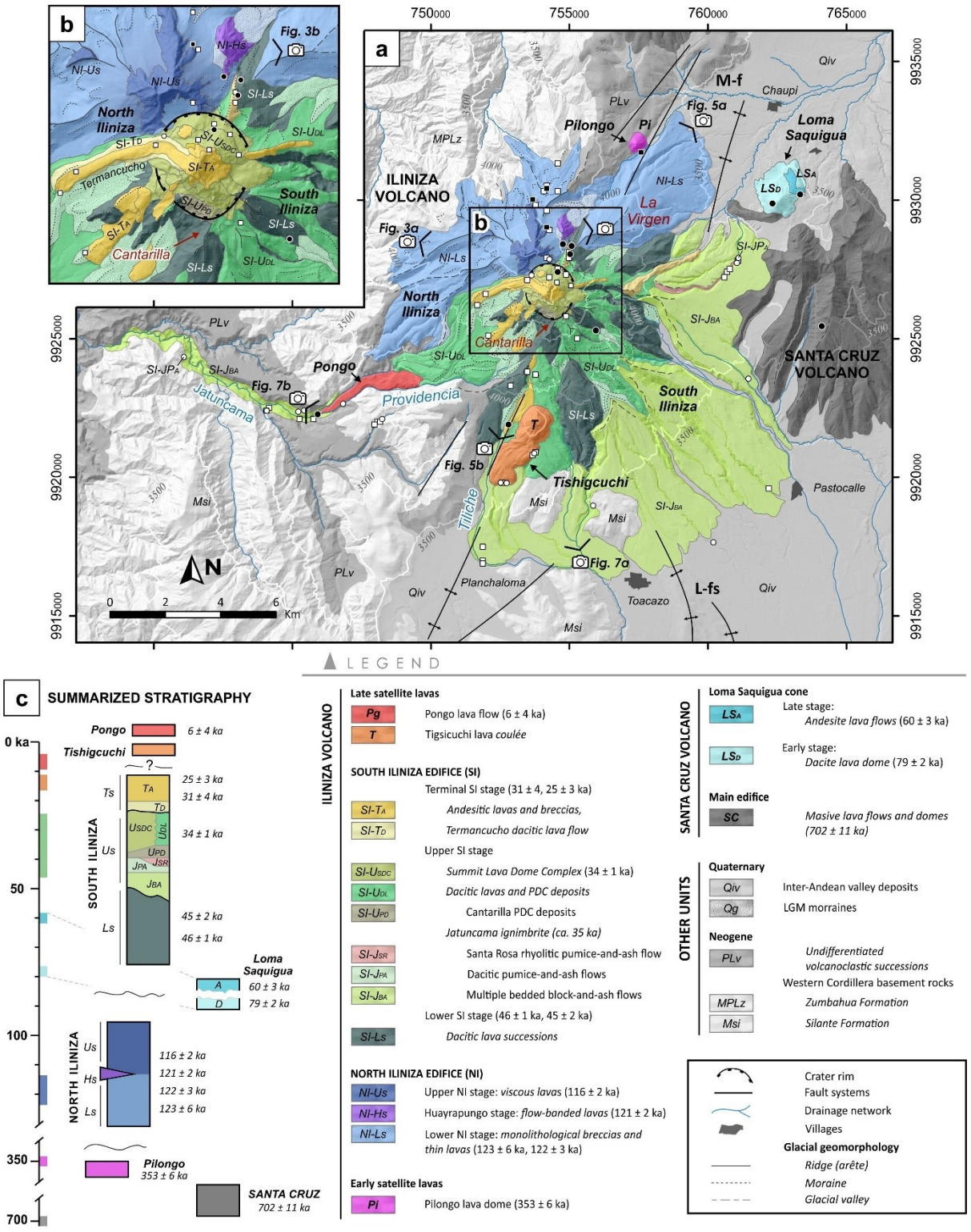

Figure 6.4. *Simplified geological map of Iliniza volcano after considering our new ages (Fig. 6.2) and field observations, as well as those from Hidalgo (2001) and Hidalgo et al. (2007). Sample sites are shown according to Figure 6.2 caption. Local fault systems are symbolized with black lines. M-f: Machachi Fault; L-fs: northern segment of Latacunga Fault System.*

The eruptive history of Iliniza volcano concluded with the emission of the **Pongo lava flow (T)** and the extrusion of the **Tishigcuchi dome coulee (Pg)**. Unfortunately, our attempts to date samples from the Tishigcuchi dome were unsuccessful due to the high atmospheric contamination exhibited by their groundmass phases and the advanced weathering of the crystalline phases. Nevertheless, we estimate the Tigsichuchi dome age between 20 and 8 ka based on stratigraphic and morphological relationships. Conversely, the Pongo andesitic lava flow, located to the southwest of Iliniza volcano (Fig. 6.4), was dated at 6 ± 4 ka. This result confirms that the activity of the Iliniza volcano extended into the Holocene. In addition, we acknowledge that this age reaches the limits of the K-Ar Cassignol-Gillot technique. Therefore, we strongly suggest the use of alternative dating techniques, such as radiocarbon dating, to constrain the Holocene activity of Iliniza volcano. Unfortunately, the source of the Pongo lava couldn't be clearly identified upstream. Given the size of the lava flow and its Holocene age, its upper parts should be still observable as they could not have been completely eroded or covered by younger deposits. Thus, an origin from a satellite vent located at the southwestern base of Iliniza volcano is suspected. The Tishigcuchi dome yields a present-day volume of 339 ± 41 × 10^{-3} km^3, whereas the Pongo lava flow reaches a volume of 73 ± 18 × 10^{-3} km^3.

6.2.1.3 Implications for hazard assessment

The Iliniza edifices developed separately in time, in contrast to other twin-peaked volcanoes such as Mojada-Fuya Fuya (Robin et al., 2009) in the Ecuadorian arc, or Yucamane-Calientes (Rivera et al., 2020) in the Peruvian , for instance. Note that the evolution of Iliniza and Santa Cruz volcanoes also included long-lasting quiescence periods, which is also the case for other volcanoes in the region such as Cotopaxi (Hall and Mothes, 2008a), Pichincha (Robin et al., 2010), Atacazo-Ninahuilca (Hidalgo, 2006), and Tungurahua (Bablon et al., 2018). Moreover, the eruptive history of both volcanoes, specially of Santa Cruz volcano, illustrate that even ancient volcanoes are susceptible to reactivation and can exhibit any kind of eruptive activity, even several thousand years after their main activity.

Volcanoes located on the Western Cordillera (Volcanic Front) usually incorporated dacitic magmas at the end of their eruptive histories. This magma composition resulted in eruptive styles characterized by Pelean and Plinian eruptions, regional tephra fallouts, the extrusion of dacitic domes, and the generation of block-and-ash flows produced by the collapse of these domes (e.g., von Hillebrandt, 1989; Hidalgo et al., 2008; Mothes and Hall, 2008b; Robin et al., 2008b; Bernard et al., 2014; Andrade et al., 2021). By contrast, the late eruptive products of Iliniza volcano showed andesitic compositions. Based on the proposed eruptive history, we infer that the most probable eruptive scenario could be dominated by the emission of lava flows and/or the formation of low-viscous lava domes, whose subsequent collapse may produce PDCs and minor tephra fallouts. The apparent migration of the active vents through time, from northern to southern locations, favors an eruptive scenario possibly taking place from a fissure located on the southern flank of South Iliniza. Nevertheless, an eruption in higher areas is not excluded. We note that the occurrence of high explosive eruptions (VEI ~5) is generally rare in the recent history of Iliniza volcano. Therefore, we consider that the occurrence of a highly explosive event such as the Jatuncama phase is less probable in the near future.

While the occurrence of sector collapse events is commonly reported in the eruptive history of several volcanoes of the Volcanic Front (e.g., Hidalgo, 2006; Bernard et al., 2008; Robin et al., 2010; Almeida et al., 2019), we have not identified avalanche deposits or morphologic evidence suggesting the occurrence of such events at Iliniza volcano. However, the location of Iliniza above an active strike-slip fault system (Egüez and Yepes, 1994; Hidalgo, 2001), the extent of the hydrothermal weathering, and the steeper slopes observed on its highest flanks increase the potential destabilization of its edifices and thus the probability of a sector collapse event. Alternatively, the thick fallout deposits of the Cotopaxi volcano accumulated on the Iliniza and Santa Cruz flanks present multiple landslide scarps (Hall et al., 2017a). Therefore, we emphasize the potential occurrence of multiple, rather small volume, landslides affecting these deposits, and moreover if a nearby earthquake or reactivation of the Cotopaxi volcano occurs. Furthermore, these poorly consolidated deposits could be easily remobilized during rainy seasons generating secondary lahars. Finally, this work proposes several hypotheses to consider in future studies dedicated to the evaluation of the threat of a potential activity of Iliniza volcano.

6.3 Geochronological evolution of the Ecuadorian volcanic arc

6.3.1 New K-Ar ages obtained for the central segment volcanoes

The present PhD thesis work focuses on the group of volcanoes located around the Guayllabamba basin (Inter-Andean Valley), between latitudes 0.1° N and 0.7°S. Together with those of the sub-Andean zone, they will be considered as the central segment of the volcanic arc in the following. In order to constrain the eruptive history of this area, which was poorly known prior to this study, we have collected more than 70 rock samples for geochemical and geochronological analysis, following the methods described in Chapter 2.

A detailed review of the literature has indicated that the eruptive histories of the Atacazo, Antisana, Cayambe, Chacana, Cotopaxi, Chalupas-Quilindaña, Mojanda-Fuya Fuya, Pichincha and Pululahua volcanoes were reasonably well defined. Conversely, no geochronological information was found for eleven volcanoes in this area, although some of them had complete studies on their stratigraphy and general geochemistry, such as Almas Santas (Chemin, 2004), Ilinizas (Hidalgo, 2001, 2002; Hidalgo et al., 2007) or Rumiñahui (Starr, 1984) volcanoes. On the other hand, the reliability of the scarce geochronological data of Ilaló (Barberi et al., 1988), Casitagua (Geotérmica Italiana, 1989) and Pasochoa (Opdyke et al., 2006) volcanoes had been questioned (see Chapter 4 and 5). Furthermore, we found that the ancient stages of Cotopaxi (Bigazzi et al., 1992; Hall and Mothes, 2008a), an active and dangerous volcano located south of the study area, remained poorly defined, and therefore we have included this volcano in our study. Three K-Ar ages were recently acquired for the satellite domes of Casitagua volcano (Pacheco, 2013; Alvarado et al., 2014), which are separated from the main edifice by the Monjas valley. Thus, as no geochronological data is available for the main edifice of Casitagua, we have also included it in our study. Finally, an eroded dome from the Holocene Pululahua complex was dated in the framework of the collaboration with Andrade et al. (2021). Therefore, the volcanoes sampled for our study are Almas Santas, Casitagua, Chacana (southern pre-caldera lavas), Corazón, Cotopaxi, Coturco, Ilaló, Pambamaca, Pasochoa, Pululahua, Puntas, Rumiñahui and Sincholagua, in

addition to the already described Iliniza and Santa Cruz volcanoes. Lastly, a sample from the Sumaco volcano, located in the Sub-Andean zone of the central segment, was also analyzed.

A summary of the new ages acquired in this study is presented in Table 6.2. As introduced in Section 6.1, as many as a hundred new K-Ar ages were obtained by the GEOPS laboratory during the last five years using the Cassignol-Gillot dating technique. Figure 6.5b presents the new results obtained in the present PhD thesis, together with previous K-Ar ages also acquired in the GEOPS laboratory (Fig. 6.5a).

Table 6.2. *K-Ar ages obtained during this study. Columns indicate, from left to right to right, sample name, volcano to which it belongs, sample nature and stratigraphic unit, sampling site location and coordinates (WGS 84, Zone 17S), fraction on which the dating was carried out (GM: groundmass; Plag: plagioclase phenocrysts), and the age obtained in ka.*

Sample	Volcano	Unit	Location	Longitude (m)	Latitude (m)	Analyzed fraction	Mean age
19EQ36	Almas Santas	Andesitic lavas, *Cerro Azul*	E flank	734605	9929768	GM	364 ± 7 ka
19EQ43	Almas Santas	Andesitic lavas, *Tangan lavas*	S flank	740786	9934033	GM	374 ± 7 ka
20EQ50*	Atacazo	Dacite block, *S avalanche*	S flank	762881	9950592	GM	149 ± 6 ka
20EQ51a	Casitagua	Lava flow, *main edifice*	E flank	780148	9992110	GM	785 ± 15 ka
20EQ52a	Casitagua	Lava flow, *main edifice*	SE flank	782567	9995974	GM	878 ± 13 ka
20EQ85	Chacana	Lava flow, *pre-caldera series*	Antisanilla valley, S flank	795498	9951500	GM	2228 ± 34 ka
19EQ05	Corazón	Lava flow, *Late stage*	SW flank	756746	9939943	GM	67 ± 4 ka
19EQ07	Corazón	Lava flow, *Late stage*	S flank	759112	9938136	GM	95 ± 3 ka
19EQ08	Corazón	Lava flow, *Early stage*	Summit pyramid	759536	9940634	GM	178 ± 32 ka
19EQ10	Corazón	Lava flow, *Late stage*	S flank	759148	9940026	GM	86 ± 3 ka
19EQ11	Corazón	Lava flow, *Cerro Bómboli*	N flank	759847	9950892	GM	91 ± 10 ka
19EQ13	Corazón	Lava flow, *Early stage*	N flank	761280	9946424	GM	75 ± 7 ka
20EQ84	Corazón	Lava flow, *Early stage*	Summit pyramid	759883	9940775	GM	175 ± 30 ka
20EQ77	Cotopaxi	Obsidian flow, *Barrancas stage*	Base of Morurco peak	783660	9920417	GM	537 ± 11 ka
20EQ78	Cotopaxi	Lava flow, *Morurco stage*	Morurco peak, S flank	782119	9919377	GM	334 ± 5 ka
20EQ88	Cotopaxi	Lava flow, *Morurco stage*	Tanipamba (Pita lavas)	786939	9949596	GM	295 ± 10 ka
20EQ54	Coturco	Lava flow, *main edifice*	Summit peak	802112	9976733	GM, Plag	1959 ± 28 ka
19EQ01	Ilaló	Lava flow, *main edifice*	E flank	784978	9973735	GM	1273 ± 20 ka
19EQ47	Ilaló	Lava flow, *main edifice*	N flank	787784	9972350	GM	1112 ± 22 ka

Sample	Volcano	Unit	Location	Longitude (m)	Latitude (m)	Analyzed fraction	Mean age
19EQ02	Iliniza	Lava flow, *SI-Ls stage*	S Iliniza, E flank	755922	9925321	GM	46 ± 1 ka
19EQ17	Iliniza	Lava flow, *NI-Hs stage*	Huayrapungo peak	754734	9928425	GM	121 ± 2 ka
19EQ18	Iliniza	Lava flow, *SI-Ls stage*	S Iliniza, N flank	755052	9928362	GM	45 ± 2 ka
19EQ23b	Iliniza	Lava dome, *SI-U_{SDC} stage*	S Iliniza, summit pyramid	754550	9927424	GM	34 ± 1 ka
19EQ25	Iliniza	PDC deposit, *SI-T_A stage*	S Iliniza, N flank	754997	9928069	GM	25 ± 3 ka
20EQ72	Iliniza	Lava flow, *SI-T_A: Tiliche lavas*	S Iliniza, S flank	752778	9921934	GM	31 ± 4 ka
20EQ75	Iliniza	Lava flow, *Pongo lava*	Pongo valley	745904	9922305	GM	6 ± 4 ka
SIL 11	Iliniza	Lava flow, *NI-Ls stage*	N Iliniza, N flank	754150	9930434	GM	123 ± 6 ka
SIL 18	Iliniza	Lava flow, *NI-Us stage*	N Iliniza, N flank	754151	9929036	GM	116 ± 2 ka
SIL 20	Iliniza	Lava flow, *NI-Us stage*	N Iliniza, N flank	753648	9930031	GM	122 ± 3 ka
SIL 25	Iliniza	Dome block, *Pilongo dome*	Pilongo valley	757550	9931731	GM	353 ± 6 ka
20EQ56	Pambamarca	Lava flow, *main edifice*	NW flank	805673	9997815	GM	1374 ± 21 ka
20EQ60	Pambamarca	Lava flow, *main edifice*	Summit area	809077	9991663	GM	1261 ± 18 ka
20EQ62	Pambamarca	Rhyolitic dome, *summit area*	Jamby Machay dome	810553	9989550	Plag	1273 ± 20 ka
19EQ30	Pasochoa	Lava flow, *main edifice*	E flank	786494	9948763	GM	450 ± 7 ka
19EQ32	Pasochoa	Lava flow, *main edifice*	NW flank	783362	9951701	GM	441 ± 9 ka
19EQ33	Pasochoa	Lava flow, *main edifice*	N flank	781758	9952313	GM	459 ± 7 ka
19EQ34	Pasochoa	Lava flow, *main edifice*	N flank	780987	9953901	GM	472 ± 8 ka
19EQ37	Pasochoa	Lava flow, *main edifice*	S flank	781599	9945191	GM	423 ± 10 ka
PUL-M	Pululahua	Dacite block, *Unit I: domes*	Maucaquito dome	780700	10007000	GM	4 ± 3 ka
20EQ66	Puntas	Lava flow, *main edifice*	E flank	809562	9981566	GM	1132 ± 16 ka
20EQ67b	Puntas	Lava flow, *main edifice*	E flank	807261	9982195	GM	1084 ± 17 ka
20EQ68	Puntas	Lava flow, *main edifice*	E flank	806008	9982702	GM	1128 ± 16 ka
19EQ27	Rumiñahui	Lava flow, *Late HK lavas*	E flank	779336	9933840	Plag	202 ± 8 ka
19EQ03	Santa Cruz	Lava flow, *Loma Saquigua*	N flank	763281	9930218	GM	60 ± 3 ka
19EQ44	Santa Cruz	Lava flow, *main edifice*	S flank	764061	9925476	GM	702 ± 11 ka
20EQ69	Santa Cruz	Dacite dome, *Loma Saquigua*	S flank	762285	9929891	GM	79 ± 2 ka
19EQ41	Sincholagua	Lava flow, *main edifice*	W flank	790298	9939301	GM	312 ± 6 ka
SUM-EPN-01	Sumaco	Andesite block, *S avalanche*	S flank (Tigre river)	874100	9919800	GM	228 ± 4 ka

**Sample from Bablon* (2018) *with original code 17EQ59. Negative age results caused by high atmospheric contamination were not included.*

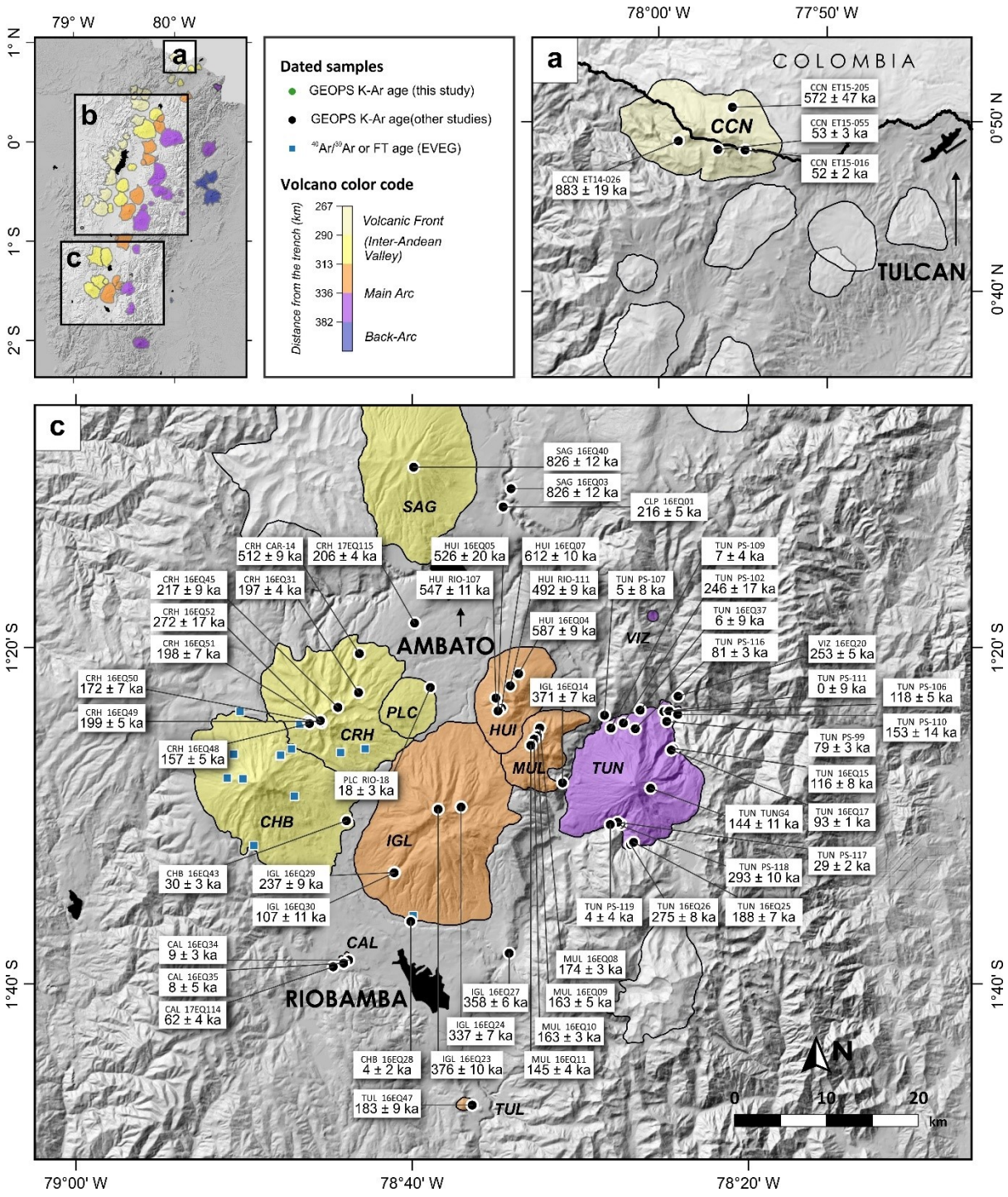

Figure 6.5. *(Caption provided in next page).*

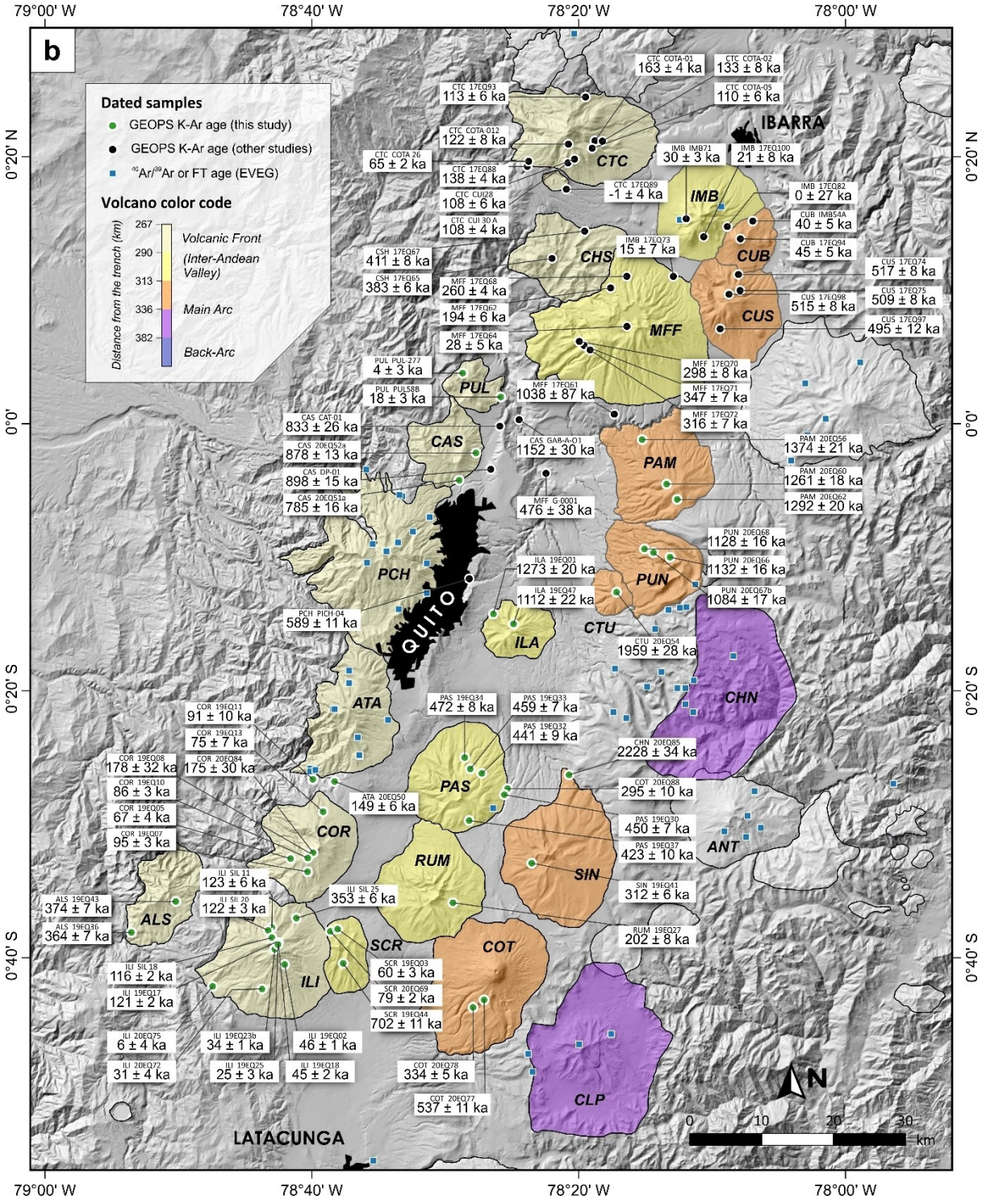

Figure 6.5. *Summary of the K-Ar ages acquired by the GEOPS laboratory. Samples from this study represented as green dots (Chapters 3, 4 and 5; Andrade et al., 2021), and from other studies as solid dots (Alvarado et al., 2014; Almeida et al., 2019; Telenchana, 2017; Bablon, 2018; Bablon et al., 2018, 2019, 2020a, 2020b). Sampled volcanoes are colored in function to their distance to the trench. Location of $^{40}Ar/^{39}Ar$ and obsidian Fission Track (FT) dated samples compiled in the EVEG database (Chapter 5) shown in blue squares. Abbreviations of volcano names as in Table 6.1.*

Based on the new ages, stratigraphic and morphological observations, it is now possible to describe the evolution of volcanism in the central segment. As noted in Chapter 5 and Figure 6.5b, the oldest edifices occur in the surroundings of the Guayllabamba basin, becoming younger towards the north and south of this area. A summary of the eruptive history of the studied volcanoes is presented below from north to south and in terms of their oldest ages.

6.3.1.1 Volcanism in the Guayllabamba valley

Located in the Estern Cordillera, the **Chacana caldera** (**CHN**; 4493 m asl.; Lat. 0°21'S; Long. 78°15'W) is the oldest dated volcanic landform in the central segment (Fig. 6.6). Although several $^{40}Ar/^{39}Ar$ ages were published (Opdyke et al., 2006), their age spectra showing perturbed patterns and the low precision of their corresponding isochron ages limit our knowledge of the timing of its activity. However, the best-defined ages revealed a low explosive volcanism (compared to the posterior caldera forming activity) which occurred at ~2.4 Ma. We obtained a K-Ar age of 2228 ± 34 ka for an andesitic lava sampled from the lowest exposed section of the Antisanilla valley sequence, located south of the Chacana caldera (Fig. 6.6). On the western outer flank of the present-day caldera, a new volcanic activity resulted in construction of the **Coturco volcano** (**CTU**; 3572 m asl.; Lat. 0°21'S; Long. 78°28'W). A summit lava was dated at 1959 ± 28 ka. The constructed edifice reached ~7.5 km in diameter, being a small-sized stratovolcano compared to the more recent surrounding edifices.

The eruptive history of Chacana continued with the caldera formation stage, where several series of lavas were emitted, and voluminous ignimbrite sequences were formed (Hall and Mothes, 2008c; Villares, 2010; Pilicita, 2013; Beate and Urquizo, 2015). The eastern outer flank sequences ((Fig. 6.7) were dated by obsidian fission tracks between 1350 ± 90 and 1580 ± 70 ka, whereas the uppermost sequence of obsidian flows was dated at 810 ± 50 ka (Bigazzi et al., 1997, 2005; Opdyke et al., 2006).

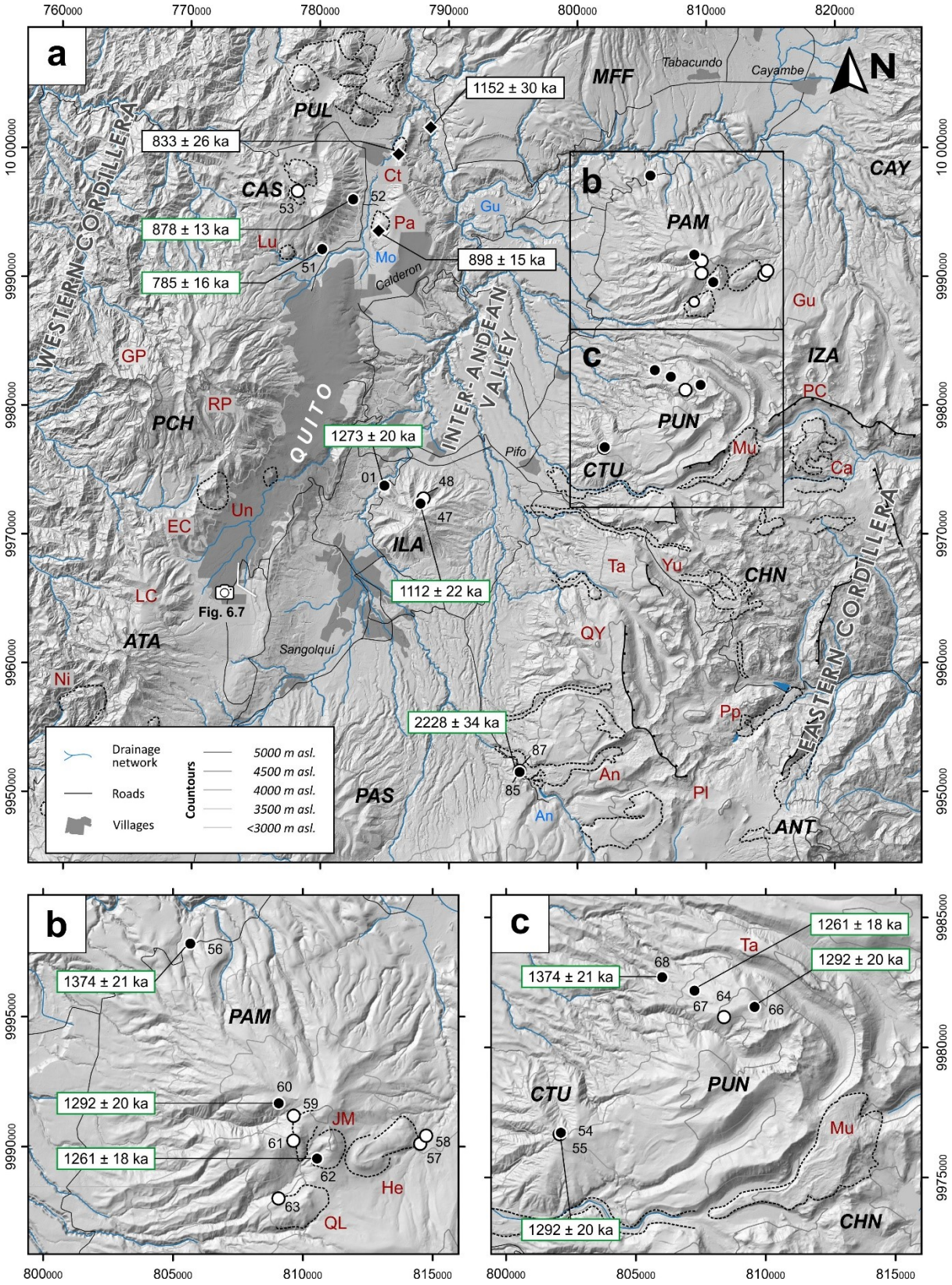

Figure 6.6. *(Caption provided in next page).*

Figure 6.6. *Hill-shaded digital surface model of the northern Guayllabamba basin showing the sampling locations and geochronological results. Numbers correspond to the last two digits of sample name (19EQxx or 20EQxx according to the recollection year). K-Ar dated samples are represented with solid symbols. K-Ar ages from Alvarado et al., (2014). Volcanoes shown as black letters as in Table 6.1. Volcanic landforms shown as red letters. An: Antisanilla; Ca: Callejones; Ct: Catequilla; EC: El Cinto; GP: Guagua Pichincha; Gu: Gualimburo; He: Herradura; JM: Jambi Machay; LC: La Carcacha; Mu: Mullumica; Ni: Ninahuilca; Pa: Pacpo; PC: Pucará Chico; Pl: Plaza de Armas series; Pp: Papallacta Flow; QL: Quito Loma; QY: Quiscatola-Yanaurcu series; RP: Rucu Pichincha; Ta: Tablones series; Yu: Yuyos flow. Rivers and valleys represented as blue letters. An: Antisanilla; Gu: Guayllabamba; Mo: Monjas.*

The subsequent resurgent activity of Chacana produced the uplift and arching of the caldera floor, as evidenced by the increase of the grainsize of the fluvial deposits accumulated inside the caldera depression (Hall and Mothes, 2008c; Villares, 2010; Pilicita, 2013). Several lava and obsidian flows were emitted during the Chacana resurgence stage. The oldest lava flows were dated as early as ~726 ka (Pilicita, 2013), while the most recent ones correspond to the historic Antisanilla (AD 1728) and Papallacta (AD 1773) lava flows (Fig. 6.6). Noteworthy are the Plinian eruptions related to the Mullumica and Callejones centers, which are recorded in two metric-size layers of pumice fallouts (Pifo layers) recognized in the Guayllabamba valley. Our attempts to date several pumice samples from the Pifo layers were unsuccessful due to their high atmospheric contamination. Several volumetric obsidian flows, dated between 180 and 200 ka (Bigazzi et al., 1992), were emitted from Mullumica and Callejones following these explosive eruptions (Fig. 6.6). We emphasize that the eruptive history of Chacana is more complex than described above, thus a detailed review of the cited references is strongly recommended for a complete understanding of Chacana caldera.

We obtained three K-Ar ages for **Pambamarca** volcano (**PAM**; 4078 m asl.; Lat. 0°08'S; Long. 78°21'W). This edifice is located on the outer northwestern flank of the Chacana caldera. Our results suggest that the main edifice of Pambamarca volcano is constituted by sucessions of andesitic lavas and monolithological breccias. An andesitic lava sampled at the base of the northern flank of Pabamarca yielded a K-Ar age of 1374 ± 21 ka, while a lava sampled in the summit area was dated at 1261 ± 18 ka (Fig. 6.6). The andesitic activity of Pambamarca was followed by the extrusion of several rhyolitic

domes in the summit area (Fig. 6.6b). For instance, the Jambimachay dome, developed close to the Quitoloma dome, was dated at 1261 ± 18 ka. The Jambimachay dome, close to the Quitoloma dome, gave a K-Ar age of 1292 ± 20 ka measured on plagioclase phenocrysts. This age from Jambimachay is consistent with the others acquired from the Pambamarca andesitic stage, so the existence of inherited argon biasing this result appears to not be a strong concern here. The most recent activity of Pambamarca corresponds to the extrusion of the Herradura dome *coulee* (Fig. 6.6b), formed by andesitic lavas rich in biotite, amphibole, and pyroxene. The location in the higher areas of Pambamarca and the limited glacial erosion suggest that this dome was extruded after the LGM. More precisely, the glaciers formed during the last cycle reached their maximum extensions at ~35 and ~28 ka, at altitudinal limits similar to the location of the Herradura dome, i.e., ~3750 m asl. Our attempts to date this dome were unsuccessful. Geochemical analyses revealed an unusual K_2O enrichment at low SiO_2 content, thus the Herradura lava is classified as a basaltic andesite belonging to the Shoshonitic series, which are rather common in back-arc volcanoes (e.g., Hoffer et al., 2008; Garrison et al., 2017). However, the composition field of Herradura is consistent with the Yuyos lava of the Chacana caldera (Fig. 6.6a; Chiaradia et al., 2014), Cono La Virgen from Cayambe (Samaniego et al., 2005), and the Cuyuja lavas from Antisana volcano (Hall et al., 2017b, 2017b), thus suggesting that the petrogenetic processes behind its origin may be more widespread than previously thought.

Immediately to the south, **Puntas** volcano (**PUN**; 4558 m asl.; Lat. 0°19'S; Long. 78°21'W) was constructed by a succession of andesitic lavas, whereas the summit area is dominated by voluminous sequences of monolithological breccias. We obtained three ages ranging between 1084 ± 17 and 1132 ± 16 ka for the western flank and summit area of Puntas volcano (Fig. 6.6c). The presence of a gently west-sloping *planèze* formed between Puntas and Pambamarca is a noticeable feature (Fig. 6.6a and 6.7). This volcanic landform corresponds to a thick ignimbrite deposit known as El Tablón, which remains undated. Morphologies containing similar sequences are observed to the south of Puntas. These ignimbrite deposits have been related to the Chacana caldera formation stage (Hall and Mothes, 2008c; Beate and Urquizo, 2015). Consequently, our ages for Puntas and Pambamarca define the older

age bound of the highly explosive episode that formed the El Tablón ignimbrite. Later, the Pleistocene glaciations carved deep and wide glacial valleys around the Puntas volcano (Fig. 6.6c).

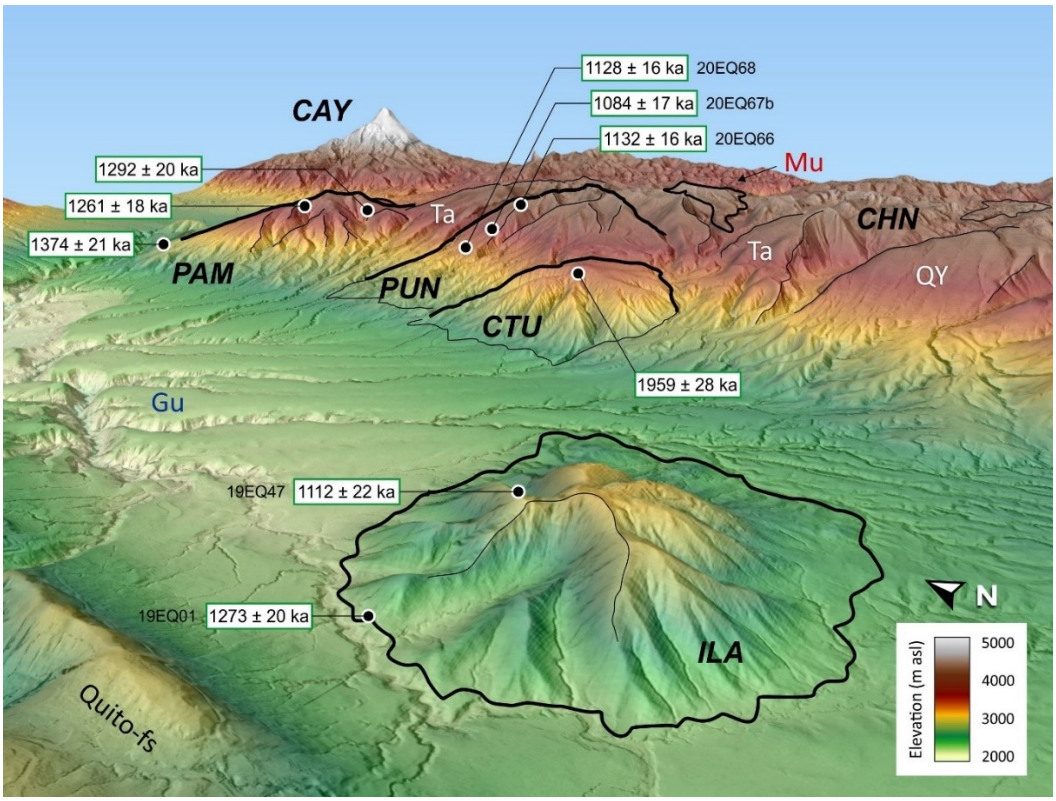

Figure 6.7. *3D model of the Guallabamba valley (Gu), looking northeast. The outer flank of the Chacana caldera (CHN), formed by the Quiscatola-Yanaurcu (QY) and Tablones (Ta) series, cover the edifices of Coturco (CTU), Puntas (PUN), and Pambamarca (PAM) volcanoes. Ilaló (ILA) is the only stratovolcano in the Inter-Andean valley. CAY: Cayambe; Mu: Mullumica lavas; Quito-fs: Quito fault system. Relative position of the model provided in Figure 6.6.*

Ilaló volcano (**ILA**; 3188 m asl.; Lat. 0°26'S; Long. 78°42'W) is located in the Inter-Andean Valley, to the west of the Puntas, Pambamarca and Chacana volcanoes (Fig. 6.7). This volcano was mainly formed by successions of massive andesitic lavas. We obtained two K-Ar groundmass ages corresponding to lava outcrops located at the northern base of the volcano, dated at 1273 ± 20 ka (19EQ47), and on its northern flank, dated at 1112 ± 18 ka (Fig. 6.6a). These results demonstrate that the eruptive activity of Ilaló was contemporaneous with that of the Pambamarca and Puntas volcanoes. A whole-rock K-Ar age at 1620 ± 160 ka was previously reported for Ilaló (Barberi et al., 1988). Although the corresponding study does not provide further information on the sampling site, it is

probable that the dated sample belongs to outcrop 19EQ47, which is located in an easily accessible position next to a highway that runs along the base of the western and northeastern flank of Ilaló (Mothes pers. comm.). We interpret the ages as due to the analysis of whole-rock, which often biases the obtained values towards too old ages as explained in Chapter 2 and elsewhere (Quidelleur et al., 1999, 2022). Although a sector collapse of the western flank was suggested to explain the depression located in this area (Fig. 6.7), we presume that this structure was rather formed by erosion given the presence of an E-W ridge that runs along the valley floor leading to the summit area and the lack of exposed debris avalanche deposits. This type of amphitheater-like depressions created by erosion have also been observed in nearby volcanoes such as Cusín volcano (Bablon et al., 2020a).

To the north of Ilaló, two andesitic lava flows were reported and dated in the Inter-Andean valley (Fig. 6.6). To the northeast, a lava flow located in the upper section of the Guayllabamba valley, interpreted as an eruptive activity ocurred prior to the Mojanda-Fuya Fuya volcanic complex (pre-Mojanda lavas; Bablon et al., 2020a) was dated at 1038 ± 87 ka. Conversely, a sequence of basaltic andesite lavas located at the bottom of the Guayllabamba valley to the northwest of Ilaló and west of pre-Mojanda, was dated at 1152 ± 30 ka (Pacheco, 2013). This flow was interpreted as part of the volcanic and volcanoclastic sequences of the **Pisque** Formation, but the emission source was not identified (Pacheco, 2013; Alvarado et al., 2014). The stratigraphic position of both lavas and their ages, together with the results from Pambamarca, Puntas, Chacana, and Coturco volcanoes, provide new temporal constrains for the sedimentary sequences of the Guayllabamba basin. Thus, in the light of these new ages, we strongly recommend to review the stratigraphy proposed by Villagomez (2003) and Pacheco (2013) for a complete understanding of the Guayllabamba basin sequences.

The activity of the **Pichincha** volcanic complex (**PCH**; 4776 m asl.; Lat. 0°17'S; Long. 78°60'W), located to the west of Ilaló on the margin between of the Western Cordillera and the Inter-Andean valley (Fig. 6.6), began with the construction of the *El Cinto edifice (EC)* dated by $^{40}Ar/^{39}Ar$ at 1112 ± 24 ka (Robin et al., 2010). Then, volcanic activity migrated 9 km to the north forming the mostly andesitic *Rucu Pichincha edifice (RP)* between ~850 and ~262 ka. The eruptive history of Rucu Pichincha includes a sector collapse of its western flank and its subsequent reconstruction. Further west,

the *Guagua Pichincha edifice (GP)*, mostly dacitic in composition, rests upon the western side of Rucu Pichincha (Robin et al., 2010). Its construction started as early as 52 ± 4 ka, and its most recent activity occurred between AD 1999 and 2001 (Robin et al., 2008b). This edifice was also affected by two sector collapses. South of the El Cinto edifice lies *La Carcacha volcano* (LC; 3880 m asl.; Lat. 0°19'S; Long. 78°36'W), an older edifice (~1290 ka; Hidalgo, 2006) of the **Atacazo-Ninahuilca** volcanic complex (**ATA**; 4455 m asl.; Lat. 0°36'S; Long. 78°62'W). The main Atacazo cone-building stages took place between ~190-220 and ~83-91 ka, followed by the extrusion of several satellite domes around ~71 ka (Hidalgo, 2006), and the Holocene high-explosive activity (VEI 4) of the *Ninahuilca dome complex* (Ni; Hidalgo et al., 2008). A block collected from an avalanche deposit located south of Atacazo (20EQ50 in Chapter 4, 17EQ59 in Bablon, 2018) yielded a K-Ar age of 149 ± 6 ka. The Sr and Th contents compared to LILE (e.g., Ba) and LREE (e.g., La) of this sample are consistent with those observed in Atacazo lavas instead of those of Corazón volcano (Chapter 4, Fig. C1), thus, suggesting a possible extension of the Lower Atacazo volcanic activity up to ~150 ka.

The volcanic activity continued to the north forming the **Casitagua** volcano (**CAS**; 3519 m asl.; Lat. 0°33'S; Long. 78°48'W). Casitagua was constructed by pyroclastic sequences and andesitic lava flows. Its summit area is truncated by a caldera-like depression filled by dacitic domes. We have dated two lavas outcropping on the eastern and southern flanks of Casitagua, obtaining two K-Ar ages of 785 ± 16 and 878 ± 13 ka, respectively (Fig. 6.6). A dacite sample collected from the southern inner flank of the caldera-like depression showed strong evidence for weathering during the thin section analysis and was discarded for K-Ar dating. Thus, this sequence could not be dated. Our ages are consistent with those previously acquired in the eastern border of the Monjas valley (Fig. 6.6). In detail, the *Catequilla* andesitic dome (Ct) was dated at 833 ± 26 ka, while the *Pacpo* dacitic dome (Pa) was dated at 898 ± 15 ka (Pacheco, 2013). The origin of the caldera-like depression remains uncertain. We did not find thick pyroclastic deposits suggesting the occurrence of a highly explosive event, such as the one that formed a similar caldera-like depression at **Pululahua** volcano (**PUL**; 3357 m asl.; Lat. 0°05'N; Long. 78°49'W) and generated a voluminous pumiceous PDC sequence (Andrade et al., 2021). Alternatively, we infer that the western flank of the Casitagua was affected by a sector collapse followed by the

extrusion of the intra-depression domes. Finally, the Casitagua andesite PDC deposits reported on the western border of the Mojas valley were tilted by the activity of the Quito fault system (Pacheco, 2013). Notably, the lacustrine sequences deposited over the this PDC series (San Miguel Formation), were also disturbed by this fault system (Villagomez, 2003; Pacheco, 2013).

6.3.1.2 The Machachi volcanic cluster

As previously described, the oldest volcanic activity (~2.4 to ~700 ka) of the Quaternary arc seems to be concentrated around the Guayllabamba valley, with Ilaló being the only stratovolcano located inside the Inter-Andean valley until the construction of the **Santa Cruz** volcano (**SCR**; 3978 m asl.; Lat. 0°39'S; Long. 78°38'W) farther south. Santa Cruz volcano is located in the inter-Andean valley, 30 km to the south of the Atacazo volcano (Fig. 6.8). As described in Chapter 4 and Section 6.2.1.1, the Santa Cruz activity was dated in this study to 702 ± 11 ka. Our data suggest a renewed activity ocurred between ~79-60 ka which formed the *Loma Saquigua dome* (Ls). After the intermediate eruptive stage in the Central Segment, volcanic activity increases significantly. A dozen new volcanoes developed to the south of the Guayllabamba basin, in an area 70 km wide (E-W) and 40 km long (N-S), forming the Machachi volcanic cluster. The term "volcanic cluster" refers to the high number of volcanoes constructed in a relatively small area and in a short period of time.

Cotopaxi volcano (**COT**; 5897 m asl.; Lat. 0°41'S; Long. 78°26'W) is located to the east of Santa Cruz, on the western edge on the Eastern Cordillera (Fig. 6.8). Its eruptive history started with an ancient rhyolite caldera (CT-I Barrancas stage), whose explosive and effusive deposits are preserved on Cotopaxi's present-day southern flank. Two fission track ages of 0.56 ± 0.04 and 0.54 ± 0.05 Ma have been reported from biotite-rich obsidians (Bigazzi et al., 1997). We have obtained a consistent and well-defined K-Ar age of 537 ± 11 ka for a voluminous obsidian flow outcropping at the base of the Morourco peak, 3.8 km to the south of the Cotopaxi present-day summit (Fig. 6.9). Unfortunately, the sampling site of the obsidians analyzed by Bigazzi et al. (1997) were not provided. However, the geochemical and petrographic similarities observed between our samples and those of Bigazzi et al.

(1997), including the occurrence of biotite and scarce quartz, suggest that we have successfully dated obsidian samples from the same sequence by applying two different techniques.

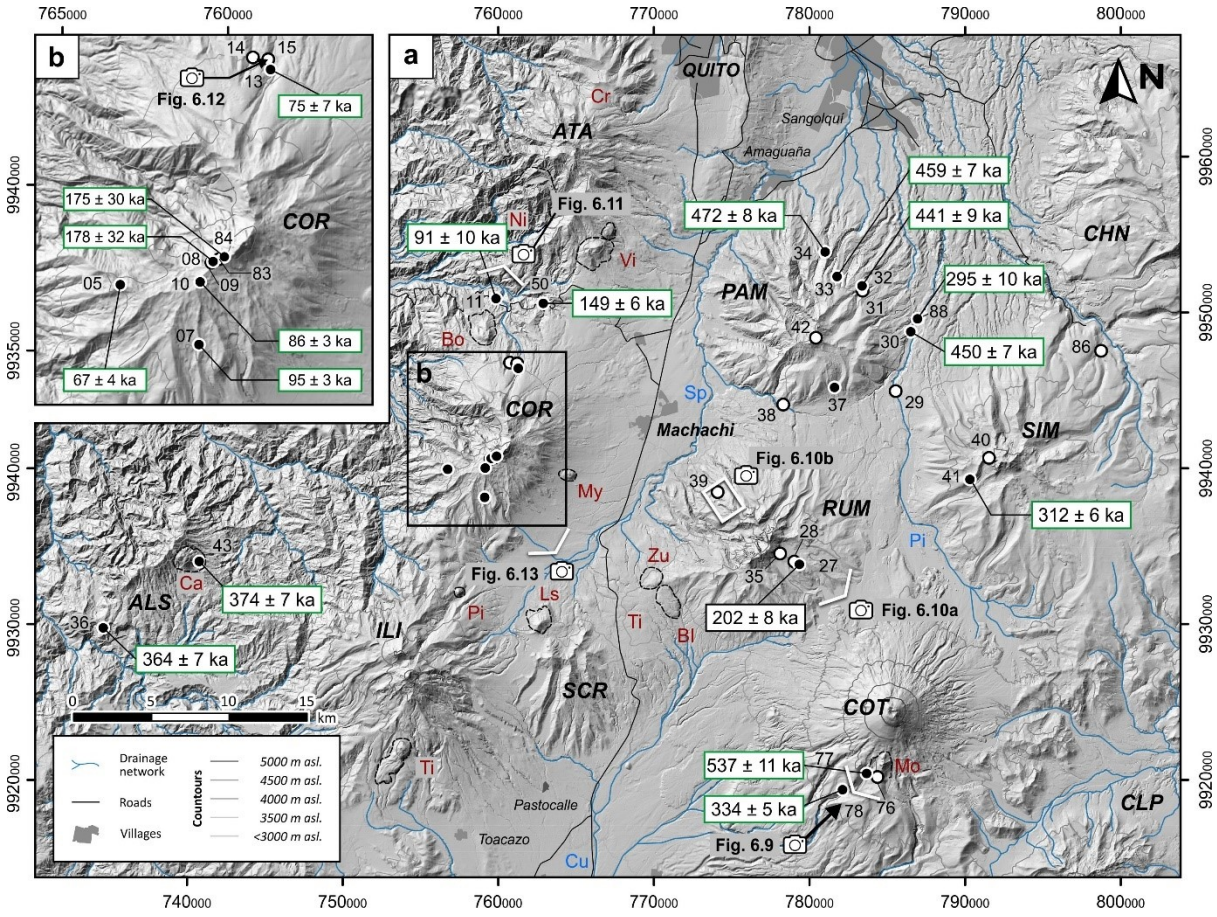

Figure 6.8. *Hill-shaded digital surface model of the Machachi volcanic cluster showing our sampling locations and geochronological results. Numbers correspond to the last two digits of sample name (19EQxx or 20EQxx according to the recollection year). K-Ar dated samples are represented with solid symbols. Volcanoes shown as black letters (see Table 6.1). Satellite domes and cones shown as red letters. Bl: Boliche; Bo: Bomboli; Ca: Cerro Azul; LC: La Carcacha; Ls: Loma Saquigua; Vi: La Viudita; Mo: Morurco; My: Moya; Ni: Ninahuilca; Ti: Tishigcuchi; Tp: Tiopullo; Pi: Pilongo; Zu: Zunfana. Rivers and valleys represented as blue letters. Cu: Cutuchi; Pi: Pita; Sp: San Pedro.*

The Cotopaxi-I caldera is overlain by a sequence of andesitic lavas and breccias associated with the Morurcu peak (CT-I Morurco stage), a remnant volcanic neck located at the southern Cotopaxi caldera rim. We obtained a K-Ar age of 334 ± 5 ka for an andesitic lava belonging to the uppermost sequence exposed in the Santa Barbara plain, 3 km south of Morurco peak (Fig. 6.9). In addition, a voluminous andesite lava, which flowed ~40 km northward in the Pita river valley was associated to

the CT-I Morurco stage (Hall and Mothes, 2008a). The ages of the rhyolite and andesite sequences are not well constrained. The Pita lava has been sampled at the Tanipamba locality, east of Pasochoa volcano, yielding a K-Ar age of 295 ± 10 ka, which is close to that obtained for the Santa Barbara plain andesite series. The most recent eruptive history of Cotopaxi was described in detail by Hall and Mothes (2008a). In summary, the Cotopaxi II-a stage was characterized by highly explosive eruptions that occurred at the beginning of the Holocene. Several Plinian eruptions generated volumetric ash flows and left thick layers of rhyolitic pumice fallouts in the region. These deposits are also known as the rhyolitic F-series of the Cotopaxi volcano, and are used in the area as stratigraphic markers. Subsequently, the magma composition changed from rhyolitic to andesitic showing relatively lower explosive eruptions. This activity was predominant during the Cotopaxi II-b stage, which formed the present-day volcanic cone (Fig. 6.9).

Figure 6.9. *View of the southern flank of the Cotopaxi volcano showing the deposits of the Barrancas, Morurco and Cotopaxi IIb stages. (*) The sampling site 20EQ78 shown corresponds to a lava flow outcropping at the same stratigraphic position. The real sampling site corresponds to an andesitic lava located 1.3 km south of the one shown in the picture.*

Pasochoa volcano (**PAS**; 4199 m asl.; Lat. 0°28'S; Long. 78°29'W) lies in the Inter-Andean valley, 25 km northwest of Cotopaxi volcano. The Pasochoa edifice is mainly formed by voluminous sequences of basaltic andesite lavas and monogenetic breccias. The long-term erosion has exposed several dyke systems in the summit area. Five K-Ar ages were acquired for this volcano, outlining a

mostly effusive eruptive history occurring between 472 ± 8 and 423 ± 10 ka (Fig. 6.8). A $^{40}Ar/^{39}Ar$, three steps only, plateau age of 1.33 ± 0.30 Ma was obtained for a lava flow on the eastern flank of Pasochoa (Opdyke et al., 2006). The corresponding isochron yielded a poorly-defined age of 1.93 ± 2.88 Ma with a $^{40}Ar/^{36}Ar$ initial ratio of 271 ± 116, suggesting a high contamination by atmosphere. We excluded this result based on the low quality of these data and on its paleomagnetic polarity. More precisely, the normal polarity reported by Opdyke et al. (2006) for this flow disagrees with the reverse paleomagnetic polarity of the Matuyama Chron (i.e., 0.77 to 2.58 Ma; Cohen and Gibbard, 2019), but rather indicates a Brunhes Chron age (i.e., <0.77 Ma; Cohen and Gibbard, 2019).

The **Rumiñahui** volcano (**RUM**; 4722 m asl.; Lat. 0°35'S; Long. 78°30'W) is located directly south of Pasochoa (Fig. 6.8). This volcano is formed by thick sequences of andesitic monolithological breccias and sparse lava flows (Starr, 1984). These series are well exposed in the summit area of Rumiñahui, where the high degree of erosion has also exposed the dike network of the central conduit of the edifice (Fig. 6.10). A series of comparatively less eroded lava flows were identified outcropping mainly on the eastern and western flanks of Rumiñahui. These andesitic lavas have a higher K_2O content compared to the basal andesitic series (Starr, 1984). Unfortunately, their high weathering state prevented us to obtain a groundmass or plagioclase K-Ar age for these lower andesitic series. However, we propose that emplacement of the older Rumiñahui volcano occurred as late as ~300 ka, as suggested by the necessary presence of a prominent edifice at the location of Rumiñahui volcano for channeling the Pita lava flows (295 ± 10 ka) northward from the Morurco cone (Cotopaxi-I volcano) to its terminal position east of Pasochoa volcano (Fig. 6.8). Moreover, the long duration erosion phase deduced from the widespread dike exposures in the summit area suggests that Rumiñahui may be even older than proposed. Furthermore, we obtained a K-Ar age at 207 ± 9 ka performed on plagioclase phenocrysts for a lava flow located on the western flank of Rumiñahui (Fig. 6.10). This lava belongs to the Late High-K andesitic series (Fig. 3; Chapter 4). In view of a possible bias caused by inherited argon, this lava may have been emitted even after the K-Ar age that we have obtained. Consequently, this age is considered as an older bound of the late High-K stage of the Rumiñahui volcano.

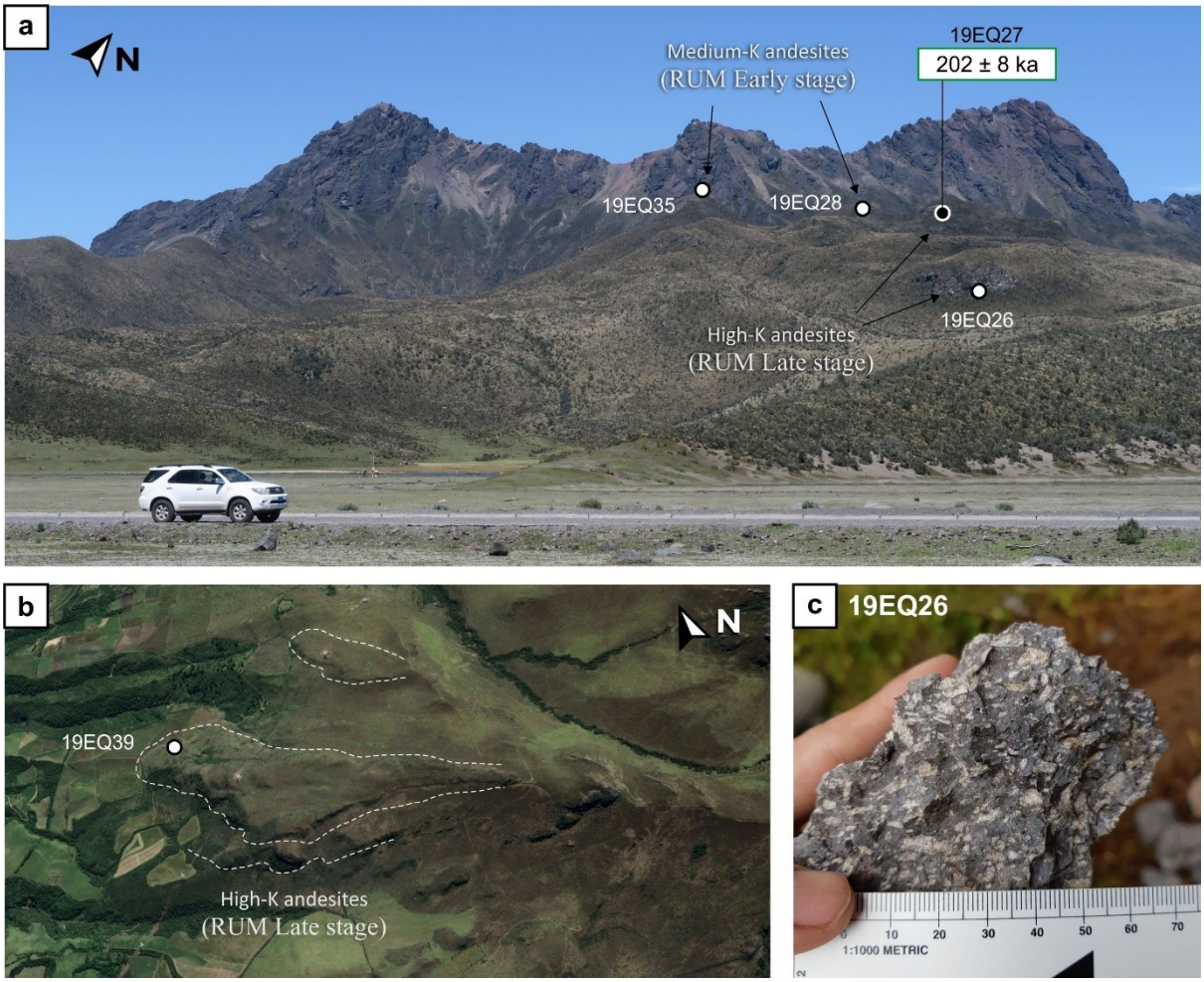

Figure 6.10. *Rumiñahui volcano.* ***a)*** *Photograph of the west flank of the volcano showing its advanced state of erosion and the location of samples collected from the high and medium K andesite series.* ***b)*** *Google satellite image of the west flank of Rumiñahui showing the low eroded morphology of the high-K andesitic lavas.* ***c)*** *Photograph of sample 19EQ26 showing the porphyritic texture exhibited by the high-K andesite lavas.*

Sincholagua volcano (**SIN**; 4873 m asl.; Lat. 0°32'S; Long. 78°22'W) is located to the east of Rumiñahui and Pasochoa volcanoes, on the western border of the Eastern Cordillera. Its edifice is mostly formed by successions of andesitic and dacitic lavas. The scarce lava exposures, its high weathering degree, and the few access routes prevented an adequate sampling of the Sincholagua volcano. However, a lava sampled on the western flank, near the summit area, yielded a K-Ar age of 312 ± 6 ka (Fig. 6.8). This value suggests the occurrence of an eruptive activity at Sincholagua contemporary to the Cotopaxi-I Morurco stage, and possibly to the Rumiñahui high-K late stage.

Volcanism in the Western Cordillera seems to have started with the activity of the **Almas Santas** volcano (**ALS**; 3786 m asl.; Lat. 0°35'S; Long. 78°51'W). Its main edifice is formed by voluminous andesitic lava sequences and scarce monolithologic breccias (Chemin, 2004). We sampled a thick lava flow showing metric-sized columnar jointing outcropping in the Tangan locality, situated at the base of the southern flank of Almas Santas. The resulting age was 374 ± 7 ka (Fig. 6.8). We also collected a sample from an outcrop located at the base of the *Cerro Azul satellite dome (Ca)*, yielding a consisted age of 364 ± 7 ka (Fig. 6.8). It should be noted that this sample corresponds to an andesitic lava of the lower Almas Santas series, rather than to the Cerro Azul dacitic activity. Other PDC deposits, dacitic to rhyolitic in composition, were reported on the southern flank of Almas Santas (Chemin, 2004). This activity represents the latter stage of Almas Santas volcano. Unfortunately, the rainforest cover and the high degree of weathering prevented the sampling of this late series. The eruptive history of Almas Santas volcano was concluded with the sector collapse of its northern flank (Chemin, 2004).

El Corazón (**COR**; 4784 m asl.; Lat. 0°32'S; Long. 78°40'W) is one of the youngest volcanoes of the Machachi volcanic cluster. This volcano is located to the west of the Pasochoa and Rumiñahui volcanoes, on the eastern border of the Western Cordillera. The andesitic composition of the volcanic products of Corazón shows no significant geochemical changes, thus its cone-building stages were only distinguished through stratigraphic relationships and geochronological data (Fig. 6.8). Our observations suggest that the Corazón volcano was formed in two main cone-building stages. The early Corazón stage corresponds to the series of lava flows and sparse monolotologic breccias which form the Corazón basal edifice. These sequences are better exposed in the present-day summit pyramid. This structure is formed by a succession of andesitic lavas, each a few meters thick. We obtained two consistent ages at 175 ± 30 and 178 ± 32 ka for these lavas. The relatively high uncertainty of these ages is due to a high atmospheric contamination present in the sampled lavas. At the northern base of Corazón volcano, a sample collected from the lower andesitic lava sequence of the Quitasol valley was dated by $^{40}Ar/^{39}Ar$ at 190 ± 10 ka (plateau age; M. Fornari pers. com.; Fig. 6.11). This result is consistent with our ages acquired from the summit lava sequence.

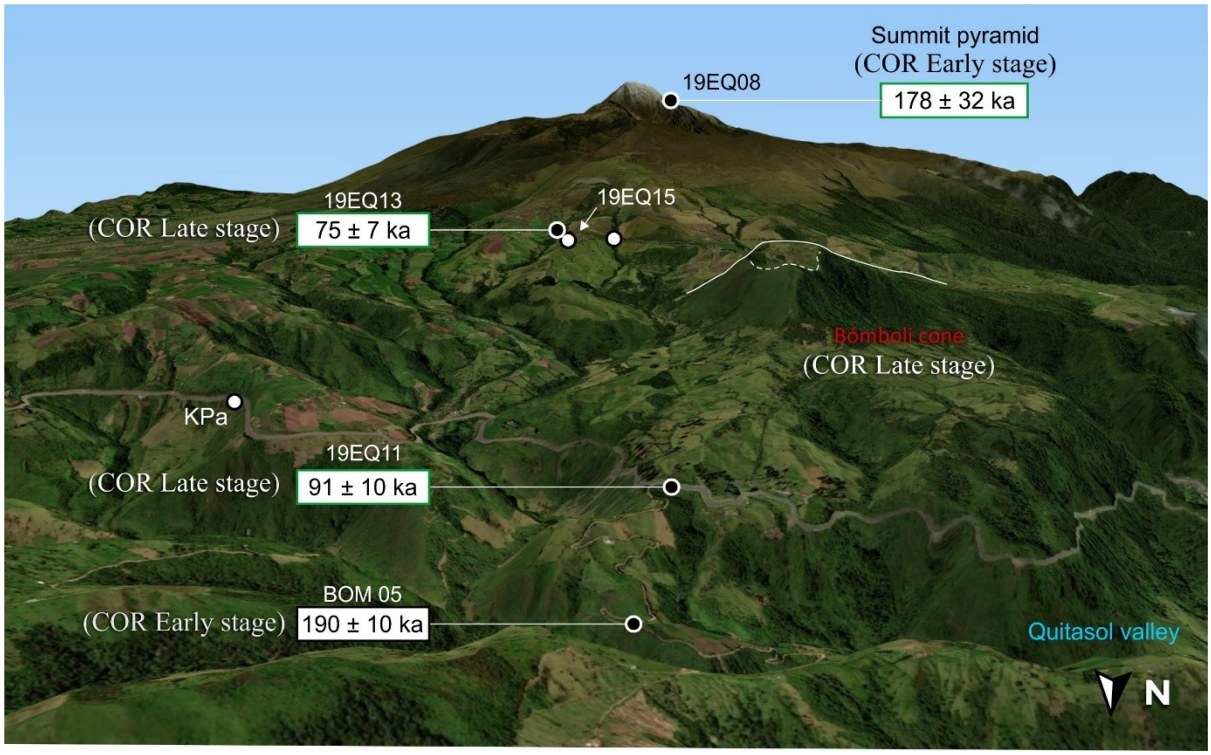

Figure 6.11. *3D model of the northern flank of Corazón volcano showing the location of the sampling sites and the ages obtained. The oldest ages are found towards the bottom of the Quitasol valley, as well as at the summit area. KPa: Outcrop of the Cretaceous Pallatanga unit.*

The Corazón basal edifice was overlain by sequences of monolithic breccias and thick lava flows belonging to the late Corazón stage. We collected multiple samples from outcrops located on the northern, southern, and southwestern flanks of Corazón, obtaining five K-Ar ages ranging from 67 ± 4 to 95 ± 3 ka (Fig. 6.8). A lava sampled at the base of the Cerro Bomboli satellite cone, which was dated at 91 ± 10 ka, deserves special mention. This lava flow is located on the northern flank of the Corazón volcano, stratigraphically above the sequence dated at 190 ± 10 ka by M. Fornari (Fig. 6.11). This result is consistent with our ages acquired from the summit lava sequence and supports the hypothesis of two cone-building stages at Corazón volcano. In addition, we identified a sequence of andesitic fallouts located on the northern flank of Corazón, to the south of the Cerro Bomboli cone (Fig. 6.12). The low erosion grade of this sequence, the lapilli grain size, and the low cover of recent deposits suggest that these andesitic fallouts were emitted from a nearby young source. Unfortunately, we were unable to obtain additional information regarding the source or age of this sequence. However, it is suspected that these tephras were emitted during a recent eruptive event of Cerro Bomboli cone. The eruptive history of Corazón volcano concluded with the sector collapse of its eastern flank.

Figure 6.12. *Tephra sequence found at sampling site 19EQ15 located to the south of the Bómboli satellite cone. See Figure 6.11 for relative location of the sampling site on the northern flank of Corazón volcano.*

We propose that the outcropping of older sequences in the Corazón summit area, instead of younger ones, could be explained by the intensive erosion experienced in this area (Fig. 6.13). In detail, during the construction of a volcanic edifice, the oldest erupted products are accumulated at the center of the edifice and are subsequently overlain by younger deposits forming the outer flanks. Episodes of high erosion, such as glacial cycles, remove the volcanic materials from the uppermost areas progressively exposing the edifice core formed by older sequences. The Corazón edifice has a conical shape whose summit is truncated near 4000 m asl. (Fig. 6.13) which roughly corresponds to the altitudinal limit of the LGM (e.g., Clapperton, 1986, 1990; Heine, 2000, 2011). Moreover, multiple glacial moraines up to tens of meters thick are found above this altitudinal limit. The glacial cirques converge in a single horn corresponding to the summit pyramid formed by ancient lava sequences.

Finally, **Iliniza** (**ILI**; 5248 m asl.; Lat. 0°40'S; Long. 78°43'W) was one of the last volcanoes to be formed in the Machachi volcanic cluster. As presented in detail in Chapter 3 and Section 6.2.1.2, Iliniza volcano is made up of two superimposed stratovolcanoes formed between ~124-116 ka and ~45-25 ka, respectively. The twin-peaked volcano is surrounded by the Pilongo (~353 ka) and Tishigcuchi (probably Holocene) domes. The Pongo lava flow (~6 ka) represents its most recent activity (Hidalgo et al., 2007; Santamaría et al., submitted).

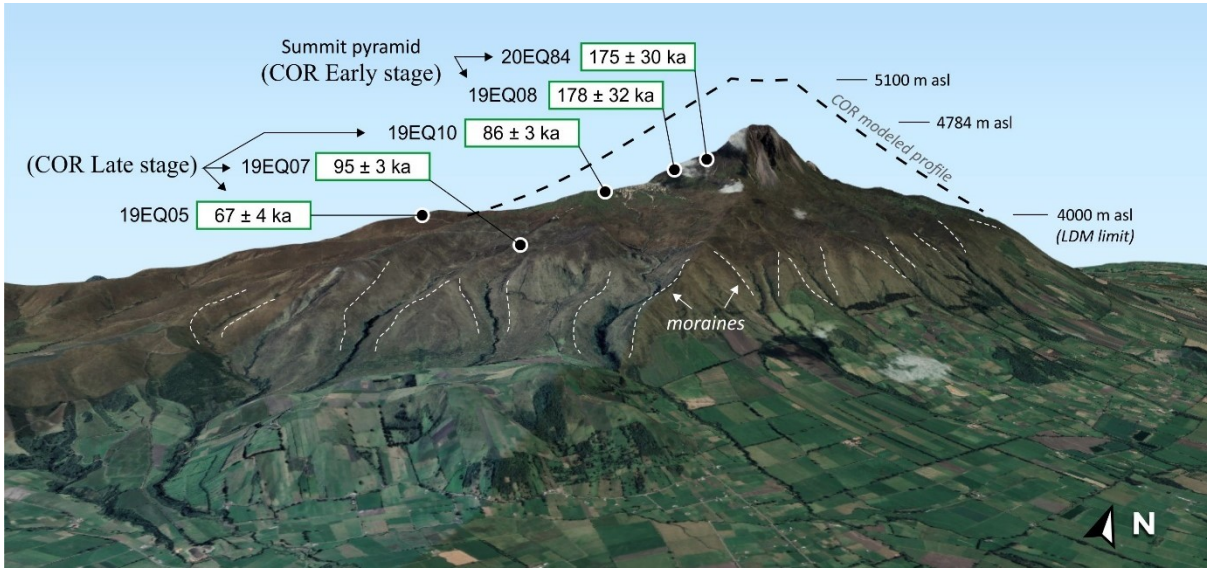

Figure 6.13. *3D model of the Corazón volcano looking northwest. Glacial erosion removed the volcanic material from the summit of the volcano, thus exposing the older sequences of the edifice core. Note the numerous moraines located around 4000 m asl.*

6.3.2 Volcanism at the Ecuadorian volcanic arc scale

6.3.2.1 Compilation of geochronological data

The extensive geochronological work carried out in the volcanic arc, including the GEOPS-IRD-IGEPN geochronological project for the last few years, provided more than 200 new radiometric ages ($^{40}Ar/^{39}Ar$, K-Ar, and Fission Track ages) acquired for more than 50 volcanoes of the Ecuadorian arc. In order to constrain the Pleistocene eruptive history of the Ecuadorian arc, we have updated the "Ecuadorian Volcanic Events and Geochronological database" (EVEG; Santamaría, 2017), by adding the most recent data while removing the low-quality ages (see Chapter 5).

The first questions that arise when reviewing the Quaternary Ecuadorian volcanism are how to distinguish one "volcano" from others, and how many volcanoes were identified. We followed the "volcano-as-eruptive-subsystem" definition of Szakács (2010), in which a volcano corresponds to the shallowest magma reservoir, all magma plumbing pathways, and the volcanic edifice at the surface. Although subsurface studies are desirable to distinguish the eruptive subsystem from others, we focused on the final landforms created which should be spatially distinguished from others. In this way, those eruptive subsystems that show spatial and/or temporal overlapping landforms were considered as single volcanoes. For instance, the Rucu Pichincha and Guagua Pichincha stratovolcanoes were considered as a single volcano (Pichincha volcanic complex; Robin et al., 2010) instead of two independent structures as in the catalog offered by Bernard and Andrade (2011).

Based on the preceding considerations, a thorough bibliographic review combined with new field works led to the identification of 77 individual volcanoes in the Ecuadorian arc (Chapter 1: Fig. 1.14). As detailed in Chapters 1 and 5, the distribution of volcanoes is not homogeneous. In fact, seven across-arc segments can be distinghished according to the number of volcanoes located in each area. The boundaries between each segment is defined by lines perpendicular to the N70°E axis formed by the Volcanic Front volcanoes. In agreement with the Andrade (2009) proposal, these segments were named according to the largest city located in each segment as shown in Figure 6.14.

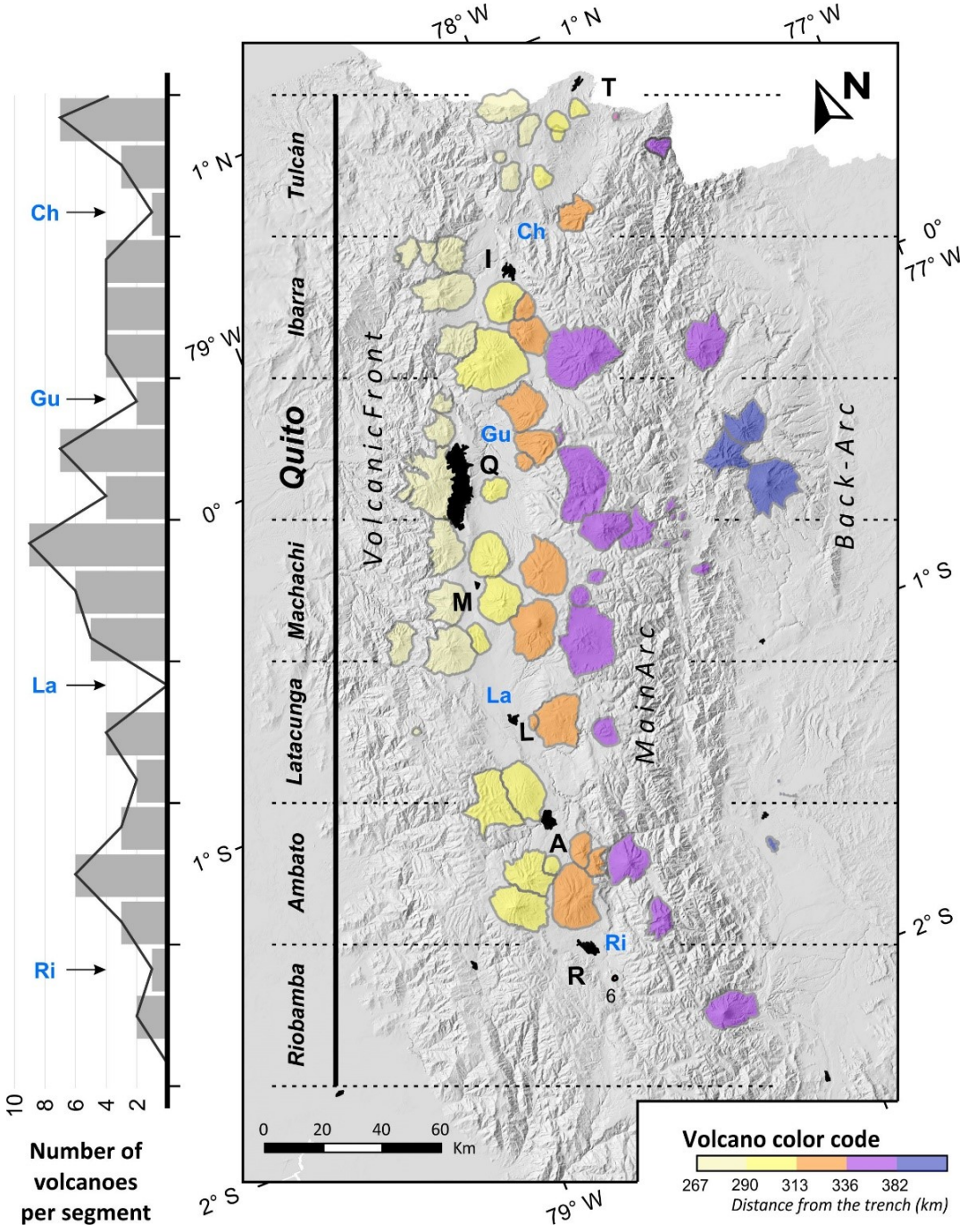

Figure 6.14. *Segmentation of the Ecuadorian volcanic arc. Ech section is named in function of the main city contained, which are represented in black letters. T: Tulcán, I: Ibarra; Q: Quito (Ecuador's capital city); M: Machachi; L: Latacunga; A: Ambato; R: Riobamba. Volcanoes' shapes taken from Bernard and Andrade (2011), and are colored according to their distance from the trench. Main basins represented as blue letters. Ch: Chota; Gu: Guayllabamba; La: Latacunga; Ri: Riobamba.*

6.3.2.2 Eruptive history of the Ecuadorian volcanic arc

The assemblage of geochronological data compiled in the EVEG database allowed us to summarize the cone-building stages of the volcanoes of the Ecuadorian arc, before constraining the eruptive history of the whole arc. Nevertheless, several volcanoes still have scarce geochronological information, especially those located in the Tulcán segment and the Sub-Andean zone (Back-arc). However, the available geochronological data suggest that the eruptive history of the Ecuadorian arc occurred in three stages, with an increasing number of active volcanoes through time, as follows.

Early stage: 2.5 to 1.4 Ma

It can be noted that sampling of the oldest units, and their consequent dating, remains scarce. Therefore, the eruptive history described during the Early Stage can only be considered as preliminary and subjected to revision as additional data is obtained in the future. However, the largest volcanic activity seems to be restricted to the central area of the arc, corresponding to the **Quito segment**. Here, intense volcanism occurred in the Eastern Cordillera forming the early volcanic sequences of Chacana (CHA) around ~2400 ka. The eruptive activity of Coturco volcano took place on the western flank of Chacana around 1954 ± 28 ka. Mostly effusive volcanic activity, with a comparative limited volume, was reported in the back-arc of the **Ambato segment**, 130 km to the south of Chacana caldera. In this area, several andesitic fissural lava flows were emitted near the present-day town of Puyo. Two lavas were dated by $^{40}Ar/^{39}Ar$ at 2670 ± 60 and 1920 ± 100 ka (Hoffer et al., 2008). The dense rainforest cover prevented detailed mapping of this area. Nevertheless, the Cacalurcu cones (CAC) were identified as the source of the oldest lava flow (Hoffer et al., 2008; Ball, 2015).

We note that two unreliable whole-rock K-Ar ages at 1850 ± 190 and 1850 ± 240 ka (Lavenu et al., 1995; Opdyke et al., 2006) were obtained from a sequence of basaltic andesite lavas north of Chinibano volcano (CNB; Eastern Cordillera). However, based on the erosional features and by comparison with other eroded volcanoes, we suggest that this volcano could have been constructed during the intermediate stage of the Ecuadorian arc.

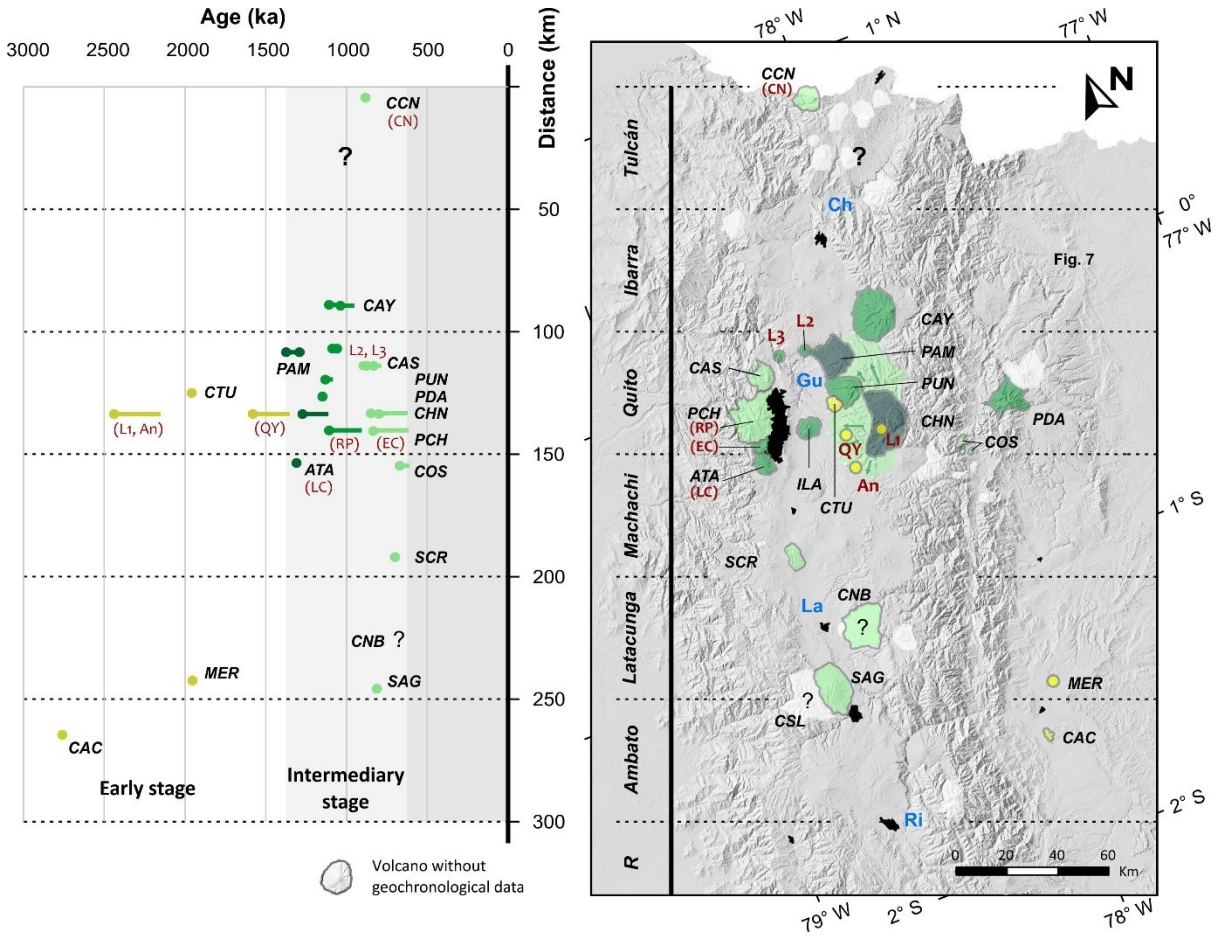

Figure 6.15. *Sketch of the Early (yellow) and Intermediary (green) stages of eruptive history of the Ecuadorian arc. The structures crated during the Intermediary stage colored by age: 1.4-1.2 Ma (dark green), 1.2-1.0 Ma (green), and 1.0-0.6 Ma (light green). The locations of the Pre-Chacana (L1), Mera (MER), Pre-Mojanda (L2), and Pisque (L3) eruptive centers are undefined, thus they are represented as oversized dots. Volcanoes shown as black letters according to Table 6.1. Landforms referred in the text shown as red letters. An: Antisanilla; EC: El Cinto; LC: La Carcacha; Ni: Ninahuilca; RP: Rucu Pichincha; QY: Quiscatola-Yanaurcu series. Valleys represented as blue letters. An: Antisanilla; Ch: Chota; Gu: Guayllabamba; La: Latacunga; Ri: Riobamba.*

Intermediate stage: 1.4 to 0.6 Ma

The volcanic activity increased during this stage in the **Quito segment** and extended to the adjacent Ibarra and Machachi segments. In the Western Cordillera, the Pambamarca and Puntas volcanoes were constructed to the northwest of Chacana between 1260-1370 and 1080-1130 ka (Section 6.3.1.1), respectively. Further north, the earliest activity of the Cayambe volcanic complex (CAY) was represented by the formation of the Viejo Cayambe andesitic edifice (CAY-VC), dated between 1108

± 11 and 1050 ± 5 ka (Samaniego et al., 2005). The eruptive history of Viejo Cayambe concluded with a large magnitude caldera-forming eruption (Samaniego et al., 2005). Southwards, the lowest lava flow sequences exposed on the western outer flank of Chacana, dated between 1350 ± 90 and 1580 ± 70 ka, seems to be roughly contemporaneous with the activity of Pambamarca volcano. Nevertheless, the ignimbrite deposits and obsidian flows forming the uppermost sequences, which also surrounds the Puntas and Pambamarca volcanoes, seems to be much younger as suggested by an obsidian flow dated at 810 ± 50 ka (Bigazzi et al., 2005). The southern Chacana volcanism was also dated at ~726 ka (Pilicita, 2013).

The Ilaló volcano developed between 1112 ± 22 and 1273 ± 20 ka in the Inter-Andean valley. It was followed by effusive eruptions that produced the Pisque (northwest of Ilaló) and pre-Mojanda (northeast of Ilaló) lavas at 1152 ± 30 ka and 1038 ± 87 ka, respectively (Pacheco, 2013; Alvarado et al., 2014; Bablon et al., 2020a). Towards the end of the Intermediate Stage, at 702 ± 11 ka, the Santa Cruz volcano developed 50 km to the south of Ilaló. The $^{40}Ar/^{39}Ar$ ages acquired from the Atacazo-Ninahuilca volcanic complex (Western Cordillera) place the activity of La Carcacha edifice (ATA-LC) at ~1300 ka (Hidalgo, 2006). North of La Carcacha, the earliest activity of the Pichincha volcano is represented by the El Cinto edifice (PCH-EC) dated at 1112 ± 24 ka (Robin et al., 2010). It was followed by the construction of the Rucu Pichincha edifice (PCH-RP) as early as ~850 ka (Robin et al., 2010). The earliest activity of the Pan de Azúcar volcano (Quito segment, sub-Andean zone) occurred at 1150 ± 10 ka (Hoffer, 2008). Several obsidian pebbles were identified in the Cosanga River 30 km southwest of Pan de Azúcar. Two fission-track ages suggest that some of these obsidians were produced from eruptions dated at 670 ± 6 and 290 ± 20 ka (Bellot-Gurlet et al., 2008).

Less extensive volcanic activity occurred on the western border of the Inter-Andean valley in the **Tulcan and Ambato segments**. A K-Ar age at ~880 ka places the volcanic activity of the Cerro Negro edifice during the Intermediate Stage (Telenchana, 2017; Bablon, 2018). This edifice belongs to the homonymous Chiles-Cerro Negro volcanic complex located 120 km north of Chacana. The Sagoatoa volcano is located at a similar distance to the south of Chacana. This edifice was active between 826 ± 12 and 799 ± 12 ka (Bablon et al., 2019).

Late stage: from 600 ka

During the Late Stage of the Ecuadorian volcanic arc, a striking increase in the number of active volcanoes can be observed in almost all segments with at least 50 volcanoes active during this period. Although nearly twenty volcanoes remain poorly studied (most of them from the Tulcán segment), we suspect that most of these volcanoes probably correspond to this stage of the arc or possibly to the intermediate stage. Geochronological data is available only for the Chiles-Cerro Negro volcanic complex (570 to 50 ka; Telenchana, 2017; Bablon, 2018) and the Holocene eruption of Soche volcano (9.6 ka; Beate, 1994). The detailed eruptive history of the Ibarra, Ambato and Riobamba segments were presented in detail by previous dedicated studies (Bablon et al., 2019, 2020a), whereas that of the Quito and Machachi segments are presented in Chapters 4 and 5, and summarized in Section 6.3.1. Corresponding references are provided in Section 6.1 as well as in the EVEG database.

As shown in Figure 6.16, most of the volcanic activity seems to extend through time from the Quito segment to the adjacent segments forming the volcanic clusters of Ibarra and Machachi. The Ibarra volcanic cluster is composed by the Mojanda-Fuya Fuya (600 to <28 ka), Cushnirrumi (~400 ka), Cayambe (Nevado Cayambe: 400 to 0 ka), Chachimbiro (400 to 5 ka), Cotacachi-Cuicocha (170 to 3 ka), Yanaurcu de Piñan (170 to 60 ka), Imbabura (<50 to <4 ka), and Cubilche (45 to ~30 ka) volcanoes, as well as the undated Pilavo and Parulo (younger than the LGM, i.e., ~20 ka) volcanoes. El Reventador volcano (350? to 0 ka), located in the Sub-Andean zone, also belongs to the Ibarra segment. Only the Pichincha (Rucu Pichicha: 850 to 150 ka; Guagua Pichincha: 50 to 0 ka) and Chacana (800 to 0 ka) volcanoes remained active in the Quito segment. Nevertheless, the northern Chacana series, also named as Izambi volcano, were dated at ~370 ka, whereas the Herradura Dome of Pambamaca volcano could have been formed after de LGM. The Sumaco volcano (250 to 0 ka) was constructed in the Sub-Andean zone whereas the Pululahua dome complex (18 to 2 ka) appeared in the Western Cordillera during or close to the Holocene.

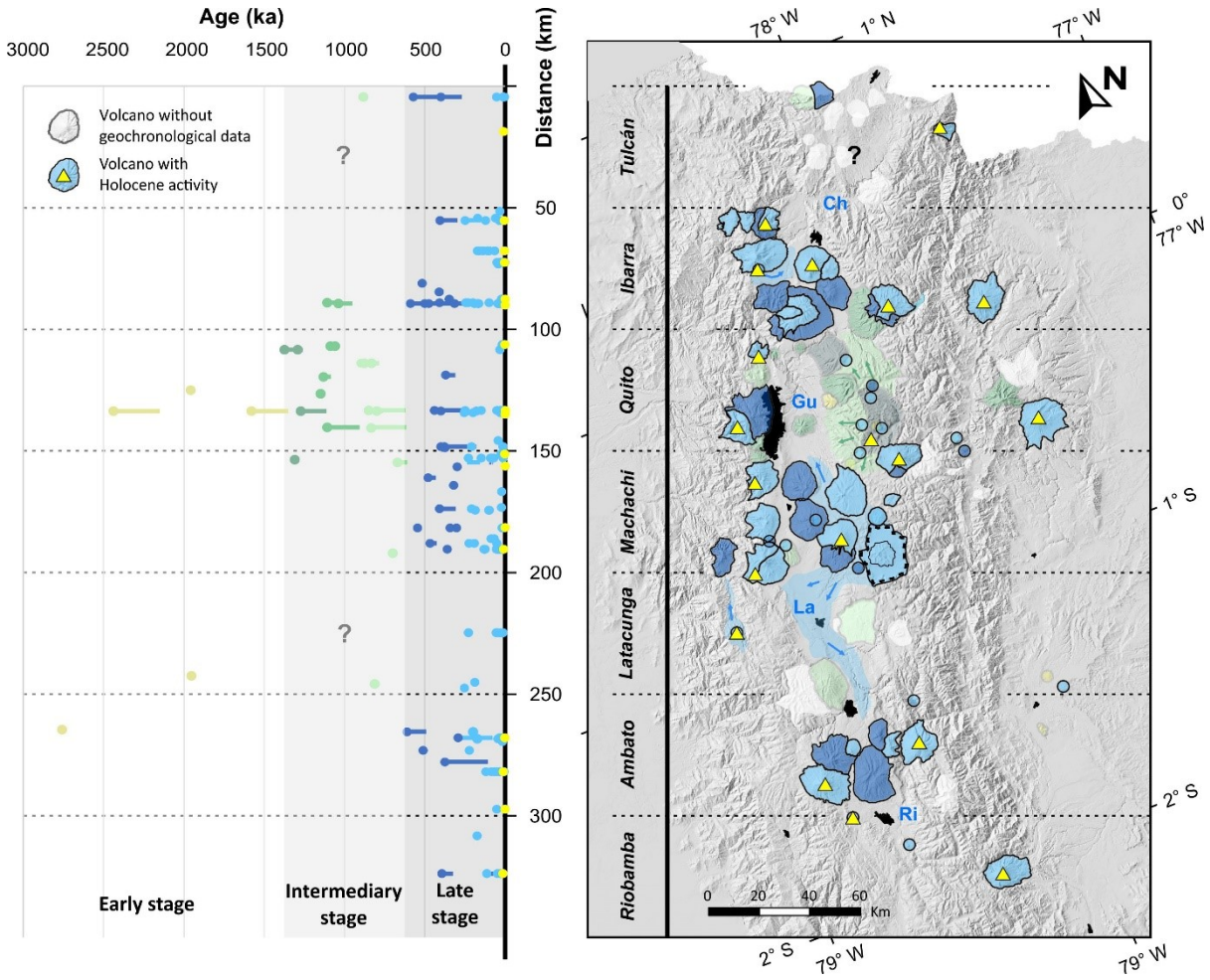

Figure 6.16. *Sketch of the Late (blue) stage of eruptive history of the Ecuadorian arc. Structures crated during this stage colored by age: 600-300 ka (dark blue) and <300 ka (light blue). Locations of small eruptive centers (<5 km in diameter) represented as oversized dots. Volcanoes with Holocene activity highlighted with yellow triangles. See Figure 1.14 for a detailed view of volcano names.*

The Machachi volcanic cluster is composed by the Cotopaxi (Barrancas stage: ~540 ka; Morurco stage: 340 to 300 ka; Cotopaxi-II stage: 12 to 0 ka), Chalupas-Quilindaña (pre-caldera lavas: 460 to 420 ka; Chalupas ignimbrite: 216 ka; Quilindaña edifice: 190 to >44 ka), Antisana (400 to 0 ka), Rumiñahui (>400 to ~200 ka), Pasochoa (470 to 420 ka), Iliniza (Pilongo dome: ~350 ka; North Iliniza: ~120 ka; South Iliniza: 45 to 6 ka), Sincholagua (~310 ka), Almas Santas (~370 ka), Atacazo-Ninahuica (230 to 2 ka), Corazón (190 to 90 ka), Santa Cruz (Loma Saquigua: 80 to 60 ka), Huañuna (10 ka) and Chaupiloma volcanoes, as well as the volcanoes related to the Aliso rhyolitic complex (290 to 3 ka) located at the border of the Eastern Cordillera. Sparse volcanism occurred in the Latacunga segment.

The Quilotoa caldera (0.8 ka) is the only volcano of the Western Cordillera in this segment. No ages are reported for the eroded Putzalagua dome, located on the eastern border of the Inter-Andean valley. Further east, multiple fissure eruptions formed the youngest stage of Chinibano volcano (Fig. 6.17). The lack of glacial erosion suggests that this activity probably occurred after the LGM.

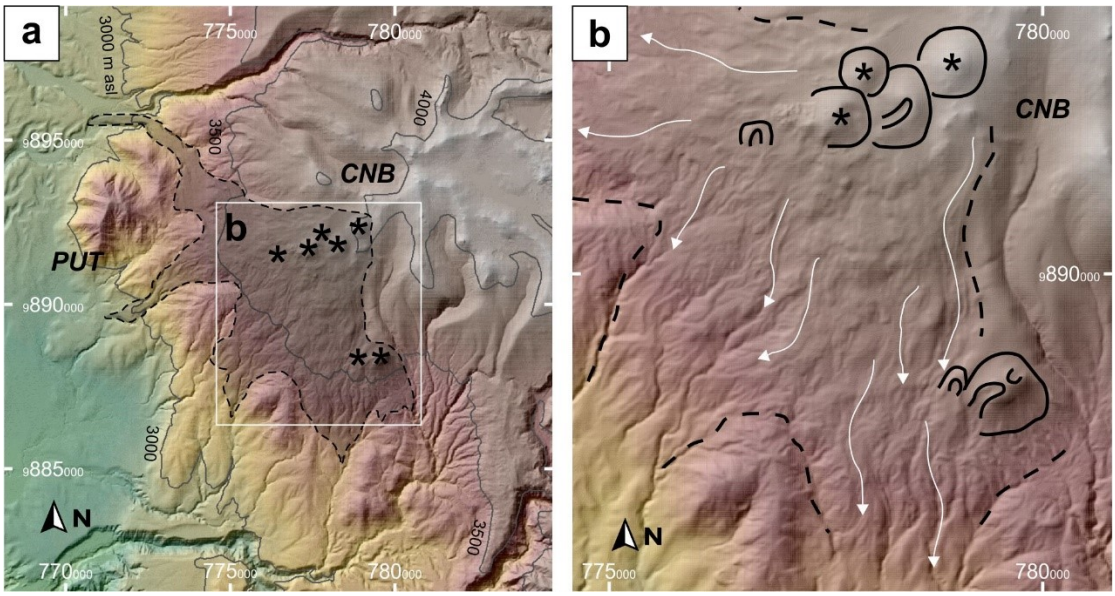

Figure 6.17. *Hill-shaded digital surface model of the southwestern flank of Chinibano volcano (CNB) showing the morphologies related to its young fissure lavas (shaded area enclosed by dashed lines). Scoria cones represented as asterisks in panel* ***a****, and with bold lines in panel* ***b****.*

Numerous volcanic edifices were formed to the south of the Latacunga basin forming the Ambato volcanic cluster. Huisla (610 to 490 ka), Igualata (370 to 110 ka), Tungurahua (290 to 0 ka), Carihuairazo (Tzunantza dome: 510 ka; Carihuairazo edifice: 270 to 160 ka), Vizcaya (250 ka), Mulmul (175 to 145 ka), Chimborazo (120 to 1 ka), and Puñalica (18 ka) volcanoes belong to the Ambato cluster, which also includes the Tulabug (Licto; 180 ka) and Calpi (60 and 9 ka) cones located in the Riobamba segment. The undated Altar volcano lies 20 km to the south of Tungurahua volcano, in the Eastern Cordillera. Fissure eruptions formed the Puyo cones (190 ka) in the Sub-Andean zone, 55 km to the east of Tungurahua. Sangay volcano (380 to 0 ka), located in the Western Cordillera 60 km to the south of Tungurahua volcano, is the southernmost volcano of the Ecuadorian arc.

Of the 77 Quaternary volcanoes identified in the Ecuadorian arc, 25 experienced eruptive activity during the Holocene. These volcanoes are listed in the Section 5.3.3 of Chapter 5.

6.4 Relationship between volcanism and tectonics

The eruptive history of the whole volcanic arc reveals that the spatial distribution of volcanoes through time is relatively heterogeneous across the arc. No patterns of migration from east to west or vice versa are noted. However, volcanic activity spread from the center of the arc to the north and south forming several volcanic clusters during the last 600 ka. Although the construction of the new volcanoes appears as relatively random in space and time, especially during the Late-Stage, the new edifices were emplaced over inherited crustal structures (Litherland and Aspden, 1992). For instance, the Volcanic Front forms a N-S corridor coincident with the Pujilí suture. This ancient structure separates the Cretaceous basaltic and ophiolite rocks (e.g., San Juan, Pallatanga, and Pilatón Formations) from the Eocene volcanic units (e.g., Macuchi Formation) in the Western Cordillera (Hughes and Bermúdez, 1997; Hughes and Pilatasig, 2002; Vallejo et al., 2019). Chapter 5 provides further detailed information on other volcanic alignments and their relationship to the inherited tectonic structures of the crust.

Although several active fault systems (fs) have been identified in the Ecuadorian Andes (Fig. 6.18; Egüez et al., 2003; Fiorini and Tibaldi, 2012; Alvarado et al., 2016), few volcanic landforms can be linked to the displacement and spatial distribution of the Quaternary fault systems (Andrade, 2009). Surprisingly, only a few volcanoes are found near or over the CCPP-fs (Fig. 6.18), the major tectonic structure in Ecuador connecting several transpresive and reverse subsystems from the Gulf of Guayaquil to the eastern border of the Eastern Cordillera (Alvarado et al., 2016). As discussed in Chapters 4 and 5, the limited correlation between the Quaternary fault system arrangement and the distribution of volcanism, suggests that the basement inherited structures played a predominant role in the magma ascension and distribution of the volcanic edifices, while active tectonics controlled second-order morphological features.

We also notice that the oldest volcanic areas from the Quito and Ambato (back-arc) segments are located over key slab structures, i.e., the projection of the Carnegie ridge onto the young Nazca crust (Gutscher et al., 1999), and the suggested flexure of the slab (Yepes et al., 2016), respectively. We speculate that the thermal regime of the young Nazca crust and the Carnegie Ridge favored magma

generation since the Early Pleistocene in Quito segment. This hypothesis is supported by the large variation in the magma geochemical compositions observed for the central zone of the arc (Ibarra, Quito and Machachi segments) as were described in Chapters 1 and 5. For instance, large variations in the fluid-mobile to fluid-immobile ratios (e.g., Ba/Th), the strong Y and HREE depletions observed in some young lavas, as well as variations in Pb-Sr-Nb isotopic compositions, can be linked to the subduction of these slab structures, as previously suggested (e.g., Gutscher et al., 1999; Garrison et al., 2006; Ancellin et al., 2017a; Narvaez et al., 2018; Bellver-Baca et al., 2020; Chiaradia et al., 2021)

The above described eruptive history of the Ecuadorian Arc supports the proposal of Bablon et al. (2019), where the apparent southward and northward extension of volcanism was probably influenced by changes in the slab geometry independent of the Grijalva FZ displacement. Unfortunately, the changes in the magma generation and transport zones that drove the increase in volcanism at 600 ka is not yet identified. We speculate that they may be related to variations in the crustal stress field and/or variations in slab geometry somewhat unrelated to its displacement (e.g., Royden and Husson, 2006; Billen and Hirth, 2007). On the other hand, the timing of the increase in the volcanic activity seems to coincide with other regional tectonic events, such as: (1) the cessation of the Late Pliocene WNW–ESE compressional phase registered in the Chota basin (Barragán et al., 1996; Winkler et al., 2005); (2) the formation the Quito-Latacunga microblock resulting from the eastward transferring of deformation zone related to the North Andean Sliver (Alvarado et al., 2016); and (3) the Late Pleistocene increase of the subsidence and deposition rates observed in the Gulf of Guayaquil which was interpreted an increased motion of the North Andean Sliver (Witt et al., 2006; Witt and Bourgois, 2010; Loayza et al., 2013). This readjustment in the upper crust dynamics during the Pleistocene may reflect changes in slab geometry, as well as changes in the depth, residence time, and ascent rate of magmas in the crust. Thus, this could explain the random occurrence of volcanoes through time in the Ecuadorian arc. Nonetheless, a further analysis of the temporal relationship between these tectonic events and the whole arc volcanism should be discussed in a focused survey.

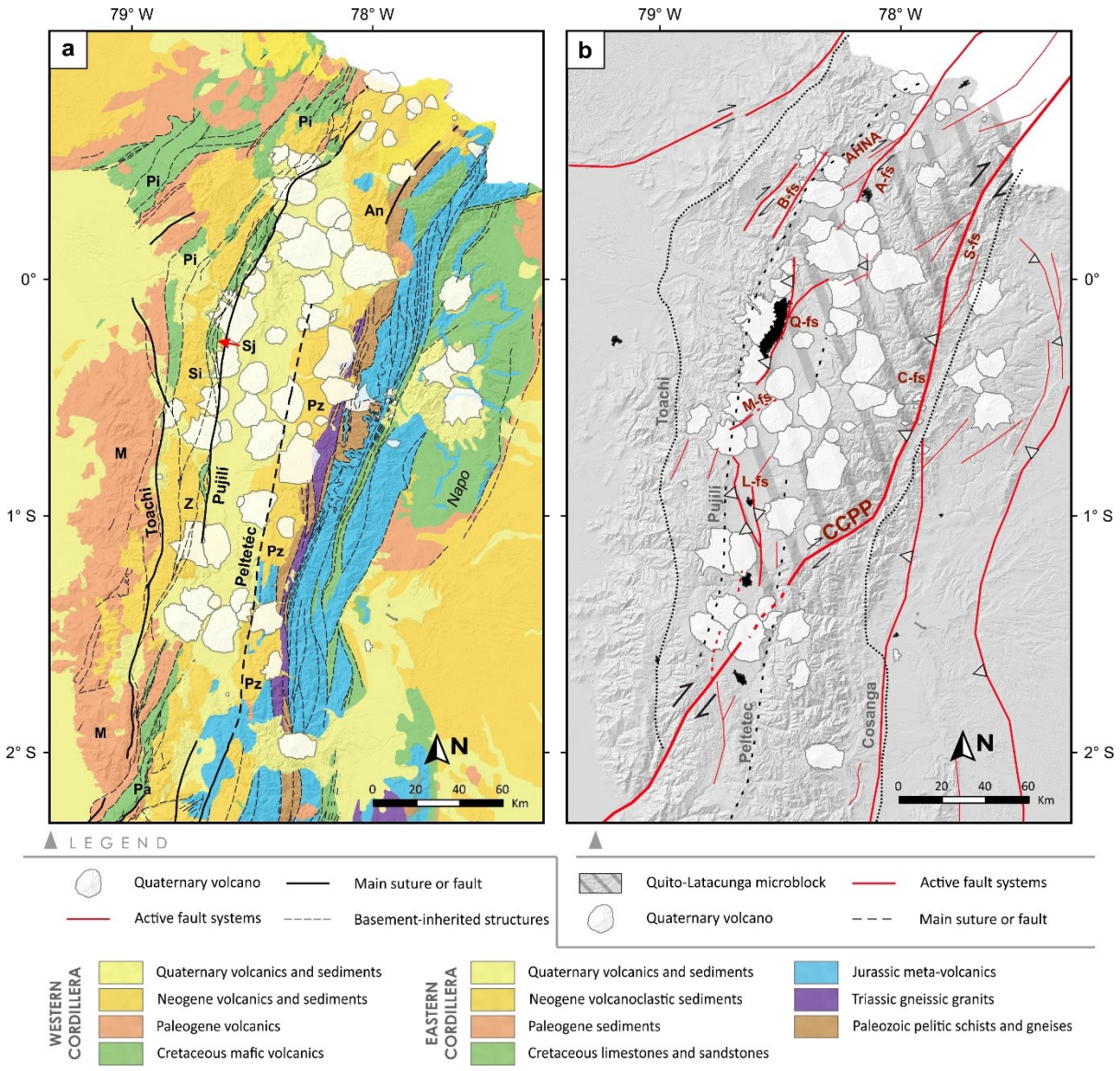

Figure 6.18. a) *Synthetic geological map of the central and northern Ecuadorian Andes showing the basement-inherited structures beneath the volcanic arc (Modified from Hughes and Bermúdez, 1997; Litherland et al., 1994; Egüez et al., 2017; Vallejo et al., 2019). Geological units represented as black letters. An: Angochagua; M: Macuchi; Pa: Pallatanga; Pi: Pilatón; Pz: Pizayambo; Si: Silante; Sj: San Juan; Z: Zumbahua.* ***b)*** *Tectonic map of the same area describing the active faults as red lines. A-fs: Ambi; B-fs: Billecocha; C-fs: Cosanga; L-fs: Latacunga; M: Machachi; Q-fs: Quito; and S-fs: Salado fault systems as red letters.*

Chapter 7

Research group ascending the Iliniza volcano. The photograph offers a view of the Machachi valley. From left to right: Corazón, Pasochoa, and Rumiñahui volcanoes. The Pilongo dome appears near the left edge of the picture.

Chapter 7

Conclusions and perspectives

This work has provided the first radiometric ages for several volcanoes in the central segment of the Ecuadorian arc and supplied better defined ages for volcanoes with scarce geochronological data constraining their oldest cone-building stages (e.g., Hall and Mothes, 2008a; Pacheco, 2013). Coupled with new field work, our ages allowed us to reconstruct the eruptive history of this region. Moreover, using these data combined with observations from previous contributions (e.g., Hidalgo, 2006; Robin et al., 2010; Samaniego et al., 2012; Alvarado et al., 2014; Bablon et al., 2019, 2020a), we have been able to describe the eruptive history of the whole volcanic arc for the first time.

The first part of the present PhD work consisted in a detailed study of Iliniza, a twin-peaked compound volcano located 50 km south of the capital city of Ecuador, Quito, and the nearby Santa Cruz volcano for comparison purposes. We have acquired 14 groundmass K-Ar ages from these volcanoes which, coupled with new field work and previous findings by Hidalgo (2001, 2002) and Hidalgo et al. (2007), allowed us to constrain the development of Iliniza volcano over time. Unlike previously proposed, the oldest volcanic activity, dated at 702 ± 11 ka, has been identified for Santa Cruz volcano. After a long quiescent period, its activity resumed at 79 ± 2 ka and 60 ± 3 ka forming the small-volume Loma Saquigua dome. The early activity of Iliniza corresponds to the extrusion of the rhyodacitic Pilongo dome at 353 ± 6 ka. The twin-peaked shape of the Iliniza volcano was due to the construction of two superimposed edifices built in several stages. The North Iliniza edifice was mainly formed by andesitic lavas and monolithological breccias dated between 116 ± 2 and 123 ± 6 ka. The eruptive history of this older edifice included the formation of the Huayrapungo satellite peak at 121 ± 2 ka. After a period of apparent quiescence, the eruptive activity resumed 1.7 km to the southwest forming

the South Iliniza edifice over the remnants of the North Iliniza edifice. The uppermost dacitic lavas of the South Iliniza basal edifice were dated at 46 ± 1 and 45 ± 2 ka. Our results suggest the occurrence of a highly explosive phase which destroyed the summit of this basal edifice and formed a volumetric dacitic pyroclastic succession at its base. The estimated minimum bulk volume of the Jatuncama ignimbrite deposits is 2.1 km^3, corresponding to a VEI 5 eruption. The subsequent eruptive activity rebuilt the South Iliniza edifice with the emplacement of a summit dome complex, dated at 34 ± 1 ka.

Unlike other volcanoes of the Volcanic Front, the latest eruptive activity of the South Iliniza edifice included the emission of multiple andesitic lava flows dated between 31 ± 4 and 25 ± 3 ka. The most recent eruptive history of Iliniza volcano included the extrusion of the Tishigcuchi satellite dome and the emission of the Pongo lava flow probably from a satellite vent. Both structures are located at the base of the southern flank of Iliniza volcano. We obtained a Holocene K-Ar age of 6 ± 4 ka for the Pongo lava. Based on these lines of geological and geochronological evidence, we support the hypothesis that the Iliniza volcano must be considered as a potentially active volcanic center. We acknowledge that these ages are at the edge of the K-Ar dating method. Therefore, we strongly suggest that further detailed research on the recent eruptive history of Iliniza should use, when possible, complementary geochronological methods especially suited to this age range, such as radiocarbon dating.

Our results provide a good overview of the behavior of the Iliniza volcano through time and support the hypothesis that it must be considered as a potentially active volcano. Accordingly, further detailed studies are required to improve the volcanic hazard assessment of Iliniza volcano. For instance, additional detailed studies on the stratigraphy of the Jatuncama ignimbrite deposits, including radiocarbon dating, could help to understand the eruptive dynamics associated with this unit. Furthermore, the detailed description and extension of the terminal andesitic units of the South Iliniza edifice deserve particular attention. Given that these units were formed during the most recent stages of Iliniza, the knowledge of the eruptive dynamics associated with their formation is important to better to define the future eruptive scenarios in case of a potential reactivation of Iliniza volcano.

The second part of this PhD study has a more regional scope. Thirty new K-Ar dates allowed us to describe the eruptive history of the central area of the volcanic arc, from latitudes 0.1° N to 0.7° S. Our sampling focused on the volcanoes of the Guayllabamba basin, located in the Inter-Andean valley. Based on our findings, we have updated the geochronological database presented by Santamaria (2017) in order to acquire a complete overview of the development of the Quaternary volcanism in the Ecuadorian Andes. At least 77 Quaternary volcanoes compose the Ecuadorian arc formed in three main stages with an overall marked increase in the number of active volcanoes. Our data suggest that the oldest documented volcanic activity was concentrated primarily around the Guayllabamba basin. More specifically, this early stage of volcanism involved the activity of Chacana volcano, dated here at 2228 ± 34 ka and at ~2400 ka by Opdyke et al. (2006), and Coturco volcano, dated here at 1959 ± 28 ka. Furthermore, various fissure eruptions occurred several kilometers south of Guayllabamba, in the back-arc of the present-day southern termination of the arc. This volcanism was dated between 2670 ± 60 and 1920 ± 100 ka (Hoffer et al., 2008). Considering that the sampling, and subsequent dating, of the oldest volcanic sequences of the arc was not exhaustive, we cannot reject the hypothesis of the occurrence of volcanism in other areas of the arc during the early stage. We observed that the Miocene-Pliocene volcanic sequences of the Eastern Cordillera (i.e., Pisayambo and Angochahua Formations) for instance, are not properly mapped or dated, and therefore, they may contain unidentified Pleistocene volcanic units as suggested by our results. Therefore, we recommend carrying out further cartographic and geochronological studies of these units.

Subsequently, during the intermediate stage (~1400 to 600 ka), several volcanic edifices were constructed mainly around the Guayllabamba basin. Our ages suggest that the Pambamarca (1374 ± 21 to 1261 ± 18 ka), Ilaló (1273 ± 20 to 1112 ± 18 ka), Puntas (1132 ± 16 to 1084 ± 17 ka), and Casitagua (878 ± 13 to 785 ± 16 ka) volcanoes were active during this stage, together with Santa Cruz volcano (702 ± 11 ka). These volcanoes complement the previously dated Chacana (1350 ± 90 to 1580 ± 70 ka, and ~810-726 ka; Bigazzi et al., 1997, 2005; Opdyke et al., 2006; Pilicita, 2013), Atacazo-Ninahuilca (La Carcacha: ~1300 ka; Hidalgo, 2006), Pichincha (El Cinto: 1112 to 910 ka; Rucu Pichincha: ~850 to ~150 ka; Robin et al., 2010), and Cayambe (Viejo Cayambe: ~1100 to 1050 ka; Samaniego et al.,

2005) volcanoes. This increase in activity also includes two lava flows north of the Guayllabamba basin dated at 1152 ± 30 ka and 1038 ± 87 ka (Pacheco, 2013; Alvarado et al., 2014; Bablon et al., 2020a). Several kilometers to the north, the early activity of the Cerro Negro edifice (Chiles-Cerro Negro volcanic complex) occurred at ~880 ka (Telenchana, 2017; Bablon, 2018). Meanwhile, the Sagoatoa volcano show evidences for activity between 826 ± 12 and 799 ± 12 ka, several km to the south of Guayllabamba (Bablon et al., 2019). Scarce information is available for back-arc volcanism. One age at 1150 ± 10 ka was provided for Pan de Azúcar volcano (Hoffer, 2008), while several obsidian pebbles found in the nearby Cosanga river, dated at 670 ± 6 and 290 ± 20 ka (Bellot-Gurlet et al., 2008), suggest an active volcanism on the eastern border of the Eastern Cordillera (Mothes and Hall, 2008a; Hall and Mothes, 2010). Considering the rhyolitic composition of these lavas, as well as, their temporal extension into the Holocene (Hall and Mothes, 2010), the identification of their emission sources is highly desirable in order to assess the hazard associated with these volcanoes.

The third stage (<600 ka) showed a marked increase in the number of active volcanoes. Several volcanic clusters, defined as a high concentration of volcanoes in relatively small areas of a few square kilometers, were formed in the volcanic arc. We have provided the first radiometric ages of the Machachi volcanic cluster, located south of the Guayllabamba basin. These K-Ar ages have allowed us to describe the eruptive history of the Cotopaxi (Barrancas stage: ~540 ka; Morurco stage: 340 to 300 ka), Rumiñahui (>400 to ~200 ka), Pasochoa (470 to 420 ka), Iliniza (Pilongo dome: ~350 ka; North Iliniza: ~120 ka; South Iliniza: 45 to 6 ka), Sincholagua (~310 ka), Almas Santas (~370 ka), Corazón (190 to 90 ka), and Santa Cruz (Loma Saquigua: 80 to 60 ka) volcanoes, in addition to the already dated Chalupas-Quilindaña (pre-caldera lavas: 460 to 420 ka; Chalupas ignimbrite: 216 ka; Quilindaña edifice: 190 to >44 ka; Hammersley, 2003; Bablon et al., 2020b; Córdova et al., 2020), Antisana (~400 to 0 ka Hall et al., 2017b), Huañuna (~10 ka) and Chaupiloma volcanoes (Clapperton et al., 1997; Hall and Mothes, 2008a; Hall et al., 2017b). We note that the evolutionary history of at least a dozen volcanoes remains poorly documented. Volcanoes that still require geochronological and stratigraphic studies are Chinibano, Cerro Negro, Reventador, Sangay, Sumaco, Soche and the volcanoes of the Tulcan segment. The volcanoes Pambamarca and Mojanda-Fuya Fuya deserve a special mention since

the limited erosion of their summit dome complexes suggests that their last eruptive activity probably occurred during the Holocene.

As previously discussed, the Quaternary volcanism in Ecuador shows no clear migration patterns as a function of its distance from the trench, i.e., from east to west or vice versa. Nevertheless, the earliest volcanism at each stage seems to be preferentially located at the border of the Eastern Cordillera and the Inter-Andean Valley. Conversely, the volcanism showed a gradual extension to the north and south of the Guayllabamba basin, also referred to as the central segment of the arc. Note that there is no evidence for a sustained activity in the southern back-arc between the early and late stages. The old fissure lavas emited near the Puyo city seems to be comparatively much smaller in volume, and thus not significant at arc-scale (Hoffer, 2008; Hoffer et al., 2008; Ball, 2015). Despite these overall observations, the order of spatial emplacement of volcanism through time seems to be rather random within each stage of the Ecuadorian arc eruptive history. Nevertheless, the final spatial distribution of the volcanoes seems to be primarily influenced by the inherited tectonic structures of the continental crust, while Quaternary tectonic activity apparently played a secondary role. More in detail, the N-S volcanic corridors described in multiple contributions (e.g., Hall, 1977; Hall and Beate, 1991; Litherland and Aspden, 1992) are mostly coincident with fault and suture zones of continental crust (e.g., Litherland et al., 1994; Hughes and Bermúdez, 1997; Boland et al., 2000; Egüez et al., 2017), while comparatively few volcanoes are located directly above the multiple Quaternary NE-SW fault systems (e.g., Tibaldi et al., 2007; Andrade, 2009; Alvarado et al., 2016). However, this hypothesis requires further research as only few detailed studies are available on the relationship between the Quaternary tectonic activity and the development of the volcanic landforms in the Ecuadorian arc (e.g., Andrade et al., 2019; Baize et al., 2020b). To this regard, the volcanoes that could require further analyses as they are located above or close to active fault systems are Cayambe, Cotacachi, Cotopaxi, Rumiñahui, and Iliniza volcanoes.

Notably, the central segment of the arc, and its unusually high number of volcanoes formed from ~2.4 Ma ago, spatially overlaps with the inland projection of the Carnegie ridge and the young Nazca crust. The proposed eruptive history suggests that subduction of these structures contributed to

the development and expansion of the Ecuadorian volcanism overtime. We acknowledge that the geochemical data acquired throughout our study show the same compositional changes previously described by others (e.g., Hidalgo et al., 2007, 2012; Chiaradia et al., 2009, 2014; Schiano et al., 2010; Ancellin et al., 2017b; Bellver-Baca et al., 2020). Our data allowed us to distinguish and better define the stratigraphic units of the studied volcanoes rather than providing further evidence for the understanding of the petrogenetic processes involved in Ecuadorian magmas genesis. Nevertheless, the present research provides insights into the identification of volcanoes that, with better adapted geochemical surveys, may contribute to the distinction of such processes on broader time scales. For instance, isotope and/or fluid inclusion geochemical analyses from volcanoes such as Chacana-Coturco (~2.4 Ma), Puntas-Pambamarca-Ilaló (~1.2 Ma), and Atacazo-Corazón-Pasochoa (<0.4 Ma) offer a suitable temporal context to study the effects of changes in the petrogenetic processes of the Ecuadorian magmas. These analyses will allow to distinguish whether the across-arc and along-arc zonation of incompatible trace elements, interpreted as reflections of the change in the subduction component (e.g., Ancellin et al., 2017; Narvaez et al., 2018), are time-dependent or time-independent. Besides, it is possible that the overall adakitic signature observed in the better sampled younger magmas of the arc may in fact be also present for the older ones. For instance, we note that the Coturco summit lava and the Pambamarca dacitic domes, dated at 1959 ± 28 ka and 1292 ± 20 ka respectively, show a slight depletion in Y and HREE relative to LREE. This hypothesis of older adakitic signatures should be further investigated through dedicated geochemical studies.

Finally, the substantial dataset provided in this PhD study and the inferred development of the Ecuadorian volcanism could be compared with other segments of the Andean arc or with other arcs worldwide. For instance, the proposed eruptive history suggests that the development of the arc was favored by the subduction of an aseismic oceanic ridge (i.e., Carnegie ridge) with specific thermal conditions, rather than being hindered, as observed in the Central Andes by the Nazca and Juan Fernandez ridges (e.g., Gutscher et al., 2000b; Chen et al., 2001; Porter et al., 2012; Ramos and Folguera, 2009). Therefore, it could be interesting to compare the geochronology, geochemistry and

tectonics of both areas in order to better understand the relationship between the development of volcanic arcs and the subduction of such structures.

References

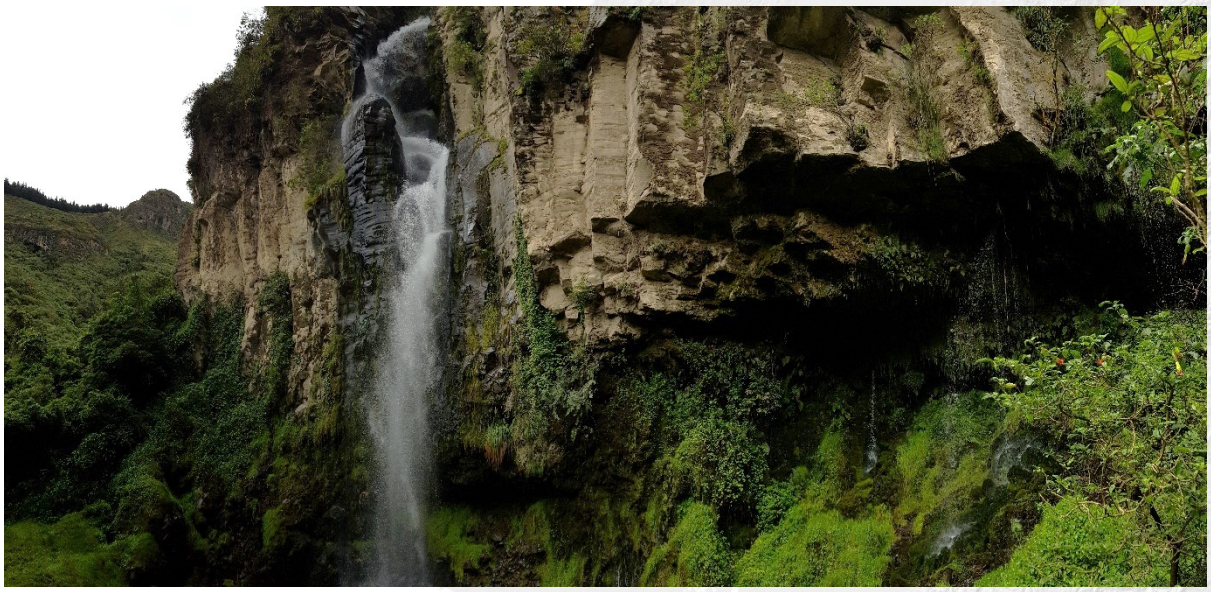

Columnar jointing exhibited by the Pongo lava flow, southwest of Iliniza volcano.

A

Aguirre, L., Atherton, M.P., 1987. Low-grade metamorphism and geotectonic setting of the Macuchi Formation, Western Cordillera of Ecuador. Journal of Metamorphic Geology 5, 473–494. https://doi.org/10.1111/j.1525-1314.1987.tb00397.x

Allaby, M., 2020. A Dictionary of Geology and Earth Sciences, 5th ed, A Dictionary of Geology and Earth Sciences. Oxford University Press.

Almeida, M., 2016. Estudio Petrográfico y Geoquímico del Volcán Cotacachi - Provincia de Imbabura (Engineer memoir). Escuela Politécnica Nacional, Quito, Ecuador.

Almeida, M., Bablon, M., Andrade, D., Hidalgo, S., Quidelleur, X., Samaniego, P., 2019. New constraints on the geological and chronological evolution of the Cotacachi-Cuicocha Volcanic Complex (Ecuador). Presented at the 8th International Symposium on Andean Geodynamics (ISAG), Quito, Ecuador.

Alvarado, A., Audin, L., Nocquet, J.M., Jaillard, E., Mothes, P., Jarrín, P., Segovia, M., Rolandone, F., Cisneros, D., 2016. Partitioning of oblique convergence in the Northern Andes subduction zone: Migration history and the present-day boundary of the North Andean Sliver in Ecuador. Tectonics 35, 1048–1065. https://doi.org/10.1002/2016TC004117

Alvarado, A., Audin, L., Nocquet, J.M., Lagreulet, S., Segovia, M., Font, Y., Lamarque, G., Yepes, H., Mothes, P., Rolandone, F., Jarrín, P., Quidelleur, X., 2014. Active tectonics in Quito, Ecuador, assessed by geomorphological studies, GPS data, and crustal seismicity. Tectonics 33, 67–83. https://doi.org/10.1002/2012TC003224

Ancellin, M.-A., Samaniego, P., Vlastélic, I., Nauret, F., Gannoun, A., Hidalgo, S., 2017a. Across-arc versus along-arc Sr-Nd-Pb isotope variations in the Ecuadorian volcanic arc. Geochem. Geophys. Geosyst. 18, 1163–1188. https://doi.org/10.1002/2016GC006679

Ancellin, M.-A., Samaniego, P., Vlastélic, I., Nauret, F., Gannoun, A., Hidalgo, S., 2017b. Across-arc versus along-arc Sr-Nd-Pb isotope variations in the Ecuadorian volcanic arc. Geochemistry, Geophysics, Geosystems 18, 1163–1188. https://doi.org/10.1002/2016GC006679

Anderson, M., Alvarado, P., Zandt, G., Beck, S., 2007. Geometry and brittle deformation of the subducting Nazca Plate, Central Chile and Argentina. Geophys J Int 171, 419–434. https://doi.org/10.1111/j.1365-246X.2007.03483.x

Andrade, S.D., 2009. The influence of active tectonics on the structural development and flank collapse of Ecuadorian arc volcanoes (Ph.D. thesis). Clermont-Ferrand 2, Clermont-Ferrand, France.

Andrade, S.D., 2002. Estudio Geovolcanológico del complejo Volcánico Pululahua (Engineer memoir). Escuela Politécnica Nacional, Quito, Ecuador.

Andrade, S.D., Martin, H., Monzier, M., 2014. Restricciones y un Posible Modelo Para la Génesis de los Magmas del Volcán Pululahua (Ecuador). Revista Politécnica 33.

Andrade, S.D., Müller, A.V., Vasconez, F.J., Beate, B., Aguilar, J., Santamaría, S., 2021. Pululahua dome complex, Ecuador: eruptive history, total magma output and potential hazards. Journal of South American Earth Sciences 106, 103046. https://doi.org/10.1016/j.jsames.2020.103046

Andrade, S.D., van Wyk de Vries, B., Robin, C., 2019. Imbabura volcano (Ecuador): The influence of dipping-substrata on the structural development of composite volcanoes during strike-slip faulting. Journal of Volcanology and Geothermal Research, Geological data in volcanology: collection, organisation and applications 385, 68–80. https://doi.org/10.1016/j.jvolgeores.2018.11.017

Arriagada, C., Roperch, P., Mpodozis, C., Cobbold, P.R., 2008. Paleogene building of the Bolivian Orocline: Tectonic restoration of the central Andes in 2-D map view. Tectonics 27. https://doi.org/10.1029/2008TC002269

Aspden, J.A., Bonilla, W., Duque, P., 1995. The El Oro metamorphic complex, Ecuador: geology and economic mineral deposits, Overseas geology and mineral resources. British Geological Survey, Keyworth, Nottingham.

Aspden, J.A., Fortey, N., Litherland, M., Viteri, F., Harrison, S.M., 1992a. Regional S-type granites in the Ecuadorian Andes: Possible remnants of the breakup of western Gondwana. Journal of South American Earth Sciences 6, 123–132. https://doi.org/10.1016/0895-9811(92)90002-G

Aspden, J.A., Harrison, S.H., Rundle, C.C., 1992b. New geochronological control for the tectono-magmatic evolution of the metamorphic basement, Cordillera Real and El Oro Province of Ecuador. Journal of South American Earth Sciences 6, 77–96. https://doi.org/10.1016/0895-9811(92)90019-U

Aspden, J.A., Litherland, M., 1992. The geology and Mesozoic collisional history of the Cordillera Real, Ecuador. Tectonophysics, Andean geodynamics 205, 187–204. https://doi.org/10.1016/0040-1951(92)90426-7

B

Bablon, M., 2018. Reconstruction de l'histoire des volcans de l'arc équatorien : contraintes pour l'évolution chronologique de l'arc andin et pour l'évaluation du risque volcanique (Ph.D. thesis). Université Paris Saclay (COmUE), Orsay, France.

Bablon, M., Quidelleur, X., Samaniego, P., Le Pennec, J.-L., Audin, L., Jomard, H., Baize, S., Liorzou, C., Hidalgo, S., Alvarado, A., 2019. Interactions between volcanism and geodynamics in the southern termination of the Ecuadorian arc. Tectonophysics 751, 54–72. https://doi.org/10.1016/j.tecto.2018.12.010

Bablon, M., Quidelleur, X., Samaniego, P., Le Pennec, J.-L., Lahitte, P., Liorzou, C., Bustillos, J.E., Hidalgo, S., 2018. Eruptive chronology of Tungurahua volcano (Ecuador) revisited based on new K-Ar ages and geomorphological reconstructions. Journal of Volcanology and Geothermal Research 357, 378–398. https://doi.org/10.1016/j.jvolgeores.2018.05.007

Bablon, M., Quidelleur, X., Samaniego, P., Le Pennec, J.-L., Santamaría, S., Liorzou, C., Hidalgo, S., Eschbach, B., 2020a. Volcanic history reconstruction in northern Ecuador: insights for eruptive and erosion rates on the whole Ecuadorian arc. Bull Volcanol 82, 11. https://doi.org/10.1007/s00445-019-1346-1

Bablon, M., Quidelleur, X., Siani, G., Samaniego, P., Le Pennec, J.-L., Nouet, J., Liorzou, C., Santamaría, S., Hidalgo, S., 2020b. Glass shard K-Ar dating of the Chalupas caldera major

eruption: Main Pleistocene stratigraphic marker of the Ecuadorian volcanic arc. Quaternary Geochronology 57, 101053. https://doi.org/10.1016/j.quageo.2020.101053

Baby, P., Rivadeneira, M., Barragán, R., Christophoul, F., 2013. Thick-skinned tectonics in the Oriente foreland basin of Ecuador. Geological Society, London, Special Publications 377, 59–76. https://doi.org/10.1144/SP377.1

Baby, P., Rivadeneira, M., Christophoul, F., Barragan, R., 1999. Style and timing of deformation in the Oriente Basin of Ecuador. Presented at the Fourth International Symposium on Andean Geodynamics, University of Goettingen (Germany), pp. 68–72.

Baize, S., Audin, L., Alvarado, A., Jomard, H., Bablon, M., Champenois, J., Espin, P., Samaniego, P., Quidelleur, X., Le Pennec, J.-L., 2020a. Active Tectonics and Earthquake Geology Along the Pallatanga Fault, Central Andes of Ecuador. Front. Earth Sci. 8. https://doi.org/10.3389/feart.2020.00193

Baize, S., Audin, L., Alvarado, A., Jomard, H., Bablon, M., Champenois, J., Espin, P., Samaniego, P., Quidelleur, X., Le Pennec, J.-L., 2020b. Active Tectonics and Earthquake Geology Along the Pallatanga Fault, Central Andes of Ecuador. Frontiers in Earth Science 8, 193. https://doi.org/10.3389/feart.2020.00193

Baksi, A., 2007. A quantitative tool for detecting alteration in undisturbed rocks and minerals—II: Application to argon ages related to hotspots, in: Foulger, G.R., Jurdy, D.M. (Eds.), Plates, Plumes, and Planetary Processes, Special Paper of the Geological Society of America. pp. 305–333. https://doi.org/10.1130/2007.2430(16)

Baldock, J.W., 1982. Geology of Ecuador: explanatory bulletin of the National Geological Map of the Republic of Ecuador. Ministerio de Recursos Naturales y Energéticos, Dirección General de Geología y Minas, Quito, Ecuador.

Ball, P., 2015. Geochemical Analysis of Ecuadorian Back-Arc Lavas (Master's thesis). University of Oxford, Oxford, UK.

Barazangi, M., Isacks, B.L., 1976. Spatial distribution of earthquakes and subduction of the Nazca plate beneath South America. Geology 4, 686–692. https://doi.org/10.1130/0091-7613(1976)4<686:SDOEAS>2.0.CO;2

Barba, D., Robin, C., Samaniego, P., Eissen, J.-P., 2008. Holocene recurrent explosive activity at Chimborazo volcano (Ecuador). Journal of Volcanology and Geothermal Research, Recent and active volcanism in the Ecuadorian Andes 176, 27–35. https://doi.org/10.1016/j.jvolgeores.2008.05.004

Barberi, F., Coltelli, M., Ferrara, G., Innocenti, F., Navarro, J.M., Santacroce, R., 1988. Plio-quaternary volcanism in Ecuador. Geological Magazine 125, 1–14.

Barckhausen, U., Ranero, C.R., Cande, S.C., Engels, M., Weinrebe, W., 2008. Birth of an intraoceanic spreading center. Geology 36, 767–770. https://doi.org/10.1130/G25056A.1

Barragán, R., Baudino, R., Marocco, R., 1996. Geodynamic evolution of the Neogene intermontane Chota basin, Northern Andes of Ecuador. Journal of South American Earth Sciences 9, 309–319. https://doi.org/10.1016/S0895-9811(96)00016-8

Barragán, R., Christophoul, F., White, H., Baby, P., Rivadeneira, M., Ramírez, F., Rodas, J., 2004. Estratigrafía secuencial del cretácico de la Cuenca Oriente del Ecuador, in: Baby, P., Rivadeneira, M., Barragán, R. (Eds.), La Cuenca Oriente: Geología y Petróleo, Travaux de l'IFEA. Institut français d'études andines, Lima, pp. 45–68.

Barragan, R., Geist, D., Hall, M., Larson, P., Mark Kurz, 1998. Subduction controls on the compositions of lavas from the Ecuadorian Andes. Earth and Planetary Science Letters 154, 153–166. https://doi.org/10.1016/S0012-821X(97)00141-6

Beate, B., 1994. El Soche: Un volcán activo en la Provincia de Sucumbíos, Ecuador - primeros datos descriptivos, in: Lachowicz, H. (Ed.), . Presented at the Terceras Jornadas en Ciéncias de la Tierra, Facultad de Geologia, Escuela Politécnica Nacional, Quito, Ecuador, pp. 9–10.

Beate, B., Monzier, M., Spikings, R., Cotten, J., Silva, J., Bourdon, E., Eissen, J.-P., 2001. Mio–Pliocene adakite generation related to flat subduction in southern Ecuador: the Quimsacocha volcanic center. Earth and Planetary Science Letters 192, 561–570. https://doi.org/10.1016/S0012-821X(01)00466-6

Beate, B., Urquizo, M., 2015. Geothermal Country Update for Ecuador: 2010-2015, in: Proceedings World Geothermal Congress. pp. 19–24.

Béguelin, P., Chiaradia, M., Beate, B., Spikings, R., 2015. The Yanaurcu volcano (Western Cordillera, Ecuador): A field, petrographic, geochemical, isotopic and geochronological study. Lithos 218–219, 37–53. https://doi.org/10.1016/j.lithos.2015.01.014

Bello-González, J.P., Contreras-Reyes, E., Arriagada, C., 2018. Predicted path for hotspot tracks off South America since Paleocene times: Tectonic implications of ridge-trench collision along the Andean margin. Gondwana Research 64, 216–234. https://doi.org/10.1016/j.gr.2018.07.008

Bellot-Gurlet, L., Dorighel, O., Poupeau, G., 2008. Obsidian provenance studies in Colombia and Ecuador: obsidian sources revisited. Journal of Archaeological Science 35, 272–289. https://doi.org/10.1016/j.jas.2007.03.008

Bellver-Baca, M.T., Chiaradia, M., Beate, B., Beguelin, P., Deriaz, B., Mendez-Chazarra, N., Villagómez, D., 2020. Geochemical evolution of the Quaternary Chachimbiro Volcanic Complex (frontal volcanic arc of Ecuador). Lithos 356–357, 105237. https://doi.org/10.1016/j.lithos.2019.105237

Berger, G.W., York, D., 1981. Geothermometry from 40Ar39Ar dating experiments. Geochimica et Cosmochimica Acta 45, 795–811. https://doi.org/10.1016/0016-7037(81)90109-5

Bernard, B., Andrade, D., 2011. Volcanes Cuaternarios del Ecuador Continental. IGEPN Poster Informativo.

Bernard, B., Hidalgo, S., Robin, C., Beate, B., Quijozaca, J., 2014. The 3640–3510 BC rhyodacite eruption of Chachimbiro compound volcano, Ecuador: a violent directed blast produced by a satellite dome. Bull Volcanol 76, 849. https://doi.org/10.1007/s00445-014-0849-z

Bernard, B., van Wyk de Vries, B., Barba, D., Leyrit, H., Robin, C., Alcaraz, S., Samaniego, P., 2008. The Chimborazo sector collapse and debris avalanche: deposit characteristics as evidence of emplacement mechanisms. Journal of Volcanology and Geophysical Research 176, 36–43.

Bès de Berc, S., Soula, J.C., Baby, P., Souris, M., Christophoul, F., Rosero, J., 2005. Geomorphic evidence of active deformation and uplift in a modern continental wedge-top–foredeep transition: Example of the eastern Ecuadorian Andes. Tectonophysics, Andean Geodynamics: 399, 351–380. https://doi.org/10.1016/j.tecto.2004.12.030

Bigazzi, G., Coltelli, M., Hadler, N.J.C., Araya, A.M.O., Oddone, M., Salazar, E., 1992. Obsidian-bearing lava flows and pre-Columbian artifacts from the Ecuadorian Andes: First new multidisciplinary data. Journal of South American Earth Sciences 6, 21–32. https://doi.org/10.1016/0895-9811(92)90014-P

Bigazzi, G., Coltelli, M., Halder, J., Osorio, A.M., 1997. Provenance studies of obsidian artefacts using fission track analyses in South America: an overview. Presented at the Congreso Internacional del Americanistas (ICA), Quito, Ecuador, pp. 1–16.

Bigazzi, G., Hadler Neto, J.C., Iunes, P.J., Osório Araya, A.M., 2005. Fission-track dating of South American natural glasses: an overview. Radiation Measurements, Proceedings of the 2nd Latin American Symposium on Nuclear Tracks 39, 585–594. https://doi.org/10.1016/j.radmeas.2004.09.006

Billen, M.I., Hirth, G., 2007. Rheologic controls on slab dynamics. Geochemistry, Geophysics, Geosystems 8. https://doi.org/10.1029/2007GC001597

Boland, M., Ibadango, E., Pilatasig, L.F., McCourt, W., Aspden, J.A., Hughen, R., Beate, B., 2000. Geology of the Cordillera Occidental of Ecuador between 0°00’ and 1°00’N (No. 10), Proyecto de Desarrollo Minero y Control Ambiental. Cogidem - Brithis Geological Survey, Quito.

Bourdon, E., Eissen, J.-P., Gutscher, M.-A., Monzier, M., Hall, M.L., Cotten, J., 2003. Magmatic response to early aseismic ridge subduction: the Ecuadorian margin case (South America). Earth and Planetary Science Letters 205, 123–138. https://doi.org/10.1016/S0012-821X(02)01024-5

Bourdon, E., Eissen, J.-P., Monzier, M., Robin, C., Martin, H., Cotten, J., Hall, M., 2002. Adakite-like Lavas from Antisana Volcano (Ecuador): Evidence for Slab Melt Metasomatism Beneath Andean Northern Volcanic Zone. Journal of Petrology 43, 199–217. https://doi.org/10.1093/petrology/43.2.199

Bristow, C.R., 1973. Guide to the geology of the Cuenca Basin, Southern Ecuador. Ecuadorian Geological and Geophysical Society, Quito.

Bryant, J.A., Yogodzinski, G.M., Hall, M.L., Lewicki, J.L., Bailey, D.G., 2006. Geochemical Constraints on the Origin of Volcanic Rocks from the Andean Northern Volcanic Zone, Ecuador. Journal of Petrology 47, 1147–1175. https://doi.org/10.1093/petrology/egl006

C

Cassignol, C., Gillot, P.-Y., 1982. Range and effectiveness of unspiked potassium-argon dating: experimental groundwork and applications, in: Odin, G.S. (Ed.), Numerical Dating in Stratigraphy. John Wiley & Sons, pp. 159–179.

Cediel, F., 2019. Phanerozoic Orogens of Northwestern South America: Cordilleran-Type Orogens. Taphrogenic Tectonics. The Maracaibo Orogenic Float. The Chocó-Panamá Indenter, in: Cediel, F., Shaw, R.P. (Eds.), Geology and Tectonics of Northwestern South America: The

Pacific-Caribbean-Andean Junction, Frontiers in Earth Sciences. Springer International Publishing, Cham, pp. 3–95. https://doi.org/10.1007/978-3-319-76132-9_1

Cediel, F., Shaw, R.P., Cceres, C., 2003. Tectonic Assembly of the Northern Andean Block 815–848.

Chemin, S., 2004. Le volcan quaternaire Almas Santas (Cordillère occidentale, Equateur). Etude volcanologique, minéralogique et géochimique (Master's thesis). Université de Lausanne, Lausanne, Suisse.

Chen, P.-F., Bina, C.R., Okal, E.A., 2001. Variations in slab dip along the subducting Nazca Plate, as related to stress patterns and moment release of intermediate-depth seismicity and to surface volcanism. Geochemistry, Geophysics, Geosystems 2. https://doi.org/10.1029/2001GC000153

Chiaradia, M., Bellver-Baca, M.T., Valverde, V., Spikings, R., 2021. Geochemical and isotopic variations in a frontal arc volcanic cluster (Chachimbiro-Pulumbura-Pilavo-Yanaurcu, Ecuador). Chemical Geology 574, 120240. https://doi.org/10.1016/j.chemgeo.2021.120240

Chiaradia, M., Müntener, O., Beate, B., 2014. Quaternary Sanukitoid-like Andesites Generated by Intracrustal Processes (Chacana Caldera Complex, Ecuador): Implications for Archean Sanukitoids. Journal of Petrology 55, 769–802. https://doi.org/10.1093/petrology/egu006

Chiaradia, M., Müntener, O., Beate, B., Fontignie, D., 2009. Adakite-like volcanism of Ecuador: lower crust magmatic evolution and recycling. Contrib Mineral Petrol 158, 563–588. https://doi.org/10.1007/s00410-009-0397-2

Christophoul, F., Burgos, J.D., Baby, P., Soula, J.-C., Bès de Berc, S., Dávila, C., Rosero, M., 2004. Dinámica de la Cuenca de ante-país Oriente desde el paleógeno, in: Baby, P., Rivadeneira, M., Barragán, R. (Eds.), La Cuenca Oriente: Geología y Petróleo, Travaux de l'IFEA. Institut français d'études andines, Lima, pp. 92–113.

Clapperton, C.M., 1990. Glacial and volcanic geomorphology of the Chimborazo-Carihuairazo Massif, Ecuadorian Andes. Earth and Environmental Science Transactions of The Royal Society of Edinburgh 81, 91–116. https://doi.org/10.1017/S0263593300005174

Clapperton, C.M., 1986. Glacial geomorphology, Quaternary glacial sequence and palaeoclimatic inferences in the Ecuadorian Andes, in: Gardiner, V. (Ed.), International Geomorphology, Part II. Wiley, London, pp. 843–870.

Clapperton, C.M., Hall, M., Mothes, P., Hole, M.J., Still, J.W., Helmens, K.F., Kuhry, P., Gemmell, A.M.D., 1997. A Younger Dryas Icecap in the Equatorial Andes. Quaternary Research 47, 13–28. https://doi.org/10.1006/qres.1996.1861

Cochrane, R., Spikings, R., Gerdes, A., Ulianov, A., Mora, A., Villagómez, D., Putlitz, B., Chiaradia, M., 2014. Permo-Triassic anatexis, continental rifting and the disassembly of western Pangaea. Lithos 190–191, 383–402. https://doi.org/10.1016/j.lithos.2013.12.020

Cohen, K.M., Gibbard, P.L., 2019. Global chronostratigraphical correlation table for the last 2.7 million years, version 2019 QI-500. Quaternary International, SI: Quaternary International 500 500, 20–31. https://doi.org/10.1016/j.quaint.2019.03.009

Coira, B., Davidson, J., Mpodozis, C., Ramos, V.A., 1982. Tectonic and magmatic evolution of the Andes of northern Argentina and Chile. Earth-Science Reviews, Magmatic Evolution of the Andes 18, 303–332. https://doi.org/10.1016/0012-8252(82)90042-3

Collot, J.-Y., Michaud, F., Alvarado, A., Marcaillou, B., Sosson, M., Ratzov, G., Migeon, S., Calahorrano, A., Pazmino, A., 2009. Visión general de la morfología submarina del margen convergente de Ecuador-Sur de Colombia: implicaciones sobre la transferencia de masa y la edad de la subducción de la Cordillera de Carnegie, in: Collot, J.-Y., Sallares, V., Pazmiño, A. (Eds.), Geología y Geofísica Marina y Terrestre Del Ecuador Desde La Costa Continental Hasta Las Islas Galápagos. CNDM-INOCAR-IRD, Guayaquil, Ecuador, pp. 47–74.

Conway, C.E., Townsend, D.B., Leonard, G.S., Wilson, C.J.N., Calvert, A.T., Gamble, J.A., 2015. Lava-ice interaction on a large composite volcano: a case study from Ruapehu, New Zealand. Bull Volcanol 77, 21. https://doi.org/10.1007/s00445-015-0906-2

Córdova, M.D., Mothes, P.A., Gaunt, H.E., Salgado, J., 2020. Post-Caldera Eruptions at Chalupas Caldera, Ecuador: Determining the Timing of Lava Dome Collapse, Hummock Emplacement and Dome Rejuvenation. Front. Earth Sci. 8. https://doi.org/10.3389/feart.2020.548251

Cotten, J., Le Dez, A., Bau, M., Caroff, M., Maury, R.C., Dulski, P., Fourcade, S., Bohn, M., Brousse, R., 1995. Origin of anomalous rare-earth element and yttrium enrichments in subaerially exposed basalts: Evidence from French Polynesia. Chemical Geology 119, 115–138. https://doi.org/10.1016/0009-2541(94)00102-E

D

Dallmeyer, R.D., Lecorche, J.P., 1990. 40Ar/39Ar polyorogenic mineral age record in the northern Mauritanide orogen, West Africa. Tectonophysics, International IGCP Conference Project 233 177, 81–107. https://doi.org/10.1016/0040-1951(90)90275-D

Dalrymple, G.B., Lanphere, M.A., Pringle, M.S., 1988. Correlation diagrams in 40Ar/39Ar dating: Is there a correct choice? Geophysical Research Letters 15, 589–591. https://doi.org/10.1029/GL015i006p00589

de Silva, S., Lindsay, J.M., 2015. Chapter 15 - Primary Volcanic Landforms, in: Sigurdsson, H. (Ed.), The Encyclopedia of Volcanoes (Second Edition). Academic Press, Amsterdam, pp. 273–297. https://doi.org/10.1016/B978-0-12-385938-9.00015-8

DeMets, C., Gordon, R.G., Argus, D.F., 2010. Geologically current plate motions. Geophysical Journal International 181, 1–80. https://doi.org/10.1111/j.1365-246X.2009.04491.x

Díaz, M., Baby, P., Rivadeneira, M., Christophoul, F., 2004. El pre-aptense en la cuenca oriente ecuatoriana, in: Baby, P., Rivadeneira, M., Barragán, R. (Eds.), La Cuenca Oriente: Geología y Petróleo. Institut français d'études andines, Lima, pp. 23–44.

Dibacto, S., Lahitte, P., Karátson, D., Hencz, M., Szakács, A., Biró, T., Kovács, I., Veres, D., 2020. Growth and erosion rates of the East Carpathians volcanoes constrained by numerical models: Tectonic and climatic implications. Geomorphology 368, 107352. https://doi.org/10.1016/j.geomorph.2020.107352

Dodson, M.H., 1973. Closure temperature in cooling geochronological and petrological systems. Contr. Mineral. and Petrol. 40, 259–274. https://doi.org/10.1007/BF00373790

Dunkley, P., Gaibor, A., 1997. Geology of the Cordillera Occidental of Ecuador between 2°00' and 3°00'S (No. 2), Proyecto de Desarrollo Minero y Control Ambiental. Cogidem - Brithis Geological Survey, Quito.

Duque-Trujillo, J.F., Hermelin, M., Toro, G.E., 2016. The Guamuéz (La Cocha) Lake, in: Hermelin, M. (Ed.), Landscapes and Landforms of Colombia, World Geomorphological Landscapes. Springer International Publishing, Cham, pp. 203–210. https://doi.org/10.1007/978-3-319-11800-0_17

Dürkefälden, A., Hoernle, K., Hauff, F., Wartho, J.-A., van den Bogaard, P., Werner, R., 2019. Age and geochemistry of the Beata Ridge: Primary formation during the main phase (~89 Ma) of the Caribbean Large Igneous Province. Lithos 328–329, 69–87. https://doi.org/10.1016/j.lithos.2018.12.021

E

Egbue, O., Kellogg, J., 2010. Pleistocene to Present North Andean "escape." Tectonophysics 489, 248–257. https://doi.org/10.1016/j.tecto.2010.04.021

Egüez, A., 1986. Evolution Cénozoïque de la cordillere occidentale septentrionale d'Equateur (0°15' LS a 1°10' LS). Les minéralisations associées. Mémoires des sciences de la Terre de l'Université Pierre et Marie Curie. Univ. Pierre et Marie Curie, Paris 6, Paris.

Egüez, A., Alvarado, A., Yepes, H., Machette, M.N., Costa, C., Dart, R.L., 2003. Database and map of Quaternary faults and folds of Ecuador and its offshore regions. US Geological Survey Open-File Report 03-289 71. https://doi.org/10.3133/ofr03289

Egüez, A., Gaona, M., Albán, A., 2017. Mapa Geológico de la República del Ecuador.

Egüez, A., Yepes, H., 1994. Estudio neotectonico y de peligro sismico para el Proyecto Hidroelectrico Toachi. Instituto Ecuatoriano de Electrificacion - INECEL, Quito, Ecuador.

Elger, K., Oncken, O., Glodny, J., 2005. Plateau-style accumulation of deformation: Southern Altiplano. Tectonics 24. https://doi.org/10.1029/2004TC001675

Espurt, N., Funiciello, F., Martinod, J., Guillaume, B., Regard, V., Faccenna, C., Brusset, S., 2008. Flat subduction dynamics and deformation of the South American plate: Insights from analog modeling. Tectonics 27. https://doi.org/10.1029/2007TC002175

F

Fiorini, E., Tibaldi, A., 2012. Quaternary tectonics in the central Interandean Valley, Ecuador: Fault-propagation folds, transfer faults and the Cotopaxi Volcano. Global and Planetary Change, Coupled deep Earth and surface processes in System Earth: monitoring, reconstruction and process modeling 90–91, 87–103. https://doi.org/10.1016/j.gloplacha.2011.06.002

Fleck, R.J., Sutter, J.F., Elliot, D.H., 1977. Interpretation of discordant 40Ar/39Ar age-spectra of mesozoic tholeiites from antarctica. Geochimica et Cosmochimica Acta 41, 15–32. https://doi.org/10.1016/0016-7037(77)90184-3

Flores, G.E., Pizarro-Araya, J., 2006. The Andes mountain range uplift as a vicariant event in the Pimeliinae (Coleoptera :Tenebrionidae) in Southern South America. Publications du musée des Confluences 10, 95–102.

G

Gaibor, J., Hochuli, J.P.A., Winkler, W., Toro, J., 2008. Hydrocarbon source potential of the Santiago Formation, Oriente Basin, SE of Ecuador. Journal of South American Earth Sciences 25, 145–156. https://doi.org/10.1016/j.jsames.2007.07.002

Garner, E.L., Murphy, T.J., Gramlich, J.W., Paulsen, P.J., Barnes, I.L., 1975. Absolute Isotopic Abundance Ratios and the Atomic Weight of a Reference Sample of Potassium. J Res Natl Bur Stand A Phys Chem 79A, 713–725. https://doi.org/10.6028/jres.079A.028

Garrison, J., Davidson, J., Reid, M., Turner, S., 2006. Source versus differentiation controls on U-series disequilibria: Insights from Cotopaxi Volcano, Ecuador. Earth and Planetary Science Letters 244, 548–565. https://doi.org/10.1016/j.epsl.2006.02.013

Garrison, J.M., Davidson, J.P., 2003. Dubious case for slab melting in the Northern volcanic zone of the Andes. Geology 31, 565–568. https://doi.org/10.1130/0091-7613(2003)031<0565:DCFSMI>2.0.CO;2

Garrison, J.M., Sims, K.W.W., Yogodzinski, G.M., Escobar, R.D., Scott, S., Mothes, P., Hall, M.L., Ramon, P., 2017. Shallow-level differentiation of phonolitic lavas from Sumaco Volcano, Ecuador. Contrib Mineral Petrol 173, 6. https://doi.org/10.1007/s00410-017-1431-4

Geotérmica Italiana, 1989. Mitigación del riesgo volcánico en el área metropolitana de Quito (Informe final No. 2). INEMIN, DGCS, Pisa, Italy.

Germa, A., Lahitte, P., Quidelleur, X., 2015. Construction and destruction of Mont Pelée volcano: Volumes and rates constrained from a geomorphological model of evolution. Journal of Geophysical Research: Earth Surface 120, 1206–1226. https://doi.org/10.1002/2014JF003355

Germa, A., Quidelleur, X., Gillot, P.Y., Tchilinguirian, P., 2010. Volcanic evolution of the back-arc Pleistocene Payun Matru volcanic field (Argentina). Journal of South American Earth Sciences 29, 717–730. https://doi.org/10.1016/j.jsames.2010.01.002

Germa, A., Quidelleur, X., Lahitte, P., Labanieh, S., Chauvel, C., 2011. The K–Ar Cassignol–Gillot technique applied to western Martinique lavas: A record of Lesser Antilles arc activity from 2Ma to Mount Pelée volcanism. Quaternary Geochronology 6, 341–355. https://doi.org/10.1016/j.quageo.2011.02.001

Gillot, P.-Y., Cornette, Y., Max, N., Floris, B., 1992. Two reference materials, Trachytes MDO-G and ISH-G, for Argon Dating (K-Ar and 40Ar/39Ar) of Pleistocene and Holocene rocks. Geostandards Newsletter 16, 55–60. https://doi.org/10.1111/j.1751-908X.1992.tb00487.x

Gillot, P.Y., Hildenbrand, A., Lefèvre, J.C., Albore-Livadie, C., 2006. The K/Ar dating method: principle, analytical techniques, and application to Holocene volcanic eruptions in Southern Italy. Acta Vulcanologica 18, 55–66.

Gómez Tapias, J., Montes, N.E., Nivia, A., Diederix, H., 2005. Geological Map of Colombia 2015.

Gómez Tapias, J., Schobbenhaus, C., Montes Ramírez, N., 2019. Geological Map of South America.

Grosse, P., Ochi Ramacciotti, M.L., Escalante Fochi, F., Guzmán, S., Orihashi, Y., Sumino, H., 2020. Geomorphology, morphometry, spatial distribution and ages of mafic monogenetic volcanoes of the Peinado and Incahuasi fields, southernmost Central Volcanic Zone of the Andes. Journal

of Volcanology and Geothermal Research 401, 106966. https://doi.org/10.1016/j.jvolgeores.2020.106966

Grosse, P., Orihashi, Y., Guzmán, S.R., Sumino, H., Nagao, K., 2018. Eruptive history of Incahuasi, Falso Azufre and El Cóndor Quaternary composite volcanoes, southern Central Andes. Bull Volcanol 80, 1–26. https://doi.org/10.1007/s00445-018-1221-5

Grove, T., Parman, S., Bowring, S., Price, R., Baker, M., 2002. The role of an H2O-rich fluid component in the generation of primitive basaltic andesites and andesites from the Mt. Shasta region, N California. Contrib Mineral Petrol 142, 375–396. https://doi.org/10.1007/s004100100299

Grove, T.L., Till, C.B., Krawczynski, M.J., 2012. The Role of H2O in Subduction Zone Magmatism. Annual Review of Earth and Planetary Sciences 40, 413–439. https://doi.org/10.1146/annurev-earth-042711-105310

Guillier, B., Chatelain, J.-L., Jaillard, É., Yepes, H., Poupinet, G., Fels, J.-F., 2001. Seismological evidence on the geometry of the Orogenic System in central-northern Ecuador (South America). Geophysical Research Letters 28, 3749–3752. https://doi.org/10.1029/2001GL013257

Gutscher, M.-A., 2002. Andean subduction styles and their effect on thermal structure and interplate coupling. Journal of South American Earth Sciences, Flat-Slab Subduction in the Andes 15, 3–10. https://doi.org/10.1016/S0895-9811(02)00002-0

Gutscher, M.-A., Malavieille, J., Lallemand, S., Collot, J.-Y., 1999. Tectonic segmentation of the North Andean margin: impact of the Carnegie Ridge collision. Earth and Planetary Science Letters 168, 255–270. https://doi.org/10.1016/S0012-821X(99)00060-6

Gutscher, M.-A., Maury, R., Eissen, J.-P., Bourdon, E., 2000a. Can slab melting be caused by flat subduction? Geology 28, 535–538. https://doi.org/10.1130/0091-7613(2000)28<535:CSMBCB>2.0.CO;2

Gutscher, M.-A., Spakman, W., Bijwaard, H., Engdahl, E.R., 2000b. Geodynamics of flat subduction: Seismicity and tomographic constraints from the Andean margin. Tectonics 19, 814–833. https://doi.org/10.1029/1999TC001152

H

Hall, M.L., 1977. El volcanismo en el Ecuador. Instituto Panamericano de Geografía e Historia, Quito.

Hall, M.L., Beate, B., 1991. El volcanismo plio cuaternario en los Andes del Ecuador, in: El paisaje volcánico de la sierra ecuatoriana: geomorfología, fenómenos volcánicos y recursos asociados, Estudios de Geografia. Corporación Editora Nacional, Quito, pp. 5–17.

Hall, M.L., Mothes, P., 2010. New active rhyolitic eruption centers - Eastern foot of the Ecuadorian Andes, in: Abstracts Volume. Presented at the Cities on Volcanoes 6th, Tenerife, Spain, p. 44.

Hall, M.L., Mothes, P., 2008a. The rhyolitic–andesitic eruptive history of Cotopaxi volcano, Ecuador. Bull Volcanol 70, 675–702. https://doi.org/10.1007/s00445-007-0161-2

Hall, M.L., Mothes, P., 2008b. Volcanic impediments in the progressive development of pre-Columbian civilizations in the Ecuadorian Andes. Journal of Volcanology and Geothermal Research, Volcanoes and Human History 176, 344–355. https://doi.org/10.1016/j.jvolgeores.2008.01.039

Hall, M.L., Mothes, P., Vallance, J., Alvarado, A., 2017a. Deslizamientos del Yacupungo, in: Cabero, A., Zúñiga, M.A., Le Pennec, J.-L., Narváez, D., Hernández, M.J., Nocquet, J.M., Gómez, F.V. (Eds.), Memorias VIII Jornadas En Ciencias de La Tierra. Presented at the VIII Jornadas en Ciencas de la Tierra, EPN Editorial, Quito, Ecuador, pp. 85–87.

Hall, M.L., Mothes, P.A., 2008c. The Chacana caldera complex in Ecuador, in: Volume 3: Collapse Calderas Workshop. Presented at the IOP Conference Series: Earth and Environmental Science (EES), IOP Publishing, Querétaro, Mexico. https://doi.org/10.1088/1755-1307/3/1/012004

Hall, M.L., Mothes, P.A., Samaniego, P., Militzer, A., Beate, B., Ramón, P., Robin, C., 2017b. Antisana volcano: A representative andesitic volcano of the eastern cordillera of Ecuador: Petrography, chemistry, tephra and glacial stratigraphy. Journal of South American Earth Sciences 73, 50–64. https://doi.org/10.1016/j.jsames.2016.11.005

Hall, M.L., Robin, C., Beate, B., Mothes, P., Monzier, M., 1999. Tungurahua Volcano, Ecuador: structure, eruptive history and hazards. Journal of Volcanology and Geothermal Research 91, 1–21. https://doi.org/10.1016/S0377-0273(99)00047-5

Hall, M.L., Samaniego, P., Le Pennec, J.L., Johnson, J.B., 2008. Ecuadorian Andes volcanism: A review of Late Pliocene to present activity. Journal of Volcanology and Geothermal Research, Recent and active volcanism in the Ecuadorian Andes 176, 1–6. https://doi.org/10.1016/j.jvolgeores.2008.06.012

Hall, M.L., Wood, C.A., 1985. Volcano-tectonic segmentation of the northern Andes. Geology 13, 203–207. https://doi.org/10.1130/0091-7613(1985)13<203:VSOTNA>2.0.CO;2

Hammersley, L.C., 2003. Isotopic evidence for the relative roles of fractional crystallization, crustal assimilation and magma supply in the generation of large volume rhyolitic eruptions (Ph.D. thesis). University of California, Berkeley, CA.

Hampton, S.J., Cole, J.W., 2009. Lyttelton Volcano, Banks Peninsula, New Zealand: Primary volcanic landforms and eruptive centre identification. Geomorphology 104, 284–298. https://doi.org/10.1016/j.geomorph.2008.09.005

Hanuš, V., Vaněk, J., 1978. Morphology of the andean wadati-benioff zone, andesitic volcanism, and tectonic features of the nazca plate. Tectonophysics 44, 65–77. https://doi.org/10.1016/0040-1951(78)90063-X

Harford, C.L., Pringle, M.S., Sparks, R.S.J., Young, S.R., 2002. The volcanic evolution of Montserrat using 40Ar/39Ar geochronology. Geological Society, London, Memoirs 21, 93–113. https://doi.org/10.1144/GSL.MEM.2002.021.01.05

Harpp, K.S., Wanless, V.D., Otto, R.H., Hoernle, K., Werner, R., 2005. The Cocos and Carnegie Aseismic Ridges: a Trace Element Record of Long-term Plume–Spreading Center Interaction. J Petrology 46, 109–133. https://doi.org/10.1093/petrology/egh064

Heine, K., 2011. Chapter 57 - Late Quaternary Glaciations of Ecuador, in: Ehlers, J., Gibbard, P.L., Hughes, P.D. (Eds.), Developments in Quaternary Sciences, Quaternary Glaciations - Extent and Chronology. Elsevier, pp. 803–813. https://doi.org/10.1016/B978-0-444-53447-7.00057-X

Heine, K., 2000. Tropical South America during the Last Glacial Maximum: evidence from glacial, periglacial and fluvial records. Quaternary International, Quaternary palaeohydorlogy of South America 72, 7–21. https://doi.org/10.1016/S1040-6182(00)00017-3

Hey, R., 1977. Tectonic evolution of the Cocos-Nazca spreading center. GSA Bulletin 88, 1404–1420. https://doi.org/10.1130/0016-7606(1977)88<1404:TEOTCS>2.0.CO;2

Hidalgo, S., 2006. Les intéractions entre magmas calco-alcalins "classiques" et adakitiques: exemple du complexe volcanique Atacazo-Ninahuilca (Equateur) (Ph.D. thesis). Université Blaise Pascal - Clermont-Ferrand II, Clermont-Ferrand, France.

Hidalgo, S., 2002. Géochimie du complexe volcanique des Iliniza: pétrogenèse de séries à affinité adakitique de l'arc équatorien (DEA Report). Université Blaise Pascal, Clermont-Ferrand.

Hidalgo, S., 2001. Estudio geovolcanológico del complejo volcánico Iliniza (Engineer memoir). Escuela Politécnica Nacional, Quito.

Hidalgo, S., Gerbe, M.C., Martin, H., Samaniego, P., Bourdon, E., 2012. Role of crustal and slab components in the Northern Volcanic Zone of the Andes (Ecuador) constrained by Sr–Nd–O isotopes. Lithos 132–133, 180–192. https://doi.org/10.1016/j.lithos.2011.11.019

Hidalgo, S., Monzier, M., Almeida, E., Chazot, G., Eissen, J.-P., van der Plicht, J., Hall, M.L., 2008. Late Pleistocene and Holocene activity of the Atacazo–Ninahuilca Volcanic Complex (Ecuador). Journal of Volcanology and Geothermal Research, Recent and active volcanism in the Ecuadorian Andes 176, 16–26. https://doi.org/10.1016/j.jvolgeores.2008.05.017

Hidalgo, S., Monzier, M., Martin, H., Chazot, G., Eissen, J.-P., Cotten, J., 2007. Adakitic magmas in the Ecuadorian Volcanic Front: Petrogenesis of the Iliniza Volcanic Complex (Ecuador). Journal of Volcanology and Geothermal Research 159, 366–392. https://doi.org/10.1016/j.jvolgeores.2006.07.007

Hildenbrand, A., Marques, F.O., Catalão, J., 2018. Large-scale mass wasting on small volcanic islands revealed by the study of Flores Island (Azores). Scientific Reports 8, 13898. https://doi.org/10.1038/s41598-018-32253-0

Hoffer, G., 2008. Fusion partielle d'un manteau métasomatisé par un liquide adakitique : approches géochimique et expérimentale de la genèse et de l'évolution des magmas de l'arrière-arc équatorien (Ph.D. thesis). Université Blaise Pascal - Clermont-Ferrand II, Clermont-Ferrand, France.

Hoffer, G., Eissen, J.-P., Beate, B., Bourdon, E., Fornari, M., Cotten, J., 2008. Geochemical and petrological constraints on rear-arc magma genesis processes in Ecuador: The Puyo cones and Mera lavas volcanic formations. Journal of Volcanology and Geothermal Research, Recent and active volcanism in the Ecuadorian Andes 176, 107–118. https://doi.org/10.1016/j.jvolgeores.2008.05.023

Hughes, R.A., Bermúdez, R., 1997. Geology of the Cordillera Occidental of Ecuador between 0°00' and 1°00'S (No. 4), Proyecto de Desarrollo Minero y Control Ambiental. Cogidem - Brithis Geological Survey, Quito.

Hughes, R.A., Pilatasig, L.F., 2002. Cretaceous and Tertiary terrane accretion in the Cordillera Occidental of the Andes of Ecuador. Tectonophysics, Andean Geodynamics ISAG 4 345, 29–48. https://doi.org/10.1016/S0040-1951(01)00205-0

Hungerbühler, D., Steinmann, M., Winkler, W., Seward, D., Egüez, A., Peterson, D.E., Helg, U., Hammer, C., 2002. Neogene stratigraphy and Andean geodynamics of southern Ecuador. Earth-Science Reviews 57, 75–124. https://doi.org/10.1016/S0012-8252(01)00071-X

I-J

INIGEMM, 2017. Hoja Geológica Zamora.

Isacks, B.L., 1988. Uplift of the Central Andean Plateau and bending of the Bolivian Orocline. Journal of Geophysical Research: Solid Earth 93, 3211–3231. https://doi.org/10.1029/JB093iB04p03211

Jacques, J., 2003. A tectonostratigraphic synthesis of the Sub-Andean basins: inferences on the position of South American intraplate accommodation zones and their control on South Atlantic opening. Journal of the Geological Society 160, 703–717. https://doi.org/10.1144/0016-764902-089

Jaillard, E., 1997. Discusión de algunos problemas estratigraficos de la cuenca oriental ecuatoriana, in: Sintesis Estratigrafica y Sedimentologica Del Cretaceo y Paleogeno de La Cuenca Oriental Del Ecuador. ORSTOM - Petroproduccion, pp. 37–47.

Jaillard, E., Ordonez, M., Benitez, S., Berrones, G., Jiménez, N., Montenegro, G., Zambrano, I., 1995. Basin development in an accretionary, oceanic-floored fore-arc setting : Southern coastal Ecuador during Late Cretaceous-Late Eocene time, in: Tankard, A.J., Suarez S., R., Welsink, H.J. (Eds.), Petroleum Basins of South America, AAPG Memoir. AAPG, Tulsa, pp. 615–631.

Jaillard, E., Soler, P., 1996. Cretaceous to early Paleogene tectonic evolution of the northern Central Andes (0–18°S) and its relations to geodynamics. Tectonophysics, Geodynamics of The Andes 259, 41–53. https://doi.org/10.1016/0040-1951(95)00107-7

Jones, R.E., De Hoog, J.C.M., Kirstein, L.A., Kasemann, S.A., Hinton, R., Elliott, T., Litvak, V.D., 2014. Temporal variations in the influence of the subducting slab on Central Andean arc magmas: Evidence from boron isotope systematics. Earth and Planetary Science Letters 408, 390–401. https://doi.org/10.1016/j.epsl.2014.10.004

Jordan, T.E., Isacks, B.L., Allmendinger, R.W., Brewer, J.A., Ramos, V.A., Ando, C.J., 1983. Andean tectonics related to geometry of subducted Nazca plate. GSA Bulletin 94, 341–361. https://doi.org/10.1130/0016-7606(1983)94<341:ATRTGO>2.0.CO;2

K

Kay, S.M., Ramos, V.A., Dickinson, W.R., 2009. Backbone of the Americas: Shallow Subduction, Plateau Uplift, and Ridge and Terrane Collision. Geological Society of America.

Kehrer, W., van der Kaaden, G., 1980. Notes on the Geology of Ecuador with Special Reference - to the Western Cordillera. Geologisches Jahrbuch B, 5–57.

Kendrick, E., Bevis, M., Smalley, R., Brooks, B., Vargas, R.B., Lauría, E., Fortes, L.P.S., 2003. The Nazca–South America Euler vector and its rate of change. Journal of South American Earth Sciences 16, 125–131. https://doi.org/10.1016/S0895-9811(03)00028-2

Kennan, L., Lamb, S.H., Hoke, L., 1997. High-altitude palaeosurfaces in the Bolivian Andes: evidence for late Cenozoic surface uplift. Geological Society, London, Special Publications 120, 307–323. https://doi.org/10.1144/GSL.SP.1997.120.01.20

Kennan, L., Pindell, J.L., 2009. Dextral shear, terrane accretion and basin formation in the Northern Andes: best explained by interaction with a Pacific-derived Caribbean Plate? Geological Society, London, Special Publications 328, 487–531. https://doi.org/10.1144/SP328.20

Kennerley, J.B., 1971. Geology of the Llanganates area, Ecuador. Inst. Geol. Sci. (London) Overseas Div. Report 23, 13.

Kerr, A.C., Aspden, J.A., Tarney, J., Pilatasig, L.F., 2002. The nature and provenance of accreted oceanic terranes in western Ecuador: geochemical and tectonic constraints. Journal of the Geological Society 159, 577–594. https://doi.org/10.1144/0016-764901-151

Kerr, A.C., Tarney, J., 2005. Tectonic evolution of the Caribbean and northwestern South America: The case for accretion of two Late Cretaceous oceanic plateaus. Geology 33, 269–272. https://doi.org/10.1130/G21109.1

Kessel, R., Schmidt, M.W., Ulmer, P., Pettke, T., 2005. Trace element signature of subduction-zone fluids, melts and supercritical liquids at 120–180 km depth. Nature 437, 724–727. https://doi.org/10.1038/nature03971

Koch, C.D., Delph, J., Beck, S.L., Lynner, C., Ruiz, M., Hernandez, S., Samaniego, P., Meltzer, A., Mothes, P., Hidalgo, S., 2021. Crustal thickness and magma storage beneath the Ecuadorian arc. Journal of South American Earth Sciences 110, 103331. https://doi.org/10.1016/j.jsames.2021.103331

Kopp, H., Flueh, E.R., Papenberg, C., Klaeschen, D., 2004. Seismic investigations of the O'Higgins Seamount Group and Juan Fernández Ridge: Aseismic ridge emplacement and lithosphere hydration. Tectonics 23. https://doi.org/10.1029/2003TC001590

Kuiper, Y.D., 2002. The interpretation of inverse isochron diagrams in 40Ar/39Ar geochronology. Earth and Planetary Science Letters 203, 499–506. https://doi.org/10.1016/S0012-821X(02)00833-6

L

LaFemina, P., Dixon, T.H., Govers, R., Norabuena, E., Turner, H., Saballos, A., Mattioli, G., Protti, M., Strauch, W., 2009. Fore-arc motion and Cocos Ridge collision in Central America. Geochemistry, Geophysics, Geosystems 10. https://doi.org/10.1029/2008GC002181

Lahitte, P., Dibacto, S., Karátson, D., Gertisser, R., Veres, D., 2019. Eruptive history of the Late Quaternary Ciomadul (Csomád) volcano, East Carpathians, part I: timing of lava dome activity. Bull Volcanol 81, 27. https://doi.org/10.1007/s00445-019-1286-9

Lahitte, P., Samper, A., Quidelleur, X., 2012. DEM-based reconstruction of southern Basse-Terre volcanoes (Guadeloupe archipelago, FWI): Contribution to the Lesser Antilles Arc construction rates and magma production. Geomorphology, Volcano Geomorphology: landforms, processes and hazards 136, 148–164. https://doi.org/10.1016/j.geomorph.2011.04.008

Lamb, S., Davis, P., 2003. Cenozoic climate change as a possible cause for the rise of the Andes. Nature 425, 792–797. https://doi.org/10.1038/nature02049

Lavenu, A., Baudino, R., Ego, F., 1996. Stratigraphie des dépôts tertiaires et quaternaires de la dépression interandine d'Equateur (entre 0° et 2°15'S). Bulletin de l'Institut Français d' Etudes Andines 25, 1–15.

Lavenu, A., Noblet, C., Bonhomme, M.G., Egüez, A., Dugas, F., Vivier, G., 1992. New K-Ar age dates of Neogene and Quaternary volcanic rocks from the Ecuadorian Andes: Implications for the relationship between sedimentation, volcanism, and tectonics. Journal of South American Earth Sciences 5, 309–320. https://doi.org/10.1016/0895-9811(92)90028-W

Lavenu, A., Winter, T., Dávila, F., 1995. A Pliocene–Quaternary compressional basin in the Interandean Depression, Central Ecuador. Geophysical Journal International 121, 279–300. https://doi.org/10.1111/j.1365-246X.1995.tb03527.x

Le Pennec, J.-L., de Saulieu, G., Samaniego, P., Jaya, D., Gailler, L., 2013. A Devastating Plinian Eruption at Tungurahua Volcano Reveals Formative Occupation at ∼1100 cal BC in Central Ecuador. Radiocarbon 55, 1199–1214. https://doi.org/10.1017/S0033822200048116

Le Pennec, J.L., Jaya, D., Samaniego, P., Ramón, P., Moreno Yánez, S., Egred, J., van der Plicht, J., 2008. The AD 1300–1700 eruptive periods at Tungurahua volcano, Ecuador, revealed by historical narratives, stratigraphy and radiocarbon dating. Journal of Volcanology and Geothermal Research, Recent and active volcanism in the Ecuadorian Andes 176, 70–81. https://doi.org/10.1016/j.jvolgeores.2008.05.019

Le Pennec, J.-L., Ramón, P., Robin, C., Almeida, E., 2016. Combining historical and 14C data to assess pyroclastic density current hazards in Baños city near Tungurahua volcano (Ecuador). Quaternary International, Volcanic Activity and Human Society 394, 98–114. https://doi.org/10.1016/j.quaint.2015.06.052

Le Pennec, J.L., Ruiz, A.G., Eissen, J.P., Hall, M.L., Fornari, M., 2011. Identifying potentially active volcanoes in the Andes: Radiometric evidence for late Pleistocene-early Holocene eruptions at Volcán Imbabura, Ecuador. Journal of Volcanology and Geothermal Research 206, 121–135. https://doi.org/10.1016/j.jvolgeores.2011.06.002

Lebras, M., Mégard, F., Dupuy, C., Dostal, J., 1987. Geochemistry and tectonic setting of pre-collision Cretaceous and Paleogene volcanic rocks of Ecuador. GSA Bulletin 99, 569–578. https://doi.org/10.1130/0016-7606(1987)99<569:GATSOP>2.0.CO;2

Lee, J.-Y., Marti, K., Severinghaus, J.P., Kawamura, K., Yoo, H.-S., Lee, J.B., Kim, J.S., 2006. A redetermination of the isotopic abundances of atmospheric Ar. Geochimica et Cosmochimica Acta 70, 4507–4512. https://doi.org/10.1016/j.gca.2006.06.1563

Litherland, M., Aspden, J.A., 1992. Terrane-boundary reactivation: A control on the evolution of the Northern Andes. Journal of South American Earth Sciences 5, 71–76. https://doi.org/10.1016/0895-9811(92)90060-C

Litherland, M., Aspden, J.A., Jemielita, R.A., 1994. The metamorphic belts of Ecuador, Overseas Memoir Institute of Geological Sciences. British Geological Survey, Keyworth, Nottingham.

Liu, S., Currie, C.A., 2016. Farallon plate dynamics prior to the Laramide orogeny: Numerical models of flat subduction. Tectonophysics 666, 33–47. https://doi.org/10.1016/j.tecto.2015.10.010

Loayza, T.G., Proust, J.-N., Michaud, F., Collot, J.-Y., 2013. Evolution Pléistocène du Système de canyons du Golfe de Guayaquil (Equateur): Contrôles paléo-climatiques et tectoniques. Presented at the 14e Congrès Français de Sédimentologie, Paris, Francia.

Lonsdale, P., 2005. Creation of the Cocos and Nazca plates by fission of the Farallon plate. Tectonophysics 404, 237–264. https://doi.org/10.1016/j.tecto.2005.05.011

Luzieux, L.D.A., Heller, F., Spikings, R., Vallejo, C.F., Winkler, W., 2006. Origin and Cretaceous tectonic history of the coastal Ecuadorian forearc between 1°N and 3°S: Paleomagnetic, radiometric and fossil evidence. Earth and Planetary Science Letters 249, 400–414. https://doi.org/10.1016/j.epsl.2006.07.008

M

Mamberti, M., Lapierre, H., Bosch, D., Jaillard, E., Hernandez, J., Polvé, M., 2004. The Early Cretaceous San Juan Plutonic Suite, Ecuador: a magma chamber in an oceanic plateau? Can. J. Earth Sci. 41, 1237–1258. https://doi.org/10.1139/e04-060

Manchuel, K., Régnier, M., Béthoux, N., Font, Y., Sallarès, V., Díaz, J., Yepes, H., 2011. New insights on the interseismic active deformation along the North Ecuadorian–South Colombian (NESC) margin. Tectonics 30. https://doi.org/10.1029/2010TC002757

Marcaillou, B., Charvis, P., Collot, J.-Y., 2006. Structure of the Malpelo Ridge (Colombia) from seismic and gravity modelling. Mar Geophys Res 27, 289–300. https://doi.org/10.1007/s11001-006-9009-y

Marín-Cerón, M.I., Leal-Mejía, H., Bernet, M., Mesa-García, J., 2019. Late Cenozoic to Modern-Day Volcanism in the Northern Andes: A Geochronological, Petrographical, and Geochemical Review, in: Cediel, F., Shaw, R.P. (Eds.), Geology and Tectonics of Northwestern South America: The Pacific-Caribbean-Andean Junction, Frontiers in Earth Sciences. Springer International Publishing, Cham, pp. 603–648. https://doi.org/10.1007/978-3-319-76132-9_8

Martinod, J., Guillaume, B., Espurt, N., Faccenna, C., Funiciello, F., Regard, V., 2013. Effect of aseismic ridge subduction on slab geometry and overriding plate deformation: Insights from analogue modeling. Tectonophysics 588, 39–55. https://doi.org/10.1016/j.tecto.2012.12.010

Martinod, J., Husson, L., Roperch, P., Guillaume, B., Espurt, N., 2010. Horizontal subduction zones, convergence velocity and the building of the Andes. Earth and Planetary Science Letters 299, 299–309. https://doi.org/10.1016/j.epsl.2010.09.010

Martinod, J., Regard, V., Letourmy, Y., Henry, H., Hassani, R., Baratchart, S., Carretier, S., 2016. How do subduction processes contribute to forearc Andean uplift? Insights from numerical models. Journal of Geodynamics, Subduction and Orogeny 96, 6–18. https://doi.org/10.1016/j.jog.2015.04.001

Mayes, C.L., Lawver, L.A., Sandwell, D.T., 1990. Tectonic history and new isochron chart of the south Pacific. Journal of Geophysical Research: Solid Earth 95, 8543–8567. https://doi.org/10.1029/JB095iB06p08543

McCourt, W., Duque, P., Pilatasig, L.F., 1997. Geology of the Cordillera Occidental of Ecuador between 1°00’ and 2°00’S (No. 3), Proyecto de Desarrollo Minero y Control Ambiental. Cogidem - Brithis Geological Survey, Quito.

McDougall, I., Harrison, T.M., 1999. Geochronology and Thermochronology by the 40Ar/39Ar Method. Oxford University Press.

McGeary, S., Nur, A., Ben-Avraham, Z., 1985. Spatial gaps in arc volcanism: The effect of collision or subduction of oceanic plateaus. Tectonophysics, Collision Tectonics: Deformation of Continental Lithosphere 119, 195–221. https://doi.org/10.1016/0040-1951(85)90039-3

Merrihue, C., Turner, G., 1966. Potassium-argon dating by activation with fast neutrons. Journal of Geophysical Research (1896-1977) 71, 2852–2857. https://doi.org/10.1029/JZ071i011p02852

Meschede, M., Barckhausen, U., 2001. The relationship of the Cocos and Carnegie ridges: age constraints from paleogeographic reconstructions. Int J Earth Sci 90, 386–392. https://doi.org/10.1007/s005310000155

Meschede, M., Barckhausen, U., 2000. Plate Tectonic Evolution of the Cocos-Nazca Spreading Center. Proc. ODP, Sci. Results, Fluid, Mass, and Thermal Fluxes in the Pacific Margin of Costa Rica 170, 1–10. https://doi.org/doi:10.2973/odp.proc.sr.170.009.2000

Michaud, F., Witt, C., Royer, J.-Y., 2009. Influence of the subduction of the Carnegie volcanic ridge on Ecuadorian geology: Reality and fiction, in: Ramos, V.A., Dickinson, W.R., Kay, S.M. (Eds.), Backbone of the Americas: Shallow Subduction, Plateau Uplift, and Ridge and Terrane Collision, Memoir - Geological Society of America. The Geological Society of America, pp. 217–228. https://doi.org/10.1130/2009.1204(10)

Mitchell, J.G., 1968. The argon-40argon-39 method for potassium-argon age determination. Geochimica et Cosmochimica Acta 32, 781–790. https://doi.org/10.1016/0016-7037(68)90012-4

Monzier, M., Robin, C., Samaniego, P., Hall, M.L., Cotten, J., Mothes, P., Arnaud, N., 1999. Sangay volcano, Ecuador: structural development, present activity and petrology. Journal of Volcanology and Geothermal Research 90, 49–79. https://doi.org/10.1016/S0377-0273(99)00021-9

Morell, K.D., 2015. Late Miocene to recent plate tectonic history of the southern Central America convergent margin. Geochemistry, Geophysics, Geosystems 16, 3362–3382. https://doi.org/10.1002/2015GC005971

Mothes, P.A., Hall, M.L., 2008a. Rhyolitic calderas and centers clustered within the active andesitic belt of Ecuador's Eastern Cordillera, in: Volume 3: Collapse Calderas Workshop. Presented at the IOP Conference Series: Earth and Environmental Science, IOP Publishing, Querétaro, Mexico, p. 012007. https://doi.org/10.1088/1755-1307/3/1/012007

Mothes, P.A., Hall, M.L., 2008b. The plinian fallout associated with Quilotoa's 800 yr BP eruption, Ecuadorian Andes. Journal of Volcanology and Geothermal Research, Recent and active volcanism in the Ecuadorian Andes 176, 56–69. https://doi.org/10.1016/j.jvolgeores.2008.05.018

Murcia, H., Borrero, C., Németh, K., 2019. Overview and plumbing system implications of monogenetic volcanism in the northernmost Andes' volcanic province. Journal of Volcanology and Geothermal Research, Maar and environmental change - monogenetic volcanism in changing environments 383, 77–87. https://doi.org/10.1016/j.jvolgeores.2018.06.013

N

Narvaez, D.F., Rose-Koga, E.F., Samaniego, P., Koga, K.T., Hidalgo, S., 2018. Constraining magma sources using primitive olivine-hosted melt inclusions from Puñalica and Sangay volcanoes (Ecuador). Contrib Mineral Petrol 173, 1–25. https://doi.org/10.1007/s00410-018-1508-8

Nier, A.O., 1950. A Redetermination of the Relative Abundances of the Isotopes of Carbon, Nitrogen, Oxygen, Argon, and Potassium. Phys. Rev. 77, 789–793. https://doi.org/10.1103/PhysRev.77.789

Norabuena, E.O., Dixon, T.H., Stein, S., Harrison, C.G.A., 1999. Decelerating Nazca-South America and Nazca-Pacific Plate motions. Geophysical Research Letters 26, 3405–3408. https://doi.org/10.1029/1999GL005394

Núñez, A., Gómez, J., Rodríguez, G., 2001. Vulcanismo básico al sureste de la ciudad de Ibagué, departamento del Tolima (Colombia). Presented at the VIII Congreso Colombiano de Geología, Manizales, Colombia.

Nur, A., Ben-Avraham, Z., 1983. Volcanic gaps due to oblique consumption of aseismic ridges. Tectonophysics, Third Annual Symposium of the Geodynamics Research Program, Texas A & M University 99, 355–362. https://doi.org/10.1016/0040-1951(83)90112-9

O-P

O'Connor, J.M., Stoffers, P., Wijbrans, Jan.R., Worthington, T.J., 2007. Migration of widespread long-lived volcanism across the Galápagos Volcanic Province: Evidence for a broad hotspot melting anomaly? Earth and Planetary Science Letters 263, 339–354. https://doi.org/10.1016/j.epsl.2007.09.007

Opdyke, N.D., Hall, M., Mejia, V., Huang, K., Foster, D.A., 2006. Time-averaged field at the equator: Results from Ecuador. Geochemistry, Geophysics, Geosystems 7. https://doi.org/10.1029/2005GC001221

Pacheco, D., 2013. Estudio Geológico de las formaciones Cuaternarias en la zona San Antonio de Pichincha - Pomasqui (Engineer memoir). Escuela Politécnica Nacional, Quito, Ecuador.

Pallares, C., Quidelleur, X., Debreil, J.A., Antoine, C., Sarda, P., Tchilinguirian, P., Delpech, G., Gillot, P.-Y., 2019. Quaternary evolution of the El Tromen volcanic system, Argentina, based on new K-Ar and geochemical data: Insights for temporal evolution of magmatic processes between arc and back-arc settings. Journal of South American Earth Sciences 90, 338–354. https://doi.org/10.1016/j.jsames.2018.12.022

Pallares, C., Quidelleur, X., Gillot, P.-Y., Kluska, J.-M., Tchilinguirian, P., Sarda, P., 2016. The temporal evolution of back-arc magmas from the Auca Mahuida shield volcano (Payenia Volcanic Province, Argentina). Journal of Volcanology and Geothermal Research 323, 19–37. https://doi.org/10.1016/j.jvolgeores.2016.04.043

Pardo-Casas, F., Molnar, P., 1987. Relative motion of the Nazca (Farallon) and South American Plates since Late Cretaceous time. Tectonics 6, 233–248. https://doi.org/10.1029/TC006i003p00233

Peccerillo, A., Taylor, S.R., 1976. Geochemistry of eocene calc-alkaline volcanic rocks from the Kastamonu area, Northern Turkey. Contr. Mineral. and Petrol. 58, 63–81. https://doi.org/10.1007/BF00384745

Pedraza Garcia, P., Vargas, C.A., Monsalve J., H., 2007. Geometric model of the Nazca plate subduction in southwest Colombia. Earth Sciences Research Journal 11, 124–134.

Pilger, R.H., 1981. Plate reconstructions, aseismic ridges, and low-angle subduction beneath the Andes. GSA Bulletin 92, 448–456. https://doi.org/10.1130/0016-7606(1981)92<448:PRARAL>2.0.CO;2

Pilicita, B.F., 2013. Estudio de fuentes termales, fallas geológicas, descarga de calor en la Caldera de Chacana y el aprovechamiento actual del recurso geotérmico (Engineer memoir). Escuela Politécnica Nacional, Quito, Ecuador.

Porter, R., Gilbert, H., Zandt, G., Beck, S., Warren, L., Calkins, J., Alvarado, P., Anderson, M., 2012. Shear wave velocities in the Pampean flat-slab region from Rayleigh wave tomography: Implications for slab and upper mantle hydration. Journal of Geophysical Research: Solid Earth 117. https://doi.org/10.1029/2012JB009350

Portner, D.E., Rodríguez, E.E., Beck, S., Zandt, G., Scire, A., Rocha, M.P., Bianchi, M.B., Ruiz, M., França, G.S., Condori, C., Alvarado, P., 2020. Detailed Structure of the Subducted Nazca Slab into the Lower Mantle Derived From Continent-Scale Teleseismic P Wave Tomography. Journal of Geophysical Research: Solid Earth 125, e2019JB017884. https://doi.org/10.1029/2019JB017884

Potts, L.V., Hernandez, O., von Frese, R.R., Schmidt, M., 2005. Architecture of the Northwest Andean Microplates. AGU Spring Meeting Abstracts 43, T43D-05.

Pousse-Beltran, L., Vassallo, R., Audemard, F., Jouanne, F., Carcaillet, J., Pathier, E., Volat, M., 2017. Pleistocene slip rates on the Boconó fault along the North Andean Block plate boundary, Venezuela. Tectonics 36, 1207–1231. https://doi.org/10.1002/2016TC004305

Pradler, J., Singh, B., Yavin, I., 2013. On an unverified nuclear decay and its role in the DAMA experiment. Physics Letters B 720, 399–404. https://doi.org/10.1016/j.physletb.2013.02.033

Pratt, W.T., Duque, P., Ponce, M., 2005. An autochthonous geological model for the eastern Andes of Ecuador. Tectonophysics, Andean Geodynamics: 399, 251–278. https://doi.org/10.1016/j.tecto.2004.12.025

Pratt, W.T., Figueroa, J., Flores, B., 1997. Geology of the Cordillera Occidental of Ecuador between 3°00' and 4°00'S (No. 1), Proyecto de Desarrollo Minero y Control Ambiental. Cogidem - Brithis Geological Survey, Quito.

Pure, L.R., Leonard, G.S., Townsend, D.B., Wilson, C.J.N., Calvert, A.T., Cole, R.P., Conway, C.E., Gamble, J.A., Smith, T. 'Bubs,' 2020. A high resolution 40Ar/39Ar lava chronology and edifice construction history for Tongariro volcano, New Zealand. Journal of Volcanology and Geothermal Research 403, 106993. https://doi.org/10.1016/j.jvolgeores.2020.106993

Q

Quidelleur, X., Carlut, J., Soler, V., Valet, J.-P., Gillot, P.-Y., 2003. The age and duration of the Matuyama–Brunhes transition from new K–Ar data from La Palma (Canary Islands) and revisited 40Ar/39Ar ages. Earth and Planetary Science Letters 208, 149–163. https://doi.org/10.1016/S0012-821X(03)00053-0

Quidelleur, X., Gillot, P.-Y., Carlut, J., Courtillot, V., 1999. Link between excursions and paleointensity inferred from abnormal field directions recorded at La Palma around 600 ka. Earth and Planetary Science Letters 168, 233–242. https://doi.org/10.1016/S0012-821X(99)00061-8

Quidelleur, X., Gillot, P.-Y., Soler, V., Lefèvre, J.-C., 2001. K/Ar dating extended into the last millennium: Application to the youngest effusive episode of the Teide Volcano (Spain). Geophysical Research Letters 28, 3067–3070. https://doi.org/10.1029/2000GL012821

Quidelleur, X., Michon, L., Famin, V., Geffray, M.-C., Danišík, M., Gardiner, N., Rusquet, A., Zakaria, M.G., 2022. Holocene volcanic activity in Anjouan Island (Comoros archipelago) revealed by new Cassignol-Gillot groundmass K–Ar and 14C ages. Quaternary Geochronology 67, 101236. https://doi.org/10.1016/j.quageo.2021.101236

Quinteros, J., Sobolev, S.V., 2013. Why has the Nazca plate slowed since the Neogene? Geology 41, 31–34. https://doi.org/10.1130/G33497.1

R

Raczek, I., Stoll, B., Hofmann, A.W., Peter Jochum, K., 2001. High-Precision Trace Element Data for the USGS Reference Materials BCR-1, BCR-2, BHVO-1, BHVO-2, AGV-1, AGV-2, DTS-1, DTS-2, GSP-1 and GSP-2 by ID-TIMS and MIC-SSMS. Geostandards Newsletter 25, 77–86. https://doi.org/10.1111/j.1751-908X.2001.tb00789.x

Ramos, V.A., 1999. Plate tectonic setting of the Andean Cordillera. Episodes 22, 183–190. https://doi.org/10.18814/epiiugs/1999/v22i3/005

Ramos, V.A., Folguera, A., 2009. Andean flat-slab subduction through time. Geological Society, London, Special Publications 327, 31–54. https://doi.org/10.1144/SP327.3

Renne, P.R., Mulcahy, S.R., Cassata, W.S., Morgan, L.E., Kelley, S.P., Hlusko, L.J., Njau, J.K., 2012. Retention of inherited Ar by alkali feldspar xenocrysts in a magma: Kinetic constraints from Ba zoning profiles. Geochimica et Cosmochimica Acta 93, 129–142. https://doi.org/10.1016/j.gca.2012.06.029

Renne, P.R., Swisher, C.C., Deino, A.L., Karner, D.B., Owens, T.L., DePaolo, D.J., 1998. Intercalibration of standards, absolute ages and uncertainties in 40Ar/39Ar dating. Chemical Geology 145, 117–152. https://doi.org/10.1016/S0009-2541(97)00159-9

Révillon, S., Hallot, E., Arndt, N.T., Chauvel, C., Duncan, R.A., 2000. A Complex History for the Caribbean Plateau: Petrology, Geochemistry, and Geochronology of the Beata Ridge, South Hispaniola. The Journal of Geology 108, 641–661. https://doi.org/10.1086/317953

Reynaud, C., Jaillard, É., Lapierre, H., Mamberti, M., Mascle, G.H., 1999. Oceanic plateau and island arcs of southwestern Ecuador: their place in the geodynamic evolution of northwestern South America. Tectonophysics 307, 235–254. https://doi.org/10.1016/S0040-1951(99)00099-2

Riel, N., Guillot, S., Jaillard, E., Martelat, J.-E., Paquette, J.-L., Schwartz, S., Goncalves, P., Duclaux, G., Thebaud, N., Lanari, P., Janots, E., Yuquilema, J., 2013. Metamorphic and geochronogical study of the Triassic El Oro metamorphic complex, Ecuador: Implications for high-temperature metamorphism in a forearc zone. Lithos 156–159, 41–68. https://doi.org/10.1016/j.lithos.2012.10.005

Rivera, M., Samaniego, P., Vela, J., Le Pennec, J.-L., Guillou, H., Paquette, J.-L., Liorzou, C., 2020. The eruptive chronology of the Yucamane-Calientes compound volcano: A potentially active edifice of the Central Andes (southern Peru). Journal of Volcanology and Geothermal Research 393, 106787. https://doi.org/10.1016/j.jvolgeores.2020.106787

Robertson, K.G., Lage, A.F., L, J.L.C., 2002. Geomorfología volcánica, actividad reciente y clasificación en Colombia. Cuadernos de Geografía: Revista Colombiana de Geografía 11, 37–76.

Robin, C., Eissen, J.-P., Samaniego, P., Martin, H., Hall, M., Cotten, J., 2009. Evolution of the late Pleistocene Mojanda–Fuya Fuya volcanic complex (Ecuador), by progressive adakitic involvement in mantle magma sources. Bulletin of Volcanology 71, 233–258. https://doi.org/10.1007/s00445-008-0219-9

Robin, C., Eissen, J.-P., Samaniego, P., Martin, H., Hall, M., Cotten, J., 2008a. Evolution of the late Pleistocene Mojanda–Fuya Fuya volcanic complex (Ecuador), by progressive adakitic involvement in mantle magma sources. Bull Volcanol 71, 233. https://doi.org/10.1007/s00445-008-0219-9

Robin, C., Hall, M., Jimenez, M., Monzier, M., Escobar, P., 1997. Mojanda volcanic complex (Ecuador): development of two adjacent contemporaneous volcanoes with contrasting eruptive styles and magmatic suites. Journal of South American Earth Sciences 10, 345–359. https://doi.org/10.1016/S0895-9811(97)00030-8

Robin, C., Samaniego, P., Le Pennec, J.-L., Fornari, M., Mothes, P., van der Plicht, J., 2010. New radiometric and petrological constraints on the evolution of the Pichincha volcanic complex (Ecuador). Bull Volcanol 72, 1109–1129. https://doi.org/10.1007/s00445-010-0389-0

Robin, C., Samaniego, P., Le Pennec, J.-L., Mothes, P., van der Plicht, J., 2008b. Late Holocene phases of dome growth and Plinian activity at Guagua Pichincha volcano (Ecuador). Journal of Volcanology and Geothermal Research, Recent and active volcanism in the Ecuadorian Andes 176, 7–15. https://doi.org/10.1016/j.jvolgeores.2007.10.008

Romeuf, N., Aguirre, L., Soler, P., Feraud, G., Jaillard, E., Ruffet, G., 1995. Middle Jurassic volcanism in the Northern and Central Andes. Andean Geology 22, 245–259. https://doi.org/10.5027/andgeoV22n2-a08

Rossel, P., Oliveros, V., Ducea, M.N., Charrier, R., Scaillet, S., Retamal, L., Figueroa, O., 2013. The Early Andean subduction system as an analog to island arcs: Evidence from across-arc geochemical variations in northern Chile. Lithos 179, 211–230. https://doi.org/10.1016/j.lithos.2013.08.014

Royden, L.H., Husson, L., 2006. Trench motion, slab geometry and viscous stresses in subduction systems. Geophysical Journal International 167, 881–905. https://doi.org/10.1111/j.1365-246X.2006.03079.x

S

Samaniego, P., Barba, D., Robin, C., Fornari, M., Bernard, B., 2012. Eruptive history of Chimborazo volcano (Ecuador): A large, ice-capped and hazardous compound volcano in the Northern Andes. Journal of Volcanology and Geothermal Research 221–222, 33–51. https://doi.org/10.1016/j.jvolgeores.2012.01.014

Samaniego, P., Martin, H., Monzier, M., Robin, C., Fornari, M., Eissen, J.-P., Cotten, J., 2005. Temporal Evolution of Magmatism in the Northern Volcanic Zone of the Andes: The Geology and Petrology of Cayambe Volcanic Complex (Ecuador). Journal of Petrology 46, 2225–2252. https://doi.org/10.1093/petrology/egi053

Samaniego, P., Monzier, M., Robin, C., Hall, M.L., 1998. Late Holocene eruptive activity at Nevado Cayambe Volcano, Ecuador. Bull Volcanol 59, 451–459. https://doi.org/10.1007/s004450050203

Samaniego, P., Robin, C., Chazot, G., Bourdon, E., Cotten, J., 2010. Evolving metasomatic agent in the Northern Andean subduction zone, deduced from magma composition of the long-lived Pichincha volcanic complex (Ecuador). Contrib Mineral Petrol 160, 239–260. https://doi.org/10.1007/s00410-009-0475-5

Samper, A., Quidelleur, X., Boudon, G., Le Friant, A., Komorowski, J.C., 2008. Radiometric dating of three large volume flank collapses in the Lesser Antilles Arc. Journal of Volcanology and Geothermal Research 176, 485–492. https://doi.org/10.1016/j.jvolgeores.2008.04.018

Santamaría, S., 2017. Catálogo de eventos volcánicos ocurridos en el Ecuador continental desde el Plioceno y análisis de la frecuencia eruptiva (Engineer memoir). Escuela Politécnica Nacional, Quito, Ecuador.

Santamaría, S., Quidelleur, X., Hidalgo, S., Samaniego, P., Le Pennec, J.-L., Liorzou, C., Lahitte, P., Córdova, M., Espin, P., submitted. Geochronological evolution of the potentially active Iliniza Volcano (Ecuador) based on new K-Ar ages. Journal of Volcanology and Geothermal Research.

Schaen, A.J., Jicha, B.R., Hodges, K.V., Vermeesch, P., Stelten, M.E., Mercer, C.M., Phillips, D., Rivera, T.A., Jourdan, F., Matchan, E.L., Hemming, S.R., Morgan, L.E., Kelley, S.P., Cassata, W.S., Heizler, M.T., Vasconcelos, P.M., Benowitz, J.A., Koppers, A.A.P., Mark, D.F., Niespolo, E.M., Sprain, C.J., Hames, W.E., Kuiper, K.F., Turrin, B.D., Renne, P.R., Ross, J., Nomade, S., Guillou, H., Webb, L.E., Cohen, B.A., Calvert, A.T., Joyce, N., Ganerød, M., Wijbrans, J., Ishizuka, O., He, H., Ramirez, A., Pfänder, J.A., Lopez-Martínez, M., Qiu, H., Singer, B.S., 2020. Interpreting and reporting 40Ar/39Ar geochronologic data. GSA Bulletin 133, 461–487. https://doi.org/10.1130/B35560.1

Schiano, P., Monzier, M., Eissen, J.-P., Martin, H., Koga, K.T., 2010. Simple mixing as the major control of the evolution of volcanic suites in the Ecuadorian Andes. Contrib Mineral Petrol 160, 297–312. https://doi.org/10.1007/s00410-009-0478-2

Schütte, P., Chiaradia, M., Beate, B., 2010. Geodynamic controls on Tertiary arc magmatism in Ecuador: Constraints from U–Pb zircon geochronology of Oligocene–Miocene intrusions and regional age distribution trends. Tectonophysics 489, 159–176. https://doi.org/10.1016/j.tecto.2010.04.015

Schwarz, W.H., Trieloff, M., 2007. Intercalibration of 40Ar–39Ar age standards NL-25, HB3gr hornblende, GA1550, SB-3, HD-B1 biotite and BMus/2 muscovite. Chemical Geology 242, 218–231. https://doi.org/10.1016/j.chemgeo.2007.03.016

Seton, M., Müller, R.D., Zahirovic, S., Gaina, C., Torsvik, T., Shephard, G., Talsma, A., Gurnis, M., Turner, M., Maus, S., Chandler, M., 2012. Global continental and ocean basin reconstructions since 200Ma. Earth-Science Reviews 113, 212–270. https://doi.org/10.1016/j.earscirev.2012.03.002

Siebert, L., Simkin, T., Kimberly, P., 2011. Volcanoes of the World: Third Edition. University of California Press.

Singer, B.S., Wijbrans, J.R., Nelson, S.T., Pringle, M.S., Feeley, T.C., Dungan, M.A., 1998. Inherited argon in a Pleistocene andesite lava: 40Ar/39Ar incremental-heating and laser-fusion analyses of plagioclase. Geology 26, 427–430. https://doi.org/10.1130/0091-7613(1998)026<0427:IAIAPA>2.3.CO;2

Skinner, S.M., Clayton, R.W., 2013. The lack of correlation between flat slabs and bathymetric impactors in South America. Earth and Planetary Science Letters 371–372, 1–5. https://doi.org/10.1016/j.epsl.2013.04.013

Skinner, S.M., Clayton, R.W., 2011. An Evaluation of Proposed Mechanisms of Slab Flattening in Central Mexico. Pure Appl. Geophys. 168, 1461–1474. https://doi.org/10.1007/s00024-010-0200-3

Sobolev, S.V., Babeyko, A.Y., 2005. What drives orogeny in the Andes? Geology 33, 617–620. https://doi.org/10.1130/G21557AR.1

Somoza, R., 1998. Updated Nazca (Farallon)—South America relative motions during the last 40 My: implications for mountain building in the central Andean region. Journal of South American Earth Sciences 11, 211–215. https://doi.org/10.1016/S0895-9811(98)00012-1

Somoza, R., Ghidella, M.E., 2012. Late Cretaceous to recent plate motions in western South America revisited. Earth and Planetary Science Letters 331–332, 152–163. https://doi.org/10.1016/j.epsl.2012.03.003

Spikings, R., Cochrane, R., Villagomez, D., Van der Lelij, R., Vallejo, C., Winkler, W., Beate, B., 2015. The geological history of northwestern South America: from Pangaea to the early collision of the Caribbean Large Igneous Province (290–75Ma). Gondwana Research 27, 95–139. https://doi.org/10.1016/j.gr.2014.06.004

Spikings, R., Crowhurst, P.V., 2004. (U–Th)/He thermochronometric constraints on the late Miocene–Pliocene tectonic development of the northern Cordillera Real and the Interandean Depression, Ecuador. Journal of South American Earth Sciences 17, 239–251. https://doi.org/10.1016/j.jsames.2004.07.001

Spikings, R., Crowhurst, P.V., Winkler, W., Villagomez, D., 2010. Syn- and post-accretionary cooling history of the Ecuadorian Andes constrained by their in-situ and detrital thermochronometric

record. Journal of South American Earth Sciences 30, 121–133. https://doi.org/10.1016/j.jsames.2010.04.002

Spikings, R., Reitsma, M.J., Boekhout, F., Mišković, A., Ulianov, A., Chiaradia, M., Gerdes, A., Schaltegger, U., 2016. Characterisation of Triassic rifting in Peru and implications for the early disassembly of western Pangaea. Gondwana Research 35, 124–143. https://doi.org/10.1016/j.gr.2016.02.008

Spikings, R., Seward, D., Winkler, W., Ruiz, G.M., 2000. Low-temperature thermochronology of the northern Cordillera Real, Ecuador: Tectonic insights from zircon and apatite fission track analysis. Tectonics 19, 649–668. https://doi.org/10.1029/2000TC900010

Spikings, R., Winkler, W., Hughes, R.A., Handler, R., 2005. Thermochronology of allochthonous terranes in Ecuador: Unravelling the accretionary and post-accretionary history of the Northern Andes. Tectonophysics, Andean Geodynamics: 399, 195–220. https://doi.org/10.1016/j.tecto.2004.12.023

Spikings, R., Winkler, W., Seward, D., Handler, R., 2001. Along-strike variations in the thermal and tectonic response of the continental Ecuadorian Andes to the collision with heterogeneous oceanic crust. Earth and Planetary Science Letters 186, 57–73. https://doi.org/10.1016/S0012-821X(01)00225-4

Starr, J.P., 1984. Geology and petrology of Rumiñahui volcano, Ecuador (Master's thesis). Departament of Geology of the University the Oregon, Oregon, USA.

Steiger, R.H., Jäger, E., 1977. Subcommission on geochronology: Convention on the use of decay constants in geo- and cosmochronology. Earth and Planetary Science Letters 36, 359–362. https://doi.org/10.1016/0012-821X(77)90060-7

Steinmann, M., 1997. The Cuenca basin of southern Ecuador: tectono-sedimentary history and the Tertiary Andean evolution (Ph.D. thesis). ETH Zurich, Switzerland. https://doi.org/10.3929/ethz-a-001843356

Steinmann, M., Hungerbühler, D., Seward, D., Winkler, W., 1999. Neogene tectonic evolution and exhumation of the southern Ecuadorian Andes: a combined stratigraphy and fission-track approach. Tectonophysics 307, 255–276. https://doi.org/10.1016/S0040-1951(99)00100-6

Stern, C.R., 2004. Active Andean volcanism: its geologic and tectonic setting. Revista geológica de Chile 31, 161–206. https://doi.org/10.4067/S0716-02082004000200001

Sun, S.-S., McDonough, W.F., 1989. Chemical and isotopic systematics of oceanic basalts: implications for mantle composition and processes. Geol. Soc. Lond. Spec. Publ. 42, 313–345. https://doi.org/10.1144/GSL.SP.1989.042.01.19

Syracuse, E.M., van Keken, P.E., Abers, G.A., 2010. The global range of subduction zone thermal models. Physics of the Earth and Planetary Interiors, Special Issue on Deep Slab and Mantle Dynamics 183, 73–90. https://doi.org/10.1016/j.pepi.2010.02.004

Szakács, A., 2010. From a definition of volcano to conceptual volcanology. https://doi.org/10.1130/2010.2470(05)

Székely, B., Karátson, D., 2004. DEM-based morphometry as a tool for reconstructing primary volcanic landforms: examples from the Börzsöny Mountains, Hungary. Geomorphology 63, 25–37. https://doi.org/10.1016/j.geomorph.2004.03.008

T

Taboada, A., Rivera, L.A., Fuenzalida, A., Cisternas, A., Philip, H., Bijwaard, H., Olaya, J., Rivera, C., 2000. Geodynamics of the northern Andes: Subductions and intracontinental deformation (Colombia). Tectonics 19, 787–813. https://doi.org/10.1029/2000TC900004

Tavera, H., Buforn, E., 2001. Source mechanism of earthquakes in Peru. Journal of Seismology 5, 519–540. https://doi.org/10.1023/A:1012027430555

Taylor, S.R., McLennan, S.M., 1985. The continental crust: Its composition and evolution. Blackwell Scientific Pub.,Palo Alto, CA.

Telenchana, E., 2017. Estudio Geovulcanológico del volcán Chiles - Provincia del Carchi (Tesis de Ingeniería). Escuela Politécnica Nacional.

Telenchana, E., Hidalgo, S., Bernard, B., Beate, B., Bablon, M., Quidelleur, X., 2019. Lithological units of Chiles Volcano, in: Abstract Volume of the 8th International Symposium on Andean Geodynamics. Presented at the 8th International Symposium on Andean Geodynamics, Quito, Ecuador.

Thorpe, R.S., 1984. The Tectonic Setting of Active Andean Volcanism, in: Harmon, R.S., Barreiro, B.A. (Eds.), Andean Magmatism: Chemical and Isotopic Constraints. Birkhäuser, Boston, MA, pp. 4–8. https://doi.org/10.1007/978-1-4684-7335-3_1

Tibaldi, A., Rovida, A., Corazzato, C., 2007. Late Quaternary kinematics, slip-rate and segmentation of a major Cordillera-parallel transcurrent fault: The Cayambe-Afiladores-Sibundoy system, NW South America. Journal of Structural Geology 29, 664–680. https://doi.org/10.1016/j.jsg.2006.11.008

Tolstykh, M.L., Naumov, V.B., Yarmolyuk, V.V., 2017. Adakites and adakitic melts: Compositions of rocks, quenched glasses, and inclusions in minerals. Petrology 25, 304–317. https://doi.org/10.1134/S0869591117020059

Toro, J., 2007. Enregistrement des surrections liées aux accrétions de terrains océaniques : les sédiments crétacé-paléogènes des Andes d'Equateur (Ph.D. thesis). Université Joseph Fourier - Grenoble I, Grenoble.

Tschopp, H.J., 1953. Oil Explorations in the Oriente of Ecuador, 1938–1950. AAPG Bulletin 37, 2303–2347. https://doi.org/10.1306/5CEADD94-16BB-11D7-8645000102C1865D

Tsunematsu, K., Bonadonna, C., 2015. Grain-size features of two large eruptions from Cotopaxi volcano (Ecuador) and implications for the calculation of the total grain-size distribution. Bull Volcanol 77, 1–12. https://doi.org/10.1007/s00445-015-0949-4

Turner, G., 1971. Argon 40-argon 39 dating: the optimization of irradiation parameters. Earth and Planetary Science Letters 10, 227–234. https://doi.org/10.1016/0012-821X(71)90010-0

Turner, G., Miller, J.A., Grasty, R.L., 1966. The thermal history of the Bruderheim meteorite. Earth and Planetary Science Letters 1, 155–157. https://doi.org/10.1016/0012-821X(66)90061-6

V

Vallejo, C., 2007. Evolution of the Western Cordillera in the Andes of Ecuador (Late Cretaceous-Paleogene) (Ph.D. thesis). University of Aberdeen, Zürich.

Vallejo, C., Almagor, S., Romero, C., Herrera, J.L., Escobar, V., Spikings, R., Winkler, W., Vermeesch, P., 2020. Sedimentology, Provenance and Radiometric Dating of the Silante Formation: Implications for the Cenozoic Evolution of the Western Andes of Ecuador. Minerals 10, 929. https://doi.org/10.3390/min10100929

Vallejo, C., Spikings, R., Horton, B.K., Luzieux, L., Romero, C., Winkler, W., Thomsen, T.B., 2019. Chapter 8 - Late cretaceous to miocene stratigraphy and provenance of the coastal forearc and Western Cordillera of Ecuador: Evidence for accretion of a single oceanic plateau fragment, in: Horton, B.K., Folguera, A. (Eds.), Andean Tectonics. Elsevier, pp. 209–236. https://doi.org/10.1016/B978-0-12-816009-1.00010-1

Vallejo, C., Spikings, R., Luzieux, L., Winkler, W., Chew, D., Page, L., 2006. The early interaction between the Caribbean Plateau and the NW South American Plate. Terra Nova 18, 264–269. https://doi.org/10.1111/j.1365-3121.2006.00688.x

Vallejo, C., Winkler, W., Spikings, R., Luzieux, L., Heller, F., Bussy, F., 2009. Mode and timing of terrane accretion in the forearc of the Andes in Ecuador. Geological Society of America Memoirs 204, 197–216. https://doi.org/10.1130/2009.1204(09)

Valverde, V., 2014. Las avalanchas de escombros provenientes del volcán sangay: caracterización petrográfica-geoquímica (Engineer memoir). Escuela Politécnica Nacional, Quito, Ecuador.

Vargas, C.A., Mann, P., 2013. Tearing and Breaking Off of Subducted Slabs as the Result of Collision of the Panama Arc-Indenter with Northwestern South AmericaTearing and Breaking Off of Subducted Slabs as the Result of Collision of the Panama Arc-Indenter. Bulletin of the Seismological Society of America 103, 2025–2046. https://doi.org/10.1785/0120120328

Vasconez, F.J., 2015. Estimación de la masa de magma contenida en los depósitos del Complejo Volcánico Pululahua (CVP) (Engineer memoir). Escuela Politécnica Nacional, Quito, Ecuador.

Vezzoli, L., Apuani, T., Corazzato, C., Uttini, A., 2017. Geological and geotechnical characterization of the debris avalanche and pyroclastic deposits of Cotopaxi Volcano (Ecuador). A contribute to instability-related hazard studies. Journal of Volcanology and Geothermal Research 332, 51–70. https://doi.org/10.1016/j.jvolgeores.2017.01.004

Villagómez, D., 2003. Evolución geológica Plio cuaternaria del valle Interandino central en Ecuador zona Quito Guayllabamba San Antonio (Engineer memoir). Escuela Politécnica Nacional, Quito, Ecuador.

Villagomez, D., 2003. Evolución Geológica Plio-cuaternaria del Valle Interandino Central en Ecuador (zona de Quito-Guayllabamba-San Antonio de Pichincha) (Engineer memoir). Escuela Politécnica Nacional, Quito, Ecuador.

Villagómez, D., Spikings, R., Magna, T., Kammer, A., Winkler, W., Beltrán, A., 2011. Geochronology, geochemistry and tectonic evolution of the Western and Central cordilleras of Colombia. Lithos 125, 875–896. https://doi.org/10.1016/j.lithos.2011.05.003

Villares, F., 2010. Estudio geovulcanologico de la zona sur de la caldera Chacana, provincias de Napo - Pichincha (Engineer memoir). Escuela Politécnica Nacional, Quito, Ecuador.

Villares, F., Garcia-Casco, A., Blanco-Quintero, I.F., Montes, C., Reyes, P.S., Cardona, A., 2020. The Peltetec ophiolitic belt (Ecuador): a window to the tectonic evolution of the Triassic margin of western Gondwana. International Geology Review 0, 1–25. https://doi.org/10.1080/00206814.2020.1830313

von Hillebrandt, C., 1989. Estudio geovolcanológico del complejo volcánico Cuicocha-Cotacachi y sus aplicaciones, Provincia de Imbabura (Master's thesis). Escuela Politécnica Nacional, Quito, Ecuador.

W-Y

Werner, R., Hoernle, K., Barckhausen, U., Hauff, F., 2003. Geodynamic evolution of the Galápagos hot spot system (Central East Pacific) over the past 20 m.y.: Constraints from morphology, geochemistry, and magnetic anomalies. Geochemistry, Geophysics, Geosystems 4. https://doi.org/10.1029/2003GC000576

White, W.M., McBirney, A.R., Duncan, R.A., 1993. Petrology and geochemistry of the Galápagos Islands: Portrait of a pathological mantle plume. Journal of Geophysical Research: Solid Earth 98, 19533–19563. https://doi.org/10.1029/93JB02018

Wijbrans, J.R., Pringle, M.S., Koppers, A. a. P., Scheveers, R., 1995. Argon geochronology of small samples using the Vulkaan argon laserprobe. Proceedings of the Royal Netherlands Academy of Arts and Sciences 2, 185–218.

Winkler, W., Villagómez, D., Spikings, R., Abegglen, P., Tobler, St., Egüez, A., 2005. The Chota basin and its significance for the inception and tectonic setting of the inter-Andean depression in Ecuador. Journal of South American Earth Sciences, Cenozoic Andean Basin Evolution 19, 5–19. https://doi.org/10.1016/j.jsames.2004.06.006

Witt, C., Bourgois, J., 2010. Forearc basin formation in the tectonic wake of a collision-driven, coastwise migrating crustal block: The example of the North Andean block and the extensional Gulf of Guayaquil-Tumbes Basin (Ecuador-Peru border area). GSA Bulletin 122, 89–108. https://doi.org/10.1130/B26386.1

Witt, C., Bourgois, J., Michaud, F., Ordoñez, M., Jiménez, N., Sosson, M., 2006. Development of the Gulf of Guayaquil (Ecuador) during the Quaternary as an effect of the North Andean block tectonic escape. Tectonics 25. https://doi.org/10.1029/2004TC001723

Witt, C., Reynaud, J.Y., Barba, D., Poujol, M., Aizprua, C., Rivadeneira, M., Amberg, C., 2019. From accretion to forearc basin initiation: The case of SW Ecuador, Northern Andes. Sedimentary Geology 379, 138–157. https://doi.org/10.1016/j.sedgeo.2018.11.009

Yepes, H., Audin, L., Alvarado, A., Beauval, C., Aguilar, J., Font, Y., Cotton, F., 2016. A new view for the geodynamics of Ecuador: Implication in seismogenic source definition and seismic hazard assessment. Tectonics 35, 1249–1279. https://doi.org/10.1002/2015TC003941

Annexes

Research group ascending the Iliniza volcano. The photograph offers a view of the Machachi valley. From left to right: Corazón, Pasochoa, and Rumiñahui volcanoes. The Pilongo dome appears near the left edge of the picture.

Annexes

Contents

Volcanic history reconstruction in northern Ecuador: insights for eruptive and erosion rates on the whole Ecuadorian arc

Bablon, M., Quidelleur, X., Samaniego, P., Le Pennec, J.-L., Santamaría, S., Liorzou, C., Hidalgo, S., Eschbach, B. *(Bulletin of Volcanology, 2020)* 376

Glass shard K-Ar dating of the Chalupas caldera major eruption: Main Pleistocene stratigraphic marker of the Ecuadorian volcanic arc

Bablon, M., Quidelleur, X., Siani, G., Samaniego, P., Le Pennec, J.-L., Nouet, J., Liorzou, C., Santamaría, S., Hidalgo, S. *(Quaternary Geochronology, 2020)* 378

Pululahua dome complex, Ecuador: eruptive history, total magma output and potential hazards

Andrade, S.D., Müller, A.V., Vasconez, F.J., Beate, B., Aguilar, J., Santamaría, S. *(Journal of South American Earth Sciences, 2021)* 380

Instituto Geofísico – Escuela Politécnica Nacional, the Ecuadorian Seismology and Volcanology Service

Ramón, P., Vallejo, S., Mothes, P., Andrade, D., Vásconez, F., Yepes, H., Hidalgo, S., Santamaría, S. *(Volcanica, 2021)* 382

New groundmass K-Ar ages of Iliniza Volcano, Ecuador

Santamaria, S., Quidelleur, X., Hidalgo. S., Samaniego, P., Le Pennec, J.-L. *(ISAG 2019)* 384

Bulletin of Volcanology (2020) 82:11
https://doi.org/10.1007/s00445-019-1346-1

RESEARCH ARTICLE

Volcanic history reconstruction in northern Ecuador: insights for eruptive and erosion rates on the whole Ecuadorian arc

Mathilde Bablon[1,2] · Xavier Quidelleur[1] · Pablo Samaniego[3,4] · Jean-Luc Le Pennec[3,4] · Santiago Santamaría[1] · Céline Liorzou[5] · Silvana Hidalgo[4] · Bastien Eschbach[1]

Received: 15 March 2019 / Accepted: 27 November 2019
© International Association of Volcanology & Chemistry of the Earth's Interior 2020

Abstract

In the northern Andes, the Ecuadorian arc presents a large number of Quaternary volcanoes, spread over a rather restricted area. The origin of this volcanic clustering is not well understood, and only a few chronological data older than the Holocene are available in northern Ecuador to document the arc development stages. In this study, we present new K-Ar ages obtained on lava flow and pumice samples for Cushnirumi, Mojanda, Fuya Fuya, Imbabura, Cubilche, and Cusín volcanoes, located about 40 km north of Quito, the Ecuador's capital city. Our results show that the volcanic activity in the northern part of the Ecuadorian arc started at least at ~ 1 Ma and that construction of volcanoes mainly occurred during the last 500 ka. Together with the radiometric data, numerical reconstructions of the paleomorphology of the volcanoes are used to estimate the volume of emitted magmas and the amount of eroded material in order to quantify their eruptive and erosion rates. Emission rates of Ecuadorian volcanoes range between < 0.2 and 3.6 ± 2.1 km^3/kyr. Highest rates are obtained for volcanoes constructed over time periods shorter than 100 kyr by sporadic eruptive pulses, whereas lowest rates are calculated over longer periods that include quiescence phases. Erosion rates range between 0.02 ± 0.01 and 0.14 ± 0.09 km^3/kyr and highlight that volcanic edifices whose activity ended recently are rapidly dismantled by physicochemical processes. Finally, the spatial distribution of Quaternary volcanoes as well as the spatio-temporal evolution of lava geochemistry may reflect the progressive influence of the Carnegie Ridge at depth.

Keywords Ecuador · K-Ar dating · Volcanic arc · Eruptive rates · Erosion · Volumes

Highlights

The Quaternary volcanic activity of northern Ecuador started at least at ~ 1 Ma.

Volcanoes grew during sporadic activity pulses separated by quiescence periods.

Erosion processes depend on the exposure duration and on rock weathering.

The volcanism spatial distribution may be related to the Carnegie Ridge subduction.

Eruptive rates do not seem to be linked to the plate convergence velocity.

Editorial responsibility: R. Cioni; Deputy Executive Editor: J. Tadeucci

Electronic supplementary material The online version of this article (https://doi.org/10.1007/s00445-019-1346-1) contains supplementary material, which is available to authorized users.

✉ Xavier Quidelleur
xavier.quidelleur@u-psud.fr

Mathilde Bablon
mathilde.bablon@geoazur.unice.fr

[1] GEOPS, Université Paris-Sud, CNRS, Université Paris-Saclay, Rue du Belvédère, 91405 Orsay, France

[2] Université Côte d'Azur, CNRS, IRD, Observatoire de la Côte d'Azur, Géoazur, Sophia Antipolis, 06560 Valbonne, France

[3] Laboratoire Magmas et Volcans, Université Clermont Auvergne, CNRS, IRD, OPGC, F-63000 Clermont-Ferrand, France

[4] Instituto Geofísico, Escuela Politécnica Nacional, Ladrón de Guevara E11-253, Ap, 2759 Quito, Ecuador

[5] Université de Bretagne Occidentale, Domaines Océaniques IUEM, 29280 Plouzané, France

Published online: 06 January 2020

Quaternary Geochronology 57 (2020) 101053

Contents lists available at ScienceDirect

Quaternary Geochronology

journal homepage: http://www.elsevier.com/locate/quageo

Research paper

Glass shard K-Ar dating of the Chalupas caldera major eruption: Main Pleistocene stratigraphic marker of the Ecuadorian volcanic arc

Mathilde Bablon [a,b], Xavier Quidelleur [a,*], Giuseppe Siani [a], Pablo Samaniego [c,d], Jean-Luc Le Pennec [c,d], Julius Nouet [a], Céline Liorzou [e], Santiago Santamaría [a], Silvana Hidalgo [d]

[a] Université Paris-Saclay, CNRS, GEOPS, Orsay, 91405, France
[b] Université Côte d'Azur, CNRS, IRD, Observatoire de la Côte d'Azur, Géoazur, Sophia Antipolis, 06560, Valbonne, France
[c] Laboratoire Magmas et Volcans, Université Clermont Auvergne, CNRS, IRD, OPGC, F-63000, Clermont-Ferrand, France
[d] Instituto Geofísico, Escuela Politécnica Nacional, Ladrón de Guevara E11-253, Ap. 2759, Quito, Ecuador
[e] Université de Bretagne Occidentale, Laboratoire Géosciences Océan, IUEM, 29280, Plouzané, France

ARTICLE INFO

Keywords:
K-Ar dating
Glass shards
Ecuador
Chalupas
Ignimbrite eruption

ABSTRACT

New K-Ar ages obtained on juvenile pumice glass shards indicate that the Chalupas ignimbrite, one of the main Pleistocene tephra markers of the Ecuadorian arc, was emplaced at 216 ± 5 ka. Morphology and major and trace element contents of the glass shards are similar to those of ash layers from deep-sea cores and allow correlation between continental deposits and marine tephra layers. Based on biostratigraphy and $\delta^{18}O$ data, the age models of these cores support our K-Ar age. Fine ashes from the Chalupas eruption column have been found about 1000 km away from the source caldera, and the estimated deposit volume of both ignimbrite and co-ignimbrite deposits ranges from 200 to 265 km^3. This suggests that the Chalupas event could have been strong enough to reach the stratosphere and inject large amount of SO_2 in both hemispheres, possibly impacting global temperatures. In addition, the age of the Chalupas ignimbrite obtained here could provide a new radiometric constraint for the age of isotope stage 7 recorded in orbitally-tuned $\delta^{18}O$ deep-sea cores. This study highlights the relevance of K-Ar dating applied to small glass shards from massive ignimbrite deposits, and the potential that it represents to improve risk assessments in volcanic zones where dating crystals is not possible. Finally, detailed tephrochronology of deep-sea cores and correlation between marine ash-layers and continental volcanic deposits constitute a strong tool to investigate the eruptive history of an active volcanic arc whose proximal products have been eroded or deeply buried by younger deposit sequences.

1. Introduction

Major explosive caldera-forming eruptions are colossal volcanic phenomenon that can eject large volumes of tephra and volatiles into the atmosphere and spread tephra over wide areas. Such events can impact the local population, infrastructures and natural environment, namely the climate system at regional and even global scales (e.g. McCormick et al., 1995; Robock, 2000; Cole-Dai, 2010). Tephrochronology is a powerful tool for dating and correlating deposit sequences scattered over large areas. The method consists in comparing tephra features, such as their age or position in the stratigraphic column, their chemical and mineralogical composition, as well as glass shard morphology, in order to match the deposits associated with a single volcanic event (e.g., Lowe, 2011). Consequently, tephrochronology allows us to investigate magmatic processes, recurrence and impact of past major eruptions, and hence better define the volcanic hazards and its frequency-magnitude relationships. As the time period between tephra emission and deposit is mostly on the order of hours or days (Robock, 2000; Mills, 2000; Rose and Durant, 2009), dating tephra fallouts is a robust way to determine the age of the corresponding eruption. The $^{40}Ar/^{39}Ar$ single grain dating method applied on K-rich minerals, such as sanidine, biotite and even plagioclase crystals, is commonly used to date tephra older than ~50 ka, i.e. for which ^{14}C age determination is not possible. For instance, this technique has been used to accurately date the Young Toba Tuff and investigate the relationship between this major eruptive event and global cooling (e.g., Williams et al., 2009; Storey et al., 2012; Mark et al., 2014), or to date the Yellowstone Tuffs and study the eruptive history of the caldera (e.g., Ellis et al., 2012; Matthews et al., 2015). In offshore

* Corresponding author.
E-mail address: xavier.quidelleur@u-psud.fr (X. Quidelleur).

https://doi.org/10.1016/j.quageo.2020.101053

Available online 6 February 2020
1871-1014/© 2020 Elsevier B.V. All rights reserved.

Contents lists available at ScienceDirect

Journal of South American Earth Sciences

journal homepage: www.elsevier.com/locate/jsames

Pululahua dome complex, Ecuador: eruptive history, total magma output and potential hazards

S. Daniel Andrade [a], Anais Vásconez Müller [b,*], Francisco J. Vasconez [a], Bernardo Beate [c], Jorge Aguilar [a], Santiago Santamaría [d]

[a] Instituto Geofísico, Escuela Politécnica Nacional, Ladrón de Guevara E11-253, Quito, Ecuador
[b] School of Earth Sciences, University of Bristol, Bristol, BS8 1RJ, UK
[c] Departamento de Geología, Escuela Politécnica Nacional, Ladrón de Guevara E11-253, Quito, Ecuador
[d] GEOPS, Université Paris-Sud, CNRS, Université Paris-Saclay, Rue du Belvédère, 91405, Orsay, France

ARTICLE INFO

Keywords:
Pululahua
Lava dome
Total magma-output
Eruptive style transitions
Volcanic hazards

ABSTRACT

Pululahua is a potentially active dome complex located 15 km north of Quito. It is composed of sixteen dacitic-andesitic lava domes located inside and around a semi-rectangular depression. We divide its eruptive history into: (1) a first member characterized by effusive lava dome growth and collapse (Units I and II, >18–12 ka), (2) a second member consisting of at least four explosive eruptive phases (VEI ~4), responsible for the formation of a caldera-like depression (Unit III, 2.6–2.3 ka cal BP), and (3) a final member encompassing partially explosive dome growth inside the depression (Unit IV, 2.2 ka cal BP). Rock samples show no significant geochemical changes over time, except for a slight decrease in SiO_2 and a minor increase in MgO and Fe_2O_3 towards younger magmas. In addition, based on field measurements, a total minimum bulk volume of all domes and pyroclastic deposits is estimated at ~5.75 ± 0.14 km^3, yielding a dense rock equivalent of ~4.24 ± 0.1 km^3 and a total erupted magma mass of 10.58 ± 0.16 E+12 kg. Finally, we put forward three future hazard scenarios that could affect the population in the proximal area (>70 k people): (1) an unrest period involving increased seismic events, volcanic gas emissions and potentially small phreatic explosions, (2) the effusive and/or slightly explosive growth and destruction of lava domes accompanied by block-and-ash flows and tephra fall, and (3) large explosive events (VEI ~4) that generate regional tephra fall and massive pyroclastic density currents.

1. Introduction

The Pululahua dome complex is located in the Western Cordillera of the Ecuadorian Andes (0.044° N, 78.48° W), 5 km north of the equator and 15 km north of the capital, Quito (Fig. 1a). It is considered one of twenty potentially active volcanoes in Ecuador (Hall et al., 2008), with its last eruption having occurred in the late Holocene (Hall and Mothes, 1994). The Pululahua complex is made up of at least sixteen lava domes, of which eleven are located around and five within a 13 km^2 sub-rectangular depression (Fig. 1b). The flanks of the domes dipping towards the depression are very steep to the NE, E and S, while the depression shows a breaching towards the northwest through which the Blanco river drains it (Figs. 1 and 2). The bottom of the depression lies at an altitude of 2400 m above sea level (masl), and Pululahua's highest peak (Sincholahua dome) reaches up to 3356 masl. The village of Pululahua, located on the flat depression floor, is inhabited by ~50 families who use it as agricultural land or for touristic purposes, including various hostels and a number of holiday and weekend cottages. Moreover, highly populated towns (>70 k people) such as San Antonio and Calacalí reach up to Pululahua's southern flank (Fig. 1b).

The few studies undertaken at Pululahua over the last three decades have focused on specific aspects of this dome complex. For instance, Papale and Rosi (1993), Pallini (1996) and Volentik et al. (2010) studied a Plinian tephra fall eruption which took place around 2.4 ka under weak to no-wind conditions. Papale and Rosi (1993) found a volume of 0.75 km^3, a mass discharge rate (MDR) of 2 E+8 kg/s and a Plinian column of 28–36 km height. In contrast, Pallini (1996) proposed 0.58 km^3 and 2-3 E+8 kg/s MDR for the same deposit, while Volentik et al. (2010) calculated a volume of 0.5 ± 0.15 km^3, a column height of 30 ± 3 km and an eruption duration of 72 ± 47 min for the same tephra layer. In all cases, the results indicate that it corresponds to a VEI 4 eruption (Newhall and Self, 1982). In addition, Petriello (2007) proposed some

* Corresponding author.
E-mail addresses: anaisvasconez@gmail.com, a.vasconez.2019@bristol.ac.uk (A.V. Müller).

https://doi.org/10.1016/j.jsames.2020.103046
Received 30 July 2020; Received in revised form 11 November 2020; Accepted 16 November 2020

REPORT VOLCANICA

Instituto Geofísico – Escuela Politécnica Nacional, the Ecuadorian Seismology and Volcanology Service

Patricio Ramón*, Silvia Vallejo*, Patricia Mothes, Daniel Andrade, Francisco J. Vásconez, Hugo Yepes, Silvana Hidalgo, Santiago Santamaría
Instituto Geofísico de la Escuela Politécnica Nacional, Quito, Ecuador.

Abstract

Ninety-eight Quaternary volcanoes have been identified in the Ecuadorian Andes and the Galápagos Islands, from them, nine experienced at least one eruption in the last twenty years. Additionally, about 35 % of the Ecuadorian population live in areas that could be affected by future volcanic eruptions. The *Instituto Geofísico of the Escuela Politécnica Nacional* (IG-EPN) monitors and evaluates Ecuador's volcanic hazards: nineteen volcanic hazard maps and hundreds of related articles have been published as a result of its research. The monitoring networks include eighteen volcanoes, with more than 266 stations, which also form the basis for early warning systems at several volcanoes. Volcanic activity is widely communicated by the IG-EPN through periodic information published in different media (website and social networks). Ecuadorian volcanoes will erupt in the future and, therefore, the IG-EPN continuously updates its monitoring and hazard assessment practices and improves communication channels and protocols to successfully fulfil its responsibilities.

Este artículo está disponible en español: https://doi.org/10.30909/vol.04.S1.93112 [PDF ES].

1 Introduction

Ecuador is divided into four physiographical regions: Coast, Mountain Range, Amazon and the Galápagos Islands, and 98 volcanoes are distributed in the last three regions (Figure 1). The origin of volcanism in Ecuador is subject to the subduction of the Nazca plate underneath the South American plate, which produces the continental Northern Andean Volcanic Zone (NVZ) and to the presence of a hot spot south of the Galápagos Spreading Center that gives rise to intense volcanism of the Galápagos archipelago (Figure 1). Since 1983 volcanoes have been monitored in Ecuador, and in this time volcanic eruptions have occurred from both sources: on the mainland, Guagua Pichincha (1999–2001), Tungurahua (1999–2016), Reventador (2002–present), Cotopaxi (2015), and Sangay (continuous) volcanoes; and along the Galápagos Archipelago, Sierra Negra (2005, 2018), Fernandina (1984, 1988, 1991, 1995, 2005, 2009, 2017, 2018, 2019, 2020), Cerro Azul (1998, 2008), and Wolf (2015) volcanoes. Based on the statistical database of the *Instituto Nacional de Estadística y Censos* from 2010 [INEC 2010], at least 35 % of the Ecuadorian population settle in these regions and could be subject to the impacts of volcanic activity.

In this work, we present an overview of the volcanism of Ecuador, as well as the different techniques that the *Instituto Geofísico de la Escuela Politécnica Nacional* (IG-EPN), the institute in charge of monitoring and evaluation of volcanic hazards, applies for the daily monitoring of volcanoes on both the mainland and the Galápagos Islands. We also outline the hazard management that the IG-EPN scientists and technicians carry out together with authorities, and with communities principally.

1.1 Volcanic activity in Ecuador

Volcanoes in Ecuador are classified based on their last eruptive activity as:

1. Extinct or dormant: if their last eruption occurred during the Pleistocene.
2. Active: for volcanoes that last erupted during the Holocene. This includes volcanoes that erupted during historical time (since 1532, time of the Spanish Conquest).
3. In Eruption: for volcanoes that are currently erupting or had an eruption within the last two years (i.e. 2018–2020).

On the mainland, 76 volcanic centers have been identified (Figure 1A), 52 of them are extinct, 24 are active and 2 of them are currently in eruption (i.e., Reventador and Sangay). Offshore, the Galápagos Islands host 22 volcanoes distributed over the Archipelago (Figure 1B): the youngest volcanoes are located at the western islands, and the oldest at the eastern islands [Allan and Simkin 2000], 12 of these volcanoes are extinct, 10 are active and 2 of them had an eruption within the last two years (i.e., Fernandina and Sierra Negra) [Santamaria and Bernard 2018; Vásconez et al. 2018].

*Corresponding authors:
pramon@igepn.edu.ec; svallejo@igepn.edu.ec

8th International Symposium
on Andean Geodynamics
(ISAG)

New groundmass K-Ar ages of Iliniza Volcano, Ecuador

S. Santamaria[1, 2], X. Quidelleur[1], S. Hidalgo[2], P. Samaniego[3] J.L. Le Pennec[3]

[1]GEOPS, Université Paris-Sud, CNRS, Université Paris-Saclay, Rue du Belvédère, Bât. 504, 91405 Orsay, France
[2]Instituto Geofísico, Escuela Politécnica Nacional, Ap. 17-01-2759, Quito, Ecuador
[3]Laboratoire Magmas et Volcans, Université Clermont Auvergne - CNRS - IRD, 6 Avenue Blaise Pascal, 63178 Aubière, France

Previous studies demonstrated the existence of a marked temporal geochemical variation of several long-lived volcanoes of the Ecuadorian arc (e.g. Cayambe, Mojanda-Fuya Fuya, Pichincha, Atacazo-Ninahuilca), that includes an evolution from typical calk-alcaline arc magmas present at the older edifices to adakite-like compositions in the younger edifices. Two non-exclusive models have been proposed to explain such a systematic evolution, including a progressive change of the nature of the subduction component, and/or a change in the modalities of the magmatic differentiation in the crust. The purpose of this study is to constrain the temporal evolution of Iliniza volcano, an eruptive center located in the volcanic front of the Ecuadorian arc and that also shows these geochemical signature. Iliniza is a twin-peaked composed volcano, comprising two main edifices: North and South Iliniza, and two satellite domes: Pilongo and Tishigcuchi. The whole volcano is located closely to the west of the eroded Santa Cruz volcano , partially covering its western flank. On the basis of the previous work of Hidalgo et al. (2007), we collected several rock samples from Santa Cruz volcano and the main geological units of Iliniza volcano for petrology, geochemistry and dating using the K-Ar Cassignol-Gillot technique performed on groundmass. The preliminary ages obtained show that Santa Cruz volcano was active at about 700 ka, which represents an older bound for Iliniza volcano. The older age from Iliniza volcano corresponds to Pilongo dome, which is located on its northern flank and yields an age around 350 ka. Stratigraphic relationships suggesting that Iliniza began its construction with the North Iliniza edifice are supported by our dating results, which indicate an age around 125 ka. For South Iliniza edifice, we obtained ages between 50 and 25 ka, this suggests that construction of the North Iliniza edifice should have finished earlier than 50 ka. The last phase of Iliniza eruptive activity corresponds to the Tishigcuchi dome emplaced over the southern flank of South Iliniza. Since the F-rhyolite series fallout deposits from Cotopaxi volcano (13-5.9 ka; Hall and Mothes, 2008) cover the entire volcano, Tishigcuchi's activity must have occurred before 13 ka. Based on morphology, it is even possible that the activity of South Iliniza edifice could have been extended until this last date. Coupling these new ages with the geochemical data we found that the geochemical change occurred in Iliniza volcano almost at the same time period compared to other long-lived volcanic centers. Finally, the numerical reconstructions of Iliniza's main morphologies allowed the calculation of their construction and quiescent erosion rates providing a detailed view of this volcano and enable comparison with other volcanic centers from Ecuadorian Arc.

Hall, M., & Mothes, P. (2008). The rhyolitic–andesitic eruptive history of Cotopaxi volcano, Ecuador. Bulletin of Volcanology, 70(6), 675-702.
Hidalgo, S., Monzier, M., Martin, H., … & Cotten, J. (2007). Adakitic magmas in the Ecuadorian volcanic front: petrogenesis of the Iliniza volcanic complex (Ecuador). Journal of Volcanology and Geothermal Research, 159(4), 366-392.

université PARIS-SACLAY

ÉCOLE DOCTORALE
Sciences mécaniques et énergétiques, matériaux et géosciences (SMEMAG)

Titre : Reconstruction de l'histoire éruptive des volcans du centre de l'arc équatorien : contraintes pour l'évolution spatio-temporelle du volcanisme andin et pour l'évaluation du risque associé

Mots clés : Géochronologie, Volcanologie, Équateur, Géochimie, Tectonique, Andes

Résumé : L'arc équatorien est composé d'au moins 77 volcans Quaternaire. Malgré les multiples études conduites au cours des dernières décennies, l'histoire éruptive de plusieurs de ces volcans reste inconnue. Pour contraindre l'histoire éruptive de l'ensemble de l'arc, et en particulier de son segment central, nous avons acquis 50 nouveaux âges K-Ar appartenant à 15 volcans de cette région. Nous avons d'abord effectué une étude détaillée de l'Iliniza, un volcan non daté avec des indices morphologiques d'une activité Holocène. Nos âges K-Ar, combinés avec de nouvelles données stratigraphiques, ont montré qu'Iliniza a été formé par la superposition de deux stratovolcans construits depuis ~125 ka. Ils ont également confirmé une activité holocène de ce volcan à ~6 ka. L'histoire éruptive de l'Iliniza comprend un événement hautement explosif (VEI 5) qui s'est produit à ~35 ka. A l'échelle régionale, nos résultats ont été intégrés dans la base de données EVEG, qui inclue une centaine d'âges K-Ar, également acquis au laboratoire GEOPS pour d'autres segments de l'arc. L'ensemble des données nous a permis de démontrer que le volcanisme du Quaternaire en Équateur s'est développé en trois stades. Le premier stade s'est produit entre ~2.4 et ~1.4 Ma en étant essentiellement concentré dans le segment central. Il a été suivi d'une augmentation modérée de l'activité au Nord et au Sud de segment central, entre ~1.4 et ~0.6 Ma. Une expansion rapide du volcanisme dans tout l'arc équatorien a commencé à ~0.6 Ma avec la présence de plus de 50 volcans actifs au cours de ce dernier stade. Enfin, nous proposons différentes hypothèses sur la relation entre le volcanisme et le contexte géodynamique de l'Équateur.

Title: Reconstruction of the eruptive history of central Ecuador volcanoes: constraints on the spatio-temporal evolution of the Andean volcanism and for the assessment of associated hazards

Keywords: Geochronology, Volcanology, Ecuador, Geochemistry, Tectonics, Andes

Abstract: The Ecuadorian arc is composed of at least 77 Quaternary volcanoes. Despite the multiple studies carried out in the last two decades, the timing of development of many of these volcanoes remain unclear. In order to constrain the eruptive history of the whole volcanic arc, with emphasis on its central segment, we have acquired 50 new K-Ar ages belonging to 15 volcanoes from this region. First, a detailed study was conducted for Iliniza, an undated volcano with morphological evidence of Holocene activity. Our K-Ar ages, together with new stratigraphic data, showed that Iliniza was formed by the superposition of two stratovolcanoes built since ~125 ka, and confirmed a Holocene activity at ~6 ka. The Iliniza eruptive history included a high explosive event (VEI 5) at ~35 ka. For a regional scope, our results were integrated in the EVEG database, including ~100 K-Ar ages also acquired at the GEOPS laboratory for other segments. The complete data demonstrated that Quaternary volcanism in Ecuador developed in three stages. The early stage, occurred at ~2.4 to ~1.4 Ma, was mostly concentrated in the central segment. It was followed by a moderate, both northward and southward, increase in activity between ~1.4 and ~0.6 Ma. The rapid expansion of volcanism throughout the arc began at ~0.6 Ma when more than 50 volcanoes were active. Finally, we offer different hypotheses regarding the relationship between volcanism and the geodynamic setting of Ecuador.

Maison du doctorat de l'Université Paris-Saclay
2ème étage aile ouest, Ecole normale supérieure Paris-Saclay
4 avenue des Sciences,
91190 Gif sur Yvette, France